

University of Nottingham
UK | CHINA | MALAYSIA

Faculty of Engineering – Department of Civil Engineering

A MULTIPLE ALGORITHM APPROACH TO THE ANALYSIS OF GNSS TIME SERIES FOR DETECTING ANOMALOUS BEHAVIOURS, GEOHAZARDS AND METEOROLOGICAL EVENTS

By

MOHAMMED HABBOUB

Thesis submitted to the University of Nottingham for the degree of Doctor of Philosophy

January, 2019

ABSTRACT

In this study, a multiple algorithm approach to the analysis of GNSS time series for detecting anomalous behaviours, geohazards and meteorological events is proposed. This multiple algorithm approach includes the novel use of temporal analysis, spatial analysis and a combined (temporal and spatial) analysis. The main concept of this approach is to first model the normal and expected behaviour of the temporal and spatial dependencies of initial GNSS time series. Then, to assess the differences between the modelled temporal and spatial dependencies and new GNSS time series. More specifically, in the temporal analysis algorithm, an Artificial Neural Network is used to extract the temporal dependency of the GNSS station coordinate or troposphere time series. On the other hand, the spatial autoregressive model is used for the spatial analysis algorithm, assuming that the GNSS coordinate or troposphere time series from a network of stations are spatially dependent. Finally, for the combined analysis algorithm, the two above methods of the temporal and the spatial analysis algorithms are adjusted and combined. This multiple algorithm approach was examined using: (i) the long-term, daily GPS coordinate time series of the BIGF network of stations in the British Isles; (ii) the 1Hz GPS coordinate time series of the GEONET stations in Japan for the Tohoku-Oki 2011 Mw9.0 earthquake; (iii) the long-term, hourly GPS troposphere time series of the BIGF network of stations in the British Isles. It was demonstrated in these case studies that the temporal analysis algorithm proved to be effective in detecting rapid changes in GNSS time series of varying magnitudes. These changes can be site-specific (e.g. an offset) or of a large scale (e.g. an earthquake or a meteorological event). On the other hand, the spatial analysis algorithm is more suitable for spatially uncorrelated, slow-paced and small magnitude changes in GNSS time series, while the combined analysis algorithm seems to be less beneficial in the detection of anomalous behaviours, but may be useful to diagnose and clarify the reasons that lead to the detected anomalous behaviours. The research suggests that the multiple algorithm approach could be very useful in supporting the operation of existing GNSS networks and in the analysis of GNSS coordinate and troposphere time series.

DEDICATION

This research is lovingly dedicated to my parents who dealt with my absence with a smile. Their support, encouragement and unconditional love have been what sustains me through my life.

ACKNOWLEDGEMENTS

I want to express my sincere gratitude to my supervisors Dr Panos Psimoulis and Dr Richard Bingley for their support, patience, guidance and motivation throughout my Master and PhD degrees. Their helpful comments, insights, and proofreading remarks are highly appreciated. I have been extremely lucky to have supervisors who genuinely cared about my work, and who responded to my questions and queries so promptly.

Besides my supervisors, I also would like to thank Dr Chris Hill for his insightful suggestions obtained during the 1st and 2nd year assessments. Moreover, I want to thank him and Dr Nigel Penna in advance for assessing this thesis.

My genuine thanks also go to the University of Nottingham which has funded this research through the Dean of Engineering Research Scholarship for International Excellence. The services of the British Isles continuous GNSS Facility (BIGF), funded by the Natural Environment Research Council (NERC) and the United Kingdom Research and Innovation (UKRI), in providing archived GNSS products to this study; the Met Office Integrated Data Archive System (MIDAS UK) and the British Atmospheric Data Centre (BADC) are also gratefully acknowledged.

Last but not the least, I would like to thank my parents and my sisters for being in my life.

DECLARATION

The research described in this thesis was conducted in the Nottingham Geospatial Institute and Department of Civil Engineering at the University of Nottingham between October 2015 and Jan 2019. I declare that the work is my own and has not been submitted for a degree of another university.

Mohammed Habboub

January 2019

TABLE OF CONTENTS

ABSTRACT ..... **i**
DEDICATION ..... **ii**
ACKNOWLEDGEMENTS ..... **iii**
DECLARATION ..... **iv**
TABLE OF CONTENTS ..... **v**
LIST OF FIGURES ..... **viii**
LIST OF TABLES ..... **xvii**
LIST OF ABBREVIATIONS ..... **xviii**
1 CHAPTER 1: INTRODUCTION **1**
1.1 Research motivation 1
1.2 Research aim and objectives 2
1.3 Research significance and contributions 4
1.4 Thesis structure and outline 5
1.5 Publications list 6
2 Chapter 2: GNSS TIME SERIES IN NETWORK MONITORING APPLICATIONS **8**
2.1 GNSS Time Series in Monitoring and Early Warning (EW) Systems 8
2.2 GNSS Time Series in Tectonic Plate Movement and Vertical Land Movement Studies 9
2.3 GNSS Time Series in Earthquake Studies 14
2.4 GNSS Time Series in Tropospheric Integrated Water Vapour Studies 19
2.5 Summary 22
3 CHAPTER 3: TEMPORAL DEPENDENCY IN GNSS TIME SERIES **23**
3.1 Modelling the Temporal Dependency 23
3.1.1 Parametric Models 24
3.1.2 Non-parametric Models 27
3.2 Temporal Analysis of GNSS Time Series 34
3.2.1 Linear Trend Estimation in Long-Term GNSS Time Series 35
3.2.2 Offset Estimation and Detection in Long-Term GNSS Time Series 38
3.3 Summary 41
4 CHAPTER 4: SPATIAL DEPENDENCY **43**
4.1 Modelling the Spatial Dependency 43
4.1.1 Spatial Interpolation Models 44
4.1.2 Spatial Autocorrelation Indices 46
4.1.3 Spatial Regression Models 47
4.2 Spatial Analysis of GNSS Time Series 49
4.3 Summary 53
5 CHAPTER 5: THE DEVELOPMENT OF A MULTIPLE ALGORITHM APPROACH TO THE ANALYSIS OF GNSS TIME SERIES **54**
5.1 The Concept of the Multiple Algorithm Approach 54

5.2 Data Segmentation 56
5.3 Correction of Offsets due to Documented Changes 58
5.3.1 The 1st Offset Correction Approach 58
5.3.2 The 2nd Offset Correction Approach 59
5.3.3 Validation of the 2nd step of the algorithm. 60
5.4 Estimation of the Main Characteristics of the Training Dataset 60
5.5 Application of the Multiple Algorithm Approach on the Training Dataset 62
5.5.1 The Temporal Analysis Algorithm 62
5.5.2 The Spatial Analysis Algorithm 65
5.5.3 The Combined Analysis Algorithm 67
5.6 Application of the Multiple Algorithm Approach on the Testing Dataset 68
5.7 Summary 72
6 CHAPTER 6: THE ANALYSIS OF THE LONG-TERM, DAILY GPS COORDINATE TIME SERIES OF THE BIGF NETWORK OF STATIONS IN THE BRITISH ISLES. ... 73
6.1 Network and Datasets 73
6.2 Results 75
6.2.1 Offset correction approaches 75
6.2.2 The Multiple analysis algorithm approach 87
6.3 Analysis 90
6.3.1 Offset correction approaches 90
6.3.2 The performance of the multiple analysis algorithm approach 92
6.3.3 A classification of the anomalous behaviours in the GPS coordinate time series of the BIGF network 96
6.4 Discussion 113
6.5 Summary 118
7 CHAPTER 7: THE ANALYSIS OF THE 1Hz GPS COORDINATE TIME SERIES OF THE GEONET STATIONS IN JAPAN FOR THE TOHOKU-OKI 2011 MW9.0 EARTHQUAKE 119
7.1 Network and Data 119
7.2 Analysis 122
7.3 Results 125
7.4 Discussion 131
7.4.1 The temporal analysis algorithm 131
7.4.2 The spatial analysis algorithm 132
7.4.3 The combined analysis algorithm 133
7.5 Summary 135
8 CHAPTER 8: THE ANALYSIS OF THE LONG-TERM, HOURLY GPS TROPOSPHERE TIME SERIES OF THE BIGF NETWORK OF STATIONS IN THE BRITISH ISLES. . 136
8.1 Datasets 136
8.2 Data processing 138
8.3 Results 140
8.3.1 The multiple algorithm approach residuals thresholds 140

8.3.2 The multiple algorithm approach in the detection of meteorological events 143
8.4 Discussion 143
8.4.1 Example#1 144
8.4.2 Example#2 160
8.5 Summary 171
9 CHAPTER 9: CONCLUSIONS AND RECOMMENDATIONS. 173
9.1 Conclusions 173
9.2 Recommendations for further research 178
References 179
APPENDIX A 208
Validation of the 2nd step of the algorithm. 208
APPENDIX B 220
NAR-ANN evaluation 220
APPENDIX C 223
The analysis of the long-term, daily GNSS coordinate time series of the BIGF network in the British Isles 223
APPENDIX D 311
The days on which meteorological events were detected by the multiple algorithm approach. 311
Example 1: Stations considered as having meteorological events using different cut-off frequencies. 321
Example 2: Stations considered as having meteorological events using different cut-off frequencies 347

LIST OF FIGURES

Figure 1-1 Amplitude versus duration diagram presenting where the three case studies fit alongside various geohazards 4

Figure 2-1 ITRF2008 horizontal station velocities with formal error less than 0.2mm/yr. 10

Figure 2-2 The estimates of velocity fields in central Japan using the improved time series data (red lines) and the original ones (black lines) in the different time periods. 13

Figure 2-3 Strain rate comparison in the time domain. 16

Figure 2-4 Locations where permanent GPS stations are used along with EEW 16

Figure 2-5 a)The first 15 seconds of the acceleration record of MYG011 strong-motion site for the Mw9.0 Tohoku 2011 earthquake and b) the computed corresponding STA/LTA ratio with the threshold for the detection of first seismic wave arrival..... 19

Figure 2-6 Comparisons between GPS, radiosonde and United Kingdom Met Office (UKMO) model of IWV estimates and forecast. 20

Figure 2-7 The discretisation of GPS DD observations from GPS satellites (x & y) to stations (a & b) through finite ellipsoidal voxel grids 21

Figure 3-1 Representation of the procedure of (a) the training stage and (b) the prediction stage of NAR-ANN. 31

Figure 3-2 Comparison of the simulation results (a) Back-Propagation Neural Network (BPN); (b) Cascade- Forward Back-Propagation Neural Network (CFN); (c) Adaptive Filter Neural Network (ADFN); (d) Extended Kalman Filter Neural Network (EKFN) 33

Figure 3-3: Velocity bias from an annual sinusoidal signal versus data span showing the maximum possible bias (max) and root mean square bias (RMS). 36

Figure 3-4: A graphical representation of white, flicker/pink, and random walk noises on the frequency spectrum using a log-log scale..... 37

Figure 3-5 SOPAC offsets (a) description and (b) magnitude distribution since 1995 for over 340 sites (560 offsets)..... 39

Figure 3-6 A simulated GPS daily coordinate time series. The vertical dashed black lines show dates of simulated offsets. 41
Figure 4-1 The distance and spatial weight matrix of 4 stations located on a line with a 1km distance in between each location 44
Figure 4-2 The ΔN time series for 7 stations before (up) and after (bottom) removing the CME using the weighted stacking method. 50
Figure 4-3 The analysed network consisted of 88 permanent stations unevenly distributed all over Europe and adjacent areas. 51
Figure 4-4 (a) The raw time series of the ΔE component in mm (light blue) and its spectral analysis (grey) (b) the spatially correlated term CME (light blue) and its spectral analysis (green) ; (c) the filtered residual time series after the subtraction of CME contributions (light blue) and its spectral analysis (red).. 52
Figure 5-1 A flowchart of the five main steps used in the proposed multiple algorithm approach 56
Figure 5-2 The GPS coordinate time series of SHOB station (ΔE component). Where the blue-dashed line represents the end of the training dataset and the magenta-dashed line shows the epoch of a documented change. 58
Figure 5-3 Flowcharts showing (a) the 1st offset and (b) the 2nd offset correction approaches. Dotted lines represent information extracted from the training dataset and used in the testing dataset. 60
Figure 5-4 Spectrum analysis using DFT with the determined cut-off frequency (red arrow), which separates the white noise (yellow-dashed line), represented by a flat spectral, from the rest of the signal (green dashed line) 61
Figure 5-5 The detrended time series (black) and low-frequency time series (red) for the training dataset related to the GPS coordinate time series of SHOB station (ΔE component). 62
Figure 5-6 The low-frequency time series (black) and its predicted values using NAR-ANN (red) for the training dataset related to the GPS coordinate time series of SHOB station (ΔE component). 64

Figure 5-7 The temporal analysis residuals time series (black) and its corresponding thresholds (red) for the training dataset related to the GPS coordinate time series of SHOB station (ΔE component).. 65
Figure 5-8 (a) The low-frequency time series (black) and its estimated values using the SAR model (red) along with (b) the spatial analysis residuals time series (black)_and its corresponding thresholds (red). 66
Figure 5-9 (a) The temporal analysis residuals time series (black) and its estimated values using the SAR model (red) along with (b) the combined analysis residuals and their corresponding thresholds. 67
Figure 5-10 The third, fourth and fifth steps of the (a) temporal, (b) spatial, and (c) combined analysis algorithms. Dotted lines represent information extracted from the training dataset and used in the testing dataset. 70
Figure 5-11 (a) the 'corrected' time series, (b) the detrended and low-frequency time series, (c) the low-frequency time series and it is predicted values using NAR-ANN, (d) the temporal analysis residuals time series and its corresponding thresholds, (e) the low-frequency time series and its estimated values using the SAR model, (f) the spatial analysis residuals time series and its corresponding thresholds, (g) the temporal analysis residuals and its estimated values using the SAR model, and (h) the combined analysis residuals time series and its corresponding thresholds, related to the GPS coordinate time series of SHOB station (ΔE component). Where the blue-dashed line represents the end of the training dataset and the magenta-dashed line shows the epoch of a documented change. 71
Figure 6-1 Selected stations of the British Isles continuous GNSS Facility 75
Figure 6-2 Stations which have significant or insignificant differences in their offset (left semicircle) and linear trend estimates (right semicircle) from the 1st and 2nd offset correction approaches, in their: (a) ΔN; (b) ΔE; and (c) ΔU components. 84
Figure 6-3 Horizontal station velocities derived from (a) the 1st (orange) and 2nd (blue) offset correction approaches, and (b) the differences between these velocity estimates and their uncertainties. 85

Figure 6-4 Vertical station velocities derived from: (a) the 1st offset correction approach; (b) the 2nd offset correction approach, and(c) the difference between these velocity estimates. 86
Figure 6-5 The detrended time series of SHOB station (ΔE) using the 1st (red) and the 2nd (black) offsets correction approaches. 90
Figure 6-6 The residuals thresholds of the (a) temporal, (b) spatial and (c) combined analysis of the ΔN component, (d) temporal, (e) spatial and (f) combined analysis of the ΔE component and (g) temporal, (h) spatial and (i) combined analysis of the ΔU components using the 2nd offset correction approach. 93
Figure 6-7 The percentage differences between the temporal and combined analysis residuals thresholds for (a) ΔN, (b) ΔE and (c) ΔU components. 94
Figure 6-8 TEDD Station (ΔN) – (a) Corrected displacement time series, (b) detrended and low-frequency time series, the (c) Temporal, (d) Spatial and (e) combined analysis residuals with their corresponding thresholds 95
Figure 6-9 The detrended ΔN component of TEDD station along with its five closest stations which are spatially weighted (on the right) according to their in-between Euclidian distance, alongside with detected anomalies using the temporal (blue), spatial (red) and combined (green) analysis algorithms. 96
Figure 6-10 The same as Figure 6-8, for HERT Station (ΔN component) using the 2nd offset correction approach 98
Figure 6-11 The same as Figure 6-8, for CLAW station (ΔN component) using the 2nd offset correction approach. 100
Figure 6-12 The same as Figure 6-8, for KEYW station (ΔN component) using the 2nd offset correction approach. 100
Figure 6-13 The same as Figure 6-8, for DUNG station (ΔE component) using the 2nd offset correction approach. 101
Figure 6-14 The same as Figure 6-8, for FARB station (ΔE component) using the 2nd offset correction approach. 101

Figure 6-15 The same as Figure 6-8, for HOOB station (ΔE component) using the 2nd offset correction approach. 102
Figure 6-16 The same as Figure 6-8, for KELO station (ΔE component) using the 2nd offset correction approach. 102
Figure 6-17 The same as Figure 67, for KING station (ΔE component) using the 2nd offset correction approach. 103
Figure 6-18 The same as Figure 6-8, for NCAS station (ΔE component) using the 2nd offset correction approach. 103
Figure 6-19 The same as Figure 6-8, for POOL station (ΔE component) using the 2nd offset correction approach. 104
Figure 6-20 The same as Figure 6-8, for SABB station (ΔE component) using the 2nd offset correction approach. 105
Figure 6-21 The same as Figure 6-8, for SWTG station (ΔE component) using the 2nd offset correction approach. 105
Figure 6-22 The same as Figure 6-8, for ESKD station (ΔU component) using the 2nd offset correction approach. 106
Figure 6-23 The same as Figure 6-22, for HELS station (ΔU component) using the 2nd offset correction approach. 106
Figure 6-24 The same as Figure 6-22, for KELO station (ΔU component) using the 2nd offset correction approach. 107
Figure 6-25 The same as Figure 6-22, for MART station (ΔU component) using the 2nd offset correction approach. 107
Figure 6-26 The same as Figure 6-22, for PBIL station (ΔU component) using the 2nd offset correction 108
Figure 6-27 The same as Figure 6-8, for PBIL station (ΔN component) using the 2nd offset correction approach. 109
Figure 6-28 The same as Figure 6-22, for CAML station (ΔU component) using the 2nd offset correction approach. 110

Figure 6-29 The same as Figure 6-22, for SABB station (ΔU component) using the 2nd offset correction approach. 110
Figure 6-30 The same as Figure 6-8, for ABER Station (ΔN component) using the 2nd offset correction approach. 111
Figure 6-31 The same as Figure 6-8, for ABER Station (ΔE component) using the 2nd offset correction approach. 112
Figure 6-32 the Temporary (black) and On-going (red) anomalous behaviours classification of (a) ΔN (b) ΔE (c) ΔU components of BIGF GNSS network 117
Figure 7-1 The permanent 2D (North and East) displacements at the GEONET stations after the Tohoku-Oki 2011 Mw 9.0 earthquake used in this case study..... 120
Figure 7-2 The permanent 3D displacements for a sample of 14 stations (black points) located next to the earthquake epicentre (red star) and in the middle of the GEONET, arranged from East (i.e. station ID:550) to West (i.e. Station ID:231) showing the variation of the 3D permanent displacements across the network a few minutes before and after the earthquake (red-dashed line). 121
Figure 7-3 A sample of the spectral analysis using DFT for the 14 stations shown in Figure 7-2..... 123
Figure 7-4 Detected arrival time of the seismic motion vs. distance from the earthquake epicentre for the temporal and spatial analysis algorithms when using different distance exponents ($\alpha = 2$ at the left and $\alpha = 3$ at the right), with cap distances of 100km, with a cap distance of 200km and with all stations (i.e. with no cap distance applied), in the GEONET case study. The trend-line expressing the P-wave velocity, commonly assumed approximately equal to a 6km/s. 127
Figure 7-5 Same as Figure 7-4 but for the temporal and combined analysis algorithms. 128
Figure 7-6 Percent difference in the detected arrival time of the seismic motion between the basic algorithm and the spatial, temporal and combined analysis algorithms in the GEONET case study. 129

Figure 7-7 Spatial distribution of the elapsed time of first detection of the geohazard and at which stations (marked by filled circles), as well as the stations with potential events (marked by hollow circles) through a time slice of 5 seconds using the (a) basic algorithm (black), (b) temporal analysis algorithm (blue), (c) spatial analysis algorithm (red), (d) combined analysis algorithm with $\boldsymbol{\alpha = 2}$ (green), (e) combined analysis algorithm with $\boldsymbol{\alpha = 3}$ (green), in the GEONET case study. 130
Figure 8-1 (a) The selected stations of the British Isles continuous GNSS Facility (BIGF) (b) the location of the rain gauges available from the MIDAS dataset. 138
Figure 8-2 A sample of the spectral analysis of IWV using DFT for 9 stations.. 140
Figure 8-3 The summation of the rain gauge readings (blue) and the number of stations (orange) considered as having meteorological events detected by the temporal (a,b), spatial (c,d), and combined (e,f) analysis algorithms, with a cut-off frequency of **0.25 cycle/day**. Grey strips indicate where hourly rain gauges readings exceed 10mm at any of the rain gauges. 145
Figure 8-4 The summation of the rain gauge readings (blue) and the number of stations (orange) considered as having meteorological events detected by the temporal (a,b), spatial (c,d), and combined (e,f) analysis algorithms, with a cut-off frequency of **0.5 cycle/day**. Grey strips indicate where the hourly rain gauge readings exceed 10mm at any of the rain gauges. 146
Figure 8-5 The summation of the rain gauge readings (blue) and the number of stations (orange) considered as having meteorological events detected by the temporal (a,b), spatial (c,d), and combined (e,f) analysis algorithms, with a cut-off frequency of **1 cycle/day**. Grey strips indicate where the hourly rain gauge readings exceed 10mm at any of the rain gauges. 147
Figure 8-6 The IWV time series of 20 stations along with epochs considered as either potential events (hollow) or meteorological events (filled) using the temporal (high IWV: dark blue, and low IWV: light blue), the spatial (high IWV: red, and low IWV: orange), and the combined (high IWV: dark green, and low IWV: light green) analysis algorithms, with **0.25 cycle/day** as a cut off frequency (y-axis grid:25 $kg.m^{-2}$). 150

Figure 8-7 Same as Figure 8-6 but showing the temporal analysis residuals only. 150
Figure 8-8 Same as Figure 8-6 but showing the spatial analysis residuals only..... 151
Figure 8-9 Same as Figure 8-6 but showing the combined algorithm residuals only. .. 151
Figure 8-10 Rain gauge readings (coloured dots) and stations considered as having either potential events (hollow symbols)or meteorological events (filled symbols), with **0.25 cycle/day** as a cut-off frequency. 155
Figure 8-11 Rain gauge readings (coloured dots) and stations considered as having either potential events (hollow symbols) or meteorological events (filled symbols), with **0.5 cycle/day** as a cut-off frequency. 156
Figure 8-12 Rain gauge readings (coloured dots) and stations considered as having either potential events (hollow symbols) or meteorological events (filled symbols), with **1 cycle/day** as a cut-off frequency. 157
Figure 8-13 Same as Figure 8-7 but showing the temporal analysis residuals with **0.5 cycle/day** as a cut-off frequency. 158
Figure 8-14 Same as Figure 8-8 but showing the spatial analysis residuals with **0.5 cycle/day** as a cut-off frequency.. 158
Figure 8-15 Same as Figure 8-7 but showing the temporal analysis residuals with **0.5 cycle/day** as a cut-off frequency. 159
Figure 8-16 Same as Figure 8-8 but showing the spatial analysis residuals with **1 cycle/day** as a cut-off frequency. 159
Figure 8-17 The summation of the rain gauge readings (blue) and the number of stations (orange) considered as having meteorological events detected by the temporal (a,b), spatial (c,d), and combined (e,f) analysis algorithms, with a cut-off frequency of **0.25 cycle/day**. Grey strips indicate where the hourly rain gauge reading exceeds 10mm at any of the rain gauges. 163
Figure 8-18 The summation of the rain gauge readings (blue) and the number of stations (orange) considered as having meteorological events detected by the temporal (a,b), spatial (c,d), and combined (e,f) analysis algorithms, with a cut-off frequency of **0.5**

cycle/day. Grey strips indicate where the hourly rain gauge reading exceeds 10mm at any of the rain gauges. 164
Figure 8-19 The summation of the rain gauge readings (blue) and the number of stations (orange) considered as having meteorological events detected by the temporal (a,b), spatial (c,d), and combined (e,f) analysis algorithms, with a cut-off frequency of **1 cycle/day**. Grey strips indicate where the hourl yrain gauge reading exceeds 10mm at any of the rain gauges. 165
Figure 8-20 The IWV time series of 20 stations along with epochs considered as either potential events(hollow) or meteorological events (filled) using the temporal (high IWV: dark blue, and low IWV: light blue), the spatial (high IWV: red, and low IWV: orange), and the combined (high IWV: dark green, and low IWV: light green) analysis algorithms, with **0.25 cycle/day** as a cut off frequency (y-axis grid:25 $kg.m^{-2}$). 166
Figure 8-21 Same as Figure 8-20 but showing the temporal residuals 166
Figure 8-22 Same as Figure 8-20 but showing the temporal residuals 167
Figure 8-23 Same as Figure 8-20 but showing the temporal residuals 167
Figure 8-24 Rain gauge readings (coloured dots) and stations considered as having either potential events (hollow symbols) or meteorological events (filled symbols), with **0.25 cycle/day** as a cut-off frequency. 168
Figure 8-25 Rain gauge readings (coloured dots) and stations considered as having either potential events (hollow symbols) or meteorological events (filled symbols), with **0.5 cycle/day** as a cut-off frequency. 169
Figure 8-26 Rain gauge readings (coloured dots) and stations considered as having either potential events (hollow symbols) or meteorological events (filled symbols), with **1 cycle/day** as a cut-off frequency. 170
Figure 9-1 Amplitude versus duration diagram presenting where the temporal and spatial analysis algorithms fit alongside the three cases studies. 177

LIST OF TABLES

Table 3-1 Prediction errors using Nonlinear Autoregressive Artificial Neural Network (NAR-ANN), a fuzzy neural network (FNN), or a Kalman filter (KF) 32

Table 4-1 Different spatial regression models based on the Manski (1993) model, and the least squares model 48

Table 6-1 ΔN component offsets (mm) and trends (mm/yr)..... 78

Table 6-2 ΔE component offsets (mm) and trends (mm/yr). 80

Table 6-3 ΔU component offsets (mm) and trends (mm/yr)..... 82

Table 6-4 The residuals threshold values and the number of anomalies for the three components using the temporal (T), spatial (S) and combined (C) analysis algorithms. 88

Table 6-5 The same as Table 6-4, by applying the spatial and temporal analysis algorithms using the 1st offset correction approach. 89

Table 6-6 The percentages of each classification within the BIGF network in the ΔN, ΔE and ΔU components. 113

Table 7-1 Summary of the configurations used in the spatial and combined analysis algorithms. 124

Table 8-1 The temporal (T), spatial (S) and combined (C) residuals thresholds (kg.m-2) using different cut-off frequencies 142

LIST OF ABBREVIATIONS

ADFN	Adaptive Filter Neural Network
ANN	Artificial Neural Network
AR	Autoregressive
ARCH	Autoregressive Conditional Heteroskedasticity
ARFIMA	Autoregressive Fractionally Integrated Moving Average
ARIMA	Autoregressive Integrated Moving Average
ARMA	Autoregressive Moving Average
ARMAX	Autoregressive Moving Average with eXogenous input
ARX	Autoregressive with eXogenous input
BADC	British Atmospheric Data Centre
BIGF	British Isles continuous GNSS Facility
BPN	Back-Propagation Neural Network
BSW	Bernese GNSS software
CATS	Create and Analyse Time Series
CFN	Cascade- Forward Back-Propagation Neural Network
CME	Common-Mode Error
CORS	Continuously Operating Reference Stations
CPU	Central Processing Unit
DD	Double Difference
DFT	Discrete Fourier Transform
DGPS	Differential GPS
EEW	Earthquake Early Warning
EKFN	Extended Kalman Filter Neural Network
EOF	Empirical Orthogonal Function
ETS	Episodic tremor and slip
EW	Early Warning
FNN	Fuzzy neural network
FODITS	Find Outliers and Discontinuities in Time Series
GEONET	GPS Earth Observation NETwork
GIM	Global Ionosphere Map
G-larmS	Geodetic Alarm System
GLONASS	Russian Global Navigation Satellite System
GNSS	Global Navigation Satellite Systems
GPS	Global Positioning System
IGS	International GNSS Service
INS	Inertial Navigation System
InSAR	Interferometric synthetic aperture radar
IQR	InterQuartile Range
ITRF	International Terrestrial Reference Frame
IWD	Inverse Distance Weighting
IWV	Integrated Water Vapour
KF	Kalman Filter
LSTM	Long Short Term Memory

LTA	Long-Term Average
MA	Moving Average
MIDAS	Met Office Integrated Data Archive System
MLE	Maximum Likelihood Estimation
NAR	Non-linear Autoregressive
NAR-ANN	Non-linear AutoRegressive Artificial Neural Network
NERC	Natural Environment Research Council
NEU	North, East and Up
NMA	Non-linear Moving Average
NNR	No-Net Rotation
MORVEL	Mid-Ocean Rigid Velocity
NUVEL	Northwest University Velocity
OLS	Ordinary Least-Squares
OSGB	Ordnance Survey of Great Britain
PCA	Principal Component Analysis
PPP	Precise Point Positioning
PW	Precipitable Water (PW)
REVEL	REcent plate VELocities
RINEX	Receiver INdependent EXchange
RMS	Root-Mean-Square
SAR	Spatial AutoRegressive
SINEX	Solution INdependent EXchange
SLR	Satellite Laser Ranging
SOPAC	Scripps Orbit and Permanent Array Center
STA	Short-Term Average
STARS	Sequential t-test Analysis of Regime Shifts
UK	United Kingdom
UKMO	United Kingdom Met Office
UTC	Coordinated Universal Time
VLBI	Very Long Baseline Interferometry
VTEC	Vertical Total Electron Content
WRMS	Weighted Root-Mean-Square
WSF	Weighted Spatial Filtering
ZHD	Zenith Hydrostatic Delay
ZTD	Zenith Total Delay
ZWD	Zenith Wet Delay

CHAPTER 1: INTRODUCTION

In this chapter, a brief background to the research topic and the research motivation are presented in section 1.1. Then, the research aim and objectives are given in section 1.2. After that, the research significance and contribution to knowledge is discussed in section 1.3. Finally, a general overview of the thesis structure is shown in section 1.4.

1.1 Research motivation

The use of networks of continuous GNSS stations to monitor geophysical and meteorological phenomena has been very popular in recent years (Allen and Kanamori 2003; Matsumura et al. 2011; Galvan et al. 2012; Colombelli et al. 2013; Melgar et al. 2015), as they can provide accurate and precise estimates of station coordinates and troposphere parameters, and significant variations in these can be used to indicate a geohazard related to crustal/land movements or meteorological events. However, the operation of these networks requires a rapid analysis and interpretation of the collected data, particularly to distinguish between variations in station coordinates caused by real movements of a station and those which represent anomalous behaviours, and to distinguish between site-specific anomalies and large-scale events (e.g. geohazards; Bock and Melgar 2016).

The literature shows that the majority of studies have tended to analyse the GNSS coordinate time series of each station individually (i.e. station by station) for the purpose of: (i) estimating linear trends (Santamaría-Gómez et al. 2011; Serpelloni et al. 2013; Griffiths and Ray 2016), (ii) estimating periodic signals (Penna et al. 2007; Davis et al. 2012; Amiri-Simkooei 2013; Chen et al. 2013), (iii) noise characterisation (Williams 2003a; Amiri-Simkooei et al. 2007; Amiri-Simkooei 2009; Montillet et al. 2013), and (iv) offset detection and correction (Williams 2003b; Gazeaux et al. 2013; Bruni et al. 2014; Montillet et al. 2015). Many GNSS coordinate time series analysis software packages have been developed, well tested and documented (e.g. Create and Analyse Time Series

software, CATS (Williams 2008), Hector (Bos et al. 2013) and est-noise (Langbein 2008)) for these purposes.

However, the majority of these studies do not consider the spatial correlation between the stations in the analysis process except for removing the common-mode error (CME) (Nikolaidis 2002; Gruszczynski et al. 2015; Tian and Shen 2016), while in some other cases, some spatial capabilities have been added to the time series analysis, but these spatial capabilities were limited to presentation purposes (Grapenthin and Freymueller 2011), spatial checking and filtering false alarms and outliers (Psimoulis et al. 2018b), or assessing the change in the relative displacement between stations (Crowell et al. 2009).

1.2 Research aim and objectives

The aim of this research is to develop a multiple algorithm approach to the analysis of GNSS time series for detecting anomalous behaviours, geohazards and meteorological events. The multiple algorithm approach is based on spatial analysis, temporal analysis and combined (temporal and spatial) analysis, which were used to develop three algorithms. The main concept of this approach is to first model the normal and expected behaviour of the temporal and spatial dependencies of initial GNSS time series. Then, to assess the differences between the modelled temporal and spatial dependencies and new GNSS time series for the purpose of detecting anomalies related to anomalous behaviours, geohazards and meteorological events.

More specifically, in the temporal analysis algorithm, an Artificial Neural Network is used to extract the temporal dependency of the GNSS station coordinate or troposphere time series; therefore, any station that behaves differently to the model created based on its historical record will be considered as having anomalies. On the other hand, the spatial autoregressive model is used for the spatial analysis algorithm, assuming that the GNSS coordinate or troposphere time series from a network of stations are spatially dependent; consequently, any station that behaves differently to its surrounding stations will be considered as having anomalies. Finally, for the combined analysis algorithm, the two

above methods of the temporal and the spatial analysis algorithms are adjusted and combined.

To evaluate the multiple algorithm approach, it was applied in three different case studies. The case studies were chosen to cover different aspects; the size of the network (e.g. small vs large networks), the length of the time series (e.g. long-term vs short-term time series) and the temporal resolution of the time series (daily vs 1Hz time series), as well as the dynamics (e.g. high-frequency vs low-frequency), the size (large vs small) and the type (spatially correlated vs site-specific) of the chosen phenomena (Figure 1-1). The three different case studies are:

- **The first case study** which is based on the analysis of the long-term, daily GPS coordinate time series of the BIGF network of stations in the British Isles, and was seen as a relatively small network (<100 stations) with long-term (>5 years) daily time series. The anomalies which were expected to be monitored would be of a small and site-specific phenomenon (e.g. any anomalous behaviours in the time series).
- **The second case study** which is based on the analysis of the 1Hz GPS coordinate time series of the GEONET stations in Japan for the Tohoku-Oki 2011 MW9.0 Earthquake, and was seen as a relatively large network (>800 stations) with short-term (<1 day), 1Hz time series with a large and spatially correlated phenomenon to be monitored (e.g. the Tohoku-Oki 2011 M_W9.0 earthquake).
- **The third case study** which is based on the analysis of the long-term hourly GPS troposphere time series of the BIGF network of stations in the British Isles, and was seen as a challenge to examine the performance of the approach on a totally different dataset that is not directly related to crustal/land movements and its ability to detect meteorological events (e.g. rain).

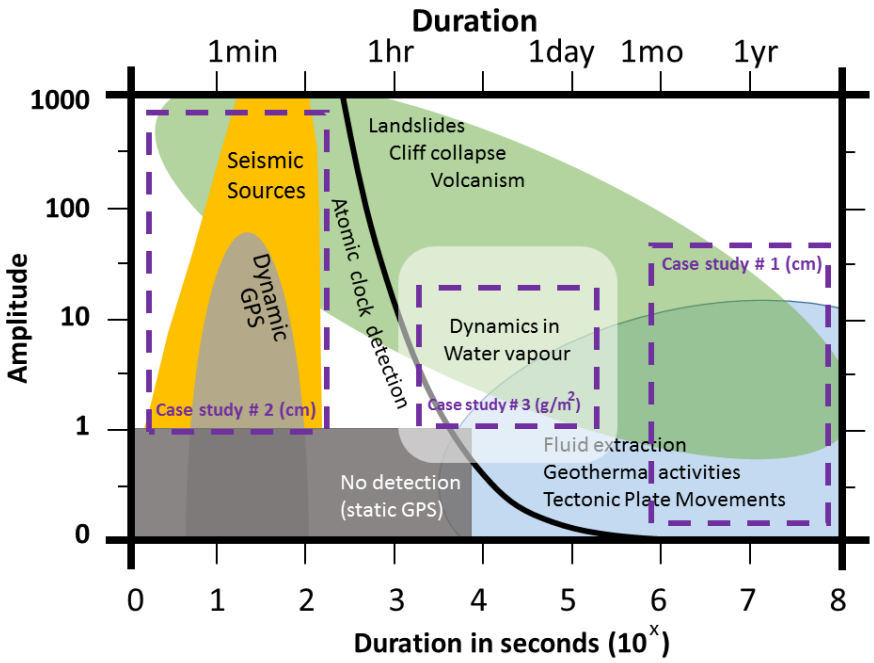


Figure 1-1 Amplitude versus duration diagram presenting where the three case studies fit alongside various geohazards adopted form (Psimoulis et al. 2018b)

1.3 Research significance and contributions

The main novelty of the developed approach is that unlike other approaches, it does not use the whole GNSS coordinate or troposphere time series, but uses a first part of them as a reference to determine the characteristics (i.e. any offsets, a linear trend, and periodic parameters) of the time series. Then, the remainder of the GNSS coordinate or troposphere time series is examined as to whether they follow the modelled time series using analysis in the time and space domains. This concept should be appealing to administrators of GNSS networks as the first period of a GNSS station lifespan are less vulnerable to wear and tear problems (e.g. antenna corrosion) than the years to follow.

Moreover, this multiple algorithm approach includes a novel use of temporal analysis, spatial analysis and combined (temporal and spatial) analysis. More specifically, most of the studies in the literature are based on the joint estimation of a parametric model, which requires a prior assumption of the modelled function (e.g. annual and semi-annual signals), with a stochastic noise model, together within the analysis of the GNSS time

series. On the other hand, in this research, the behaviour of GNSS time series will be analysed regarding the time-history of the corresponding stations using a non-parametric modelling (e.g. Nonlinear AutoRegressive Artificial Neural Network) which does not require any prior assumption about the structure of the modelled function used, and has the potential to bring more flexibility in the modelling process. It is worthy to mention that Artificial Neural Networks have been used previously in GNSS, but mainly in applications such as GNSS/INS integration (Wang et al., 2007; Nguyen-H and Zhou, 2010), and de-noising GNSS signals in the use of structural monitoring (Akyılmaz et al., 2004; Kaloop and Hu, 2015); however, no previous studies have used it in the detection of anomalous behaviours, geohazards and meteorological events. Moreover, no previous studies have tested the use of spatial regression as a method to analyse the spatial dependency in the GNSS time series as previously discussed.

Consequently, the behaviour of GNSS coordinate and troposphere time series will be analysed not only regarding the time-history of the corresponding stations but also their spatial relationship, creating a new perspective in GNSS network applications that goes beyond the use of conventional GNSS coordinate time series analysis software packages.

1.4 Thesis structure and outline

This thesis is organised into nine chapters as follows:

- **Chapter 2:** This chapter focuses on the use of GNSS time series in monitoring geohazards and meteorological events, where a general introduction on the use of GNSS time series in monitoring and early warning systems is given.
- **Chapter 3:** In this chapter, an introduction to the concept of modelling the temporal dependency is given, and the parametric and non-parametric models, as the main two ways of modelling of the temporal dependency, are discussed.
- **Chapter 4:** In this chapter, the concept of spatial dependency and its application in GNSS time series is discussed by introducing the concept of spatial dependency and the most common methods used to model it.

- **Chapter 5:** In this chapter, the methodology used in the development of the multiple algorithm approach to the analysis of GNSS time series is illustrated. The chapter illustrates where this new methodology stands in relation to other methods in the previous literature.
- **Chapter 6:** In this chapter, the multiple algorithm approach will be evaluated using the first case study; the analysis of the daily GPS coordinate time series of the BIGF network of stations in the British Isles.
- **Chapter 7:** In this chapter, the multiple algorithm approach will be evaluated using a second case study; the analysis of the 1Hz GPS coordinate time series of the GEONET stations in Japan for the Tohoku-Oki 2011 MW9.0 Earthquake.
- **Chapter 8:** In this chapter, the multiple algorithm approach will be evaluated using a third case study; the analysis of the long-term hourly GPS troposphere time series of the BIGF network of stations in the British Isles.
- **Chapter 9** contains the conclusions and recommendations based on the findings of the study, and directions for future work are also suggested

1.5 Publications list

- **Conferences**
  - A Multiple Algorithm Approach to the Analysis of GNSS Coordinate Time Series for Detecting Geohazards and Anomalies *[Poster presentation: European Geosciences Union General Assembly – Vienna 23-28 April 2017].*
  - Detecting Anomalous Behaviours in the GNSS Coordinate Time Series of the NERC British Isles continuous GNSS Facility (BIGF) Network *[Poster presentation: European Geosciences Union General Assembly – Vienna 23-28 April 2017].*
  - Detecting Meteorological Events in the GNSS IWV Time Series of the NERC British Isles continuous GNSS Facility (BIGF) network *[Poster presentation: European Geosciences Union General Assembly – Vienna 23-28 April 2017].*

- [To be presented] Temporal and Spatial Analysis of GNSS network data for detection of anomalies [*Poster presentation:* Joint International Symposium on Deformation Monitoring – Athens 15-17 May 2019]

- **Competitions**
  - Finalist presenter in the one-minute presentation PhD madness competition at the University of Nottingham – May 2016.
  - Poster presenter in the Engineering showcase competition at the University of Nottingham – May 2017.

- **Journal papers**
  - [Under revision] A Multiple Algorithm Approach to the Analysis of GNSS Coordinate Time Series for Detecting Geohazards and Anomalies *[Journal of Geophysical Research Solid Earth]*
  - [Draft to be submitted] Detecting Anomalous Behaviours in GNSS Coordinate Time Series: A case study of the British Isles continuous GNSS Facility (BIGF) Network *[Journal of Geophysical Research Solid Earth]*

Chapter 2: GNSS TIME SERIES IN NETWORK MONITORING APPLICATIONS

This chapter focuses on the use of GNSS time series in detecting geohazards and meteorological events. More specifically, section 2.1 gives a general introduction on the use of GNSS time series in monitoring and early warning systems. Then, the following three sections discuss further where GNSS time series fit alongside existing models and sensors in: tectonic plate movement and vertical land movement studies (section 2.2); earthquake studies (section 2.3); and tropospheric integrated water vapour studies (section 2.4).

2.1 GNSS Time Series in Monitoring and Early Warning (EW) Systems

Monitoring and Early Warning (EW) systems for the detection of geohazards are usually based on networks of sensors and are related to developments in geospatial engineering (Bhattacharya et al. 2012), which enable the protection of infrastructure and populations, and the mitigation of long-term consequences (Kubo et al. 2011; Michoud et al. 2013).

The development of GNSS technology in the sense of: the establishment and operation of permanent GPS networks (Bock and Melgar 2016); higher data recording rates (e.g. up to 100Hz) (Moschas et al. 2014; Häberling et al. 2015; Zhou et al. 2018); and the use of GPS alone or multiple satellite systems, such as GPS with GLONASS, BeiDou, and/or Galileo (Zhao et al. 2014; Teunissen et al. 2014; Msaewe et al. 2017) all enable the creation of GNSS products in the form of time series, which can provide information on ground deformation (Houlié et al. 2006; Reilinger et al. 2006; Liu et al. 2017; Psimoulis et al. 2018b) and troposphere/ionosphere activity (Wielgosz et al. 2005; Jin 2012), all of which are related to geohazards.

More specifically, GNSS coordinate time series are used in applications related to: plate tectonics (DeMets et al., 2000; Sella et al., 2002; Hollenstein et al., 2003; Grenerczy et al., 2005; Reilinger et al., 2006); vertical land movements (Teferle et al., 2006;

Grapenthin and Freymueller, 2011); and the estimation of earthquake magnitude (Blewitt et al., 2006; Edwards et al., 2010; Jin, 2012; Wright et al., 2012; Psimoulis et al., 2018a) and earthquake characteristics (Geng et al., 2013; Melgar et al., 2013; Psimoulis et al., 2014; Ganas et al., 2015; Montillet et al., 2015; Michel et al., 2017). Furthermore, GNSS coordinate time series have also been used in other applications related to tsunamis (Ohta et al., 2012; Titov et al., 2016), hydrological loading (Bevis et al., 2002; Tregoning et al., 2009) and ionospheric storms (Wielgosz et al., 2005).

However, it is worthy to note that it is not always that easy to draw a line between different geophysical phenomena as one can lead to or contribute to another. For example, tectonic plate movements and earthquakes.

2.2 GNSS Time Series in Tectonic Plate Movement and Vertical Land Movement Studies

The theory of plate tectonics, which suggests that the continents were once one large land mass that has undergone processes that gave rise to several tectonic plates, was confirmed by the mid-1950s (Bastos et al. 2010). Tectonic plate movements are those which describe the motion of the earth's crust which are most evident between the plate boundaries. These boundaries could be: divergent boundaries, where the plates are moving away from each other; convergent boundaries, where the plates are going under each other; or transform boundaries, where the plates slide horizontally past each other.

Initially, in order to model these movements, several datasets were used including ocean floor magnetic anomalies (Briais et al. 1993; DeMets et al. 1994), transform faults and earthquake slip vectors (Minster et al. 1974; Deng and Sykes 1995; D'Agostino et al. 2008), transform fault azimuths (Minster and Jordan 1978; Chu and Gordon 1999; Bird 2003), mid-ocean ridge spreading rates (Macdonald 1982; Stampfli and Borel 2002; Langmuir et al. 2013), and magnetic lineations (Uyeda and Miyashiro 1974; Weissel et al. 1977; Hsu et al. 2004) averaged over a period of 3 to 5 million years (Bock and Melgar 2016). Then, the NUVEL-1 model (DeMets et al. 1990), and its later version NUVEL-1A

(DeMets et al. 1994), was introduced, which proposed a more advanced, No-Net-Rotation (NNR) model. This model was different from previous models in the sense that it represents absolute movements, assuming that the total angular momentum of all tectonic plates should be zero (DeMets and Dixon 1999; DeMets et al. 2010; Wang et al. 2018; Yu et al. 2018; Chagas de Melo and Assumpção 2018). However, the use of such models based on geological data averaged over millions of years may yield biased estimates for some tectonic plates that are speeding up, slowing down, or changing direction (Sella et al. 2002). Figure 2-1 shows the major tectonic plate boundaries in green along with the ITRF2008 horizontal station velocities.

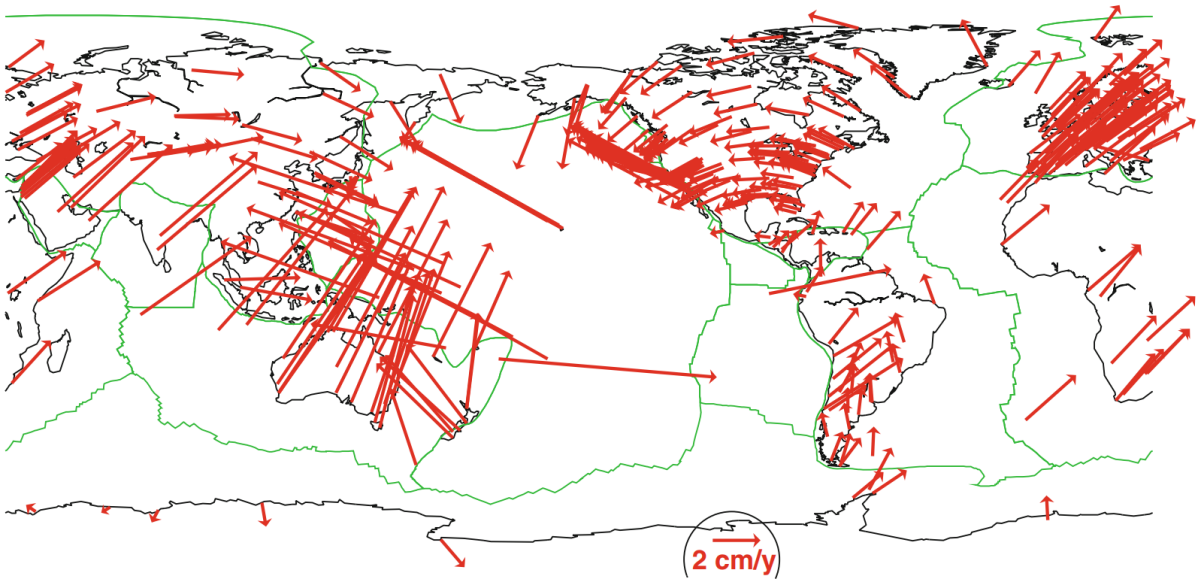


Figure 2-1 ITRF2008 horizontal station velocities with formal error less than 0.2mm/yr. Major plate boundaries are shown in green (Altamimi et al. 2011)

On the other hand, since their evolution, space geodetic methods have been used for the same purpose of measuring tectonic plate movements. For example, using Very Long Baseline Interferometry (VLBI), which measures the delay in arrival time of the signal from distant celestial objects (Argus and Gordon 1991; Sato 1993; Bock and Melgar 2016; Tong et al. 2018), and Satellite Laser Ranging (SLR), which determines the distance to a satellite by measuring the round trip time of a light pulse that is sent to the satellite (Smith et al. 1990; Sengoku 1998; Hofmann et al. 2018), the distances between stations that are thousands of kilometres apart can be derived with millimetre accuracy. Such space

geodetic methods provide estimates of horizontal station velocities which agree with the tectonic plate movements obtained with NUVEL-1A within 95% confidence (Sella et al. 2002). Then, since the mid-1990s, GPS (now GNSS) began to be used as an alternative to VLBI and SLR, although the latter still play a very important role in supporting the realisation of the celestial reference system, the determination of the Earth's geocentre the determination of the Earth's rotation, and the realisation of the International Terrestrial Reference Frame (Männel and Rothacher 2012; Plank et al. 2017).

With its lower costs, in terms of setting up and operating, GPS (or GNSS) stations acting as continuously operating reference stations (CORS) can be used to form permanent GPS (or GNSS) networks. The Permanent GPS network in California (Dong and Bock 1989; Larsen and Reilinger 1992; Feigl et al. 1993) and in Japan (Feigl et al. 1990; Shimada and Bock 1992; Tsuji et al. 1995; Miyazaki et al. 1996) are examples of the earliest permanent networks that were established on a regional and national scale. On a different scale, since 1994, the International GNSS Service (IGS) network has provided a global permanent GPS (and then GNSS) network (currently >300 active CORS) and significantly contributes in all GNSS applications by providing the precise orbit determination and Earth orientation parameters and terrestrial reference frame realisation (Altamimi et al. 2011; Rebischung et al. 2012; Klos et al. 2016).

GNSS coordinate time series from these permanent GNSS networks, consisting of daily coordinate estimates at each station over many years, can be used in detecting inter-plate (i.e. between the tectonic plates) and intra-plate (i.e. within the tectonic plate) deformations. Moreover, these time series can also provide more accurate estimates of tectonic plate movements than the previously mentioned technologies, assuming that their horizontal station velocities represent the movements of the tectonic plate on which they are located. In order to reach the requisite level of accuracy, the analysis of a GNSS coordinate time series demands considering all aspects involved in the GNSS process (He et al. 2017) and usually includes: estimating a linear trend (Santamaría-Gómez et al. 2011; Serpelloni et al. 2013; Griffiths and Ray 2016) and periodic signals (Penna et al.

2007; Davis et al. 2012; Amiri-Simkooei 2013; Chen et al. 2013); modelling the time series noise (Williams 2003a; Amiri-Simkooei et al. 2007; Amiri-Simkooei 2009; Montillet et al. 2013); and correcting potential offsets (Williams 2003b; Gazeaux et al. 2013; Bruni et al. 2014; Montillet et al. 2015) (See chapter 3). It can also include the detection of low-frequency motions and filtering of the common-mode error spatially (Wdowinski et al. 1997; Nikolaidis 2002; Liu et al. 2015; Tian and Shen 2016) (see chapter 4).

It has been shown that GNSS coordinate time series can be used to record all phases of the deformation cycle and, hence, to improve plate motion models. REcent VELocity (REVEL) (Sella et al. 2002) and Mid-Ocean Rigid Velocity (MORVEL) (DeMets et al. 2010) are examples of such improved models, which showed general agreement with NUVEL-1A (DeMets et al. 1994). However, the REVEL model (Sella et al. 2002), which used horizontal station velocities derived from GPS over the period of 1993 to 2000 to study 19 tectonic plates, showed some deviations from previous geological plate motion models, revealing the limitations of these previous models. On the other hand, in the MORVEL model (DeMets et al. 2010), 25 tectonic plates were modelled to estimate the Euler vectors (Deng and Sykes 1995), using horizontal station velocities derived from GPS along with earthquake slip vectors, and other geological data (DeMets et al., 2000; Sella et al., 2002; Hollenstein et al., 2003; Grenerczy et al., 2005; Reilinger et al., 2006).

In addition to the models mentioned above, several studies have also used GNSS coordinate time series with stochastic as well as deterministic models to study plate tectonic movements and the crustal deformation. For example, Li et al. (2000) used 2 years of GPS data to model the crustal deformation in central Japan. In this case, the authors used the Autoregressive Moving Average (ARMA) method to de-noise the time series, assuming only white noise is considered. Then, they detected the data discontinuities using Kalman filtering. Finally, they obtained the velocities and strain fields in central Japan using the de-noised time series in a least-squares collocation method (Figure 2-2). Jin et al. (2007) analysed 7 years of GPS data from 85 CORS and around

1000 campaign stations to study the micro-plate tectonics in Northeast Asia, and modelled the tectonic movements with rigid block rotations and elastic deformation.

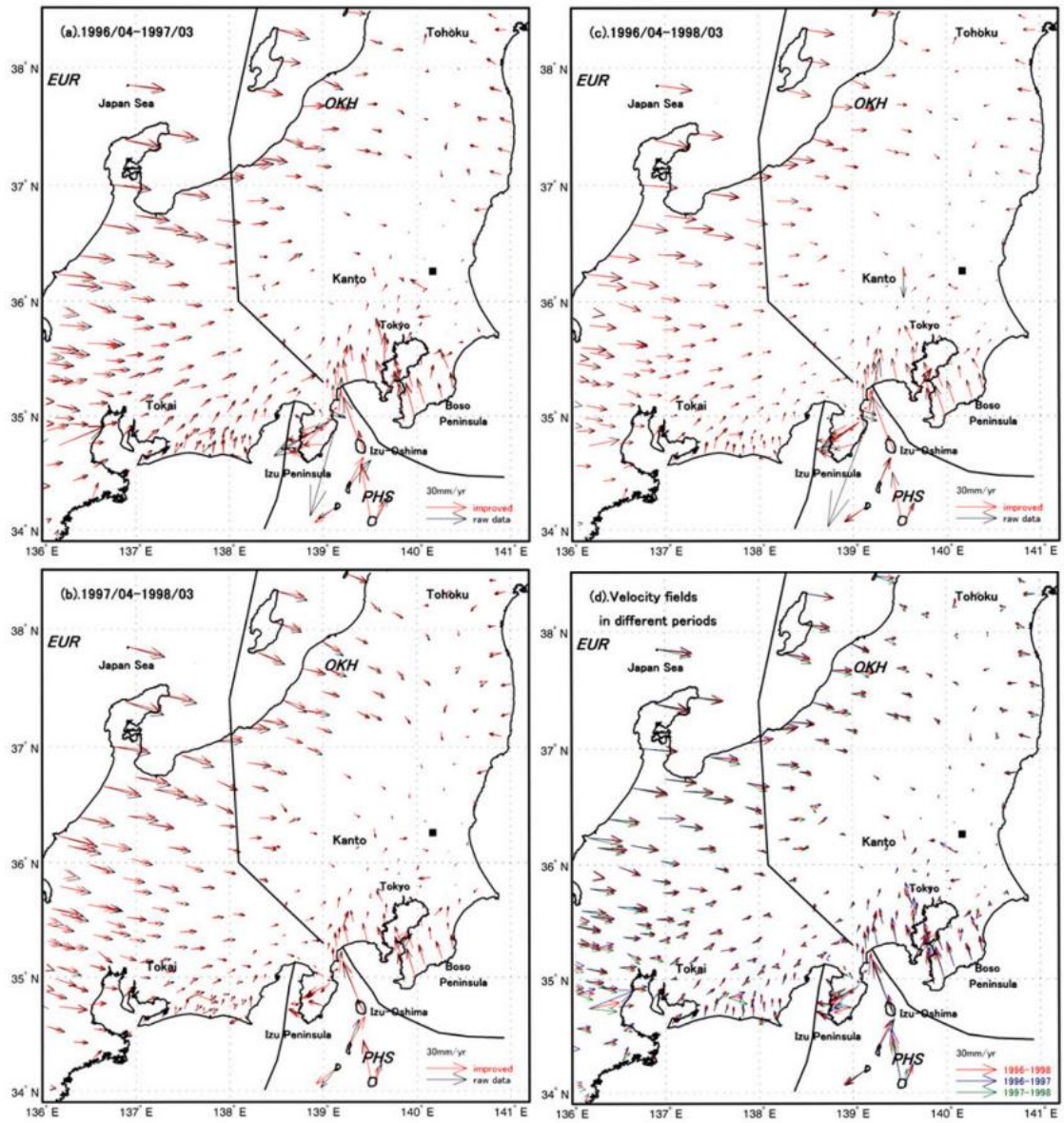


Figure 2-2 The estimates of velocity fields in central Japan using the improved time series data (red lines) and the original ones (black lines) in the different time periods (Li et al. 2000).

GNSS coordinate time series have not only been used to study tectonic plate movements, based on horizontal station velocities, but have also been used to great effect in the study of vertical land movements, based on the vertical station velocities. For example, Teferle

et al. (2008) used 5 years of GPS data from more than 30 CORS to analyse the vertical land movements in Western Europe. The authors used both Maximum Likelihood Estimation (MLE) (Williams 2003a; Langbein 2012) and Principal Component Analysis (PCA) (Dong et al. 2006; Liu et al. 2015), also known as Empirical Orthogonal Function (EOF), to analyse the time series. The authors also concluded that: the stochastic properties of the time series confirmed the presence of coloured noise; combining the use of MLE and PCA analyses led to determine highly accurate vertical station velocity estimates as it considers the spatial and temporal dependencies (See Chapters 3 and 4); and the PCA analysis revealed that the characteristics of the common-mode error time series are affected by the GPS processing strategy.

Similarly, Serpelloni et al. (2013b) used GPS data from more than 800 CORS and analysed their long-term coordinate time series in order to generate a synoptic view of contemporary vertical deformation rates in the Euro-Mediterranean region. The authors estimated and removed common mode errors in the time series using PCA, which they found to have a significant gain in the signal-to-noise ratio. The authors also analysed the data using MLE analysis to estimate the vertical station velocities and found it evident that there are significant vertical velocity gradients in regions characterized by null to low tectonic activity.

However, some researchers (Dong et al. 2006; Liu et al. 2015; Shen et al. 2016) see the use of PCA to estimate correlations statistically as being fairly complicated and prefer to use the correlation between nearby stations, as a function of the in-between distance. These methods will be discussed further in chapter 4.

2.3 GNSS Time Series in Earthquake Studies

In terms of earthquake studies, it is usually considered that the dynamic range of signals is quite wide and cannot be covered by a single type of sensor. For example, GNSS are considered as low-gain sensors which directly measure strong motion and can be used in studies to quantify tectonic plate movements and permanent deformation of the Earth's

crust. However, it may be seen as being less suitable for detecting small and moderate earthquakes (<M_w 6) (Colombelli et al. 2013) and not suitable when co-seismic ground displacement starts to be evident with the arrival of the S wave (i.e. later than the P wave arrival) (Colombelli et al. 2013; Minson et al. 2015).

In contrast, seismological instruments are considered as high-gain sensors as they can measure weak motion and small amplitude signals. However, such high-gain sensors may clip if a large amplitude signal or a close-range event occurs, affecting the accuracy of any absolute displacements derived (Crowell et al. 2009). On the other hand, the dynamic range of GNSS has no upper limit (Bock and Melgar 2016). Moreover, the mechanism of installing GNSS and seismic instruments varies too as the later are located in boreholes to minimize any atmospheric effects, while GNSS stations are located in an open-sky environment. Furthermore, seismological instruments are considered locally aligned (i.e. with respect to an inertial reference frame) while GNSS instruments are globally aligned (i.e. with the global terrestrial reference frame).

Therefore, GNSS and seismological instruments are often used together as they cover a broad range of frequencies of dynamic and static surface displacements as shown in Figure 2-3, which shows the complementary nature of both types of sensor. More specifically, it is shown how GPS is more sensitive than ultra-precise strainmeters at periods greater than a few months and that high-rate GPS sensitivity extends into the seismic domain (Bock and Melgar 2016).

This combination of using GNSS and seismological instruments together started with Blewitt et al. (1993) and Bock et al. (1993) to determine the static displacements (i.e. also referred to as Earth Geodesy) and with Nikolaidis *et al.* (2001) and Larson *et al.* (2003) to measure the dynamic displacement (i.e. also referred to as GNSS Seismology). Then, it was adopted by other researchers (Allen and Ziv 2011; Bock et al. 2011; Crowell et al. 2012; Wright et al. 2012; Colombelli et al. 2013). Such a combination is also adopted when large permanent GNSS networks are used for Earthquake Early Warning (EEW) as shown in, but not limited to, Figure 2-4

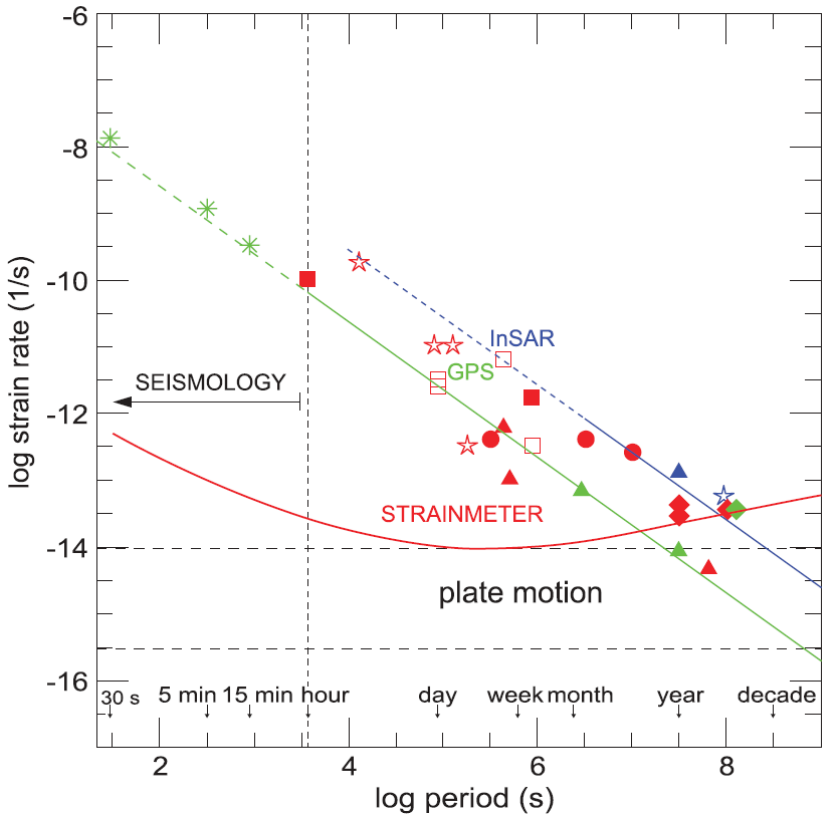


Figure 2-3 Strain rate comparison in the time domain. The GPS (green) is more sensitive than ultra-precise strainmeters at periods greater than a few months. The coloured symbols denote different types of transients that have been measured with a GPS and InSAR including post-seismic deformation (triangles), slow earthquakes (squares), long-period aseismic deformation (creep, diamonds), pre-seismic transients (circles), and volcanic transients (stars). High-rate GPS sensitivity extends into the seismic domain. (Bock and Melgar 2016)

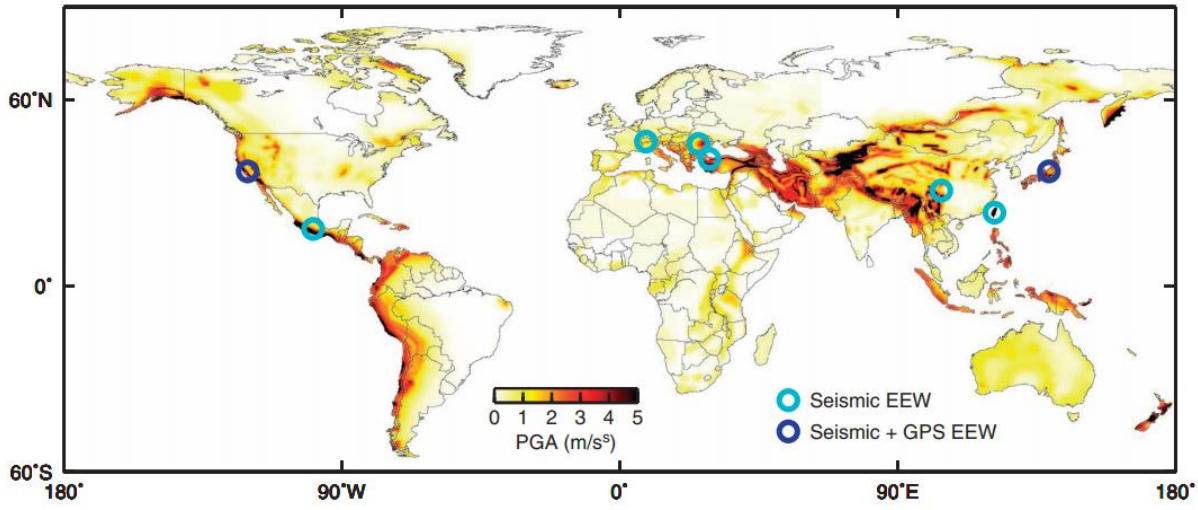


Figure 2-4 Locations where permanent GPS stations are used along with EEW along with a thematic map shows the peak ground acceleration with 10% probability of exceedance in 50 years from the Global Seismic Hazard Assessment Program (Minson et al. 2015)

In such cases, high-rate (i.e. 1Hz or higher) GNSS coordinate time series, usually derived from Precise Point Positioning (PPP), are used in real- or near real-time, to complement existing early-warning systems and to provide the amplitude of the co-seismic displacement, other characteristics of the monitored earthquake, and the seismic wave detection (Suarez et al., 2009; Perez-Campos et al., 2013)), or to predict the generation of tsunamis (Blewitt et al., 2009).

The basic concept of the methods and approaches used for earthquake early warning is called the "frontal detection" method. In this approach, once a ground shaking is detected at a station, a warning is issued ahead to those in a buffer zone. The warning time ranges from a few seconds to several minutes according to the distance from the epicentre. This approach is in operation in Japan, Mexico, and Taiwan (Bock and Melgar 2016). However, most of the subsequent studies that integrated GNSS instruments with seismological instruments have used GNSS for estimating the earthquake characteristics rather than for detecting the earthquake itself (apart from Crowell et al. (2009)). For example, Allen and Ziv (2011) focused on the applicability of using GNSS coordinate time series for earthquake early warning systems and concluded that GNSS could be vital for earthquake early warning systems, especially during large magnitude earthquakes, as they can provide an estimate of the permanent co-seismic static displacement, which is hard to extract from accelerometer data. Moreover, since the GNSS-based estimate is independent, integrating this with seismically derived information would be valuable.

Colombelli et al. (2013) used an algorithm developed by Allen and Ziv (2011) to extract the 'permanent static offset' from 1 Hz coordinate time series based on GPS by developing a strategy that does not require prior assumptions about the earthquake, as their strategy estimates a preliminary, quick magnitude and then the model upgrades this preliminary estimation to be increased in size. They tested this proposed strategy by simulating real-time environments for three earthquakes; the Mw 9.0, 2011 Tohoku-Oki earthquake, the Mw 8.3, 2003 Tokachi-Oki earthquakes, and the Mw 7.2, 2010 El Mayor-Cucapah earthquake. The accuracy of the ground shaking prediction using the GPS-based

magnitude and finite extent is significantly better than existing seismology-based point source approaches. However, it should be noted that in this study GPS was used to estimate the earthquake magnitude, with seismometers being used to detect the earthquake and to trigger the estimation of the earthquake magnitude.

Grapenthin et al. (2014) discussed the use of the 'Geodetic alarm system' (G-larmS) (Johanson et al. 2014) as an extensible geodetic, earthquake early warning system that analyses coordinate time series from real-time GPS. However, G-larmS uses the P-wave detected by seismic alarm systems to trigger its own processing to then estimate earthquake characteristics.

Following Allen (1978), in all of the above-mentioned studies, and others (Ohta et al. 2012; Psimoulis et al. 2018b), there is the analysis of the short-term average (STA) and the long-term average (LTA) of the GNSS coordinate time series (Figure 2-5). These methods compare the instantaneous displacement derived from the differencing of the short-term and long-term averages against the noise of the time series, derived from the standard deviation of the STA and LTA. On the other hand, probabilistic approaches such as Bayesian inversion (Minson et al. 2014) and artificial neural networks (Käufl et al. 2014) have also been used to identify earthquake characteristics.

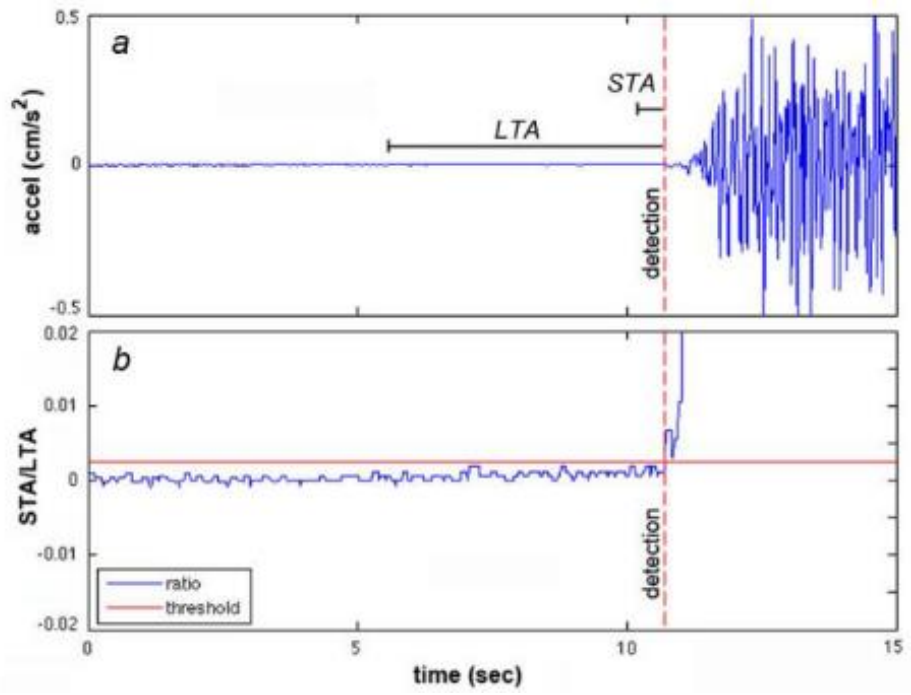


Figure 2-5 a)The first 15 seconds of the acceleration record of MYG011 strong-motion site for the Mw9.0 Tohoku 2011 earthquake and b) the computed corresponding STA/LTA ratio with the threshold for the detection of first seismic wave arrival(Psimoulis et al. 2018b).

2.4 GNSS Time Series in Tropospheric Integrated Water Vapour Studies

In addition to GNSS coordinate time series, it is also possible to form GNSS tropospheric time series by taking advantage of the delaying effect of the neutral atmosphere on the GNSS signal. This tropospheric delay is usually solved for as a Zenith Total Delay (ZTD), in the zenith direction at a station, and is a function of atmospheric pressure, water vapour, and temperature. Over the last 20 years, there has been great interest in using such ZTD estimates through what has become known as "GNSS meteorology". The ZTD is a sum of the total effect of the hydrostatic component (i.e. zenith hydrostatic delay, ZHD) and the wet component (i.e. zenith wet delay, ZWD). As the ZHD can be modelled very precisely using surface pressure measurements it is then possible to extract the ZWD which, in turn, can be related to Integrated Water Vapour (IWV), which is quantified in mass per unit area (e.g. kg/m2), or precipitable water (PW), which is quantified as the equivalent height of a liquid water column (e.g. mm).

In terms of weather forecasting using numerical weather models, GNSS meteorology is seen as a complementary method to existing meteorological sensors and models for the following two reasons: very short-term moisture surges are not easy to detect using existing meteorological methods (e.g. satellite, radar, radiosonde and surface dew point observations); and the temporal resolution of GNSS can be much smaller than that of existing meteorological methods (e.g. 15 minutes compared to 12 or 24 hours using radiosonde measurements).

Many early studies assessed the quality of GNSS tropospheric IWV time series in relation to the water vapour derived from existing meteorological means. For example, *Baker et al.* (2001) and *Glowacki et al.* (2006) compared with radiosonde estimates and concluded that both datasets were in a good agreement (Figure 2-6).

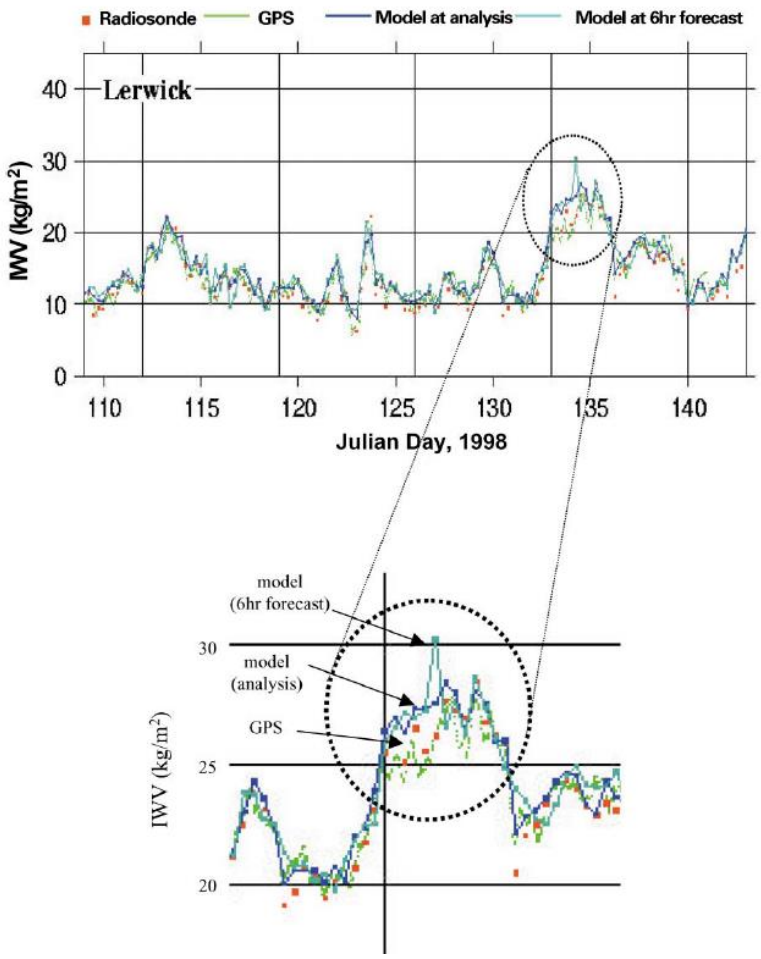


Figure 2-6 Comparisons between GPS, radiosonde and United Kingdom Met Office (UKMO) model of IWV estimates and forecast(Baker et al. 2001).

While other studies have looked into the impact of using GNSS tropospheric IWV time series on weather forecasting. Tomassini et al. (2002) showed that GNSS revealed a diurnal cycle which existing meteorological models did not detect. However, Gendt et al. (2004) showed that GNSS only led to a 2% improvement for the relative humidity in a 12-hour forecast whereas Jones (2010) concluded that 2D maps of the IWV derived from GNSS are potentially useful to the forecasting community, but had the most potential impact in relation to organised thunderstorms.

GPS tomography, on the other hand, may be seen as a development of using the time series for reconstructing a 4D distribution of water vapour in the troposphere using a local GPS network as the method provides the spatial and temporal distribution of water vapour content in the troposphere (Perler et al. 2011; Wilgan et al. 2017). The integrated measurements of wet delays are extracted from each satellite-to-station link, which are used as the primary observable through a finite 3D ellipsoidal grid field to estimate the 3D structure of WV with a time evolving variable (Figure 2-7).

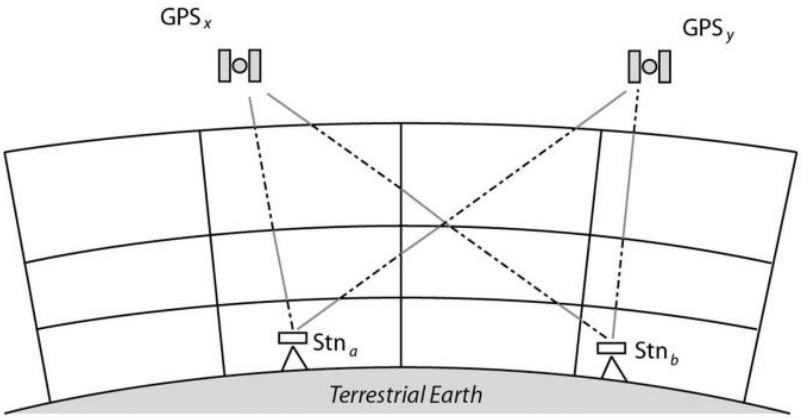


Figure 2-7 The discretisation of GPS DD observations from GPS satellites (x & y) to stations (a & b) through finite ellipsoidal voxel grids (Manning 2013).

In addition to its use in weather forecasting, GNSS meteorology could also be potentially useful in long-term monitoring, for example, positive trends in IWV time series can be seen as an indicator of climate change. However, since these need long periods (greater than 20 years) of consistent data, they are less common in the literature (Sherwood et al.

2010; Stocker et al. 2014). Furthermore, there have also been some studies on the usefulness of GNSS ionospheric time series in detecting earthquakes and tsunamis (Cahyadi and Heki 2013; Heki and Enomoto 2013) using the change in the vertical total electron content (VTEC).

2.5 Summary

This chapter has introduced the use of GNSS time series in detecting geohazards and meteorological events, and summarised where GNSS time series fit alongside existing models and sensors in: tectonic plate movement and vertical land movement studies; earthquake studies; and tropospheric integrated water vapour studies. These sections were chosen as such to be consistent with the case studies used in this research, as discussed in Chapter 1, and presented in Chapters 6, 7 and 8.

The next chapters will consider the general nature of such GNSS time series, in terms of their temporal dependency and spatial dependency.

CHAPTER 3: TEMPORAL DEPENDENCY IN GNSS TIME SERIES

In this chapter, an introduction to the concept of temporal dependency is given. In the first section (section 3.1), the modelling of temporal dependency in time series is introduced while the two sub-sections (sub-sections 3.1.1 and 3.1.2) discuss the difference between parametric and non-parametric models as ways to extract the temporal dependency from a time series. In this respect, Autoregressive, Moving Average and Kalman Filter models are illustrated in sub-section 3.1.1 as examples of parametric models, while Artificial Neural Network models are introduced in sub-section 3.1.2 as an example of a non-parametric model. Then in the following section (section 3.2), the discussion is focussed on the temporal analysis of GNSS time series, where it is shown how the extraction of the temporal dependency can be used to estimate the linear trend as well as to detect and/or estimate offsets in long-term GNSS time series.

3.1 Modelling the Temporal Dependency

Temporal dependency is mainly used in stochastic models, where the value of each observation (or measurement) at a time is a function of the values of previous observations within a level of uncertainty (Maybeck 1982). The form of which these observations are ordered in relation to each other is called a time series. Literature defines time series as "a sequence of measurements [or observations] of the variable of interest, usually collected at regular time intervals" (Shigueo and Junior 2012), or, more simply, as "a collection of observations made chronologically" (Fu 2011).

Since time series have an explicit order dependence between observations, researchers have used this to analyse the temporal dependency between observation values, where the goal is to develop mathematical models that provide plausible descriptions from sample data, which can then be used to predict future observation values of the time series or to perform other analyses (e.g. clustering (Iorio et al. 2016), indexing (Camerra et al.

2010), segmentation (Durán-Rosal et al. 2016) and classification (Bagnall et al. 2016)) of phenomena which are related to time.

In order to determine the temporal dependency between the values in a time series, it is necessary to start from a model of the form:

$$\boldsymbol{y_t} = \boldsymbol{f}(\boldsymbol{y_{t-1}}, \boldsymbol{y_{t-2}}, \dots) + \boldsymbol{\epsilon_t} \qquad \text{Equation 3-1}$$

where y_t is the observation value of interest at the current time t, $f(.)$ is a function that maps $\boldsymbol{y_{t-1}}, \boldsymbol{y_{t-2}}, \dots$ into $\boldsymbol{y_t}$ and ϵ_t is a sequence of independent (or uncorrelated) random variables with a mean equal to zero and a variance equal to σ^2, or so-called white noise.

The structure of the function $f(.)$ can either be considered known (i.e. parametric models) or unknown (i.e. non-parametric models) (Chen et al. 1997).

3.1.1 Parametric Models

Methods based on parametric models are the most commonly used in previous literature concerned with time series analysis and forecasting. These methods use past observations to develop a mathematical model which captures the underlying data generating process for the time series. In these models, there is assumed to be a priori knowledge about the structure of the function $f(.)$ as it is identified from some parametric characteristics so that the value of interest is obtained by specifying a fixed finite number of parameters. This approach is particularly useful when there is a lack of a satisfactory 'explanatory model' (Adhikari and Agrawal 2013; Gershenfeld and Weigend 2018). Autoregressive (AR) models and Moving Average (MA) models are the most common in this category (Connor et al. 1994; Ji et al. 2005; Billings 2013; Cohen 2014; Gershenfeld and Weigend 2018).

Autoregressive (AR) Models

Autoregressive (AR) models are used to study the effect of internal memory as the value of interest is predicted using a linear combination of its past values. The mathematical form of this model is as follows (Connor et al. 1994):

$$y_t = \sum_{i=1}^{p} \beta_i y_{t-i} + \epsilon_t \quad where \quad \epsilon_t \sim N(0, v) \qquad \text{Equation 3-2}$$

where y_t is the observation value of interest at the current time t, $\beta_1, \ldots, \beta_i$ are fixed constants to be determined, and ϵ_t is assumed to be white noise.

Moving Average (MA) Models

In Moving Average (MA) models, rather than using past values in a regression, the residual errors from forecasts of a time series act as another source of information to be modelled which, in turn, can be used to correct the forecasts. The mathematical form of these models is as follows (Connor et al. 1994):

$$y_t = \sum_{j=0}^{q} \alpha_j \epsilon_{t-j} \quad where \quad \epsilon_t \sim N(0, v) \qquad \text{Equation 3-3}$$

where y_t is the observation value of interest at the current time t, $\alpha_1, \ldots, \alpha_j$ are fixed constants to be determined, $\alpha_0 = 1$, and ϵ_t is assumed to be white noise.

Hybrid Models

Many other techniques found in previous literature are effectively modified versions of these two models in some form. For example, Autoregressive Moving Average (ARMA), Autoregressive Integrated Moving Average (ARIMA), and Autoregressive Fractionally Integrated Moving Average (ARFIMA) models (Xiong and Yeung 2002; Adhikari and Agrawal 2013) all use a linear combination of both past values and past forecast errors, while Autoregressive with eXogenous input (ARX) and Autoregressive Moving Average with eXogenous input (ARMAX) models (Billings 2013) use an external variable as an additional parameter (Li et al. 2000; Xu et al. 2002; Garrison et al. 2002; Tomáš Bacigál 2004; Jiann-Shiou Yang 2005; Park and Gao 2008; Koyama and Tanaka 2010;

Tanikawara et al. 2010; Bogusz and Kontny 2011; Djouadi et al. 2011; Lim et al. 2013; Soundy et al. 2015).

Even though all of these models are powerful, easy to use and computationally effective, ultimately they are linear models which make them suitable for linear systems only. Therefore, non-linear models were developed to overcome this issue. These non-linear models have the same concept as the linear models; however, the difference is that the functions used to combine the parameters are more sophisticated than using the weighted sum. Examples of such non-linear models are Non-linear Autoregressive (NAR), Non-linear Moving Average (NMA), and Autoregressive Conditional Heteroskedasticity (ARCH) (Zhang 2007; Diaconescu 2008; Billings 2013; Adhikari and Agrawal 2013).

Kalman Filter (KF) Models

Even though the Kalman filter is considered a parametric model, it has the potential to surpass the conventional models because it is an adaptive model which constantly updates its $f(.)$ at each new epoch. However, its drawback is that it focuses on the short-term dependency rather than long-term dependency.

The Kalman Filter (KF) model assumes at time t the true state, x_t , is evolved from the state at $\mathrm{t}-1$, x_{t-1}, according to Equation 3-4, while at time t an observation y_t of the true state x_t is made according to Equation 3-5.

$$x_t = \mathbf{F}_t x_{t-1} + \mathbf{B}_t u_t + \boldsymbol{w_t} \qquad \text{Equation 3-4}$$

$$y_t = \mathbf{H}_t x_t + \boldsymbol{v_t} \qquad \text{Equation 3-5}$$

where x_t is the system state at the current time t, $\mathbf{F}_t$ is the state transition model which is applied to the previous state x_{t-1}. $\mathbf{B}_t$ is the control-input model which is applied to the control vector u_t, w_t is the process noise which is assumed to be drawn from a zero mean multivariate normal distribution with covariance of the process noise, $\mathbf{Q_k}$: $w_t \sim \boldsymbol{N}(\mathbf{0}, \mathbf{Q_k})$. $\mathbf{H}_t$ is the observation model which maps the true state space into the observed, and $\boldsymbol{v_t}$ is the observation noise which is assumed to be zero mean Gaussian white noise with covariance of the observation noise , $\mathbf{R_k}$: $w_t \sim \boldsymbol{N}(\mathbf{0}, \mathbf{R_k})$.

3.1.2 Non-parametric Models

As detailed in section 3.1.1, parametric models have a prior assumption about the structure of the function used. For this reason, they can be considered as being more vulnerable to 'bias errors' due to the simplification made by introducing an assumption, which leads to them having a lower predictive performance on complex problems. On the other hand, with non-parametric models, there is no prior assumption about the structure of the function $f(.)$ used, and it is allowed to have a more general form than that used in parametric models. Machine Learning algorithms are considered the most common non-parametric methods used to extract the temporal dependency, as in machine learning the aim is to automatically learn and recognise patterns in large amounts of data (Krollner et al. 2010) by learning a target function (sometimes called a mapping function) that best maps input observation values (e.g. past observations) into an output observation value (e.g. the current observation), where the form of this function is unknown (Bradley 1997; Stockwell and Peterson 2002; Rasmussen and Williams 2006; Drozdov et al. 2009; Wernick et al. 2010).

Artificial Neural Network (ANN) Models

The Artificial Neural Network (ANN) is one of the most common machine learning algorithms used in generic time series analysis (Peralta et al. 2010; Fu 2011; Adhikari and Agrawal 2013). The intuition behind it is to mimic the human brain and its connected neurons, and ANN is a supervised learning problem that gives a way of defining a complex, non-linear form of the target function, with weights to fit the given data (Geng 2007).

Figure 3-1 represents the main principles of the Non-linear AutoRegressive Artificial Neural Network (NAR-ANN) model, where it consists of two input observation values, y_{t-1} and y_{t-2}, one hidden layer containing three neurons, and one output predicted value, $\hat{y}_t$, of the observed value, y_t, and the solid arrows represent the weights that are to be optimised.

Each single neuron works as a computational unit that adds up the weighted inputs and passes them to a so-called "activation function" which, in turn, controls the neuron output. The error in the estimation (i.e. the difference between the predicted value and true value) represents how optimal the weights are. Accordingly, this error will be propagated backwards, in a process called "back propagation" (Hecht-Nielsen 1989), by apportioning it to each assigned weight according to the amount each weight is responsible for, in order to minimize this error through a technique called "gradient descent".

The activation function in each neuron works as a gate to pass or stop the flow of the computation from each input. It can be as simple as a step function (i.e. 1: pass or 0: stop), a linear function, or one of the S-shaped functions (e.g. sigmoid, hyperbolic tangent). However, the most common activation function is the sigmoid function (Equation 3-6 and 3-7) as it provides a smooth non-linearity to the solution and makes the ANN better in discovering non-linear relationships between the input observation values and the output observation values, which makes it better than step and linear functions. Moreover, the sigmoid function is preferred to any other S-shaped function because it is easier to do calculations with it than it is with the other S-shaped functions.

$$T_i = \frac{1}{1 + e^{-a_i}} \qquad \text{Equation 3-6}$$

$$a_i = b_i + \sum_{j=1}^{p} g_{ij} y_j \qquad \text{Equation 3-7}$$

where T_i is the output observation value of the sigmoid function at neuron i, a_i is the weighted sum at the neuron i from the input of the neurons in the previous layer, b_i is the bias term of the neuron i, and g_{ij} are the weights to be optimized connecting the p inputs (i.e. $p = 2$) to neuron i.

As mentioned before, the assigned weights are optimized, to get the closest estimation of the desired outputs in a process called gradient descent which can be summarized as follows (Burges et al. 2005; Zinkevich et al. 2010; Ghosh 2012).

1. Assign initial random values to the weights to be optimized, θ, where it is preferable that these random values are small.
2. Estimate the desired output, $\hat{\boldsymbol{y}}_{\boldsymbol{t}}$, based on these initial weight values and then compare it to the true value, $\boldsymbol{y}_{\boldsymbol{t}}$, using the cost function, $J(\theta)$, shown in Equation 3-8.
3. Calculate the derivative of the cost function, $\nabla_{\theta} J(\theta)$, with respect to each weight value to give the slope of the function, which represents the direction to move the weight values in order to get a lower cost on the next iteration.
4. Specify a learning rate parameter, η, which controls how much the weight values can change on each update; where a large η leads to large jumps in the weight values while a small η leads to a slow learning process.
5. Update the weight values using Equation 3-9.
6. Repeat this process until the cost function is close enough to zero or no further improvements in cost can be achieved.

$$\boldsymbol{J(\theta)} = \frac{\mathbf{1}}{\mathbf{2}} \sum_{\boldsymbol{i}} (\boldsymbol{y}_{\boldsymbol{t}} - \hat{\boldsymbol{y}}_{\boldsymbol{t}})^{\mathbf{2}} \qquad \text{Equation 3-8}$$

$$\theta = \theta - \eta \, \nabla_{\theta} J(\theta) \qquad \text{Equation 3-9}$$

Here it should be noted that gradient descent is the most basic optimization technique, and there are more-advanced and sophisticated techniques that are derived from it such as the Bayesian Regularization training function (Diaconescu 2008; Ali 2009) and the Levenberg-Marquardt (Kumar and K.Rajasekhar 2017) which are also mentioned in previous literature.

ANN models, as with all non-parametric models, are less vulnerable to 'bias errors' but are more vulnerable to 'variance errors', which are due to the nature of the algorithm behaviour regarding different datasets. As a result, an "overfitting problem" can

happen when a model learns the details and noise in the data to the extent that it negatively impacts the performance of the model on new data. To overcome this problem, it is always recommended to split the dataset into training and testing datasets, and to optimize the weights using the training dataset and then evaluate the ANN model's performance on a new dataset (i.e. the testing dataset), with the training dataset being between 65%-80% of the entire dataset (Crowther and Cox 2005; Lean Yu et al. 2006).

Since the performance of the ANN model depends on so many factors, such as the chosen architecture (i.e. the number of layers, the number of neurons), the optimization process, and the amount of data used (Dietterich and Kong 1995), it is always recommended to examine different ANN architectures in order to assess their Normalised Mean Square Error (Equation 3-10) or Root Mean Square Error (Equation 3-12).

$$NMSE = \frac{1}{N}\sum_{i=1}^{N}\frac{(\hat{y}_i - y_i)^2}{\left(\frac{1}{N}\sum_{i=1}^{N}\hat{y}_i\right)\times\left(\frac{1}{N}\sum_{i=1}^{N}y_i\right)} \qquad \text{Equation 3-10}$$

$$RMSE = \frac{1}{N}\sum_{i=1}^{N}(\hat{y}_i - y_i)^2 \qquad \text{Equation 3-11}$$

Where N is the number of epochs within the time series dataset, and $\hat{y}_i$ is the predicted observation value of y_i.

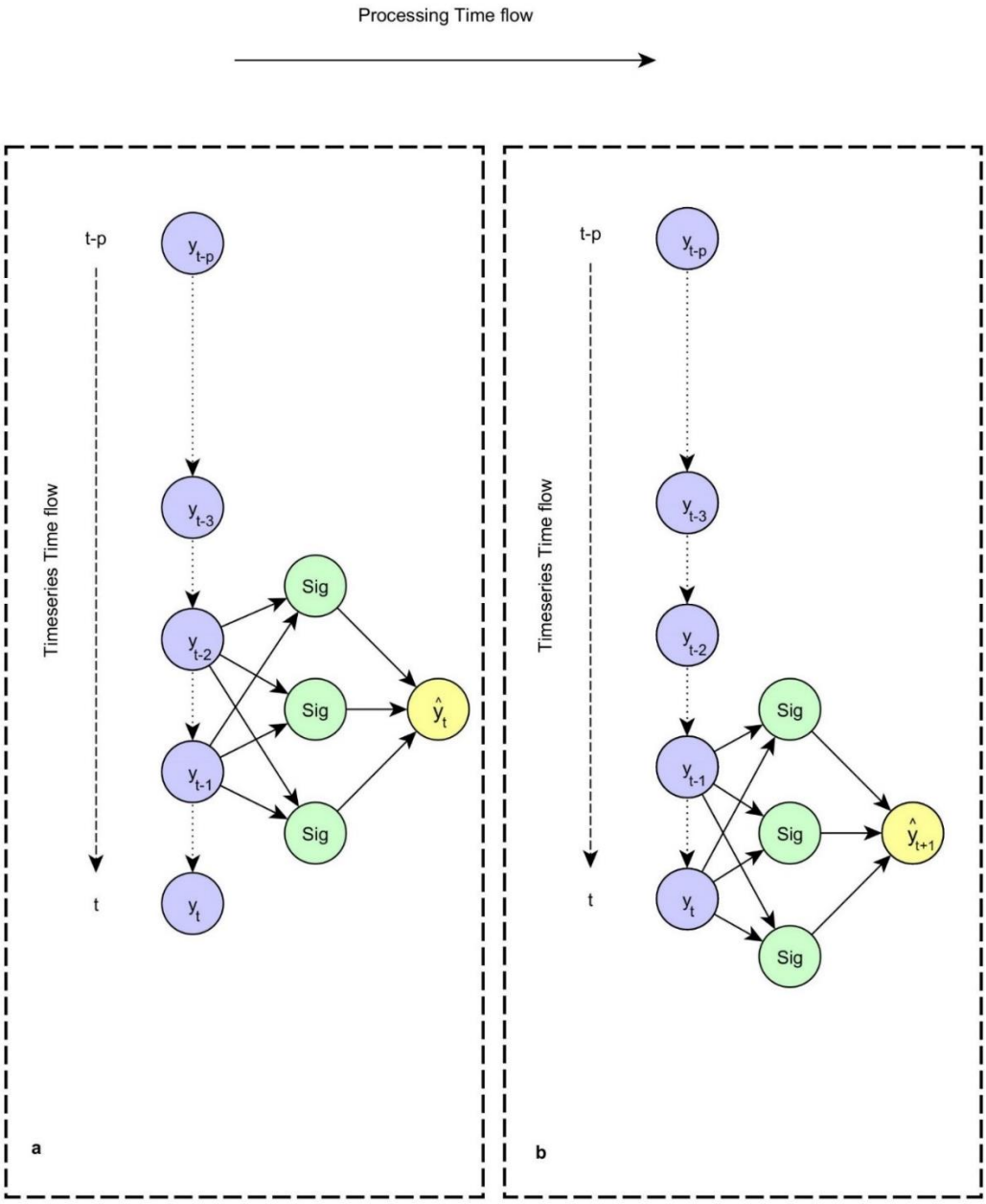


Figure 3-1 Representation of the procedure of (a) the training stage and (b) the prediction stage of NAR-ANN. In the training stage, y_{t-1} and y_{t-2} are used to estimate y_t as $\hat{y}_t$ using sigmoid (sig) functions, and the weights of the functions are defined in the training stage.

Aside from its use in GNSS time series analysis, ANN has been used in GNSS/ INS integration. For example, Nguyen-H & Zhou (2010) used ANN to develop a more efficient and faster method for processing the GPS signal, in the case of INS signal loss, without losing the accuracy of the data. While Wang et al. (2007) presented the use of an ANN as

an aid to Kalman filtering, in order to improve the navigation solutions from an integrated GPS/INS georeference system.

ANN is also used in estimating atmospheric error as well; Hernández-Pajares et al. (1997) in their research used ANN to model a 2-D ionospheric electron distribution using the IGS network data. El-Naggar (2013) used ANN to model the regional behaviour of the ionosphere. He estimated the Vertical Total Electron Content (VTEC) for void areas and to avoid the gap which occurs between the results of the Global Ionosphere Map (GIM) from two consecutive sessions using ANN to produce a high-resolution ionospheric model to serve the single frequency receiver.

Furthermore, ANN has also been used as a tool to assess differential GNSS corrections. For example, Mosavi (2006) illustrated a new approach for predicting differential GPS (DGPS) corrections using Nonlinear Autoregressive Artificial Neural Network (NAR-ANN), a fuzzy neural network (FNN), or a Kalman filter (KF), and presented experimental test results with real data to emphasize that the performance of NAR is better than FNN and KF when considering a trade-off between accuracy and speed (Table 3-1). Geng (2007) also applied both a NAR-ANN and a Kalman filter to predict DGPS corrections and concluded that NAR-ANN provides correction data with a significant accuracy improvement.

Table 3-1 Prediction errors using Nonlinear Autoregressive Artificial Neural Network (NAR-ANN), a fuzzy neural network (FNN), or a Kalman filter (KF) (Mosavi 2006)

PARAMETERS	**NAR**			**KF**			**FNN**		
	X	**Y**	**Z**	**X**	**Y**	**Z**	**X**	**Y**	**Z**
AVERAGE (METERS)	0.0011	0.0052	-0.00005	0.0346	0.0318	0.0321	0.8665	0.6133	0.2041
RMS	0.3508	0.3694	0.3325	0.3410	0.3512	0.3223	1.8415	2.1439	1.3472
VARIANCE	0.0001	0.0117	0.0105	0.0001	0.0001	0.0001	0.0026	0.0042	0.0018
CPU TIME (MS)	4			10			37		

Additionally, in structural monitoring, Kaloop & Hu (2015) used ANN with four prediction models for the learning algorithms (back-propagation, cascade-forward back-propagation,

an adaptive filter, and an extended Kalman filter) and suggested that ANN can be used for de-noising the observations, specifically for the GPS displacement components of structures (Figure 3-2).

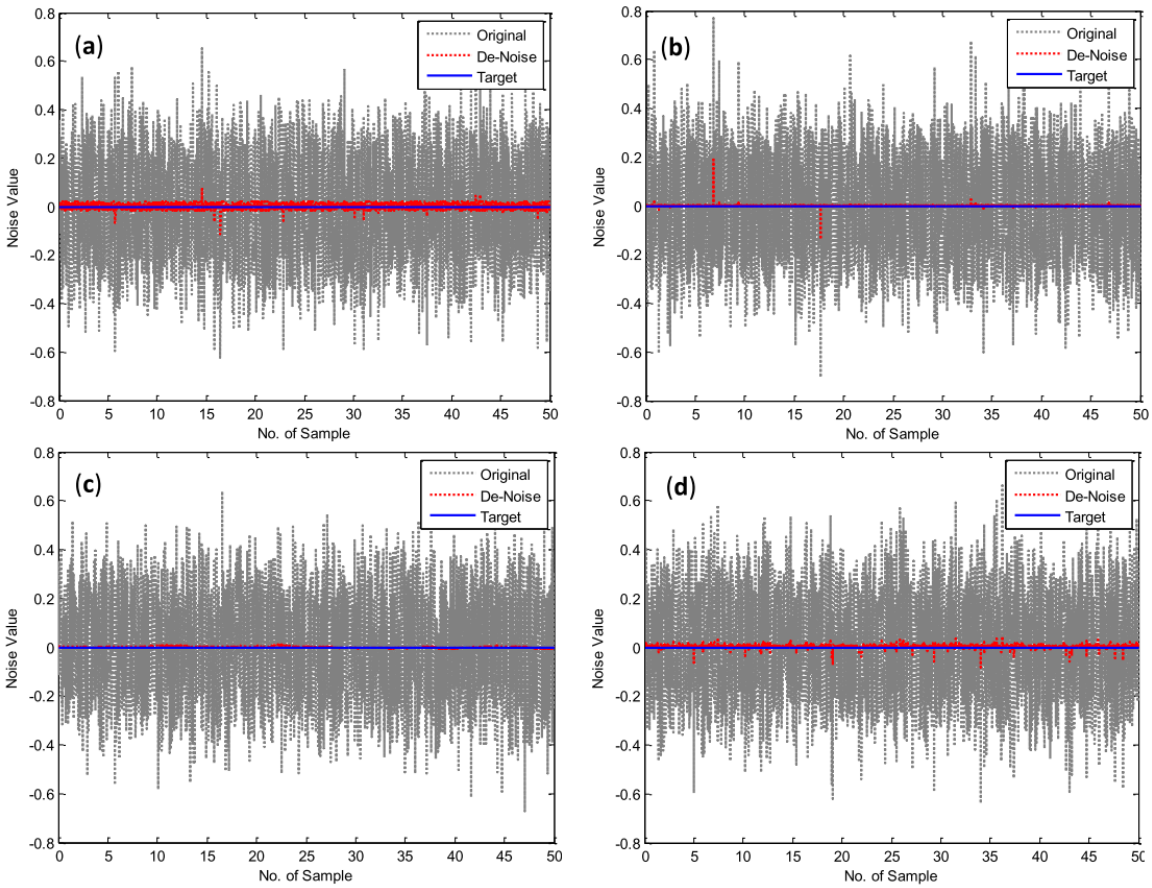


Figure 3-2 Comparison of the simulation results (a) Back-Propagation Neural Network (BPN); (b) Cascade- Forward Back-Propagation Neural Network (CFN); (c) Adaptive Filter Neural Network (ADFN); (d) Extended Kalman Filter Neural Network (EKFN) (Kaloop and Hu 2015).

From the above, it can be concluded that the Kalman filter has more advantages than the other parametric models (e.g. AR and MA) as its ability to update its parameters with each epoch is seen as useful in dealing with streaming data\measurements as GNSS time series. On the other hand, with the Artificial Neural Network as a non-parametric model, in addition to its ability to update its parameters with each epoch, the mapping function is not explicitly written, but learned from provided examples (i.e. training dataset), while in the Kalman Filter, some prior models of the signal (e.g. linear or non-linear) and noise type (e.g. Gaussian noise) should be addressed to estimate the filter parameters in a way

which is optimal. Moreover, ANN surpasses the Kalman filter in the sense of its ability to extract the temporal dependency in both long and short-term memories, depending on how many previous epochs are included, while the Kalman filter only provides predictions that reflect short-term memory. Therefore, for GNSS time series applications, non-parametric models (e.g. the use of an Artificial Neural Network) can be considered as being more flexible than parametric models.

3.2 Temporal Analysis of GNSS Time Series

Studying the temporal dependency of GNSS time series acquired more attention in the literature after Larson & Agnew (1991) who examined the precision and accuracy of a 3-year GPS coordinate time series to conclude that, at that time, the accuracy is up to 30 mm and 80mm, in the plan and vertical components respectively, while the precision is 2mm and 17mm, in the plan and vertical components respectively.

Since then, the accuracy and precision of GNSS time series have improved which, in turn, makes it one of the predominant tools in geodetic studies (Bock and Melgar 2016). This improvement can be attributed to: denser local, regional and global networks of GNSS stations, through international collaboration; more accurate precise ephemeris which can be used by end users; and better GNSS processing software packages with improved modelling of all of the various systematic biases and errors (Blewitt 1993; Segall and Davis 1997; Xu et al. 2002; Bastos et al. 2010; He et al. 2017).

Larson & Agnew (1991) has been followed by a multitude of detailed researches which have examined GNSS coordinate time series more thoroughly (Blewitt 1993; Segall and Davis 1997; He et al. 2017) and tried to address the issues which affect the accuracy of such time series including: linear trend estimation (Santamaría-Gómez et al. 2011; Serpelloni et al. 2013; Griffiths and Ray 2016); periodic signals (Penna et al. 2007; Davis et al. 2012; Amiri-Simkooei 2013; Chen et al. 2013); noise characterisation (Williams 2003a; Amiri-Simkooei et al. 2007; Amiri-Simkooei 2009; Montillet et al. 2013); and offset

estimation and detection (Williams 2003b; Gazeaux et al. 2013; Bruni et al. 2014; Montillet et al. 2015).

3.2.1 Linear Trend Estimation in Long-Term GNSS Time Series

Linear trend estimation is a vital step in the analysis of long-term GNSS time series, especially in tectonic plate movement studies (DeMets et al. 2000; Sella et al. 2002; Hollenstein et al. 2003; Grenerczy et al. 2005; Reilinger et al. 2006).

The linear trend is usually estimated using least squares and following Equation 3-12 (Williams 2003a):

$$\begin{aligned} y_i = y_0 + rt_i &+ \mathrm{p}_{ann} * \sin(2\pi f_{ann} t_i) \\ &+ \mathrm{q}_{ann} * \cos(2\pi f_{ann} t_i) \\ &+ \mathrm{p}_{semi} * \sin(2\pi f_{semi} t_i) \\ &+ \mathrm{q}_{semi} * \cos(2\pi f_{semi} t_i) + \varepsilon_i \end{aligned} \qquad \text{Equation 3-12}$$

where y_i is the observation value of the time series at epoch i, y_0 is the linear trend intercept, r is the linear trend, t_i is the time at epoch i, $f_{ann} and\ f_{semi}$ are the frequencies of annual and semi-annual periodic signals (1 and 2 cycle/yr. respectively), the parameters $\mathrm{p}_{ann,}\ \mathrm{p}_{semi,}\ \mathrm{q}_{ann}$ and q_{semi} are related to the amplitude and phase shift of the annual and semi-annual periodic signals, and ε_i is the error term.

As can be seen from Equation 3-11, linear trend estimation is clearly affected by periodic signals within the time series. In terms of velocities based on long-term linear trend estimates, Blewitt & Lavallée (2002) presented Figure 3-3, and showed that velocity biases can become unacceptably large if a data span of less than 2.5 years is used, even if periodic signals are taken into account, and recommended that to minimise velocity biases, data spans of an integer-plus-half year span should be used, with a data span of more than 4.5 years, i.e. 4.5, 5.5, 6.5 years etc..

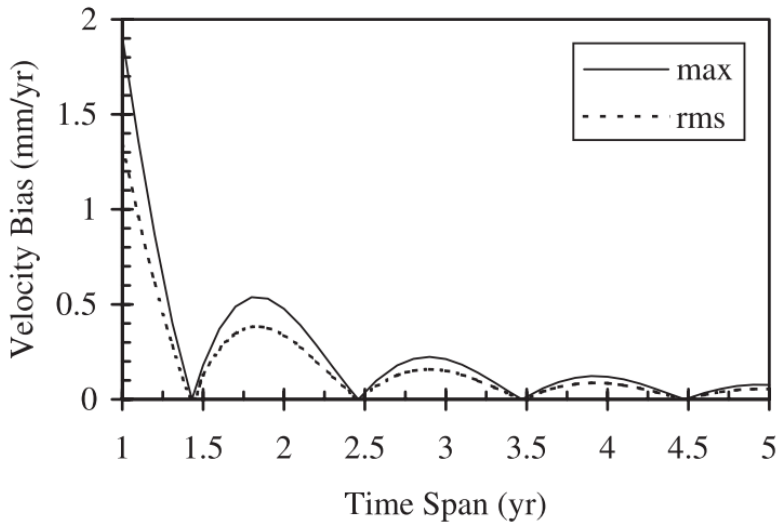


Figure 3-3: Velocity bias from an annual sinusoidal signal versus data span showing the maximum possible bias (max) and root mean square bias (RMS) (Blewitt and Lavallée 2002).

Moreover, it has been shown that careful consideration needs to be given to the uncertainties associated with long-term linear trend estimates (Williams 2003a), which are affected by sources of noise from satellite orbit errors, atmospheric delays, and loading effects that are not completely mitigated in GNSS processing, and long-term monument stability (Hackl et al. 2011).

The power-law process is commonly used to describe the noise in GNSS time series (Mao et al. 1999; Williams 2003a, 2004; Amiri-Simkooei et al. 2007; Klos et al. 2016) as described in Equation 3-12.

$$P_x(f) = P_0 \left(\frac{f}{f_0}\right)^k \qquad \text{Equation 3-13}$$

where f is the temporal frequency, P_0 and f_0 are normalising constants, and k is the spectral index, which equals 0, -1 and -2 in the cases of white noise (a random signal with a flat power spectral density), flicker/pink noise (a signal with a frequency spectrum such that the power spectral density is inversely proportional to the frequency), and random walk noise (a signal correlated to its previous states) respectively. Figure 3-4 illustrates a graphical representation of these three types of noise on the frequency spectrum.

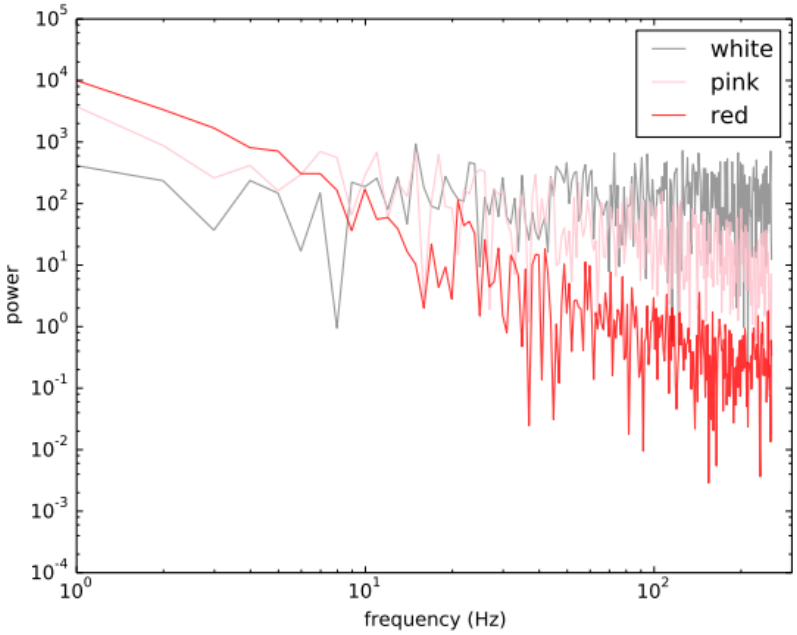


Figure 3-4: A graphical representation of white, flicker/pink, and random walk noises on the frequency spectrum using a log-log scale (Allen B. Downey 2014)

Accordingly, the uncertainties associated with long-term linear trend estimates differ based on the noise type assumed in the GNSS time series, as shown in the following equations (Williams 2003a):

$$\sigma_{\hat{r}_{white}} = \sqrt{\frac{12 * a^2}{\Delta T^2 * (N^3 - \mathrm{N})}} \qquad \text{Equation 3-14}$$

$$\sigma_{\hat{r}_{flicker}} = \sqrt{\frac{9 * b_{-1}^2}{16 * \Delta T^2 * (N^3 - \mathrm{N})}} \qquad \text{Equation 3-15}$$

$$\sigma_{\hat{r}_{RW}} = \sqrt{\frac{b_{-2}^2}{(N-1)\Delta T}} \qquad \text{Equation 3-16}$$

where N is the time series length, ΔT is the sampling rate, a is the magnitude of white noise, b_{-1} is the magnitude of flicker noise, and b_{-2} is the magnitude of random-walk noise.

In order to estimate the noise magnitudes, a and b_k, Equation 3-17 can be used (Williams 2003a):

$$\mathbf{C}_x = a^2\mathbf{I} + b_k^2\mathbf{J_k} \qquad \text{Equation 3-17}$$

where $\mathbf{C}_x$ is the covariance matrix for the measurements y_i, $\mathbf{I}$ is the identity matrix, and $\mathbf{J_k}$ is the covariance matrix for the appropriate coloured noise which is computed by means of fractional differencing.

Alternatively, the noise magnitudes, a and b_{-1} can be calculated empirically using the following equations that are a function of the WRMS of a de-trended GNSS time series (Zhang et al. 1997; Williams 2003a).

$$a(N) = 0.613 * WRMS(N) + 0.259 \qquad \text{Equation 3-18}$$

$$a(E) = 0.767 * WRMS(E) - 0.183 \qquad \text{Equation 3-19}$$

$$a(H) = 0.843 * WRMS(H) - 1.772 \qquad \text{Equation 3-20}$$

$$b_{-1}(N) = 1.139 * WRMS(N) + 0.117 \qquad \text{Equation 3-21}$$

$$b_{-1}(E) = 1.041 * WRMS(E) - 0.342 \qquad \text{Equation 3-22}$$

$$b_{-1}(H) = 0.668 * WRMS(H) + 5.394 \qquad \text{Equation 3-23}$$

3.2.2 Offset Estimation and Detection in Long-Term GNSS Time Series

It is almost inevitable that GNSS time series become contaminated by offsets (and outliers). Williams (2003a) suggested that an offset typically occurs about every 9 years and Gazeaux et al. (2013) suggested that, in the case of SOPAC, offsets were mostly due to: equipment (receiver and antenna) changes; seismic events; or unknown reasons as shown in Figure 3-5.

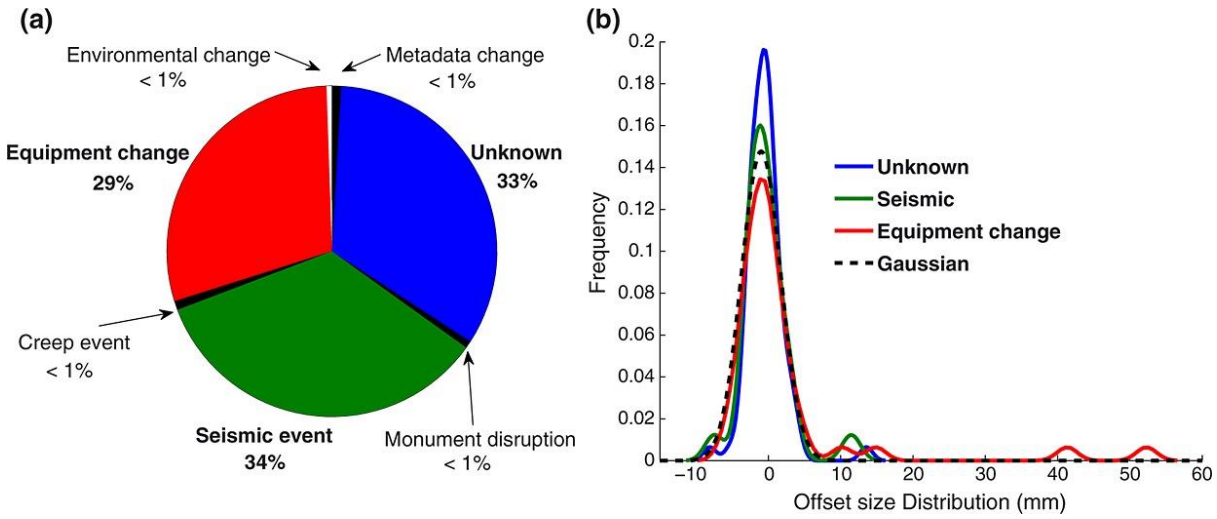


Figure 3-5 SOPAC offsets (a) description and (b) magnitude distribution since 1995 for over 340 sites (560 offsets) (Gazeaux et al. 2013).

If not corrected for, such offsets have a general effect to decrease the accuracy and reliability of time series analysis, including linear trend estimation and noise analysis. Moreover, depending on its nature, an un-corrected offset may not only affect the time series in which it exists, but its effect may propagate from one station to another via the processing, network adjustment or realization of the reference frame (Williams 2003b).

Estimating the Magnitude of Offsets in GNSS Time Series

If the epoch at which an offset occurred is known, for example if it is related to an equipment change or a seismic event, it is possible to estimate the magnitude of the offset. For this, the weighted mean method is considered the most common and follows the form of Equation 3-12 but with taking into consideration the offsets as shown in the following Equations 3-23 and 3-24 (Williams 2004; Montillet et al. 2015).

$$\begin{aligned} y_i \;=\; y_0 + rt_i \;+ \boldsymbol{op_i} &+ \mathrm{p}_{ann} * \sin(2\pi f_{ann} t_i) \\ &+ \mathrm{q}_{ann} * \cos(2\pi f_{ann} t_i) \\ &+ \mathrm{p}_{semi} * \sin(2\pi f_{semi} t_i) \\ &+ \mathrm{q}_{semi} * \cos(2\pi f_{semi} t_i) + \varepsilon_i \end{aligned} \qquad \text{Equation 3-24}$$

$$\sigma_{\hat{x}_{off}} = \sqrt{\frac{a^2 * N * (N^2 - 1)}{M(N^3 - N - 4 * N^2 * M + 6 * N * M^2 - 3 * M^3 + M)}} \qquad \text{Equation 3-25}$$

where y_i is the observation value of the time series at epoch i, y_0 is the linear trend intercept, r is the linear trend, t_i is the time at epoch i, o is the magnitude of the offset, p_i is the Heaviside function (p_i =1 if $t_i \geq t_{offset}$ and $p_i = 0$ elsewhere), $f_{ann} and\ f_{semi}$ are the frequencies of annual and semi-annual periodic signals (1 and 2 cycle/yr. respectively), the parameters $p_{ann,}\ p_{semi,}\ q_{ann}$ and q_{semi} are relate to the amplitude and phase shift of the annual and semi-annual periodic signals, ε_i is the error term, $\sigma_{\hat{x}_{off}}$ is the uncertainty associated with the offset estimate, a is the magnitude of white noise, N is the time series length, and M = $\sum_{i=1}^{N} p_i$.

On the other hand, the mean method is another way to estimate the magnitude of an offset by simply averaging the time series for a few weeks before and after the epoch at which the offset occurred, and then subtracting the mean values from each other (Blewitt 1993; Bock et al. 2004). This method is fast and simple which makes it suitable for real-time analysis. However, the uncertainties of the offset estimates are usually larger than those obtained using the weighted mean method (Montillet et al. 2015).

Detecting the Time of Occurrence of Offsets in GNSS Time Series

If the epoch at which an offset occurred is not known, for example if it is related to an unknown reason, it is also possible to attempt to detect the time of occurrence of the offset (Williams 2003b). Clearly automated techniques for this would be preferable and there have been various proposed and tested, including: the likelihood maximization approach with different penalty functions (Picard et al. 2005); a shifting means Hidden Markov Model approach (Kehagias et al. 2006); FODITS (Find Outliers and Discontinuities in Time Series) which is a detection tool integrated within the Bernese GNSS Software (Ostini et al. 2008); and the Sequential t-test Analysis of Regime Shifts (STARS) Bruni *et al.*, (2014).

Gazeaux *et al.*, (2013) illustrated several different techniques (manual and automated) to detect the time of occurrence of offsets in GNSS time series, and showed that manual methods almost always give better results than automated or semi-automated

methods, but are reliant on visual inspection of the GNSS time series. Figure 3-6 illustrates the offsets detected by the best method, SDPWMANL, as concluded by Gazeaux *et al.*, (2013), which happens to be a manual method and the worst method, MAK2PIEE, as concluded by Gazeaux *et al.*, (2013), which happens to be an automated method. The study also concluded that most of the automated techniques work well in terms of detecting the times of occurrence of the largest offsets while the weak point of most was the high rate of false positives (i.e. detecting an offset that was not simulated).

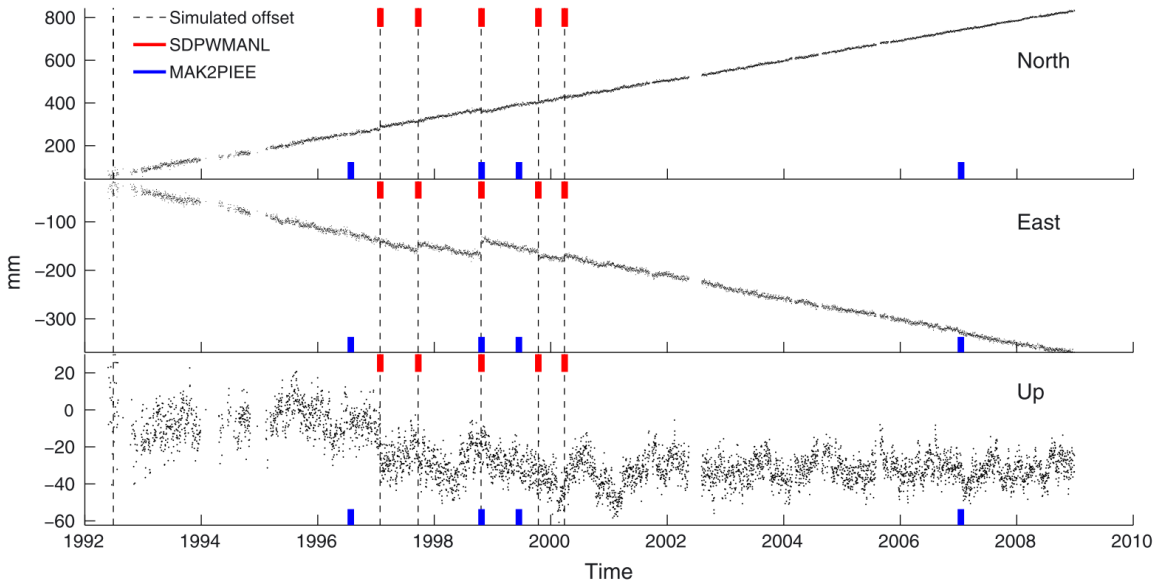


Figure 3-6 A simulated GPS daily coordinate time series. The vertical dashed black lines show dates of simulated offsets. The red and blue markers represent, respectively, the offsets detected by two different methods (SDPWMANL and MAK2PIEE).

3.3 Summary

This chapter introduced the use of parametric and non-parametric models as ways to extract the temporal dependency from a time series. It was discussed how non-parametric models (e.g. the use of an Artificial Neural Network) can be considered as being more flexible as they do not require a prior assumption about the structure of the function used. The chapter also discussed how GNSS time series are analysed temporally showing how the extraction of the temporal dependency can be used to estimate the linear trend as well as to detect and/or estimate offsets in long-term GNSS time series. These provide the

background for Chapter 5, where the specific methodology used in this research is developed.

The next chapter will further consider the general nature of such GNSS time series, not in terms of their temporal dependency, but in terms of their spatial dependency.

CHAPTER 4: SPATIAL DEPENDENCY

In this chapter, the concept of spatial dependency and its application in GNSS time series will be discussed. The first section (section 4.1) introduces the concept of spatial dependency and the most common methods used to model it, by assessing the spatial correlation in a dataset and building spatial regression models. Then, in section 4.2, spatial dependency in GNSS time series is illustrated highlighting the applications discussed in previous literature.

4.1 Modelling the Spatial Dependency

With spatial dependency, a variable is a function of space as its observation value in one location is related to the observation values of that variable in other locations (Fischer and Nijkamp 2014; Thanos et al. 2016). Tobler (1970) defines spatial dependency as "everything is related to everything else, but near things are more related than distant things". This spatial relationship between locations is expressed by the so-called "spatial weights matrix" which represents the spatial influence of the locations of observed values relative to each other. Spatial weights are based on the distances between the locations of these observation values, which may be expressed as 'Power Distance Weights' (Equation 4-1), 'Exponential Distance Weights' (Equation 4-2), or 'Radial Distance Weights' (Equation 4-3):

$$w_{ij} = \frac{d_{ij}^{-\alpha}}{\sum_{j \neq i} d_{ij}^{-\alpha}} \qquad \text{Equation 4-1}$$

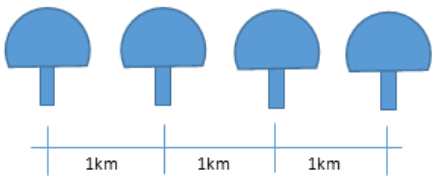
$$w_{ij} = \frac{e^{-\alpha d_{ij}}}{\sum_{j \neq i} e^{-\alpha d_{ij}}} \qquad \text{Equation 4-2}$$

$$w_{ij} = \begin{cases} 1 & 0 \leq d_{ij} \leq d \\ 0 & d_{ij} > d \end{cases} \qquad \text{Equation 4-3}$$

where w_{ij} is the spatial weight which reflects the spatial influence of an observation at a location j on the desired location i, d_{ij} is the Euclidean distance between location j and location i, and $\boldsymbol{\alpha}$ is the distance exponent value which identifies the 'distance decay

function'. The $\boldsymbol{\alpha}$ value ranges between 1 to 3 (de Mesnard 2013) to reflect linear (Neidell 2004), parabolic (Fann et al. 2012) and cubic (Bell 2006) decay functions respectively, n is the number of observed locations, and d is a cap distance (i.e. threshold distance).

Even though selecting between these equations objectively is still a pending question which remains to be resolved, the Power Distance Weights (Equation 4-1) is the most common decay function used (Getis 2009; Dubé and Legros 2011; Seya et al. 2013; Shen et al. 2016). Moreover, Chen (2012) concluded that the use of Power Distance Weights is suitable for complex and large-scale systems, while the Exponential Distance Weights is more suitable for simple and small-scale systems with local correlation. He also suggested that if the geographical phenomenon is local, the Radial Distance Weights may suffice. In any case it is important to note that the spatial weight matrix is a symmetrical hollow matrix; it is symmetrical as $\boldsymbol{w_{12} = w_{21}}$ since $\boldsymbol{d_{12} = d_{21}}$, and it is hollow as the weight between a location and itself is always set to zero, i.e. $\boldsymbol{w_{ii} = 0}$. Figure 4-1 shows an example of the spatial weight matrix for 4 stations using Equation 4-1 with $\alpha = 1$.



$$D = \begin{bmatrix} 0 & 1.0 & 2.0 & 3.0 \\ 1.0 & 0 & 1.0 & 2.0 \\ 2.0 & 1.0 & 0 & 1.0 \\ 3.0 & 2.0 & 1.0 & 0 \end{bmatrix} \quad W = \begin{bmatrix} 0 & 0.6 & 0.3 & 0.1 \\ 0.4 & 0 & 0.4 & 0.2 \\ 0.2 & 0.4 & 0 & 0.4 \\ 0.1 & 0.3 & 0.6 & 0 \end{bmatrix}$$

Figure 4-1 The distance and spatial weight matrix of 4 stations located on a line with a 1km distance in between each location using Equation 4-1 with $\alpha = 1$

The spatial dependency concept lays the foundation for almost all aspects concerning spatial analysis including: spatial interpolation models; spatial autocorrelation indices; and spatial regression models. In the following sub-sections, the basic concepts behind each one of these models are illustrated.

4.1.1 Spatial Interpolation Models

Spatial interpolation is a way of estimating the observation value at a desired location from a limited number of georeferenced observation values at other locations, where actual

observation values are not available at the certain location. It is used extensively in Engineering Surveying, for example to estimate the elevation at a desired location based on the elevations at other locations in a geodetic network. Shepard's method, which is also known as 'Inverse Distance Weighting' (IDW) (Shepard 1968; Dobesch et al. 2007; Yao et al. 2013), and 'Kriging' (Krige 1952; Oliver and Webster 1990; Jeffrey et al. 2001; Govaerts and Vervoort 2010; Yao et al. 2013) are the most common models used for this purpose.

In IDW, more importance is attributed to the closer points, which can be seen as an application of Tobler's law (Tobler 1970). A weight is assigned to an observation value based on the inverse of the distance between the location of that observation value and the desired location for the estimated observation value, with consideration of a specific $\boldsymbol{\alpha}$ value (Equation 4-1). Then, to estimate the observation value at the desired location, each observation value is multiplied by its corresponding weight (Equation 4-4).

$$y_i = \sum_{j=1}^{n} w_{ij} y_j \qquad \text{Equation 4-4}$$

where y_i is the observation value to be estimated at a desired location i, y_j is the actual observation value at another location j, w_{ij} is the spatial weight, and n is the number of other locations.

Kriging, on the other hand, avoids the arbitrary nature of IDW by choosing the right value of the distance exponent $\boldsymbol{\alpha}$ and linking the variation of observation values to their distances in a relation called a "semi-variogram" (Zimmerman and Zimmerman 1991; Zhang et al. 1995; Carr and De Miranda 1998).

Kriging has the same general form of Equation 4-4, but the weights are derived more objectively based on the distance between the other locations with actual observation values and the desired location for the estimated observation value, as well as the overall spatial correlation of the locations using a least-squares approach to minimize the variance

of error between the estimated value and the true value at a location, which makes it a very complicated and computationally-heavy (Pesquer et al. 2011; de Mesnard 2013).

So, even though spatial interpolation models are very useful in generating continuous data from a limited number of actual observation values, they do not state to what extent the data is spatially correlated. Spatial autocorrelation indices, on the other hand, do.

4.1.2 Spatial Autocorrelation Indices

Spatial autocorrelation indices are used to describe the overall spatial correlation between georeferenced observation values. Geary's index (Geary 1954) and Moran's index (Moran 1950) are the most common forms of spatial autocorrelation indices used in the literature (Assunção and Reis 1999; Da Silva et al. 2008; Moons et al. 2009; Song et al. 2011; Chen 2013; Fischer and Nijkamp 2014).

Spatial autocorrelation indices start with the null hypothesis that the data are random and have no spatial correlations. Rejecting this Null hypothesis means that there is a spatial structure (i.e. a correlation) within the observation values, considering the inverse of the distance in generating the spatial weights matrix (Equation 4-1). Spatial autocorrelation indices use the general matrix cross-product statistic (Hubert et al. 1981): Moran's index considers the deviation of the observation values of a variable at two locations i and j from the mean (Equation 4-5); while Geary's index considers the squared differences of the value at locations i and j (Equation 4-6).

$$I = \frac{N \sum_i \sum_j w_{ij} (y_i - \bar{y})(y_j - \bar{y})}{\sum_i \sum_j w_{ij} \sum_i (y_i - \bar{y})^2} \qquad \text{Equation 4-5}$$

$$C = \frac{(N-1) \sum_i \sum_j w_{ij} (y_i - y_j)^2}{2 \sum_i \sum_j w_{ij} \sum_i (y_i - \bar{y})^2} \qquad \text{Equation 4-6}$$

Spatial autocorrelation indices are effective tools to examine the spatial correlation in a set of georeferenced observation values. However, they are limited to this purpose and considered as a diagnostic tool rather than a modelling tool. Spatial regression, on the other hand, can be used in modelling the spatial dependencies.

4.1.3 Spatial Regression Models

Spatial regression models can be seen as an extension to the Ordinary Least-Squares (OLS) model which takes into account spatial dependency by exploring the relationship between dependent and independent variables of georeferenced locations. Equations 4-7 and 4-8 below show the most general form of the spatial regression model, namely 'the Manski (1993) Model'.

$$Y = \rho \boldsymbol{W} Y + \boldsymbol{X}\beta + \boldsymbol{W}\boldsymbol{X}\theta + u \qquad \text{Equation 4-7}$$

$$u = \lambda \boldsymbol{W} u + \varepsilon \qquad \text{Equation 4-8}$$

where Y is a N × 1 vector of observation values across space, ρ is the so-called "spatial autoregressive coefficient" to be estimated using Maximum Likelihood Estimation (MLE) (LeSage 2008; Elhorst 2010), W is an $N \times N$ matrix describing the spatial arrangement of the spatial units in the sample, X is a $N \times k$ matrix which describes the explanatory variables, β, just as for θ, represents a $K \times 1$ vector of fixed but unknown parameters, u are the spatial residuals, λ is the spatial autocorrelation coefficient, and ε are the spatial residuals when assumed to be white noise. While, w_{ij} is the spatial weight which reflects the spatial influence of unit j on unit i, d_{ij} is the Euclidean distance between unit j and unit i, and $\boldsymbol{\alpha}$ is the distance exponent value which identifies the distance decay function.

Collectively, the studied values, Y, are a function of: internal interaction effects, $\rho \boldsymbol{W} Y$; external interaction effects, $\boldsymbol{W}\boldsymbol{X}\theta$; and correlated effects, $\lambda \boldsymbol{W} u$, which consider the effect of any unobserved explanatory variables by correlating the residuals spatially. In addition to the spatial dependency, the Manski (1993) model also takes into consideration the explanatory variables, $\boldsymbol{X}\beta$, at each spatial unit (Elhorst 2010). The spatial dependency is expressed by a function of the relative distance between the locations of the spatial units, which is known as the spatial weights matrix, $\boldsymbol{W}$ (Getis 2009; Dubé and Legros 2011; Seya et al. 2013; Shen et al. 2016).

As an example of applying the Manski (1993) model in studying the Integrated Water Vapour (IWV) values, the values of IWV at each station in the GNSS network, Y, may be seen as a function of: internal interaction effects between the IWV value at a station and the IWV values at the surrounding stations taking into consideration the spatial weights assigned to each station, $\rho \boldsymbol{W} Y$; external interaction effects between the IWV at a station and any explanatory variables (e.g. temperature or pressure) at the surrounding stations with the consideration of the spatial weights assigned to each station, $\boldsymbol{W}\boldsymbol{X}\theta$; the effects between the IWV at a station and the explanatory variables at that station, $\boldsymbol{X}\beta$; and the effect of any unobserved explanatory variables which may appear in the residuals, $\lambda \boldsymbol{W} u$.

From the Manski (1993) model, different simplified versions can be derived based on the purpose of the analysis. For example, by assuming that there is no internal interaction, $\rho \boldsymbol{W} Y$, the 'Spatial Durbin Error model' is derived, while the 'Kelejan-Preucha model' is used when no external interaction, $\boldsymbol{W}\boldsymbol{X}\theta$, is assumed. Table 4-1 shows a variety of different spatial regression models based on the Manski (1993) model, and the least squares model.

Table 4-1 Different spatial regression models based on the Manski (1993) model, and the least squares model (Elhorst 2010).

$\rho = 0$	$Y = \boldsymbol{X}\beta + \boldsymbol{W}\boldsymbol{X}\theta + u$ $u = \lambda \boldsymbol{W} u + \varepsilon$	Spatial Durbin Error model
$\theta = 0$	$Y = \rho \boldsymbol{W} Y + \boldsymbol{X}\beta + u$ $u = \lambda \boldsymbol{W} u + \varepsilon$	Kelejan-Preucha model
$\lambda = 0$	$Y = \rho \boldsymbol{W} Y + \boldsymbol{X}\beta + \boldsymbol{W}\boldsymbol{X}\theta + \varepsilon$	Spatial Durbin model
$\rho = 0, \theta = 0$	$Y = \boldsymbol{X}\beta + u$ $u = \lambda \boldsymbol{W} u + \varepsilon$	Spatial Error model
$\theta = 0, \lambda = 0$	$Y = \rho \boldsymbol{W} Y + \boldsymbol{X}\beta + \boldsymbol{W}\boldsymbol{X}\theta + \varepsilon$	Spatial Lag model
$\beta = 0, \theta = 0, \lambda = 0$	$Y = \rho \boldsymbol{W} Y$	Spatial AutoRegressive model
$\rho = 0, \beta = 0, \theta = 0, \lambda = 0$	$Y = \boldsymbol{X}\beta + \varepsilon$	Least squares model

Considering Table 4-1, it is clear that spatial regression models are adaptable to the purpose of the study and the available data, which makes them very effective for different case studies.

4.2 Spatial Analysis of GNSS Time Series

It was suggested by Williams et al. (2004) and Amiri-Simkooei (2009) that part of the noise in the GNSS coordinate time series of any pair of nearby GNSS stations are correlated. However, despite this, the use of spatial analysis of GNSS coordinate time series is not as common in previous literature as the use of temporal analysis (Bock and Melgar 2016), and spatial analysis is typically limited to the removal of a so-called "common-mode error" (CME) within a regional network of stations, by averaging techniques operated on the residual time series (i.e. after 'cleaning' the GNSS coordinate time series for outliers and offsets, and removing any long-term linear trends). All of the averaging techniques are seen as a development of a method called "stacking" (Equation 4-9), which was first introduced by Wdowinski et al. (1997), or "weighted stacking" (Equation 4-10) as used by Nikolaidis (2002) (Figure 4-2).

$$CME_t^i = \frac{\sum_{i=1}^{n} R_t^i}{n} \qquad \text{Equation 4-9}$$

$$CME_t^i = \frac{\sum_{j=1}^{n} \frac{R_t^i}{\sigma_i^2}}{\sum_{j=1}^{n} \frac{1}{\sigma_i^2}} \qquad \text{Equation 4-10}$$

where CME_t^i is the common-mode error at a station i at time t, R_t^i is the coordinate residual for the station i at time t, σ_i^2 is the inverse of the square of the RMS of the station coordinate, and n is the number of stations.

Here it should be mentioned that the stacking and weighted stacking techniques do not introduce any spatial weighting based on the distances between the stations, but are based solely on an averaging process. However, more recent studies have used spatial weighting instead of the averaging processes: Gruszczyński et al. (2015), for example, removed the CME by dividing the local GNSS networks into concentric ring-shaped areas and correlating the stations according to their distances from the network barycentre (Equations 4-11) and is illustrated in Figure 4-3 ; while Tian and Shen (2016) introduced another similar technique to remove the CME, namely, 'Weighted Spatial Filtering' (WSF) which introduces

the spatial correlation between two stations as a function of Lin's concordance correlation coefficient, based on the correlation between the residuals of the stations and the square radial distance between these stations, as shown in Equations 4-11, 4-12 and 4-13 and illustrated in Figure 4-4.

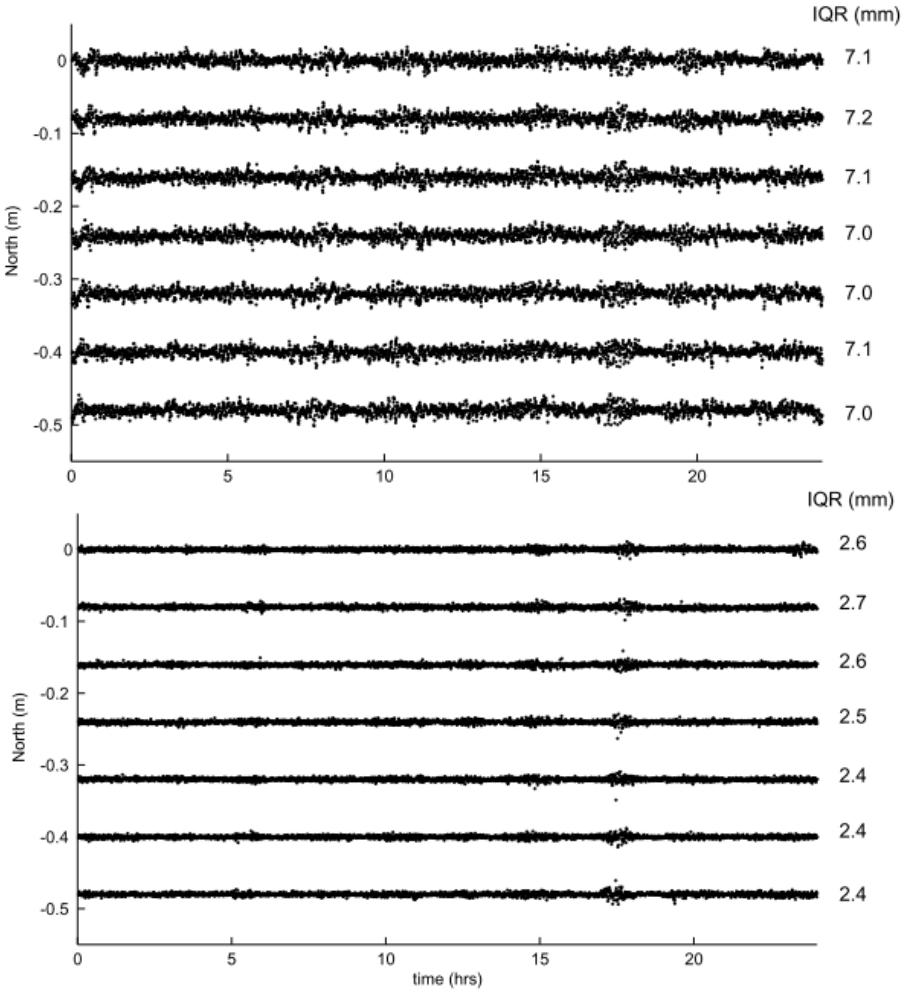


Figure 4-2 The ΔN time series for 7 stations before (up) and after (bottom) removing the CME using the weighted stacking method. The interquartile range (IQR) describes the scatter of data about the median for each day (Nikolaidis 2002)

$$CME_t^i = \frac{\sum_{i=1}^{n} \frac{R_t^i}{l_i}}{\sum_{i=1}^{n} \frac{1}{l_i}} \qquad \text{Equation 4-11}$$

$$CME_t^i = \frac{\sum_{i=1}^{n} \frac{R_t^i}{\sigma_i^2} \times w_{ij} \times r_{ij}}{\sum_{i=1}^{n} \frac{1}{\sigma_i^2} \times w_{ij} \times r_{ij}} \qquad \text{Equation 4-12}$$

$$w_{ij} = e^{-\left(\frac{d_{ij}^2}{\tau_i^2}\right)} \qquad \text{Equation 4-13}$$

where CME_t^i is the common-mode error at station i at time t, R_t^i is the coordinate residual for the station i at time t, l_i is the distance from the network barycentre to station i, σ_i^2 is the inverse of the square of the RMS of the station coordinate, w_{ij} is the spatial weight between stations i and j, r_{ij} is Lin's concordance correlation coefficient between stations i and j, d_{ij} is the distance between stations i and j, and τ_i is a distance weighting constant to regulate weighting by distance between n stations.

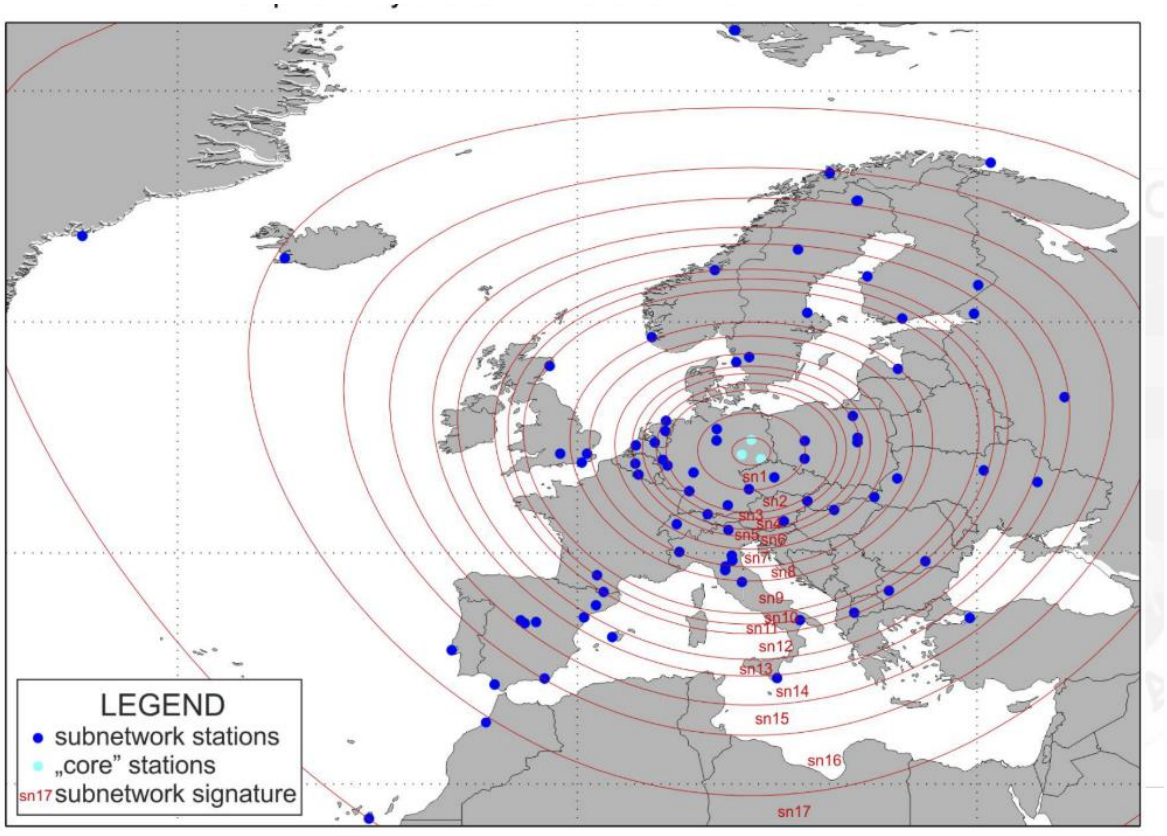


Figure 4-3 The analysed network consisted of 88 permanent stations unevenly distributed all over Europe and adjacent areas. Stations are divided into 17 ring-shaped subnetworks. Three "core" stations are located near to the centre of rings (network barycentre)(Gruszczynski et al. 2015).

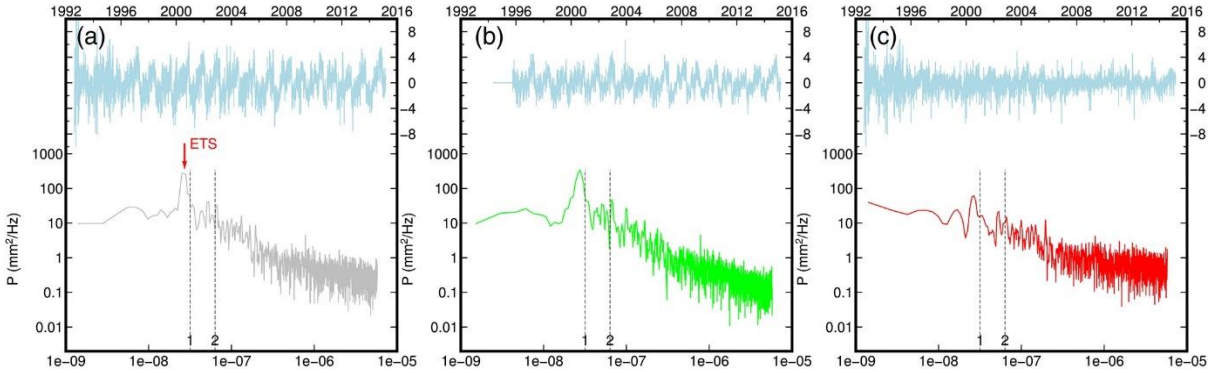


Figure 4-4 (a) The raw time series of the ΔE component in mm (light blue) and its spectral analysis (grey) (b) the spatially correlated term CME (light blue) and its spectral analysis (green) ; (c) the filtered residual time series after the subtraction of CME contributions (light blue) and its spectral analysis (red). The arrow in Figure a points to the frequency peak of Cascadia episodic tremor and slip (ETS) events. The vertical dashed lines indicate harmonics of 1 and 2 cpy (Tian and Shen 2016).

However, correlating with r_{ij} (Equation 4-11) may be seen as having the effect of future days affecting the past, as whole time series are used to estimate r_{ij} . Consequently, the CME_{t-p}^{i} (where $0 < p < t$) will be affected by the coordinates from the time interval $[p - t]$ as it is embedded in the r_{ij} estimation. Furthermore, by comparing the Tian and Shen (2016) technique to spatial regression techniques, it can be seen that in the latter, y_i is regressed with its neighbouring station y_j epoch by epoch, which prevents past data being affected by future data. Moreover, by having the fact that ρ is one estimated value for all stations, spatial regression can be seen as a balance between the overall strength of spatial dependencies, represented by ρ, and the relative strength of individual stations, represented by $\boldsymbol{w_{ij}}$ (LeSage 1998).

Moreover, in GNSS time series, spatial regression models are preferred to spatial interpolation models due to the fact that the measured value at a location will only be reflected in the estimated coefficient, ρ , but not in the estimated observation value, $\hat{y}_i$. While in spatial interpolation models, the estimated observation value at a location will be mostly affected by the measured value at that location, which in turn makes that estimation biased; in other words, if a station's measured observation value is anomalous, the estimated observation value at that station will be closer to that anomalous value, and consequently the anomaly may be masked. Furthermore, spatial regression models are

preferred to spatial autocorrelation indices as the latter provide an overall index measuring the degree of spatial influence exerted by something over its neighbours (Fischer and Nijkamp 2014) with no site-specific estimation of the observation value, while the former provides both.

As discussed earlier in Chapter 2, there are other ways to add spatial capabilities into analysis used to detect/analyse geohazards (especially earthquakes) using GNSS networks (Crowell et al. 2009; Grapenthin and Freymueller 2011; Psimoulis et al. 2018b). However, in those studies the spatial analysis was used solely for assessing the relative displacement between stations (Crowell et al. 2009), or for filtering outliers (Psimoulis et al. 2018b), rather than for analysing the spatial dependency between stations, as discussed in this chapter.

4.3 Summary

In this chapter, the concept of spatial dependency and the most common tools used to extract it were discussed and it was illustrated that, amongst the various spatial dependency models, spatial regression models give station-specific estimations (which autocorrelation models do not); are simple (when compared to spatial interpolation models); and can be extended using exogenous variables. Due to these reasons, spatial regression models were selected to be a part of the specific methodology used in this research, which is detailed in Chapter 5. Moreover, this chapter also showed that spatial analysis of GNSS coordinate time series is not very common in previous literature and, therefore, its consideration alongside temporal analysis in the specific methodology used in this research is somewhat novel.

The next chapter details the development of the specific methodology used in this research, which is based on the use of multiple algorithms to analyse GNSS time series.

CHAPTER 5: THE DEVELOPMENT OF A MULTIPLE ALGORITHM APPROACH TO THE ANALYSIS OF GNSS TIME SERIES

In this chapter, the methodology used in the development of a multiple algorithm approach to the analysis of GNSS time series will be illustrated. The first section (Section 5.1) shows where this new methodology stands in relation to other methods in the previous literature which were discussed in previous chapters. Then, the five main steps of this methodology are presented in the following sections (Sections 5.2 to 5.6) showing how the temporal, spatial and combined analysis algorithms fit into this approach.

5.1 The Concept of the Multiple Algorithm Approach

As discussed in the previous chapters, the majority of previous studies have involved the analysis of GNSS time series individually (i.e. station by station) without considering the whole GNSS network in the analysis process (see Chapter 3), apart from a few previous studies which have considered the spatial dependency between stations to remove the so-called common-mode error (CME) (Nikolaidis 2002; Gruszczynski et al. 2015; Tian and Shen 2016) as presented in Chapter 4. Other previous studies, on the other hand, have added some spatial capabilities to their analysis in detecting/analysing earthquakes (see Chapter 2). Nevertheless, these spatial capabilities were limited to spatial checking and the filtering of false alarms and outliers (Psimoulis et al. 2018b), or assessing the change in the relative displacement between stations (Crowell et al. 2009). The aim of this chapter is to develop a multiple algorithm approach to the analysis of GNSS time series that takes into consideration both temporal and spatial dependencies.

The main concept of this approach is to model the normal and expected behaviour of the temporal and spatial dependencies of the GNSS time series. Then, to assess the difference between these modelled expected behaviours and the actual GNSS time series.

More specifically, in the temporal analysis algorithm, an Artificial Neural Network (ANN) is used to extract the temporal dependency of the GNSS station time series from its time-history; such that, any station that then behaves differently to its previous time-history will be considered as exhibiting anomalies. On the other hand, the spatial autoregressive model is used for the spatial analysis algorithm, assuming that the GNSS time series from a network of stations are spatially dependent; consequently, any station that behaves differently to its surrounding stations will be considered as exhibiting anomalies. Finally, for the combined analysis algorithm, the two above methods of the temporal and the spatial analysis algorithms are adjusted and combined. In this latter approach, the GNSS time series will be analysed not only regarding the time-history of the corresponding stations but also their spatial relationship, leading to a new perspective in GNSS network applications.

In the following sections, the proposed multiple algorithm approach will be separated into five main steps, as illustrated in Figure 5-1, namely: [1] data segmentation, where the data will be split into a training dataset and a testing dataset; [2] the correction of offsets due to documented changes, which is an essential step for accurate linear trend estimations; [3] estimation of the main characteristics of the training dataset; [4] application of the multiple algorithm approach on the training dataset; and finally, [5] application of the multiple algorithm on the testing dataset.

The first three steps are essential as they lead to 'clean' time series which are then used in the later steps. It is also worth mentioning that other geodetic time series analysis software packages, e.g. Create and Analyze Time Series software, CATS (Williams 2008), Hector (Bos et al. 2013), and est-noise (Langbein 2008) only cover the first three steps and essentially enable offset correction and noise analysis, in order to provide linear and periodic trend estimates. The fourth and fifth steps, therefore, are seen as an improvement on these software packages; with the fourth and fifth steps being the core steps of this proposed multiple algorithm approach as the temporal, spatial and combined analysis algorithms are applied on the training dataset and the testing dataset respectively.

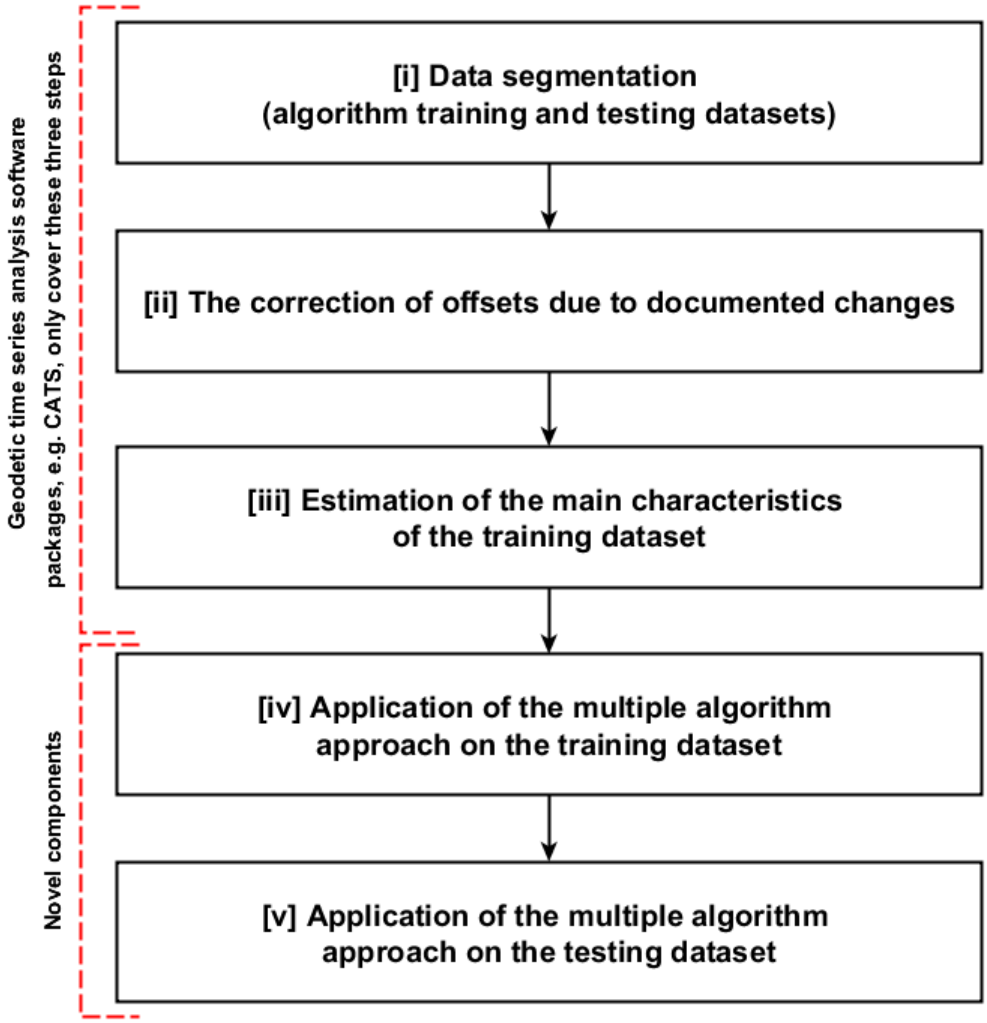


Figure 5-1 A flowchart of the five main steps used in the proposed multiple algorithm approach

5.2 Data Segmentation

In conventional GNSS time series analysis, concerned with detecting anomalies and outliers, the whole time series is analysed to extract the descriptive statistics which are then used in the later decision process (Box et al. 2013). These methods suit applications which assume that these estimated descriptive statistics are constant throughout the lifespan of the GNSS time series. Moreover, they suit applications concerning post-processing analysis rather than real-time analysis.

More advanced methods have been used in GNSS time series analysis, to extract and compare the descriptive statistics of two sliding windows, usually long-term and short-

term windows, for a more realistic temporal analysis (Allen 1978; Ohta et al. 2012; Psimoulis et al. 2018b). Yet, in most of these methods, the short term window is a sub-group of the long-term window, which makes the descriptive statistics of the former embedded in the descriptive statistics of the latter, and any decisions based on this performance may be biased. In computer science machine learning studies (Peralta et al. 2010; Fu 2011; Adhikari and Agrawal 2013), on the other hand, data is usually split into two separate datasets, a training dataset and a testing dataset. The training dataset is then used to extract the characteristics embedded in it while the testing dataset is left as an independent dataset (i.e. also called "unseen" or "out of sample" data) used only to evaluate the model.

Following the same strategy, in the proposed multiple algorithm approach the GNSS time series will be chronologically split into two datasets, i.e. an algorithm training dataset and an algorithm testing dataset. Whereby the training dataset will be assumed to be the reference to which the testing dataset is compared. On the one hand, this prevents the testing dataset from affecting the training dataset. On the other hand, it mimics the scenario of running the multiple algorithm approach in real-time as the algorithm will be tested using unseen data.

Since the training dataset is assumed to represent the expected normal behaviour of a GNSS station it should be, or at least assumed to be, anomaly-free. Moreover, it should also represent 70%-80% of the entire dataset (Crowther and Cox 2005; Lean Yu et al. 2006). Then, through time, it is possible to extend the training dataset by including new data, as long as this represents expected normal behaviour.

This concept should be appealing to administrators of new GNSS networks as the first period of a GNSS station's lifespan (represented by the training dataset) is usually less vulnerable to wear and tear problems (e.g. antenna corrosion) than the years to follow (represented by the testing dataset).

Figure 5-2 shows the ΔE component of the GPS coordinate time series of SHOB station in BIGF network along with the epoch representing the end of the training dataset (blue-dashed line) and the epochs of any documented changes (magenta-dashed line) which will be dealt with in the next section.

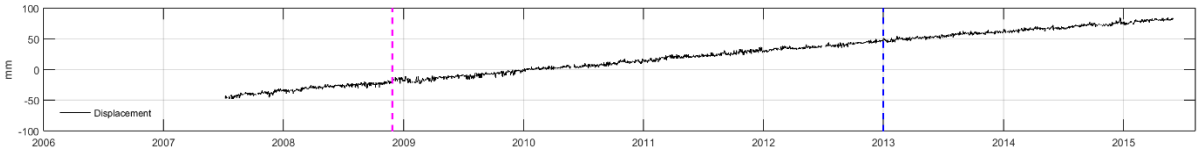


Figure 5-2 The GPS coordinate time series of SHOB station (ΔE component). Where the blue-dashed line represents the end of the training dataset and the magenta-dashed line shows the epoch of a documented change.

5.3 Correction of Offsets due to Documented Changes

As discussed in sub-section 3.2.2 in Chapter 3, the presence of offsets in GNSS coordinate time series can have a negative effect on the accuracy and the reliability of the time series analysis, as well as the velocity, estimates that are based on a linear trend. Therefore, any offsets due to documented changes should be corrected. For this purpose, two methods are used and examined in this research, referred to as the 1st and 2nd offset correction approaches, as illustrated in Figure 5-3.

5.3.1 The 1st Offset Correction Approach

In the 1st offset correction approach, the conventional use of the weighted mean method (Equation 3-24 in Chapter 3) (Williams 2003b; Montillet et al. 2015) is applied to the whole dataset in order to correct the offsets in both the training and testing datasets.

This offset correction approach assumes that the station performs consistently throughout its lifespan. However, this is not always the case (Griffiths and Ray 2016) as sometimes the station has a degradation in its performance due to site-specific reasons (e.g. antenna corrosion, or monumentation instability), or due to larger-scale reasons (e.g. water pumping). Clearly, these potential reasons violate the assumption

that the station behaves consistently throughout its lifespan. Moreover, Montillet *et al.* (2015) suggested that for an accurate offset estimate, at least 2 years of data after the offset are required, which makes this method less suitable for real-time analysis. Therefore, in addition to this approach, a 2nd offset correction approach is proposed and used in this research.

5.3.2 The 2nd Offset Correction Approach

The 2nd offset correction approach first applies the weighted mean method on the training dataset, in order to correct any documented offsets within. This approach assumes that the station only performs consistently throughout its training dataset, which agrees with the concept of data segmentation discussed in Section 5.2. As a result, the testing dataset will not influence the training dataset by any means and this approach should be more suitable than the 1st offset correction approach for real-time applications.

Then, if there are any offsets due to documented changes in the testing dataset, the estimated linear trend from the training dataset is extended to detrend windows of n-days before and after the epoch of the documented change, and then the mean values are subtracted from each other, which may be seen as a development on the conventional averaging method (Blewitt 1993; Bock et al. 2004; Montillet et al. 2015). The width of these windows, n, is subject to the data availability and how close the analysis is to a real-time scenario. In this research, a window of 30 days was used when dealing with long-term GNSS coordinate time series.

In both approaches, if the training or testing datasets have offsets due to documented changes, they will be shifted accordingly. This resultant 'corrected' time series will then be used in the next step.

The underlying reason behind using both offset correction approaches, rather than just using the 2nd offset correction approach, is that comparing between them has the potential to help understand the data even more, as will be discussed in Chapter 6.

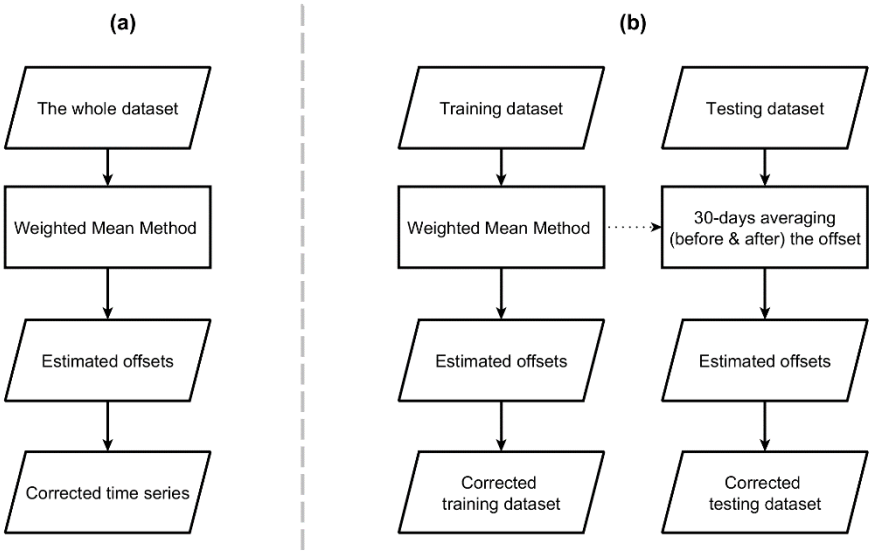


Figure 5-3 Flowcharts showing (a) the 1st offset and (b) the 2nd offset correction approaches. Dotted lines represent information extracted from the training dataset and used in the testing dataset.

5.3.3 Validation of the 2nd step of the algorithm.

To validate that the 2nd step of the algorithm (Figure 5-1), i.e. the correction of offsets due to documented changes, agrees with CATS outcomes, the offset magnitude estimations and their uncertainties using both CATS software (provided by BIGF) and the 1st offset correction approach are compared in Tables A1-A3 (see appendix), along with the differences (CATS minus 1st) in the estimates and their corresponding uncertainties (columns K-O). The tables show the differences (CATS minus 1st) in the offset estimates are within their corresponding uncertainties. In other words, the offset magnitude and the trend estimations using the 1st offset correction approach (Equation 3-24 in Chapter 3) are in agreement with CATS outcomes considering the associated level of uncertainties. This validation is important especially for the first case study (Section 6.2.1) where the 1st and 2nd offset correction approaches will be compared.

5.4 Estimation of the Main Characteristics of the Training Dataset

In this step, the main characteristics (i.e. linear trend and noise characteristics) of the training dataset will be estimated based on the corrected time series. Since the long-term linear trend, due to tectonic plate movements, is considered a deterministic part of the

training dataset, it will be estimated using the Least Squares method (see Equation 3-11 in Chapter 3) and removed from the training dataset, resulting in a 'detrended' time series (Figure 5-5). At this stage, annual and semi-annual signals can also be taken into consideration, assuming that their amplitudes and phases are constant throughout the lifespan of the time series (He et al. 2017). However, in this research, it is preferred not to include them because this assumption is not always the case, i.e. the amplitudes and phases can vary within a time series (Davis et al. 2012; Chen et al. 2013).

The frequencies of the detrended time series are then analysed using Discrete Fourier Transform DFT spectrum to determine a cut-off frequency (red arrow), which separates the white noise (yellow-dashed line), represented by a flat spectrum, from the rest of the signal (green dashed line), as shown in Figure 5-4. This is done by incrementally calculating the average of the amplitude from the highest frequency (the right side in Figure 5-4) towards the lowest frequency. The cut-off frequency is determined when this average starts to significantly change.

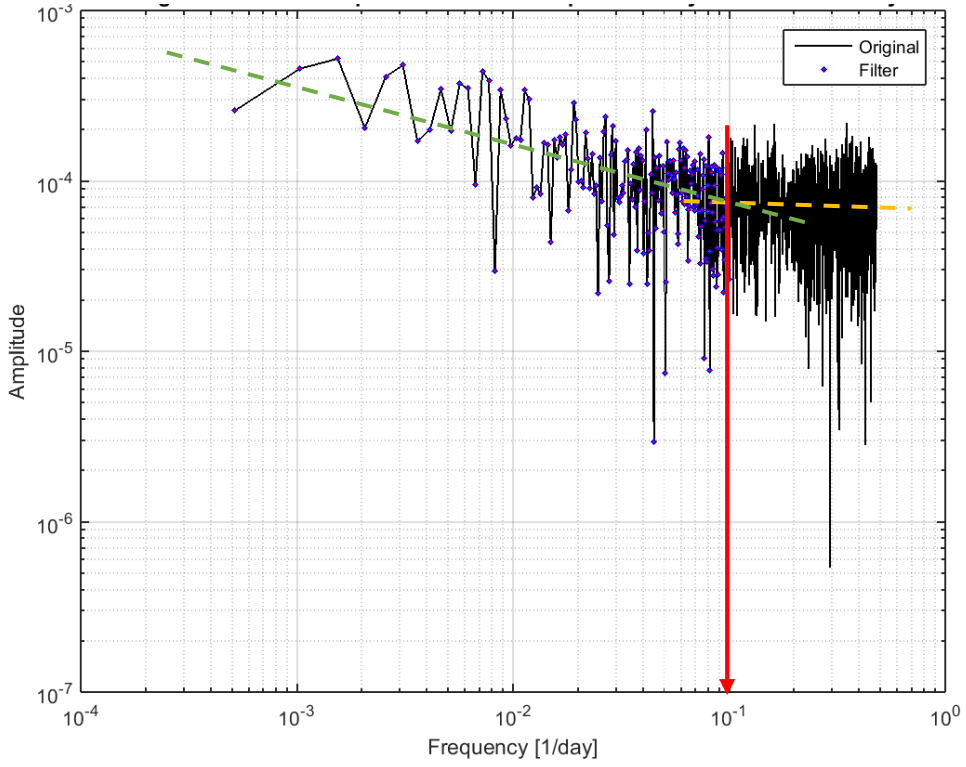


Figure 5-4 Spectrum analysis using DFT with the determined cut-off frequency (red arrow), which separates the white noise (yellow-dashed line), represented by a flat spectral, from the rest of the signal (green dashed line)

All frequencies higher than the cut-off frequency are then filtered out of the detrended time series by using a first-order Butterworth filter (Boore et al. 2002; Colombelli et al. 2013), with filtering of the white noise leading to a less noisy time series that can be used to extract the expected normal behaviour of the station. This resultant time series will be referred to as the 'low frequency' time series (see Figure 5-5) on which the three analysis algorithms (temporal, spatial and combined) will be applied in the next two steps. Figure 5-10 given later shows where this third step fits in with the subsequent fourth and fifth steps.

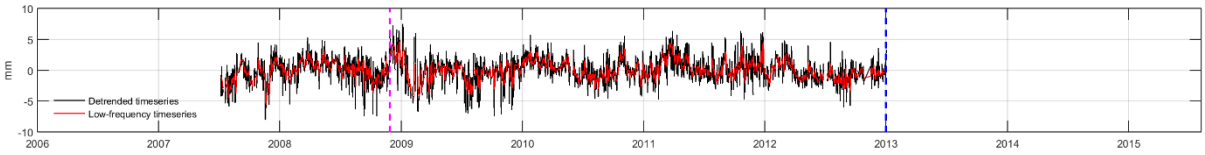


Figure 5-5 The detrended time series (black) and low-frequency time series (red) for the training dataset related to the GPS coordinate time series of SHOB station (ΔE component). Where the blue-dashed line represents the end of the training dataset and the magenta-dashed line shows the epoch of a documented change.

5.5 Application of the Multiple Algorithm Approach on the Training Dataset

In this step, the temporal and the spatial dependencies of the GNSS time series are analysed. Figure 5-10 given later shows how this fourth step fits in with the previous third step and the subsequent fifth step.

5.5.1 The Temporal Analysis Algorithm

In this analysis, the low-frequency time series of each single station[1], i, is assumed to be correlated in time and the NAR-ANN[2] (Equation 5-1) is used to predict the next

[1] The notation used is this chapter is that a superscript *(1, 2, …, N)* represents the GNSS stations while a subscript *t* represents the time. If no superscript is used, it represents a vector of the values of all stations at a given time. Similarly, if no subscript is used, it represents the time series of a value at a given station.
[2] MATLAB Deep Learning Toolbox was used in this research

observation value at the next epoch of the low-frequency time series, y_t^i ,by using the two previous epochs (Hagan et al. 1996; Zhang 2007).

$$\widehat{y_t^i} = f\left(y_{t-1}^i, y_{t-2}^i\right) \qquad \text{Equation 5-1}$$

where $\widehat{y_t^i}$ is the observation value of the low-frequency time series for station i at time t, and f is a sigmoid mapping function (see Sub-section 3.1.2 in Chapter 3).

As explained in Chapter 3, the NAR-ANN splits the dataset into training and testing datasets to optimize the weights using the training dataset and then evaluate the NAR-ANN model's performance on a new dataset (i.e. the testing dataset), with the training dataset being between 65%-80% of the entire dataset (Crowther and Cox 2005; Lean Yu et al. 2006). This split of training and testing NAR-ANN is shouldn't be confused with algorithm training and testing datasets as the former is just to validate and test the performance of NAR-ANN on new data, which is all done in the algorithm training stage, while the algorithm training and testing datasets are to test the performance of the whole algorithm.

Different NAR-ANN architectures were examined, (i.e. the number of layers, number of neurons) using both Bayesian Regularization (Diaconescu, 2008; Ali, 2009) and Levenberg-Marquardt (Kumar and K.Rajasekhar, 2017) training functions and their Normalised Mean Square Error (NMSE) and Root Mean Square Errors (RMSE) were assessed.

It was found that the overall performance of Bayesian Regularization is better than Levenberg-Marquardt as the latter seems to be more vulnerable to overfitting than the former. This can be noticed as the difference in NMSE between the training dataset and the testing dataset is larger using Levenberg-Marquardt. When the Bayesian Regularization method is used, the different architectures give close estimates of NMSE in both training and testing datasets.

A 2-layers network with 10 neurons per layer was found to be the most optimal using the Bayesian Regularization training function for both case studies in Chapter 6 (see

Tables A-4 to A-7 in the appendix) and Chapter 7 (see Tables A-8 in the appendix), while a 2-layers network with 20 neurons per layer was found to be the most optimal using Bayesian Regularization training function for the third case study in Chapter 8 (see Tables A-9 in the appendix).

More previous epochs could be used to predict the next epoch which leads to extract a longer temporal dependency; however, if more previous epochs are used (say p epochs), it will be less suitable for real-time analysis as it would require p consecutive epochs to be available after each missing observation value (i.e. each gap) in the time series. Consequently, each missing observation value in the raw data will be followed by p missing observation values in the predicted low-frequency time series, $\widehat{y_t^i}$. Therefore, only two previous epochs are used in this research, leading to, for example, Figure 5-6.

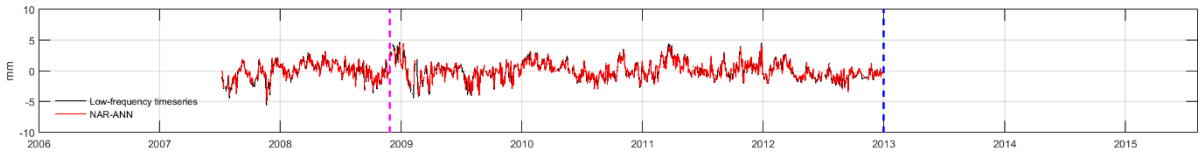


Figure 5-6 The low-frequency time series (black) and its predicted values using NAR-ANN (red) for the training dataset related to the GPS coordinate time series of SHOB station (ΔE component). Where the blue-dashed line represents the end of the training dataset and the magenta-dashed line shows the epoch of a documented change.

Then, the predicted low-frequency time series, $\widehat{y_t^i}$, is subtracted from the detrended time series,x_t^i , resulting in the temporal analysis residuals, δ_t^i (Equation 5-2).

$$\delta_t^i = x_t^i - \widehat{y_t^i} \qquad \text{Equation 5-2}$$

where δ_t^i is the temporal residual for station i at time t, x_t^i is the detrended time series for station i at time t, and $\widehat{y_t^i}$ is the predicted observation value of the low-frequency time series for station i at time t.

Here, it is worth mentioning that the temporal analysis residuals, δ^i, include all of the high-frequency components (i.e. > the cut-off frequency) and any abnormalities in the low-frequency components that the NAR-ANN could not predict. This makes the value of the cut-off frequency less sensitive as the filtered noise will not be ignored

but will be embedded in the temporal analysis residuals. Moreover, this cut-off frequency can be used to optimize the algorithm to suit different applications and different phenomena, assuming that the NAR-ANN will only learn the temporal dependency within the so-called low-frequency time series.

Finally, the mean μ and standard deviation σ of temporal analysis residuals, δ^i , of the algorithm training dataset of each station are used to define the 'temporal analysis residuals thresholds' by adopting the range $\mu \pm 3\sigma$, leading to, for example, Figure 5-7. These temporal analysis residuals thresholds will then be used later in the fifth step of the multiple algorithm approach.

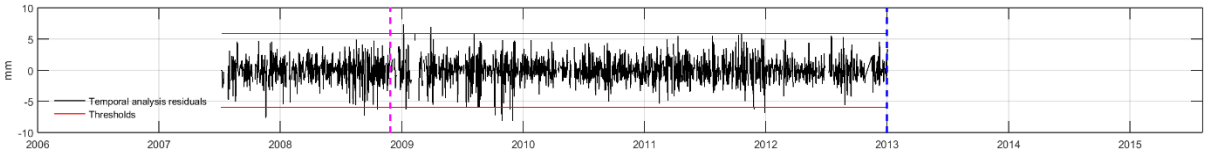


Figure 5-7 The temporal analysis residuals time series (black) and its corresponding thresholds (red) for the training dataset related to the GPS coordinate time series of SHOB station (ΔE component). Where the blue-dashed line represents the end of the training dataset and the magenta-dashed line shows the epoch of a documented change.

However, since this analysis compares each station individually to its history, further analysis may be required to analyse the collective behaviour of a set of stations. Therefore, in parallel with the temporal analysis algorithm, the spatial analysis algorithm is applied in order to study the collective behaviour of the low-frequency component of the time series, while the combined analysis algorithm is used in order to study the collective behaviour of the temporal residuals of the time series.

5.5.2 The Spatial Analysis Algorithm

In this analysis, the low-frequency time series at each station within the GNSS network, y_t , are assumed to be spatially correlated at a specific epoch. A simplified version of the Manski (1993) model, the Spatial AutoRegressive (SAR)[3] Model

[3] MATLAB Spatial Econometrics Toolbox is used in this research

(Equation *5-3*), is adopted due to a lack of explanatory variables (i.e. external time series - see Sub-section 4.1.3 in Chapter 4) (LeSage 2008):

$$y_t = \rho \boldsymbol{W} y_t + \varepsilon_t \qquad \text{Equation 5-3}$$

$$\boldsymbol{w_{ij}} = \frac{\boldsymbol{d_{ij}^{-\alpha}}}{\sum_{j \neq i} \boldsymbol{d_{ij}^{-\alpha}}} \qquad \text{Equation 5-4}$$

where y_t is a N × 1 vector which represents the values of the low-frequency time series at all N stations at a certain time (i.e. $[y_t^1, y_t^2, y_t^3, \dots y_t^N]^T$), ρ is the spatial autoregressive parameter to be estimated using Maximum Likelihood Estimate (MLE) (LeSage 2008; Elhorst 2010), $\boldsymbol{W}$ is the N × N spatial weight matrix which defines the spatial relation between these N stations, and ε_t is the spatial residuals when assumed to be white noise at time t. While, w_{ij} is the spatial weight which reflects the spatial influence of station j on station i, d_{ij} is the Euclidean distance between station j and station i, and $\boldsymbol{\alpha}$ is the distance exponent value which identifies the distance decay function. As discussed earlier in Chapter 4, the distance exponent value $\boldsymbol{\alpha}$ can be determined according to the phenomenon being analysed.

The spatial regression runs independently for each epoch of the time series during the training stage. The accumulated time series of the spatial analysis residuals at each station, ε^i (Figure 5-8a), are used to compute its mean μ and standard deviation σ. Finally, the range $\mu \pm 3\sigma$ defines the 'spatial analysis residuals thresholds' to be used in the fifth step of this multiple algorithm approach, leading to, for example, Figure 5-8b.

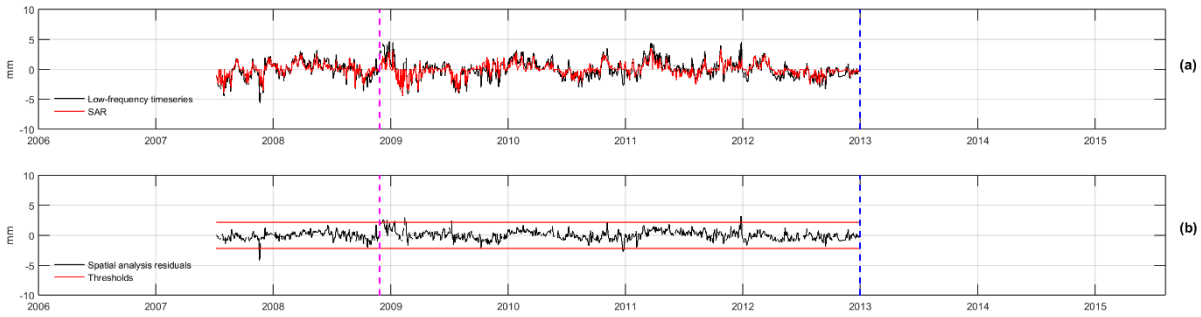


Figure 5-8 (a) The low-frequency time series (black) and its estimated values using the SAR model (red) along with (b) the spatial analysis residuals time series (black)_and its corresponding

thresholds (red). Where the blue-dashed line represents the end of the training dataset and the magenta-dashed line shows the epoch of a documented change.

5.5.3 The Combined Analysis Algorithm

The purpose of the combined analysis algorithm is to analyse the temporal analysis residuals spatially. As stated above, the temporal analysis residuals contain the white noise and any abnormalities in the low-frequency time series and it would be worth to check whether the source of these abnormalities are spatially correlated with the surrounding stations or not.

Therefore, the temporal analysis residuals at each station within the GNSS network, δ_t , at a specific epoch are assumed to be spatially correlated and, in a similar way to the spatial analysis algorithm, the SAR model is used (Equation 5-5).

$$\delta_t = \rho \boldsymbol{W} \delta_t + \upsilon_t \qquad \text{Equation 5-5}$$

where δ_t is N × 1 vector represents the values of the temporal analysis residuals of all stations at time t (i.e. $[\delta_t^1, \delta_t^2, \delta_t^3, \dots \delta_t^N]^T$), ρ is the spatial autoregressive parameter, and υ_t is the combined analysis residuals when assumed to be white noise, leading to, for example, Figure 5-9.

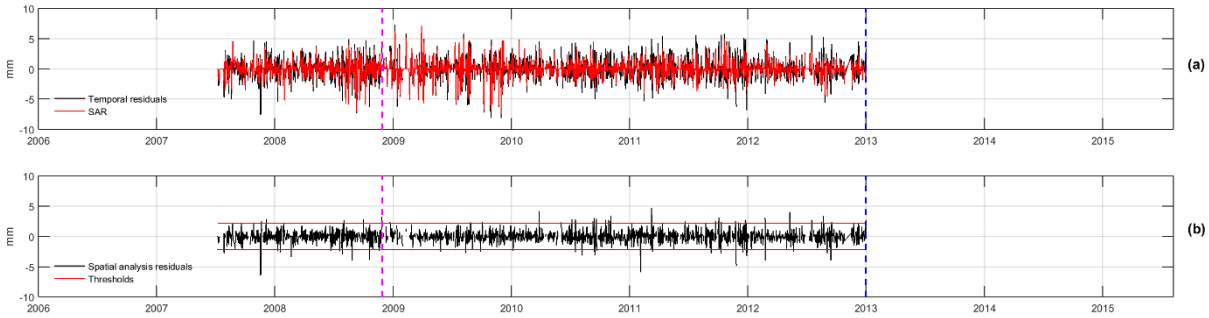


Figure 5-9 (a) The temporal analysis residuals time series (black) and its estimated values using the SAR model (red) along with (b) the combined analysis residuals and their corresponding thresholds. Where the blue-dashed line represents the end of the training dataset and the magenta-dashed line shows the epoch of a documented change.

5.6 Application of the Multiple Algorithm Approach on the Testing Dataset

In this step, all the main characteristics estimated from the algorithm training dataset, determined from the third step, as the linear trends and desired cut-off frequencies corresponding to white noise will be used to detrend and to filter the white noise from the algorithm testing dataset. Then, for the temporal analysis algorithm, the trained NAR-ANNs per time series, determined from the fourth step, are used to predict each epoch in the algorithm testing dataset from its two previous epochs, while SAR model is used in both spatial and combined analysis algorithms, epoch by epoch. Finally, the residuals statistics, determined from the fourth step, are applied to the testing dataset as thresholds to determine any anomalous behaviours, as shown in Figure 5-10.

In the temporal analysis, anomalies are detected and identified as potential events when the value of the high-frequency component at a station is higher than it used to be or when there is significant abnormal behaviour in the low-frequency component (e.g. a large offset that is not related to a documented change) which NAR-ANN could not predict (see Figure 5-11d). Whenever an anomaly is detected and identified as a potential event, a spatial search is conducted, to check if any of the surrounding stations[4] also have potential events at that epoch. If the potential event occurs at one station only, then it is considered to be a site-specific anomaly, while if potential events occur at more than one station collectively, then they are considered to represent a wider anomaly. These wide anomalies could be related to large-scale land movements (e.g. earthquakes or landslides) or atmospheric events (e.g. tropospheric event). In this research, earthquakes and meteorological events are considered.

In the spatial analysis, anomalies are detected and identified as potential events when the relative behaviour of the low-frequency component between the surrounding stations

[4] A certain number of stations may be specified based on the density of the GNSS network and the phenomena to be monitored/detected.

seems less spatially correlated than it used to be, as the spatial analysis residuals values get larger when there is a weak spatial correlation at that epoch, which may indicate that one or a sub-set of the stations are behaving differently to their surrounding stations (see Figure 5-11f). On the other hand, in the combined analysis, anomalies are detected and identified as potential events when the temporal analysis residuals seem less spatially correlated than they used to be, which indicates that the temporal analysis residuals at one or a sub-set of the stations are behaving differently to their surrounding stations (see Figure 5-11h). In a similar manner to the temporal analysis, a spatial search is conducted to filter out any site-specific anomalies from any wider anomaly which could be related to a geohazard or a meteorological event.

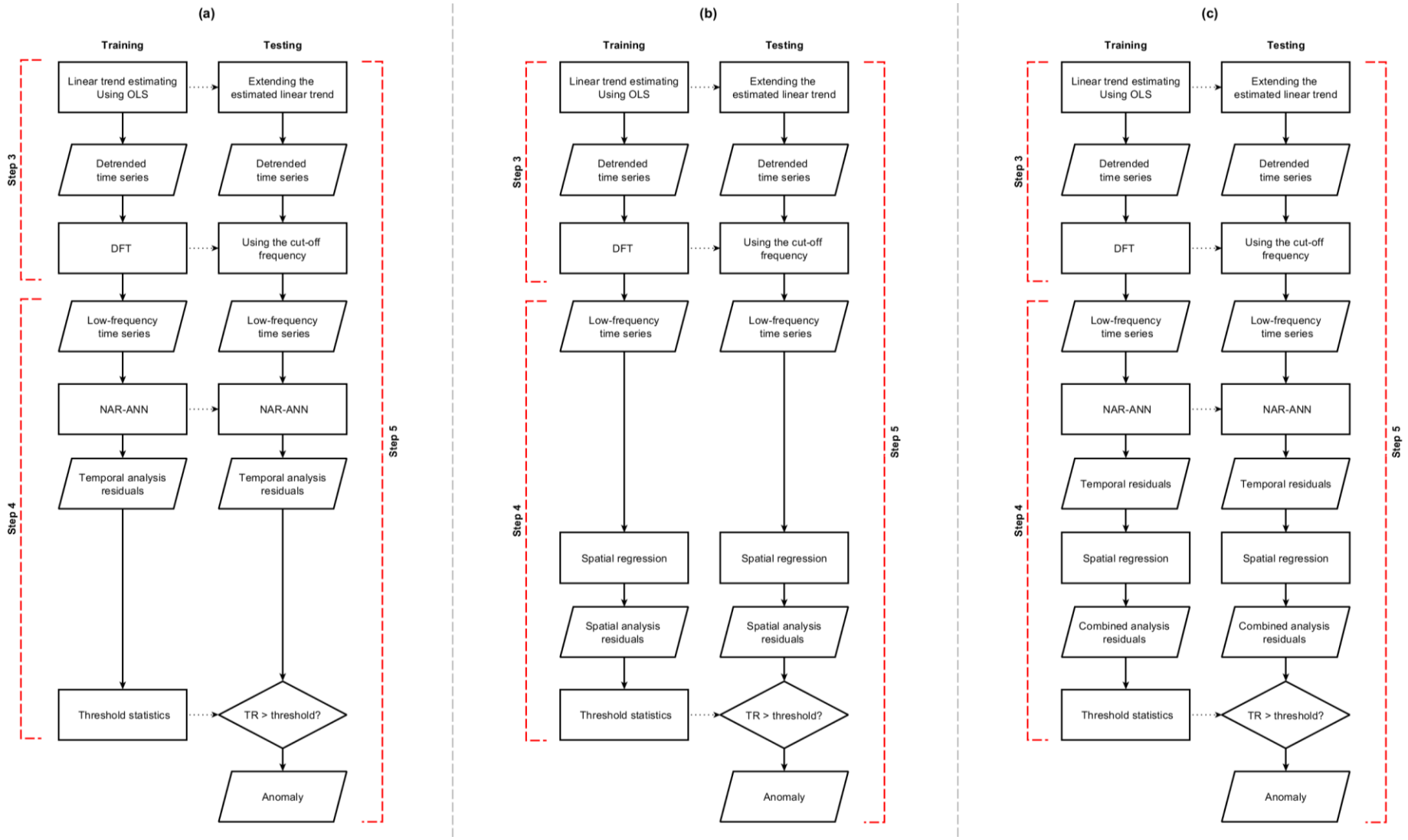


Figure 5-10 The third, fourth and fifth steps of the (a) temporal, (b) spatial, and (c) combined analysis algorithms. Dotted lines represent information extracted from the training dataset and used in the testing dataset.

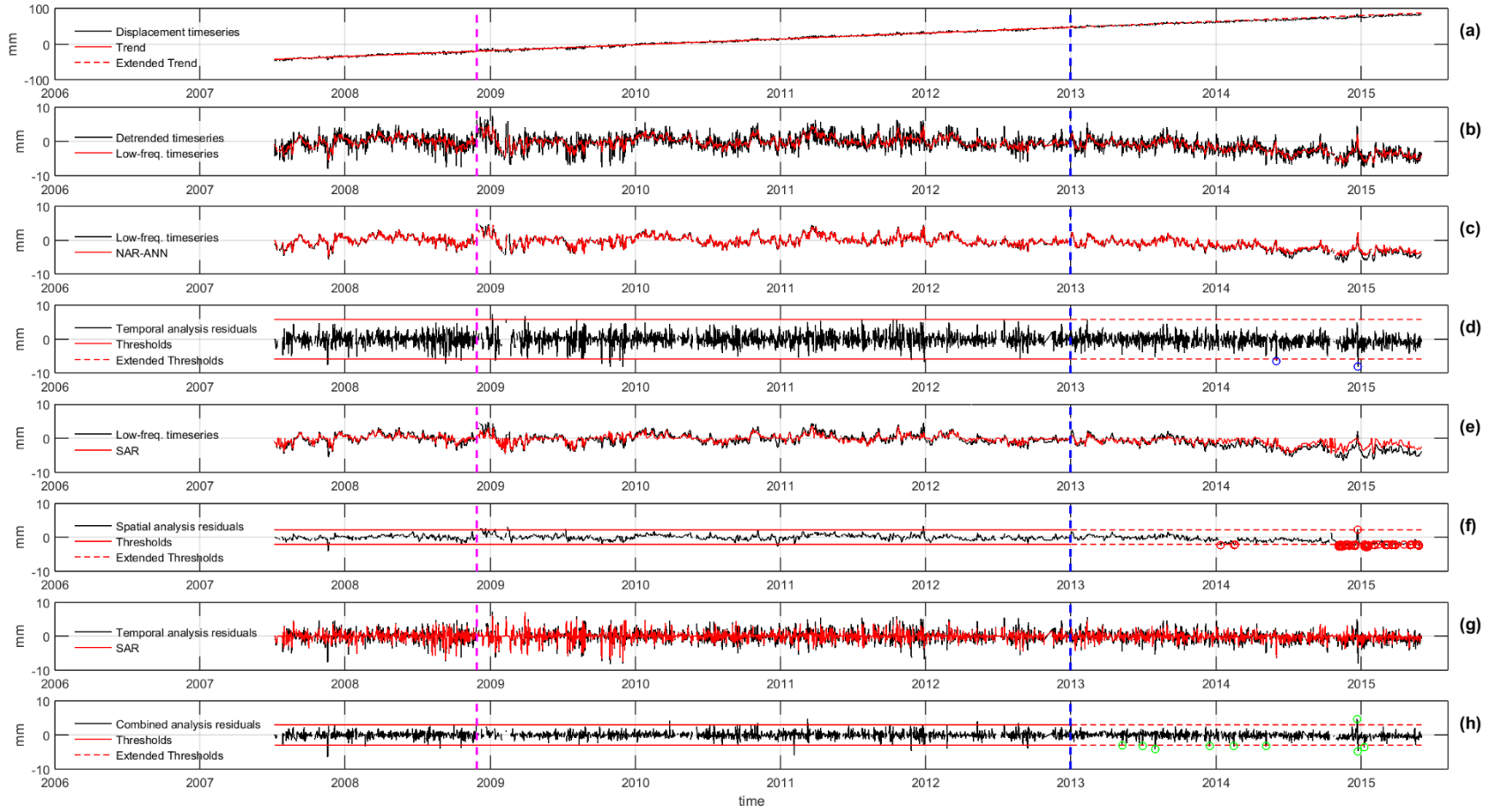


Figure 5-11 (a) the 'corrected' time series, (b) the detrended and low-frequency time series, (c) the low-frequency time series and it is predicted values using NAR-ANN, (d) the temporal analysis residuals time series and its corresponding thresholds, (e) the low-frequency time series and its estimated values using the SAR model, (f) the spatial analysis residuals time series and its corresponding thresholds, (g) the temporal analysis residuals and its estimated values using the SAR model, and (h) the combined analysis residuals time series and its corresponding thresholds, related to the GPS coordinate time series of SHOB station (ΔE component). Where the blue-dashed line represents the end of the training dataset and the magenta-dashed line shows the epoch of a documented change.

5.7 Summary

In this chapter, the methodology used in the development of a multiple algorithm approach to the analysis of GNSS time series was discussed, along with illustrations of the five main steps of that methodology. It was shown that by following this approach, GNSS time series for a network of stations can be analysed not only regarding the time-history of each corresponding station but also in relation to their spatial relationship, leading to a new perspective on GNSS network applications.

In the next chapters, the multiple algorithm approach will be evaluated by applying it in three different case studies, for the analysis of:

(i) The long-term, daily GPS coordinate time series of the BIGF network of stations in the British Isles.

(ii) The 1Hz GPS coordinate time series of the GEONET stations in Japan, for the Tohoku-Oki 2011 Mw9.0 earthquake.

(iii) The long-term, hourly GPS tropospheric parameter time series of the BIGF network of stations in the British Isles.

CHAPTER 6: THE ANALYSIS OF THE LONG-TERM, DAILY GPS COORDINATE TIME SERIES OF THE BIGF NETWORK OF STATIONS IN THE BRITISH ISLES.

In this chapter, the multiple algorithm approach will be evaluated using the first case study; the analysis of the daily GPS coordinate time series of the BIGF network of stations in the British Isles. The case studies were chosen to cover different aspects; the size of the network (e.g. small vs large networks), the length of the time series (e.g. long-term vs short-term time series) and the temporal resolution of the time series (e.g. daily vs 1Hz time series), as well as the dynamics (e.g. high-frequency vs low-frequency), the size (large vs small) and the type (spatially correlated vs site-specific) of the chosen phenomena. This case study can be seen as a relatively small network (<100 stations) with long-term (>5 years) daily time series. Moreover, the phenomenon to be monitored is any anomalous behaviour in the time series which can be seen as a small and site-specific phenomenon. In the next section, the network and the data used will be illustrated. Then, the results will be analysed and discussed.

6.1 Network and Datasets

The British Isles continuous GNSS Facility (BIGF) has been operating since 1997 and providing data and products for ~160 continuously recording GNSS stations for more than twenty years (BIGF; Hansen et al. 2012). Such data and products have been used in case studies in many other researches (Bingley et al. 2001; Dong et al. 2002; Allinson et al. 2004; Teferle et al. 2006, 2008; Penna et al. 2007; Williams and Penna 2011; Hansen et al. 2012; Liu et al. 2015).

The BIGF network data are processed with Bernese GNSS software version 5.2 (BSW5.2) using GPS only resulting in cartesian (XYZ) coordinate estimates as output. The current research was based on using daily SINEX files that were provided as long-term, daily GPS coordinate time series of ΔN, ΔE, ΔU (NEU) displacements with respect to reference

coordinates. As a part of this process, any days that had one or more of the NEU displacements identified as an outlier at that stage were removed before the derived products were provided by BIGF; an outlier being defined as a residual greater than three times the weighted RMS of a linear de-trended time series with offsets due to documented changes accounted for.

Furthermore, in this research, the focus was on time series from the start of July 2007 to the end of September 2015, which was the limit of the BIGF derived products that were provided, as most of the stations were active over this time 8.25 year period and processed with the same processing configuration. Any station that does not cover this period was removed in order to eliminate short time series and lead to better trend extraction, spectral analysis, and NAR-ANN learning, resulting finally in 87 stations (Figure 6-1). Then, the dataset was split into: (i) the algorithm training dataset and (ii) the algorithm testing dataset. The algorithm training dataset length was 5.5 years to mitigate the effect of annual and semi-annual signals when estimating any linear trends (Blewitt and Lavallée 2002). On the other hand, the algorithm testing dataset was chosen to start in January 2013 and end in September 2015, such that its length was 2.75 years, which represents around 33% of the used data. Here it can be noted that this concept may be particularly appealing to administrators of new networks of GNSS stations as the first years of a station lifespan should be less vulnerable to wear and tear problems (e.g. antenna corrosion) than the years to follow; however, it is, of course, always possible to extend the algorithm training dataset as time goes by, as long as it can still be assumed to represent the expected normal behaviour of a station.

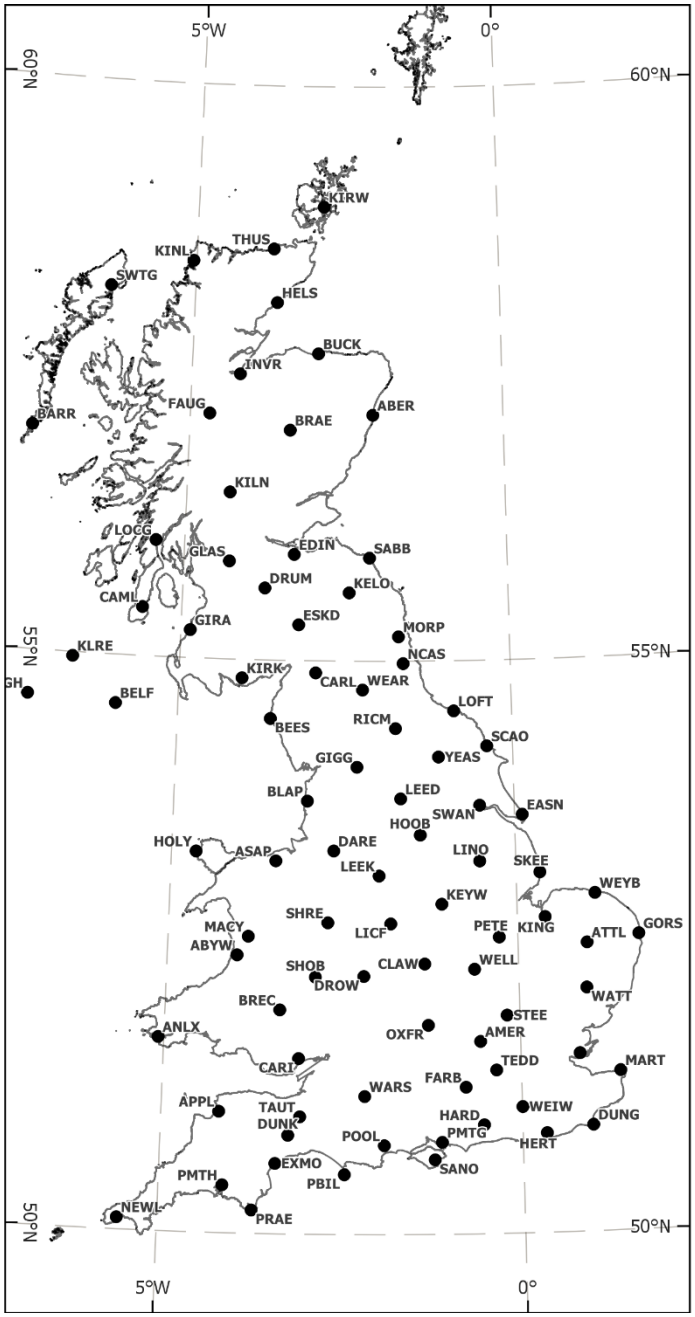


Figure 6-1 Selected stations of the British Isles continuous GNSS Facility (BIGF).

6.2 Results

6.2.1 Offset correction approaches

The pre-defined times of occurrence of any documented changes (i.e. receiver and/or antenna equipment changes) at each station were also provided by BIGF; the magnitudes

of any offsets (at these pre-defined times of occurrence) were estimated and corrected as a part of this research.

As discussed in chapter 5, two offset correction approaches were examined; the 1st approach is the conventional approach of applying the weighted mean method (Williams 2003b; Montillet et al. 2015) on the whole dataset, and the 2nd approach being where the weighted mean method was applied only on the algorithm training dataset to correct any documented offsets within, while the averaging method was used to correct any offsets in the algorithm testing dataset.

Tables 6-1 to 6-3 show the offset and linear trend estimates and their uncertainties based on the two offset correction approaches, along with the differences (1st minus 2nd) in the estimates and their corresponding uncertainties (columns K-O). The difference in the estimates is considered significant if the offset and linear trend estimates met the following conditions:

$$o_1 - o_2 > \sqrt{\sigma_{\hat{1}_{off}}^2 + \sigma_{\hat{2}_{off}}^2} \qquad \text{Equation 6-1}$$

$$r_1 - r_2 > \sqrt{\sigma_{\hat{1}_r}^2 + \sigma_{\hat{2}_r}^2} \qquad \text{Equation 6-2}$$

where o_1 and o_2 are the offsets estimated by the 1st and 2nd approaches respectively, $\sigma_{\hat{1}_{off}}$ and $\sigma_{\hat{2}_{off}}$ are their associated uncertainties (see Equation 3-24). Similarly, r_1 and r_2 are the linear trends estimated by the 1st and 2nd approaches and $\sigma_{\hat{1}_r}$ and $\sigma_{\hat{2}_r}$ are their associated uncertainties (see Equations 3-13 and 3-14).

Figure 6-2 shows the stations which have significant or insignificant differences in their offset (left semicircle) and linear trend estimates (right semicircle) from the two offset correction approaches, in the three components, ΔN, ΔE and ΔU respectively. Figure 6-3 and 6-4 represent the horizontal and vertical station velocities based on the linear trend estimates when using the two offset correction approaches, as well as the differences (1st minus 2nd) in the estimates and their corresponding uncertainties.

Tables 6-1 to 6-3 show that the two offset correction approaches gave different estimates for the magnitude of the offsets in the algorithm training dataset. The tables show that 71.6%, 79.0% and 69.0% of the stations have at least one offset estimate with a significant difference between the two offset correction approaches in ΔN, ΔE and ΔU respectively, while 11.1%, 79.0% and 7.4% of the stations have a significant difference in their linear trend estimates in ΔN, ΔE and ΔU respectively which will be discussed further in the Section 6.3.1.

Table 6-1 ΔN component offsets (mm) and trends (mm/yr). 1st offset correction approach vs 2nd offset correction approach. Dark shaded areas indicate offsets in the algorithm testing dataset.

	1st approach					2nd approach					The difference (1st – 2nd)				
	(A)	(B)	(C)	(D)	(E)	(F)	(G)	(H)	(I)	(J)	(K)	(L)	(M)	(N)	(O)
	Offset#1	Offset#2	Offset#3	Offset#4	Trend	Offset#1	Offset#2	Offset#3	Offset#4	Trend	Offset#1	Offset#2	Offset#3	Offset#4	Trend
ABER	6.83±0.19	-	-	-	14.72±0.32	9.41±0.44	-	-	-	14.26±0.34	-2.58±0.48	-	-	-	0.47±0.46
ABYW	-10.17±0.13	-1.29±0.14	-	-	16.46±0.22	-10.47±0.16	-0.32±0.29	-	-	16.6±0.34	0.3±0.21	-0.97±0.32	-	-	-0.13±0.4
AMER	-2.66±0.09	-	-	-	16.32±0.2	-2.74±0.11	-	-	-	16.34±0.31	0.08±0.14	-	-	-	-0.02±0.37
ANLX	-6.55±0.1	-	-	-	16.37±0.21	-6.46±0.13	-	-	-	16.34±0.33	-0.09±0.16	-	-	-	0.03±0.39
APPL	14.43±0.13	-4.44±0.1	-	-	16.67±0.21	14.53±0.14	-4.18±0.12	-	-	16.56±0.32	-0.1±0.19	-0.26±0.16	-	-	0.12±0.39
ASAP	-2.39±0.1	-	-	-	16.51±0.22	-2.81±0.12	-	-	-	16.66±0.34	0.42±0.16	-	-	-	-0.15±0.4
ATTL	6.31±0.09	-	-	-	16.16±0.19	6.06±0.11	-	-	-	16.26±0.29	0.25±0.14	-	-	-	-0.09±0.35
BARR	-2.25±0.18	-4.93±0.09	-	-	16.65±0.2	-2.61±0.18	-5.46±0.11	-	-	16.91±0.3	0.36±0.25	0.53±0.14	-	-	-0.26±0.36
BEES	-0.47±0.13	-	-	-	14.62±0.32	1.6±0.13	-	-	-	13.76±0.37	-2.07±0.18	-	-	-	0.86±0.49
BELF	0.03±0.12	-	-	-	16.52±0.21	-0.3±0.13	-	-	-	16.66±0.32	0.33±0.18	-	-	-	-0.14±0.38
BLAP	0.06±0.09	-	-	-	15.5±0.21	-0.99±0.12	-	-	-	15.96±0.32	1.05±0.15	-	-	-	-0.46±0.38
BRAE	0.09±0.12	-	-	-	16.73±0.28	-0.58±0.15	-	-	-	17.01±0.41	0.67±0.19	-	-	-	-0.28±0.49
BREC	-3.41±0.12	-	-	-	16.51±0.27	-3.57±0.15	-	-	-	16.57±0.41	0.16±0.19	-	-	-	-0.05±0.49
BUCK	-0.16±0.09	-	-	-	16.62±0.21	-0.09±0.12	-	-	-	16.62±0.32	-0.07±0.15	-	-	-	0±0.38
CAML	-18.65±0.13	-	-	-	15.5±0.3	-18.52±0.16	-	-	-	15.43±0.46	-0.13±0.21	-	-	-	0.07±0.55
CARI	14.28±0.09	-	-	-	16.47±0.21	13.99±0.12	-	-	-	16.56±0.32	0.29±0.15	-	-	-	-0.09±0.38
CARL	1.54±0.09	-	-	-	16.41±0.2	1.24±0.11	-	-	-	16.54±0.31	0.3±0.14	-	-	-	-0.13±0.37
CLAW	-15.53±0.09	-	-	-	15.97±0.2	-14.55±0.11	-	-	-	15.56±0.31	-0.98±0.14	-	-	-	0.42±0.37
DARE	-3.59±0.09	-	-	-	16.37±0.21	-3.79±0.12	-	-	-	16.43±0.33	0.2±0.15	-	-	-	-0.06±0.39
DROW	6.47±0.09	-	-	-	16.63±0.2	5.83±0.11	-	-	-	16.86±0.3	0.64±0.14	-	-	-	-0.23±0.36
DRUM	1.28±0.09	-	-	-	16.48±0.2	0.89±0.11	-	-	-	16.64±0.31	0.39±0.14	-	-	-	-0.16±0.37
DUNG	-0.25±0.09	-	-	-	16.08±0.19	-0.37±0.11	-	-	-	16.13±0.29	0.12±0.14	-	-	-	-0.05±0.35
EASN	0.7±0.08	-	-	-	16.16±0.18	0.85±0.11	-	-	-	16.12±0.29	-0.15±0.14	-	-	-	0.04±0.34
EDIN	2.79±0.1	-	-	-	16.66±0.21	2.64±0.12	-	-	-	16.71±0.33	0.15±0.16	-	-	-	-0.05±0.39
ESKD	-1.25±0.1	0.48±0.1	-0.27±0.11	0.36±0.11	16.24±0.22	-1.77±0.12	0.07±0.14	-0.31±0.12	0.15±0.12	16.56±0.34	0.52±0.16	0.41±0.17	0.04±0.16	0.21±0.16	-0.32±0.4
EXMO	-7.89±0.1	0.44±0.11	0.08±0.12	1.42±0.11	16.3±0.23	-8.24±0.13	0.21±0.15	-0.13±0.13	1.22±0.15	16.51±0.35	0.35±0.16	0.23±0.19	0.21±0.18	0.2±0.19	-0.21±0.42
FARB	-2.26±0.09	-	-	-	16.89±0.21	-2.01±0.12	-	-	-	16.8±0.32	-0.25±0.15	-	-	-	0.09±0.38
FAUG	-7.41±0.1	-	-	-	16.75±0.23	-7.56±0.13	-	-	-	16.81±0.35	0.15±0.16	-	-	-	-0.07±0.42
GIGG	0.88±0.1	-	-	-	16.34±0.22	0.64±0.12	-	-	-	16.44±0.34	0.24±0.16	-	-	-	-0.09±0.41
GIRA	-10.2±0.09	-	-	-	16.62±0.2	-10.23±0.11	-	-	-	16.65±0.3	0.03±0.14	-	-	-	-0.04±0.35
GLAS	-0.13±0.1	-	-	-	17.03±0.22	-0.39±0.12	-	-	-	17.14±0.33	0.26±0.16	-	-	-	-0.1±0.39
GORS	-9.3±0.09	-	-	-	16.44±0.19	-9.25±0.11	-	-	-	16.41±0.29	-0.05±0.14	-	-	-	0.03±0.35
HARD	-4.5±0.1	-	-	-	16.16±0.23	-4.77±0.13	-	-	-	16.26±0.35	0.27±0.16	-	-	-	-0.1±0.42
HELS	7.75±0.11	-	-	-	16.13±0.24	7.52±0.13	-	-	-	16.21±0.36	0.23±0.17	-	-	-	-0.08±0.44
HERT	3.61±0.16	-	-	-	16.41±0.25	3.89±0.16	-	-	-	16.26±0.34	-0.28±0.23	-	-	-	0.15±0.42
HOLY	-9.92±0.09	-	-	-	16.58±0.21	-10.34±0.12	-	-	-	16.75±0.32	0.42±0.15	-	-	-	-0.17±0.38
HOOB	-5.5±0.09	-	-	-	15.66±0.2	-5.98±0.11	-	-	-	15.86±0.31	0.48±0.14	-	-	-	-0.21±0.36
INVR	-16.45±0.1	-	-	-	16.64±0.22	-16.72±0.12	-	-	-	16.79±0.32	0.27±0.16	-	-	-	-0.14±0.39
KELO	-3.59±0.09	1.41±0.1	-	-	16.54±0.19	-4.29±0.11	0.83±0.12	-	-	16.91±0.3	0.7±0.14	0.58±0.16	-	-	-0.37±0.35

Table 6-1 continued

	1st approach					2nd approach					The difference (1st – 2nd)				
	(A)	(B)	(C)	(D)	(E)	(F)	(G)	(H)	(I)	(J)	(K)	(L)	(M)	(N)	(O)
KILN	Offset#1	Offset#2	Offset#3	Offset#4	Trend	Offset#1	Offset#2	Offset#3	Offset#4	Trend	Offset#1	Offset#2	Offset#3	Offset#4	Trend
KING	-5.02±0.09	-	-	-	16.17±0.19	-5.14±0.11	-	-	-	16.22±0.3	0.12±0.14	-	-	-	-0.05±0.36
KINL	0.37±0.1	-	-	-	16.14±0.21	-0.32±0.12	-	-	-	16.44±0.31	0.69±0.16	-	-	-	-0.3±0.38
KIRK	-5.45±0.09	-	-	-	15.47±0.2	-5.75±0.11	-	-	-	15.62±0.3	0.3±0.14	-	-	-	-0.15±0.36
KIRW	0.15±0.09	-	-	-	16.76±0.19	0.24±0.11	-	-	-	16.75±0.28	-0.09±0.14	-	-	-	0.01±0.34
KLRE	9.55±0.13	-	-	-	16.7±0.21	9.26±0.15	-	-	-	16.79±0.32	0.29±0.2	-	-	-	-0.1±0.38
LEED	-0.99±0.09	-	-	-	16.26±0.21	-1.23±0.12	-	-	-	16.37±0.32	0.24±0.15	-	-	-	-0.11±0.38
LEEK	-6.97±0.09	-	-	-	16.3±0.19	-7.29±0.11	-	-	-	16.41±0.3	0.32±0.14	-	-	-	-0.12±0.35
LICF	-9.69±0.09	-	-	-	16.53±0.19	-9.42±0.11	-	-	-	16.4±0.29	-0.27±0.14	-	-	-	0.13±0.34
LINO	4.32±0.09	-	-	-	16.26±0.19	4.92±0.11	-	-	-	16.02±0.29	-0.6±0.14	-	-	-	0.24±0.35
LOCG	0.18±0.11	-	-	-	16.6±0.24	0.33±0.14	-	-	-	16.55±0.37	-0.15±0.18	-	-	-	0.04±0.44
LOFT	1.57±0.09	-	-	-	16.34±0.2	1.36±0.11	-	-	-	16.42±0.31	0.21±0.14	-	-	-	-0.08±0.36
MACY	-7.32±0.11	-	-	-	16.44±0.26	-8.09±0.14	-	-	-	16.76±0.39	0.77±0.18	-	-	-	-0.32±0.47
MART	-7.51±0.09	4.37±0.11	-	-	16.57±0.2	-7.27±0.12	2.99±0.26	-	-	16.48±0.31	-0.24±0.15	1.38±0.28	-	-	0.1±0.37
NCAS	0.05±0.09	-	-	-	16.03±0.21	0.07±0.12	-	-	-	16.05±0.32	-0.02±0.15	-	-	-	-0.02±0.38
NEWL	-4.76±0.13	1.89±0.11	-13.6±0.12	-	15.33±0.24	-4.63±0.14	2.23±0.14	-11.07±0.34	-	15.19±0.36	-0.13±0.19	-0.34±0.18	-2.53±0.36	-	0.14±0.44
OMGH	3.59±0.14	-	-	-	16.62±0.22	2.94±0.15	-	-	-	16.87±0.33	0.65±0.21	-	-	-	-0.26±0.39
OXFR	-4.12±0.09	-	-	-	16.4±0.19	-4.13±0.11	-	-	-	16.39±0.3	0.01±0.14	-	-	-	0.01±0.36
PBIL	-27.61±0.1	-	-	-	15.21±0.24	-29.98±0.12	-	-	-	16.16±0.32	2.37±0.16	-	-	-	-0.95±0.4
PETE	-4.67±0.08	-	-	-	16.32±0.19	-4.79±0.11	-	-	-	16.36±0.29	0.12±0.14	-	-	-	-0.04±0.34
PMTH	-1.1±0.09	-	-	-	16.44±0.21	-0.97±0.12	-	-	-	16.36±0.32	-0.13±0.15	-	-	-	0.07±0.38
POOL	-5.21±0.1	-	-	-	16.12±0.21	-5.3±0.12	-	-	-	16.15±0.32	0.09±0.16	-	-	-	-0.03±0.38
PRAE	2.55±0.1	-	-	-	15.89±0.21	2.52±0.13	-	-	-	15.92±0.33	0.03±0.16	-	-	-	-0.04±0.39
RICM	-9.16±0.09	-	-	-	16.31±0.2	-8.8±0.12	-	-	-	16.18±0.31	-0.36±0.15	-	-	-	0.13±0.37
SABB	-12.12±0.1	-	-	-	16.66±0.23	-13.06±0.12	-	-	-	17.05±0.32	0.94±0.16	-	-	-	-0.39±0.39
SANO	-2.22±0.11	-	-	-	15.61±0.25	-4.09±0.13	-	-	-	16.31±0.37	1.87±0.17	-	-	-	-0.7±0.44
SCAO	-23.43±0.1	-	-	-	14.33±0.22	-22.87±0.12	-	-	-	14.13±0.33	-0.56±0.16	-	-	-	0.2±0.4
SHOB	1.85±0.1	-	-	-	16.73±0.22	1.26±0.12	-	-	-	16.96±0.32	0.59±0.16	-	-	-	-0.23±0.39
SHRE	-7.6±0.09	-	-	-	16.56±0.2	-7.74±0.12	-	-	-	16.6±0.31	0.14±0.15	-	-	-	-0.04±0.37
SKEE	-3.07±0.09	-	-	-	16.31±0.19	-3.36±0.11	-	-	-	16.43±0.29	0.29±0.14	-	-	-	-0.12±0.35
STEE	-11.04±0.09	0.01±0.1	-0.73±0.1	-	16.26±0.2	-11.42±0.11	-0.25±0.13	-0.88±0.12	-	16.49±0.31	0.38±0.14	0.26±0.16	0.15±0.16	-	-0.23±0.37
SWAN	1.55±0.09	-	-	-	16.35±0.19	1.74±0.11	-	-	-	16.29±0.3	-0.19±0.14	-	-	-	0.06±0.36
SWTG	6.36±0.11	-	-	-	17.2±0.2	5.92±0.26	-	-	-	17.16±0.35	0.44±0.28	-	-	-	0.04±0.4
TAUT	-4.81±0.11	-	-	-	16.7±0.26	-5.3±0.14	-	-	-	16.88±0.39	0.49±0.18	-	-	-	-0.17±0.47
THUS	-4.24±0.09	-	-	-	16.7±0.19	-4.2±0.1	-	-	-	16.69±0.28	-0.04±0.13	-	-	-	0.01±0.33
WARS	3392.13±0.11	-1.58±0.1	23.25±0.11	-	16.13±0.24	3392.26±0.13	-1.33±0.13	23.58±0.13	-	15.98±0.34	-0.13±0.17	-0.25±0.16	-0.33±0.17	-	0.16±0.42
WEAR	-1.02±0.13	-	-	-	16.42±0.29	-1.32±0.15	-	-	-	16.53±0.43	0.3±0.2	-	-	-	-0.12±0.52
WEIW	-0.04±0.1	-	-	-	16.22±0.22	-0.44±0.13	-	-	-	16.38±0.34	0.4±0.16	-	-	-	-0.15±0.41
WELL	-4.45±0.09	-	-	-	16.15±0.19	-3.99±0.11	-	-	-	15.96±0.3	-0.46±0.14	-	-	-	0.19±0.36
WEYB	-1.89±0.09	-	-	-	15.9±0.19	-1.91±0.11	-	-	-	15.92±0.29	0.02±0.14	-	-	-	-0.02±0.35
YEAS	8.73±0.09	-	-	-	16.35±0.19	8.82±0.11	-	-	-	16.32±0.3	-0.09±0.14	-	-	-	0.03±0.35

Table 6-2 ΔE component offsets (mm) and trends (mm/yr). 1st offset correction approach vs 2nd offset correction approach. Dark shaded areas indicate offsets in the algorithm testing dataset.

	1st approach					2nd approach					The difference (1st – 2nd)				
	(A)	(B)	(C)	(D)	(E)	(F)	(G)	(H)	(I)	(J)	(K)	(L)	(M)	(N)	(O)
	Offset#1	Offset#2	Offset#3	Offset#4	Trend	Offset#1	Offset#2	Offset#3	Offset#4	Trend	Offset#1	Offset#2	Offset#3	Offset#4	Trend
ABER	10.99±0.21	-	-	-	14.19±0.28	6.52±0.54	-	-	-	14.47±0.26	4.47±0.58	-	-	-	-0.29±0.38
ABYW	-20.4±0.12	-6.74±0.13	-	-	15.77±0.16	-20.42±0.15	-4.9±0.28	-	-	15.77±0.27	0.02±0.19	-1.84±0.31	-	-	0±0.31
AMER	-1.14±0.08	-	-	-	16.99±0.15	-2.2±0.1	-	-	-	17.41±0.22	1.06±0.13	-	-	-	-0.42±0.27
ANLX	10.67±0.09	-	-	-	15.87±0.16	9.27±0.12	-	-	-	16.39±0.25	1.4±0.15	-	-	-	-0.53±0.3
APPL	12.83±0.11	-0.1±0.08	-	-	17.03±0.15	12.94±0.12	-0.21±0.1	-	-	17.06±0.23	-0.11±0.16	0.11±0.13	-	-	-0.02±0.27
ASAP	-1.72±0.1	-	-	-	15.4±0.18	-2.11±0.12	-	-	-	15.52±0.28	0.39±0.16	-	-	-	-0.13±0.33
ATTL	-2.79±0.08	-	-	-	16.99±0.14	-3.96±0.1	-	-	-	17.46±0.21	1.17±0.13	-	-	-	-0.46±0.26
BARR	4.79±0.16	-0.9±0.08	-	-	13.51±0.15	4.58±0.17	-1.21±0.1	-	-	13.64±0.23	0.21±0.23	0.31±0.13	-	-	-0.14±0.27
BEES	12.12±0.11	-	-	-	13.77±0.21	12.68±0.13	-	-	-	13.52±0.28	-0.56±0.17	-	-	-	0.25±0.35
BELF	-5.33±0.16	-	-	-	14.71±0.23	-7.54±0.16	-	-	-	15.52±0.32	2.21±0.23	-	-	-	-0.81±0.39
BLAP	2.16±0.08	-	-	-	15.35±0.15	1.04±0.11	-	-	-	15.76±0.23	1.12±0.14	-	-	-	-0.41±0.28
BRAE	-0.27±0.1	-	-	-	14.51±0.17	-1.09±0.12	-	-	-	14.82±0.26	0.82±0.16	-	-	-	-0.31±0.31
BREC	0.65±0.09	-	-	-	16.21±0.17	-0.72±0.11	-	-	-	16.73±0.25	1.37±0.14	-	-	-	-0.52±0.3
BUCK	0.65±0.09	-	-	-	14.46±0.16	-0.41±0.11	-	-	-	14.85±0.25	1.06±0.14	-	-	-	-0.39±0.3
CAML	-39.73±0.11	-	-	-	13.72±0.19	-41.55±0.12	-	-	-	14.41±0.26	1.82±0.16	-	-	-	-0.69±0.33
CARI	3.29±0.1	-	-	-	15.98±0.19	1.62±0.13	-	-	-	16.63±0.28	1.67±0.16	-	-	-	-0.65±0.34
CARL	2.85±0.09	-	-	-	15.37±0.15	1.45±0.11	-	-	-	15.89±0.23	1.4±0.14	-	-	-	-0.52±0.28
CLAW	-1.15±0.08	-	-	-	16.83±0.14	-2.04±0.1	-	-	-	17.15±0.22	0.89±0.13	-	-	-	-0.32±0.26
DARE	-4.22±0.09	-	-	-	16.11±0.16	-6.01±0.11	-	-	-	16.8±0.24	1.79±0.14	-	-	-	-0.69±0.28
DROW	-2.07±0.09	-	-	-	16.22±0.15	-3.59±0.11	-	-	-	16.81±0.23	1.52±0.14	-	-	-	-0.6±0.28
DRUM	0.7±0.09	-	-	-	15.02±0.15	-0.51±0.11	-	-	-	15.48±0.23	1.21±0.14	-	-	-	-0.46±0.28
DUNG	-9.83±0.08	-	-	-	17.75±0.14	-11.03±0.1	-	-	-	18.21±0.22	1.2±0.13	-	-	-	-0.46±0.26
EASN	-3.69±0.08	-	-	-	16.43±0.14	-5.02±0.11	-	-	-	16.94±0.22	1.33±0.14	-	-	-	-0.51±0.27
EDIN	1.91±0.09	-	-	-	14.78±0.15	0.36±0.1	-	-	-	15.37±0.23	1.55±0.13	-	-	-	-0.59±0.28
ESKD	1.56±0.1	1.61±0.11	-0.14±0.12	0.18±0.12	14.95±0.18	-0.45±0.13	-0.05±0.15	-0.72±0.13	-1.02±0.13	16.26±0.28	2.01±0.16	1.66±0.19	0.58±0.18	1.2±0.18	-1.31±0.34
EXMO	-5.29±0.1	1.24±0.1	1.11±0.11	0.04±0.11	16.53±0.17	-6.42±0.13	0.32±0.14	0.26±0.12	-0.19±0.14	17.33±0.27	1.13±0.16	0.92±0.17	0.85±0.16	0.23±0.18	-0.8±0.32
FARB	-3.5±0.09	-	-	-	17.41±0.15	-5.12±0.11	-	-	-	18.04±0.23	1.62±0.14	-	-	-	-0.62±0.27
FAUG	0.09±0.09	-	-	-	13.96±0.17	-0.6±0.11	-	-	-	14.21±0.25	0.69±0.14	-	-	-	-0.25±0.3
GIGG	4.31±0.1	-	-	-	15.88±0.18	2.86±0.12	-	-	-	16.41±0.27	1.45±0.16	-	-	-	-0.53±0.32
GIRA	-6.28±0.09	-	-	-	14.75±0.16	-7.29±0.11	-	-	-	15.12±0.24	1.01±0.14	-	-	-	-0.37±0.29
GLAS	-0.55±0.09	-	-	-	14.53±0.16	-2.05±0.11	-	-	-	15.12±0.24	1.5±0.14	-	-	-	-0.59±0.28
GORS	-5.26±0.08	-	-	-	16.96±0.14	-6.16±0.1	-	-	-	17.3±0.22	0.9±0.13	-	-	-	-0.35±0.26
HARD	-2.96±0.09	-	-	-	17.05±0.15	-4.14±0.11	-	-	-	17.51±0.23	1.18±0.14	-	-	-	-0.46±0.28
HELS	-10.88±0.1	-	-	-	13.68±0.18	-12.09±0.13	-	-	-	14.11±0.28	1.21±0.16	-	-	-	-0.43±0.33
HERT	2.44±0.19	-	-	-	16.75±0.24	2.25±0.18	-	-	-	16.77±0.32	0.19±0.26	-	-	-	-0.02±0.4
HOLY	-3.96±0.08	-	-	-	15.54±0.15	-4.88±0.11	-	-	-	15.89±0.23	0.92±0.14	-	-	-	-0.35±0.27
HOOB	4.46±0.09	-	-	-	15.61±0.16	2.55±0.11	-	-	-	16.35±0.24	1.91±0.14	-	-	-	-0.74±0.28
INVR	-5.79±0.09	-	-	-	14.16±0.16	-6.74±0.11	-	-	-	14.51±0.24	0.95±0.14	-	-	-	-0.35±0.28
KELO	8.11±0.09	-1.33±0.1	-	-	15.09±0.15	5.69±0.11	-3.58±0.11	-	-	16.37±0.23	2.42±0.14	2.25±0.15	-	-	-1.28±0.27

Table 6-2 continued

	1st approach					2nd approach					The difference (1st – 2nd)				
	(A)	(B)	(C)	(D)	(E)	(F)	(G)	(H)	(I)	(J)	(K)	(L)	(M)	(N)	(O)
KILN	Offset#1	Offset#2	Offset#3	Offset#4	Trend	Offset#1	Offset#2	Offset#3	Offset#4	Trend	Offset#1	Offset#2	Offset#3	Offset#4	Trend
KING	-10.66±0.08	-	-	-	16.8±0.15	-12.21±0.1	-	-	-	17.41±0.22	1.55±0.13	-	-	-	-0.61±0.26
KINL	4.95±0.08	-	-	-	13.6±0.15	3.85±0.1	-	-	-	14.03±0.22	1.1±0.13	-	-	-	-0.43±0.27
KIRK	-0.03±0.09	-	-	-	14.89±0.17	-1.64±0.11	-	-	-	15.5±0.24	1.61±0.14	-	-	-	-0.61±0.29
KIRW	5.16±0.08	-	-	-	13.66±0.14	4.42±0.1	-	-	-	13.95±0.21	0.74±0.13	-	-	-	-0.28±0.25
KLRE	-2.34±0.12	-	-	-	14.12±0.15	-2.68±0.14	-	-	-	14.19±0.24	0.34±0.18	-	-	-	-0.08±0.28
LEED	-6.38±0.08	-	-	-	16.06±0.15	-7.46±0.11	-	-	-	16.46±0.23	1.08±0.14	-	-	-	-0.4±0.28
LEEK	-0.65±0.1	-	-	-	16.08±0.17	-1.55±0.12	-	-	-	16.4±0.27	0.9±0.16	-	-	-	-0.32±0.32
LICF	3.3±0.09	-	-	-	16.44±0.16	1.7±0.11	-	-	-	17.05±0.23	1.6±0.14	-	-	-	-0.61±0.28
LINO	3.57±0.08	-	-	-	16.48±0.15	1.9±0.1	-	-	-	17.14±0.22	1.67±0.13	-	-	-	-0.66±0.26
LOCG	-1.67±0.11	-	-	-	14.68±0.19	-3.22±0.13	-	-	-	15.28±0.29	1.55±0.17	-	-	-	-0.6±0.35
LOFT	-1.19±0.09	-	-	-	17.58±0.15	-2.84±0.11	-	-	-	18.21±0.23	1.65±0.14	-	-	-	-0.63±0.28
MACY	-2.8±0.1	-	-	-	16.06±0.17	-4.26±0.12	-	-	-	16.63±0.26	1.46±0.16	-	-	-	-0.57±0.31
MART	-0.74±0.08	-6.35±0.09	-	-	17.17±0.14	-1.01±0.1	-6.12±0.22	-	-	17.27±0.21	0.27±0.13	-0.23±0.24	-	-	-0.1±0.25
NCAS	1.02±0.09	-	-	-	14.78±0.17	-0.8±0.12	-	-	-	15.49±0.26	1.82±0.15	-	-	-	-0.71±0.31
NEWL	-2.82±0.11	1.77±0.1	-5.1±0.1	-	14.9±0.17	-2.94±0.13	1.5±0.13	-5.56±0.27	-	15.02±0.26	0.12±0.17	0.27±0.16	0.46±0.29	-	-0.12±0.31
OMGH	-2.1±0.11	-	-	-	14.21±0.14	-2.48±0.13	-	-	-	14.3±0.22	0.38±0.17	-	-	-	-0.1±0.26
OXFR	-6.1±0.08	-	-	-	17.4±0.15	-7.66±0.1	-	-	-	17.99±0.22	1.56±0.13	-	-	-	-0.6±0.26
PBIL	-194.98±0.08	-	-	-	17.15±0.15	-196.3±0.1	-	-	-	17.68±0.22	1.32±0.13	-	-	-	-0.53±0.27
PETE	-0.01±0.08	-	-	-	16.68±0.14	-1.22±0.1	-	-	-	17.16±0.21	1.21±0.13	-	-	-	-0.47±0.25
PMTH	-4.87±0.09	-	-	-	16.4±0.16	-6.07±0.11	-	-	-	16.86±0.23	1.2±0.14	-	-	-	-0.46±0.28
POOL	-0.94±0.09	-	-	-	16.99±0.16	-3.15±0.1	-	-	-	17.85±0.22	2.21±0.13	-	-	-	-0.86±0.28
PRAE	13.95±0.09	-	-	-	16.55±0.16	12.26±0.11	-	-	-	17.19±0.23	1.69±0.14	-	-	-	-0.64±0.28
RICM	7.97±0.09	-	-	-	15.94±0.15	6.33±0.11	-	-	-	16.57±0.23	1.64±0.14	-	-	-	-0.63±0.28
SABB	-11.96±0.09	-	-	-	16.28±0.16	-11.47±0.11	-	-	-	16.09±0.24	-0.49±0.14	-	-	-	0.19±0.29
SANO	0.31±0.09	-	-	-	16.36±0.17	-1.77±0.12	-	-	-	17.18±0.25	2.08±0.15	-	-	-	-0.82±0.3
SCAO	-8.48±0.09	-	-	-	17.16±0.15	-9.48±0.11	-	-	-	17.53±0.23	1±0.14	-	-	-	-0.36±0.28
SHOB	-2.42±0.1	-	-	-	15.82±0.18	-3.97±0.11	-	-	-	16.4±0.25	1.55±0.15	-	-	-	-0.58±0.3
SHRE	4.32±0.09	-	-	-	16.16±0.16	2.78±0.11	-	-	-	16.75±0.23	1.54±0.14	-	-	-	-0.59±0.28
SKEE	-7.74±0.08	-	-	-	17.24±0.14	-9±0.1	-	-	-	17.73±0.22	1.26±0.13	-	-	-	-0.49±0.26
STEE	3.08±0.08	1.89±0.08	0.78±0.09	-	16.62±0.14	1.93±0.1	1.07±0.12	0.14±0.1	-	17.34±0.22	1.15±0.13	0.82±0.14	0.64±0.13	-	-0.72±0.26
SWAN	-0.79±0.08	-	-	-	16.35±0.15	-2.01±0.11	-	-	-	16.83±0.23	1.22±0.14	-	-	-	-0.48±0.28
SWTG	4.77±0.11	-	-	-	13.93±0.15	2.85±0.31	-	-	-	13.87±0.28	1.92±0.33	-	-	-	0.06±0.32
TAUT	-1.18±0.09	-	-	-	16.51±0.16	-2.95±0.11	-	-	-	17.25±0.23	1.77±0.14	-	-	-	-0.74±0.28
THUS	-0.15±0.08	-	-	-	13.51±0.14	-0.68±0.1	-	-	-	13.7±0.22	0.53±0.13	-	-	-	-0.18±0.26
WARS	-45.63±0.1	-1.86±0.1	132.6±0.11	-	16.86±0.18	-46.82±0.1	-3.4±0.11	131.58±0.11	-	17.92±0.23	1.19±0.14	1.54±0.15	1.02±0.16	-	-1.06±0.29
WEAR	-5.05±0.12	-	-	-	15.59±0.21	-6.6±0.14	-	-	-	16.18±0.32	1.55±0.18	-	-	-	-0.59±0.38
WEIW	2.41±0.08	-	-	-	16.96±0.14	0.95±0.1	-	-	-	17.54±0.21	1.46±0.13	-	-	-	-0.58±0.25
WELL	-6.62±0.08	-	-	-	16.76±0.15	-8.24±0.1	-	-	-	17.38±0.22	1.62±0.13	-	-	-	-0.62±0.26
WEYB	-5.29±0.08	-	-	-	16.82±0.14	-5.61±0.1	-	-	-	16.94±0.22	0.32±0.13	-	-	-	-0.12±0.26
YEAS	4.22±0.08	-	-	-	16.18±0.15	2.72±0.1	-	-	-	16.74±0.22	1.5±0.13	-	-	-	-0.56±0.26

Table 6-3 ΔU component offsets (mm) and trends (mm/yr). 1st offset correction approach vs 2nd offset correction approach. Dark shaded areas indicate offsets in the algorithm testing dataset.

	1st approach					2nd approach					The difference (1st – 2nd)				
	(A)	(B)	(C)	(D)	(E)	(F)	(G)	(H)	(I)	(J)	(K)	(L)	(M)	(N)	(O)
	Offset#1	Offset#2	Offset#3	Offset#4	Trend	Offset#1	Offset#2	Offset#3	Offset#4	Trend	Offset#1	Offset#2	Offset#3	Offset#4	Trend
ABER	-0.39±0.29	-	-	-	0.29±0.85	4.82±0.71	-	-	-	0.16±1.29	-5.21±0.77	-	-	-	0.14±1.54
ABYW	1.33±0.34	37.71±0.36	-	-	-1.65±0.9	0.07±0.4	35.26±0.75	-	-	-1.13±1.35	1.26±0.52	2.45±0.83	-	-	-0.51±1.63
AMER	15.22±0.25	-	-	-	-0.84±0.89	14.03±0.3	-	-	-	-0.31±1.34	1.19±0.39	-	-	-	-0.53±1.61
ANLX	249.05±0.21	-	-	-	-0.99±0.85	247.8±0.28	-	-	-	-0.52±1.3	1.25±0.35	-	-	-	-0.47±1.55
APPL	2.47±0.3	9.2±0.23	-	-	-0.56±0.87	3.39±0.33	8.66±0.28	-	-	-0.37±1.31	-0.92±0.45	0.54±0.36	-	-	-0.19±1.57
ASAP	8.02±0.24	-	-	-	-0.87±0.88	8.04±0.31	-	-	-	-0.92±1.35	-0.02±0.39	-	-	-	0.04±1.61
ATTL	8.16±0.25	-	-	-	-1.02±0.89	7.73±0.3	-	-	-	-0.81±1.33	0.43±0.39	-	-	-	-0.21±1.6
BARR	-9.19±0.31	28.98±0.16	-	-	-0.34±0.8	-9.59±0.32	26.14±0.2	-	-	0.8±1.2	0.4±0.45	2.84±0.26	-	-	-1.14±1.44
BEES	8.69±0.23	-	-	-	0.57±1.01	8.72±0.26	-	-	-	0.57±1.29	-0.03±0.35	-	-	-	0±1.64
BELF	6.71±0.3	-	-	-	-0.2±0.88	5.17±0.33	-	-	-	0.37±1.32	1.54±0.45	-	-	-	-0.57±1.59
BLAP	27.27±0.21	-	-	-	-0.43±0.86	24.81±0.29	-	-	-	0.57±1.31	2.46±0.36	-	-	-	-1±1.56
BRAE	9.49±0.25	-	-	-	0.96±0.89	7.87±0.31	-	-	-	1.65±1.34	1.62±0.4	-	-	-	-0.68±1.61
BREC	10.55±0.23	-	-	-	-0.64±0.87	9.92±0.3	-	-	-	-0.37±1.33	0.63±0.38	-	-	-	-0.27±1.59
BUCK	24.06±0.21	-	-	-	0.39±0.85	21.08±0.25	-	-	-	1.59±1.27	2.98±0.33	-	-	-	-1.2±1.52
CAML	14.64±0.44	-	-	-	-3.08±1.11	5.01±0.3	-	-	-	0.29±1.34	9.63±0.53	-	-	-	-3.38±1.74
CARI	9.65±0.22	-	-	-	-1.28±0.86	9.12±0.29	-	-	-	-1.04±1.31	0.53±0.36	-	-	-	-0.23±1.57
CARL	-3.41±0.23	-	-	-	0.15±0.87	-3.9±0.29	-	-	-	0.39±1.33	0.49±0.37	-	-	-	-0.24±1.59
CLAW	11.99±0.24	-	-	-	-0.84±0.88	11.68±0.3	-	-	-	-0.71±1.33	0.31±0.38	-	-	-	-0.13±1.6
DARE	13.48±0.23	-	-	-	-0.9±0.87	12.57±0.31	-	-	-	-0.5±1.34	0.91±0.39	-	-	-	-0.4±1.6
DROW	14.11±0.23	-	-	-	-1.47±0.87	14.77±0.29	-	-	-	-1.73±1.32	-0.66±0.37	-	-	-	0.27±1.57
DRUM	3.59±0.22	-	-	-	0.85±0.86	1.82±0.28	-	-	-	1.55±1.3	1.77±0.36	-	-	-	-0.69±1.56
DUNG	24.46±0.24	-	-	-	-1.55±0.88	23.44±0.3	-	-	-	-1.14±1.32	1.02±0.38	-	-	-	-0.41±1.59
EASN	10.97±0.25	-	-	-	-0.68±0.89	8.81±0.32	-	-	-	0.16±1.35	2.16±0.41	-	-	-	-0.84±1.62
EDIN	-0.93±0.21	-	-	-	0.66±0.85	-2.96±0.26	-	-	-	1.44±1.28	2.03±0.33	-	-	-	-0.79±1.54
ESKD	8.84±0.23	5.02±0.24	4.11±0.26	-1.83±0.26	-0.03±0.87	4.4±0.29	0.8±0.33	1.74±0.29	-3.38±0.29	3.13±1.32	4.44±0.37	4.22±0.41	2.37±0.39	1.55±0.39	-3.16±1.58
EXMO	20.83±0.26	3.68±0.28	-1.39±0.3	-0.9±0.29	-0.55±0.91	20±0.34	2.66±0.37	-2.28±0.33	-1.54±0.39	0.25±1.37	0.83±0.43	1.02±0.46	0.89±0.45	0.64±0.49	-0.8±1.65
FARB	29.2±0.25	-	-	-	-1.96±0.89	28.58±0.3	-	-	-	-1.74±1.32	0.62±0.39	-	-	-	-0.23±1.59
FAUG	15.18±0.21	-	-	-	1.12±0.86	13.23±0.27	-	-	-	1.9±1.31	1.95±0.34	-	-	-	-0.78±1.56
GIGG	10.3±0.24	-	-	-	-0.49±0.88	8.62±0.3	-	-	-	0.21±1.34	1.68±0.38	-	-	-	-0.7±1.6
GIRA	-3.25±0.22	-	-	-	0.93±0.86	-3.63±0.28	-	-	-	1.1±1.3	0.38±0.36	-	-	-	-0.16±1.56
GLAS	10.22±0.22	-	-	-	0.19±0.86	9.23±0.29	-	-	-	0.57±1.32	0.99±0.36	-	-	-	-0.38±1.57
GORS	22.95±0.25	-	-	-	-1.23±0.9	22.52±0.32	-	-	-	-1.05±1.35	0.43±0.41	-	-	-	-0.18±1.62
HARD	20.35±0.24	-	-	-	-1.14±0.88	20.07±0.29	-	-	-	-0.93±1.32	0.28±0.38	-	-	-	-0.21±1.58
HELS	7.54±0.35	-	-	-	-1.48±1.01	0.94±0.31	-	-	-	0.92±1.37	6.6±0.47	-	-	-	-2.4±1.7
HERT	5.88±0.38	-	-	-	-0.44±0.9	4.89±0.38	-	-	-	0.18±1.33	0.99±0.54	-	-	-	-0.62±1.61
HOLY	23.15±0.22	-	-	-	-0.8±0.86	20.17±0.28	-	-	-	0.38±1.3	2.98±0.36	-	-	-	-1.17±1.56
HOOB	0.17±0.25	-	-	-	1.45±0.89	1.39±0.32	-	-	-	0.95±1.36	-1.22±0.41	-	-	-	0.5±1.62
INVR	-5.04±0.21	-	-	-	0.96±0.86	-6.38±0.27	-	-	-	1.53±1.29	1.34±0.34	-	-	-	-0.57±1.55
KELO	18.6±0.23	5.54±0.26	-	-	-0.86±0.87	20.22±0.31	6.82±0.32	-	-	-1.7±1.33	-1.62±0.39	-1.28±0.41	-	-	0.84±1.59

Table 6-3 continued

	1st approach					2nd approach					The difference (1st – 2nd)				
	(A) Offset#1	(B) Offset#2	(C) Offset#3	(D) Offset#4	(E) Trend	(F) Offset#1	(G) Offset#2	(H) Offset#3	(I) Offset#4	(J) Trend	(K) Offset#1	(L) Offset#2	(M) Offset#3	(N) Offset#4	(O) Trend
KEYW	13.08±0.23	-	-	-	-0.82±0.88	12.38±0.29	-	-	-	-0.53±1.33	0.7±0.37	-	-	-	-0.3±1.59
KILN	4.09±0.28	-	-	-	1.15±0.92	3.7±0.33	-	-	-	1.31±1.36	0.39±0.43	-	-	-	-0.16±1.65
KING	2.36±0.23	-	-	-	-1.01±0.87	1.43±0.3	-	-	-	-0.62±1.33	0.93±0.38	-	-	-	-0.38±1.59
KINL	0.74±0.19	-	-	-	0.9±0.83	-1.12±0.23	-	-	-	1.66±1.25	1.86±0.3	-	-	-	-0.76±1.5
KIRK	11.12±0.22	-	-	-	-0.98±0.86	11.54±0.28	-	-	-	-1.13±1.3	-0.42±0.36	-	-	-	0.15±1.56
KIRW	9.55±0.2	-	-	-	0.1±0.84	6.57±0.25	-	-	-	1.3±1.27	2.98±0.32	-	-	-	-1.2±1.53
KLRE	3.28±0.3	-	-	-	0.18±0.86	3.48±0.35	-	-	-	0.12±1.31	-0.2±0.46	-	-	-	0.06±1.56
LEED	-1.64±0.23	-	-	-	-0.4±0.87	-2.73±0.29	-	-	-	0.06±1.33	1.09±0.37	-	-	-	-0.46±1.59
LEEK	10.18±0.25	-	-	-	-0.57±0.89	8.46±0.32	-	-	-	0.17±1.36	1.72±0.41	-	-	-	-0.74±1.62
LICF	16.24±0.22	-	-	-	-0.81±0.86	16.68±0.28	-	-	-	-0.99±1.3	-0.44±0.36	-	-	-	0.18±1.56
LINO	15.31±0.23	-	-	-	-0.7±0.87	15.72±0.3	-	-	-	-0.87±1.32	-0.41±0.38	-	-	-	0.17±1.58
LOCG	25.66±0.27	-	-	-	-1.03±0.91	21.78±0.28	-	-	-	0.47±1.3	3.88±0.39	-	-	-	-1.5±1.59
LOFT	14.47±0.24	-	-	-	-2.38±0.88	14.04±0.31	-	-	-	-2.21±1.35	0.43±0.39	-	-	-	-0.17±1.61
MACY	2.74±0.24	-	-	-	-0.74±0.88	0.92±0.31	-	-	-	0.1±1.35	1.82±0.39	-	-	-	-0.84±1.61
MART	89.09±0.24	-13.28±0.27	-	-	-2.38±0.87	89.28±0.3	-4.21±0.75	-	-	-2.49±1.31	-0.19±0.38	-9.07±0.8	-	-	0.11±1.58
NCAS	-59.82±0.22	-	-	-	0.59±0.86	-61.02±0.3	-4.27±0.7	-	-	1.02±1.32	1.2±0.37	4.27±0.7	-	-	-0.44±1.58
NEWL	0.26±0.26	3.56±0.23	-0.1±0.24	-	-2.64±0.86	0.25±0.28	3.26±0.29	-4.27±0.7	-	-2.53±1.29	0.01±0.38	0.3±0.37	4.17±0.74	-	-0.11±1.55
OMGH	10.63±0.31	-	-	-	0.17±0.86	10.53±0.36	-	-	-	0.18±1.31	0.1±0.48	-	-	-	-0.02±1.56
OXFR	15.27±0.23	-	-	-	-0.9±0.87	15.01±0.29	-	-	-	-0.76±1.32	0.26±0.37	-	-	-	-0.14±1.58
PBIL	26.11±0.27	-	-	-	-3.1±0.92	21.78±0.28	-	-	-	-1.5±1.3	4.33±0.39	-	-	-	-1.6±1.6
PETE	22.27±0.22	-	-	-	-0.62±0.87	22.19±0.29	-	-	-	-0.68±1.31	0.08±0.36	-	-	-	0.06±1.57
PMTH	6.7±0.25	-	-	-	-1.14±0.89	7.21±0.32	-	-	-	-1.32±1.35	-0.51±0.41	-	-	-	0.19±1.62
POOL	14.18±0.25	-	-	-	-0.86±0.9	14.25±0.31	-	-	-	-0.87±1.34	-0.07±0.4	-	-	-	0.01±1.61
PRAE	79.83±0.23	-	-	-	-1.77±0.87	80.21±0.29	-	-	-	-1.95±1.29	-0.38±0.37	-	-	-	0.18±1.56
RICM	13.97±0.24	-	-	-	-0.47±0.88	12.73±0.3	-	-	-	0.03±1.34	1.24±0.38	-	-	-	-0.51±1.6
SABB	68.91±0.48	-	-	-	-7.73±1.15	53.43±0.35	-	-	-	-0.77±1.39	15.48±0.59	-	-	-	-6.96±1.8
SANO	32.14±0.24	-	-	-	-1.32±0.88	31.24±0.31	-	-	-	-1.02±1.33	0.9±0.39	-	-	-	-0.3±1.59
SCAO	25.71±0.24	-	-	-	-1.05±0.9	23.82±0.3	-	-	-	-0.27±1.33	1.89±0.38	-	-	-	-0.78±1.6
SHOB	8.12±0.24	-	-	-	-0.56±0.91	7.93±0.3	-	-	-	-0.44±1.34	0.19±0.38	-	-	-	-0.11±1.62
SHRE	14.98±0.24	-	-	-	-0.74±0.88	13.93±0.31	-	-	-	-0.31±1.34	1.05±0.39	-	-	-	-0.43±1.6
SKEE	30.63±0.24	-	-	-	-2.23±0.88	28.5±0.31	-	-	-	-1.42±1.33	2.13±0.39	-	-	-	-0.81±1.6
STEE	19.41±0.24	-0.95±0.25	2.99±0.27	-	-1.11±0.88	18.69±0.3	-2.01±0.34	1.36±0.3	-	-0.4±1.32	0.72±0.38	1.06±0.42	1.63±0.4	-	-0.71±1.59
SWAN	14.32±0.24	-	-	-	-1.28±0.89	12.82±0.31	-	-	-	-0.67±1.35	1.5±0.39	-	-	-	-0.61±1.61
SWTG	-7.64±0.2	-	-	-	-0.76±0.8	-8.95±0.48	-	-	-	-0.69±1.42	1.31±0.52	-	-	-	-0.07±1.63
TAUT	13.27±0.31	-	-	-	-0.77±0.96	17.98±0.37	-	-	-	-2.68±1.42	-4.71±0.48	-	-	-	1.92±1.71
THUS	9.23±0.2	-	-	-	0.44±0.83	7.13±0.24	-	-	-	1.33±1.25	2.1±0.31	-	-	-	-0.88±1.5
WARS	1021.79±0.27	15.65±0.26	-503.6±0.29	-	-1.3±0.95	1020.81±0.31	16.88±0.32	-505.18±0.33	-	-1.4±1.35	0.98±0.41	-1.23±0.41	1.58±0.44	-	0.1±1.65
WEAR	9.85±0.26	-	-	-	0.04±0.9	8.67±0.33	-	-	-	0.5±1.38	1.18±0.42	-	-	-	-0.46±1.65
WEIW	19.42±0.24	-	-	-	-1.15±0.88	17.77±0.3	-	-	-	-0.51±1.33	1.65±0.38	-	-	-	-0.64±1.59
WELL	15.28±0.22	-	-	-	-0.89±0.86	14.44±0.28	-	-	-	-0.56±1.3	0.84±0.36	-	-	-	-0.33±1.56
WEYB	18.14±0.25	-	-	-	-1.34±0.89	16.84±0.32	-	-	-	-0.84±1.34	1.3±0.41	-	-	-	-0.5±1.61
YEAS	9.66±0.24	-	-	-	-0.82±0.88	7.34±0.32	-	-	-	0.05±1.35	2.32±0.4	-	-	-	-0.87±1.62

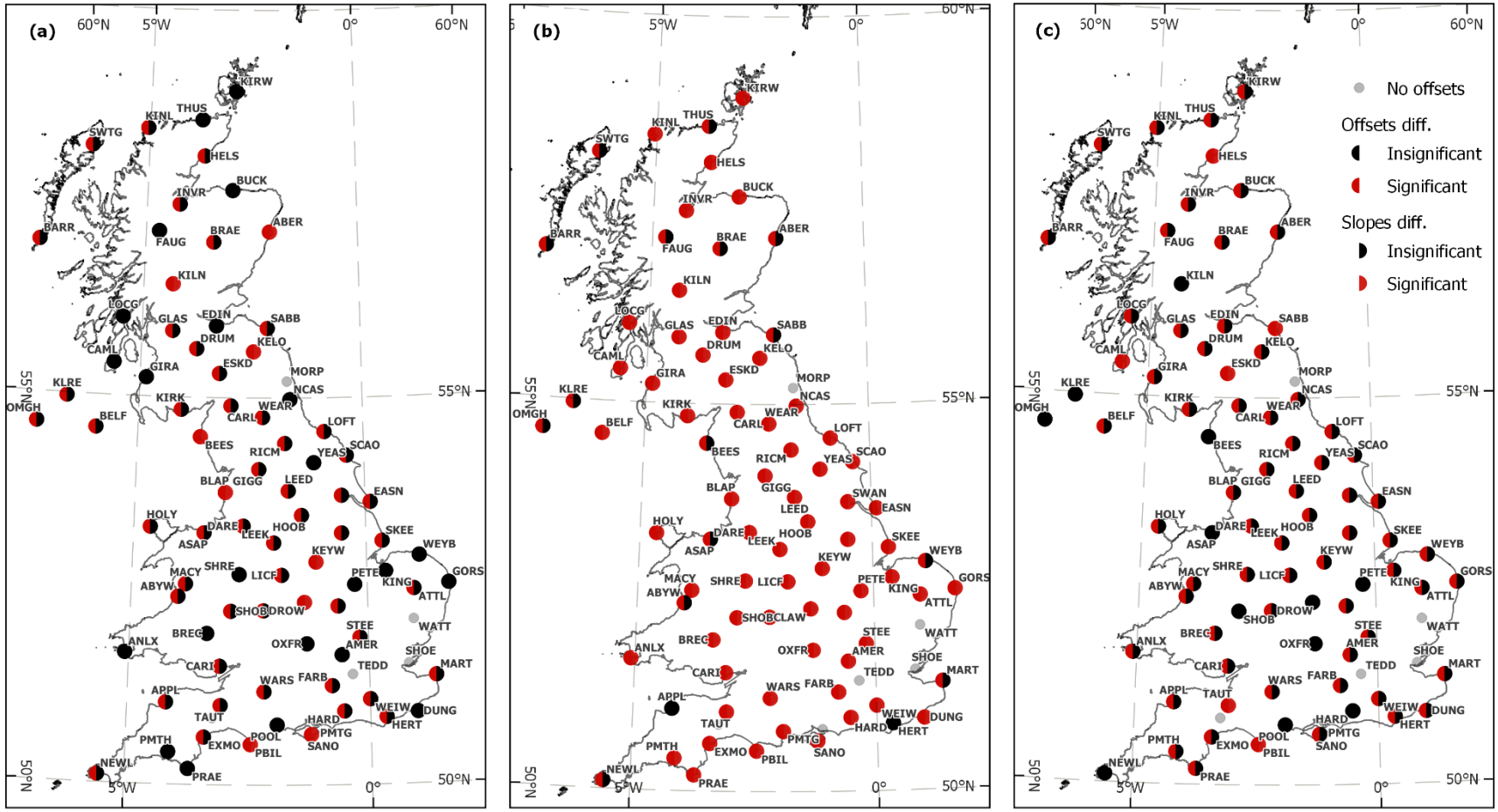


Figure 6-2 Stations which have significant or insignificant differences in their offset (left semicircle) and linear trend estimates (right semicircle) from the 1st and 2nd offset correction approaches, in their: (a) ΔN; (b) ΔE; and (c) ΔU components.

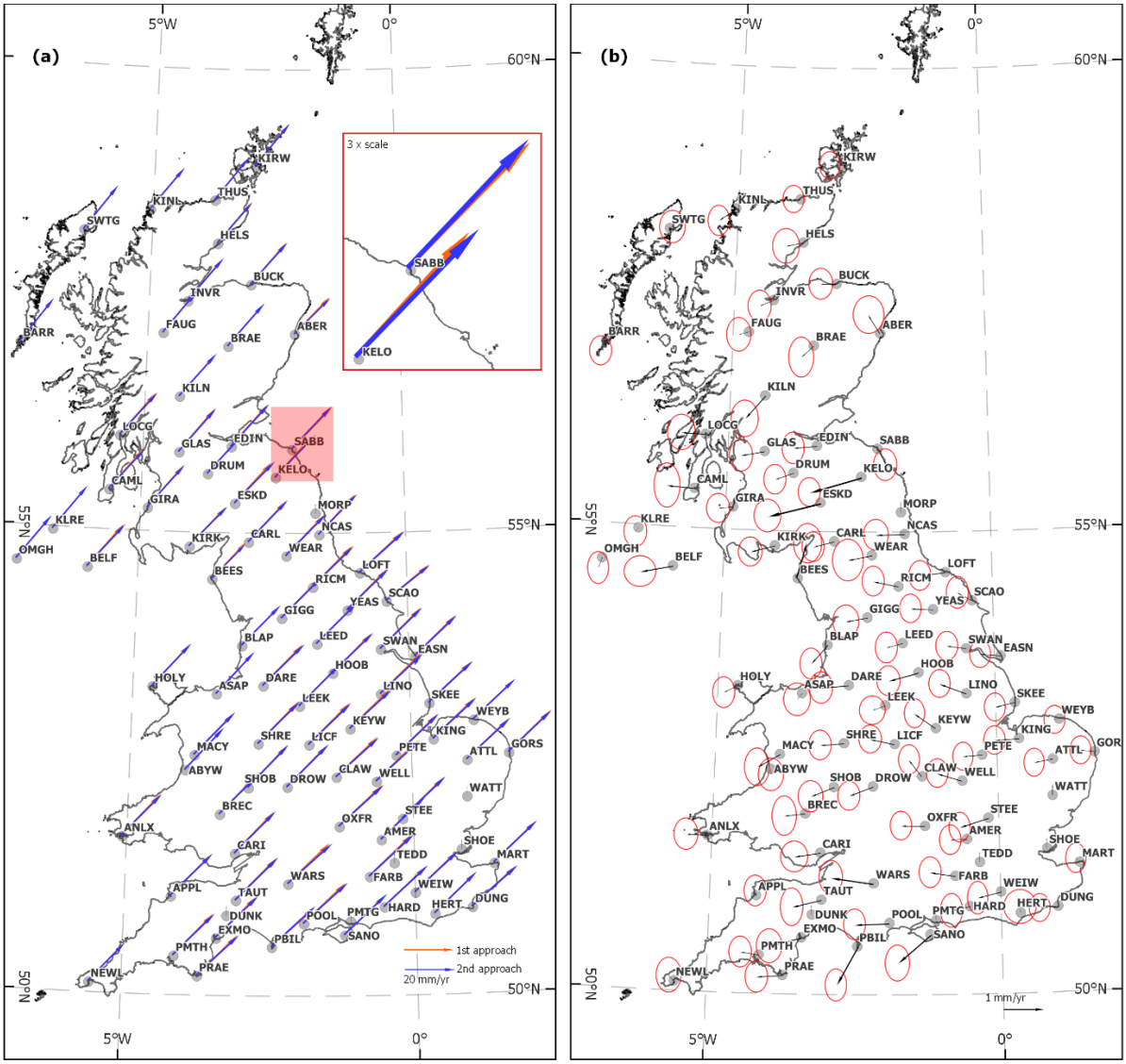


Figure 6-3 Horizontal station velocities derived from (a) the 1st (orange) and 2nd (blue) offset correction approaches, and (b) the differences between these velocity estimates and their uncertainties.

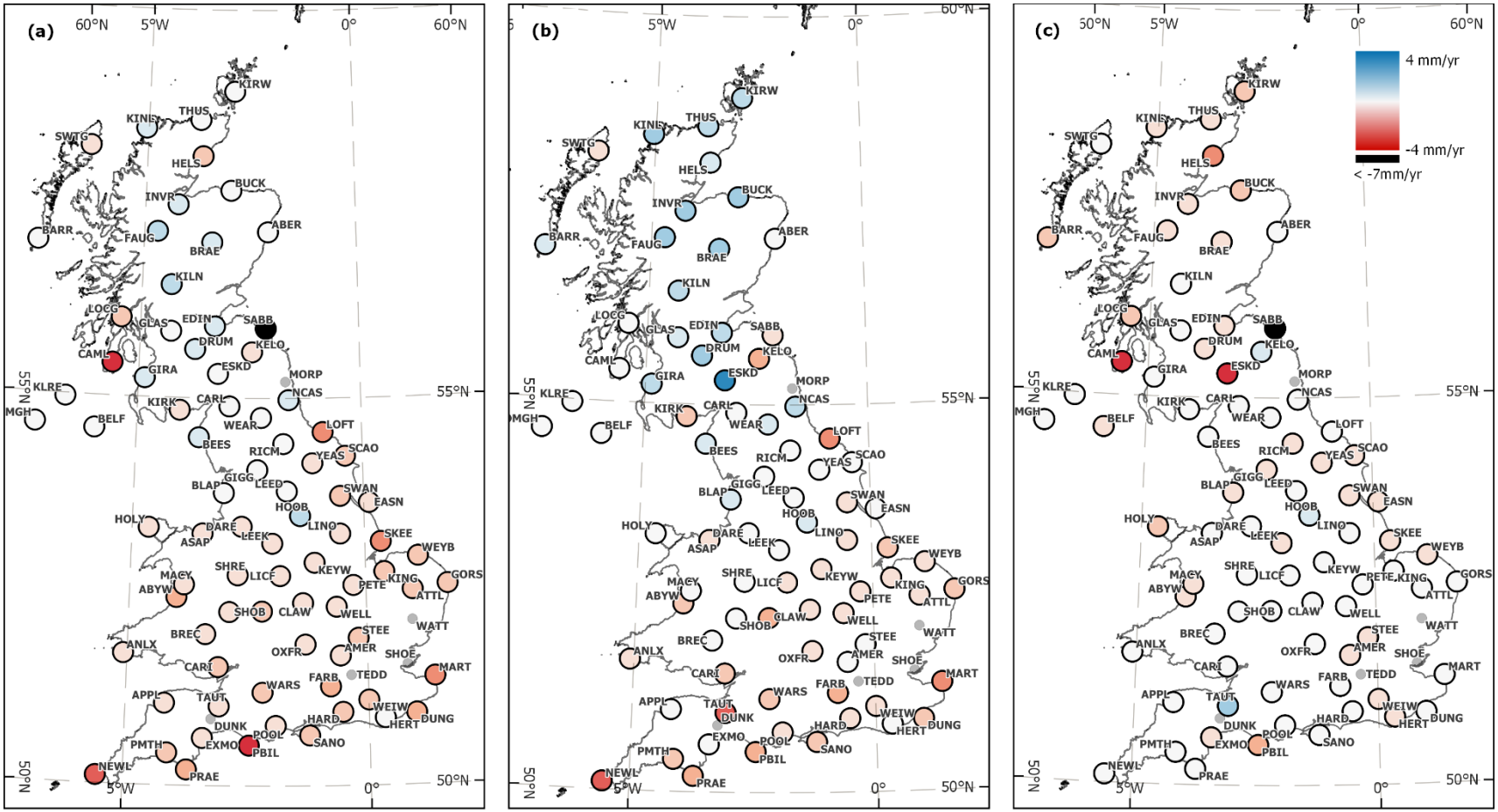


Figure 6-4 Vertical station velocities derived from: (a) the 1st offset correction approach; (b) the 2nd offset correction approach, and(c) the difference between these velocity estimates.

6.2.2 The Multiple analysis algorithm approach

Tables 6-4 and 6-5 show the residuals threshold values and the number of anomalous days for the three components, ΔN, ΔE and ΔU, as detected by the three analysis algorithms using the two offset correction approaches respectively. In addition, an asterisk is put next to the number of anomalies detected by the spatial analysis algorithm (columns E, K and Q) if >50% of the last 200 days of the algorithm testing period are considered anomalies by the spatial analysis algorithm which will be used in the classification process later in sub-section 6.3.3.

The temporal and combined residuals threshold values are generally in agreement in all components when comparing the two offset correction approaches, while the spatial residuals threshold values vary at a few stations (e.g. PBIL (ΔN), ABER (ΔE) and SABB (ΔU)) due to the existence of anomalous behaviours in their algorithm training dataset (as will be discussed later). However, it is always the case that the temporal analysis gives larger threshold values than the spatial analysis, due to the higher noise level. Consequently, the number of anomalous days detected by the spatial analysis is higher than the temporal analysis while the combined analysis is in between.

For the sake of completion, the Figures A-1 to A261 in the appendix show the corrected displacement time series, the detrended and low-frequency time series, as well as the temporal, spatial and combined analysis residuals with their corresponding thresholds of each station.

Table 6-4 The residuals threshold values and the number of anomalies for the three components using the temporal (T), spatial (S) and combined (C) analysis algorithms. Dark shaded areas indicate more than 200 anomalies identified by the spatial analysis or more than 10 anomalies identified by the temporal analysis using the 1st offset correction approach.

	ΔN						ΔE						ΔU					
	Residuals Threshold (mm)			Anomalies (days)			Residuals Threshold (mm)			Anomalies (days)			Residuals Threshold (mm)			Anomalies (days)		
	(A) T	(B) S	(C) C	(D) T	(E) S	(F) C	(G) T	(H) S	(I) C	(J) T	(K) S	(L) C	(M) T	(N) S	(O) C	(P) T	(Q) S	(R) C
ABER	5.42	3.81	3.72	29	235*	67	5.22	3.44	2.98	54	256	134	15.44	7.38	10.13	2	47	12
ABYW	5.99	2.17	4.17	3	11	2	6.01	3.02	3.82	-	10	2	20	9.16	14.75	1	2	3
AMER	5.5	2.1	2.67	1	13	8	5.39	2.43	2.33	2	1	8	18.42	5.86	8.72	5	30	6
ANLX	5.83	2.51	3.73	6	2	2	5.56	2.64	3.05	1	3	5	17.99	7.83	13.11	4	1	-
APPL	5.87	2.76	3.36	4	10	12	5.51	2.7	2.81	2	144*	6	18.66	6.96	11.33	1	14	3
ASAP	6.03	2.41	3.74	4	5	2	6.33	3.39	3.55	1	15	13	19.17	7.84	11.57	2	9	5
ATTL	5.09	2.25	2.34	6	25	15	5.15	1.76	1.81	4	29	22	17.79	5.14	8.1	9	34	31
BARR	4.91	2.56	3.37	2	11	3	5.31	5.13	3.15	-	-	6	14.08	6.75	10.43	4	73	3
BEES	5.2	4.7	2.7	7	172	7	5.89	3.78	2.81	-	36	3	16.97	5.58	9.33	-	9	10
BELF	5.56	2.71	3.73	2	-	4	6.89	5.92	4.74	5	62	16	17.83	8.28	12.48	4	3	7
BLAP	5.37	3.71	3.04	4	56	5	5.41	2.07	2.41	2	4	7	17.28	5.89	9.94	3	83	8
BRAE	7.41	5.23	5.96	11	3	19	6.39	2.77	4.34	6	11	19	17.82	9.27	13.32	5	6	12
BREC	7.5	3.24	5.3	8	16	17	6.05	2.36	3.33	-	28	5	18.95	6.22	11.4	-	20	5
BUCK	5.59	2.99	4.2	3	-	3	5.87	4.19	3.76	2	1	7	15.83	7.97	11.62	5	40	5
CAML	7.57	5.01	6	11	2	18	6.24	6.5	4.05	2	6	7	18.61	7.17	12.57	59	341*	155
CARI	5.75	2.01	3.28	6	2	7	6.28	7.99	3.85	1	-	7	18.53	6.84	10.85	-	15	8
CARL	5.16	2.47	3.18	3	12	4	5.51	2.89	2.77	-	6	11	17.9	6.9	10.16	1	10	9
CLAW	5.14	2.13	2.48	3	287*	6	5.31	1.84	2.14	3	7	7	18.03	6	9.45	6	16	9
DARE	5.35	2.73	3.14	3	1	5	5.4	2.93	2.6	4	100	15	17.39	7.19	9.65	1	-	8
DROW	5.39	1.95	2.59	5	103	10	5.53	1.78	2.45	2	54	3	18.17	5.76	9.26	-	52	7
DRUM	5.27	2.27	3.27	5	14	7	5.62	1.95	3.01	1	2	4	17.25	6.29	10.24	2	12	10
DUNG	5.13	1.55	2.22	2	47	13	5.28	1.71	2.06	1	255*	21	18.28	5.44	8.5	3	18	9
DUNK	5.41	2.49	3.5	2	4	5	5.75	2.84	3.72	1	55	4	20.15	9.46	12.1	2	1	2
EASN	4.91	1.55	2.32	3	3	1	5.29	1.54	2.07	1	36	6	18.5	5.82	9.18	3	40	3
EDIN	5.55	2.64	3.55	6	4	13	5.45	1.81	2.63	2	116	12	16.76	5.99	9.86	4	20	11
ESKD	5.69	2.39	3.53	4	11	10	6.65	3.16	4.32	6	49	18	17.77	7.57	11.43	3	352*	8
EXMO	6.26	2.8	3.39	4	-	4	6.35	2.96	4.04	6	19	12	19.66	10.33	11.68	6	3	6
FARB	5.55	2.1	2.44	2	7	9	5.43	1.89	2.16	1	331*	8	18.27	4.99	8.08	8	75	8
FAUG	6.16	2.76	4.99	1	6	5	6.02	2.5	3.91	1	8	8	16.84	7.36	12.55	2	5	2
GIGG	5.85	2.49	3.74	8	10	8	6.29	3.3	3.97	-	35	8	18.88	6.48	12.25	-	16	5
GIRA	5.14	3.04	3.22	12	8	16	5.73	3.01	3.15	-	5	8	17.49	6.64	10.91	4	64	9
GLAS	5.7	3.05	3.7	6	3	9	5.71	2.69	3.06	4	14	11	18.06	6.32	10.63	1	14	6
GORS	5.19	1.68	2.4	4	18	11	5.45	2.41	2.15	1	-	11	18.55	5.86	9.02	5	18	10
HARD	6.15	3.17	3.45	4	11	13	5.53	2.69	2.49	1	10	15	18.26	6.18	8.75	4	36	13
HELS	6.2	3.46	5.07	9	10	10	6.42	3.9	4.17	1	27	10	18.14	10.09	13.69	9	266*	14
HERT	5.94	2.89	3.2	22	109	95	6.62	3.93	4.07	24	160	86	18.58	7.31	9.22	5	61	13
HOLY	5.6	2.21	3.12	2	8	3	5.39	2.13	2.49	2	1	2	17.35	6.5	9.82	2	124	12
HOOB	5.33	2.24	3.06	5	37	5	5.59	2.06	2.93	-	292*	6	18.5	6.79	10.44	2	78	6
INVR	5.45	2.62	4.2	11	22	11	5.64	2.54	3.18	2	4	15	16.83	7.39	11.7	5	27	5
KELO	5.05	2.36	2.98	8	11	8	5.63	2.96	2.83	1	440*	21	17.19	9.85	10.52	3	306	34
KEYW	5.03	1.96	2.57	2	225*	6	5.09	1.7	2.15	2	14	9	17.39	5.34	8.92	3	18	9
KILN	7	3.48	5.75	6	199	10	6.74	2.86	4.69	3	11	8	19.86	9.89	15.01	13	28	24
KING	5.03	2.09	2.48	5	5	3	5.14	1.72	1.93	1	312*	10	17.23	7.01	8.15	3	29	14
KINL	5.15	2.57	3.45	4	72	4	5.42	2.24	2.83	2	116	8	15.49	6.61	10.93	3	10	4
KIRK	5.21	3.09	3.04	6	69	6	5.72	5.06	3.14	2	1	16	17.54	5.87	10.08	3	51	8
KIRW	4.71	2.22	3.15	7	9	6	5.07	1.96	2.46	1	9	15	15.41	6.05	9.81	2	66	4
KLRE	5.65	2.17	3.83	2	2	5	5.2	2.47	3.25	1	32	8	17.5	6.66	11.13	3	24	5
LEED	5.63	3.03	3.2	8	3	10	5.58	2.11	2.82	1	4	13	18.16	6.11	10.3	3	26	9
LEEK	5.25	2.08	3.22	2	6	6	5.58	3.89	3.17	2	2	11	18.2	8.37	11.85	1	13	3
LICF	5.06	1.52	2.48	4	58	6	5.57	1.86	2.67	4	198	12	17.41	5.75	9.34	4	30	3
LINO	4.95	1.53	2.23	5	191	10	5.22	1.9	2.09	3	117	9	17.58	5.39	8.28	3	72	15
LOCG	6.35	3.41	4.77	2	5	4	6.79	3.58	4.52	2	7	11	17.71	6.85	12.38	6	163	11
LOFT	5.38	1.98	3.2	4	9	6	5.6	2.06	2.59	1	83	15	18.06	6.78	10.01	1	12	12
MACY	7.13	3.41	5.43	2	25	14	6.25	2.9	4.07	6	73	15	18.95	9.03	13.75	1	20	7
MART	5.4	1.93	2.57	5	79	6	5.19	1.69	2.08	2	95	10	17.85	5.27	8.16	3	262*	8
MORP	5.59	6.09	3.68	3	2	5	5.58	2.93	2.91	5	124	9	17.73	11.91	11.4	2	9	3
NCAS	5.4	3.23	3.37	4	-	7	5.52	2.81	2.59	2	213*	16	17.83	8.53	10.23	2	4	6
NEWL	6.15	3.39	3.75	3	88	9	5.76	2.97	3.46	3	44	13	18.2	8.5	12.38	6	54	6
OMGH	5.67	2.53	3.83	3	24	8	5.08	2.31	3.3	3	36	4	16.86	7.87	11.55	4	11	3
OXFR	5.27	1.65	2.57	4	28	3	5.31	1.76	2.11	2	173	10	18.17	6.31	9.96	2	5	1
PBIL	5.65	2.13	2.65	11	780*	63	5.3	2.07	2.18	3	1	13	18.09	6.17	9.1	10	423*	47
PETE	5.08	2.47	2.35	3	4	6	5.16	1.67	1.88	3	-	11	17.43	5.24	8.19	3	74	6
PMTG	5.47	3.27	3.45	5	4	3	5.77	2.92	2.47	-	142*	5	17.62	6.46	9.11	4	18	2
PMTH	5.71	1.83	2.82	2	32	3	5.64	2.02	2.73	2	9	5	19.81	7.41	10.82	4	9	3
POOL	5.69	2.56	2.74	2	43	7	5.35	2	2.03	4	407*	41	19.37	6.42	9.77	4	36	4
PRAE	5.81	2.2	2.95	2	15	4	5.57	2.14	2.61	2	168	10	18.11	6.18	9.67	8	22	5
RICM	5.51	2.38	3.47	8	6	21	5.55	1.97	2.91	6	31	16	18.17	6.17	10.9	3	16	15
SABB	5.43	2.81	3.51	6	154	35	5.58	2.56	2.95	1	430*	27	18.1	12.86	11.99	171	953*	404
SANO	6.23	7.64	3.84	5	47	6	5.77	4.14	2.56	2	114	10	18.23	7.22	9.56	2	2	8
SCAO	5.32	3.28	3.21	5	20	8	5.4	2.27	2.44	1	-	7	17.8	5.37	8.93	3	81	8
SHOB	5.76	2.1	3.05	6	17	9	5.88	2.17	3.01	2	64	9	18.96	6.22	10.28	1	7	5
SHOE	5.3	1.72	2.38	3	10	15	5.37	2.17	2.03	2	29	7	17.68	6.22	8.12	5	37	5
SHRE	5.5	1.96	3.09	1	7	5	5.54	1.84	2.59	3	35	5	18.53	6.2	10.28	2	13	3
SKEE	4.9	3.07	2.3	5	-	3	5.14	1.65	1.91	4	10	12	18.09	5.18	8.4	2	110	6
STEE	5.39	1.85	2.73	5	97	11	5.37	2.05	2.16	2	9	10	18.24	5.83	9.26	3	33	14
SWAN	5.09	2.37	2.7	7	2	8	5.42	2.09	2.43	2	2	5	18.36	6.32	9.18	1	25	4
SWTG	4.69	2.92	3.35	5	-	6	5.22	2.68	2.73	2	451*	11	14.06	6.4	9.39	4	51	1
TAUT	6.5	3.81	3.97	3	31	11	5.64	3.5	2.86	3	109	11	19.95	14	11.52	5	176	4
TEDD	6.17	4.62	3.48	28	257	69	6.13	5.35	3.22	25	33	94	18.28	6.04	8.18	5	100	17
THUS	4.71	2.01	3.21	6	12	13	5.17	1.97	2.58	2	17	8	15.5	6.89	10.11	10	23	8
WARS	5.8	2.75	2.94	8	16	15	5.69	2.08	2.55	4	263	38	19.23	7.21	10.12	2	30	9
WATT	5.18	2.47	2.84	3	4	1	5.16	1.89	2.24	-	3	-	18.84	6.01	9.37	3	9	2
WEAR	7.73	4.24	6.24	10	2	9	7.45	3.55	5.43	4	33	14	19.58	8.61	13.72	-	8	3
WEIW	5.92	3.96	3.21	2	17	9	5.29	2.6	2.23	1	193*	24	18.33	5.8	9.18	7	21	1
WELL	5.22	2.34	2.42	3	6	4	5.52	1.85	2.17	1	180	5	17.53	4.79	8.05	3	26	5
WEYB	5.03	1.82	2.53	4	8	6	5.23	1.74	2.08	2	120	6	18.27	5.29	8.86	5	85	7
YEAS	5.14	2.08	3.04	4	3	6	5.3	2.54	2.61	3	8	15	17.94	6.06	9.88	1	55	13

Table 6-5 The same as Table 6-4, by applying the spatial and temporal analysis algorithms using the 1st offset correction approach.

	ΔN						ΔE						ΔU					
	Residuals Threshold (mm)			Anomalies (days)			Residuals Threshold (mm)			Anomalies (days)			Residuals Threshold (mm)			Anomalies (days)		
	(A) T	(B) S	(C) C	(D) T	(E) S	(F) C	(G) T	(H) S	(I) C	(J) T	(K) S	(L) C	(M) T	(N) S	(O) C	(P) T	(Q) S	(R) C
ABER	5.41	3.81	3.7	28	311*	69	5.22	3.16	2.98	44	497*	109	15.44	7.3	10.08	1	148	12
ABYW	5.99	2.09	4.16	3	4	2	6.02	2.52	3.81	1	8	2	20	9.18	14.74	1	2	3
AMER	5.48	2.08	2.66	1	15	8	5.4	2.51	2.33	2	-	11	18.24	6.12	8.65	5	8	6
ANLX	5.83	2.53	3.73	6	2	2	5.58	2.58	3.06	1	-	5	18	7.8	13.12	4	-	1
APPL	5.86	2.82	3.35	4	4	13	5.52	2.78	2.82	1	21	7	18.66	7.12	11.33	1	9	2
ASAP	6.04	2.41	3.75	4	6	2	6.34	3.44	3.55	1	6	14	19.17	8.05	11.55	2	4	5
ATTL	5.08	2.22	2.34	6	24	15	5.15	1.65	1.81	3	18	24	17.79	5.28	8.1	9	21	29
BARR	4.93	2.6	3.38	2	1	3	5.32	5.14	3.15	-	-	6	14.11	6.76	10.43	4	8	3
BEES	5.2	5	2.7	5	87	5	5.88	4.08	2.8	-	1	3	16.94	5.6	9.29	-	7	8
BELF	5.56	2.71	3.73	2	-	4	6.9	5.85	4.75	5	29	16	17.82	8.42	12.47	4	3	7
BLAP	5.38	3.8	3.05	4	6	6	5.42	1.94	2.41	2	6	5	17.32	6.2	9.96	3	22	7
BRAE	7.45	5.21	5.99	11	3	20	6.39	2.69	4.33	6	7	18	17.84	9.23	13.32	5	6	12
BREC	7.51	3.25	5.3	8	15	17	6.08	2.36	3.34	-	15	5	18.96	6.3	11.41	-	16	5
BUCK	5.57	2.98	4.19	3	-	3	5.87	4.2	3.76	2	-	7	15.88	8.02	11.64	5	25	4
CAML	7.57	5.01	6	11	2	19	6.24	6.52	4.04	2	1	8	18.84	10.04	12.76	3	285*	24
CARI	5.76	2	3.28	6	4	6	6.29	8.11	3.84	1	-	9	18.53	6.99	10.86	-	4	8
CARL	5.16	2.46	3.18	3	9	4	5.53	3.02	2.78	-	3	10	17.91	6.97	10.15	1	6	8
CLAW	5.16	2.3	2.49	4	61	5	5.31	1.73	2.14	3	5	6	18.04	6.07	9.45	5	8	8
DARE	5.35	2.71	3.13	3	1	6	5.42	2.9	2.6	2	3	6	17.41	7.2	9.64	1	-	7
DROW	5.39	2.03	2.58	5	25	10	5.55	1.68	2.46	1	23	4	18.17	5.78	9.25	-	17	7
DRUM	5.28	2.24	3.27	4	13	7	5.63	1.86	3.01	1	6	4	17.26	6.25	10.25	2	10	8
DUNG	5.13	1.53	2.22	2	32	13	5.28	1.62	2.07	-	138*	21	18.31	5.65	8.52	3	9	10
DUNK	5.42	2.49	3.51	2	-	5	5.75	2.6	3.72	1	16	4	20.15	9.02	12.1	2	1	2
EASN	4.91	1.56	2.31	3	3	1	5.31	1.54	2.06	1	1	7	18.53	5.92	9.2	3	6	3
EDIN	5.54	2.64	3.54	6	4	12	5.45	1.8	2.63	2	80	14	16.79	5.98	9.86	4	22	9
ESKD	5.7	2.43	3.54	4	4	9	6.66	3.25	4.33	2	9	14	17.82	7.92	11.48	3	1	6
EXMO	6.25	2.76	3.38	4	-	4	6.36	3.09	4.04	5	-	12	19.66	10.32	11.69	6	2	6
FARB	5.55	2.23	2.44	2	5	10	5.45	2.18	2.17	1	22	8	18.28	5.06	8.1	8	58	7
FAUG	6.16	2.77	4.99	1	6	5	6.04	2.46	3.92	1	13	10	16.89	7.41	12.57	2	-	2
GIGG	5.85	2.5	3.74	8	10	7	6.33	3.33	3.99	-	24	8	18.91	6.53	12.26	-	2	5
GIRA	5.14	3.04	3.22	12	10	15	5.74	3.02	3.16	-	1	9	17.51	7.14	10.89	4	33	5
GLAS	5.7	3.03	3.69	5	3	9	5.72	2.63	3.06	3	7	9	18.08	6.32	10.63	1	10	5
GORS	5.19	1.68	2.4	4	12	11	5.43	2.42	2.16	1	1	11	18.55	5.93	9.02	5	11	9
HARD	6.17	3.19	3.46	4	8	12	5.53	2.52	2.49	1	11	13	18.26	6.28	8.75	4	25	12
HELS	6.2	3.46	5.08	9	8	9	6.46	3.86	4.19	1	15	10	18.24	10.78	13.77	7	150*	11
HERT	5.93	2.89	3.19	22	99	98	6.62	3.73	4.06	22	121	88	18.65	7.71	9.23	5	39	13
HOLY	5.6	2.19	3.12	2	9	3	5.4	2	2.5	2	1	1	17.39	6.75	9.84	2	36	11
HOOB	5.33	2.24	3.05	5	13	6	5.6	2.18	2.93	-	27	4	18.49	6.89	10.42	2	18	6
INVR	5.45	2.63	4.2	12	17	10	5.66	2.45	3.18	2	4	15	16.84	7.36	11.7	4	24	4
KELO	5.06	2.44	2.98	8	2	7	5.66	3.17	2.85	2	3	16	17.28	10.37	10.53	3	67	14
KEYW	5.02	2.14	2.56	3	27	5	5.07	1.6	2.15	2	12	10	17.39	5.38	8.93	4	8	8
KILN	7.04	3.64	5.78	6	51	10	6.77	2.83	4.71	3	8	7	19.86	9.9	15	13	27	23
KING	5.03	2.09	2.47	5	5	3	5.16	1.68	1.94	-	136	8	17.24	7.15	8.15	3	23	12
KINL	5.16	2.62	3.46	4	28	4	5.43	2.17	2.84	2	12	11	15.51	6.52	10.93	4	3	3
KIRK	5.21	3.12	3.04	6	46	6	5.72	5.1	3.14	2	1	16	17.54	5.98	10.08	3	19	7
KIRW	4.72	2.23	3.16	7	5	6	5.07	1.94	2.47	2	13	16	15.44	6.06	9.82	2	16	5
KLRE	5.64	2.17	3.83	3	3	5	5.19	2.26	3.23	1	10	10	17.5	6.41	11.12	3	18	6
LEED	5.64	3.01	3.21	8	3	10	5.57	1.93	2.81	1	6	11	18.17	6.17	10.29	3	20	7
LEEK	5.25	2.07	3.23	2	4	5	5.6	3.85	3.17	2	1	11	18.23	8.38	11.88	1	7	2
LICF	5.05	1.53	2.48	4	21	6	5.6	1.82	2.69	3	72	10	17.41	5.71	9.34	4	10	3
LINO	4.95	1.55	2.24	5	80	10	5.24	1.87	2.11	3	38	10	17.58	5.39	8.27	3	21	11
LOCG	6.35	3.43	4.77	2	5	4	6.81	3.49	4.53	1	4	8	17.77	6.91	12.4	6	112	14
LOFT	5.38	2.02	3.21	4	4	6	5.65	1.96	2.61	1	25	9	18.07	6.69	10.01	1	6	12
MACY	7.14	3.39	5.44	2	15	13	6.24	2.79	4.07	5	33	14	18.98	9.17	13.77	1	2	6
MART	5.4	1.98	2.57	5	5	6	5.19	1.68	2.08	2	88	9	17.85	5.23	8.14	3	37	6
MORP	5.59	6.06	3.68	3	2	5	5.59	2.54	2.9	5	58	9	17.73	12.04	11.39	2	9	3
NCAS	5.4	3.24	3.37	4	-	7	5.6	2.7	2.61	2	20	13	17.85	8.52	10.23	2	3	6
NEWL	6.15	3.43	3.75	2	5	10	5.76	2.95	3.46	2	-	10	18.2	8.53	12.39	6	12	7
OMGH	5.67	2.55	3.83	3	12	8	5.07	2.22	3.3	3	18	3	16.86	7.91	11.55	4	10	3
OXFR	5.26	1.67	2.57	4	19	3	5.34	1.71	2.12	1	35	9	18.22	6.35	9.98	2	3	1
PBIL	5.69	2.67	2.67	5	383	24	5.33	1.91	2.19	2	2	9	18.18	7.84	9.2	10	159	39
PETE	5.09	2.45	2.36	3	1	6	5.18	1.58	1.88	3	-	11	17.43	5.33	8.18	3	35	5
PMTG	5.47	3.26	3.44	5	1	3	5.77	2.68	2.47	-	35	4	17.61	6.71	9.11	4	12	2
PMTH	5.71	1.83	2.81	2	21	4	5.66	1.93	2.74	1	6	5	19.81	7.41	10.85	4	4	2
POOL	5.69	2.62	2.75	2	16	5	5.38	2.11	2.03	3	116	13	19.36	6.54	9.75	4	22	4
PRAE	5.81	2.2	2.95	2	16	5	5.58	2.32	2.61	1	8	8	17.98	6.15	9.62	8	12	4
RICM	5.51	2.38	3.48	8	2	21	5.58	1.93	2.92	5	16	19	18.18	6.17	10.91	3	14	13
SABB	5.45	2.8	3.52	6	114	33	5.59	2.69	2.94	1	56	16	18.38	17.55	12.16	16	638	46
SANO	6.23	7.88	3.85	5	3	7	5.77	4.28	2.56	2	9	9	18.25	7.33	9.57	2	4	7
SCAO	5.31	3.31	3.21	5	4	8	5.41	2.22	2.44	1	1	6	17.83	5.46	8.95	3	37	6
SHOB	5.78	2.08	3.06	7	12	9	5.89	2.1	3	2	26	9	18.96	6.29	10.28	1	-	6
SHOE	5.29	1.72	2.38	3	8	14	5.35	1.91	2.03	1	156*	9	17.67	6.38	8.11	5	8	5
SHRE	5.5	1.94	3.09	1	8	5	5.57	1.75	2.59	3	11	7	18.55	6.33	10.29	2	7	3
SKEE	4.9	3.05	2.3	5	-	3	5.16	1.64	1.91	3	9	10	18.11	5.38	8.41	2	23	5
STEE	5.39	1.81	2.73	4	18	11	5.39	2.21	2.19	2	3	9	18.23	5.93	9.27	3	53	14
SWAN	5.09	2.37	2.7	6	1	8	5.43	2.06	2.43	2	4	6	18.38	6.35	9.19	1	8	4
SWTG	4.69	2.93	3.35	5	-	6	5.23	2.37	2.73	2	88	7	14.07	6.15	9.39	4	7	1
TAUT	6.51	3.83	3.97	2	31	11	5.65	3.43	2.86	2	36	8	19.91	14.34	11.48	5	51	3
TEDD	6.17	4.59	3.48	28	242	69	6.12	5.7	3.22	25	35	96	18.28	6.3	8.19	5	79	15
THUS	4.71	2.03	3.21	6	7	13	5.17	1.91	2.62	2	20	7	15.53	6.74	10.12	9	18	7
WARS	5.8	2.76	2.93	8	7	15	5.72	1.91	2.56	1	201	5	19.22	7.19	10.1	2	12	8
WATT	5.19	2.45	2.84	3	3	1	5.16	1.78	2.24	-	24	-	18.84	6.1	9.37	3	8	2
WEAR	7.74	4.23	6.24	9	1	9	7.48	3.44	5.44	5	27	11	19.59	8.63	13.72	-	6	3
WEIW	5.92	3.94	3.21	2	11	9	5.3	2.64	2.23	1	90	25	18.35	6.14	9.2	7	6	1
WELL	5.22	2.36	2.42	3	1	4	5.51	1.74	2.13	1	60	7	17.54	5.01	8.06	3	10	5
WEYB	5.03	1.83	2.52	4	8	5	5.22	1.68	2.07	2	80	5	18.28	5.35	8.88	5	53	7
YEAS	5.14	2.08	3.04	4	2	6	5.32	2.62	2.61	3	3	13	17.97	6.22	9.9	1	11	11

6.3 Analysis

6.3.1 Offset correction approaches

Tables 6-1 to 6-3 show that the two offset correction approaches gave different estimates for the magnitude of the offsets in the algorithm training dataset, even though the only difference between them was the length of the time series used (i.e. 8.25 vs 5.50 years in the 1st and 2nd offset correction approaches respectively). In addition, since the uncertainty is a function of the time series length, it is always smaller when using the 1st offset correction approach than when using the 2nd offset correction approach. Furthermore, the two offset correction approaches gave different estimates for the magnitude of the offsets in the few cases where an offset happens to be in the algorithm testing dataset, with the uncertainty being more when using the 2nd offset correction approach, which is similar to what Montillet et al. (2015) concluded when they compared the mean method to the weighted mean method. Figure 6-5 shows an example of the difference between the 1st (red) and the 2nd (black) offset correction approaches. It shows that the de-trended time series of SHOB station (ΔE) starts to diverge from zero at the beginning of 2014. As a result, when the whole time series is used to solve for the offset in the 1st offset correction approach, the offset at 2008 is estimated to be -2.42±0.1mm to maintain a linear trend of 15.82±0.18 mm/yr, while when the 2nd offset correction approach is used, by excluding the algorithm testing dataset, the offset is estimated to be -3.97± 0.11 mm to maintain a linear trend of 16.4±0.25 mm/yr.

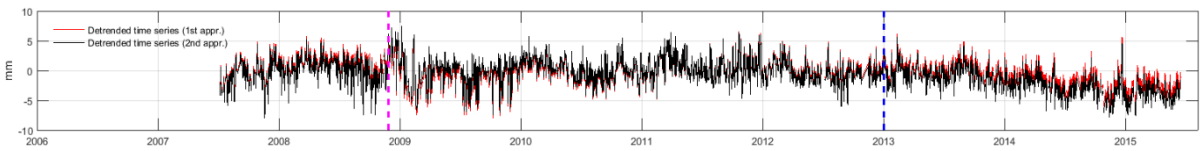


Figure 6-5 The detrended time series of SHOB station (ΔE) using the 1st (red) and the 2nd (black) offsets correction approaches.

The results in Tables 6-1 to 6-3 show that 71.6%, 79.0% and 69.0% of the stations have at least one offset estimate with a significant difference between the two offset correction approaches in ΔN, ΔE and ΔU respectively, while 11.1%, 79.0% and 7.4% of the stations

have a significant difference in their linear trend estimates in ΔN, ΔE and ΔU respectively. This is illustrated in Figure 6-2 where even though the difference in the linear trend estimate for the ΔN and ΔU component is insignificant at most of the stations, the difference in the offset estimate is significant (i.e. a red left semi-circle with a black right semi-circle). On the contrary, for the ΔE component, the differences in both the offset estimate and the linear trend estimate are significant at most of the stations (i.e. a red left semi-circle with a red right semi-circle).

It is also shown that there is no discernible systematic effect in the linear trend estimates for the ΔN component from using either of the two offset correction approaches, while for the ΔE component the estimates from using the 1st offset correction approach are almost always of smaller value than when using the 2nd offset correction approach, with the exception of ABYW, BEES, SABB and SWTG stations. Accordingly, Figure 6-3 shows that the differences between the horizontal station velocities are consistently indicating to the west at almost all of the stations, and these differences can reach more than 1mm/year, e.g. at ESKD, KELO, PBIL, SANO and WARS stations. Also, based on Table 6-3 and Figure 6-4 there is no discernible systematic effect in the linear trend estimates for the ΔU component from using either offset correction approaches, with the differences between the vertical station velocities from the 1st offset correction approach and the 2nd offset correction approach only being significant at a few stations, namely CAML, ESKD, HELS, PBIL, SABB and TAUT stations.

As a result of this analysis, it can be said that the use of the two offset correction approaches appears to reveal potential anomalous behaviours in the algorithm testing dataset at some of the stations but that, apart from visually inspecting the time series, further diagnosis of the nature of the anomalous behaviours is not possible with the currently presented statistics. In an attempt to address this issue, additional analysis is required which, in this study, is enabled by applying both temporal and spatial analysis algorithms aiming to increase our understanding of the anomalous behaviours at different stations.

6.3.2 The performance of the multiple analysis algorithm approach

The performance of the three analysis algorithms differs, as the residuals of the temporal and combined analysis are dominated by the high-frequency component of the time series and include any abnormalities in the low-frequency components that the NAR-ANN could not predict.

In contrast, the residuals of the spatial analysis are dominated by the low-frequency component of the time series, which makes it more effective for detecting long-term changes (e.g. variations in linear trend estimates). Accordingly, the spatial residuals are less noisy than the temporal and combined residuals which is reflected in their thresholds, as shown in Table 6-4, which makes the spatial analysis algorithm more sensitive in detecting smaller offsets (that are not related to documented changes) and variations in long-term trends, resulting in higher numbers of anomalous days (Table 6-4).

Looking at the spatial distribution of the residuals thresholds of the three analysis algorithms (Figure 6-6), it can be seen that the south-eastern part of the UK tends to be less noisy than the rest for the horizontal components. Since the combined analysis correlates the temporal residuals spatially, the combined analysis residuals will always be smaller in values than the temporal residuals. However, the larger the difference is between a station and its surrounding, the less spatial correlation between this station and the surrounding stations will be.

Figure 6-7 shows the differences between the temporal and the combined analysis residuals thresholds as a percentage. The larger the percentage differences between the temporal and the combined analysis residuals thresholds, the more it indicate that the nearby stations are spatially correlated. It is clear that the temporal residuals get more spatially correlated along the way toward the south-east and it seems that this correlation in the ΔE component is the highest amongst the three components.

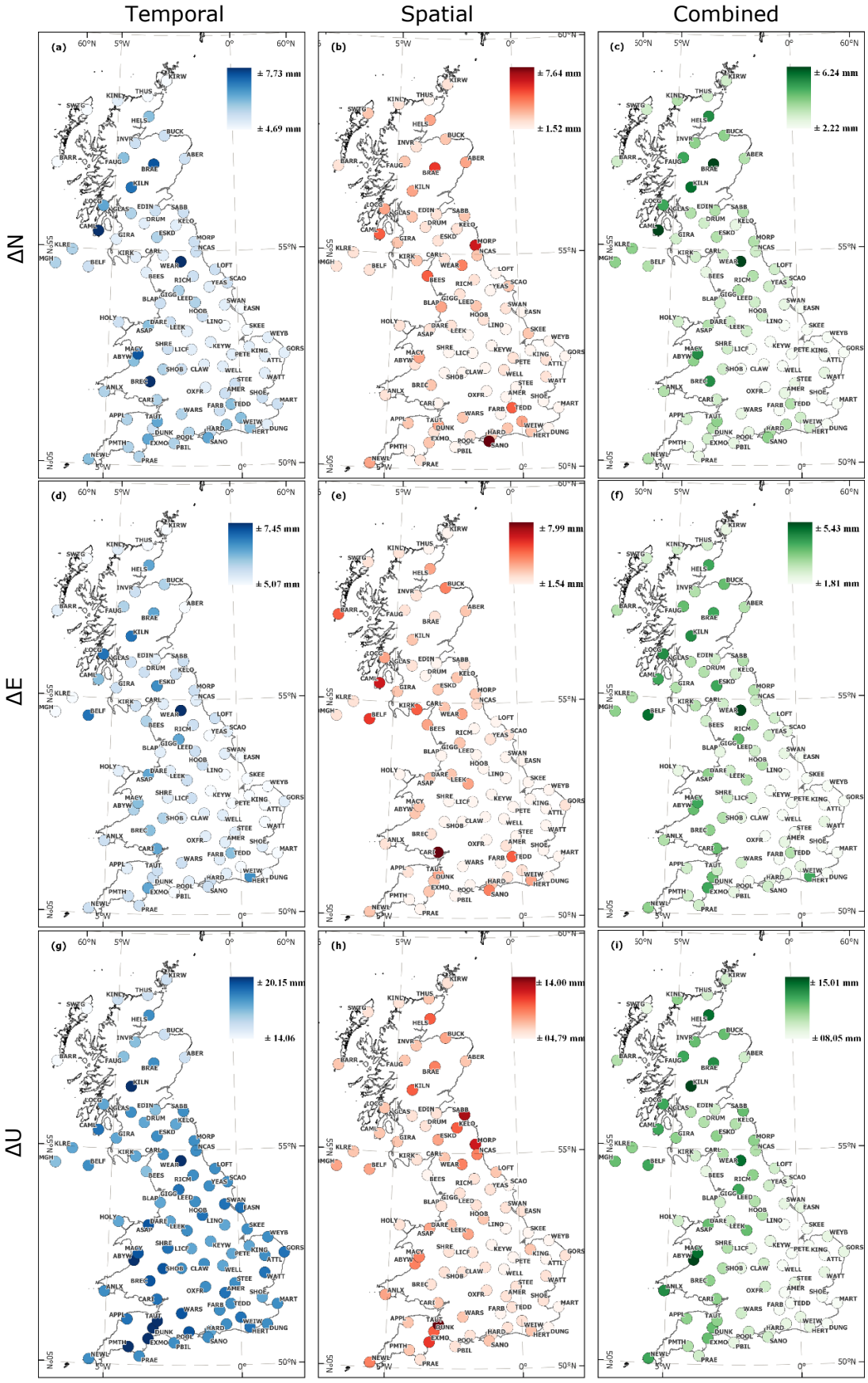


Figure 6-6 The residuals thresholds of the (a) temporal, (b) spatial and (c) combined analysis of the ΔN component, (d) temporal, (e) spatial and (f) combined analysis of the ΔE component and (g) temporal, (h) spatial and (i) combined analysis of the ΔU components using the 2nd offset correction approach.

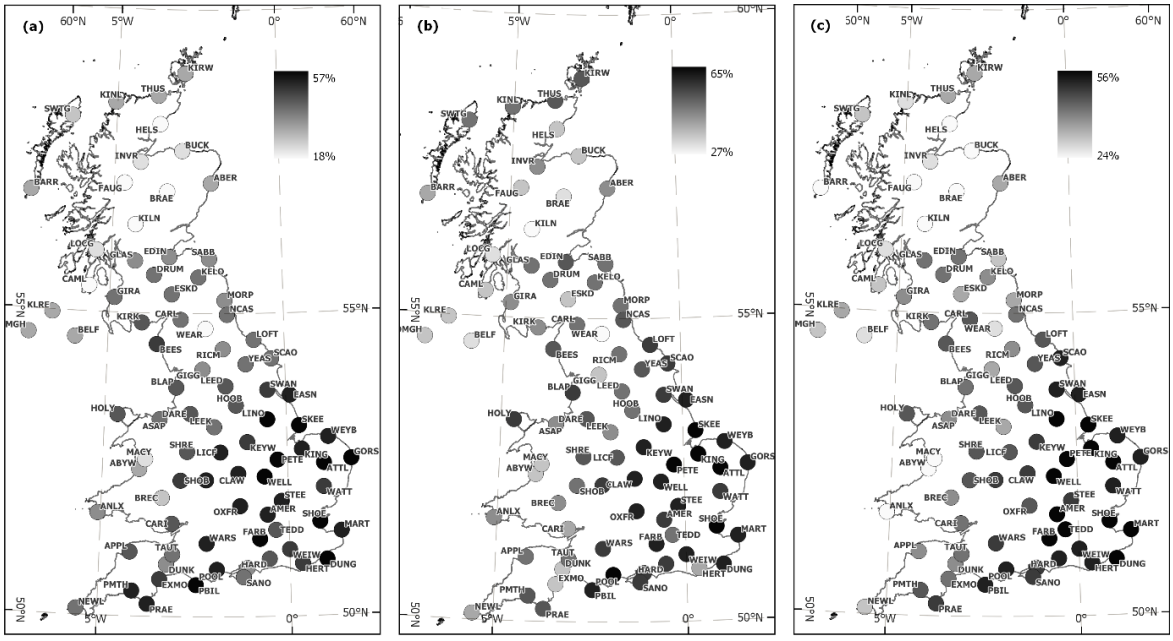


Figure 6-7 The percentage differences between the temporal and combined analysis residuals thresholds for (a) ΔN, (b) ΔE and (c) ΔU components.

As a detailed example, Figure 6-8a and 6-8b show the corrected and the de-trended time series of TEDD station (ΔN component) and illustrate how different types of anomalies can be detected by the different algorithms. Here it should be noted that the intermediate steps of low-frequency time series analysis (i.e. predicted values using NAR-ANN and estimated values using Spatial Regression) are omitted from Figure 6-8, and all subsequent figures, in order to focus on the temporal, spatial, and combined analysis residuals (i.e. Figure 6-8c, 6-8d, and 6-8e). From Figure 6-8c, 6-8d, and 6-8e, it can be seen that the three analysis algorithms identified several days of anomalous behaviour from the beginning of 2013 to the middle of 2014. However, the anomalous behaviour also continues for the spatial analysis algorithm after the middle of 2014.

Even though the combined analysis residuals are dominated by the high-frequency component, it has a higher number of anomalous days than the temporal analysis algorithm due to the reason that the thresholds of the former are narrower than the latter. In this example, most of these detected anomalies coincide with the ones detected by the temporal analysis which confirms that these anomalies are site-specific and not a result of

processing artefacts or a large-scale event as they don't appear in the surrounded stations (i.e. uncorrelated spatially).

In contrast, some of these detected anomalies do not coincide with the anomalies detected by the temporal analysis which can be seen as a high-frequency component which is spatially uncorrelated. For example, at the middle of March 2014, an anomaly existed in all the surrounding stations but TEDD (shaded area in Figure 6-9). Therefore, in the combined analysis, it was considered as a normal behaviour in all the surrounding stations but TEDD.

This could be seen as a setback to the combined analysis algorithm as it considered what seems to be anomalous as a normal behaviour just because it happened in the surrounding stations. On the other hand, this algorithm can be more useful in the stage of diagnosing the reasons that lead to an anomalous behaviour rather than in the stage of detecting the anomalous behaviour. Since the scope of research focuses on detecting anomalous behaviours in the GNSS time series, the combined analysis will not be discussed further but will be shown in the figures below for the sake of completion.

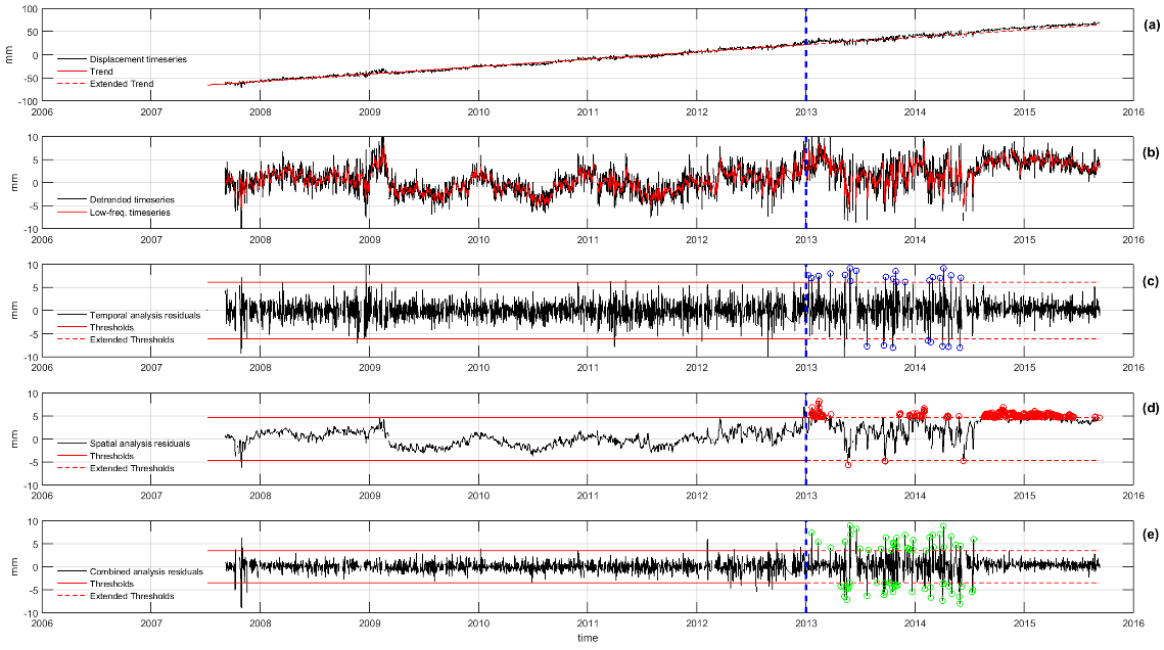


Figure 6-8 TEDD Station (ΔN) – (a) Corrected displacement time series, (b) detrended and low-frequency time series, the (c) Temporal, (d) Spatial and (e) combined analysis residuals with their corresponding thresholds

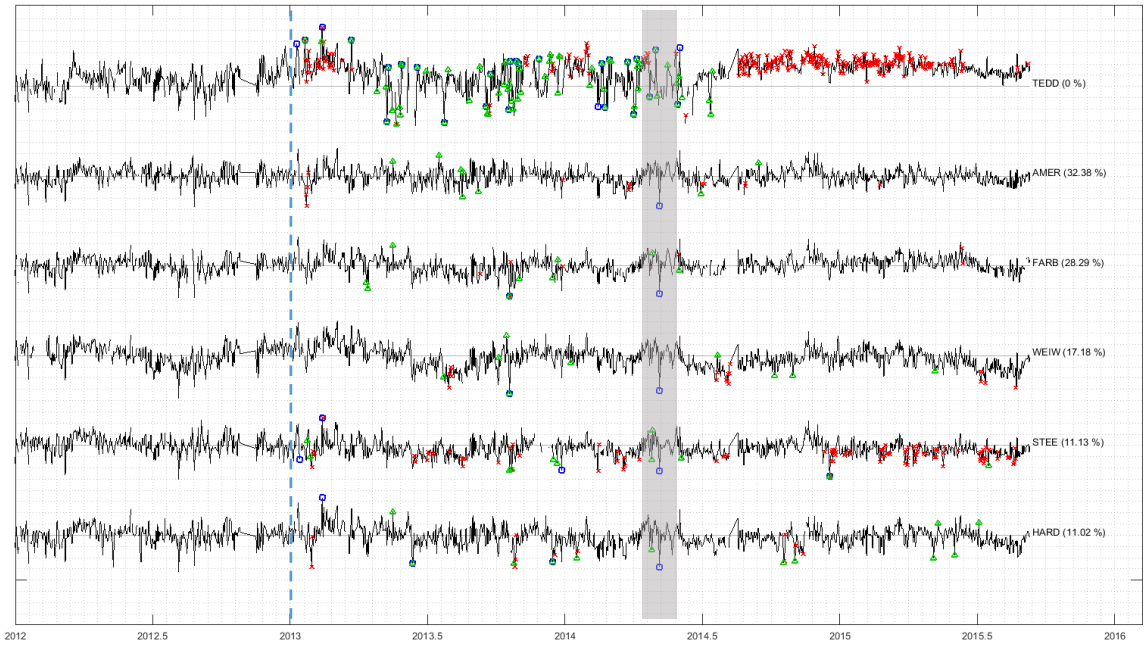


Figure 6-9 The detrended ΔN component of TEDD station along with its five closest stations which are spatially weighted (on the right) according to their in-between Euclidian distance, alongside with detected anomalies using the temporal (blue), spatial (red) and combined (green) analysis algorithms.

6.3.3 A classification of the anomalous behaviours in the GPS coordinate time series of the BIGF network

From an inspection of Table 6-4, and considering the times of occurrence of the respective anomalies for all 87 stations of the BIGF network, the anomalous behaviours can be classified into three categories: (i) temporary anomalous behaviours; (ii) on-going anomalous behaviours; (iii) periodic anomalous behaviours. In this research, temporary anomalous behaviours are defined as when anomalies appear irregularly for specific period(s) of time and disappear prior to the end of the algorithm testing dataset (i.e. <50% of the last 200 days of the algorithm testing period are anomalies). Such temporary anomalous behaviours can then be sub-classified into two types, namely: (a) high-frequency-related, i.e. anomalies identified by the temporal analysis algorithm; and (b) low-frequency-related, i.e. anomalies identified by the spatial analysis algorithm. In this research, however, on-going anomalous behaviours are defined as when anomalies appear at a certain time and continue to appear until the end of the algorithm testing dataset (i.e.

>50% of the last 200 days of the algorithm testing period are anomalies). Such on-going anomalous behaviours can then be sub-classified into two types, namely: (a) due to deviations from the linear trend; and (b) due to offsets (that are not related to documented changes). Finally, in this research, periodic anomalous behaviours is a separate class given to a station when it cannot be classified as having either temporary or on-going anomalous behaviours because it exhibits significant periodic variations over time.

From Table 6-4, it can be seen that when using the 2nd offset correction approach, there are several stations which have either temporary, on-going, or periodic anomalous behaviours worthy of further investigation, as illustrated by the relatively high number of anomalies that were identified by either the spatial and temporal analysis algorithms or both. In this respect, stations that have either more than 200 anomalies (i.e. more than ~10% of the algorithm training dataset) identified by the spatial analysis algorithm and/or more than 10 anomalies (i.e. more than ~0.5% of the algorithm training dataset) identified by the temporal analysis algorithm in Table 6-4 (columns C, D, H, I, M and N) include ABER (ΔN and ΔE components), BRAE (ΔN component), CAML (ΔN and ΔU components), CLAW (ΔN component), DUNG (ΔE component), ESKD (ΔU component), FARB (ΔE component), GIRA (ΔN component), HELS (ΔU component), HERT (ΔN and ΔE components), HOOB (ΔE component), INVR (ΔN component), KELO (ΔE and ΔU components), KEYW (ΔN component), KILN (ΔU component), KING (ΔE component), MART (ΔU component), NCAS (ΔE component), PBIL (ΔN and ΔU components), POOL (ΔE component), SABB (ΔE and ΔU components), SWTG (ΔE component), TEDD (ΔN components) and WARS (ΔE component). A sample of these is analysed in the following sub-sections. Furthermore, for completeness, Table 6-5 shows the statistics obtained when using the 1st offset correction approach, where only 11 of the 24 stations mentioned above are highlighted.

It was preferred to build the classification tree based on the temporal and spatial analysis algorithms only for the sake of simplification and because, as mentioned in section 6.3.2, the combined analysis behaviour is resembling the temporal analysis behaviour. This

resemblance will be illustrated in the figures below for completeness but will not be further discussed.

(i) Temporary anomalous behaviours

(a) *High frequency-related:* Stations (and components) in this category have been classified as such when they have a relatively low number of anomalies (i.e. <200) identified by the spatial analysis algorithm, but have a relatively high number of anomalies (i.e. >10) identified by the temporal analysis algorithm. Based on Table 6-4, it can be seen that there are several examples of this type of temporary anomalous behaviour, namely BRAE (ΔN), CAML (ΔN), GIRA (ΔN), HERT (ΔN and ΔE), INVR (ΔN), KILN (ΔU) and TEDD (ΔE). In Figure 6-10 the time series of HERT(ΔN) is presented, as a representative case of temporary high-frequency related anomalous behaviour, where the anomalies appear randomly in the residuals of the temporal analysis algorithm.

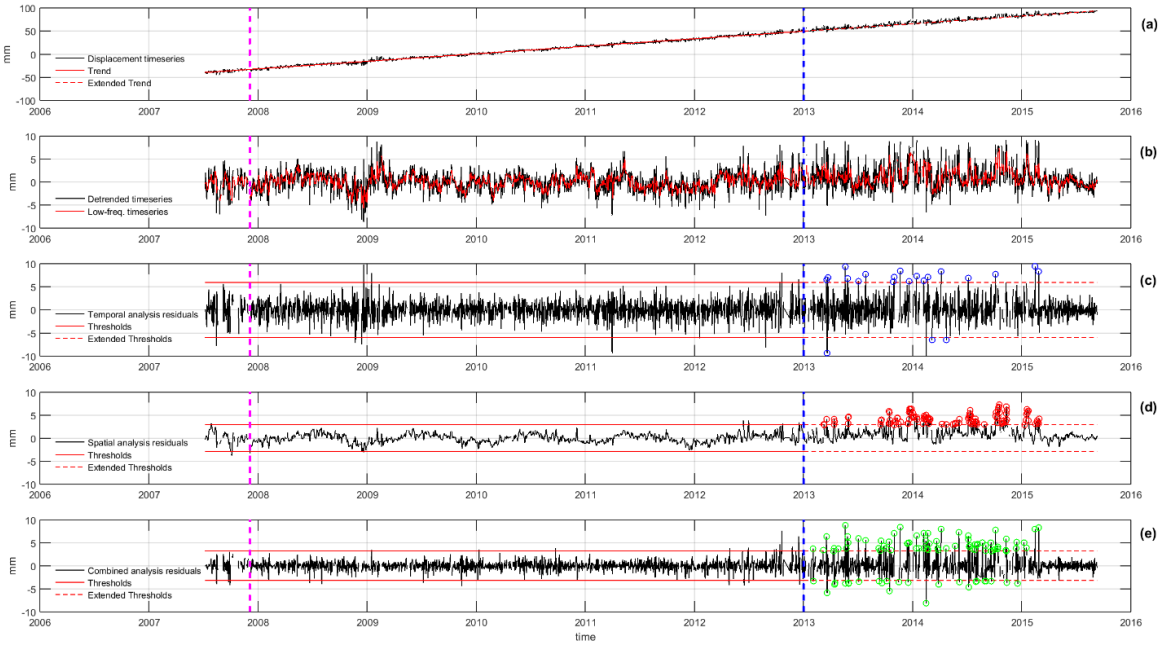


Figure 6-10 The same as Figure 6-8, for HERT Station (ΔN component) using the 2nd offset correction approach

(b) *Low frequency-related:* Stations (and components) in this category have been classified as such when they have a relatively high number of anomalies (i.e. > 200)

identified by the spatial analysis algorithm, but with <50% of the last 200 days of the algorithm testing period considered as anomalies, regardless of the number of anomalies identified by the temporal analysis algorithm. From an inspection of Table 6-4, it can be seen that KELO (ΔU), TEDD (ΔN) and WARS (ΔE) fulfil the above criteria. Figure 6-8, mentioned above, shows the TEDD (ΔN) station having 257 and 28 anomalies identified by the spatial and temporal analysis algorithms respectively, related to a sudden change in mid-2014.

(ii) On-going anomalous behaviours

(a) Due to deviations from the linear trend: This type of on-going anomalous behaviours are usually less clear and cannot always be detected visually. Stations (and components) in this category have been classified as such when they have a relatively high number of anomalies (i.e. >200) identified by the spatial analysis algorithm, with >50% of the last 200 days of the algorithm testing period considered as anomalies, but have a relatively low number of anomalies (i.e. <10) identified by the temporal analysis algorithm. From Table 6-4, it can be seen that the number of anomalies derived by the spatial analysis algorithm range between 213 and 451, while those of the temporal analysis were limited to less than 10. As can be seen from Table 6-4, such anomalous behaviour is the most common in the BIGF network, including the stations CLAW (ΔN), DUNG (ΔE), ESKD (ΔU), FARB (ΔE), HELS (ΔU), HOOB (ΔE), KELO (ΔE), KEYW (ΔN), KING (ΔE), MART (ΔU), NCAS (ΔE), PBIL (ΔU), POOL (ΔE), SABB (ΔE) and SWTG (ΔE).

In terms of the ΔN component, anomalous behaviours are identified for CLAW and KEYW. For CLAW, the anomalies are clearly related to a deviation from the linear trend that started in mid-2014 and seems to be greater than the estimated trend from the algorithm training dataset (Figure 6-11). A similar number of anomalies are identified for KEYW, again with an increased linear trend (Figure 6-12).

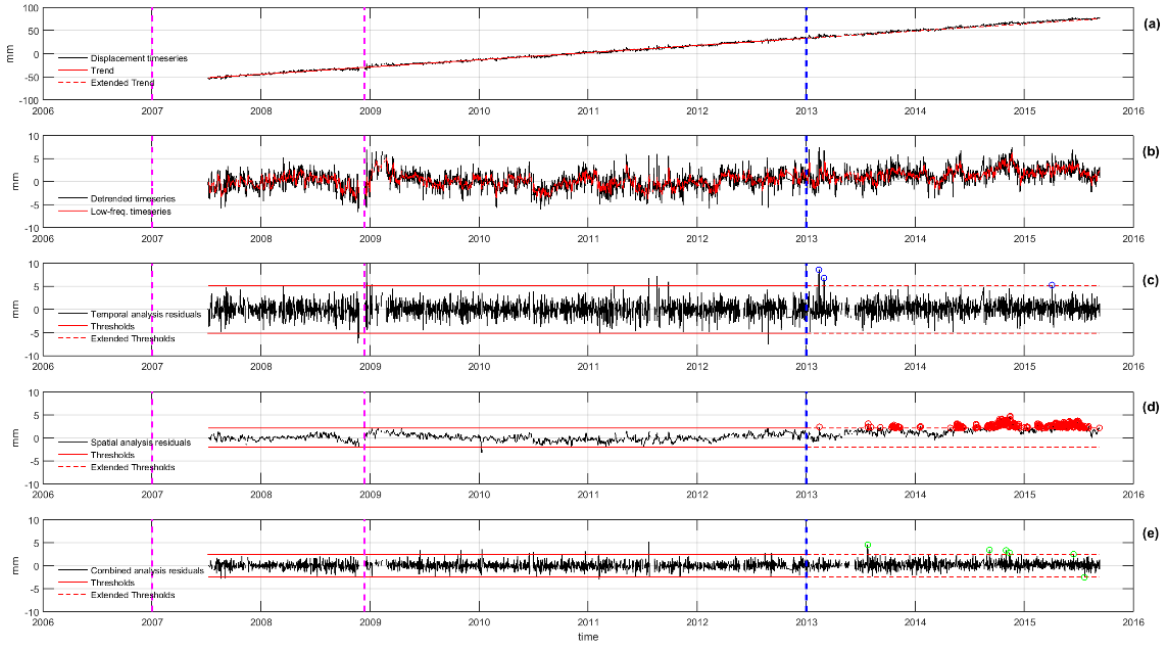


Figure 6-11 The same as Figure 6-8, for CLAW station (ΔN component) using the 2nd offset correction approach.

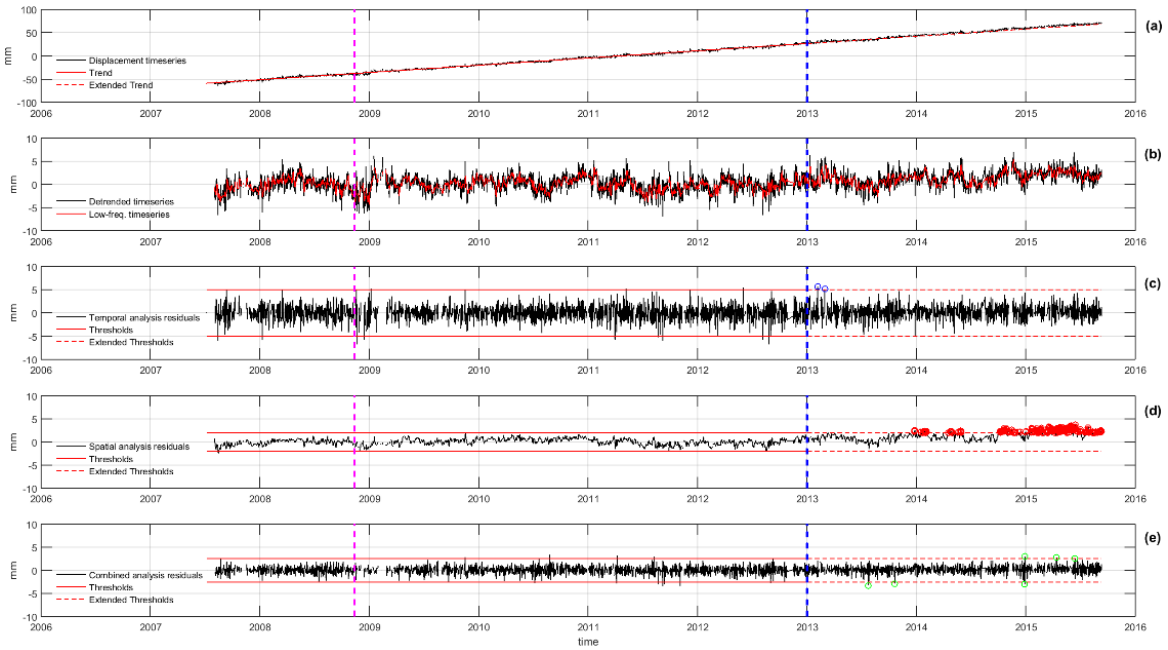


Figure 6-12 The same as Figure 6-8, for KEYW station (ΔN component) using the 2nd offset correction approach.

Regarding the ΔE component, DUNG, FARB, HOOB, KELO, KING, NCAS and POOL exhibit similar anomalous behaviours with a trend that is less than the estimated trend from the algorithm training dataset, with the anomalies starting between late 2013 and late 2014 (Figure 6-13 to Figure 6-19).

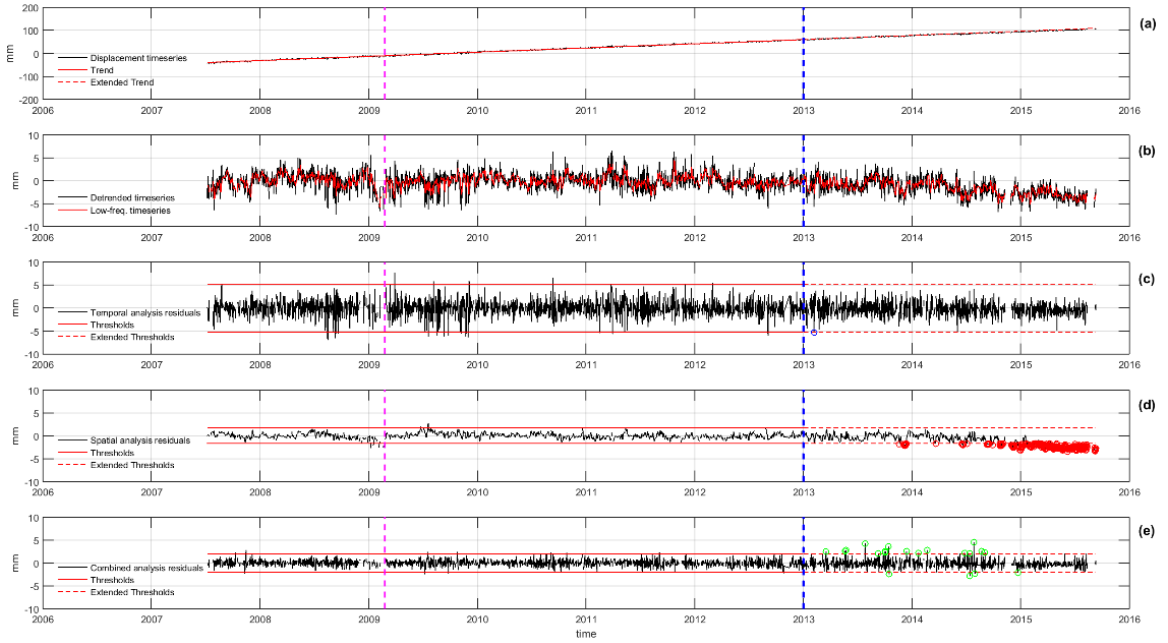


Figure 6-13 The same as Figure 6-8, for DUNG station (ΔE component) using the 2nd offset correction approach.

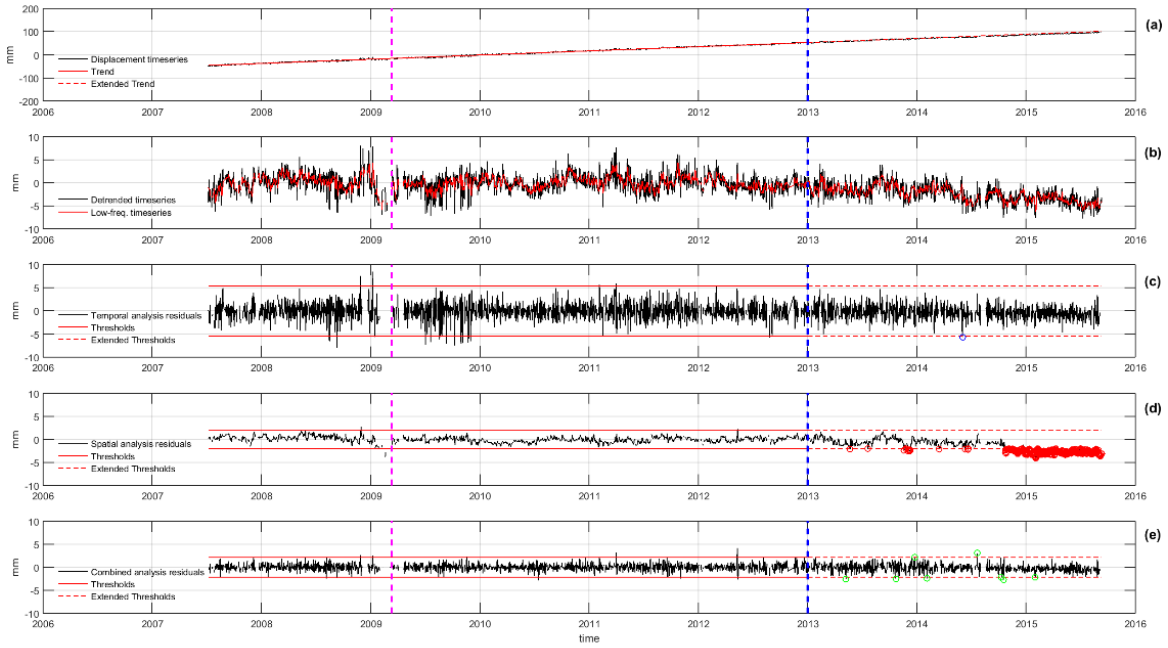


Figure 6-14 The same as Figure 6-8, for FARB station (ΔE component) using the 2nd offset correction approach.

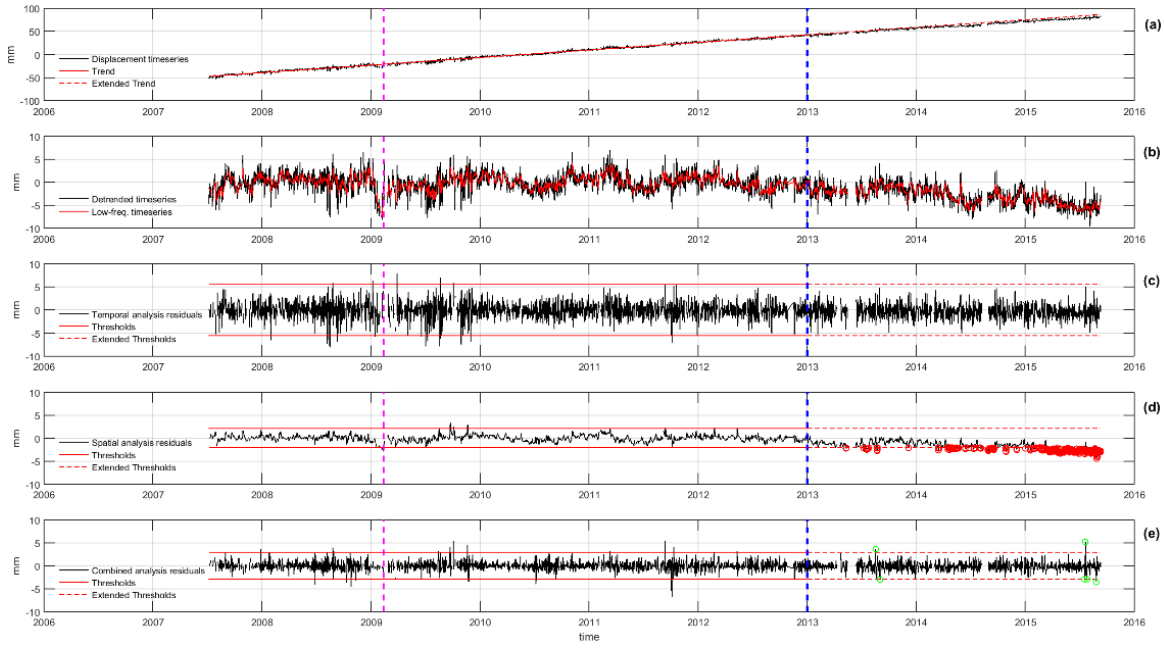


Figure 6-15 The same as Figure 6-8, for HOOB station (ΔE component) using the 2nd offset correction approach.

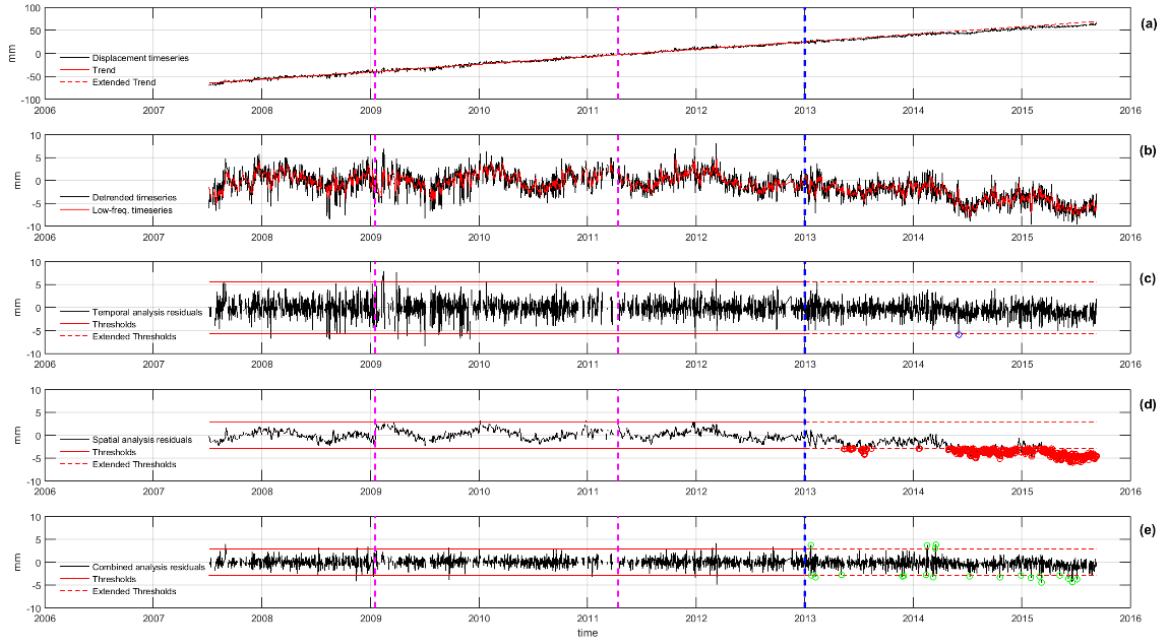


Figure 6-16 The same as Figure 6-8, for KELO station (ΔE component) using the 2nd offset correction approach.

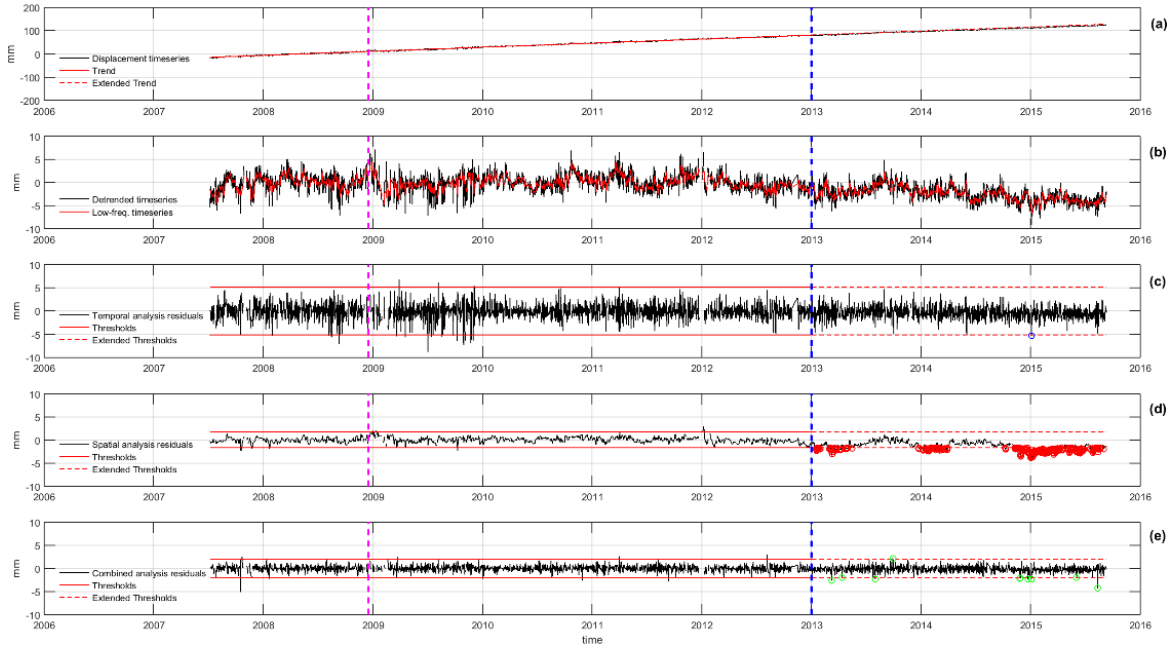


Figure 6-17 The same as Figure 67, for KING station (ΔE component) using the 2nd offset correction approach.

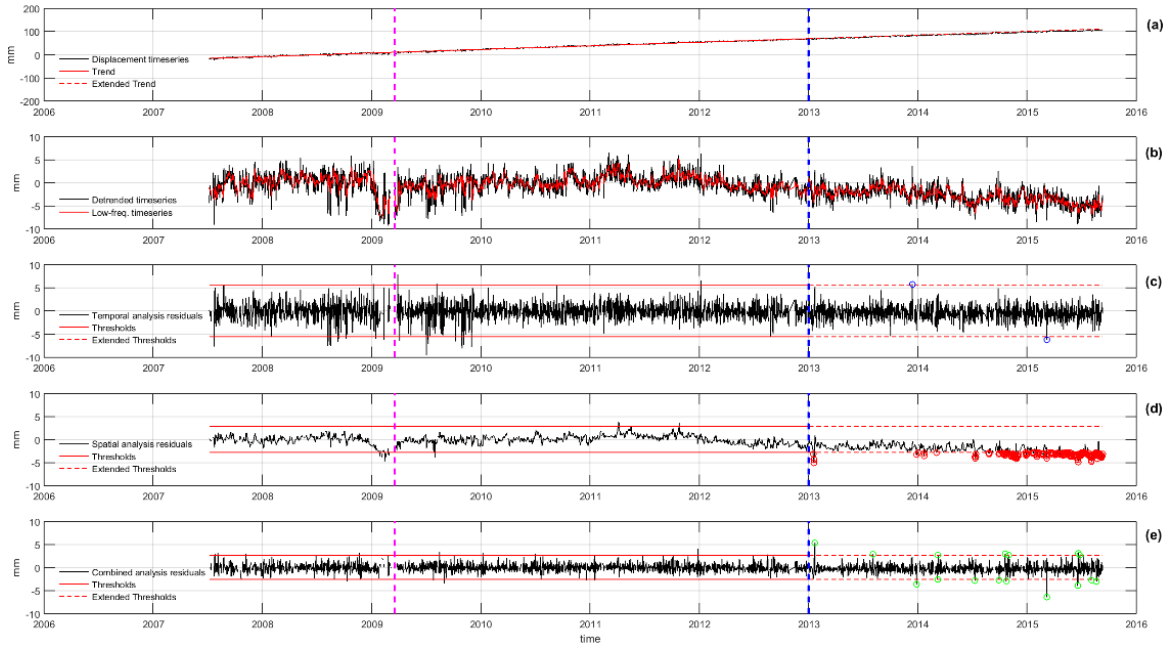


Figure 6-18 The same as Figure 6-8, for NCAS station (ΔE component) using the 2nd offset correction approach.

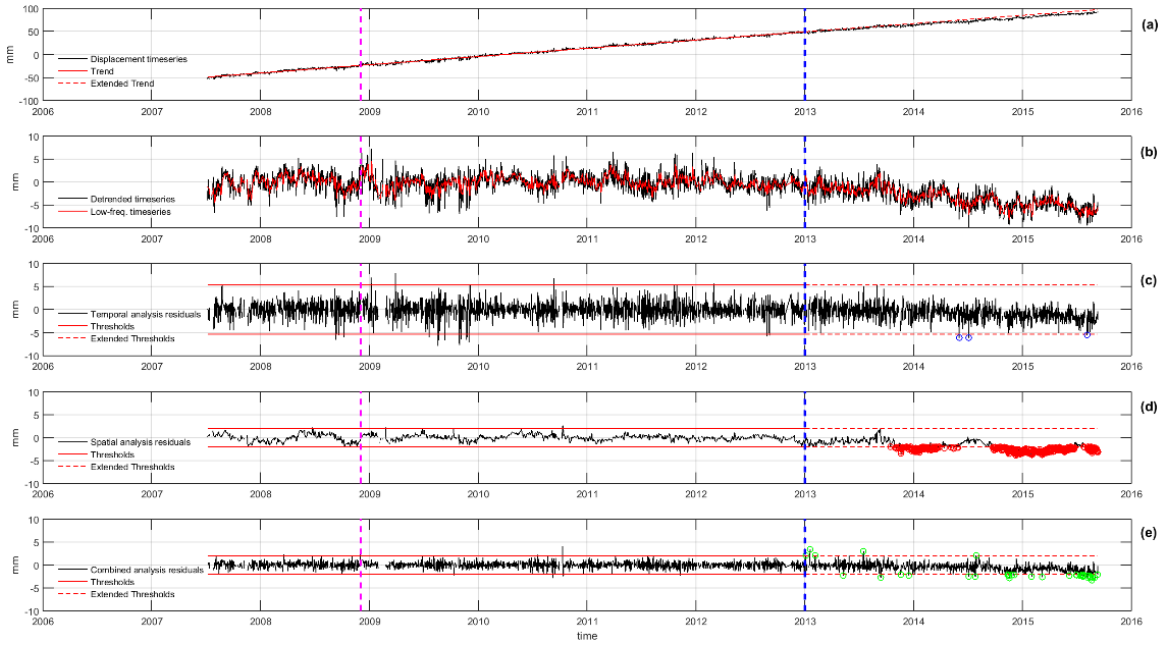


Figure 6-19 The same as Figure 6-8, for POOL station (ΔE component) using the 2nd offset correction approach.

On the other hand, SABB and SWTG seem to exhibit different behaviour. In the case of SABB, the trend seems to be greater than the estimated trend from the algorithm training dataset (Figure 6-20), which suggests that the cause of the behaviour at this station is different from the rest, especially since anomalies were also detected at the same station in the ΔU component (Figure 6-29) whereas in the case of SWTG, it is clear from Figure 6-21 that the anomalies identified by the spatial analysis algorithm coincide with a documented change (receiver and antenna replacement) in late 2013 that followed a relatively large gap in the time series of about 18 months.

In terms of the ΔU component, ESKD, HELS, KELO, MART and PBIL all exhibit anomalous behaviours (Figure 6-22 to Figure 6-26). The anomalous behaviours for ESKD, KELO and PBIL are relatively consistent, and clearly indicate a gradual deviation from the linear trend, starting between mid-2013 and early-2014 (Figure 6-22, Figure 6-24, Figure 6-26). For HELS, the anomalies appear at late-2014, and the deviation from the linear trend is more abrupt. Regarding MART, similarly to SWTG, the anomalies coincide with a

documented change (receiver and antenna replacement) in early 2015 that followed a gap in the time series of about 3 months (Figure 6-25).

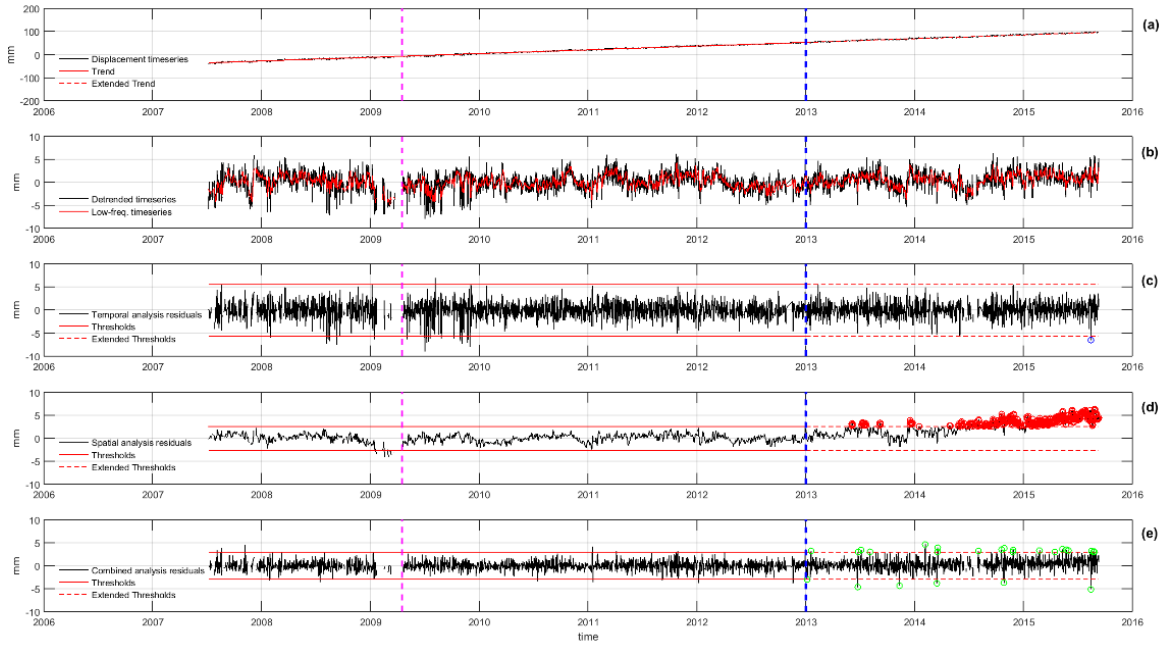


Figure 6-20 The same as Figure 6-8, for SABB station (ΔE component) using the 2nd offset correction approach.

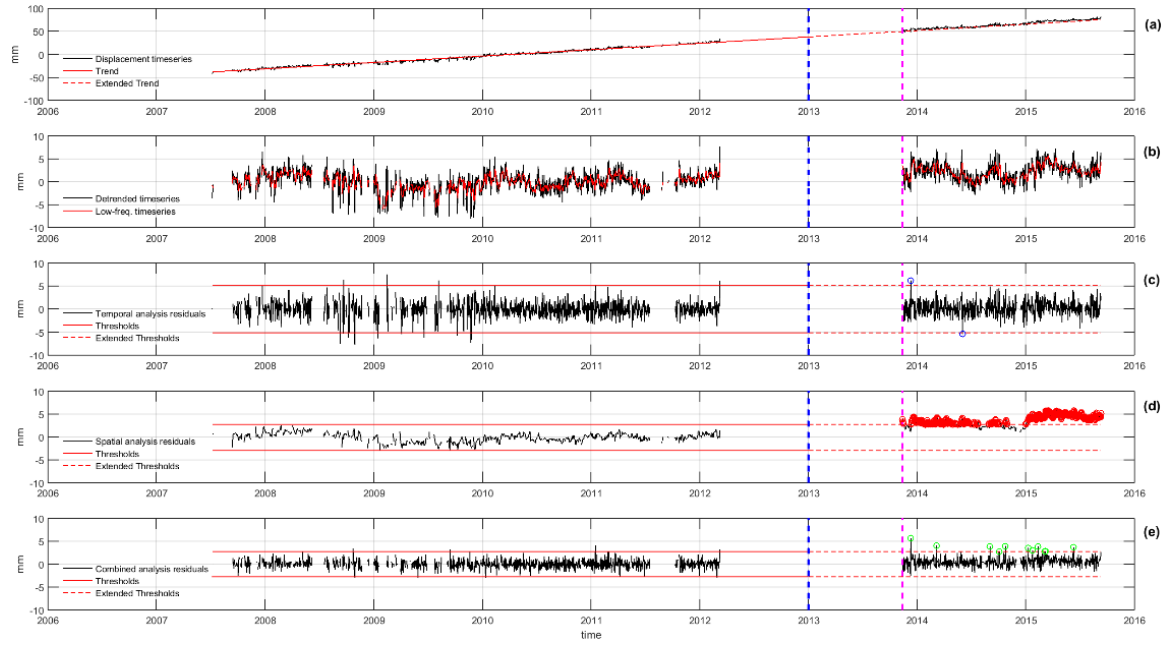


Figure 6-21 The same as Figure 6-8, for SWTG station (ΔE component) using the 2nd offset correction approach.

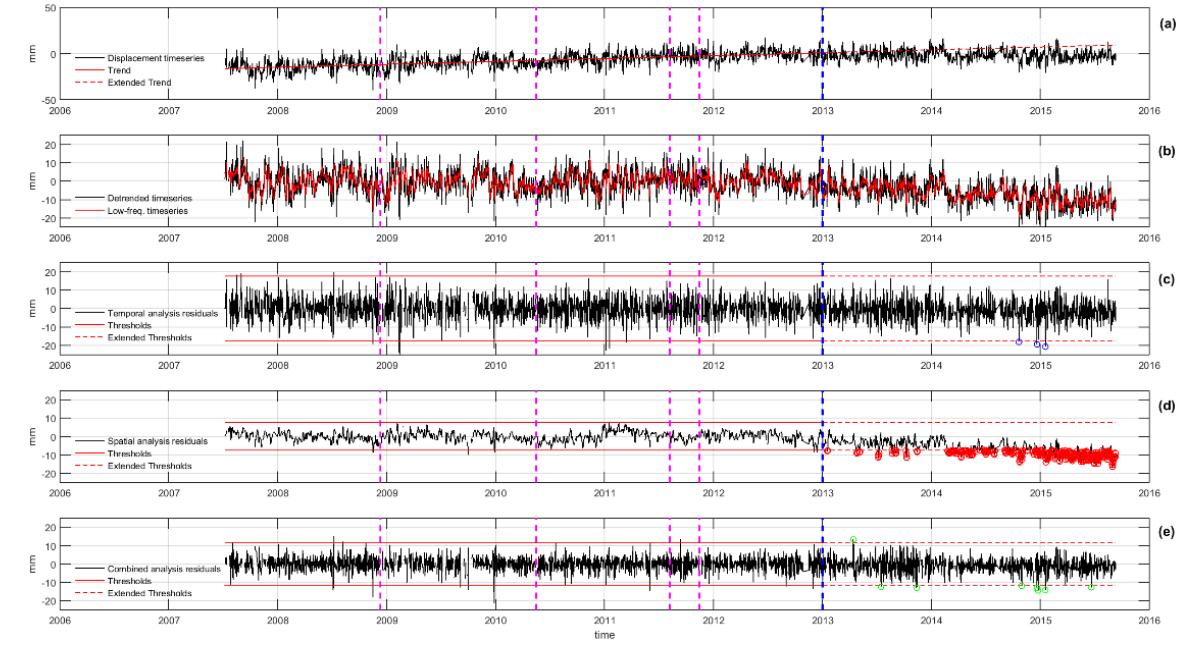


Figure 6-22 The same as Figure 6-8, for ESKD station (ΔU component) using the 2nd offset correction approach (noting that a larger Y-axis range was used for the ΔU component).

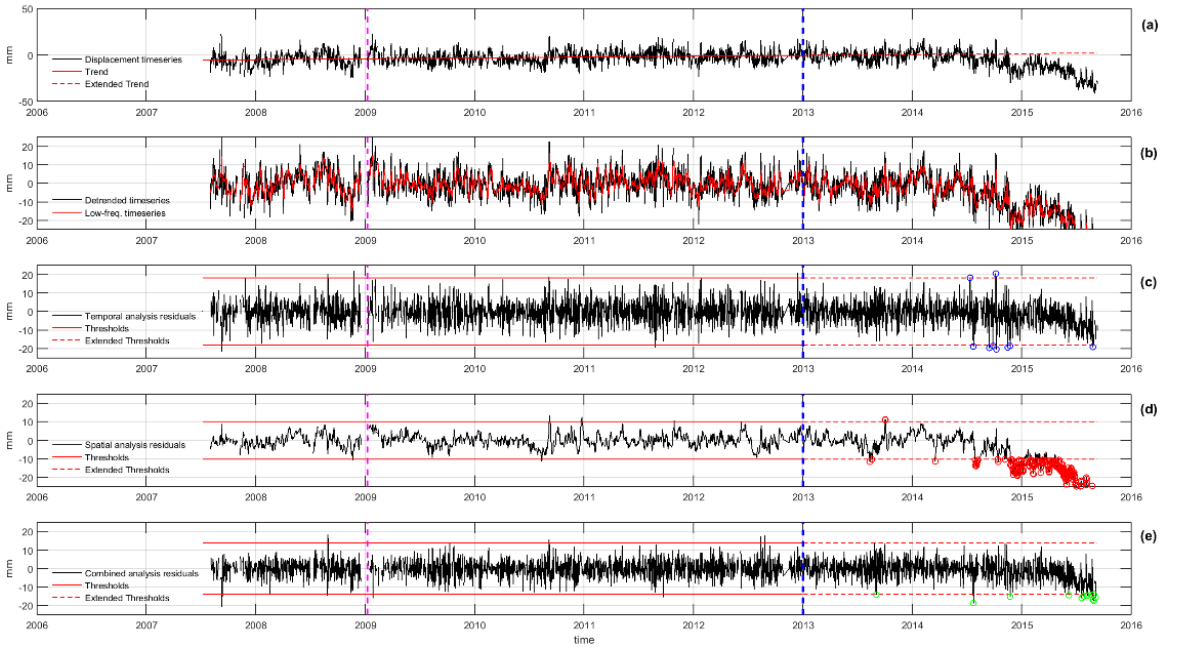


Figure 6-23 The same as Figure 6-22, for HELS station (ΔU component) using the 2nd offset correction approach.

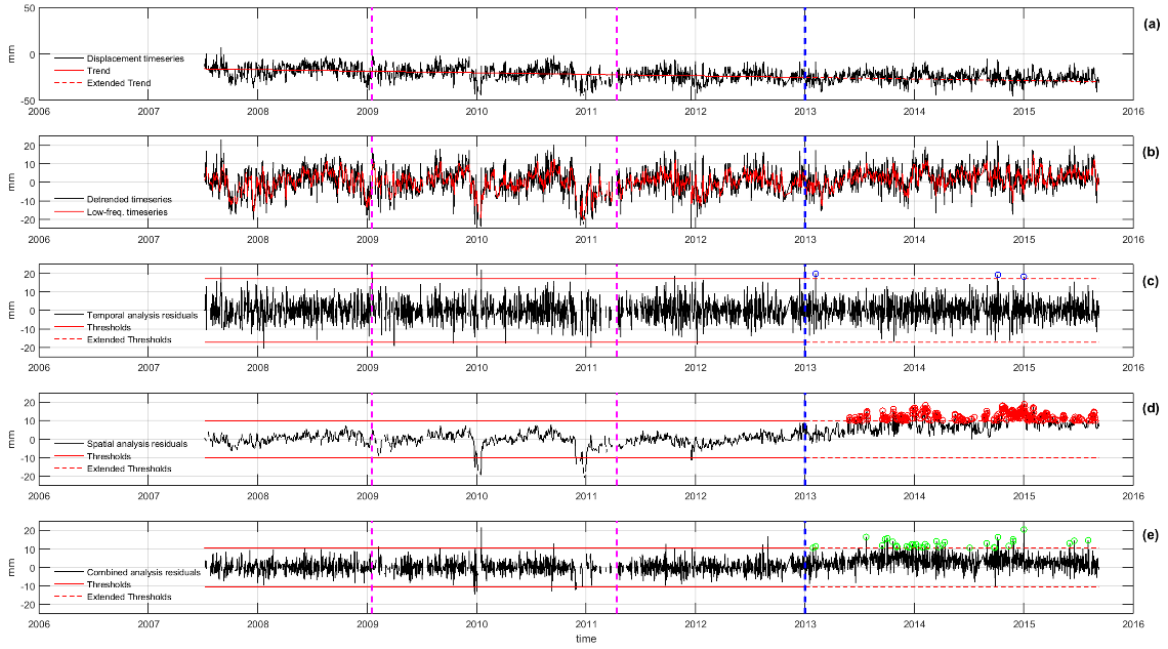


Figure 6-24 The same as Figure 6-22, for KELO station (ΔU component) using the 2nd offset correction approach.

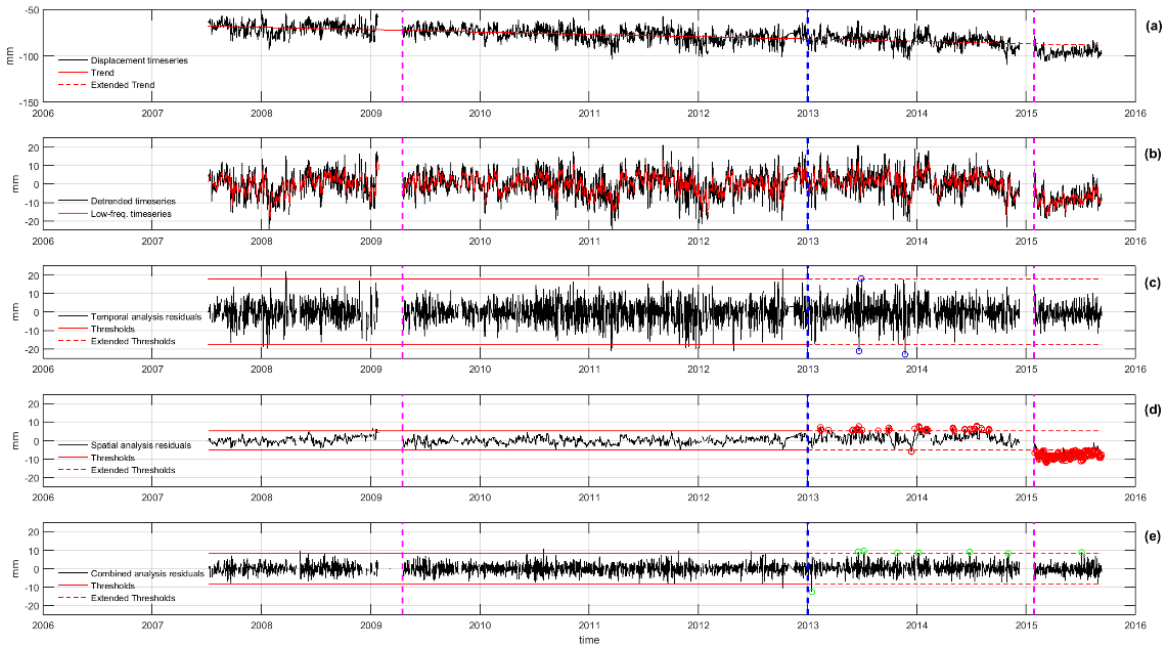


Figure 6-25 The same as Figure 6-22, for MART station (ΔU component) using the 2nd offset correction approach.

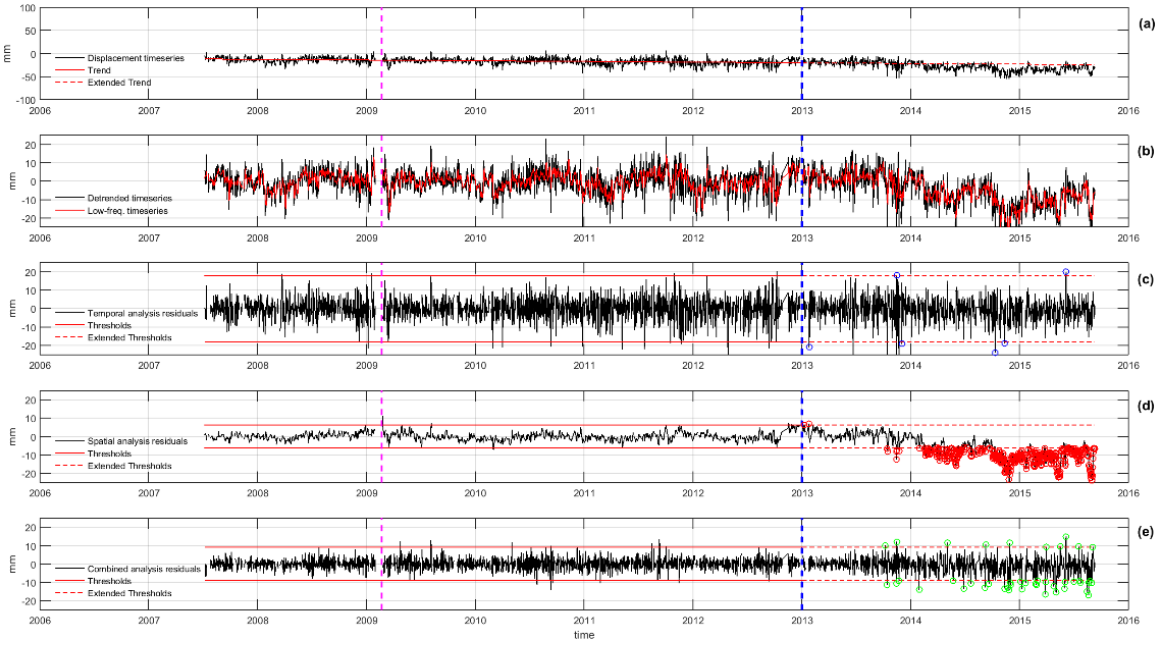


Figure 6-26 The same as Figure 6-22, for PBIL station (ΔU component) using the 2nd offset correction

Apart from those stations listed above and highlighted in Table 6-4, there are two other stations (and components) worth mentioning, that have >50% of the last 200 days of the algorithm testing period considered as anomalies but currently do not have >200 anomalies identified by the spatial analysis algorithm as their on-going anomalous behaviours are relatively recent. These are PMTG (ΔE) with 142 anomalies and PRAE (ΔE) with 168 anomalies both of which, with an extended algorithm testing dataset, could be revealed as stations with on-going anomalous behaviours due to deviations from the linear trend.

(b) Due to offsets (that are not related to documented changes): This type of on-going anomalous behaviours are usually very clear and can also be detected visually. Stations (and components) in this category have been classified as such when they have a relatively high number of anomalies (i.e. >200) identified by the spatial and temporal analysis algorithm, with >50% of the last 200 days of the algorithm testing period considered as anomalies, and have a relatively high number of anomalies (i.e. >10) identified by the temporal analysis algorithm. As can be seen from Table 6-4, this type of anomalous

behaviour is less common in the BIGF network, as it appears at only on three stations: PBIL (ΔN), and CAML (ΔU) and SABB (ΔU).

For the ΔN component of PBIL, there are 780 and 11 anomalies identified by the spatial and temporal analysis algorithms respectively, related to a gradual change taking place between early 2013 followed by a more sudden change in late 2013 (Figure 6-27). This anomalous behaviour started to be detected from the beginning of the testing period which maybe implies that if the testing dataset was chosen to start earlier in time, it would have been detected even earlier.

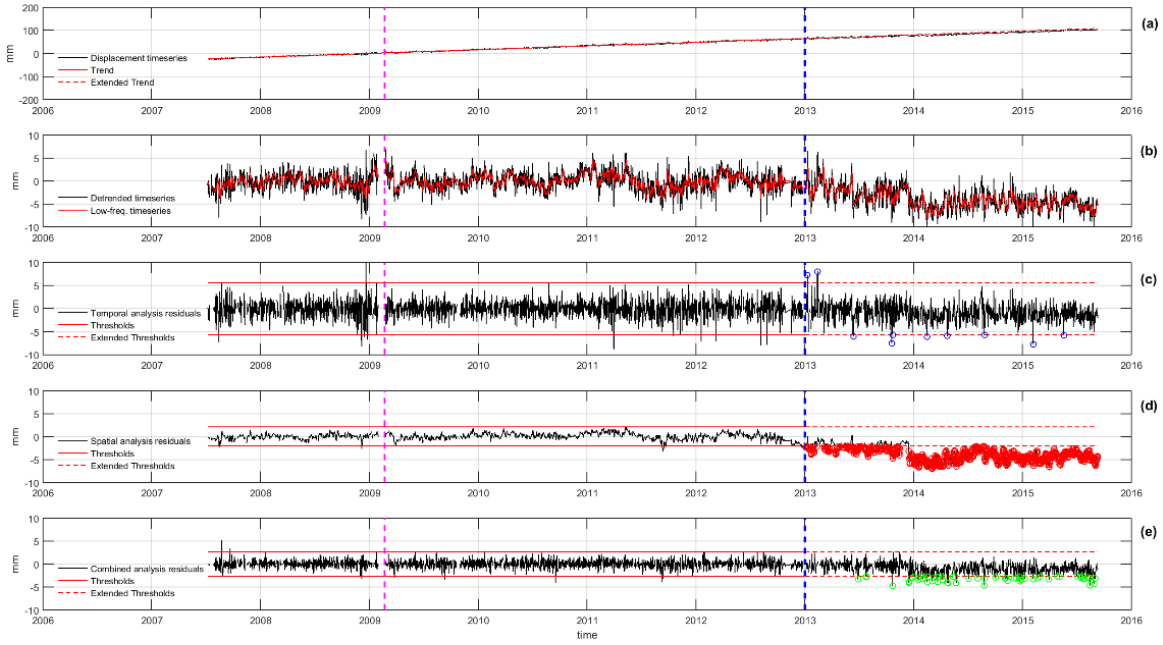


Figure 6-27 The same as Figure 6-8, for PBIL station (ΔN component) using the 2nd offset correction approach.

Furthermore, with regards to the anomalies of the ΔU component of CAML and SABB, they both appear to be related to potential local ground deformation which may be related to subsidence that took place in late-2014 (Figure 6-28) and between mid-2012 and mid-2013 (Figure 6-29), respectively. However, the number of anomalies of CAML (341-spatial and 59-temporal) and SABB (953-spatial and 171-temporal) is significantly higher than those of PBIL, reflecting the gradual appearance of these anomalies.

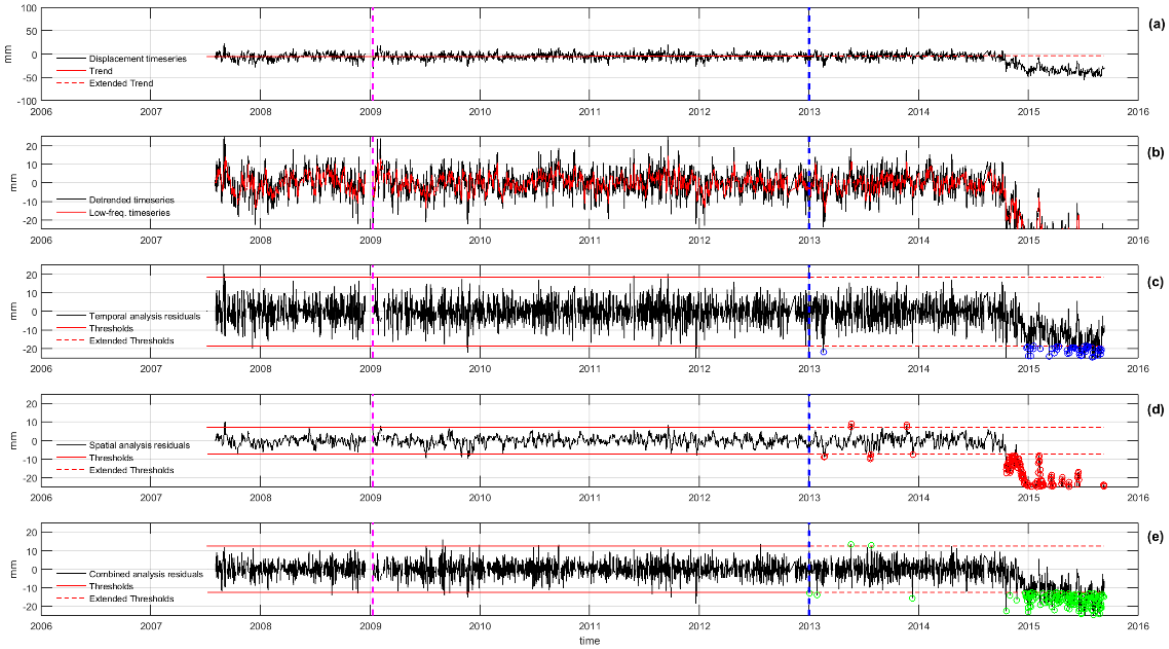


Figure 6-28 The same as Figure 6-22, for CAML station (ΔU component) using the 2nd offset correction approach.

.

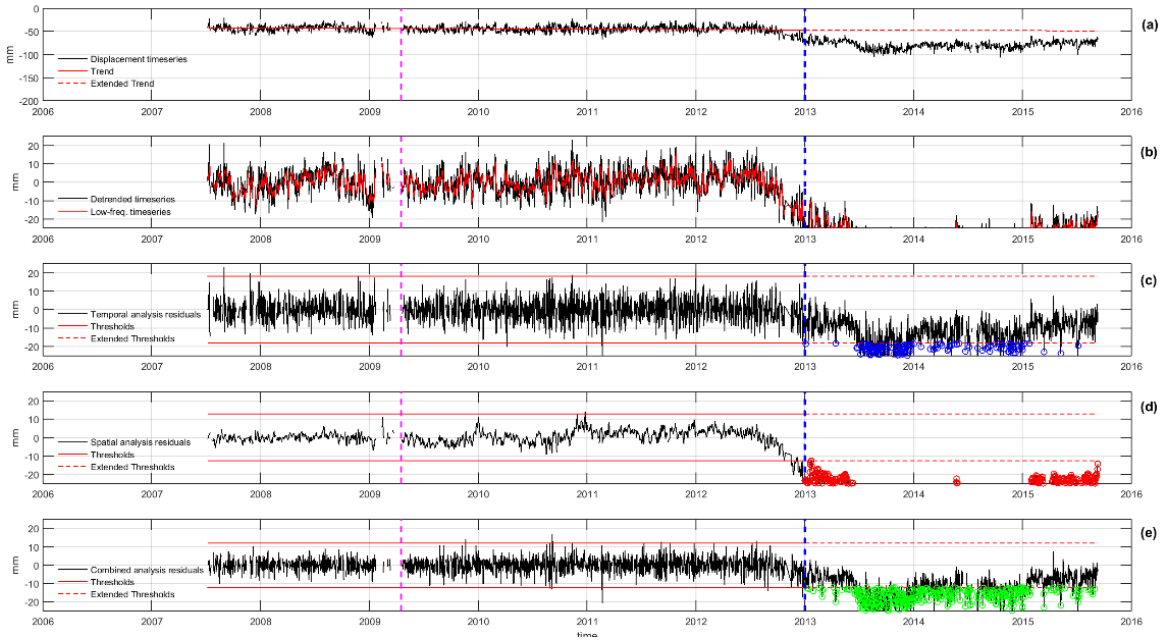


Figure 6-29 The same as Figure 6-22, for SABB station (ΔU component) using the 2nd offset correction approach.

(iii) Periodic anomalous behaviours

This type of anomalous behaviour is usually very clear, and can be detected visually. Stations (and components) in this category have been classified as such when they have

a relatively high number of anomalies (i.e. >200 and >10) identified by the spatial and temporal analysis algorithm, respectively, but where they also exhibit significant periodic variations over time. As can be seen from Table 6-4, this classification only applies to ABER (ΔN and ΔE).

For the ΔN component of ABER, there are 235 anomalies identified by the spatial analysis algorithm, with >50% of the last 200 days of the algorithm testing period considered as anomalies, and 29 anomalies identified by the temporal analysis algorithm which, without visual inspection, would lead to a classification of on-going anomalous behaviour due to offsets (that are not related to documented changes). On the other hand, in the ΔE component there are 256 anomalies identified by the spatial analysis algorithm, with <50% of the last 200 days of the algorithm testing period considered as anomalies, and 54 anomalies identified by the temporal analysis algorithm which, without visual inspection, would lead to a classification of low-frequency related temporary anomalous behaviour. However, from an inspection of Figure 6-30 and Figure 6-31, it can clearly be seen that any anomalous behaviour clearly started after a documented change that was a receiver and antenna replacement in August 2013 and that there is a distinct periodicity over the periods from November to April and from May to October each year.

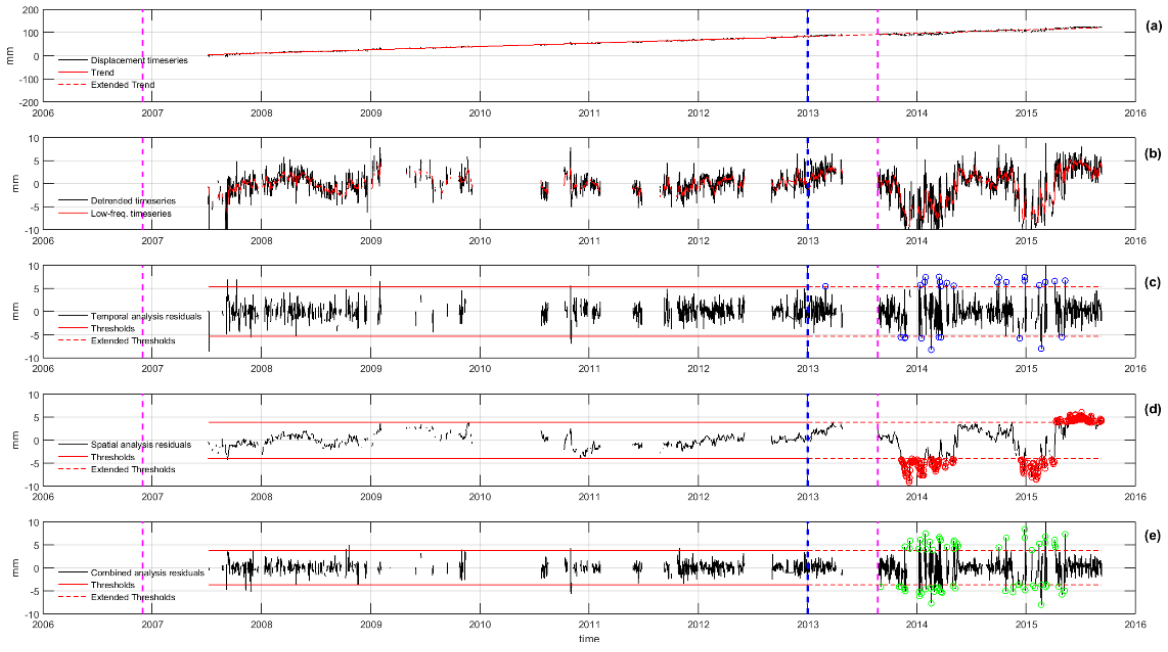


Figure 6-30 The same as Figure 6-8, for ABER Station (ΔN component) using the 2nd offset correction approach.

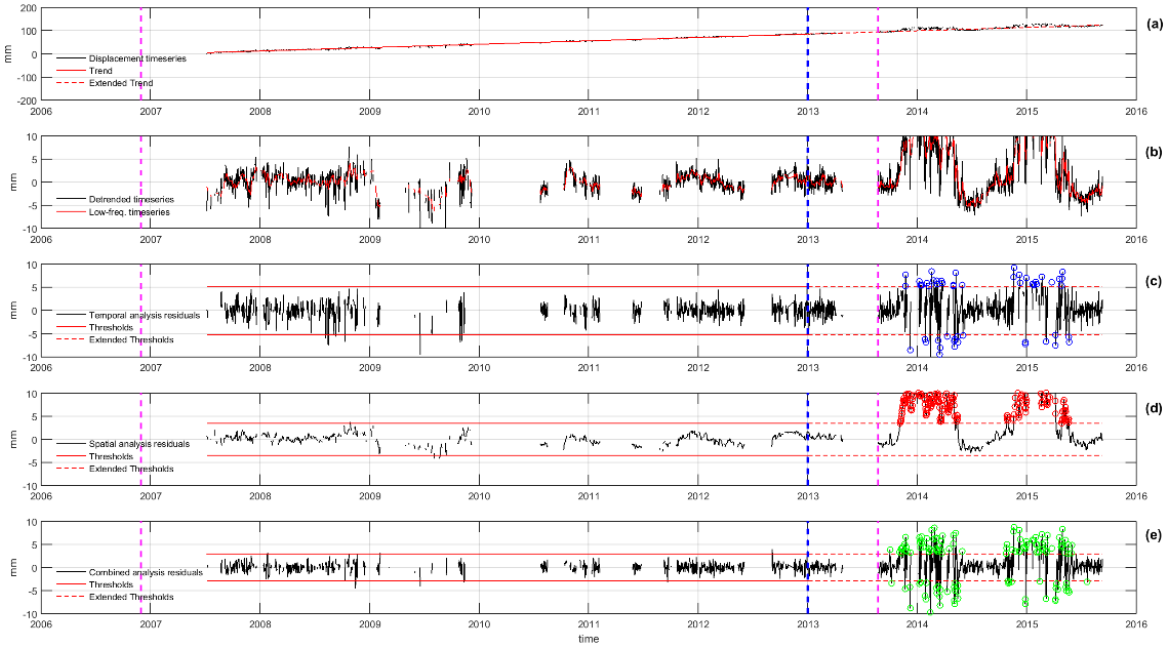


Figure 6-31 The same as Figure 6-8, for ABER Station (ΔE component) using the 2nd offset correction approach.

6.4 Discussion

The developed approach of the current study is based on the condition that the GPS coordinate time series follows a predictable behaviour for the algorithm training period, assuming that there are no offsets (that are not related to documented changes), while for the remaining algorithm testing period, the GPS coordinate time series are potentially susceptible to anomalies. This approach has enabled the definition of a classification based on different categories of anomalous behaviours, namely: (i) temporary (low or high frequency-related), (ii) on-going, due to deviations from the linear trend or due to offsets that are not related to documented changes, and (iii) periodic. In relation to the BIGF network, as it is presented in Table 6-6, the ΔE component seems to be the least 'stable' component as 85.1% of the stations were considered as having negligible anomalous behaviours while 3.4% and 10.3% were classified as having temporary and on-going anomalous behaviours, respectively. On the other hand, 88.5% and 90.8% of the stations are considered to have negligible anomalous behaviour in the ΔN and ΔU components, respectively. The ΔN component has the fewest number of on-going anomalies, 3.4%, while this percent reaches 6.9% in the ΔU component. However, the stations which have a temporary anomalous behaviour in the ΔN component, 6.9%, is more than in the ΔU component, 2.3%. This relatively low number of anomalies for the ΔU is attributed to the relatively high noise level of the component, which masks potential anomalies of moderate magnitude.

Table 6-6 The percentages of each classification within the BIGF network in the ΔN, ΔE and ΔU components.

	ΔN	**ΔE**	**ΔU**
Negligible anomalous behaviours	**88.5%**	**85.1%**	**90.8%**
Temporary anomalous behaviours	**6.9%**	**3.4%**	**2.3%**
High-frequency-related	5.7%	2.3%	1.1%
Low-frequency-related	1.1%	1.1%	1.1%
On-going anomalous behaviours	**3.4%**	**10.3%**	**6.9%**
Due to deviations from the linear trend	2.3%	10.3%	4.6%
Due to offsets (that are not related to documented changes)	1.1%	0%	2.3%
Periodic anomalous behaviours	**1.1%**	**1.1%**	**0.0%**

The developed approach revealed in the ΔE component the most stations with significant differences in their offset and linear trend estimates from the 1st and 2nd offset correction approaches (Figure 6-2), which could be due to a degradation in the reliability of the network adjustment and subsequent realisation of the reference frame over time. More specifically, for the BIGF processing the epoch of the daily solutions, which result in the station coordinate estimates, is the observed day, with the daily coordinates of the 200+ IGS stations motioned forward from the IGb08 reference epoch of 2005-01-01 to the observed day using the IGb08 station velocities. Then, to define the reference frame, no stations are fixed for the network solution, but rather an adjustment of the global network on to the IGb08 reference frame is affected using a no-net translation and no-net scale minimum constraints approach. Clearly, if the IGb08 station velocities became less reliable the further forward that they were propagated it may be that their use beyond 2013 was just a step too far. The developed approach also revealed that for the ΔE component there are: (i) the most stations with on-going anomalous behaviours (Figure 31), (ii) the largest percentage of on-going anomalous behaviours (Table 6-6) and (iii) that most of these on-going anomalous behaviours are due to deviations from the linear trend (8% of the whole network). These deviations can be seen at several of the stations in the BIGF network from early 2014 onwards and it is either because of: (i) the fact that the rate of the deviation at these stations is larger than at the surrounded stations, (ii) a site-specific reason, or (iii) a combination of these two reasons rather than merely the reference frame instability mentioned above which clearly plays a role here, too. This is clear by comparing the differences in trend between the 1st and 2nd offset correction approaches shown in Tables 6-1 to 6-3 (column O); for example, the difference in trend for HOOB (ΔE) of -0.74mm/yr is relatively larger than its surrounding stations which range between -0.66 to -0.32mm/yr. However, Tables 6-1 to 6-3 can only be used as indicators and cannot be used alone as they solely compare the trends without considering any other factors (i.e. noise level, the behaviour of other surrounding stations, and un-documented offsets in the algorithm testing dataset).

Considering Table 6-6 and Figure 6-32 further, it is also clear that the cases where there are on-going anomalous behaviours in the ΔU component were for CAML, ESKD, HELS, MART, PBIL and SABB, with the majority of these being at coastal sites. Clearly, it is not possible from the analysis carried out in this research to identify whether these stations are exhibiting anomalous behaviours due to site-specific reasons (e.g. antenna corrosion or monumentation stability issues) or due to a large-scale problem (e.g. periodic aquifer withdrawal and/or recharge). However, in terms of anecdotal evidence, the Ordnance Survey of Great Britain (OSGB) replaced the antennas at MART (on 2015-01-26), SABB (now SABS) (on 2015-12-16), and HELS station (on 2018-09-11) due to antenna corrosion. Furthermore, as part of their GNSS equipment upgrades taking place at all stations in 2018, OSGB are making a site visit to each station in order to replace the current LEICA GRX100+GNSS receiver with a SEPT POLARX5 or TRIMBLE ALLOY receiver, and to check the state of the antenna, with a view to replace it if corrosion is evident. With regards to the list of stations given above, to date (2018-10-23) these site visits have taken place at the three remaining stations (i.e. CAML, ESKD, PBIL), with no antenna replacements.

Lastly, it should be noted that the classifications of these stations can and will change through time, as the anomalous behaviour continues or stops. For example, if anomalies just started to appear at a station, it will first be considered as having recent anomalous behaviour until it reaches the limits of 200 or 10 for the spatial and temporal analysis algorithm respectively. Then, once these are reached it may be classified as having temporary anomalous behaviour which, if it continues, will then be classified as on–going anomalous behaviour. Similarly, if a station appears to have on-going anomalous behaviour and this anomalous behaviour stops, it will then be classified as having temporary anomalous behaviour. Therefore, it should also be noted that these limits (i.e. 200 and 10 for the spatial and temporal analysis algorithm respectively) are network-specific and were based on the general behaviour of the GPS coordinate time series of the BIGF network for the period of the available data. If lower limits were chosen, for instance, 100 and 5 respectively, then the overall percentage of on-going anomalous behaviours

would change from 3.4%, 10.3% and 6.9% to 2.3%, 16.1% and 8.0% in the ΔN, ΔE and ΔU components respectively. Similarly, if higher limits were chosen, for instance, 400 and 20 respectively, the percentage of the going anomalous behaviours would reduce from 3.4%, 10.3% and 6.9% to 1.1%, 4.6% and 2.3% in the ΔN, ΔE and ΔU components respectively.

.

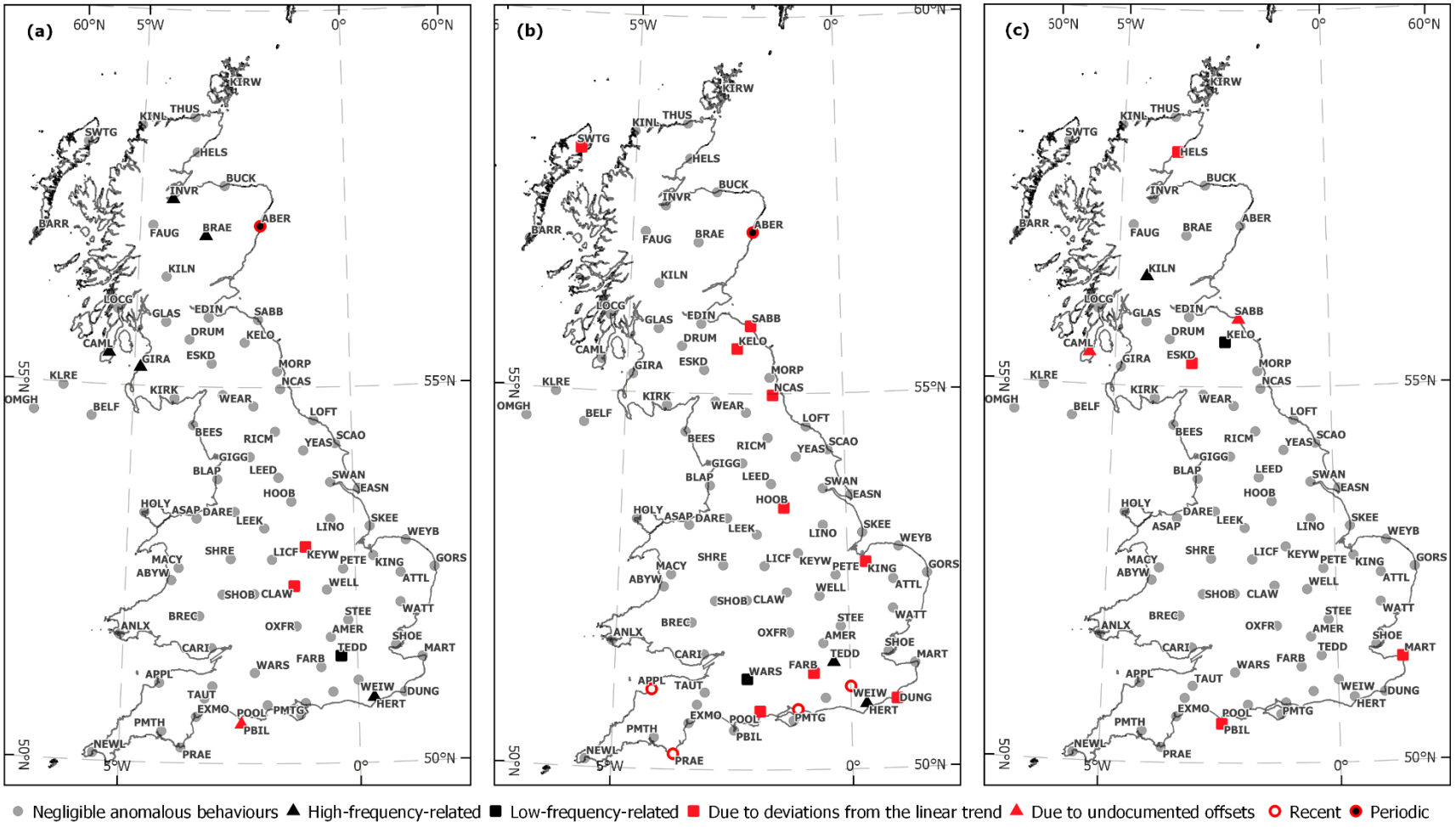


Figure 6-32 the Temporary (black) and On-going (red) anomalous behaviours classification of (a) ΔN (b) ΔE (c) ΔU components of BIGF GNSS network

6.5 Summary

In this chapter, the multiple algorithm approach was evaluated on a relatively small network with long-term daily GPS coordinate time series. This case study showed that the multiple algorithm approach was able to detect different types of anomalous behaviours (i.e. temporary and on-going). Moreover, this case study showed that the spatial analysis algorithm is preferable to be used (than the temporal and combined analysis algorithms) in the case of long-term changes (e.g. trend related anomalies). Since this case study considered a daily time series with a slow pace phenomenon, the second case study (Chapter 7) will examine the use of this multiple algorithm approach on a 1Hz GPS coordinate time series of larger network, GEONET, in Japan and in relation to a higher paced phenomenon, the Tohoku-Oki 2011 MW9.0 Earthquake.

CHAPTER 7: THE ANALYSIS OF THE 1Hz GPS COORDINATE TIME SERIES OF THE GEONET STATIONS IN JAPAN FOR THE TOHOKU-OKI 2011 MW9.0 EARTHQUAKE

In this chapter, the multiple algorithm approach will be evaluated using a second case study; the analysis of the 1Hz GPS coordinate time series of the GEONET stations in Japan for the Tohoku-Oki 2011 MW9.0 Earthquake. This case study is different from the previous case study (Chapter 6), in a sense that the GEONET is a relatively large network and the phenomenon to be monitored (i.e. the Tohoku-Oki 2011 MW9.0 earthquake) is a large, rapid and spatially correlated phenomenon which resulted in large magnitude coordinate offsets. Moreover, the used GPS coordinate time series are only for a relatively short time-period with higher temporal resolution than the previous case study. In the first section (Section 7.1), the network and the data used will be introduced. Then, in the following section (Section 7.2) the parameters used in analysing this case study are shown. Finally, in Sections 7.3 and 7.4, the results will be presented and discussed.

7.1 Network and Data

The GPS Earth Observation NETwork (GEONET) stations in Japan are considered to form one of the most dense GPS networks as it includes ~1000 GPS stations with average inter-station distances of 25-30 km (GEONET). The GEONET stations have been the subject of many studies over the last 20 years (Saito et al. 1998; Ogawa et al. 2001; Ma and Maruyama 2003, 2006, Tsugawa et al. 2004, 2007; Ma et al. 2005; Nishimura et al. 2011).

The Tohoku-Oki Mw9.0 earthquake, which was recorded by the GEONET stations, occurred at 05:46:23 UTC on March 11th 2011. Various studies have used the data from the GEONET stations to estimate the co-seismic and transient displacement, in order to model the fault rupture and earthquake characteristics (Ohta et al. 2012; Wright et al. 2012).

Figure 7-1 shows the permanent 2D (North and East) displacements at the GEONET stations after the Tohoku-Oki 2011 Mw 9.0 earthquake.

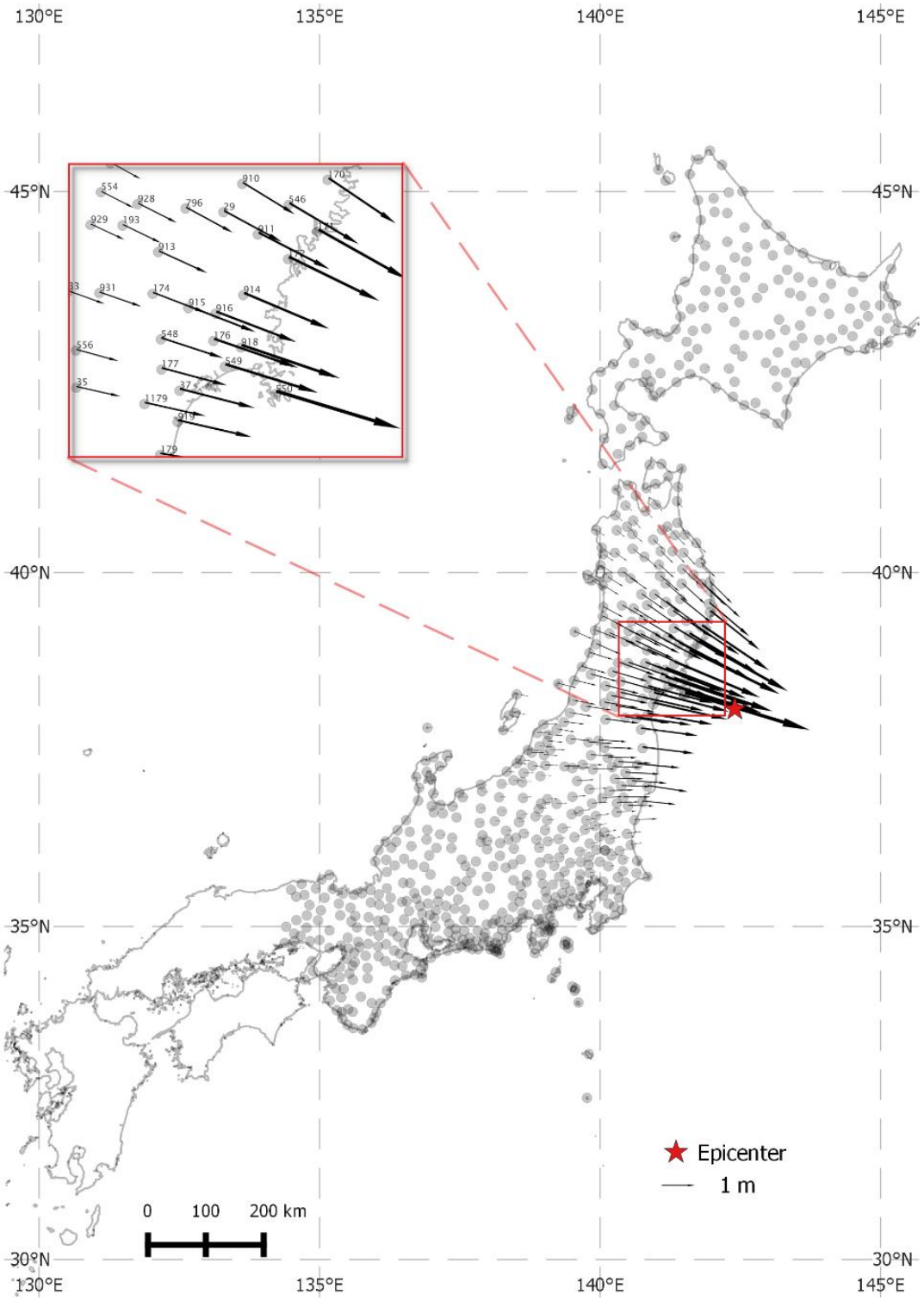


Figure 7-1 The permanent 2D (North and East) displacements at the GEONET stations after the Tohoku-Oki 2011 Mw 9.0 earthquake used in this case study

The data used in this research are the 1Hz GPS coordinate time series of North, East, Up (NEU) displacements for 847 GEONET stations, covering the period of 5 hours and 47 minutes before and 1 hour after the earthquake. These data were obtained from a PPP processing using Bernese GNSS software version 5.2 (BSW5.2), and have been successfully applied in previous studies for the definition of the earthquake characteristics (Psimoulis et al. 2014, 2015; Michel et al. 2017) and for a ground motion detection algorithm (Psimoulis et al. 2018b).

For the purpose of this study, the 1Hz GPS coordinate time series provided as North, East, Up (NEU) displacements were combined to form 1Hz GPS coordinate time series of 3D displacements. Figure 7-2 shows the 3D displacements time series for a sample of 14 stations (black points) located next to the earthquake epicentre (red star) in the middle of the GEONET, and arranged from East (i.e. station ID:550) to West (i.e. station ID:231), showing the variation of the 3D displacements across the network a few minutes before and after the earthquake (red-dashed line).

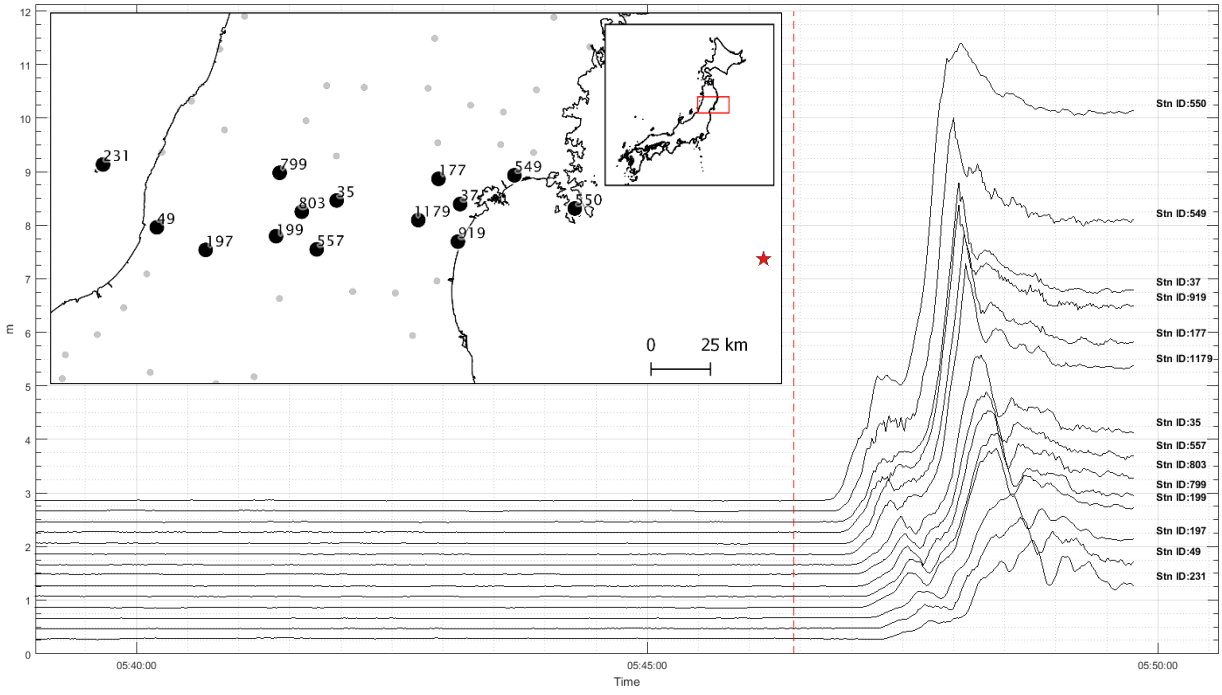


Figure 7-2 The permanent 3D displacements for a sample of 14 stations (black points) located next to the earthquake epicentre (red star) and in the middle of the GEONET, arranged from East (i.e. station ID:550) to West (i.e. Station ID:231) showing the variation of the 3D permanent displacements across the network a few minutes before and after the earthquake (red-dashed line).

7.2 Analysis

Following the methodology introduced in Chapter 5, the data were split into a training dataset, of 5 hours and 40 minutes, followed by a testing dataset, corresponding to 7 and 5 minutes before and after the earthquake.

Since the GPS coordinate time series of this case study are relatively short, linear trend estimation was not considered as it was in the previous case study (Chapter 6). However, detrending of the time series is still required to shift the time series (according to the estimated intercept) to make the spatial regression work better as the coordinate time series for all stations start from a value of 0 on their y-axis. Moreover, in this case study, during the relatively short time series, there are no documented changes and so the use of offset correction approaches were not necessary here.

The frequencies of the detrended time series were analysed using Discrete Fourier Transform (DFT) spectrum and a cut-off frequency of 0.1 Hz was identified as corresponding to white noise. Figure 7-3 shows the DFT results for the 14 stations selected above as a sample. In this figure, it can be seen that the white noise, which is shown as a random signal with a flat power spectral density, may be distinguished from the rest of the signal at 0.1 Hz (marked as a red line). This cut-off frequency of 0.1 Hz is in agreement with the range identified by Genrich & Bock (2006), namely 0.05 – 0.5 Hz, using a similar network, and close to what was identified by Colombelli et al. (2013), namely 0.075 Hz.

However, as stated in Chapter 5, it is worth mentioning that the temporal analysis residuals include all the high-frequency components (i.e. > the cut-off frequency) which makes the value of the cut-off frequency less sensitive as the filtered noise will not be removed but will be embedded in the temporal analysis residuals and, therefore, analysed in the temporal and combined analysis algorithms.

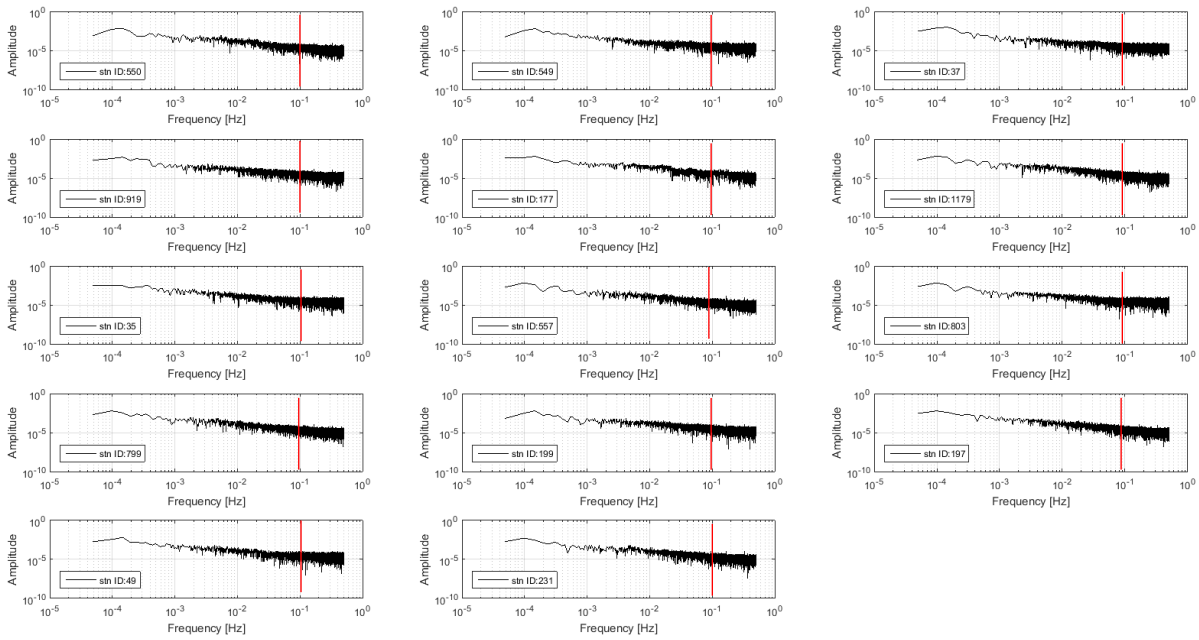


Figure 7-3 A sample of the spectral analysis using DFT for the 14 stations shown in Figure 7-2. The cut-off frequency that distinguishes the white noise, which is shown as a random signal with a flat power spectral density, and the rest of the signal is at 0.1 Hz (marked as a red line).

As illustrated in Figure 7-1, the GEONET stations form a dense network; and the offsets in the 1Hz GPS coordinate time series of 3D displacements are significantly large in magnitude (i.e. ~6m). Therefore, regarding the spatial analysis algorithm, where the spatial weights matrix derives from the geometry of the network of stations, different configurations were examined by using both the entire network and a limited number of stations, ignoring any stations that are located further than a so-called "cap distance". More specifically, three cases of spatial weight matrix were applied: one with a cap distance of 100 km; and one with a cap distance of 200km; and one using all stations (i.e. with no cap distance applied). Furthermore, two distance exponent values were used: $\alpha = 2$ and $\alpha = 3$ as summarized in Table 7-1.

Table 7-1 Summary of the configurations used in the spatial and combined analysis algorithms.

Distance exponent, $\boldsymbol{\alpha}$	Spatial regression cap		
$\boldsymbol{\alpha = 2}$	100km	200km	All stations
$\boldsymbol{\alpha = 3}$	100km	200km	All stations

Moreover, since the aim of this case study is detecting geohazards, rather than site-specific anomalous behaviours as in Chapter 6, whenever a potential event is detected a spatial search with a so-called "search buffer" is carried out in order to check if any of the surrounding stations also have potential events at that epoch. If this is the case, the algorithm considers that potential event as a geohazard and all site-specific anomalies are then eliminated (Psimoulis et al. 2018b). The search buffer of the spatial search depends on the density of the network and the phenomenon to be monitored/detected. A large search buffer may be less effective as it may include stations that are considered to be far away whereas a small search buffer could isolate stations. In this case study, a search buffer of 50 km was applied effectively, as for that distance 96% of the GEONET stations are surrounded by at least three other stations, which is consistent with Crowell et al. (2009) who used three stations or more to initiate the hypocentre estimation.

To evaluate the performance of the multiple algorithm approach, the detected anomalies were compared against those that were detected by using a method, which is based on considering as anomalies the values exceeding the range μ±3σ and fulfil the spatial search. This method, which will be called 'basic algorithm' was adopted to develop RT-SHAKE algorithm and successfully applied in Psimoulis et al. (2018a), while similar approaches have been also adopted by previous studies and in current early warning systems (Allen and Ziv, 2011; Colombelli et al., 2013).

7.3 Results

Figures 7-4 and 7-5 show the detected arrival time of the seismic motion (x-axis) at each GEONET station that was detected from the start of the earthquake, plotted against the distance of the station from the earthquake epicentre (y-axis) in order to correlate the seismic motion detection with the earthquake propagation. The results of the spatial analysis algorithm (red), the temporal analysis algorithm (blue), and the combined analysis algorithm (green) are compared against the results of the basic algorithm. The trend-line expressing the P-wave velocity, commonly assumed approximately equal to a 6km/s (Shearer 2013) is also illustrated in the figures just as a reference line. In order to compare the arrival time of each GEONET station and each algorithm against the basic algorithm, the percent difference was also calculated using the following equation:

$$\boldsymbol{percent\ difference} = \sum_{\mathbf{1}}^{\boldsymbol{n}} \left(\frac{ATBA - ATDA}{ATBA} \right) \times 100 \qquad \textit{Equation 7-1}$$

where $ATBA$ is the detected Arrival Time using the Basic Algorithm, $ATDA$ is the detected Arrival Time using the Developed Algorithm and n is the number of stations.

Figure 7-6 presents the percent differences for the three developed algorithms (temporal, spatial and combined) and the three cases of spatial weight matrix using all of the testing dataset. The higher the absolute value indicates that the difference between the two curves (i.e. the developed algorithm and the basic algorithm) is larger, while a negative sign means that the arrival time detected by the developed algorithm was later than that detected by the basic algorithm and a positive sign means that the arrival time detected by the developed algorithm is earlier than that detected by the basic algorithm.

Figure 7-7 presents the results for the basic algorithm and the three developed algorithms that were obtained when considering the first few seconds of the seismic motion arrival, and shows the spatial distribution of the elapsed time of first detection of the geohazard and at which stations. There were also considered the cases of stations indicated as potential events or geohazards. It was compared against those that were detected in the

algorithm testing dataset using the 'basic algorithm' (i.e. any value exceeds the range of $\mu \pm 3\sigma$ extracted from the detrended time series of the algorithm training dataset). The main principle of adopting this range (i.e. $\mu \pm 3\sigma$) for comparison, is it has been used in previous studies and in current early warning systems [Allen and Ziv, 2011; Colombelli et al., 2013; Psimoulis et al., 2018b].

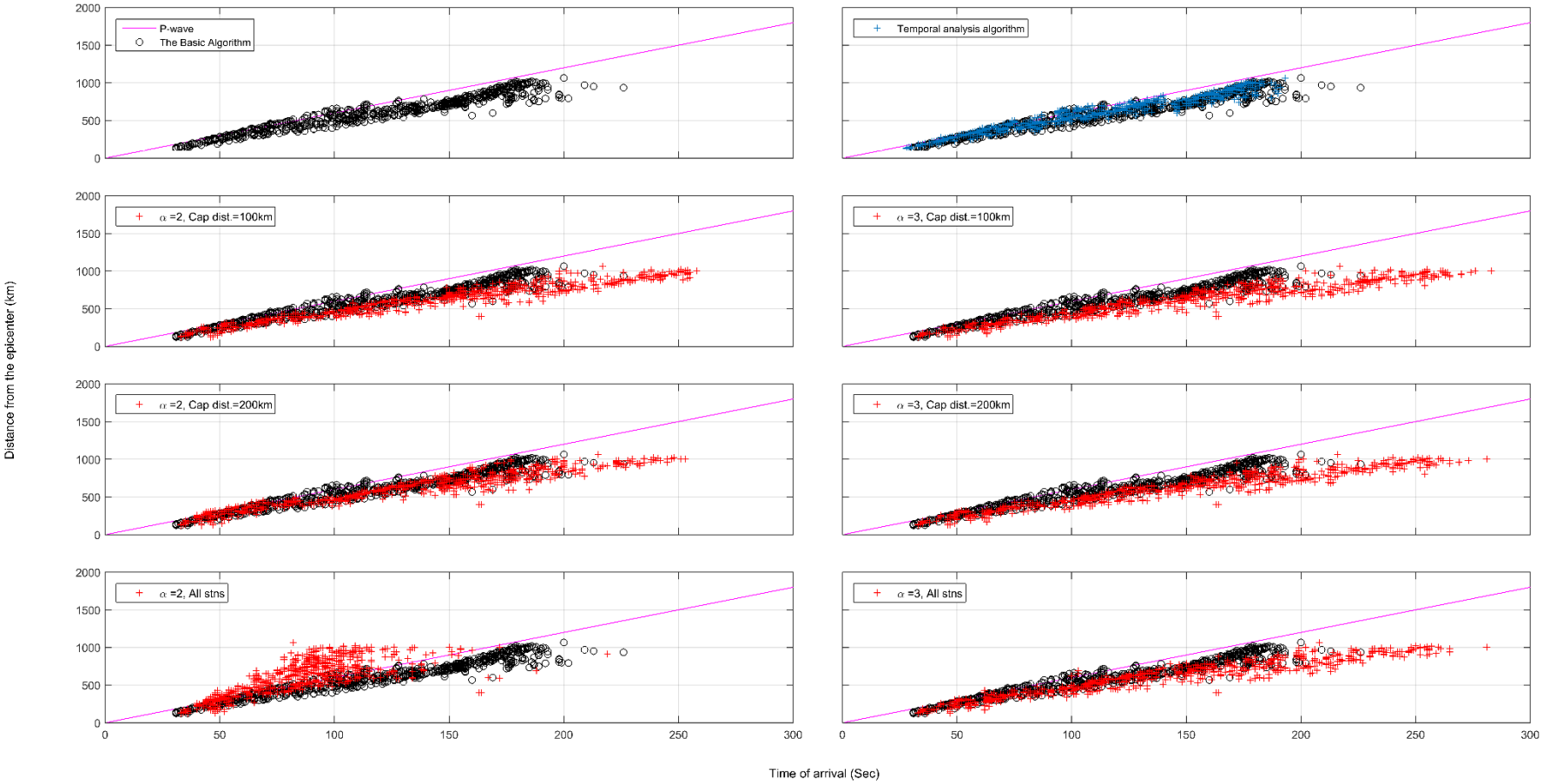


Figure 7-4 Detected arrival time of the seismic motion vs. distance from the earthquake epicentre for the temporal and spatial analysis algorithms when using different distance exponents ($\alpha = 2$ at the left and $\alpha = 3$ at the right), with cap distances of 100km, with a cap distance of 200km and with all stations (i.e. with no cap distance applied), in the GEONET case study. The trend-line expressing the P-wave velocity, commonly assumed approximately equal to a 6km/s.

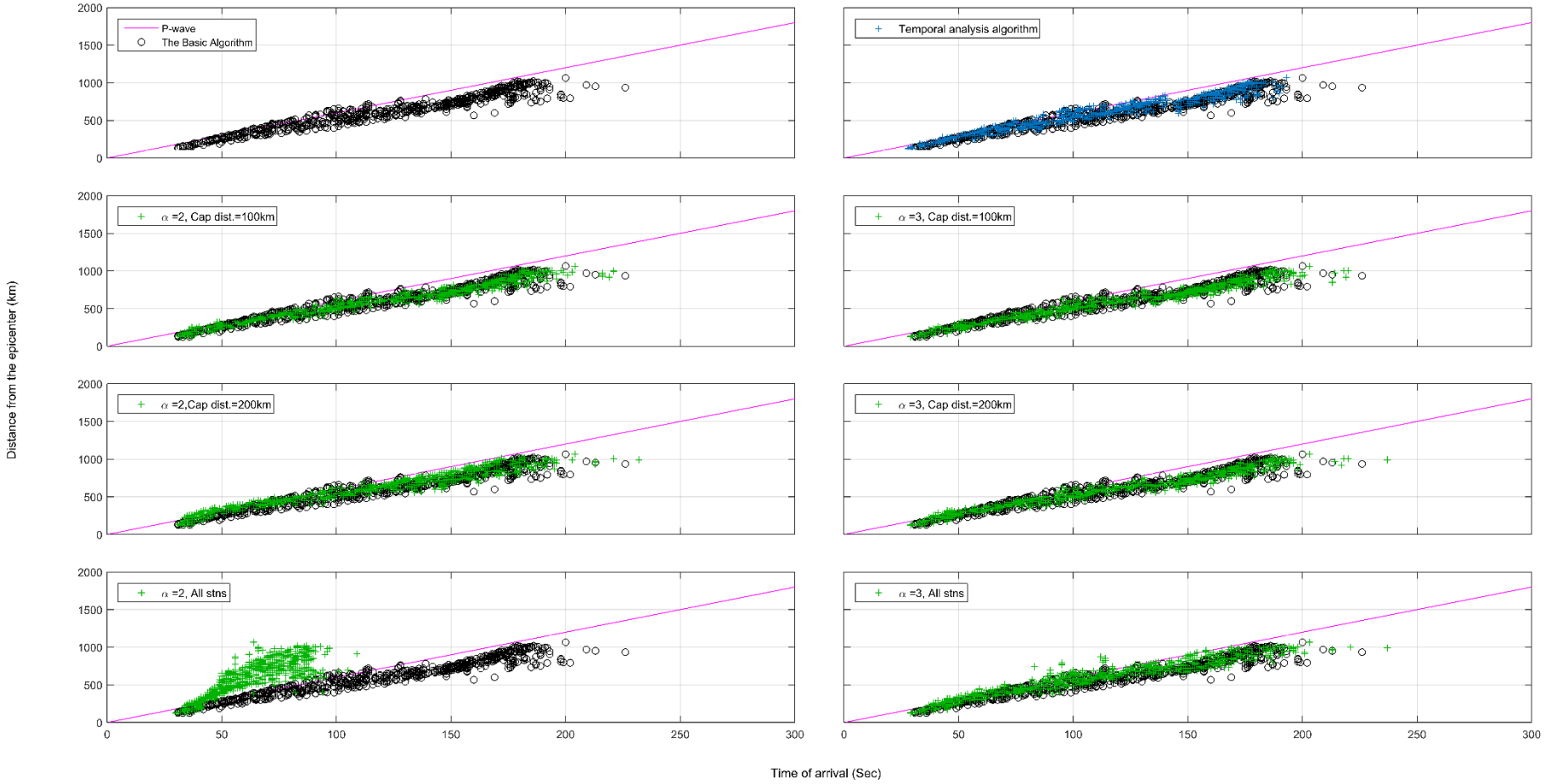
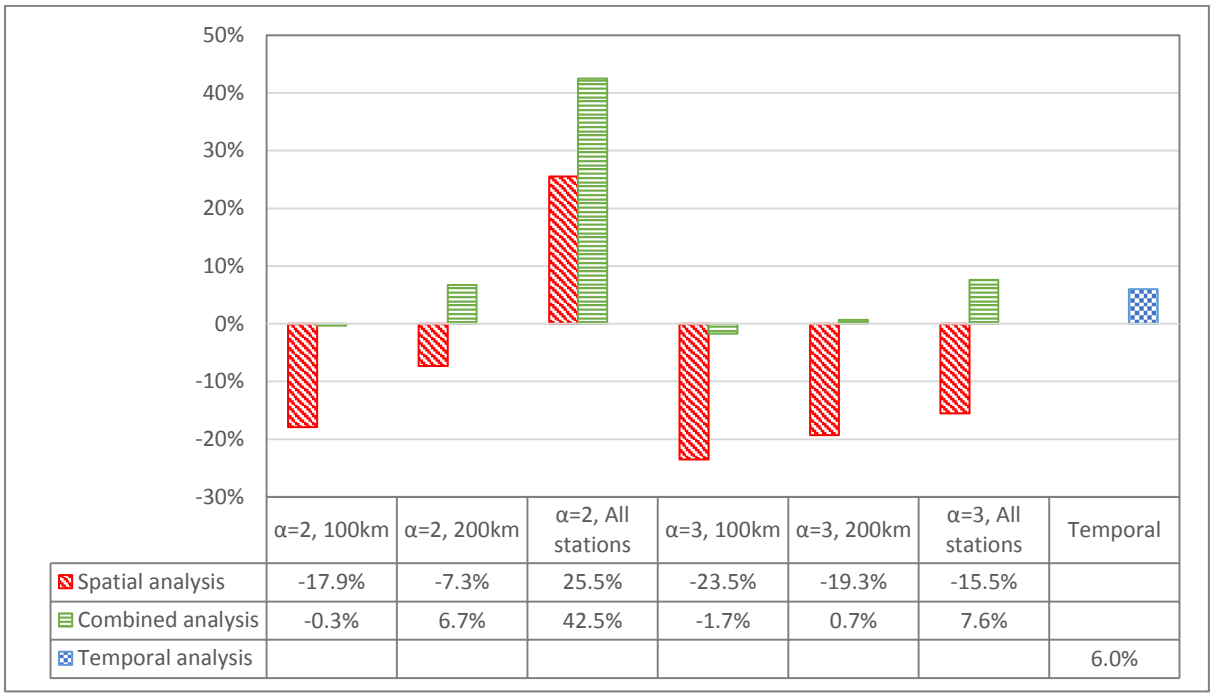


Figure 7-5 Same as Figure 7-4 but for the temporal and combined analysis algorithms.



	α=2, 100km	α=2, 200km	α=2, All stations	α=3, 100km	α=3, 200km	α=3, All stations	Temporal
Spatial analysis	-17.9%	-7.3%	25.5%	-23.5%	-19.3%	-15.5%	
Combined analysis	-0.3%	6.7%	42.5%	-1.7%	0.7%	7.6%	
Temporal analysis							6.0%

Figure 7-6 Percent difference in the detected arrival time of the seismic motion between the basic algorithm and the spatial, temporal and combined analysis algorithms in the GEONET case study.

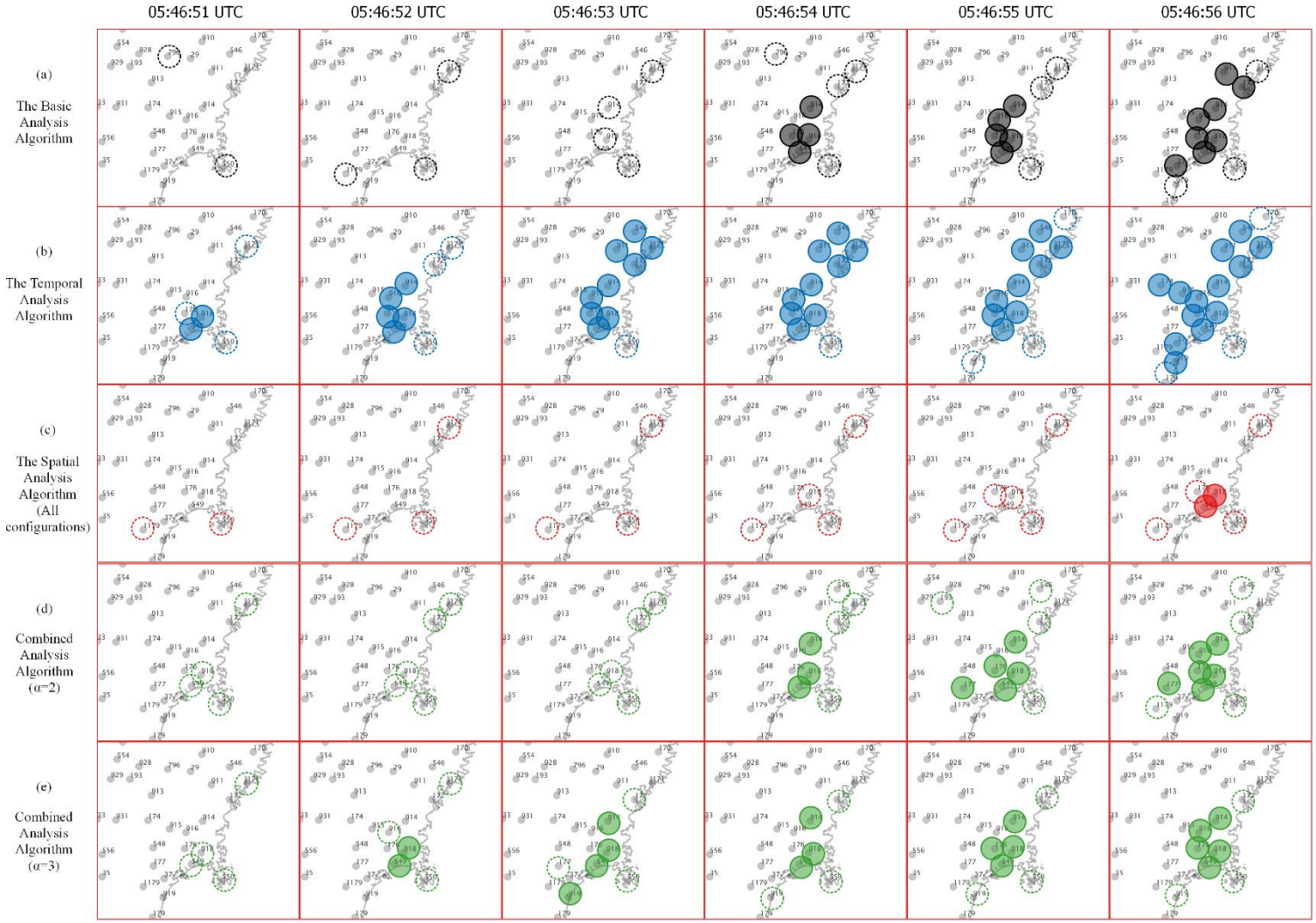


Figure 7-7 Spatial distribution of the elapsed time of first detection of the geohazard and at which stations (marked by filled circles), as well as the stations with potential events (marked by hollow circles) through a time slice of 5 seconds using the (a) basic algorithm (black), (b) temporal analysis algorithm (blue), (c) spatial analysis algorithm (red), (d) combined analysis algorithm with $\alpha = 2$ (green), (e) combined analysis algorithm with $\alpha = 3$ (green), in the GEONET case study.

7.4 Discussion

In this section, the results are discussed in terms of the temporal analysis algorithm (Sub-section 7.4.1), the spatial analysis algorithm (Sub-section 7.4.2) and the combined analysis algorithm (Sub-section 7.4.3).

7.4.1 The temporal analysis algorithm

The temporal analysis algorithm performs similar to the basic algorithm (Figure 7-4), as in both cases each station is analysed separately, with no interaction between the stations in the network. However, the temporal analysis algorithm detects the earthquake earlier than the basic algorithm (Figure 7-6), due to its higher sensitivity by using the high-frequency component, through the analysis of the time series and the spatial search. This led the temporal analysis algorithm to obtain an elapsed time of first detection of the geohazard 3 seconds earlier than the basic algorithm for the closest stations to the earthquake epicentre (Figure 7-7b). It is also expected that the temporal analysis algorithm would have performed better than the basic algorithm if the GPS time series had been of longer time period, where the impact of periodic signals and linear trends would be more evident and their efficient modelling would be possible through the ANN, as presented in Chapter 6. It is also shown in this figure that using the temporal analysis algorithm led to a wider detection (i.e. geographically) of the geohazard than with the spatial and combined analysis algorithms. This may be due to the averaging in the spatial regression (Equations 5-3 and 5-5 in Chapter 5) through using the spatial weight matrix in both the spatial and combined analysis algorithms to compare the relative behaviours. In other words, the estimated value of the spatial regression model at a station is, in a way, an average of the surrounding stations, which in the case of a station having a relatively larger displacement to its neighbours, the estimated displacement value will be smaller than the true displacement value.

7.4.2 The spatial analysis algorithm

In Figure 7-4 it can be seen that by using the spatial analysis algorithm with $\boldsymbol{\alpha} = 2$ for the spatial weights matrix, and with all stations (i.e. with no cap distance applied) leads to false detection of the arrival time of the seismic motion, as it corresponds to a propagation velocity significantly faster than that of the P-wave (i.e. 6km/s). Hence, this configuration was not further analysed; as having a large anomalous displacement at a station in the network may affect the estimates at all stations, especially if the decay function is not steep enough to dissipate this propagation (i.e. comparing with using $\boldsymbol{\alpha} = 3$).

In other words, since the spatial regression estimates the values at each station based on the values of other stations across the entire network (as no cap distance applied) simultaneously, the large displacements at the stations near the epicenter biased the estimations of the values at stations that are far from epicenter to be larger than they truly are. Consequently, this made the spatial residuals at these stations (i.e. far from the epicentre) to be large enough to exceed the spatial thresholds and considered anomalous.

However, it is worthy to mention that this effect will not appear until there are enough stations with relatively large enough values to compete with the rest of the stations. This appears clearly in the figure that even with $\boldsymbol{\alpha} = 2$ and with no cap distance, it took time (as noted in the x-axis) till the false detection occurred as will be illustrated further in Figure 7-7.

For all of the other combinations of $\boldsymbol{\alpha}$ and cap distance, the overall performance of the spatial analysis algorithm seems similar, with the general trend being that the detected arrival time of the seismic motion is slower than the P-wave and slower than the basic algorithm (Figure 7-4). This is also reflected numerically (Figure 7-6) in the percent difference values which are all negative, meaning that the detected arrival time of the seismic motion is later than that of the basic algorithm.

Furthermore, it is observed that, for a given cap distance for the spatial regression, the smaller the α used for the spatial weights matrix, the more the impact of the seismic

motion from far stations, which makes the algorithm more susceptible to false detection due to large displacements from distant stations, as in the case of a large earthquake. Therefore, the spatial analysis algorithm should be optimised by adjusting the parameter α, based on the expected coordinate offset due to the geohazard being monitored.

Figure 7-6 shows that with a 100 km cap distance, the percent difference is -23.5% and -17.9% with $\boldsymbol{\alpha} = 3$ and $\boldsymbol{\alpha} = 2$, respectively, while for a 200km cap distance and for the same values of $\boldsymbol{\alpha}$ the percent difference decreases (i.e. -19.3% and -7.3%, respectively). Likewise, for a given α, the larger the cap distance, the more susceptible the spatial analysis algorithm is to any dispacements in distant stations. Therefore, the spatial analysis algorithm should be optimised by adjusting the parameter cap distance, based on the geometry of the GNSS network.

Figure 7-7(c) illustrates the spatial distribution of the elapsed time of first detection of the geohazard and at which stations, in a time period of 5 seconds. For the different configurations of the spatial analysis algorithm, potential events are detected at stations 171, 550 and 1179 (hollow circles), but since these stations are further than the spatial buffer (i.e. 50 km) they were flagged but not considered as geohazards, until potential events also appear at their nearby stations, namely 176, 549, 918 and 550. Lastly, the geohazard is detected 2 seconds after the basic algorithm at stations 918 and 549 (filled circles), as each of these is surrounded by at least three stations which are also considered to have potential events.

7.4.3 The combined analysis algorithm

From Figure 7-5 and Figure 7-6, it is observed that the performance of the combined analysis algorithm, using Equation 7-1, sits between the performance of the spatial and temporal analysis algorithms. More specifically, it agrees with the spatial analysis algorithm in giving false detection with $\boldsymbol{\alpha} = 2$ for the spatial weights matrix and with all stations (i.e. with no cap distance applied) for the spatial regression. By using $\alpha = 2$ and a 100km cap distance, or $\alpha = 3$ and either a 100 or 200km cap distance, the performance of

the combined algorithm is similar to that of the basic algorithm as the percent difference values are small.

On the other hand, by using $\alpha = 2$ and a 200km cap distance, or $\alpha = 3$ and all the stations (i.e. with no cap distance applied), the performance of the combined analysis algorithm is consistent with that of the temporal analysis algorithm, as the detected arrival time of the seismic motion is prior to that of the basic algorithm, with the percent difference of 6.7% and 7.6%, respectively (Figure 7-6).

However, the combined analysis algorithm does differ from the spatial analysis algorithm, as the elapsed time of first detection of the geohazard (Figure 7-7d,e) depends on the configuration of the algorithm. More specifically, the first detection of the geohazard is 2 seconds before the basic algorithm when using $\boldsymbol{\alpha = 3}$, while it behaves just like the basic algorithm when using $\boldsymbol{\alpha = 2}$, which is due to the fact that the low-frequency signal is analysed by the spatial analysis algorithm, whereas the high-frequency signal is analysed by the combined analysis algorithm.

From all of the above analyses, it is demonstrated that the temporal analysis algorithm provides slightly earlier detection than the basic algorithm, while the spatial analysis algorithm gives a later detection than the basic algorithm. While the combined analysis algorithm proved to be more effective for a steeper decay function (i.e. $\alpha = 3$) which made the ground motion of station(s) easier to distinguish from that of the surrounding stations. Furthermore, when using different configurations of the parameters (α and cap distance) Figure 7-6 shows significant differences in the overall perfomance of the used configurations within an algorithm (e.g. the spatial analysis algorithm), while Figure 7-7 shows less significant differences within the same analysis algorithm. This is due to the fact that the effect at the first few stations which are affected by the geohazard, may propagate to other stations due to the simultanous nature of the spatial regression (i.e. depending on their relative displacement to other stations and the α value used).

The analysis also shows that how each algorithm behaves in such large, rapid and spatially correlated phenomenon which resulted in large magnitude coordinate offsets. The temporal analysis algorithm proved to be more effective than the spatial and combined analysis algorithms because, on one hand, only the low-frequency component is used in the spatial analysis which makes it harder to detect high-frequency phenomena as earthquakes. On the other hand, the SAR model in both spatial and combined analysis algorithms looks for stations that behave in a different way from their neighbours which makes it harder in a geohazard as earthquakes which are often regional in nature.

7.5 Summary

In this case study, the multiple algorithm approach was tested on a relatively dense network with a large and spatially correlated phenomenon, but with shorter time series when compared to the previous case study. This case study showed that the multiple algorithm approach was able to detect the arrival time of seismic motion due to the Tohoku-Oki 2011 MW9.0 Earthquake Moreover, this case study showed that the temporal analysis algorithm is preferable to be used (than the spatial and combined analysis algorithms) in the case of such large displacements. Also it is expected that the temporal analysis algorithm would be even more effective for long-period GPS time series, where the modelling of the long-period signals and linear trends need to be modelled accurately for the reliable performance of the algorithms.

Since this case study and the previous case study considered GPS coordinate time series, the third case study (Chapter 8) will examine the use of this multiple algorithm approach on GPS troposphere time series, to test its performance on a long-term and spatially dependent dataset.

CHAPTER 8: THE ANALYSIS OF THE LONG-TERM, HOURLY GPS TROPOSPHERE TIME SERIES OF THE BIGF NETWORK OF STATIONS IN THE BRITISH ISLES.

In this chapter, the multiple algorithm approach will be evaluated using a third case study; the analysis of the long-term hourly GPS troposphere time series of the BIGF network of stations in the British Isles. The aim of this chapter is to examine the performance of the algorithm on a different type of dataset that is not directly related to crustal/land movement and its ability to detect wider anomalies (i.e. meteorological events). It is worthy to mention that water vapour is a dominant but not sole factor in the rain formation process and this research does not claim that such meteorological events can be detected/predicted using Integrated Water Vapour (IWV) alone. However, it tests the ability to use the multiple algorithm approach as a complementary tool in weather nowcasting/forecasting. In the next section, a brief introduction to IWV will be shown and the datasets used will be illustrated. Then, the results of the multiple algorithm approach will be analysed and discussed.

8.1 Datasets

Integrated Water Vapour (IWV) estimates are derived from the total effect of tropospheric refraction on the GNSS signal. This total effect is known as the Zenith Total Delay (ZTD) which also can be expressed as the summation of the Zenith Hydrostatic Delay (ZHD) and Zenith Wet Delay (ZWD). The ZHD can be modelled well using the height, latitude and pressure values at each station while the ZWD is hard to model. Therefore, it is estimated by subtracting the modelled ZHD from the estimated ZTD (Equation 8-1).

$$ZWD = ZTD - ZHD. \qquad \textit{Equation 8-1}$$

The ZWD is a consequence of the presence of water vapour in the atmosphere, where an estimate of integrated water vapour can be derived from the ZWD (Calori et al. 2016) as shown in Equation 8-2.

$$IWV = \Pi * ZWD \qquad \textit{Equation 8-2}$$

where Π is a dimensionless quantity of the weighted mean temperature, refractivity constants and the ratio between the molar gas constant and molar gas of water (Calori et al. 2016). In this research, IWV estimates were the output from a processing using Bernese software version 5.2 (BSW5.2) and GPS only, and were provided, by BIGF (BIGF), as long-term hourly estimates for 72 British Isles continuous GNSS Facility (BIGF) stations (Figure 8-1a). More information and description of BIGF are given in Chapter 6.

Since the presence of water vapour across the network is highly dynamic, the Met Office Integrated Data Archive System (MIDAS UK) hourly rainfall data was used as a secondary dataset that can help to indicate the start and end of meteorological events. This data was downloaded from the British Atmospheric Data Centre (BADC) (Figure 8-1b).

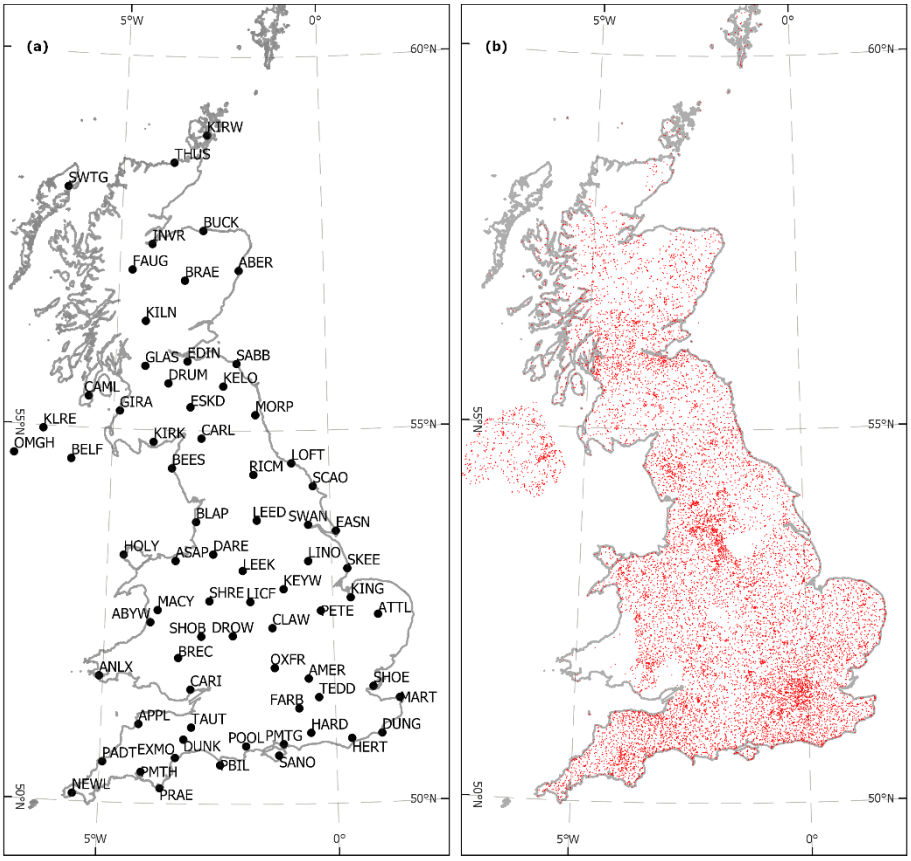


Figure 8-1 (a) The selected stations of the British Isles continuous GNSS Facility (BIGF) (b) the location of the rain gauges available from the MIDAS dataset.

8.2 Data processing

Following the 5-step methodology discussed in Chapter 5, the IWV dataset was split into an algorithm training dataset and the algorithm testing dataset. The algorithm training dataset length was chosen to be 5.5 years (i.e. July 2007 to December 2012) to mitigate the effect of annual and semi-annual signals in the estimation of the long-term trends (Blewitt and Lavallée 2002), while the rest of the dataset (January 2013 to September 2015) was used as the algorithm testing dataset which represents around 33% of the used data. No corrections or modifications were applied to the gaps and the outliers of the dataset. The influence of any documented changes reported in the GPS coordinate time series were checked manually and it was found that the IWV time series were not affected by any of these. Therefore, the 2nd step, correcting offsets related to documented changes, was skipped as implementing this step may have introduced errors into the time series.

The Discrete Fourier Transform (DFT) spectrum analysis was performed to analyse the frequencies of the detrended time series to identify the cut-off frequencies corresponding to the white noise (see Chapter 5). The spectral analysis showed that the annual and semi-annual signals are the dominant signals in all stations (the dashed green lines in Figure 8-2), while the white noise corresponds to frequencies varying between 1 cycle/day to 0.25 cycle/day as illustrated by the red strip in Figure 8-2.

As stated in Chapter 5, the cut-off frequency can be optimised based on the application and the phenomenon to be detected, assuming that NAR-ANN will only learn the temporal dependency within the so-called "low-frequency" time series (< cut-off frequency). In this study, since the phenomenon we desire is complicated and the IWV is only one factor amongst several other factors, different cut-off frequencies were examined namely, 0.25 cycle/day, 0.5 cycle/day and 1 cycle/day.

Similarly to the previous case study (chapter 7), since the aim of this case study is not detecting site-specific anomalous behaviours, but rather meteorological events, a spatial search is conducted whenever a potential event is detected at a station. This will eliminate false alarms and site-specific anomalies (Psimoulis et al. 2018b). However, instead of applying a fixed distance search, as done in the previous case study, in this case study the nearest five stations were checked; if there are three stations or more out of these five stations that have anomalous behaviour at that epoch (Crowell et al. 2009), it is considered a meteorological event. This modification was done rather than using a fixed distance for the spatial search as in Chapter 7 due to the fact that the BIGF network is less dense and by having a fixed distance for the spatial search, it may lead to unbalanced clusters of stations.

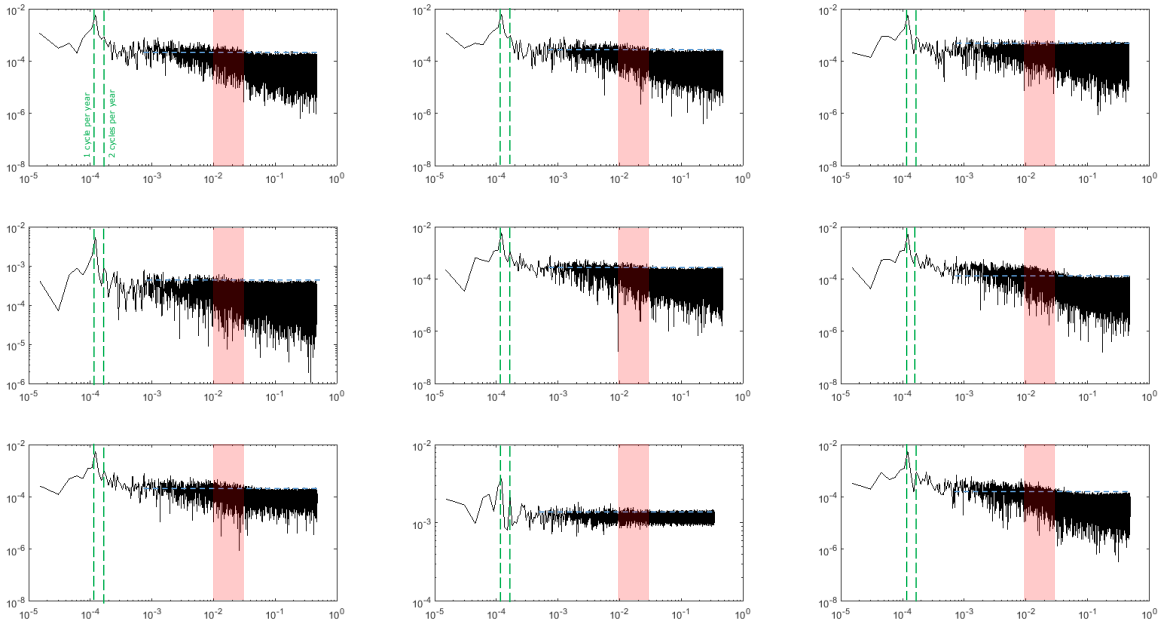


Figure 8-2 A sample of the spectral analysis of IWV using DFT for 9 stations. The red strips show the range of the examined cut-off frequency namely: 0.25 cycle/day, 0.5 cycle/day and 1 cycle/day. The dashed green lines show the annual and semi-annual cycles while the blue dashed lines are plotted to help distinguish the white noise, which is shown as a random signal with a flat power spectral density.

8.3 Results

The results will be illustrated in this section in two parts: the first part illustrates the ranges of the residuals thresholds of the temporal, spatial, and combined analysis algorithms when different cut-off frequencies are used; the second part shows the days which were flagged as having a meteorological event.

8.3.1 The multiple algorithm approach residuals thresholds

Table 8-1 shows the residuals thresholds of the temporal, spatial and combined analysis algorithms using the three values of cut-off frequencies of 0.25, 0.5 and 1 cycle/day. This table shows that the temporal analysis residuals thresholds have the widest ranges amongst the three analysis algorithms, while the spatial analysis residuals thresholds have the narrowest ranges amongst the three analysis algorithms, which suggests that IWV are highly spatially correlated even among the high frequencies, as reflected by the relatively narrow range of the combined analysis residuals thresholds.

Table 8-1 shows that the temporal analysis residuals thresholds have averages of 8.74, 7.55 and 7.06 $kg.m^{-2}$ using 0.25, 0.5 and 1 cycle/day, respectively. On the other hand,

the spatial and combined analysis residuals thresholds are very close to each other, and are fairly small; with average values for the spatial analysis residuals thresholds of 3.06, 3.24 and 3.31 $kg.m^{-2}$ using 0.25, 0.5 and 1 cycle/day, respectively, and average values for the combined analysis residuals thresholds of 3.86, 3.72 and 3.65 $kg.m^{-2}$ using 0.25, 0.5 and 1 cycle/day, respectively.

This suggests that the effect of the chosen cut-off frequency has an opposite effect on the spatial analysis as higher cut-off frequency leads to higher thresholds. This is due to the fact that when a higher cut-off frequency is used, more noise is introduced into the low-frequency time series and the values become less correlated spatially, which leads to larger value residuals and thresholds. On the other hand, when a higher cut-off frequency is used in the temporal analysis algorithm, less noise is left in the temporal residuals which lead to narrower thresholds. Furthermore, since the combined analysis algorithm uses the temporal residuals as an input to the spatial regression, the noisier temporal residuals lead to nosier combined analysis residuals.

Table 8-1 also shows, at an individual station level, that there are some variations between the stations. For example, ABER, ABYW, DUNK and SHOE stations have relatively higher thresholds in the three analysis algorithms which may indicate site-specific issues. Likewise, SWTG, NEWL and ANLX stations have large spatial and combined analysis residuals which may be a result of their locations in relation to their surrounding stations, as these three stations clearly have an unbalanced distribution of their nearest five stations. Nevertheless, this case study focuses on the large scale anomalous behaviours rather than site-specific anomalies and therefore, these site-specific issues will not be investigated further.

Table 8-1 The temporal (T), spatial (S) and combined (C) residuals thresholds (kg.m-2) using different cut-off frequencies

Cut-off	0.25 cycle/day			0.5 cycle/day			1 cycle/day		
	T	S	C	T	S	C	T	S	C
ABER	10.43	6.28	7.38	9.33	6.37	6.98	8.82	6.41	6.76
ABYW	10.56	5.51	5.08	9.33	5.35	4.76	8.78	5.28	4.6
AMER	9.12	2.15	3.13	7.91	2.28	3.05	7.4	2.35	3.03
ANLX	9.39	5.4	6.13	8.07	5.87	5.7	7.52	6.07	5.51
APPL	9.1	5.11	5	7.83	5.42	4.7	7.31	5.55	4.58
ASAP	8.61	2.46	3.7	7.43	2.66	3.61	6.95	2.74	3.58
ATTL	8.74	3.07	4.07	7.51	3.32	3.91	7	3.43	3.85
BEES	8.4	2.49	3.55	7.2	2.65	3.42	6.7	2.73	3.37
BELF	9.13	4.28	4.68	7.86	4.49	4.38	7.32	4.58	4.25
BLAP	8.53	2.79	3.71	7.31	3.01	3.58	6.81	3.11	3.53
BRAE	7.2	2.56	3.39	6.2	2.72	3.29	5.79	2.79	3.24
BREC	8.56	2.41	3.32	7.38	2.58	3.22	6.89	2.66	3.18
BUCK	7.54	2.68	3.72	6.51	2.91	3.58	6.08	3.01	3.53
CAML	8.5	3.6	4.23	7.3	3.85	4.02	6.81	3.96	3.92
CARI	9.22	3.86	4.02	7.94	4.08	3.83	7.41	4.17	3.75
CARL	8.22	2.01	3.24	7.05	2.18	3.15	6.57	2.26	3.12
CLAW	8.74	3.47	3.42	7.51	3.63	3.29	7	3.69	3.24
DARE	8.54	2.51	3.23	7.32	2.64	3.16	6.81	2.69	3.13
DROW	8.88	3.18	3.49	7.65	3.33	3.37	7.14	3.39	3.33
DRUM	7.96	2.95	2.69	6.85	2.98	2.65	6.39	3	2.63
DUNG	8.82	2.89	3.82	7.6	3.12	3.65	7.09	3.22	3.59
DUNK	10.7	5.79	5.14	9.37	5.61	4.72	8.78	5.5	4.51
EASN	8.82	2.36	3.53	7.62	2.53	3.43	7.12	2.61	3.39
EDIN	7.93	2.03	3.06	6.8	2.19	2.99	6.34	2.26	2.96
ESKD	7.86	1.65	2.8	6.76	1.77	2.76	6.3	1.83	2.75
EXMO	9.42	4.04	3.69	8.13	4.13	3.53	7.6	4.16	3.48
FARB	9.1	1.84	2.84	7.88	1.94	2.78	7.38	1.98	2.76
FAUG	7.28	2.62	3.35	6.25	2.82	3.22	5.83	2.91	3.17
GIRA	8.32	2.7	3.57	7.16	2.86	3.48	6.69	2.93	3.44
GLAS	7.95	2.49	3.2	6.8	2.64	3.09	6.33	2.72	3.05
HARD	9.17	2.42	3.13	7.94	2.56	3.06	7.43	2.62	3.04
HELS	7.66	2.22	3.4	6.62	2.39	3.3	6.19	2.47	3.26
HERT	8.94	2.54	3.67	7.74	2.72	3.56	7.24	2.8	3.52
HOLY	8.85	4.48	5.46	7.6	4.93	5.11	7.09	5.12	4.96
INVR	7.65	2.35	3.66	6.67	2.53	3.61	6.26	2.61	3.59
KELO	8.08	1.86	2.97	6.93	1.95	2.9	6.46	2	2.88
KEYW	8.54	2.18	3.14	7.33	2.33	3.08	6.83	2.39	3.06
KILN	7.5	2.43	3.54	6.46	2.62	3.43	6.03	2.7	3.38
KING	8.65	2.01	3.02	7.44	2.16	2.98	6.95	2.23	2.97
KIRK	8.49	2.57	3.52	7.29	2.73	3.41	6.8	2.8	3.37
KIRW	7.43	3.67	4.33	6.42	4.03	4.06	6	4.18	3.93
KLRE	10.02	5.41	5.13	8.78	5.44	4.79	8.23	5.46	4.64
LEED	8.44	2.35	3.66	7.26	2.55	3.56	6.77	2.64	3.52
LEEK	8.13	2.57	3.02	6.99	2.69	2.97	6.51	2.74	2.95
LICF	8.59	2.54	3.08	7.38	2.68	3	6.87	2.74	2.97
LINO	8.76	1.93	3.2	7.54	2.06	3.13	7.03	2.13	3.11
LOFT	8.27	2.03	3.38	7.13	2.2	3.29	6.66	2.28	3.26
MACY	8.98	3.64	3.98	7.72	3.71	3.77	7.2	3.74	3.7
MART	8.99	2.67	3.9	7.76	2.89	3.75	7.24	3	3.68
MORP	8.33	3.01	4.02	7.19	3.19	3.9	6.72	3.28	3.84
NEWL	9.55	5.56	6.49	8.25	6.07	6.03	7.71	6.3	5.82
OMGH	9.71	4.94	5.51	8.5	5.19	5.11	7.97	5.3	4.93
OXFR	8.83	3.56	3.94	7.61	3.77	3.78	7.11	3.86	3.73
PBIL	9.31	3.19	3.97	8	3.41	3.8	7.45	3.5	3.73
PETE	8.72	3	3.52	7.5	3.17	3.42	6.99	3.25	3.38
PMTG	9.8	2.45	3.17	8.53	2.47	3.03	7.99	2.48	2.98
PMTH	9.13	2.67	3.61	7.86	2.85	3.5	7.34	2.93	3.45
POOL	9.03	2.99	3.46	7.76	3.14	3.36	7.23	3.2	3.33
PRAE	9.46	3.03	3.8	8.14	3.26	3.63	7.58	3.36	3.56
RICM	8.16	2.17	3.6	7.05	2.39	3.51	6.58	2.48	3.48
SABB	8.26	2.63	3.6	7.09	2.84	3.44	6.61	2.93	3.38
SANO	9.26	2.79	2.88	8	2.87	2.78	7.48	2.91	2.74
SCAO	8.27	2.19	3.29	7.11	2.38	3.2	6.63	2.47	3.17
SHOB	8.9	2.04	3.18	7.67	2.16	3.1	7.16	2.21	3.08
SHOE	12.14	2.68	8.96	11.4	3	9.08	11.19	3.16	9.22
SHRE	8.65	3.11	3.52	7.44	3.3	3.41	6.94	3.37	3.36
SKEE	8.73	2.16	3.24	7.53	2.32	3.16	7.03	2.4	3.14
SWAN	8.45	1.83	3.03	7.27	1.98	2.98	6.78	2.05	2.96
SWTG	8.06	5.99	6.08	7.01	6.52	5.6	6.56	6.75	5.37
TAUT	9.11	4.76	3.68	7.85	4.79	3.44	7.33	4.8	3.35
TEDD	9.07	2.03	2.92	7.87	2.13	2.86	7.38	2.18	2.84
THUS	7.43	2.45	3.43	6.44	2.66	3.31	6.02	2.75	3.26

8.3.2 The multiple algorithm approach in the detection of meteorological events

Due to the complex nature of meteorological events, regarding their durations, overlapping behaviours and spatial coverage, the results of the multiple algorithm approach will be presented in different forms in order to try to capture a representative picture of its performance. Table D-1 , in the appendix, summarizes the days on which meteorological events were detected. For each day, the number of hours the meteorological event lasted is given, as well as the number of stations that were listed for each cut-off frequency, which gives the first indication of the intensity of each meteorological event. However, it should be noted that in some cases, meteorological events can occur across several days, while in other cases several meteorological events can be present within a single day.

Table D-1 shows that the number of days considered as having meteorological events is always higher from the temporal analysis algorithm; roughly three times higher than for the spatial analysis algorithm and two times higher than for the combined analysis algorithm. It can also be seen from Table D-1 that, in some cases, the number of hours or stations flagged using 1 cycle / day as the cut off frequency is higher than the rest, while in other cases, it is the other way around (i.e. the number of hours or stations flagged using 0.25 cycle/day as the cut off frequency is higher than the rest). Moreover, the table shows that the average number of hours for a meteorological event that was flagged by the combined analysis algorithm is the shortest (i.e. 2 hours). In order to further understand this performance, examples will, therefore, be shown using the 0.25, 0.5 and 1 cycle/day cut-off frequencies.

8.4 Discussion

In this section, detailed examples are illustrated and discussed. The examples were chosen to be representative of the majority of the cases, and are relatively long in period (i.e. several days). The first example shows the different behaviours of the temporal, spatial and combined analysis algorithms, and also shows how the different cut-off frequencies

affect the three algorithms. The second example, on the other hand, draws more attention to the behaviour of the temporal analysis algorithm corresponding to different cut-off frequencies as the temporal analysis is the most frequent, as shown in Table D-1 mentioned above.

8.4.1 Example#1

This example focuses on August 2015 when there were various incidents of localised flash flooding, mostly due to heavy downpours of rain. Figure 8-3 to 8-5 present the results of using 0.25, 0.5 and 1 cycle/day cut-off frequencies, respectively. In the first instance, these show the hourly summation of the rain at rain gauges across the network on the left-hand axis; furthermore, as an attempt to show the intensity of the rain, grey strips are put at instances where the hourly reading exceeds 10mm at any of the rain gauges. While on the right-hand axis, the number of stations which were considered to have a meteorological event as detected by the temporal, spatial, and combined analysis algorithms, either due to high or low IWV values.

Figures 8-3 to 8-5 illustrate that the three algorithms were able to detect meteorological events with different intensities for each of the three examined cut-off frequencies. The temporal analysis algorithm detected high IWV at the beginning of 9th August 2015, which does not coincide with a large amount of rain as none of the rain gauges exceeds 10mm. Moreover, it detected a meteorological event related to high IWV prior to rain on the 13th August 2015, while on the 15th August 2015 just after the rain had ended, it detected a low IWV value, which exceeded the lower threshold. Figures 8-3 to 8-5 also show that when 0.25 cycle/day is used as the cut-off frequency, more stations were considered to be having meteorological events in the temporal analysis algorithm.

The meteorological events detected by the spatial analysis algorithm, on the other hand, which take place on 11th and 12th August 2015 do not coincide with a large amount of rain, but are more related to some local intense rain as flagged by the grey zones on the 11th and 12th. Also when the 0.25 Cycle/day cut-off frequency is used for the spatial analysis algorithm, more stations were considered to be having meteorological events. Finally,

Figures 8-3 to 8-5 show that even though the combined analysis algorithm detected a few stations on 9th August 2015, a higher cut-off frequency leads to more stations being flagged.

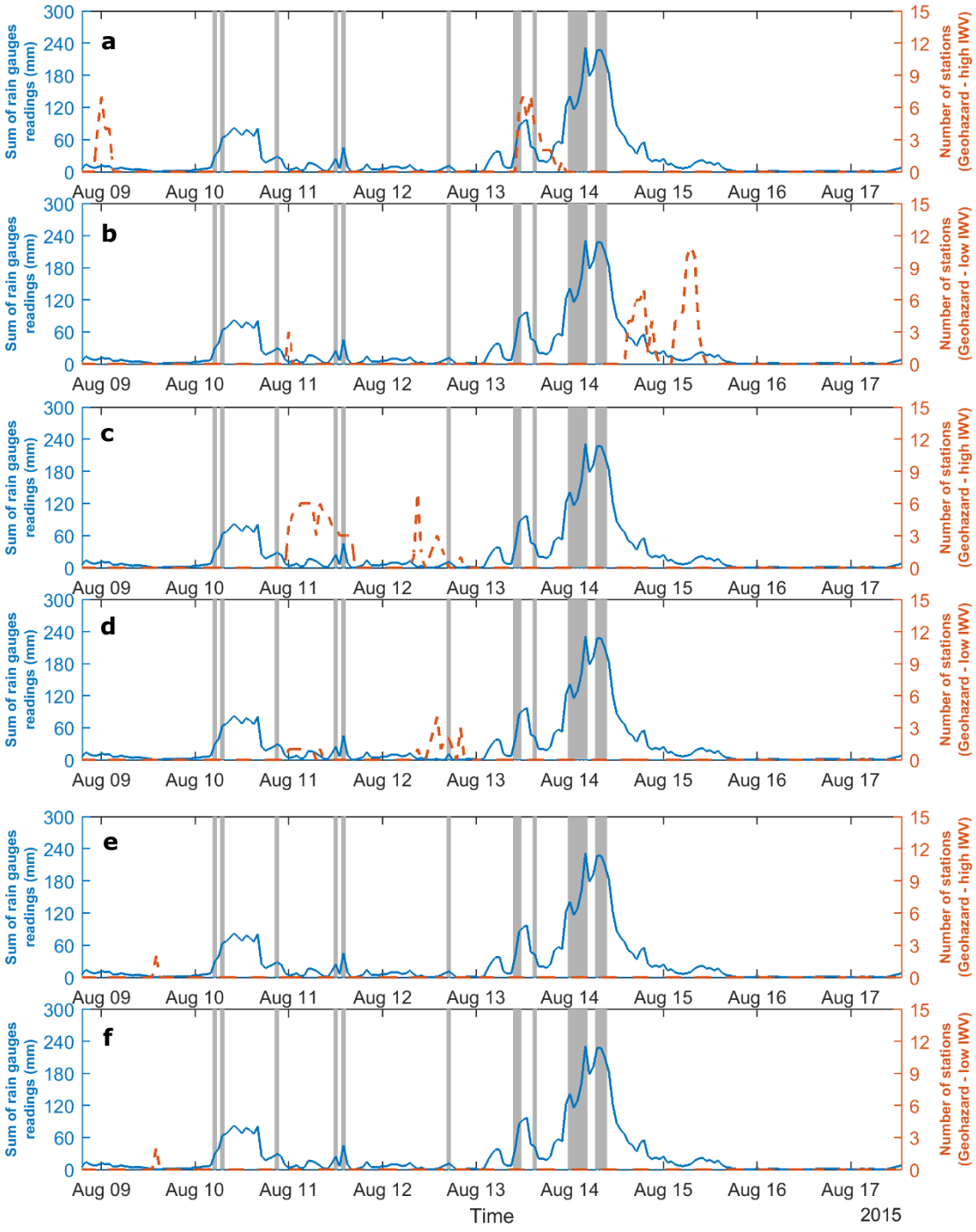


*Figure 8-3 The summation of the rain gauge readings (blue) and the number of stations (orange) considered as having meteorological events detected by the temporal (a,b), spatial (c,d), and combined (e,f) analysis algorithms, with a cut-off frequency of **0.25 cycle/day**. Grey strips indicate where hourly rain gauges readings exceed 10mm at any of the rain gauges.*

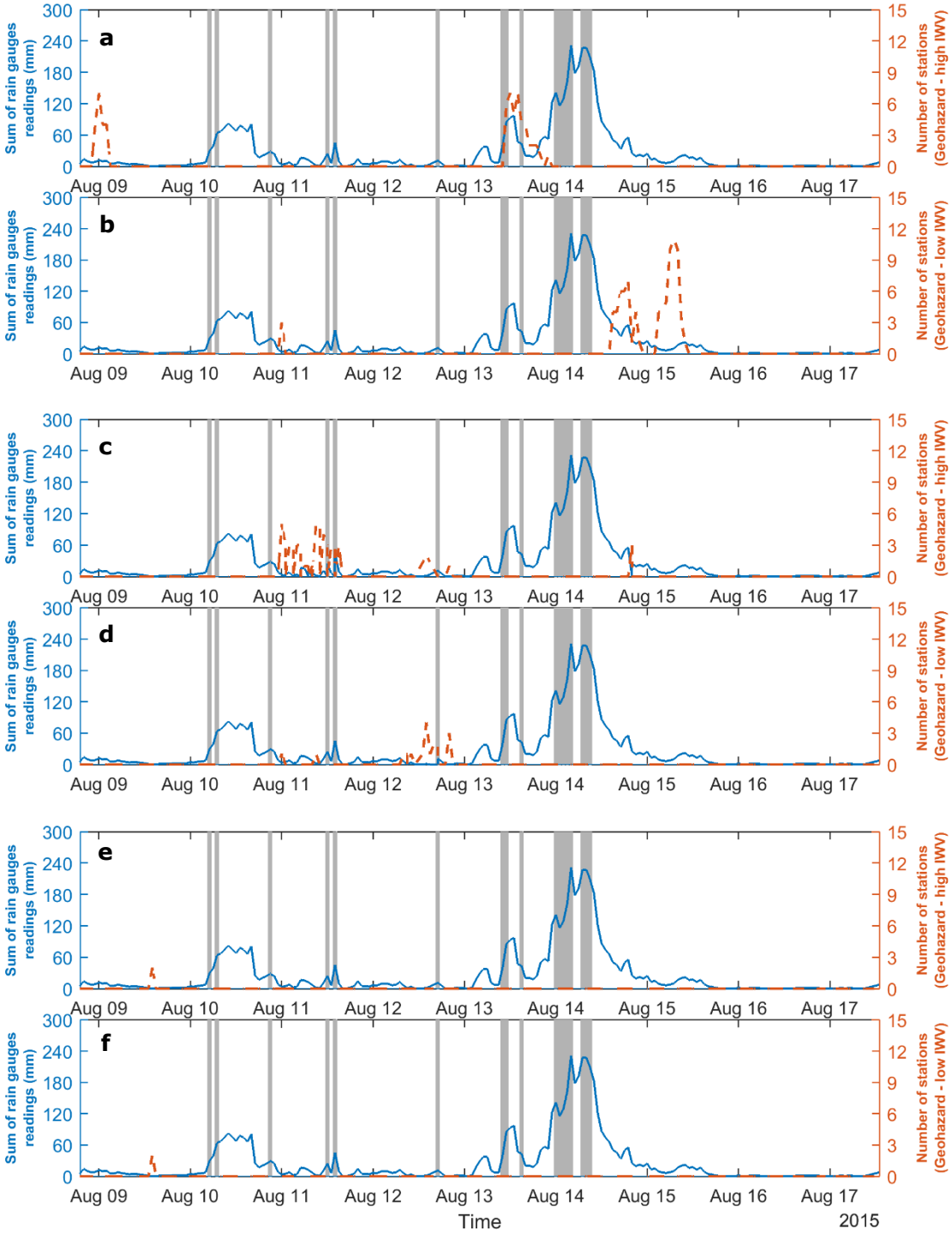


*Figure 8-4 The summation of the rain gauge readings (blue) and the number of stations (orange) considered as having meteorological events detected by the temporal (a,b), spatial (c,d), and combined (e,f) analysis algorithms, with a cut-off frequency of **0.5 cycle/day**. Grey strips indicate where the hourly rain gauge readings exceed 10mm at any of the rain gauges.*

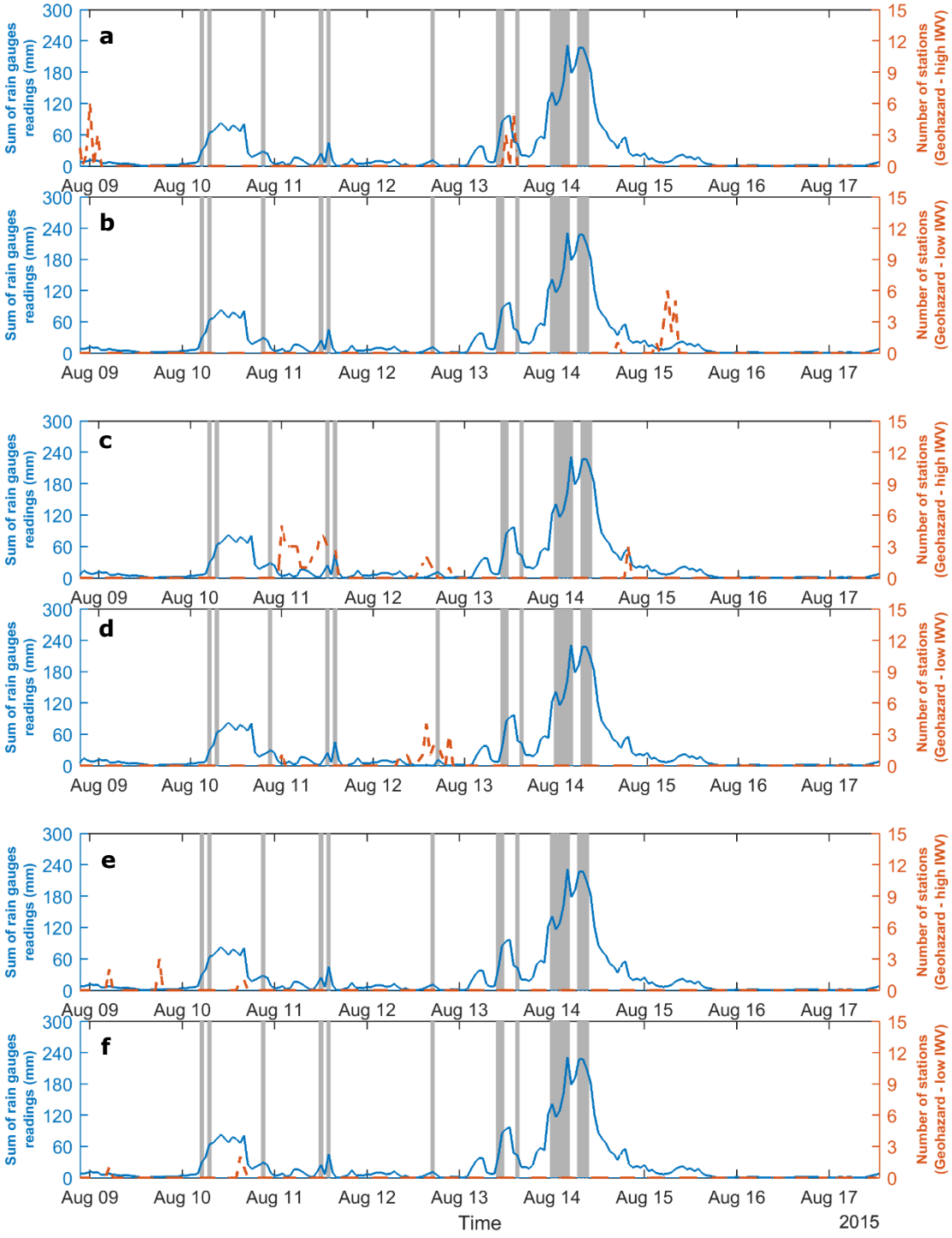


*Figure 8-5 The summation of the rain gauge readings (blue) and the number of stations (orange) considered as having meteorological events detected by the temporal (a,b), spatial (c,d), and combined (e,f) analysis algorithms, with a cut-off frequency of **1 cycle/day**. Grey strips indicate where the hourly rain gauge readings exceed 10mm at any of the rain gauges.*

To further understand the effect of different cut-off frequencies on meteorological event detection, the IWV time series of 20 stations across the BIGF network (sorted from North to South) are presented in Figure 8-6, showing the epochs with potential events (hollow symbols) and meteorological events (filled symbols) detected by the temporal (high IWV: dark blue, and low IWV: light blue), the spatial (high IWV: red, and low IWV: orange), and the combined (high IWV: dark green, and low IWV: light green) analysis algorithms.

Figure 8-6 shows how the IWV values started to increase gradually in almost all of the nearby stations during the early hours of 9th August 2015, and that the beginning of this increase was detected by the temporal analysis algorithm, but since it happened in most of the nearby stations, it was not detected by the spatial analysis algorithm. By the end of 10th August 2015, the values of IWV started to decrease again. However, this time, this decrease was not at all the stations as the IWV maintained their values at the southernmost stations (represented in this figure by SANO, HERT, HARD and TEDD stations) which makes them appear anomalous to their surrounding stations with relatively high IWV. Similarly, the spatial analysis algorithm detected anomalies at CARI station concerning it having relatively low IWV when compared to its surrounding stations. Then, on 13th August 2015, the IWV increased again at almost all of the stations, which makes the meteorological event detected by the spatial analysis algorithm disappear. Nevertheless, this increase was detected by the temporal analysis algorithm which coincides with the beginning of the strong rain event. Finally, a drop in the IWV values was also detected by the temporal analysis algorithm by the end of the meteorological event. The combined analysis algorithm, on the other hand, detects some anomalies, but these are only considered as potential events rather than meteorological events.

This variation between the three analysis algorithms is reflected by their residuals, which are shown in Figure 8-7 to 8-9. Figure 8-7 shows the temporal analysis residuals and where anomalies were only detected at the beginning and at the end of the rain, rather than during the whole period of the rain. This is due to the fact that the changes of the first event (9th – 11th August 2015) and the second event (mid 13th to mid 14th August

2015) are slow in pace, which caused them to be modelled as part of the low-frequency signal (i.e. <0.25 cycle/day) and hence not appear in the temporal analysis residuals. Figure 8-8 illustrates that the spatial analysis residuals have small values, which indicates that the values of the low-frequency component of these time series are highly spatially correlated and that the spatial regression succeeded in modelling most of the variation in these time series, hence leading to such small residuals.

Since the input to the combined analysis algorithm is the temporal residuals, it is expected to detect stations where its temporal residuals exhibit a different behaviour from surrounding stations. As shown previously in Table 8-1, these residuals are spatially correlated, resulting in a low number of detected meteorological events from the combined analysis residuals, when compared to the temporal analysis residuals.

Figure 8-9 shows the combined analysis residuals of these events which illustrates that the combined analysis algorithm detects some anomalies which coincide with where its temporal residuals are being noisy. However, after conducting the spatial search, the majority of these potential events were filtered out as they did not appear in nearby stations, which makes this algorithm less suitable for meteorological event detection. Therefore, the combined analysis algorithm will not be discussed further, but its results will be included in subsequent figures for the sake of completion.

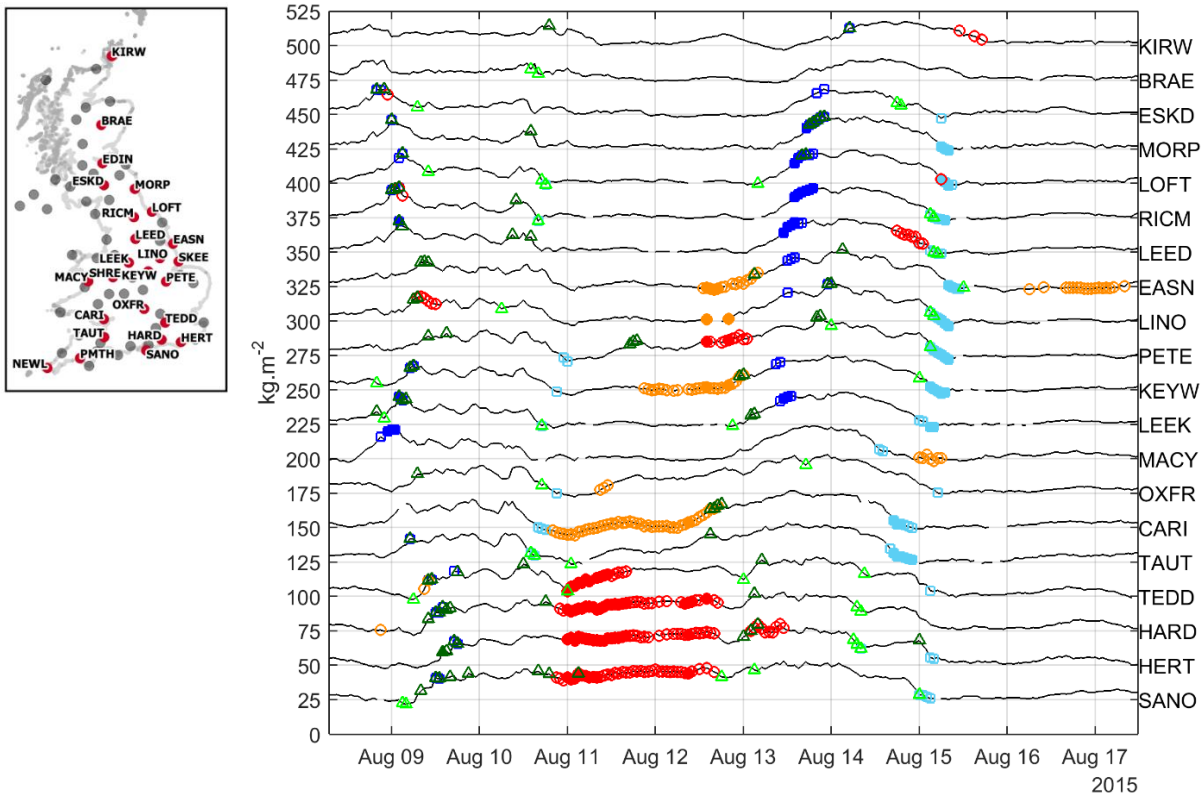


*Figure 8-6 The IWV time series of 20 stations along with epochs considered as either potential events (hollow) or meteorological events (filled) using the temporal (high IWV: dark blue, and low IWV: light blue), the spatial (high IWV: red, and low IWV: orange), and the combined (high IWV: dark green, and low IWV: light green) analysis algorithms, with **0.25 cycle/day** as a cut off frequency (y-axis grid:25 kg.m^{-2}).*

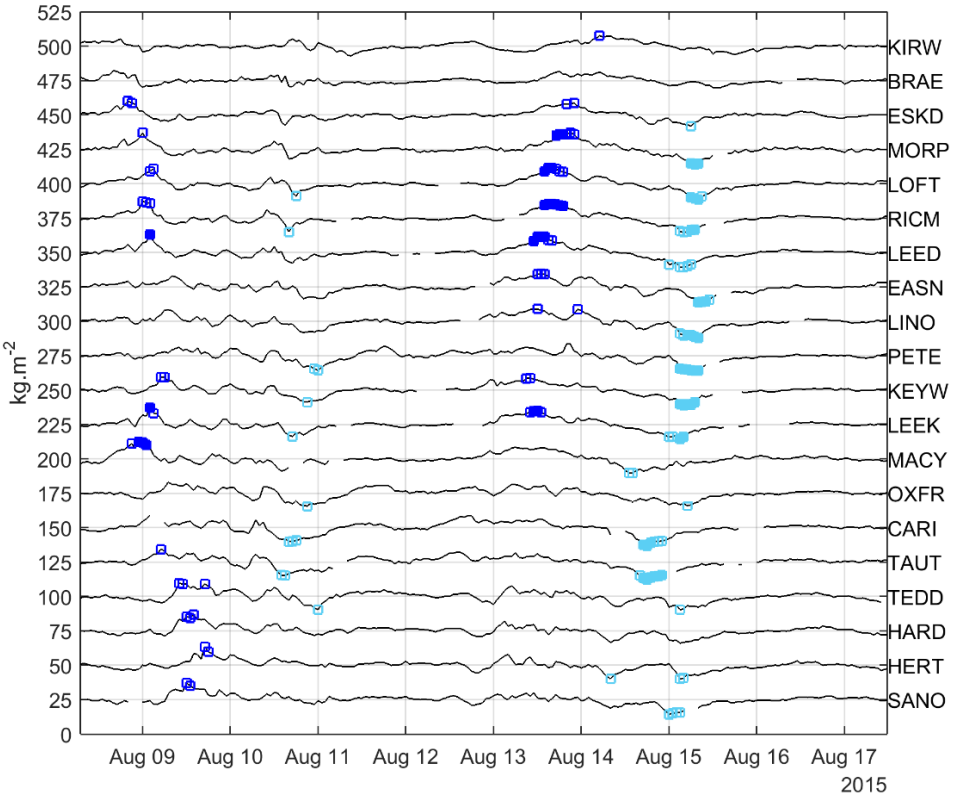


Figure 8-7 Same as Figure 8-6 but showing the temporal analysis residuals only.

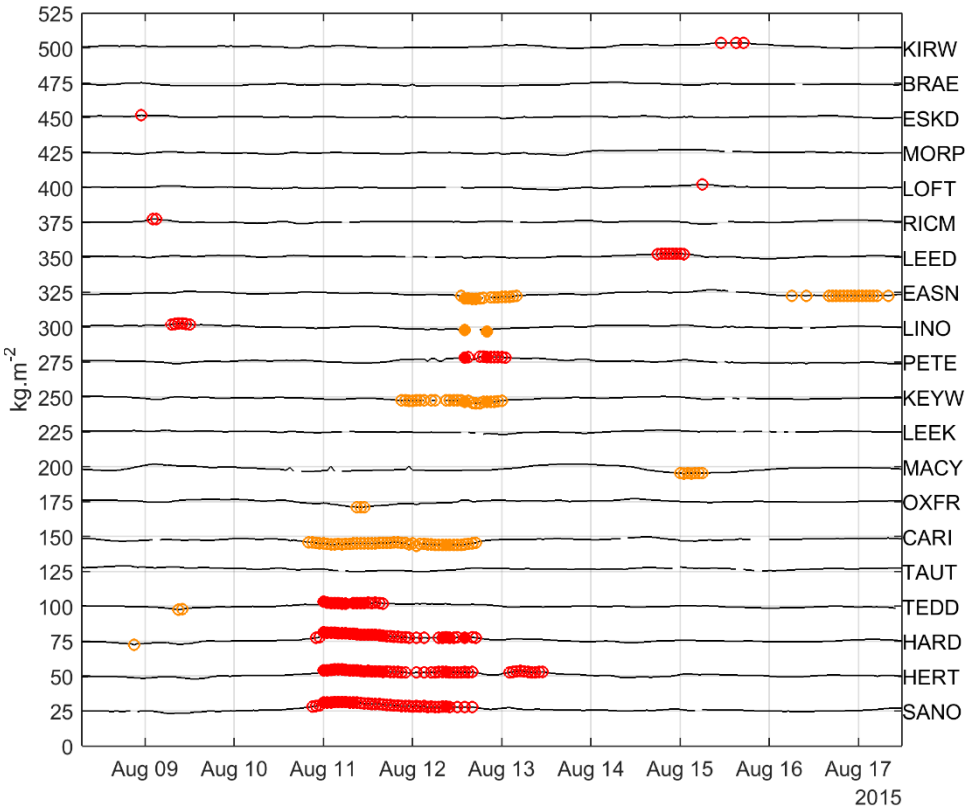


Figure 8-8 Same as Figure 8-6 but showing the spatial analysis residuals only.

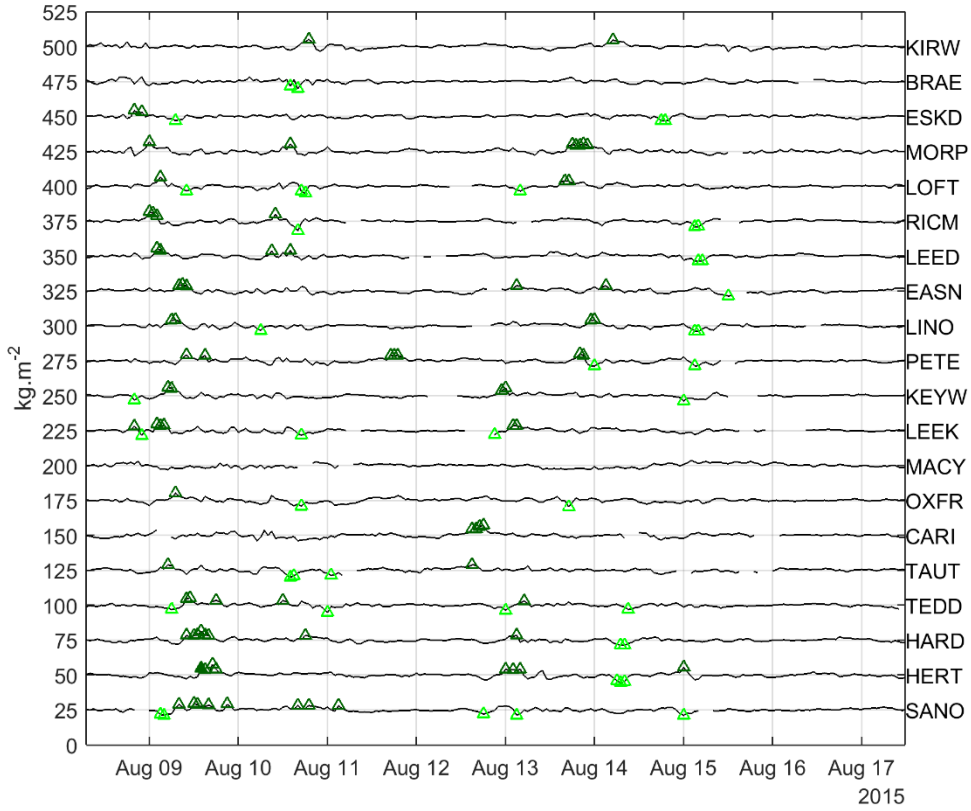


Figure 8-9 Same as Figure 8-6 but showing the combined algorithm residuals only.

To check the spatial correlation of a meteorological event, the stations and the rain gauges are illustrated in Figure 8-10, as a summary figure, which shows the rain gauges as coloured dots according to their readings, and stations with potential events as well as stations considered to have a meteorological event. Figure 8-10 also indicates whether the residuals exceed the upper boundary of the threshold or the lower boundary of the threshold. To reduce the complexity of the figures, only flagged stations and rain gauges will be shown. A 1-hour temporal resolution version of this figure is shown in the appendix (Figure D-1) where the figures present each day on a separate page.

As a general overview, Figure 8-10 shows that the spatial algorithm detects a relatively high amount of water vapour accumulated slowly in a period of 18-hours, which is then followed by a local rainfall event. On the contrary, the temporal analysis algorithm flags the locations of a high amount of water vapour, which is moving dynamically and crossing significant part of the network in a few-hour period and then followed by rainfall, as this is indicated by the rain-gauge data.

In details, Figure D-1 shows that in the early hours of 9th August 2015, even though the meteorological event detected by the temporal analysis algorithm (blue squares) did not coincide with a large amount of rain, it bounded the areas of rain and followed the same direction as the rain for 3 hours. Then, the rain dissipated even though the IWV maintained their values till the end of 10th August 2015 (as discussed earlier in relation to Figure 8-6). This explains why this algorithm did not detect the rain that started on 10th August 2015 moving from southwest to northeast. The dissipation of this event was then followed by scattered potential events indicating low IWV detected by all three analysis algorithms.

On 11th August 2015, relatively higher IWV values were detected by the spatial analysis algorithm (red circles) in southern England and lasted for nearly 2 days. During this relatively long period, rain occurred in that area at 04:00 till 07:00 then started again from 18:00 and continued till 05:00 on the next day, which in turn, reduced the IWV at some of the stations such that the meteorological events became considered as potential events. Since the spatial analysis algorithm compares the values at each epoch, it is

possibly better to look at this when the IWV is relatively high in relation to the surrounding stations rather than in relation to a station history, in addition to the fact that the thresholds are fairly small.

The relatively high values of IWV in southern England were also detected by the temporal analysis algorithm and were followed by severe thunderstorms that led to flooding on 13th, 14th and 15th August 2015. The beginning of this was detected by the temporal analysis algorithm as potential events (see 13th August 2015 at 9:00) and then as meteorological events after 2 hours (see 13th August 2015 at 11:00) and lasted for 10 hours going in the same direction as the rain. Similarly, Figure 8-10 shows that a meteorological event was detected related to low IWV values after the rain (see 14th August 2015 at 15:00) and following the rain from southwest to northeast.

This example shows how the temporal analysis algorithm can detect fast-paced meteorological events which spread across the network, in contrast to the spatial analysis algorithm which detects more local, slower paced events. This variation between the two algorithms is due to the nature of each algorithm's residuals; the temporal analysis residuals are dominated by what is considered to be high-frequency (> cut-off frequency), while the spatial analysis residuals show the uncorrelated values of surrounding stations that are considered to be low-frequency (< cut-off frequency).

Therefore, when higher cut-off frequencies are used, as illustrated in Figure 8-13 and Figure 8-14 for 0.5 cycle/day day (the complete figures are from Figure D-2 to Figure D-6 in the appendix), and in Figure 8-15 and Figure 8-16 for 1 cycle/day (the complete figures are from in Figure D-7 to Figure D-11 in the appendix), all frequencies less than these cut-off frequencies are considered as a part of the low-frequency component which leads to less noise included in the high-frequency component.

This is reflected in the temporal analysis residuals shown in Figure D-3 and Figure D-7 as comparing these with the ones shown in Figure 8-7 (i.e. using 0.25 cycle/day) it can be seen that the meteorological events appear more dominant in the residuals shown in Figure 8-7 (i.e. using 0.25 cycle/day) while they appear less dominant in the residuals shown in Figure D-3 (i.e. using 1 cycle/day), due to the slow nature of the events that lasted for a relatively long period (nearly 2 days), and as a result, part of the signal was considered in the low-frequency component when 1 cycle/day was used. Therefore, the meteorological event was detected by more stations when using 0.25 cycle/day than when using 1 cycle/day as a cut-off frequency. These variations are also clearly reflected in relation to the rain. For instance, Figure 8-10 (i.e. with 0.25 cycle/day) shows that the temporal analysis algorithm detects the meteorological event related to (i) the high IWV on 13th August from 11:00-20:00 and (ii) the low IWV on 14th August 2015 from 15:00-22:00 and 15th August 2015 from 3:00-10:00. On the other hand, Figure 8-12 (i.e. with 1 cycle/day) shows that the temporal analysis algorithm detects the meteorological event related to (i) the high IWV on 13th August 2015 only from 12:00-14:00 and (ii) the low IWV on 15th August 2015 from 05:00-08:00, as part of this event is considered in the low-frequency component.

Similarly, in the spatial analysis algorithm, fewer epochs are considered as anomalies in Figure D-4 and Figure D-8 than in Figure 8-8, as with lower cut-off frequencies the corresponding thresholds are smaller. This is illustrated by comparing the detected meteorological events using 0.25 cycle/day at 15:00 and 16:00 on 11th August 2015, and 9:00 and 10:00 on 12th August 2015 (Figure D-1) while it did not detect those when using 1 cycle/day (Figure D-11).



*Figure 8-10 Rain gauge readings (coloured dots) and stations considered as having either potential events (hollow symbols)or meteorological events (filled symbols), with **0.25 cycle/day** as a cut-off frequency.*

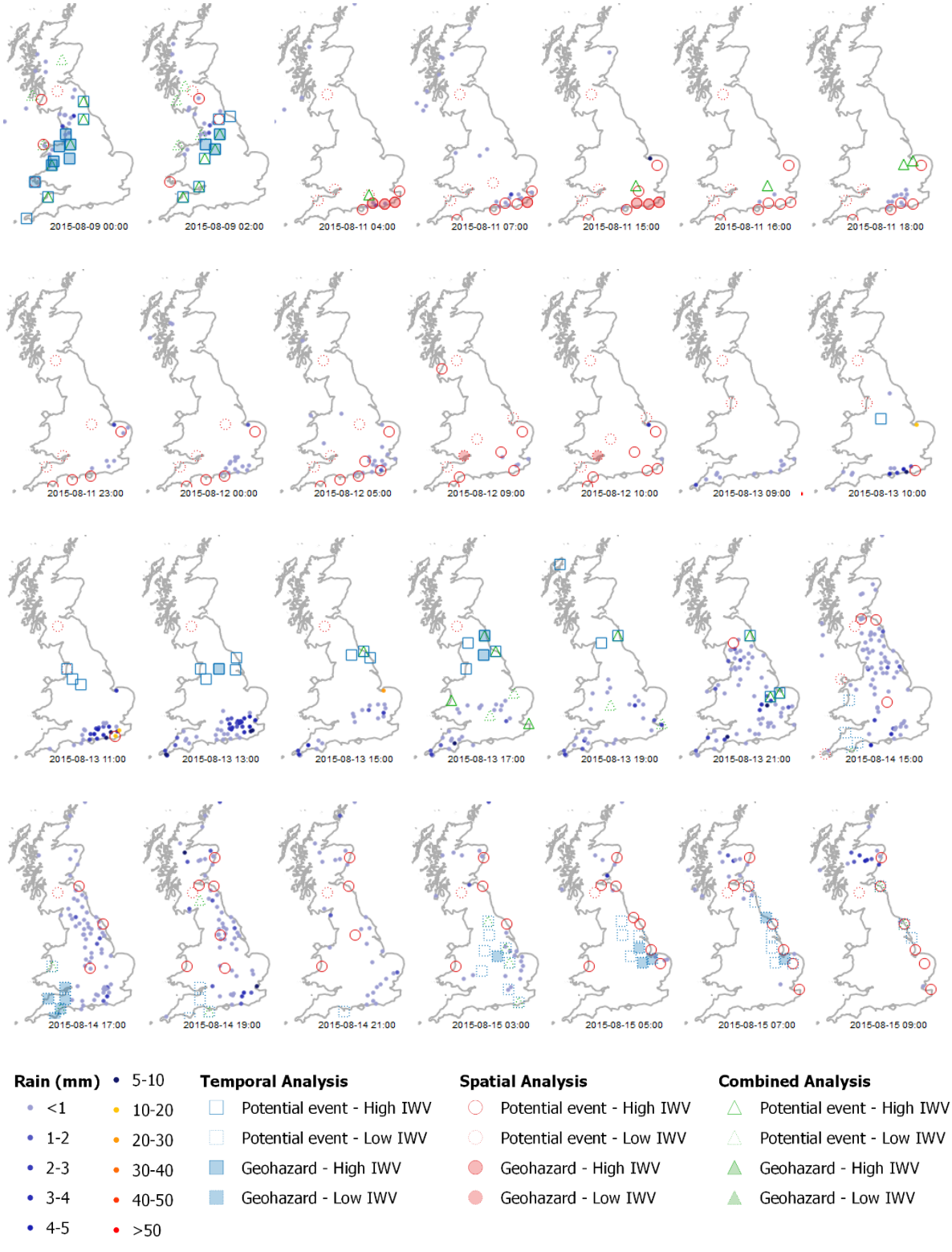


*Figure 8-11 Rain gauge readings (coloured dots) and stations considered as having either potential events (hollow symbols) or meteorological events (filled symbols), with **0.5 cycle/day** as a cut-off frequency.*

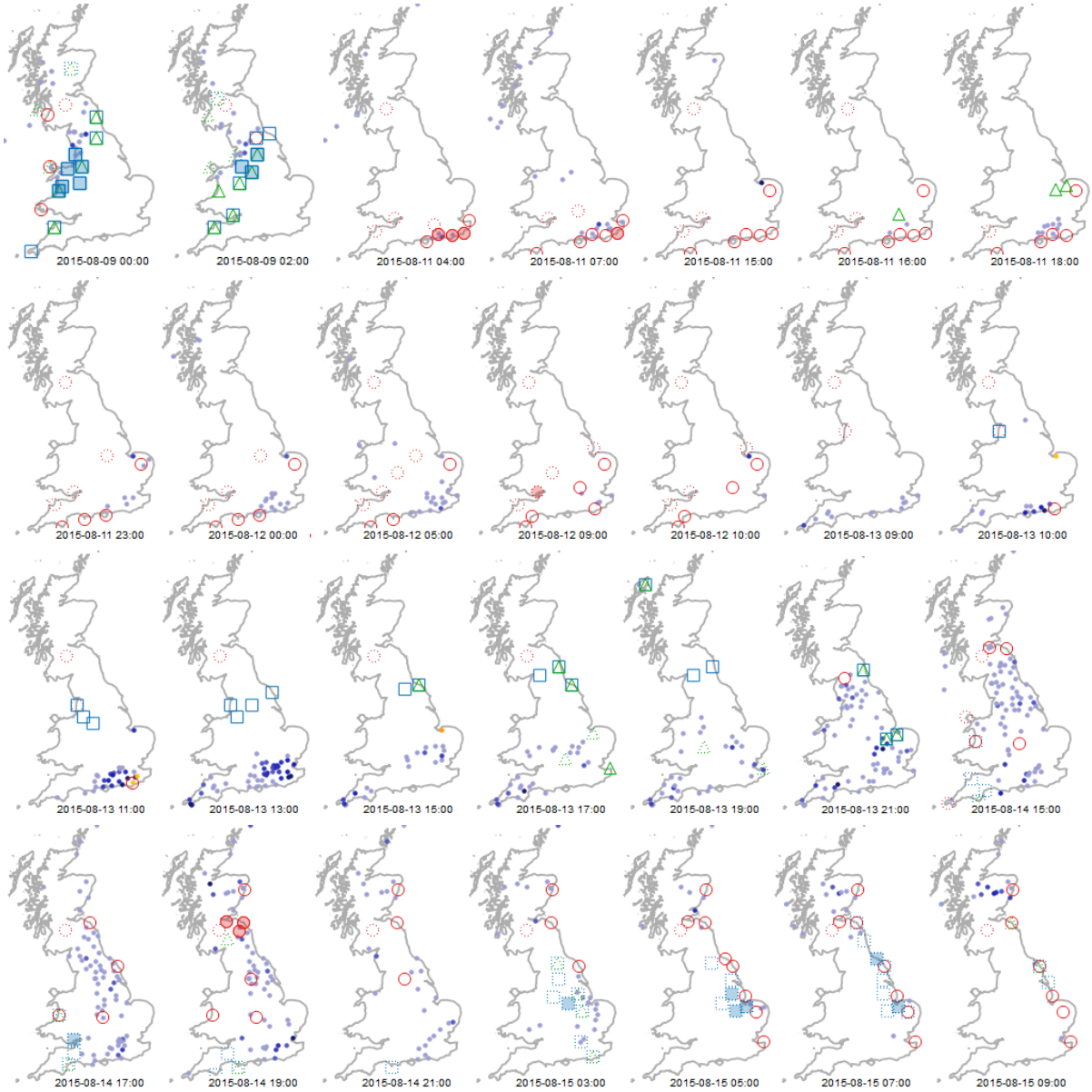


*Figure 8-12 Rain gauge readings (coloured dots) and stations considered as having either potential events (hollow symbols) or meteorological events (filled symbols), with **1 cycle/day** as a cut-off frequency.*

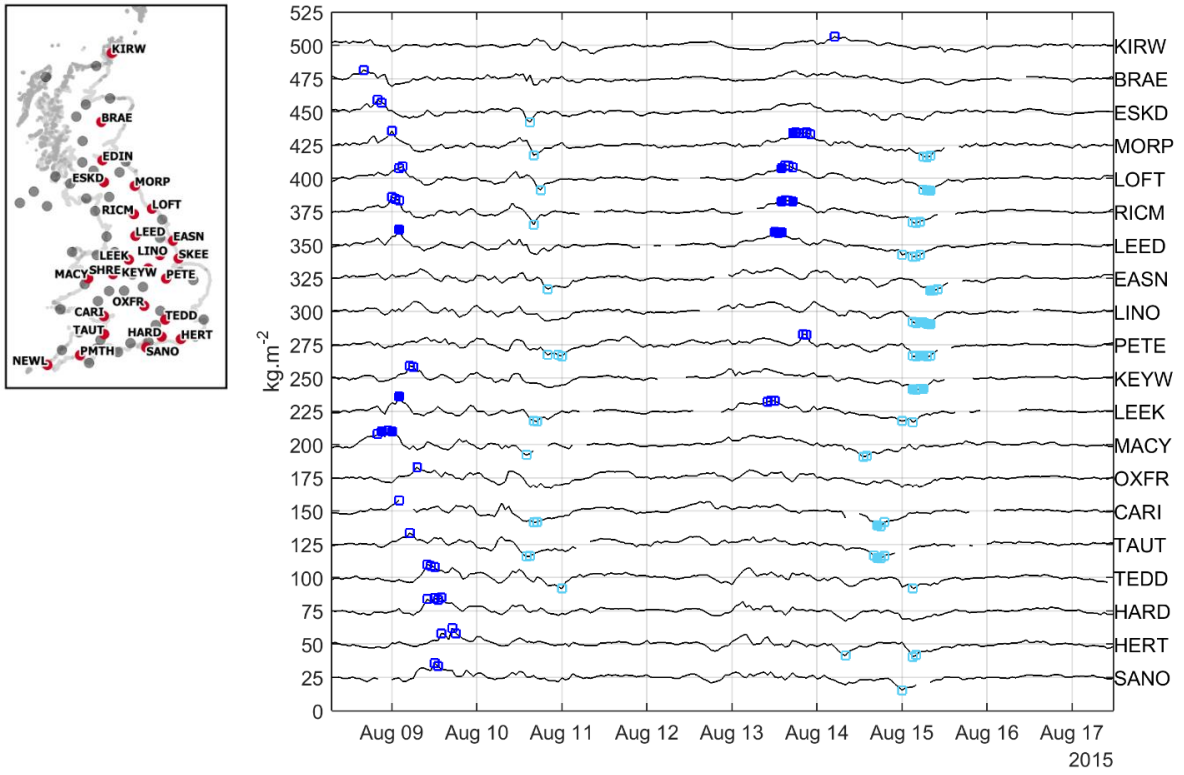


*Figure 8-13 Same as Figure 8-7 but showing the temporal analysis residuals with **0.5 cycle/day** as a cut-off frequency.*

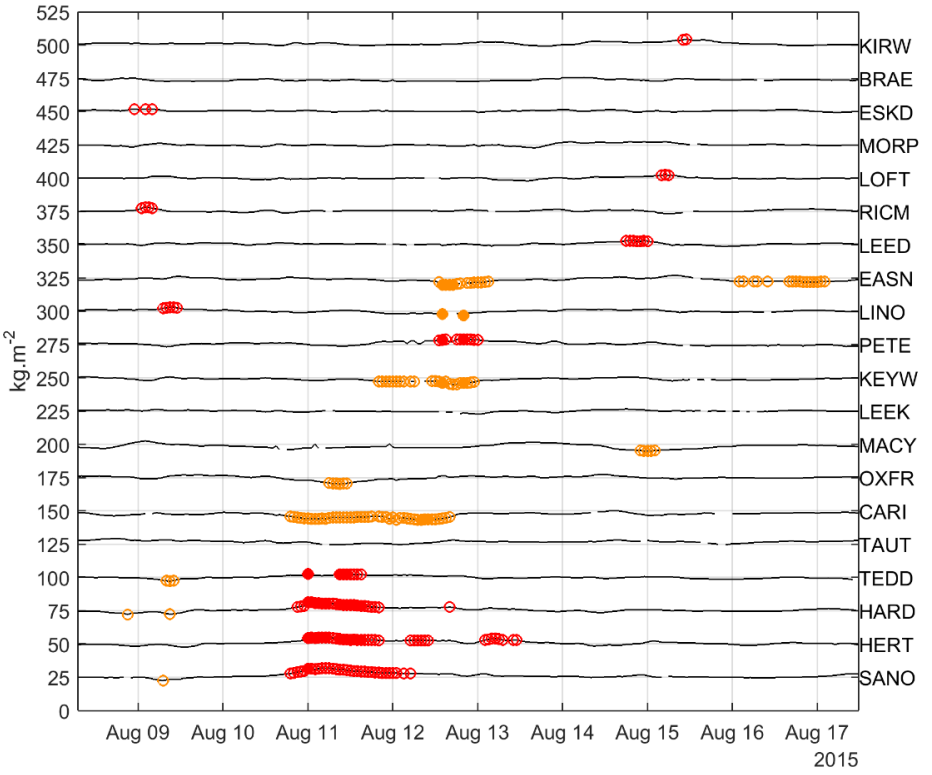


*Figure 8-14 Same as Figure 8-8 but showing the spatial analysis residuals with **0.5 cycle/day** as a cut-off frequency.*

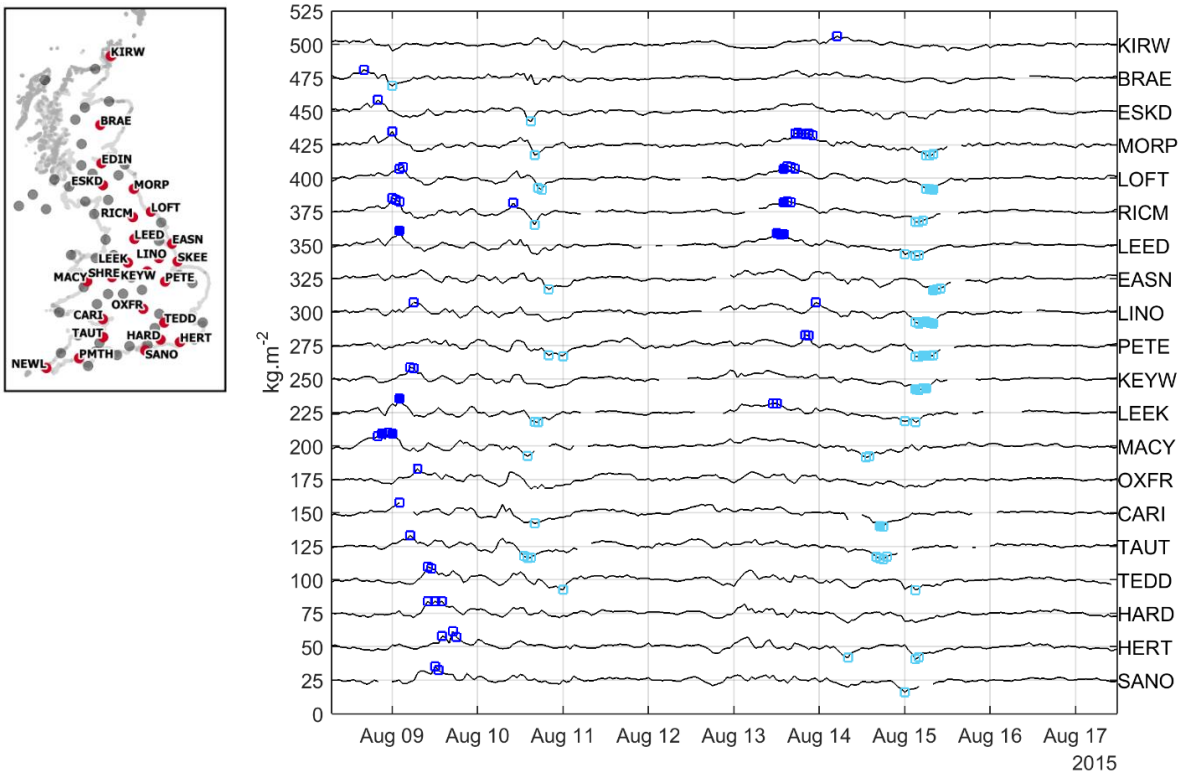


*Figure 8-15 Same as Figure 8-7 but showing the temporal analysis residuals with **0.5 cycle/day** as a cut-off frequency.*

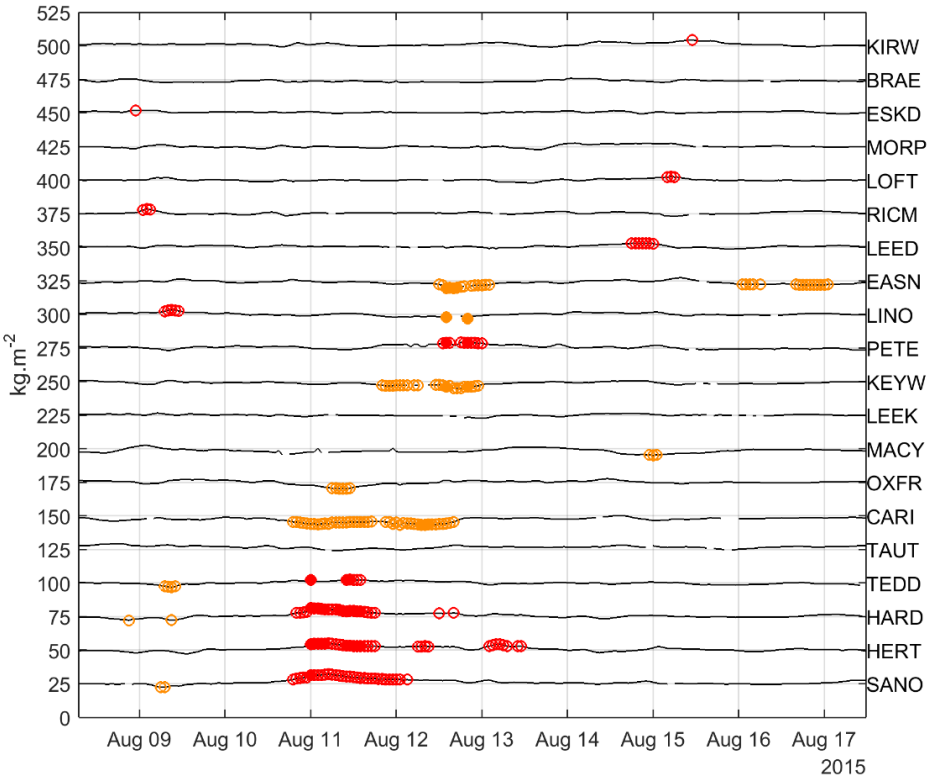


*Figure 8-16 Same as Figure 8-8 but showing the spatial analysis residuals with **1 cycle/day** as a cut-off frequency.*

8.4.2 Example#2

The second example is illustrated in Figure 8-17 to Figure 8-26 (see also Figure D-12 to Figure D-22 in the appendix). This example is different from the previous example as in this case the number of detected meteorological events increases with an increase in the cut off frequency rather than decreasing.

This example is related to rain that occurred from 25th January until 4th February 2013, when the multiple algorithm approach detected meteorological events as shown in Figure 8-17 to Figure 8-19. Despite the fact that some of these events are only detected by the temporal analysis algorithm, figures related to the spatial and the combined analysis algorithms will also be illustrated for the sake of completeness. These figures show that by choosing a higher cut-off frequency, more stations were considered as having meteorological events especially on 26th, 28th, 31st January 2013, and 3rd February 2013.

Figure 8-20, Figure D-13 and Figure D-18 show the time series of IWV for this event using 0.25, 0.5 and 1 cycle/day cut-off frequencies, respectively. These figures show how rapidly the IWV values change in this example compared to the previous example, as reflected by their time series values. Furthermore, the relatively high frequencies of IWV values are more dominant in this example, which also explains why the spatial analysis algorithm could not detect any meteorological events as most of these changes will not be part of the low-frequency component which is used as the input of the spatial analysis.

Since these rapid changes are in the frequency-range higher than the cut-off frequencies, they appear in the temporal analysis residuals (Figure 8-21, D-14 and D-19). Hence, they are detected in different intensities because of the variations in corresponding temporal analysis residuals thresholds. In other words, the temporal analysis residuals thresholds are narrower when higher cut-off frequencies are used, as shown in Table 8-1, and this leads to the fact that these changes are flagged more frequently when higher cut-off frequencies are used.

The spatial correlation between the rain and the meteorological event detection can also be seen in Figure 8-20, 8-21 and 8-22 (see Figures D-11, D-12 and D-22 for higher temporal resolution (i.e. 1-hour)) as they show that on 26th January 2013 a meteorological event related to low IWV was detected (04:00, 2:00, 2:00 respectively) following rain and going from west to east, and this was detected with different intensities according to the cut-off frequency as more stations were flagged with higher cut-off frequency which shows a more detailed description of the IWV dynamics. For example, when 0.25 cycle/day was used, meteorological events were detected at 04:00 in one station in the south-east, and at 07:00 in four stations at the south. However, when 0.5 cycle/day was used, meteorological events were detected at 02:00 in four stations in the south-west, at 03:00 in one station, at 05:00 in two stations, and at 06:00 in seven stations at the south. Similarly, when 1 cycle/day was used, meteorological events were detected at 02:00 in six stations in the south-west, at 05:00 in 10 stations, and at 06:00 in seven stations at the south.

Then, a slight and gradual increase in IWV, which coincides with an increase in the amount of rain recorded by the rain gauges as reflected by darker dots in the figures, is shown on that day from 11:00 – 16:00, but which was detected only when 0.5 and 1 cycle/day were used as cut-off frequencies from 15:00 - 17:00. The rain then started to dissipate on 27th January 2013 where a meteorological event related to the low IWV was detected from 07:00-11:00 when 0.25 cycle/day was used; from 03:00-10:00 when 0.5 cycle/day was used, and from 01:00-10:00 when 1 cycle/day was used.

On 28th January 2013, an increase in IWV for a small period of time was detected by the temporal analysis algorithm with different intensities. For a 0.25 cycle/day cut-off frequency, it was detected for one hour (Figure 8-24 at 13:00), whereas for 0.5 cycle/day it also was detected for one hour but at 12:00 instead of at 13:00 (Figure 8-25 at 12:00). Whilst when 1 cycle/day was used it was detected for 2 hours (Figure 8-26 at 12:00 and 13:00). This meteorological event was associated with rain that started around 09:00 and continued for about 12 hours.

Following that, there were several other detections of meteorological events associated with rain followed by a detection of low IWV when the rain dissipated. For example, on 29th January 2013 when 0.25 cycle/day was used, an event was detected for 4 hours (Figure 8-24 at 12:00-15:00) moving from west to east, and then low IWV was detected from 18:00-21:00 moving from north-west to south. When 0.5 and 1 cycle/day were used, the event also was detected for 3 hours from 10:00-12:00, and then at 14:00 (Figure 8-25 and Figure 8-26), and then low IWV was detected for 4 hours, from 17:00-20:00, when 0.5 cycle/day was used (Figure 8-25) and for 5 hours, from 16:00-20:00, when 1 cycle/day was used (Figure 8-26). This pattern of high IWV and low IWV associated with the start and the end of the rain then appeared in the last two days.

The figures also show that on the 1st February 2013, even though there was rain recorded by the rain gauges in the southern parts of England, it was not associated with any detections of meteorological events as the changes in the IWV time series were smoother than on the other days (Figure 8-20, Figure D-13 and Figure D-18).

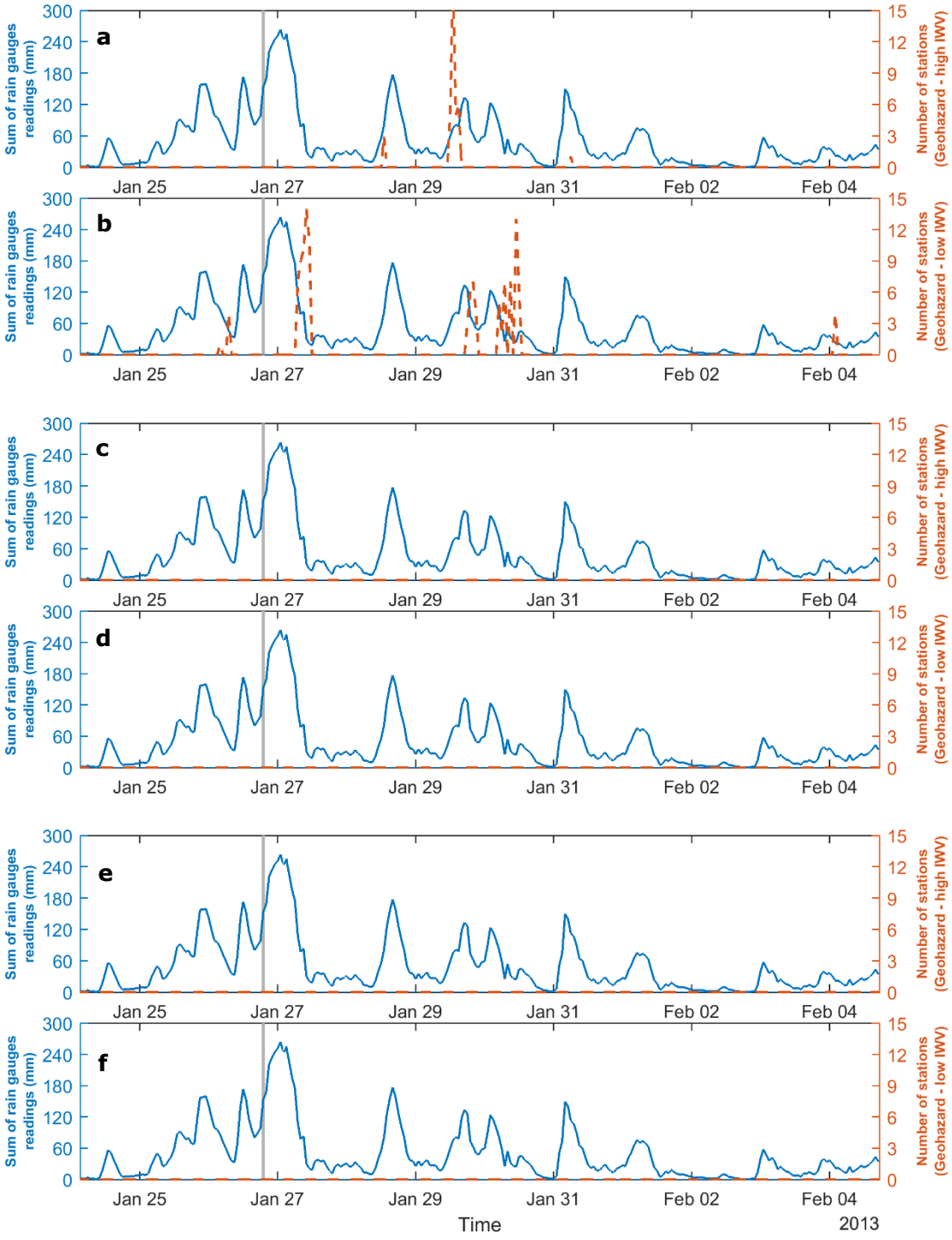


*Figure 8-17 The summation of the rain gauge readings (blue) and the number of stations (orange) considered as having meteorological events detected by the temporal (a,b), spatial (c,d), and combined (e,f) analysis algorithms, with a cut-off frequency of **0.25 cycle/day**. Grey strips indicate where the hourly rain gauge reading exceeds 10mm at any of the rain gauges.*

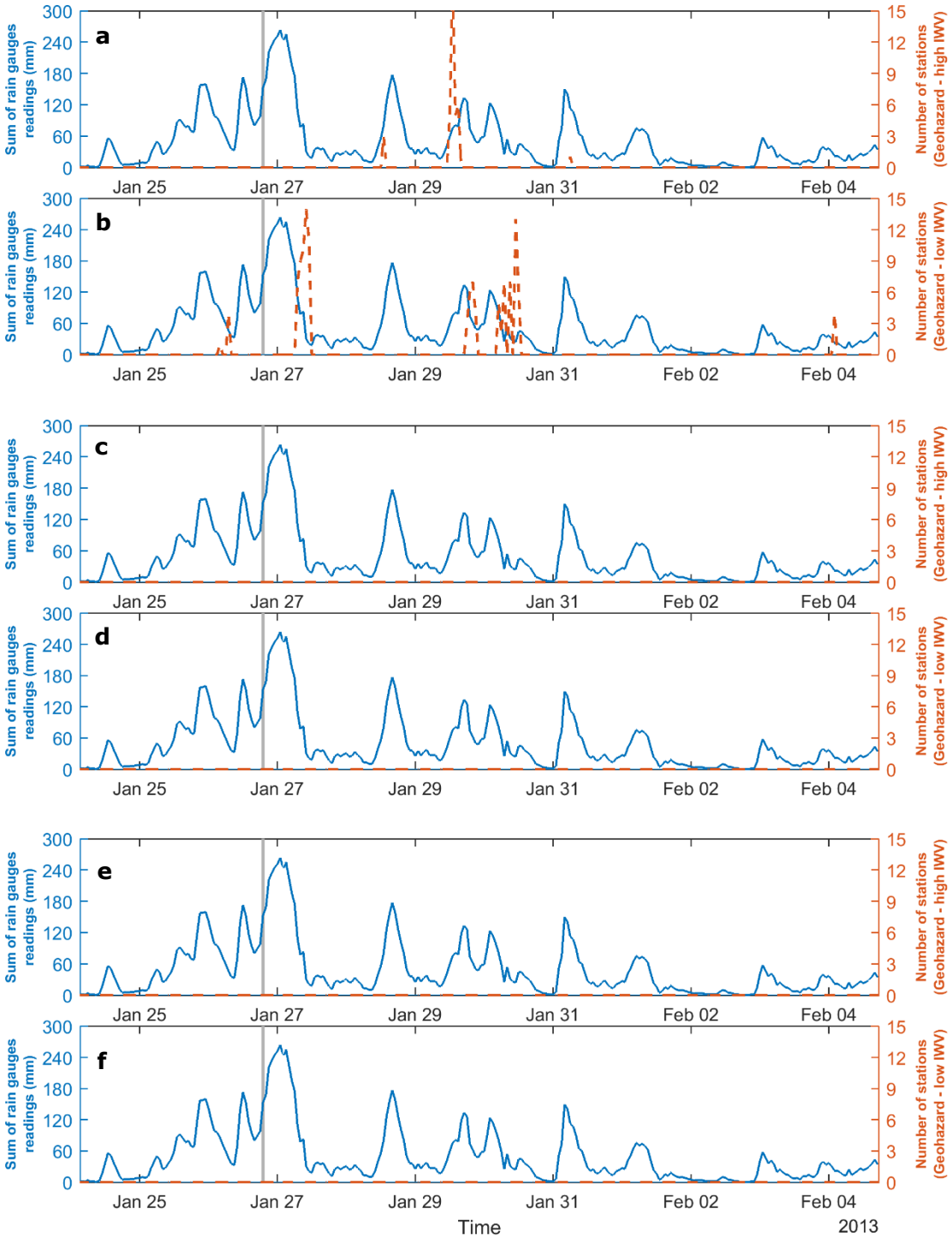


*Figure 8-18 The summation of the rain gauge readings (blue) and the number of stations (orange) considered as having meteorological events detected by the temporal (a,b), spatial (c,d), and combined (e,f) analysis algorithms, with a cut-off frequency of **0.5 cycle/day**. Grey strips indicate where the hourly rain gauge reading exceeds 10mm at any of the rain gauges.*

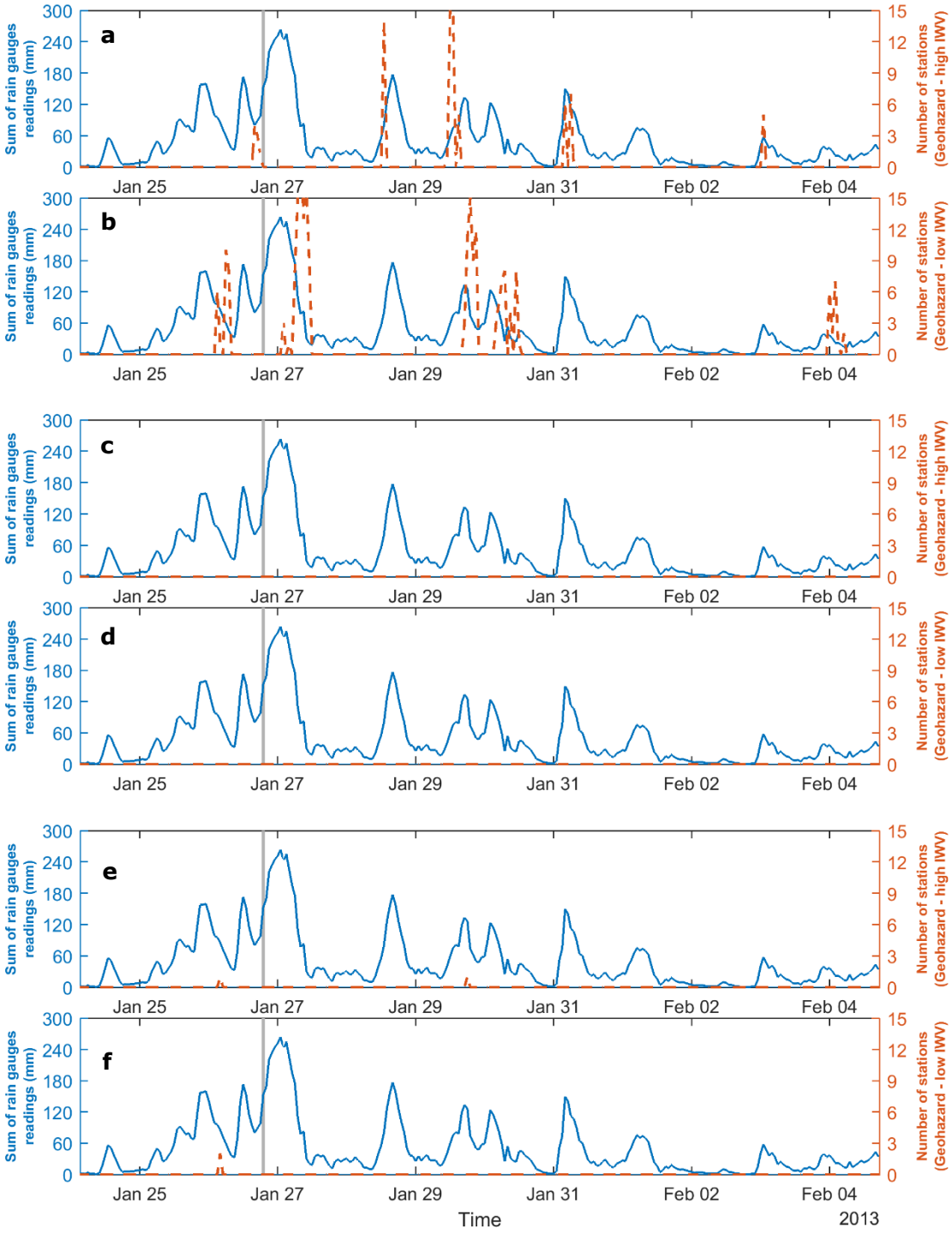


*Figure 8-19 The summation of the rain gauge readings (blue) and the number of stations (orange) considered as having meteorological events detected by the temporal (a,b), spatial (c,d), and combined (e,f) analysis algorithms, with a cut-off frequency of **1 cycle/day**. Grey strips indicate where the hourly rain gauge reading exceeds 10mm at any of the rain gauges.*

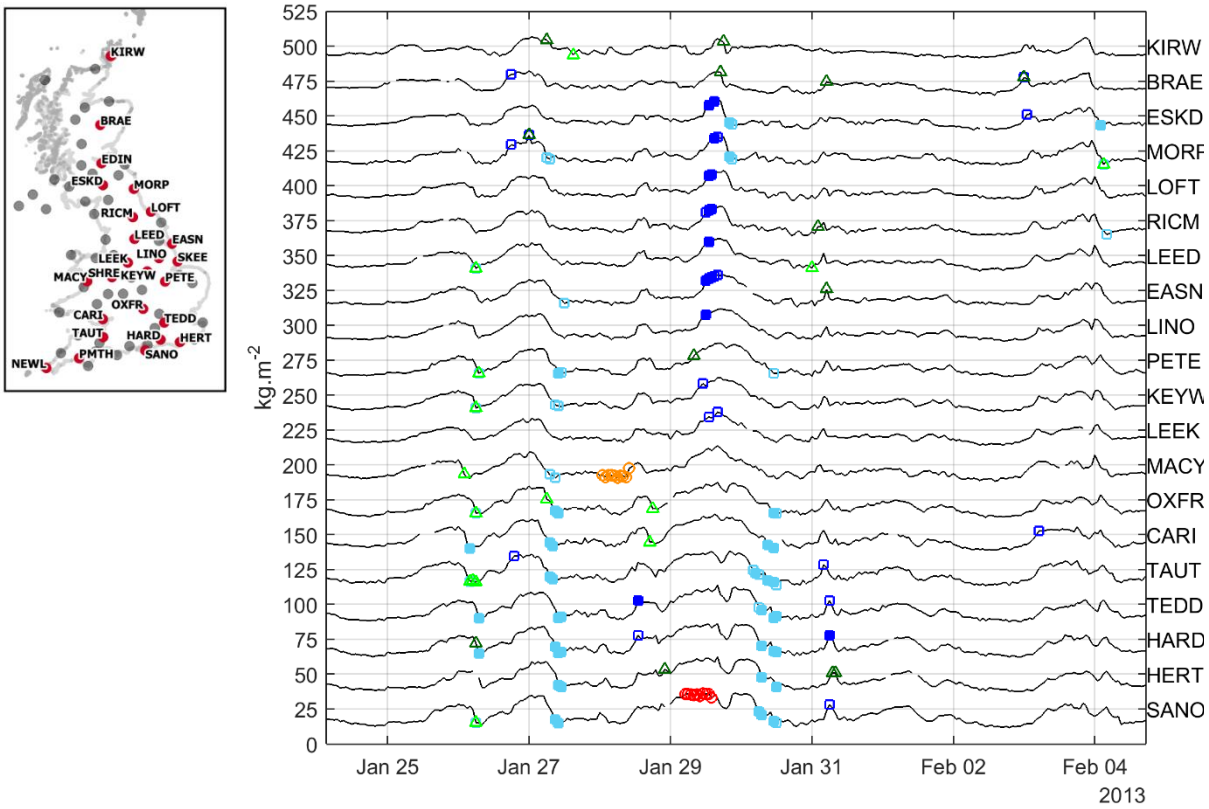


*Figure 8-20 The IWV time series of 20 stations along with epochs considered as either potential events(hollow) or meteorological events (filled) using the temporal (high IWV: dark blue, and low IWV: light blue), the spatial (high IWV: red, and low IWV: orange), and the combined (high IWV: dark green, and low IWV: light green) analysis algorithms, with **0.25 cycle/day** as a cut off frequency (y-axis grid:25 kg.m^{-2}).*

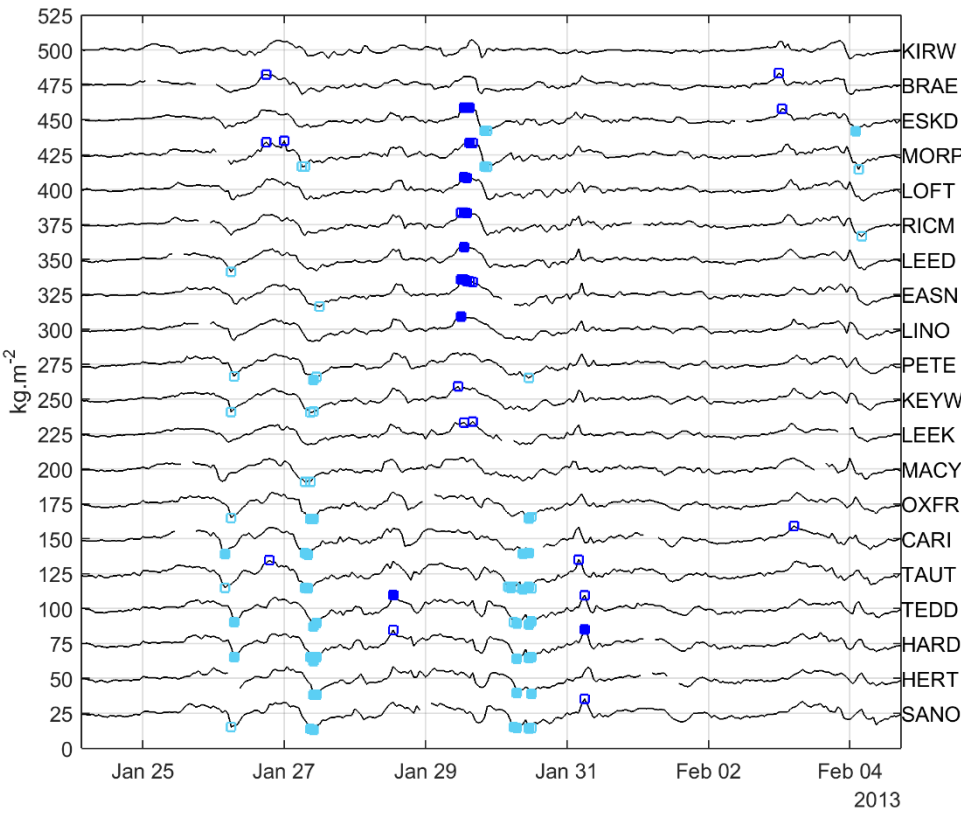


Figure 8-21 Same as Figure 8-20 but showing the temporal residuals

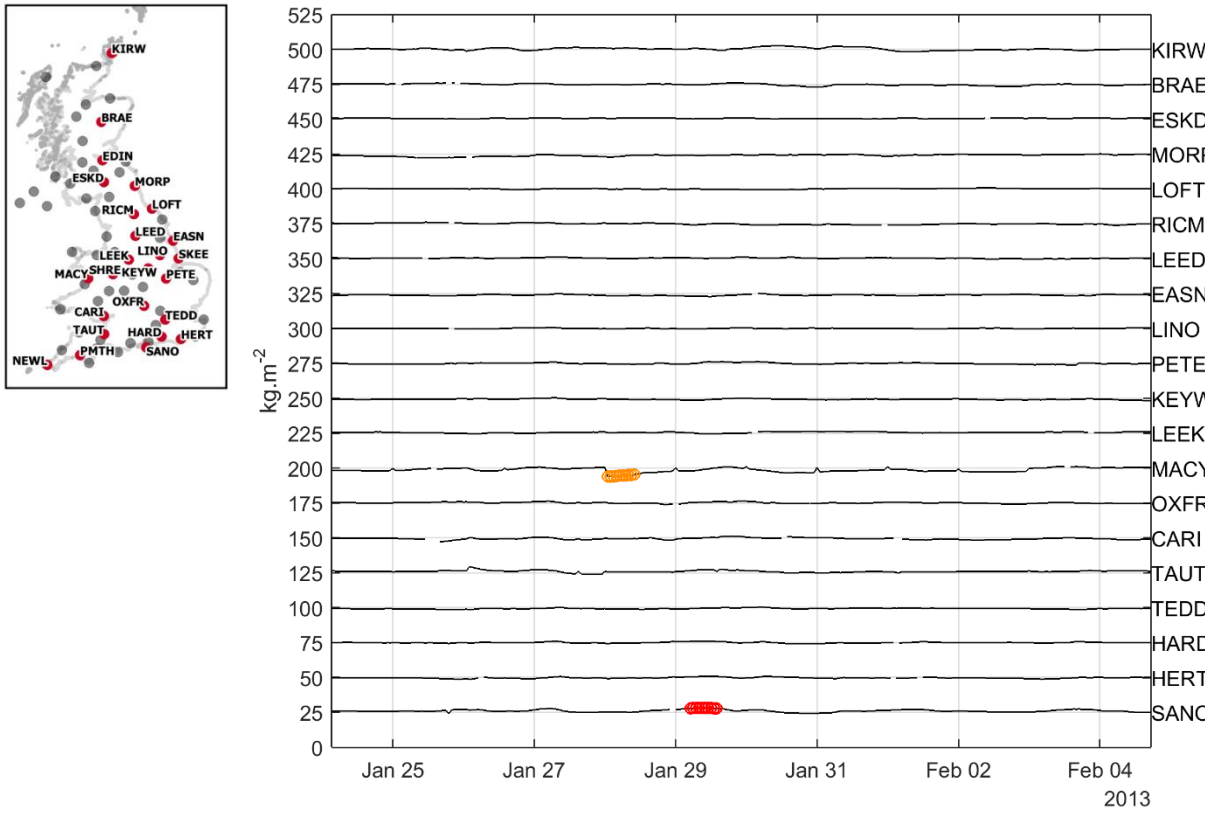


Figure 8-22 Same as Figure 8-20 but showing the temporal residuals

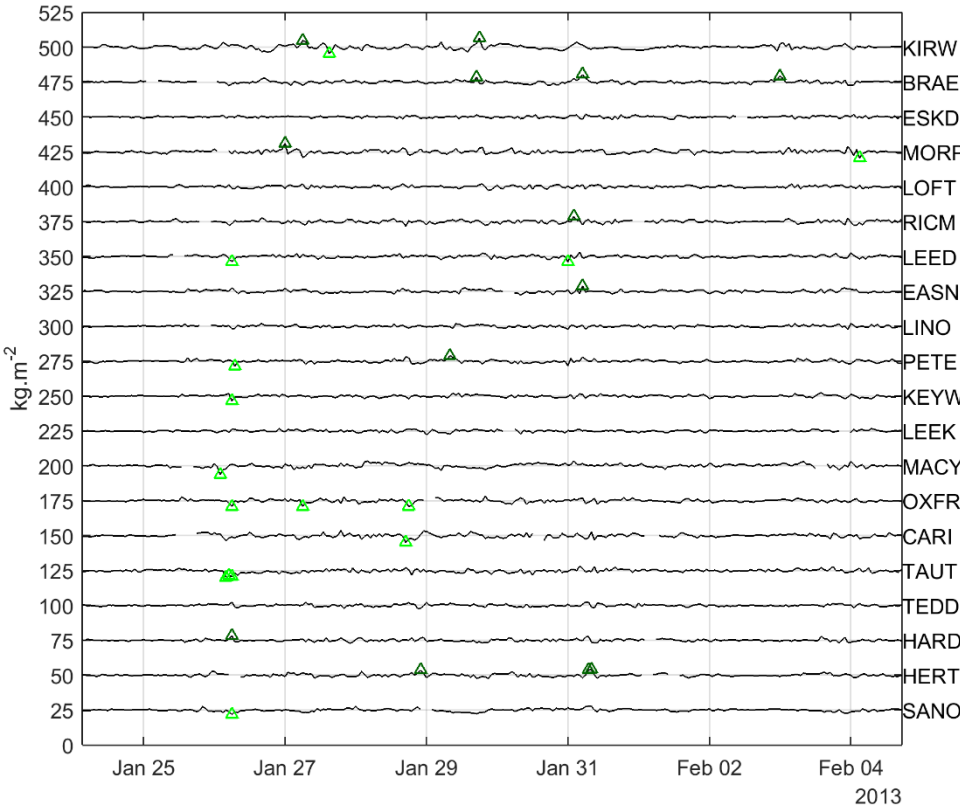


Figure 8-23 Same as Figure 8-20 but showing the temporal residuals

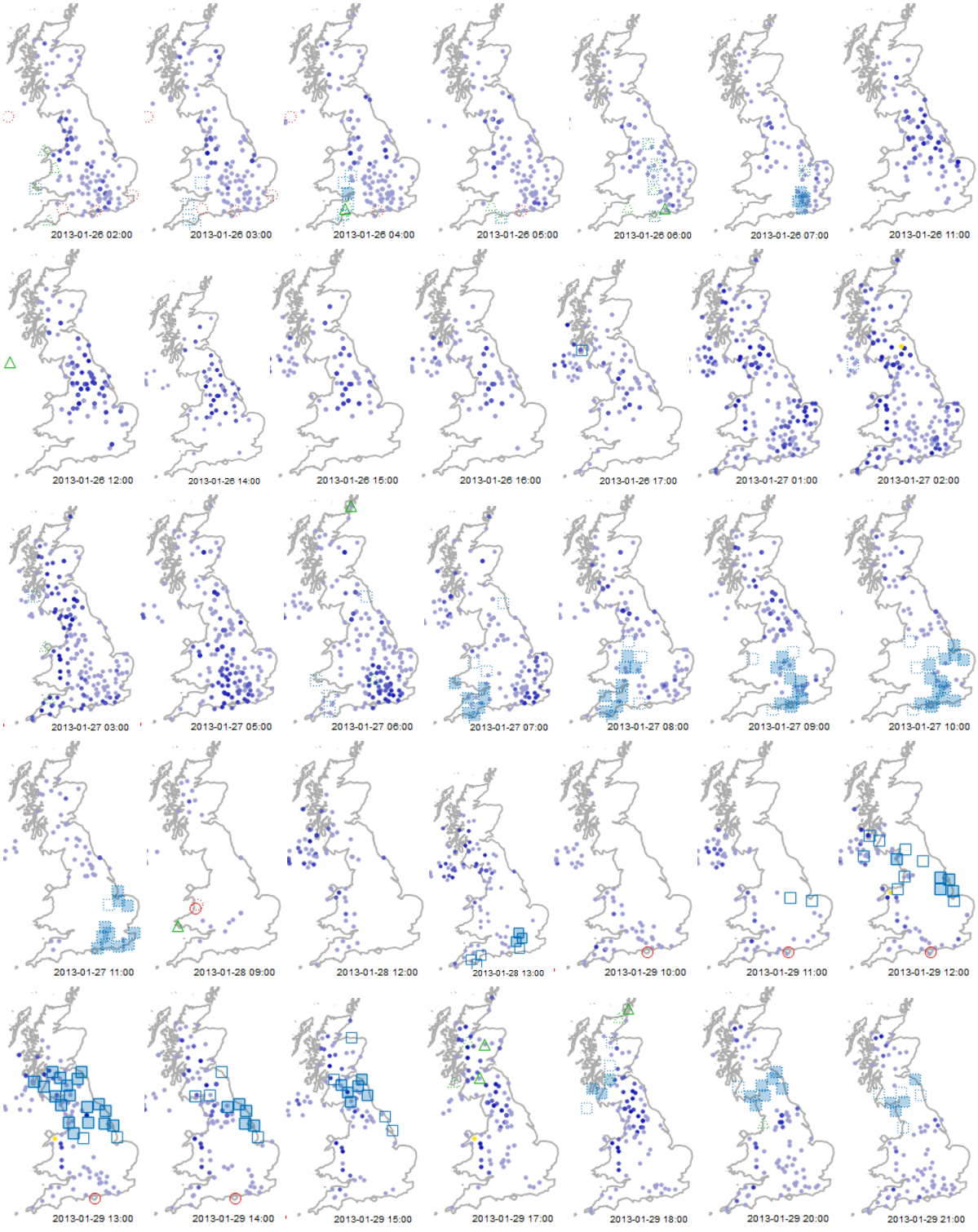


*Figure 8-24 Rain gauge readings (coloured dots) and stations considered as having either potential events (hollow symbols) or meteorological events (filled symbols), with **0.25 cycle/day** as a cut-off frequency.*

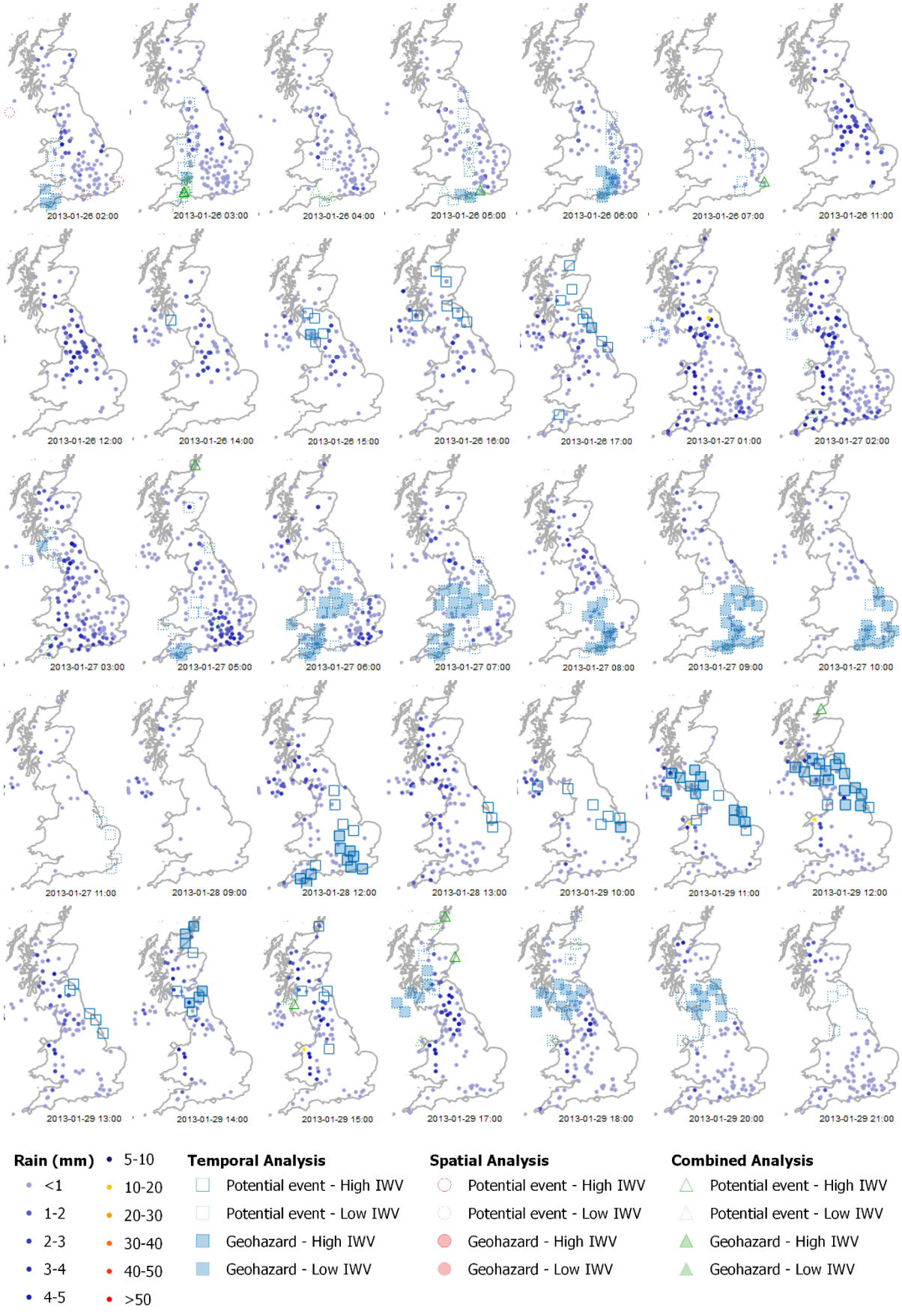


*Figure 8-25 Rain gauge readings (coloured dots) and stations considered as having either potential events (hollow symbols) or meteorological events (filled symbols), with **0.5 cycle/day** as a cut-off frequency.*

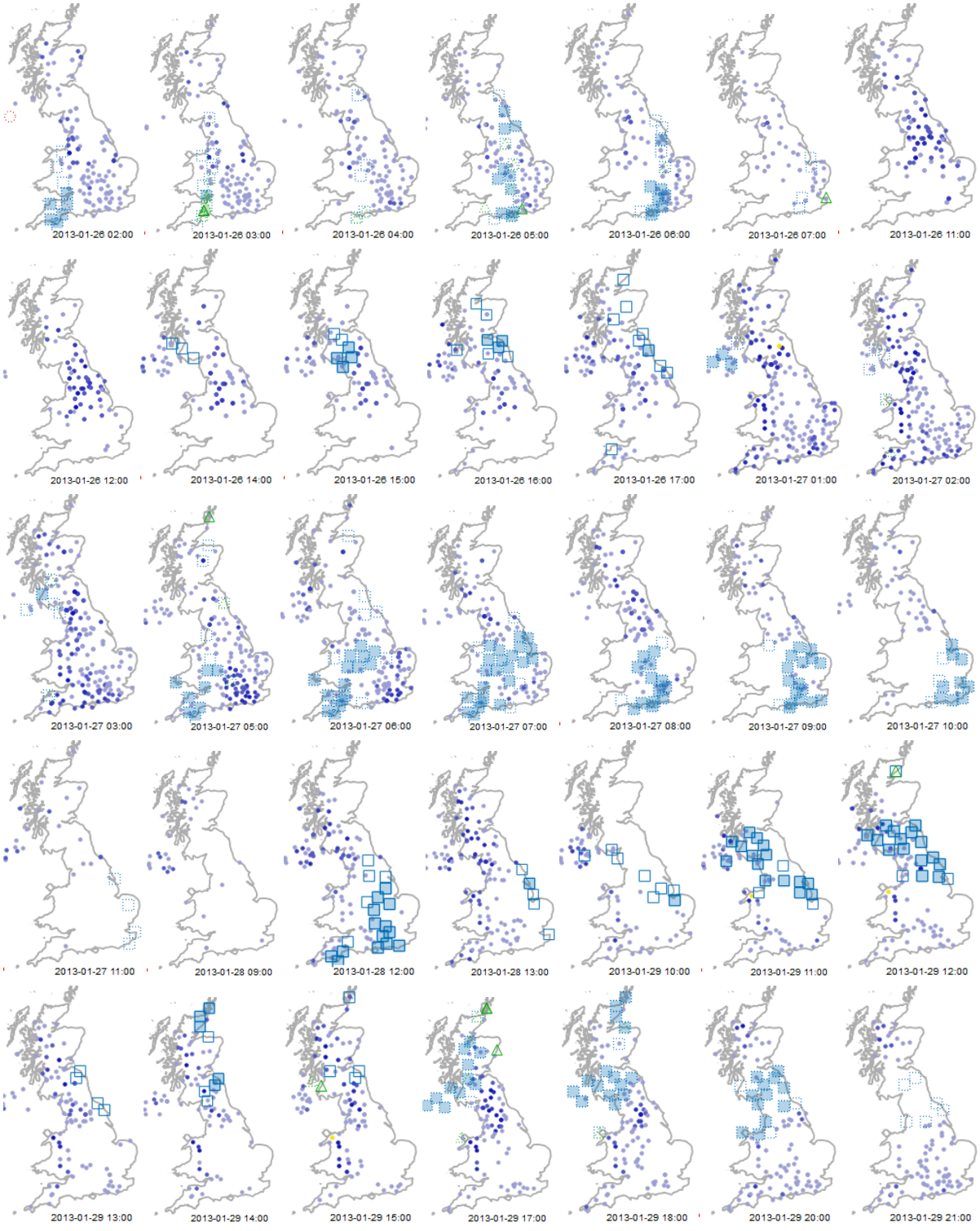


*Figure 8-26 Rain gauge readings (coloured dots) and stations considered as having either potential events (hollow symbols) or meteorological events (filled symbols), with **1 cycle/day** as a cut-off frequency.*

From the previous examples, it can be concluded that the performance of the multiple algorithm approach varies depending on the nature of the meteorological events and what is expected to be detected. The examples showed that variations in IWV time series can be more complicated than those in GPS coordinate time series, although these variations are usually more spatially correlated.

The two examples given also showed that the temporal analysis algorithm detected rapid changes in IWV better when higher cut-off frequencies are used, while it detected the beginning of slower changes in IWV better when lower cut-off frequencies are used. Such changes usually travel across the network and are related to either an increase or decrease in the IWV values which are, sometimes, associated with rain or thunderstorms. Nevertheless, the examples also showed some cases where rain occurred, but the multiple algorithm approach could not detect anything, as this rain was not associated with sudden changes in the IWV time series.

The examples also showed that the spatial analysis algorithm can be used to detect the spatial variations of the low-frequency components, which depend on the used cut-off frequencies and the meteorological events to be detected. These variations do not travel across the network and appear to be present in local parts of the network for a relatively long period of time.

Therefore, it can be concluded that using the multiple algorithm approach could have the potential to be a useful complementary tool to weather nowcasting/forecasting, especially because of the fact that the IWV values are often estimated with a higher resolution, i.e. every 15 minutes, than how often the conventional numerical weather models are run, e.g. every 6 hours, every 3 hours or every hour (Baker et al. 2001).

8.5 Summary

In this chapter, the performance of the multiple algorithm approach was evaluated using long-term hourly GPS troposphere time series of the BIGF network in the British Isles, and detected meteorological events were compared with recorded rain. It was shown that

different meteorological events have different behaviours and that there is a need to carry out several runs of the multiple algorithm approach using different cut-off frequencies in order to detect these different behaviours. The results also showed that the temporal analysis algorithm is better at detecting fast-paced changes in IWV across the network, while the spatial analysis algorithm is better at detecting more local changes in IWV values.

CHAPTER 9: CONCLUSIONS AND RECOMMENDATIONS.

In this chapter, the main conclusions of this research will be summarised in section 9.1, in relation to the three case studies presented in this thesis. Then some recommendations for future research are suggested in section 9.2.

9.1 Conclusions

A new multiple algorithm approach to detect anomalies in GNSS time series has been proposed and demonstrated. The main benefit of this approach is that a part of the dataset is considered as a reference which is used for the stochastic modelling of the GNSS time series behaviour, the remaining time series is left unconstrained and can be analysed against the corresponding time-history of the current station or spatially-correlated with other stations in a GNSS network.

The multiple algorithm approach that has been developed was applied successfully to three different case studies, that were chosen to cover different aspects; the size of the network, the length and the temporal resolution of the time series, as well as the dynamics, the size and the type of the phenomena:

- **The first case study**, the analysis of the daily GNSS coordinate time series of the BIGF network of stations in the British Isles, was seen as a relatively small network with long-term, daily time series along with site-specific phenomena to be monitored. In this case study, it was concluded that the data segmentation stage (i.e. chronologically splitting the GPS coordinate time series into training and testing datasets) is highly beneficial in detecting potential anomalous behaviours, especially those related to variations from the linear trend. Moreover, it was concluded that the developed approach detected potential anomalous behaviours of various characteristics, i.e. temporary (low or high frequency-related), on-going (due to variations from the linear trend, or due to offsets), and periodic. This case

study showed that the spatial analysis algorithm surpasses the temporal analysis algorithm in, and is particularly suited to, detecting anomalies due to variations from the linear trend, or small offsets. While the temporal analysis algorithm surpasses the spatial analysis algorithm in, and is particularly suited to, detecting rapid changes in the high-frequency component (i.e. > cut-off frequency); while the combined analysis sits in between but closer to the temporal analysis algorithm.

- **The second case study**, the analysis of the 1Hz GPS coordinate time series of the GEONET stations in Japan for the Tohoku-Oki 2011 MW9.0 Earthquake, was seen as a relatively large network with short-term time series with a large and spatially correlated phenomenon to be monitored. In this case study, it was concluded that the temporal analysis algorithm proved to be more effective than the spatial analysis algorithm in detecting large magnitude changes in the GNSS coordinate time series. Furthermore, such large magnitude changes, which appear in one small part of the network, may bias the spatial estimation of the coordinate time series of the GNSS stations of the broader network, that do not have this anomaly at the corresponding epoch. The latter phenomenon is also known as "spatial spillovers" and may result in a false triggering of the detection of the spatial analysis algorithm at those stations. The adjustment of the parameters (cap distance, α) of the spatial analysis algorithm limits these biases but still, the spatial analysis algorithm proved less effective than the temporal or combined analysis algorithms.
- **The third case study**, the analysis of the long-term hourly GPS troposphere time series of the BIGF network of stations in the British Isles, was seen as a challenge to examine the performance of the developed approach on a totally different dataset that is not directly related to crustal/land movements and its ability to detect meteorological events (e.g. rain). In this case study, it was concluded that the performance of the developed multiple algorithm approach varies depending on the nature of the meteorological events as the variations in IWV time series are more complicated than those in GPS coordinate time series, and more spatially correlated. However, in general, the temporal analysis algorithm detects the

changes in IWV which travel across a network at a fast pace, while the spatial analysis algorithm detects changes that appear to be present in local parts of the network for a relatively long period of time, whereas the combined analysis algorithm did not seem to be useful in such applications.

Therefore, in general, it was shown that the temporal analysis algorithm proved to be effective in detecting rapid changes in GNSS time series of varying magnitudes. These changes can be site-specific (e.g. large sudden offsets) or of a large scale (e.g. an earthquake or a meteorological event). Even though the behaviour of the temporal analysis algorithm works by analysing each station separately, that does not mean that it is less effective in detecting large-scale events. This is due to the fact that if this large-scale event behaves at each station differently from its historical record, it will be detected by the temporal analysis algorithm at each station. However, to differentiate between site-specific anomalies and large-scale events detected, a spatial search (i.e. buffer) should be carried out searching for anomalous behaviours at the surrounding stations at that epoch (as shown in Chapters 7 and 8).

On the other hand, the spatial analysis algorithm is more suitable for site-specific, spatially uncorrelated, slow-paced and small magnitude changes in GNSS time series (e.g. monumentation issues or antenna corrosion issues) as discussed in Chapter 9. However, the spatial analysis may be useful to detect small regional events (i.e. if a small cluster of stations behaves differently from the entire network (as shown in chapter 8). On the other hand, it would be less effective if the large scale event affects the majority of the stations in the network (as demonstrated in chapter7).

The combined analysis algorithm seems to be less beneficial in the detection of anomalous behaviours, but may be useful to diagnose and clarify the reasons that lead to the detected anomalous behaviours using the temporal analysis algorithm since the input to the combined analysis algorithm is the temporal residuals. It is expected to detect stations where its temporal residuals exhibit a different behaviour from surrounding stations.

It is worthy to mention that the three algorithms are complementing each other rather than competing as each algorithm focuses on different parts of the signal. For example, the spatial analysis algorithm focuses on the low-frequency component in the signal which makes it more effective in detecting low-frequency changes like the deviation in the trend of the time series. On the other hand, the temporal and combined analysis algorithms focus on the high-frequency component in the signal which makes them more effective in detecting high-frequency changes (e.g. earthquakes) than the spatial analysis algorithm.

Moreover, at a station, the high-frequency component of the signal will be analysed and compared to its historical behaviour using the temporal analysis algorithm, while it will be compared to other surrounding stations using the combined analysis algorithm. Similarly, the low-frequency component will be analysed and compared to its historical behaviour, to some extent, using the NAR-ANN as well as to the surrounding stations using the spatial analysis algorithm.

Nevertheless, understanding the behaviour of the GNSS time series across the network, the behaviour of the multiple algorithm approach as well as understanding the behaviour of the desired phenomena to be detected is vital. This can be summarised in Figure 9-1 which represents an approximation of where the temporal and spatial analysis algorithms fit alongside the three cases studies. It's worthy to mention that this figure is not meant to present a sharp cut of what each algorithm can detect, as each algorithm focuses on different parts of the signal (e.g. high vs low frequencies) and in the case of spatial analysis algorithm, it also depends on the behaviour of the surrounding stations; however, the figure illustrates that the temporal analysis algorithm detects high-rate changes but the ability of the algorithm decreases when changes get smaller or their rate gets slower. On the other hand, the spatial analysis algorithm detects slow rate changes but the ability of the algorithm decreases when changes get smaller or their rate gets higher.

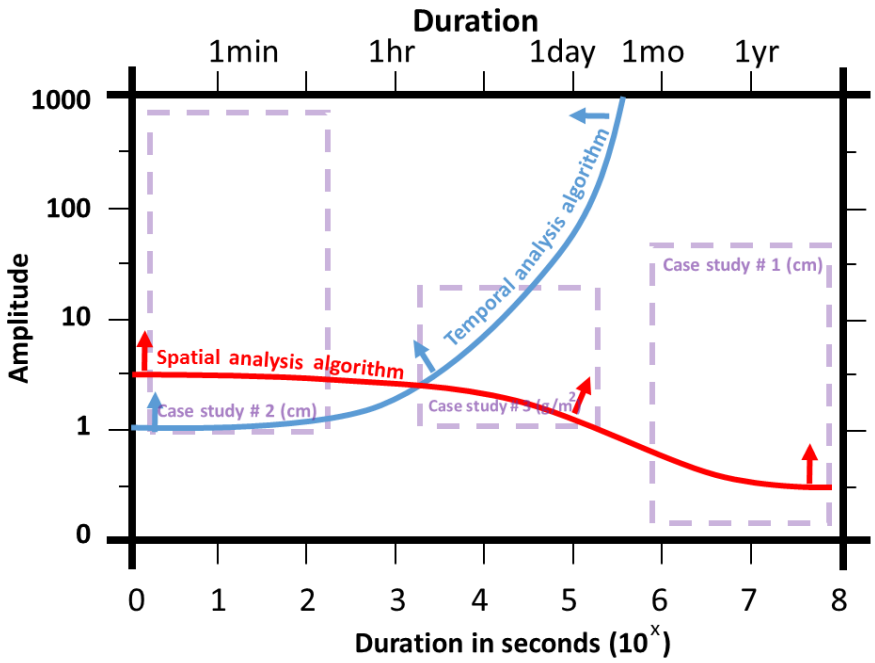


Figure 9-1 Amplitude versus duration diagram presenting where the temporal and spatial analysis algorithms fit alongside the three cases studies.

The complementary function of the three analysis algorithms, which could be implemented for real-time or near real-time applications, suggests that the multiple algorithm approach could be very useful in supporting the operation of existing GNSS networks and in the analysis of GNSS coordinate and troposphere time series. As demonstrated through the three case studies, this multiple algorithm approach has the potential to (i) contribute to the reliable operation of the GNSS networks, by detecting site-specific anomalies at GNSS stations and/or inconsistencies across the GNSS network; (ii) form part of early warning systems (e.g. earthquake early warning), where the outcome of the GNSS coordinate time series analysis can supplement and reinforce the results of existing early warning systems (e.g. seismic networks), or (iii) be used as a complementary tool for weather nowcasting/forecasting using IWV time series of a GNSS network.

9.2 Recommendations for further research

This investigation has also revealed areas where further research could be undertaken to support and validate the findings of the present study. Therefore, some recommendations for future studies are made as follows:

Firstly, the developed multiple algorithm approach has the potential to be improved by using more sophisticated models for extracting the temporal and spatial dependencies.

- For example, the temporal analysis algorithm could be tested with the use of a Long Short Term Memory (LSTM) Neural Network model, which takes into consideration any long-term temporal dependencies in the modelling process; although this does require time series with no gaps.
- Another possible way to improve the temporal dependency would be by using a Nonlinear Autoregressive Exogenous (NARX) Neural Network Model, which includes external time series values to improve the prediction of the ANN.
- Such external datasets could also be used to improve the spatial analysis algorithm by extending the SAR model to the Manski model. Furthermore, the spatial dependency could be extracted using machine learning techniques (e.g. ANN); although, this would require all of the time series to be of the same length for all stations (i.e. no gaps or discontinuities).

Secondly, concerning the first case study, the developed multiple algorithm approach should be re-run when extended, up-to-date GPS coordinate time series, using ITRF2014 instead of IGb08, are available from BIGF. This would help to identify whether the trend related anomalous behaviours are caused by computational issue (using IGb08 instead of ITRF2014) or caused by a physical change in the stations velocities. Moreover, further case studies could be investigated using other monitoring networks and time series, such as tide gauges and mean sea level.

References

Adhikari, R., Agrawal, R.K., 2013. An Introductory Study on Time Series Modeling and Forecasting. LAP Lambert Academic Publishing, Germany.

Akyılmaz, O., Çelik, R.N., Apaydın, N., Ayan, T., 2004. GPS monitoring of the Fatih Sultan Mehmet Suspension Bridge by using assessment methods of the neural networks. Int. Arch. Photogramm. Remote Sens. Spat. Inf. Sci. 34, 1–6.

Ali, A., 2009. Nonlinear multivariate rainfall-stage model for large wetland systems. J. Hydrol. 374, 338–350. doi:10.1016/j.jhydrol.2009.06.033

Allen B. Downey, 2014. Think DSP: Digital Signal Processing in Python. Green Tea Press.

Allen, R.M., Kanamori, H., 2003. The potential for earthquake early warning in Southern California. Science (80-.). 300, 786–789. doi:10.1126/science.1080912

Allen, R.M., Ziv, A., 2011. Application of real-time GPS to earthquake early warning. Geophys. Res. Lett. 38, n/a-n/a. doi:10.1029/2011GL047947

Allen, R. V., 1978. Automatic earthquake recognition and timing from single traces. Bull. Seism. Soc. Am. 68, 1521–1532. doi:10.1353/cch.2001.0013

Allinson, C.R., Clarke, P.J., Edwards, S.J., King, M.A., Baker, T.F., Cruddace, P.R., 2004. Stability of direct GPS estimates of ocean tide loading. Geophys. Res. Lett. 31. doi:10.1029/2004GL020588

Altamimi, Z., Collilieux, X., Métivier, L., 2011. ITRF2008: An improved solution of the international terrestrial reference frame. J. Geod. 85, 457–473. doi:10.1007/s00190-011-0444-4

Amiri-Simkooei, A.R., 2013. On the nature of GPS draconitic year periodic pattern in multivariate position time series. J. Geophys. Res. Solid Earth 118, 2500–2511. doi:10.1002/jgrb.50199

Amiri-Simkooei, A.R., 2009. Noise in multivariate GPS position time-series. J. Geod. 83,

175–187. doi:10.1007/s00190-008-0251-8

Amiri-Simkooei, A.R., Tiberius, C.C.J.M., Teunissen, P.J.G., 2007. Assessment of noise in GPS coordinate time series: Methodology and results. J. Geophys. Res. Solid Earth 112, B07413. doi:10.1029/2006JB004913

Argus, D.F., Gordon, R.G., 1991. Current Sierra Nevada-North America motion from very long baseline interferometry:Implications for the kinematics of the western United States. Geology 19, 1085. doi:10.1130/0091-7613(1991)019<1085:CSNNAM>2.3.CO;2

Assunção, R.M., Reis, E.A., 1999. A new proposal to adjust Moran's I for population density. Stat. Med. 18, 2147–2162. doi:10.1002/(SICI)1097-0258(19990830)18:16<2147::AID-SIM179>3.0.CO;2-I

Bagnall, A., Lines, J., Bostrom, A., Large, J., Keogh, E., Lines, J., 2016. The Great Time Series Classification Bake Off: An Experimental Evaluation of Recently Proposed Algorithms. Extended Version. Data Min. Knowl. Discov. 31, 606–660. doi:10.1007/s10618-016-0483-9

Baker, H.C., Dodson, A.H., Penna, N.T., Higgins, M., Offiler, D., 2001. Ground-based GPS water vapour estimation: Potential for meteorological forecasting. J. Atmos. Solar-Terrestrial Phys. 63, 1305–1314. doi:10.1016/S1364-6826(00)00249-2

Bastos, L., Bos, M., Fernandes, R.M., 2010. Deformation and tectonics: Contribution of GPS measurements to plate tectonics-overview and recent developments, in: Sciences of Geodesy - I: Advances and Future Directions. Springer Berlin Heidelberg, Berlin, Heidelberg, pp. 155–184. doi:10.1007/978-3-642-11741-1_5

Bell, M.L., 2006. The use of ambient air quality modeling to estimate individual and population exposure for human health research: A case study of ozone in the Northern Georgia Region of the United States. Environ. Int. 32, 586–593. doi:10.1016/j.envint.2006.01.005

Bevis, M., Scherer, W., Merrifield, M., 2002. Technical issues and recommendations related to the installation of continuous GPS stations at tide gauges. Mar. Geod. 25, 87–99. doi:10.1080/014904102753516750

Bhattacharya, D., Ghosh, J.K., Samadhiya, N.K., 2012. Review of geohazard warning systems toward development of a popular usage geohazard warning communication system. Nat. Hazards Rev. 13, 260–271. doi:10.1061/(ASCE)NH.1527-6996.0000078

BIGF, n.d. Home | BIGF - The archive for UK GNSS data = GPS + GLONASS + Galileo [WWW Document]. URL http://www.bigf.ac.uk/ (accessed 1.11.17).

Billings, S., 2013. Nonlinear system identification: NARMAX methods in the time, frequency, and spatio-temporal domains, Nonlinear System Identification: NARMAX Methods in the Time, Frequency, and Spatio-Temporal Domains. John Wiley & Sons, Ltd., UK. doi:10.1002/9781118535561

Bingley, R., Dodson, A., Penna, N., Teferle, N., Baker, T., 2001. Monitoring the vertical land movement component of changes in mean sea level using GPS: results from tide gauges in the UK. J. Geospatial Eng. 3(1), PP.9-20.

Bird, P., 2003. An updated digital model of plate boundaries. Geochemistry, Geophys. Geosystems 4. doi:10.1029/2001GC000252

Blewitt, G., 1993. Advances in Global Positioning System Technology for Geodynamics Investigations: 1978–1992, in: Contributions of Space Geodesy to Geodynamics: Technology. pp. 195–213. doi:10.1029/GD025p0195

Blewitt, G., Hammond, W.C., Kreemer, C., Plag, H.-P.P., Stein, S., Okal, E., 2009. GPS for real-time earthquake source determination and tsunami warning systems. J. Geod. 83, 335–343. doi:10.1007/s00190-008-0262-5

Blewitt, G., Heflin, M.B., Hurst, K.J., Jefferson, D.C., Webb, F.H., Zumberge, J.F., 1993. Absolute far-field displacements from the 28 June 1992 Landers earthquake

sequence. Nature 361, 340–342. doi:10.1038/361340a0

Blewitt, G., Kreemer, C., Hammond, W.C., Plag, H.P., Stein, S., Okal, E., 2006. Rapid determination of earthquake magnitude using GPS for tsunami warning systems. Geophys. Res. Lett. 33, L11309. doi:10.1029/2006GL026145

Blewitt, G., Lavallée, D., 2002. Effect of annual signals on geodetic velocity. J. Geophys. Res. 107, 2145--. doi:10.1029/2001JB000570

Bock, Y., Agnew, D.C., Fang, P., Genrich, J.F., Hager, B.H., Herring, T.A., Hudnut, K.W., King, R.W., Larsen, S., Minster, J.-B., Stark, K., Wdowinski, S., Wyatt, F.K., 1993. Detection of crustal deformation from the Landers earthquake sequence using continuous geodetic measurements. Nature 361, 337–340. doi:10.1038/361337a0

Bock, Y., Melgar, D., 2016. Physical applications of GPS geodesy: a review. Reports Prog. Phys. 79, 106801. doi:10.1088/0034-4885/79/10/106801

Bock, Y., Melgar, D., Crowell, B.W., 2011. Real-time strong-motion broadband displacements from collocated GPS and accelerometers. Bull. Seismol. Soc. Am. 101, 2904–2925. doi:10.1785/0120110007

Bock, Y., Wdowinski, S., Fang, P., Zhang, J., Williams, S., Johnson, H., Behr, J., Genrich, J., Dean, J., van Domselaar, M., Agnew, D., Wyatt, F., Stark, K., Oral, B., Hudnut, K., King, R., Herring, T., Dinardo, S., Young, W., Jackson, D., Gurtner, W., 2004. Southern California permanent GPS geodetic array: Continuous measurements of regional crustal deformation between the 1992 Landers and 1994 Northridge earthquakes. J. Geophys. Res. Solid Earth 102, 18013–18033. doi:10.1029/97jb01379

Bogusz, J., Kontny, B., 2011. Estimation of sub-diurnal noise level in GPS time series. Acta Geodyn. Geomater. 8, 273–281.

Boore, D.M., Stephens, C.D., Joyner, W.B., 2002. Comments on Baseline Correction of Digital Strong-Motion Data: Examples from the 1999 Hector Mine, California,

Earthquake. Bull. Seismol. Soc. Am. 92, 1543–1560. doi:10.1785/0120000926

Bos, M.S., Fernandes, R.M.S., Williams, S.D.P., Bastos, L., 2013. Fast error analysis of continuous GNSS observations with missing data. J. Geod. 87, 351–360. doi:10.1007/s00190-012-0605-0

Box, G.E.P., Jenkins, G.M., Reinsel, G.C., 2013. Time series analysis: Forecasting and control: Fourth edition, Time Series Analysis: Forecasting and Control: Fourth Edition. John Wiley & Sons, Inc., Hoboken, NJ. doi:10.1002/9781118619193

Bradley, A.P., 1997. The use of the area under the ROC curve in the evaluation of machine learning algorithms. Pattern Recognit. 30, 1145–1159. doi:10.1016/S0031-3203(96)00142-2

Briais, A., Patriat, P., Tapponnier, P., 1993. Updated interpretation of magnetic anomalies and seafloor spreading stages in the south China Sea: Implications for the Tertiary tectonics of Southeast Asia. J. Geophys. Res. Solid Earth 98, 6299–6328. doi:10.1029/92JB02280

Bruni, S., Zerbini, S., Raicich, F., Errico, M., Santi, E., 2014. Detecting discontinuities in GNSS coordinate time series with STARS: case study, the Bologna and Medicina GPS sites. J. Geod. 88, 1203–1214. doi:10.1007/s00190-014-0754-4

Burges, C., Shaked, T., Renshaw, E., Lazier, A., Deeds, M., Hamilton, N., Hullender, G., 2005. Learning to rank using gradient descent, in: Proceedings of the 22nd International Conference on Machine Learning - ICML '05. ACM Press, New York, New York, USA, pp. 89–96. doi:10.1145/1102351.1102363

Cahyadi, M.N., Heki, K., 2013. Ionospheric disturbances of the 2007 Bengkulu and the 2005 Nias earthquakes, Sumatra, observed with a regional GPS network. J. Geophys. Res. Sp. Phys. 118, 1777–1787. doi:10.1002/jgra.50208

Calori, A., Santos, J.R., Blanco, M., Pessano, H., Llamedo, P., Alexander, P., de la Torre, A., 2016. Ground-based GNSS network and integrated water vapor mapping during

the development of severe storms at the Cuyo region (Argentina). Atmos. Res. 176–177, 267–275. doi:10.1016/J.ATMOSRES.2016.03.002

Camerra, A., Palpanas, T., Shieh, J., Keogh, E., 2010. iSAX 2.0: Indexing and Mining One Billion Time Series, in: 2010 IEEE International Conference on Data Mining. IEEE, pp. 58–67. doi:10.1109/ICDM.2010.124

Carr, J.R., De Miranda, F.P., 1998. The semivariogram in comparison to the co-occurrence matrix for classification of image texture. IEEE Trans. Geosci. Remote Sens. 36, 1945–1952. doi:10.1109/36.729366

Chagas de Melo, B., Assumpção, M., 2018. Mantle anisotropy and asthenospheric flow around cratons in southeastern South America. Geophys. J. Int. 215, 494–506. doi:10.1093/gji/ggy288

Chen, G., Abraham, B., Bennett, G.W., 1997. Parametric and non-parametric modelling of time series - An empirical study. Environmetrics 8, 63–74. doi:10.1002/(SICI)1099-095X(199701)8:1<63::AID-ENV238>3.0.CO;2-B

Chen, Q., van Dam, T., Sneeuw, N., Collilieux, X., Weigelt, M., Rebischung, P., 2013. Singular spectrum analysis for modeling seasonal signals from GPS time series. J. Geodyn. 72, 25–35. doi:10.1016/j.jog.2013.05.005

Chen, Y., 2013. New approaches for calculating Moran's Index of spatial autocorrelation. PLoS One 8, e68336. doi:10.1371/journal.pone.0068336

Chen, Y., 2012. On the four types of weight functions for spatial contiguity matrix. Lett. Spat. Resour. Sci. 5, 65–72. doi:10.1007/s12076-011-0076-6

Chu, D., Gordon, R.G., 1999. Evidence for motion between Nubia and Somalia along the Southwest Indian ridge. Nature 398, 64–67. doi:10.1038/18014

Cohen, M.X., 2014. Analyzing Neural Time Series Data: Theory and Practice.

Colombelli, S., Allen, R.M., Zollo, A., 2013. Application of real-time GPS to earthquake

early warning in subduction and strike-slip environments. J. Geophys. Res. Solid Earth 118, 3448–3461. doi:10.1002/jgrb.50242

Connor, J.T., Martin, R.D., Atlas, L.E., 1994. Recurrent neural networks and robust time series prediction. Neural Networks, IEEE Trans. 5, 240–254.

Crowell, B.W., Bock, Y., Melgar, D., 2012. Real-time inversion of GPS data for finite fault modeling and rapid hazard assessment. Geophys. Res. Lett. 39, n/a-n/a. doi:10.1029/2012GL051318

Crowell, B.W., Bock, Y., Squibb, M.B., 2009. Demonstration of Earthquake Early Warning Using Total Displacement Waveforms from Real-time GPS Networks. Seismol. Res. Lett. 80, 772–782. doi:10.1785/gssrl.80.5.772

Crowther, P.S., Cox, R.J., 2005. A Method for Optimal Division of Data Sets for Use in Neural Networks, in: Knowledge-Based Intelligent Information and Engineering Systems. Springer, Berlin, Heidelberg, pp. 1–7. doi:10.1007/11554028_1

D'Agostino, N., Avallone, A., Cheloni, D., D'Anastasio, E., Mantenuto, S., Selvaggi, G., 2008. Active tectonics of the Adriatic region from GPS and earthquake slip vectors. J. Geophys. Res. 113, B12413. doi:10.1029/2008JB005860

Da Silva, E.C., Silva, A.C., De Paiva, A.C., Nunes, R.A., 2008. Diagnosis of lung nodule using Moran's index and Geary's coefficient in computerized tomography images. Pattern Anal. Appl. 11, 89–99. doi:10.1007/s10044-007-0081-y

Davis, J.L., Wernicke, B.P., Tamisiea, M.E., 2012. On seasonal signals in geodetic time series. J. Geophys. Res. Solid Earth 117, n/a-n/a. doi:10.1029/2011JB008690

de Mesnard, L., 2013. Pollution models and inverse distance weighting: Some critical remarks. Comput. Geosci. 52, 459–469. doi:10.1016/j.cageo.2012.11.002

DeMets, C., Dixon, T.H., 1999. New kinematic models for Pacific-North America motion from 3 Ma to present, I: Evidence for steady motion and biases in the NUVEL-1A Model. Geophys. Res. Lett. 26, 1921–1924. doi:10.1029/1999GL900405

DeMets, C., Gordon, R.G., Argus, D.F., 2010. Geologically current plate motions. Geophys. J. Int. 181, 1–80. doi:10.1111/j.1365-246X.2009.04491.x

DeMets, C., Gordon, R.G., Argus, D.F., Stein, S., 1994. Effect of recent revisions to the geomagnetic reversal time scale on estimates of current plate motions. Geophys. Res. Lett. 21, 2191–2194. doi:10.1029/94GL02118

DeMets, C., Gordon, R.G., Argus, D.F., Stein, S., 1990. Current plate motions. Geophys. J. Int. 101, 425–478. doi:10.1111/j.1365-246X.1990.tb06579.x

DeMets, C., Jansma, P.E., Mattioli, G.S., Dixon, T.H., Farina, F., Bilham, R., Calais, E., Mann, P., 2000. GPS geodetic constraints on Caribbean-North America plate motion. Geophys. Res. Lett. 27, 437–440. doi:10.1097/00003226-200101000-00021

Deng, J., Sykes, L.R., 1995. Determination of Euler pole for contemporary relative motion of Caribbean and North American plates using slip vectors of interplate earthquakes. Tectonics 14, 39–53. doi:10.1029/94TC02547

Diaconescu, E., 2008. The use of NARX neural networks to predict chaotic time series. Wseas Trans. Comput. Res. 3, 182–191.

Dietterich, T.G., Kong, E.B., 1995. Machine Learning Bias , Statistical Bias , and Statistical Variance of Decision Tree Algorithms. Mach. Learn. 255, 0–13.

Djouadi, S.M., Crilly, P., Sahyoun, S., Smith, S.F., 2011. Improved localization in GPS-denied environments using an autoregressive model and a generalized linear model. 2011 - MILCOM 2011 Mil. Commun. Conf. 760–765. doi:10.1109/MILCOM.2011.6127768

Dobesch, H., Dumolard, P., Dyras, I., Wiley InterScience (Online service), 2007. Spatial interpolation for climate data : the use of GIS in climatology and meteorology. ISTE.

Dong, D.-N., Bock, Y., 1989. Global Positioning System Network analysis with phase ambiguity resolution applied to crustal deformation studies in California. J. Geophys. Res. Solid Earth 94, 3949–3966. doi:10.1029/JB094iB04p03949

Dong, D., Fang, P., Bock, Y., Webb, F., Prawirodirdjo, L., Kedar, S., Jamason, P., 2006. Spatiotemporal filtering using principal component analysis and Karhunen-Loeve expansion approaches for regional GPS network analysis. J. Geophys. Res. Solid Earth 111, n/a-n/a. doi:10.1029/2005JB003806

Dong, X., Woodworoth, P., Moore, P., Bingley, R., 2002. Absolute calibration of the TOPEX/POSEIDON altimeters using UK tide gauges, GPS, and precise, local geoid-differences. Mar. Geod. 25, 189–204. doi:10.1080/01490410290051527

Drozdov, I., Kidd, M., Nadler, B., Camp, R.L., Mane, S.M., Hauso, O., Gustafsson, B.I., Modlin, I.M., 2009. Predicting neuroendocrine tumor (carcinoid) neoplasia using gene expression profiling and supervised machine learning. Cancer 115, 1638–1650. doi:10.1002/cncr.24180

Dubé, J., Legros, D., 2011. Using a Spatio-Temporal Weights Matrix in the Development of a Spatio-Temporal Autoregressive (STAR) Model, in: In Proceedings of the Spatial Econometric Association Annual Meetings.

Durán-Rosal, A.M., Gutiérrez-Peña, P.A., Martínez-Estudillo, F.J., Hervás-Martínez, C., 2016. Time Series Representation by a Novel Hybrid Segmentation Algorithm. Springer International Publishing, pp. 163–173. doi:10.1007/978-3-319-32034-2_14

Edwards, B., Allmann, B., Fäh, D., Clinton, J., H., K., Di Toro, G., 2010. Automatic computation of moment magnitudes for small earthquakes and the scaling of local to moment magnitude. Geophys. J. Int. 183, 407–420. doi:10.1111/j.1365-246X.2010.04743.x

El-Naggar, A.M., 2013. Artificial neural network as a model for ionospheric TEC map to serve the single frequency receiver. Alexandria Eng. J. 52, 425–432. doi:10.1016/j.aej.2013.05.007

Elhorst, J.P., 2010. Applied Spatial Econometrics: Raising the Bar. Spat. Econ. Anal. 5, 9–28. doi:10.1080/17421770903541772

Fann, N., Lamson, A.D., Anenberg, S.C., Wesson, K., Risley, D., Hubbell, B.J., 2012. Estimating the National Public Health Burden Associated with Exposure to Ambient PM2.5 and Ozone. Risk Anal. 32, 81–95. doi:10.1111/j.1539-6924.2011.01630.x

Feigl, K.L., Agnew, D.C., Bock, Y., Dong, D., Donnellan, A., Hager, B.H., Herring, T.A., Jackson, D.D., Jordan, T.H., King, R.W., Larsen, S., Larson, K.M., Murray, M.H., Shen, Z., Webb, F.H., 1993. Space geodetic measurement of crustal deformation in central and southern California, 1984-1992. J. Geophys. Res. Solid Earth 98, 21677–21712. doi:10.1029/93JB02405

Feigl, K.L., King, R.W., Jordan, T.H., 1990. Geodetic measurement of tectonic deformation in the Santa Maria Fold and Thrust Belt, California. J. Geophys. Res. 95, 2679–2699. doi:10.1029/JB095iB03p02679

Fischer, M.M., Nijkamp, P., 2014. Spatial Autocorrelation and Spatial Filtering, Handbook of Regional Science, Advances in Spatial Science. Springer Berlin Heidelberg, Berlin, Heidelberg. doi:10.1007/978-3-642-23430-9

Fu, T., 2011. A review on time series data mining. Eng. Appl. Artif. Intell. 24, 164–181. doi:10.1016/j.engappai.2010.09.007

Galvan, D.A., Komjathy, A., Hickey, M.P., Stephens, P., Snively, J., Tony Song, Y., Butala, M.D., Mannucci, A.J., 2012. Ionospheric signatures of Tohoku-Oki tsunami of March 11, 2011: Model comparisons near the epicenter. Radio Sci. 47. doi:10.1029/2012RS005023

Ganas, A., Cannavo, F., Chousianitis, K., Kassaras, I., Drakatos, G., 2015. Displacements recorded on continuous GPS stations following the 2014 M6 Cephalonia (Greece) earthquakes: Dynamic characteristics and kinematic implications. Acta Geodyn. Geomater. 12, 5–27. doi:10.13168/AGG.2015.0005

Garrison, J.L., Komjathy, A., Zavorotny, V.U., Katzberg, S.J., 2002. Wind speed measurement using forward scattered GPS signals. IEEE Trans. Geosci. Remote Sens.

40, 50–65. doi:10.1109/36.981349

Gazeaux, J., Williams, S.D.P., King, M., Bos, M., Dach, R., Deo, M., Moore, A.W., Ostini, L., Petrie, E., Roggero, M., Teferle, F.N., Olivares, G., Webb, F.H., 2013. Detecting offsets in GPS time series: First results from the detection of offsets in GPS experiment. J. Geophys. Res. Solid Earth 118, 2397–2407. doi:10.1002/jgrb.50152

Geary, R.C., 1954. The Contiguity Ratio and Statistical Mapping. Inc. Stat. 5, 115. doi:10.2307/2986645

Gendt, G., Dick, G., Reigber, C., Tomassini, M., Liu, Y., Ramatschi, M., 2004. Near real time GPS water vapor monitoring for numerical weather prediction in Germany. J. Meteorol. Soc. Japan. Ser. II 82, 361–370. doi:10.2151/jmsj.2004.361

Geng, J., Bock, Y., Melgar, D., Crowell, B.W., Haase, J.S., 2013. A new seismogeodetic approach applied to GPS and accelerometer observations of the 2012 Brawley seismic swarm: Implications for earthquake early warning. Geochemistry, Geophys. Geosystems 14, 2124–2142. doi:10.1002/ggge.20144

Geng, Y., 2007. Online DGPS correction prediction using recurrent neural networks with unscented Kalman filter, in: International Global Navigation Satellite Systems Society IGNSS Symposium, The University of New South Wales, Sydney, Australia. Citeseer, pp. 4–6.

Genrich, J.F., Bock, Y., 2006. Instantaneous geodetic positioning with 10–50 Hz GPS measurements: Noise characteristics and implications for monitoring networks. J. Geophys. Res 111, 3403. doi:10.1029/2005JB003617

GEONET, n.d. GPS Earth Obesrvation NETwork (GEONET) of Japan [WWW Document]. URL http://mekira.gsi-mc.go.jp/ENGLISH/index.html (accessed 7.26.18).

Gershenfeld, N.A., Weigend, A.S., 2018. The future of time series: Learning and understanding, Pattern Formation in the Physical and Biological Sciences. doi:10.1201/9780429493362

Getis, A., 2009. Spatial Weights Matrices. Geogr. Anal. 41, 404–410. doi:10.1111/j.1538-4632.2009.00768.x

Ghosh, A., 2012. Comparative study of Financial Time Series Prediction By Artificial Neural Network with Gradient Descent Learning. Int. J. Sci. Eng. Res. 3.

Glowacki, T.J., Penna, N.T., Bourke, W.P., 2006. Validation of GPS-based estimates of integrated water vapour for the Australian region and identification of diurnal variability. Aust. Meteorol. Mag. 55, 55(2), 131-148, June 2006.

Govaerts, A., Vervoort, A., 2010. Geostatistical Interpolation of Soil Properties in Boom Clay in Flanders. Springer, Dordrecht, pp. 219–230. doi:10.1007/978-90-481-2322-3_20

Grapenthin, R., Freymueller, J.T., 2011. The dynamics of a seismic wave field: Animation and analysis of kinematic GPS data recorded during the 2011 Tohoku-oki earthquake, Japan. Geophys. Res. Lett. 38, n/a-n/a. doi:10.1029/2011GL048405

Grapenthin, R., Johanson, I.A., Allen, R.M., 2014. Operational real-time GPS-enhanced earthquake early warning. J. Geophys. Res. Solid Earth 119, 7944–7965. doi:10.1002/2014JB011400

Grenerczy, G., Sella, G., Stein, S., Kenyeres, A., 2005. Tectonic implications of the GPS velocity field in the northern Adriatic region. Geophys. Res. Lett. 32, 1–4. doi:10.1029/2005GL022947

Griffiths, J., Ray, J., 2016. Impacts of GNSS position offsets on global frame stability. Geophys. J. Int. 204, 480–487. doi:10.1093/gji/ggv455

Gruszczynski, M., Bogusz, J., Kłos, A., Figurski, M., 2015. Studies on spatio-temporal filtering of GNSS-derived coordinates 17, 2015.

Häberling, S., Rothacher, M., Zhang, Y., Clinton, J.F., Geiger, A., 2015. Assessment of high-rate GPS using a single-axis shake table. J. Geod. 89, 697–709. doi:10.1007/s00190-015-0808-2

Hackl, M., Malservisi, R., Hugentobler, U., Wonnacott, R., 2011. Estimation of velocity uncertainties from GPS time series: Examples from the analysis of the South African TrigNet network. J. Geophys. Res. Solid Earth 116, n/a-n/a. doi:10.1029/2010JB008142

Hagan, M., Demuth, H., Beale, M., 1996. Neural network design. ecee.colorado.edu. doi:10.1007/1-84628-303-5

Hansen, D.N., Teferle, F.N., Bingley, R.M., Williams, S.D.P., 2012. New estimates of present-day crustal/land motions in the British isles based on the BIGF network, in: International Association of Geodesy Symposia. Springer Berlin Heidelberg, pp. 665–671. doi:10.1007/978-3-642-20338-1_82

He, X., Montillet, J.P., Fernandes, R., Bos, M., Yu, K., Hua, X., Jiang, W., 2017. Review of current GPS methodologies for producing accurate time series and their error sources. J. Geodyn. doi:10.1016/j.jog.2017.01.004

Hecht-Nielsen, R., 1989. Theory of the backpropagation neural network, in: International Joint Conference on Neural Networks. IEEE, pp. 593–605 vol.1. doi:10.1109/IJCNN.1989.118638

Heki, K., Enomoto, Y., 2013. Preseismic ionospheric electron enhancements revisited. J. Geophys. Res. Sp. Phys. 118, 6618–6626. doi:10.1002/jgra.50578

Hernández-Pajares, M., Juan, J.M., Sanz, J., 1997. Neural network modeling of the ionospheric electron content at global scale using GPS data. Radio Sci. 32, 1081–1089. doi:0048-6604/97/97RS-00431

Hofmann, F., Biskupek, L., Müller, J., 2018. Contributions to reference systems from Lunar Laser Ranging using the IfE analysis model. J. Geod. 92, 975–987. doi:10.1007/s00190-018-1109-3

Hollenstein, C., Kahle, H.G., Geiger, A., Jenny, S., Goes, S., Giardini, D., 2003. New GPS constraints on the Africa-Eurasia plate boundary zone in southern Italy. Geophys.

Res. Lett. 30. doi:10.1029/2003GL017554

Houlié, N., Briole, P., Bonforte, A., Puglisi, G., 2006. Large scale ground deformation of Etna observed by GPS between 1994 and 2001. Geophys. Res. Lett. 33. doi:10.1029/2005GL024414

Hsu, S.K., Yeh, Y.C., Doo, W. Bin, Tsai, C.H., 2004. New bathymetry and magnetic lineations identifications in the northernmost South China Sea and their tectonic implications. Mar. Geophys. Res. 25, 29–44. doi:10.1007/s11001-005-0731-7

Hubert, L.J., Golledge, R.G., Costanzo, C.M., 1981. Generalized Procedures for Evaluating Spatial Autocorrelation. Geogr. Anal. 13, 224–233. doi:10.1111/j.1538-4632.1981.tb00731.x

Iorio, C., Frasso, G., D'Ambrosio, A., Siciliano, R., 2016. Parsimonious time series clustering using P-splines. Expert Syst. Appl. 52, 26–38. doi:10.1016/j.eswa.2016.01.004

Jeffrey, S.J., Carter, J.O., Moodie, K.B., Beswick, A.R., 2001. Using spatial interpolation to construct a comprehensive archive of Australian climate data. Environ. Model. Softw. 16, 309–330. doi:10.1016/S1364-8152(01)00008-1

Ji, Y., Hao, J., Reyhani, N., Lendasse, A., 2005. Direct and recursive prediction of time series using Mutual information selection. Comput. Intell. Bioinspired Syst. 3512, 1010–1017. doi:10.1007/11494669_124

Jiann-Shiou Yang, J.-S., 2005. A study of travel time modeling via time series analysis, in: Proceedings of 2005 IEEE Conference on Control Applications, 2005. CCA 2005. IEEE, pp. 855–860. doi:10.1109/CCA.2005.1507236

Jin, S., 2012. GNSS atmopheric seismology: A case study of the 2008 Mw7.9 Wenchuan earthquake, in: International Geoscience and Remote Sensing Symposium (IGARSS). pp. 7504–7507. doi:10.1109/IGARSS.2012.6351896

Jin, S., Park, P.H., Zhu, W., 2007. Micro-plate tectonics and kinematics in Northeast Asia

inferred from a dense set of GPS observations. Earth Planet. Sci. Lett. 257, 486–496. doi:10.1016/j.epsl.2007.03.011

Johanson, I.A., Grapenthin, R., Allen, R.M., 2014. G-larmS: An Infrastructure for Geodetic Earthquake Early Warning, applied to Northern California. Am. Geophys. Union, Fall Meet. 2014, Abstr. id. S32C-06.

Jones, J., 2010. An assessment of the quality of GPS water vapour estimates and their use in operational meteorology and climate monitoring . PhD thesis , University of Nottingham . Univ. Nottingham. University of Nottingham.

Kaloop, M.R., Hu, J.W., 2015. Optimizing the De-Noise neural network model for GPS time-series monitoring of structures. Sensors 15, 24428–24444.

Käufl, P., Valentine, A.P., O'Toole, T.B., Trampert, J., 2014. A framework for fast probabilistic centroid-moment-tensor determination-inversion of regional static displacement measurements. Geophys. J. Int. 196, 1676–1693. doi:10.1093/gji/ggt473

Kehagias, A., Geophysics, V.F.-N.P. in, 2006, U., 2006. TIME SERIES SEGMENTATION WITH SHIFTING MEANS. Nonlinear Process. Geophys. Eur. Geosci. Union 13, 339–352.

Klos, A., Bogusz, J., Figurski, M., Gruszczynski, M., 2016. Error analysis for European IGS stations. Stud. Geophys. Geod. 60, 17–34. doi:10.1007/s11200-015-0828-7

Koyama, Y., Tanaka, T., 2010. Improvements in accurate GPS positioning using time series analysis, SICE Annual Conference 2010, Proceedings of. IEEE.

Krige, D.G., 1952. A Statistical Approach to Some Basic Mine Valuation Problems on the Witwatersrand. J. Chem. Metall. Min. Soc. South Africa 201–215. doi:10.2307/3006914

Krollner, B., Vanstone, B., Finnie, G., 2010. Financial time series forecasting with machine learning techniques : A survey. Comput. Intell. 28–30.

Kubo, T., Hisada, Y., Murakami, M., Kosuge, F., Hamano, K., 2011. Application of an earthquake early warning system and a real-time strong motion monitoring system in emergency response in a high-rise building. Soil Dyn. Earthq. Eng. 31, 231–239. doi:10.1016/J.SOILDYN.2010.07.009

Kumar, G., K.Rajasekhar, 2017. Performance analysis of Levenberg-Marquardt and Steepest Descent algorithms based ANN to predict compressive strength of SIFCON using manufactured sand. Eng. Sci. Technol. an Int. J. 20, 1396–1405. doi:10.1016/J.JESTCH.2017.07.005

Langbein, J., 2012. Estimating rate uncertainty with maximum likelihood: differences between power-law and flicker–random-walk models. J. Geod. 86, 775–783. doi:10.1007/s00190-012-0556-5

Langbein, J., 2008. Noise in GPS displacement measurements from Southern California and Southern Nevada. J. Geophys. Res. 113, B05405. doi:10.1029/2007JB005247

Langmuir, C.H., Klein, E.M., Plank, T., 2013. Petrological Systematics of Mid-Ocean Ridge Basalts: Constraints on Melt Generation Beneath Ocean Ridges. American Geophysical Union (AGU), pp. 183–280. doi:10.1029/GM071p0183

Larsen, S., Reilinger, R., 1992. Global positioning system measurements of strain accumulation across the Imperial Valley, California: 1986–1989. J. Geophys. Res. 97, 8865. doi:10.1029/92JB00428

Larson, K.M., Agnew, D.C., 1991. Application of the global positioning system to crustal deformation measurement: 1. Precision and accuracy. J. Geophys. Res. 96, 16547. doi:10.1029/91JB01275

Larson, K.M., Bodin, P., Gomberg, J., 2003. Using 1-Hz GPS Data to Measure Deformations Caused by the Denali Fault Earthquake. Science (80-.). 300, 1421–1424. doi:10.1126/science.1084531

Lean Yu, Shouyang Wang, Lai, K.K., 2006. An integrated data preparation scheme for

neural network data analysis. IEEE Trans. Knowl. Data Eng. 18, 217–230. doi:10.1109/TKDE.2006.22

LeSage, J.P., 2008. An introduction to Spatial Econometrics. Rev. d'économie Ind. 19–44. doi:10.4000/rei.3887

LeSage, J.P., 1998. Spatial econometrics. A companion to Theor. Econom. 273.

Li, J., Miyashita, K., Kato, T., Miyazaki, S., 2000. GPS time series modeling by autoregressive moving average method: Application to the crustal deformation in central Japan. Earth Planets Sp. 52, 155–162. doi:10.1186/BF03351624

Lim, C.H., Lim, T.S., Koo, V.C., Ayer, J., Lama, K., 2013. A Comprehensive New GPS-Aided SINU System Modeling using Autoregressive Model. Int. J. Adv. Robot. Syst. 1–18. doi:10.3390/s130x0000x

Liu, B., Dai, W., Liu, N., 2017. Extracting seasonal deformations of the Nepal Himalaya region from vertical GPS position time series using Independent Component Analysis. Adv. Sp. Res. doi:10.1016/j.asr.2017.02.028

Liu, B., Dai, W., Peng, W., Meng, X., 2015. Spatiotemporal analysis of GPS time series in vertical direction using independent component analysis. Earth, Planets Sp. 67, 189. doi:10.1186/s40623-015-0357-1

Ma, G., Maruyama, T., 2006. A super bubble detected by dense GPS network at east Asian longitudes. Geophys. Res. Lett. 33, L21103. doi:10.1029/2006GL027512

Ma, G., Maruyama, T., 2003. Derivation of TEC and estimation of instrumental biases from GEONET in Japan. Ann. Geophys. 21, 2083–2093. doi:10.5194/angeo-21-2083-2003

Ma, X.F., Maruyama, T., Ma, G., Takeda, T., 2005. Three-dimensional ionospheric tomography using observation data of GPS ground receivers and ionosonde by neural network. J. Geophys. Res. Sp. Phys. 110, A05308. doi:10.1029/2004JA010797

Macdonald, K.C., 1982. Mid-Ocean Ridges: Fine Scale Tectonic, Volcanic and Hydrothermal

Processes Within the Plate Boundary Zone. Annu. Rev. Earth Planet. Sci. 10, 155–190. doi:10.1146/annurev.ea.10.050182.001103

Männel, B., Rothacher, M., 2012. Co-location of GPS, SLR and VLBI in space and its impact on the TRF. AGU Fall Meet. Abstr.

Manning, T., 2013. Sensing the dynamics of severe weather using 4D GPS tomography in the Australian region. Royal Melbourne Institute of Technology (RMIT) University.

Mao, A., Harrison, C.G.A., Dixon, T.H., 1999. Noise in GPS coordinate time series. J. Geophys. Res. Solid Earth 104, 2797–2816. doi:10.1029/1998JB900033

Matsumura, M., Saito, A., Iyemori, T., Shinagawa, H., Tsugawa, T., Otsuka, Y., Nishioka, M., Chen, C.H., 2011. Numerical simulations of atmospheric waves excited by the 2011 off the Pacific coast of Tohoku Earthquake. Lett. Earth Planets Sp. 63, 885–889. doi:10.5047/eps.2011.07.015

Maybeck, P.S., 1982. Stochastic models, estimation, and control - Volume 3, Mathematics in science and engineering. Academic Press.

Melgar, D., Crowell, B.W., Bock, Y., Haase, J.S., 2013. Rapid modeling of the 2011 Mw 9.0 Tohoku-oki earthquake with seismogeodesy. Geophys. Res. Lett. 40, 2963–2968. doi:10.1002/grl.50590

Melgar, D., Crowell, B.W., Geng, J., Allen, R.M., Bock, Y., Riquelme, S., Hill, E.M., Protti, M., Ganas, A., 2015. Earthquake magnitude calculation without saturation from the scaling of peak ground displacement. Geophys. Res. Lett. 42, 5197–5205. doi:10.1002/2015GL064278

Michel, C., Kelevitz, K., Houlié, N., Edwards, B., Psimoulis, P., Su, Z., Clinton, J., Giardini, D., 2017. The Potential of High-Rate GPS for Strong Ground Motion Assessment. Bull. Seismol. Soc. Am. 107, 1849–1859. doi:10.1785/0120160296

Michoud, C., Bazin, S., Blikra, L.H., Derron, M.H., Jaboyedoff, M., 2013. Experiences from site-specific landslide early warning systems. Nat. Hazards Earth Syst. Sci. 13, 2659–

2673. doi:10.5194/nhess-13-2659-2013

Minson, S.E., Brooks, B.A., Glennie, C.L., Murray, J.R., Langbein, J.O., Owen, S.E., Heaton, T.H., Iannucci, R.A., Hauser, D.L., 2015. Crowdsourced earthquake early warning. Sci. Adv. 1. doi:10.1126/sciadv.1500036

Minson, S.E., Murray, J.R., Langbein, J.O., Gomberg, J.S., 2014. Real-time inversions for finite fault slip models and rupture geometry based on high-rate GPS data. J. Geophys. Res. Solid Earth 119, 3201–3231. doi:10.1002/2013JB010622

Minster, J.B., Jordan, T.H., 1978. Present-day plate motions. J. Geophys. Res. 83, 5331. doi:10.1029/JB083iB11p05331

Minster, J.B., Jordan, T.H., Molnar, P., Haines, E., 1974. Numerical Modelling of Instantaneous Plate Tectonics. Geophys. J. Int. 36, 541–576. doi:10.1111/j.1365-246X.1974.tb00613.x

Miyazaki, S., Tsuji, H., Hatanaka, Y., Abe, Y., Yoshimura, A., Kamada, K., Kobayashi, K., Morishita, H., Iimura, Y., 1996. Establishement of the Nationwide GPS Array (GRAPES) and its Initial Results on the Crustal Deformation of Japan. Bull. Earthq. Res. Inst. Univ. Tokyo 42, 27–41.

Montillet, J.-P., Tregoning, P., McClusky, S., Yu, K., 2013. Extracting White Noise Statistics in GPS Coordinate Time Series. IEEE Geosci. Remote Sens. Lett. 10, 563–567. doi:10.1109/LGRS.2012.2213576

Montillet, J.-P., Williams, S.D.P., Koulali, A., McClusky, S.C., 2015. Estimation of offsets in GPS time-series and application to the detection of earthquake deformation in the far-field. Geophys. J. Int. 200, 1205–1219. doi:10.1093/gji/ggu473

Moons, E., Brijs, T., Wets, G., 2009. Improving moran's index to identify hot spots in traffic safety. Stud. Comput. Intell. 176, 117–132. doi:10.1007/978-3-540-89930-3_7

Moran, P.A., 1950. Notes on continuous stochastic phenomena. Biometrika 37, 17–23. doi:10.1093/biomet/37.1-2.17

Mosavi, M.R., 2006. Comparing DGPS corrections prediction using neural network, fuzzy neural network, and Kalman filter. GPS Solut. 10, 97–107. doi:10.1007/s10291-005-0011-7

Moschas, F., Avallone, A., Saltogianni, V., Stiros, S.C., 2014. Strong motion displacement waveforms using 10-Hz precise point positioning GPS: An assessment based on free oscillation experiments. Earthq. Eng. Struct. Dyn. 43, 1853–1866. doi:10.1002/eqe.2426

Msaewe, H.A., Hancock, C.M., Psimoulis, P.A., Roberts, G.W., Bonenberg, L., de Ligt, H., 2017. Investigating multi-GNSS performance in the UK and China based on a zero-baseline measurement approach. Measurement 102, 186–199. doi:10.1016/J.MEASUREMENT.2017.02.004

Neidell, M., 2004. Air pollution, health, and socio-economic status: the effect of outdoor air quality on childhood asthma. J. Health Econ. 23, 1209–1236.

Nguyen-H, M., Zhou, C., 2010. Improving GPS/INS integration through neural networks. arXiv Prepr. arXiv1005.5115.

Nikolaidis, R., 2002. Observation of Geodetic and Seismic Deformation with the Global Positioning System. doi:University of California, San Diego

Nikolaidis, R.M., Bock, Y., de Jonge, P.J., Shearer, P., Agnew, D.C., Van Domselaar, M., 2001. Seismic wave observations with the Global Positioning System. J. Geophys. Res. Solid Earth 106, 21897–21916. doi:10.1029/2001JB000329

Nishimura, T., Munekane, H., Yarai, H., 2011. The 2011 off the Pacific coast of Tohoku Earthquake and its aftershocks observed by GEONET. Earth, Planets Sp. 63, 631–363. doi:10.5047/eps.2011.06.025

Ogawa, T., Ogawa, T., Saito, A., Saito, A., Tsugawa, T., Tsugawa, T., Fukao, S., Fukao, S., Miyazaki, S., Miyazaki, S., 2001. A new technique for mapping of total electron content using GPS network in Japan. Radio Sci. 54, 1–23.

Ohta, Y., Kobayashi, T., Tsushima, H., Miura, S., Hino, R., Takasu, T., Fujimoto, H., Iinuma, T., Tachibana, K., Demachi, T., Sato, T., Ohzono, M., Umino, N., 2012. Quasi real-time fault model estimation for near-field tsunami forecasting based on RTK-GPS analysis: Application to the 2011 Tohoku-Oki earthquake (M w 9.0). J. Geophys. Res. Solid Earth 117, n/a-n/a. doi:10.1029/2011JB008750

Oliver, M.A., Webster, R., 1990. Kriging: A method of interpolation for geographical information systems. Int. J. Geogr. Inf. Syst. 4, 313–332. doi:10.1080/02693799008941549

Ostini, L., Rolf Dach, P., Beutler, G., 2008. Analysis and Quality Assessment of GNSS-Derived Parameter Time Series. der Philosophisch-naturwissenschaftlichen Fakult¨at, der Universit¨at Bern.

Park, M., Gao, Y., 2008. Error and performance analysis of MEMS-based inertial sensors with a low-cost GPS receiver. Sensors 8, 2240–2261. doi:10.3390/s8042240

Penna, N.T., King, M.A., Stewart, M.P., 2007. GPS height time series: Short-period origins of spurious long-period signals. J. Geophys. Res. Solid Earth 112, B02402. doi:10.1029/2005JB004047

Peralta, J., Gutierrez, G., Sanchis, A., 2010. Automatic Design of Artificial Neural Networks to Forecast Time Series. III Simp. Intel. Comput. 238–242.

Perez-Campos, X., Melgar, D., Singh, S.K., Cruz-Atienza, V., Iglesias, A., Hjorleifsdottir, V., 2013. Rapid Estimation of Fault Parameters for Tsunami Warning along the Mexican Subduction Zone: A Scenario Earthquake in the Guerrero Seismic Gap. Seismol. Res. Lett. 84, 474–484. doi:10.1785/0220120156

Perler, D., Geiger, A., Hurter, F., 2011. 4D GPS water vapor tomography: new parameterized approaches. J. Geod. 85, 539–550. doi:10.1007/s00190-011-0454-2

Pesquer, L., Cortés, A., Pons, X., 2011. Parallel ordinary kriging interpolation incorporating automatic variogram fitting. Comput. Geosci. 37, 464–473.

doi:10.1016/j.cageo.2010.10.010

Picard, F., Robin, S., Lavielle, M., Vaisse, C., Daudin, J.J., 2005. A statistical approach for array CGH data analysis. BMC Bioinformatics 6, 27. doi:10.1186/1471-2105-6-27

Plank, L., Hellerschmied, A., McCallum, J., Böhm, J., Lovell, J., 2017. VLBI observations of GNSS-satellites: from scheduling to analysis. J. Geod. 91, 867–880. doi:10.1007/s00190-016-0992-8

Psimoulis, P., Behr, Y., Houlié, N., 2018. Real-time magnitude characterization of large earthquakes using the predominant period derived from 1Hz GPS data ETH Library. doi:10.3929/ethz-b-000220393

Psimoulis, P., Houlie, N., Meindl, M., Rothacher, M., 2015. Consistency of PPP GPS and strong-motion records: Case study of Mw9.0 Tohoku-Oki 2011 earthquake. Smart Struct. Syst. 16, 347–366. doi:10.12989/sss.2015.16.2.347

Psimoulis, P.A., Houlié, N., Habboub, M., Michel, C., Rothacher, M., 2018. Detection of ground motions using high-rate GPS time-series. Geophys. J. Int. 214, 1237–1251. doi:10.1093/gji/ggy198

Psimoulis, P.A., Houlié, N., Michel, C., Meindl, M., Rothacher, M., 2014. Long-period surface motion of the multipatch MW 9.0 Tohoku-Oki earthquake. Geophys. J. Int. 199, 968–980. doi:10.1093/gji/ggu302

Rasmussen, C.E., Williams, C.K.I., 2006. Bayesian Regression and Gaussian processes. Gaussian Process. Mach. Learn. Chapter 2. doi:10.1093/bioinformatics/btq657

Rebischung, P., Griffiths, J., Ray, J., Schmid, R., Collilieux, X., Garayt, B., 2012. IGS08: the IGS realization of ITRF2008. GPS Solut. 16, 483–494. doi:10.1007/s10291-011-0248-2

Reilinger, R., McClusky, S., Vernant, P., Lawrence, S., Ergintav, S., Cakmak, R., Ozener, H., Kadirov, F., Guliev, I., Stepanyan, R., Nadariya, M., Hahubia, G., Mahmoud, S., Sakr, K., ArRajehi, A., Paradissis, D., Al-Aydrus, A., Prilepin, M., Guseva, T., Evren,

E., Dmitrotsa, A., Filikov, S. V., Gomez, F., Al-Ghazzi, R., Karam, G., 2006. GPS constraints on continental deformation in the Africa-Arabia-Eurasia continental collision zone and implications for the dynamics of plate interactions. J. Geophys. Res. Solid Earth 111, n/a-n/a. doi:10.1029/2005JB004051

Saito, A., Fukao, S., Miyazaki, S., 1998. High resolution mapping of TEC perturbations with the GSI GPS network over Japan. Geophys. Res. Lett. 25, 3079–3082. doi:10.1029/98GL52361

Santamaría-Gómez, A., Bouin, M., Collilieux, X., Wöppelmann, G., 2011. Correlated errors in GPS position time series: Implications for velocity estimates. J. Geophys. Res. Solid Earth 116, B01405. doi:10.1029/2010JB007701

Sato, K., 1993. Tectonic plate motion and deformation inferred from very long baseline interferometry. Tectonophysics 220, 69–87. doi:10.1016/0040-1951(93)90224-8

Segall, P., Davis, J.L., 1997. GPS applications for geodynamics and earthquake studies. Annu. Rev. Earth Planet. Sci. 25, 301–336. doi:10.1146/annurev.earth.25.1.301

Sella, G.F., Dixon, T.H., Mao, A., 2002. REVEL: A model for Recent plate velocities from space geodesy. J. Geophys. Res. Solid Earth 107, ETG 11-1-ETG 11-30. doi:10.1029/2000JB000033

Sengoku, A., 1998. A plate motion study using Ajisai SLR data. Earth, Planets Sp. 50, 611–627. doi:10.1186/BF03352156

Serpelloni, E., Faccenna, C., Spada, G., Dong, D., Williams, S.D.P., 2013. Vertical GPS ground motion rates in the Euro - Mediterranean region : New evidence of velocity gradients at different spatial scales along the Nubia - Eurasia plate boundary GPS ground motion rates in the Euro - Mediterranean region : New evidence of velo. J . Geophys . Res . Solid Earth 118. doi:10.1002/2013JB010102

Seya, H., Yamagata, Y., Tsutsumi, M., 2013. Automatic selection of a spatial weight matrix in spatial econometrics: Application to a spatial hedonic approach. Reg. Sci. Urban

Econ. 43, 429–444. doi:10.1016/j.regsciurbeco.2013.02.002

Shearer, P.M., 2013. Introduction to Seismology. Cambridge University Press.

Shen, C., Li, C., Si, Y., 2016. Spatio-temporal autocorrelation measures for nonstationary series: A new temporally detrended spatio-temporal Moran's index. Phys. Lett. Sect. A Gen. At. Solid State Phys. 380, 106–116. doi:10.1016/j.physleta.2015.09.039

Shepard, D., 1968. A two-dimensional interpolation function for irregularly-spaced data, in: Proceedings of the 1968 23rd ACM National Conference On -. ACM Press, New York, New York, USA, pp. 517–524. doi:10.1145/800186.810616

Sherwood, S.C., Roca, R., Weckwerth, T.M., Andronova, N.G., 2010. Tropospheric water vapor, convection, and climate. Rev. Geophys. 48, RG2001. doi:10.1029/2009RG000301

Shigueo, O., Junior, O., 2012. Spatio-Temporal Prediction Methods Spatio-Temporal Prediction Methods.

Shimada, S., Bock, Y., 1992. Crustal deformation measurements in central Japan determined by a Global Positioning System Fixed-Point Network. J. Geophys. Res. 97, 12437. doi:10.1029/92JB00809

Smith, D.E., Kolenkiewicz, R., Dunn, P.J., Robbins, J.W., Torrence, M.H., Klosko, S.M., Williamson, R.G., Pavlis, E.C., Douglas, N.B., Fricke, S.K., 1990. Tectonic Motion and Deformation From Satellite Laser Ranging to LAGEOS. J. Geophys. Res. 95, 22013–22041. doi:10.1029/JB095iB13p22013

Song, M., Wang, S., Wu, J., Yang, L., 2011. A new space-time correlation coefficient and its comparison with Moran's Index on evaluation. Manag. Decis. 49, 1426–1443. doi:10.1108/00251741111173925

Soundy, A.W.R., Panckhurst, B.J., Molteno, T.C.A., 2015. Enhanced noise models for GPS positioning, in: 2015 6th International Conference on Automation, Robotics and Applications (ICARA). IEEE, pp. 28–33. doi:10.1109/ICARA.2015.7081121

Stampfli, G.M., Borel, G.D., 2002. A plate tectonic model for the Paleozoic and Mesozoic constrained by dynamic plate boundaries and restored synthetic oceanic isochrons. Earth Planet. Sci. Lett. 196, 17–33. doi:10.1016/S0012-821X(01)00588-X

Stocker, T., Qin, D., Plattner, G.-K., Tignor, M., Allen, S.K., Boschung, J., Nauels, A., Xia, Y., Bex, V., Midgley, P.M., 2014. Climate change 2013 : the physical science basis : Working Group I contribution to the Fifth assessment report of the Intergovernmental Panel on Climate Change.

Stockwell, D.R.., Peterson, A.T., 2002. Effects of sample size on accuracy of species distribution models. Ecol. Modell. 148, 1–13. doi:10.1016/S0304-3800(01)00388-X

Suarez, G., Novelo, D., Mansilla, E., 2009. Performance Evaluation of the Seismic Alert System (SAS) in Mexico City: A Seismological and a Social Perspective. Seismol. Res. Lett. 80, 707–716. doi:10.1785/gssrl.80.5.707

Tanikawara, M., Kubo, Y., Sugimoto, S., 2010. Modeling of Sensor Error Equations for Gps/Ins Hybrid Systems. Int. J. Innov. Comput. Inf. Control 6, 127–138.

Teferle, F.N., Bingley, R.M., Williams, S.D.P., Baker, T.F., Dodson, A.H., 2006. Using continuous GPS and absolute gravity to separate vertical land movements and changes in sea-level at tide-gauges in the UK. Philos. Trans. A. Math. Phys. Eng. Sci. 364, 917–930. doi:10.1098/rsta.2006.1746

Teferle, F.N., Williams, S.D.P., Kierulf, H.P., Bingley, R.M., Plag, H.-P.P., 2008. A continuous GPS coordinate time series analysis strategy for high-accuracy vertical land movements. Phys. Chem. Earth 33, 205–216. doi:10.1016/j.pce.2006.11.002

Teunissen, P.J.G., Odolinski, R., Odijk, D., 2014. Instantaneous BeiDou+GPS RTK positioning with high cut-off elevation angles. J. Geod. 88, 335–350. doi:10.1007/s00190-013-0686-4

Thanos, S., Dubé, J., Legros, D., 2016. Putting Time into Space: The Temporal Coherence of Spatial Applications in the Housing Market. Reg. Sci. Urban Econ.

doi:10.1016/j.regsciurbeco.2016.03.001

Tian, Y., Shen, Z.K., 2016. Extracting the regional common-mode component of GPS station position time series from dense continuous network. J. Geophys. Res. Solid Earth 121, 1080–1096. doi:10.1002/2015JB012253

Titov, V., Kânoğlu, U., Synolakis, C., 2016. Development of MOST for Real-Time Tsunami Forecasting. J. Waterw. Port, Coastal, Ocean Eng. 142, 03116004. doi:10.1061/(ASCE)WW.1943-5460.0000357

Tobler, W.R., 1970. A Computer Movie Simulation Urban Growth in Detroit Region. Econ. Geogr. 46, 234–240. doi:10.1126/science.11.277.620

Tomáš Bacigál, I., 2004. Multivariate Threshold Autoregressive Models in Geodesy. ISCAM.

Tomassini, M., Gendt, G., Dick, G., Ramatschi, M., Schraff, C., 2002. Monitoring of integrated water vapour from ground-based GPS observations and their assimilation in a limited-area NWP model. Phys. Chem. Earth 27, 341–346. doi:10.1016/S1474-7065(02)00010-4

Tong, X., Sandwell, D.T., Schmidt, D.A., 2018. Surface Creep Rate and Moment Accumulation Rate Along the Aceh Segment of the Sumatran Fault From L-band ALOS-1/PALSAR-1 Observations. Geophys. Res. Lett. 45, 3404–3412. doi:10.1002/2017GL076723

Tregoning, P., Watson, C., Ramillien, G., McQueen, H., Zhang, J., 2009. Detecting hydrologic deformation using GRACE and GPS. Geophys. Res. Lett. 36, n/a-n/a. doi:10.1029/2009GL038718

Tsugawa, T., Kotake, N., Otsuka, Y., Saito, A., 2007. Medium-scale traveling ionospheric disturbances observed by GPS receiver network in Japan: A short review. GPS Solut. 11, 139–144. doi:10.1007/s10291-006-0045-5

Tsugawa, T., Saito, A., Otsuka, Y., 2004. A statistical study of large-scale traveling ionospheric disturbances using the GPS network in Japan. J. Geophys. Res. Sp. Phys.

109, A06302. doi:10.1029/2003JA010302

Tsuji, H., Hatanaka, Y., Sagiya, T., Hashimoto, M., 1995. Coseismic crustal deformation from the 1994 Hokkaido-Toho-Oki Earthquake Monitored by a nationwide continuous GPS array in Japan. Geophys. Res. Lett. 22, 1669–1672. doi:10.1029/95GL01659

Uyeda, S., Miyashiro, A., 1974. Plate tectonics and the Japanese Islands: A synthesis. Bull. Geol. Soc. Am. 85, 1159–1170. doi:10.1130/0016-7606(1974)85<1159:PTATJI>2.0.CO;2

Wang, J.J., Wang, J., Sinclair, D., Watts, L., 2007. Neural network aided Kalman filtering for integrated GPS/INS geo-referencing platform, in: Proc. 5th Int. Symp. Mobile Mapping Technol. pp. 1–6.

Wang, T., Wei, S., Shi, X., Qiu, Q., Li, L., Peng, D., Weldon, R.J., Barbot, S., 2018. The 2016 Kaikōura earthquake: Simultaneous rupture of the subduction interface and overlying faults. Earth Planet. Sci. Lett. 482, 44–51. doi:10.1016/J.EPSL.2017.10.056

Wdowinski, S., Bock, Y., Zhang, J., Fang, P., Genrich, J., 1997. Southern California permanent GPS geodetic array: Spatial filtering of daily positions for estimating coseismic and postseismic displacements induced by the 1992 Landers earthquake. J. Geophys. Res. 102, 18057. doi:10.1029/97JB01378

Weissel, J.K., Hayes, D.E., Herron, E.M., 1977. Plate tectonics synthesis: The displacements between Australia, New Zealand, and Antarctica since the Late Cretaceous. Mar. Geol. 25, 231–277. doi:10.1016/0025-3227(77)90054-8

Wernick, M.N., Yang, Y., Brankov, J.G., Yourganov, G., Strother, S.C., 2010. Machine Learning in Medical Imaging. IEEE Signal Process. Mag. 27, 25–38. doi:10.1109/MSP.2010.936730

Wielgosz, P., Kashani, I., Grejner-Brzezinska, D., 2005. Analysis of long-range network RTK during a severe ionospheric storm. J. Geod. 79, 524–531. doi:10.1007/s00190-005-0003-y

Wilgan, K., Hurter, F., Geiger, A., Rohm, W., Bosy, J., 2017. Tropospheric refractivity and zenith path delays from least-squares collocation of meteorological and GNSS data. J. Geod. 91, 117–134. doi:10.1007/s00190-016-0942-5

Williams, S.D.P., 2008. CATS: GPS coordinate time series analysis software. GPS Solut. 12, 147–153. doi:10.1007/s10291-007-0086-4

Williams, S.D.P., 2004. Error analysis of continuous GPS position time series. J. Geophys. Res. 109, B03412. doi:10.1029/2003JB002741

Williams, S.D.P., 2003a. The effect of coloured noise on the uncertainties of rates estimated from geodetic time series. J. Geod. 76, 483–494. doi:10.1007/s00190-002-0283-4

Williams, S.D.P., 2003b. Offsets in Global Positioning System time series. J. Geophys. Res. 108, 16743. doi:10.1029/2002JB002156

Williams, S.D.P., Penna, N.T., 2011. Non-tidal ocean loading effects on geodetic GPS heights. Geophys. Res. Lett. 38, n/a-n/a. doi:10.1029/2011GL046940

Wright, T.J., Houlié, N., Hildyard, M., Iwabuchi, T., 2012. Real-time, reliable magnitudes for large earthquakes from 1 Hz GPS precise point positioning: The 2011 Tohoku-Oki (Japan) earthquake. Geophys. Res. Lett. 39, n/a-n/a. doi:10.1029/2012GL051894

Xiong, Y.X.Y., Yeung, D.-Y.Y.D.-Y., 2002. Mixtures of ARMA models for model-based time series clustering. 2002 IEEE Int. Conf. Data Mining, 2002. Proceedings. 717–720. doi:10.1109/ICDM.2002.1184037

Xu, L., Guo, J.J., Jiang, J.J., 2002. TIME}FREQUENCY ANALYSIS OF A SUSPENSION BRIDGE BASED ON GPS. J. Sound <ibration 254, 105–116. doi:10.1006

Yao, X., Fu, B., Lü, Y., Sun, F., Wang, S., Liu, M., 2013. Comparison of four spatial interpolation methods for estimating soil moisture in a complex terrain catchment. PLoS One 8, e54660. doi:10.1371/journal.pone.0054660

Yu, Y., Gao, S.S., Liu, K.H., Yang, T., Xue, M., Le, K.P., Gao, J., 2018. Characteristics of the Mantle Flow System Beneath the Indochina Peninsula Revealed by Teleseismic Shear Wave Splitting Analysis. Geochemistry, Geophys. Geosystems 19, 1519–1532. doi:10.1029/2018GC007474

Zhang, G.P., 2007. A neural network ensemble method with jittered training data for time series forecasting. Inf. Sci. (Ny). 177, 5329–5346. doi:10.1016/j.ins.2007.06.015

Zhang, J., Bock, Y., Johnson, H., Fang, P., Williams, S.D.P., Genrich, J., Wdowinski, S., Behr, J., 1997. Southern California Permanent GPS Geodetic Array. Error Analysis of Daily Position Estimates and Sites Velocities. J. Geophys. Res. 102, 18035–18055. doi:10.1029/97JB01380

Zhang, X.F., Van Eijkeren, J.C.H., Heemink, A.W., 1995. On the weighted least-squares method for fitting a semivariogram model. Comput. Geosci. 21, 605–608. doi:10.1016/0098-3004(94)00099-G

Zhao, S., Cui, X., Guan, F., Lu, M., 2014. A kalman filter-based short baseline RTK algorithm for single-frequency combination of GPS and BDS. Sensors (Switzerland) 14, 15415–15433. doi:10.3390/s140815415

Zhou, C., Yin, K., Cao, Y., Ahmed, B., Fu, X., 2018. A novel method for landslide displacement prediction by integrating advanced computational intelligence algorithms. Sci. Rep. 8, 7287. doi:10.1038/s41598-018-25567-6

Zimmerman, D.L., Zimmerman, M.B., 1991. A comparison of spatial semivariogram estimators and corresponding ordinary kriging predictors. Technometrics 33, 77–91. doi:10.1080/00401706.1991.10484771

Zinkevich, M., Weimer, M., Li, L., Smola, A.J., Alex, S., Weimer, M., Li, L., 2010. Parallelized Stochastic Gradient Descent. Adv. Neural Inf. Process. Syst. 23 2595–2603. doi:10.1088/0741-3335/38/11/011

APPENDIX A

Validation of the 2nd step of the algorithm.

To validate that the 2nd step of the algorithm (Figure 5-1) agrees with CATS outcomes, the offset magnitude and linear trend estimations and their uncertainties using both CATS software (provided by BIGF) and the 1st method are compared in the tables below, along with the differences (CATS minus 1st) in the estimates and their corresponding uncertainties (columns K-O).

Table A-1 ΔN component offsets and trends. CATS results vs the implementation of the 1st offset correction approach.

	CATS					1st approach					The difference (CATS – 1st approach)				
	(A)	(B)	(C)	(D)	(E)	(F)	(G)	(H)	(I)	(J)	(K)	(L)	(M)	(N)	(O)
	Offset#1	Offset#2	Offset#3	Offset#4	Trend	Offset#1	Offset#2	Offset#3	Offset#4	Trend	Offset#1	Offset#2	Offset#3	Offset#4	Trend
ABER	0.28±0.43	1.22±0.19	2.86±0.21	5.31±0.21	15.12±0.11	-0.09±0.3	1.23±0.13	2.88±0.13	5.33±0.12	15.12±0.15	0.37±0.52	-0.01±0.23	-0.02±0.25	-0.02±0.24	0±0.19
ABYW	2.49±0.15	-9.72±0.16	-2.99±0.21		16.86±0.06	2.49±0.1	-9.72±0.09	-2.99±0.13		16.86±0.12	0±0.18	0±0.19	0±0.25		0±0.14
AMER	-2.42±0.12				16.29±0.08	-2.42±0.09				16.29±0.16	0±0.15				0±0.18
ANLX	-6.13±0.13				16.4±0.1	-6.13±0.1				16.4±0.18	0±0.16				0±0.21
APPL	14.2±0.14	-4.26±0.15			16.62±0.09	14.2±0.09	-4.26±0.09			16.62±0.17	0±0.16	0±0.18			0±0.19
ASAP	-2.07±0.13				16.51±0.09	-2.07±0.09				16.51±0.17	0±0.16				0±0.19
ATTL	6.78±0.12				16.19±0.11	6.76±0.09				16.19±0.18	0.02±0.15				0±0.21
BARR	-1.97±0.23	-4.93±0.12			16.65±0.12	-2.25±0.18	-4.93±0.09			16.65±0.2	0.28±0.29	0±0.15			0±0.23
BEES	0.29±0.18				14.89±0.21	0.29±0.13				14.89±0.26	0±0.22				0±0.33
BELF	0.4±0.12				16.52±0.08	0.4±0.09				16.52±0.15	0±0.15				0±0.17
BLAP	-0.46±0.13				15.91±0.09	-0.44±0.09				15.91±0.14	-0.02±0.16				0±0.17
BRAE	0.17±0.16				16.71±0.13	0.17±0.11				16.71±0.23	0±0.2				0±0.27
BREC	-3.05±0.16				16.52±0.12	-3.05±0.11				16.52±0.22	0±0.2				0±0.25
BUCK	-0.9±0.13				16.5±0.12	-0.9±0.1				16.51±0.19	0±0.16				0±0.23

	CATS					1st approach					The difference (CATS – 1st approach)				
	(A)	(B)	(C)	(D)	(E)	(F)	(G)	(H)	(I)	(J)	(K)	(L)	(M)	(N)	(O)
	Offset#1	Offset#2	Offset#3	Offset#4	Trend	Offset#1	Offset#2	Offset#3	Offset#4	Trend	Offset#1	Offset#2	Offset#3	Offset#4	Trend
CAML	-18.6±0.19				15.51±0.19	-18.65±0.13				15.5±0.3	0.05±0.23				0±0.36
CARI	14.59±0.13				16.43±0.08	14.59±0.09				16.43±0.16	0±0.16				0±0.18
CARL	0.43±0.12	1.48±0.12			16.46±0.06	0.48±0.08	1.47±0.09			16.46±0.12	-0.05±0.15	0.01±0.15			0±0.13
CLAW	-11.38±0.11	-15.31±0.12			15.96±0.09	-11.38±0.08	-15.31±0.09			15.96±0.15	0±0.14	0±0.15			0±0.17
DARE	1.74±0.12	-4.09±0.12			16.54±0.06	1.78±0.08	-4.1±0.09			16.54±0.12	-0.04±0.15	0.01±0.15			0±0.14
DROW	6.6±0.12				16.59±0.09	6.6±0.09				16.59±0.17	0±0.15				0±0.19
DRUM	1.63±0.12				16.49±0.08	1.63±0.09				16.49±0.15	0±0.15				0±0.17
DUNG	0.01±0.12				16.11±0.08	0.01±0.09				16.11±0.15	0±0.15				0±0.17
DUNK	0.72±0.66	0.13±0.3	-0.21±0.16		16.28±0.09	0.44±0.86	0.14±0.19	-0.22±0.11		16.28±0.18	0.28±1.09	-0.01±0.36	0.01±0.2		0±0.2
EASN	0.94±0.11				16.14±0.08	0.94±0.08				16.14±0.14	0±0.14				0±0.16
EDIN	0.1±0.12	2.72±0.13			16.63±0.06	0.14±0.08	2.72±0.09			16.63±0.12	-0.04±0.15	0±0.16			0±0.14
ESKD	-1.04±0.14	0.47±0.14	-0.37±0.23	0.46±0.23	16.23±0.11	-1.04±0.09	0.47±0.1	-0.37±0.1	0.46±0.1	16.23±0.18	0±0.17	0±0.17	0±0.25	0±0.25	0±0.21
EXMO	-7.68±0.16	0.36±0.16	0.03±0.16	1.33±0.16	16.34±0.1	-7.69±0.1	0.36±0.11	0.03±0.1	1.31±0.1	16.34±0.19	0.01±0.19	0±0.19	0±0.19	0.02±0.19	-0.01±0.21
FARB	-1.82±0.13				16.86±0.1	-1.82±0.09				16.86±0.17	0±0.16				0±0.19
FAUG	-7.39±0.14				16.75±0.12	-7.41±0.1				16.75±0.23	0.02±0.17				0±0.26
GIGG	1.08±0.13				16.31±0.09	1.08±0.1				16.31±0.17	0±0.16				0±0.19
GIRA	-9.96±0.11				16.61±0.08	-9.96±0.08				16.61±0.15	0±0.14				0±0.17
GLAS	0.51±0.13	-0.11±0.13			16.84±0.07	0.55±0.09	-0.11±0.09			16.85±0.13	-0.04±0.16	0±0.16			0±0.15
GORS	-9.23±0.12				16.37±0.09	-9.24±0.09				16.37±0.17	0.01±0.15				0±0.19
HARD	-4.27±0.14				16.16±0.1	-4.27±0.1				16.16±0.18	0±0.17				0±0.2
HELS	7.79±0.15				16.13±0.14	7.75±0.11				16.13±0.24	0.04±0.18				0±0.28
HERT	3.19±0.13				16.34±0.09	3.19±0.1				16.34±0.16	0±0.16				0±0.19
HOLY	-9.62±0.12				16.6±0.09	-9.61±0.09				16.59±0.16	-0.01±0.15				0±0.18
HOOB	-5.06±0.12				15.77±0.08	-5.06±0.09				15.77±0.15	0±0.15				0±0.17
INVR	-16.8±0.12				16.75±0.06	-16.81±0.09				16.75±0.13	0.01±0.15				0±0.14
KELO	-3.6±0.12	1.58±0.13			16.49±0.09	-3.6±0.09	1.57±0.1			16.49±0.17	0±0.15	0.01±0.16			0±0.2
KEYW	-5.69±0.12				15.94±0.11	-5.72±0.09				15.94±0.2	0.03±0.15				0±0.23

	CATS					1st approach					The difference (CATS – 1st approach)				
	(A)	(B)	(C)	(D)	(E)	(F)	(G)	(H)	(I)	(J)	(K)	(L)	(M)	(N)	(O)
	Offset#1	Offset#2	Offset#3	Offset#4	Trend	Offset#1	Offset#2	Offset#3	Offset#4	Trend	Offset#1	Offset#2	Offset#3	Offset#4	Trend
KILN	-4.67±0.15				16.31±0.1	-4.67±0.11				16.31±0.2	0±0.18				0±0.22
KING	1.27±0.18	0.12±0.18	-5.45±0.12		16.18±0.06	1.27±0.07	0.12±0.07	-5.44±0.08		16.18±0.12	0±0.19	0±0.19	-0.01±0.15		0±0.14
KINL	0.41±0.13				16.14±0.13	0.37±0.1				16.14±0.21	0.04±0.16				0±0.25
KIRK	-5.38±0.12				15.44±0.1	-5.38±0.09				15.44±0.17	0±0.15				0±0.2
KIRW	0.18±0.11				16.76±0.11	0.15±0.09				16.76±0.19	0.03±0.14				0±0.22
KLRE	9.84±0.14				16.7±0.07	9.84±0.1				16.7±0.15	0±0.17				0±0.17
LEED	1.36±0.21	-0.02±0.21	-0.99±0.12		16.27±0.06	1.37±0.07	-0.03±0.08	-0.99±0.09		16.27±0.12	-0.01±0.22	0.01±0.22	0±0.15		0±0.14
LEEK	-6.65±0.12				16.43±0.08	-6.65±0.09				16.43±0.15	0±0.15				0±0.17
LICF	-9.5±0.12				16.49±0.08	-9.49±0.09				16.49±0.14	-0.01±0.15				0±0.16
LINO	4.47±0.11				16.22±0.08	4.47±0.08				16.22±0.14	0±0.14				0±0.16
LOCG	0.39±0.14				16.57±0.12	0.39±0.1				16.57±0.19	0±0.17				0±0.22
LOFT	2.01±0.12				16.39±0.09	2.01±0.09				16.39±0.17	0±0.15				0±0.19
MACY	-6.7±0.15				16.48±0.12	-6.7±0.11				16.47±0.22	0±0.18				0±0.25
MART	-7.24±0.13	4.54±0.15			16.53±0.08	-7.25±0.09	4.53±0.11			16.53±0.16	0.01±0.16	0.01±0.18			0±0.18
MORP	-8.27±0.28	-3.32±0.18			17.09±0.18	-8.2±0.19	-3.32±0.12			16.79±0.25	-0.07±0.34	0±0.22			0.3±0.3
NCAS	-0.53±0.12				16.36±0.07	-0.53±0.09				16.36±0.13	0±0.15				0±0.14
NEWL	-7.06±0.17	-1.15±0.16	-18.25±0.13		16.72±0.08	-7.03±0.1	-1.14±0.09	-18.23±0.09		16.71±0.13	-0.03±0.2	-0.01±0.19	-0.02±0.16		0.01±0.16
OMGH	3.77±0.15				16.6±0.09	3.77±0.1				16.6±0.16	0±0.18				0±0.18
OXFR	-3.94±0.12				16.37±0.09	-3.94±0.09				16.37±0.16	0±0.15				0±0.18
PBIL	-26.88±0.15				15.41±0.13	-26.87±0.11				15.4±0.19	-0.01±0.18				0±0.23
PETE	-4.43±0.11				16.31±0.07	-4.43±0.08				16.31±0.14	0±0.14				0±0.16
PMTG	2.55±0.16				16.63±0.12	2.55±0.11				16.62±0.17	0±0.2				0±0.21
PMTH	-1.08±0.13				16.4±0.08	-1.08±0.09				16.4±0.16	0±0.16				0±0.18
POOL	-4.85±0.13				16.11±0.09	-4.85±0.09				16.11±0.16	0±0.16				0±0.19
PRAE	3.02±0.13				15.95±0.11	3.02±0.1				15.95±0.19	0±0.16				0±0.22
RICM	-9.06±0.12				16.28±0.08	-9.05±0.09				16.27±0.15	-0.01±0.15				0±0.17
SABB	-12.05±0.13				16.57±0.11	-12.06±0.1				16.57±0.17	0.01±0.16				0±0.2

	CATS					1st approach					The difference (CATS – 1st approach)				
	(A)	(B)	(C)	(D)	(E)	(F)	(G)	(H)	(I)	(J)	(K)	(L)	(M)	(N)	(O)
	Offset#1	Offset#2	Offset#3	Offset#4	Trend	Offset#1	Offset#2	Offset#3	Offset#4	Trend	Offset#1	Offset#2	Offset#3	Offset#4	Trend
SANO	-1.43±0.16				15.75±0.14	-1.43±0.11				15.75±0.21	0±0.2				0±0.26
SCAO	-23.84±0.15				14.98±0.13	-23.82±0.11				14.97±0.18	-0.02±0.19				0.01±0.22
SHOB	2.01±0.13				16.73±0.1	2.01±0.09				16.73±0.18	0±0.16				0±0.2
SHOE	-4.1±0.11				16.16±0.09	-4.08±0.08				16.17±0.17	-0.02±0.14				0±0.19
SHRE	-7.35±0.12				16.58±0.08	-7.35±0.09				16.58±0.15	0±0.15				0±0.17
SKEE	-2.99±0.11				16.29±0.1	-2.99±0.08				16.29±0.17	0±0.14				0±0.19
STEE	-10.98±0.13	0.16±0.14	-0.37±0.14		16.12±0.09	-10.98±0.09	0.15±0.1	-0.39±0.09		16.13±0.17	0±0.16	0.01±0.17	0.02±0.17		-0.01±0.19
SWAN	1.81±0.12				16.29±0.08	1.8±0.09				16.29±0.15	0.01±0.15				0±0.17
SWTG	7.29±0.15				16.98±0.1	7.28±0.09				16.98±0.16	0.01±0.18				0±0.19
TAUT	-4.75±0.15				16.62±0.12	-4.75±0.11				16.62±0.2	0±0.18				0±0.23
TEDD	-	-	-	-	-	-	-	-	-	-	-	-	-	-	-
THUS	-4.2±0.11				16.7±0.11	-4.22±0.09				16.7±0.19	0.02±0.14				0±0.21
WARS	3392.54±0.24	-1.42±0.24	23.48±0.15		16.06±0.11	3392.53±0.1	-1.42±0.1	23.48±0.1		16.06±0.19	0.01±0.26	0±0.26	0±0.18		0±0.22
WATT	-	-	-	-	-	-	-	-	-	-	-	-	-	-	-
WEAR	-0.88±0.17				16.38±0.13	-0.88±0.12				16.38±0.22	0±0.21				0±0.26
WEIW	0.24±0.14				16.21±0.1	0.24±0.1				16.21±0.17	0±0.17				0±0.2
WELL	-4.05±0.12				16.17±0.11	-4.06±0.09				16.17±0.18	0.01±0.15				0±0.21
WEYB	-1.58±0.12				15.96±0.08	-1.58±0.09				15.96±0.15	0±0.15				0±0.17
YEAS	9.01±0.12				16.32±0.08	9.01±0.09				16.32±0.14	0±0.15				0±0

Table A-2 ΔE component offsets and trends. CATS results vs the implementation of the 1st offset correction approach.

	CATS					1st approach					The difference (CATS – 1st approach)				
	(A)	(B)	(C)	(D)	(E)	(F)	(G)	(H)	(I)	(J)	(K)	(L)	(M)	(N)	(O)
	Offset#1	Offset#2	Offset#3	Offset#4	Trend	Offset#1	Offset#2	Offset#3	Offset#4	Trend	Offset#1	Offset#2	Offset#3	Offset#4	Trend
ABER	0.03±0.42	1.17±0.19	1.18±0.21	8.82±0.2	14.67±0.11	0.48±0.29	1.16±0.12	1.16±0.13	8.8±0.11	14.68±0.12	-0.45±0.51	0.01±0.23	0.02±0.25	0.02±0.23	0±0.16
ABYW	1.58±0.16	-19.11±0.18	-10.63±0.24		16.68±0.09	1.59±0.11	-19.08±0.1	-10.61±0.14		16.68±0.1	-0.01±0.19	-0.03±0.21	-0.02±0.28		0.01±0.14
AMER	-0.85±0.12				17.01±0.09	-0.85±0.08				17.01±0.11	0±0.14				0±0.14
ANLX	11.09±0.14				15.91±0.12	11.09±0.09				15.91±0.14	0±0.17				0±0.18
APPL	12.02±0.14	0.21±0.15			16.96±0.1	12.02±0.08	0.2±0.08			16.96±0.12	0±0.16	0.01±0.17			0±0.15
ASAP	-0.73±0.15				15.53±0.12	-0.73±0.1				15.53±0.14	0±0.18				0±0.19
ATTL	-2.44±0.12				17.01±0.11	-2.46±0.08				17.01±0.14	0.02±0.14				0±0.18
BARR	5.09±0.24	-0.9±0.13			13.51±0.12	4.79±0.16	-0.9±0.08			13.51±0.15	0.3±0.29	0±0.15			0±0.19
BEES	12.87±0.16				14±0.17	12.86±0.11				14±0.18	0.01±0.2				0±0.25
BELF	-4.69±0.17				14.74±0.14	-4.69±0.12				14.74±0.16	0±0.21				0±0.21
BLAP	1.76±0.12				15.6±0.08	1.76±0.08				15.6±0.09	0±0.14				0±0.13
BRAE	0.02±0.14				14.51±0.11	0.02±0.09				14.51±0.15	0±0.17				0±0.18
BREC	1.04±0.13				16.22±0.11	1.04±0.09				16.22±0.14	0±0.16				0±0.17
BUCK	0.58±0.13				14.43±0.12	0.59±0.09				14.43±0.14	-0.01±0.16				0±0.19
CAML	-39.68±0.16				13.72±0.17	-39.73±0.11				13.72±0.19	0.05±0.19				0±0.26
CARI	3.94±0.15				16.09±0.13	3.94±0.1				16.09±0.15	0±0.18				0±0.2
CARL	0.36±0.12	3.02±0.12			15.35±0.06	0.35±0.07	3.02±0.07			15.35±0.08	0.01±0.14	0±0.14			0±0.1
CLAW	-0.79±0.11	-0.85±0.12			16.82±0.08	-0.78±0.07	-0.86±0.08			16.82±0.1	-0.01±0.13	0.01±0.14			0±0.13
DARE	-0.94±0.12	-3.68±0.12			15.97±0.07	-0.95±0.07	-3.68±0.07			15.97±0.08	0.01±0.14	0±0.14			0±0.11
DROW	-1.64±0.13				16.24±0.11	-1.64±0.08				16.24±0.13	0±0.16				0±0.17
DRUM	1.04±0.12				15.03±0.1	1.04±0.08				15.03±0.12	0±0.15				0±0.15
DUNG	-9.56±0.12				17.73±0.09	-9.57±0.08				17.73±0.11	0.01±0.14				0±0.14
DUNK	-2.48±0.66	0.03±0.3	-0.19±0.16		16.65±0.1	-2.83±0.78	0.03±0.18	-0.19±0.1		16.65±0.13	0.35±1.02	0±0.35	0±0.19		0±0.16
EASN	-3.39±0.12				16.43±0.09	-3.4±0.08				16.44±0.11	0.01±0.14				0±0.14
EDIN	-0.14±0.11	2.37±0.12			14.85±0.06	-0.11±0.07	2.37±0.07			14.85±0.08	-0.03±0.13	. 0±014			0±0.1

	CATS					1st approach					The difference (CATS – 1st approach)				
	(A)	(B)	(C)	(D)	(E)	(F)	(G)	(H)	(I)	(J)	(K)	(L)	(M)	(N)	(O)
	Offset#1	Offset#2	Offset#3	Offset#4	Trend	Offset#1	Offset#2	Offset#3	Offset#4	Trend	Offset#1	Offset#2	Offset#3	Offset#4	Trend
ESKD	1.91±0.17	1.48±0.16	-0.21±0.27	0±0.27	15.03±0.12	1.91±0.1	1.48±0.11	-0.21±0.11	0±0.11	15.04±0.16	0±0.2	0±0.19	0±0.29	0±0.29	0±0.2
EXMO	-4.96±0.17	1.23±0.16	1.12±0.17	0.05±0.17	16.52±0.11	-4.97±0.1	1.22±0.1	1.11±0.1	0.03±0.09	16.53±0.14	0.01±0.2	0.01±0.19	0.01±0.2	0.02±0.19	-0.01±0.18
FARB	-3.34±0.14				17.18±0.11	-3.36±0.09				17.19±0.13	0.02±0.17				-0.01±0.17
FAUG	0.13±0.14				13.96±0.12	0.09±0.09				13.96±0.17	0.04±0.17				0±0.21
GIGG	4.83±0.14				15.88±0.11	4.83±0.1				15.88±0.13	0±0.17				0±0.17
GIRA	-5.95±0.13				14.76±0.1	-5.95±0.09				14.75±0.13	0±0.16				0±0.16
GLAS	-1±0.12	0.06±0.12			14.54±0.06	-0.98±0.07	0.07±0.08			14.54±0.08	-0.02±0.14	-0.01±0.14			0±0.11
GORS	-4.83±0.12				17±0.09	-4.83±0.08				17±0.12	0±0.14				0±0.15
HARD	-2.65±0.12				17±0.09	-2.67±0.08				17.01±0.11	0.02±0.15				-0.01±0.15
HELS	-10.81±0.15				13.68±0.16	-10.88±0.1				13.68±0.18	0.07±0.18				0±0.24
HERT	1.33±0.15				16.67±0.13	1.33±0.11				16.67±0.14	0±0.18				0±0.19
HOLY	-3.52±0.12				15.61±0.1	-3.52±0.08				15.61±0.12	0±0.15				0±0.15
HOOB	4.8±0.13				15.66±0.1	4.8±0.09				15.66±0.12	0±0.16				0±0.15
INVR	-5.83±0.11				14.2±0.07	-5.79±0.08				14.2±0.09	-0.04±0.14				0.01±0.11
KELO	8.46±0.13	-1.65±0.15			15.18±0.12	8.46±0.09	-1.65±0.1			15.18±0.14	0±0.16	0±0.18			0±0.18
KEYW	-7.59±0.12				16.41±0.12	-7.64±0.08				16.41±0.14	0.05±0.15				0±0.19
KILN	-0.84±0.15				14.54±0.12	-0.85±0.1				14.55±0.16	0.01±0.18				0±0.19
KING	1.36±0.17	-1.49±0.17	-10.12±0.11		16.87±0.07	1.35±0.06	-1.48±0.06	-10.11±0.07		16.87±0.08	0.01±0.18	-0.01±0.18	-0.01±0.13		0±0.11
KINL	5±0.13				13.6±0.12	4.95±0.08				13.6±0.15	0.05±0.15				0±0.19
KIRK	0.15±0.13				14.87±0.12	0.15±0.09				14.87±0.14	0±0.16				0±0.19
KIRW	5.21±0.12				13.67±0.12	5.16±0.08				13.66±0.14	0.05±0.14				0±0.18
KLRE	-1.53±0.15				14.16±0.09	-1.53±0.09				14.16±0.11	0±0.18				0±0.15
LEED	1.36±0.2	-1.17±0.2	-5.82±0.11		16.08±0.06	1.35±0.06	-1.16±0.06	-5.81±0.07		16.08±0.08	0.01±0.21	-0.01±0.21	-0.01±0.13		0±0.1
LEEK	-0.28±0.14				16±0.12	-0.29±0.09				16.01±0.13	0.01±0.17				-0.01±0.17
LICF	3.68±0.13				16.43±0.1	3.67±0.09				16.44±0.12	0.01±0.16				0±0.15
LINO	3.95±0.12				16.44±0.09	3.94±0.08				16.45±0.11	0.01±0.14				0±0.14
LOCG	-1.43±0.15				14.62±0.13	-1.43±0.11				14.62±0.15	0±0.18				0±0.2

	CATS					1st approach					The difference (CATS – 1st approach)				
	(A)	(B)	(C)	(D)	(E)	(F)	(G)	(H)	(I)	(J)	(K)	(L)	(M)	(N)	(O)
	Offset#1	Offset#2	Offset#3	Offset#4	Trend	Offset#1	Offset#2	Offset#3	Offset#4	Trend	Offset#1	Offset#2	Offset#3	Offset#4	Trend
LOFT	-0.72±0.13				17.63±0.11	-0.72±0.08				17.63±0.13	0±0.15				0±0.17
MACY	-2.09±0.14				16.1±0.12	-2.09±0.1				16.1±0.15	0±0.17				0±0.19
MART	-0.5±0.13	-6.35±0.14			17.17±0.08	-0.51±0.08	-6.36±0.09			17.17±0.11	0.01±0.15	0.01±0.17			0±0.13
MORP	-2.92±0.21	-0.14±0.14			15.31±0.11	-2.68±0.14	-0.14±0.09			15.3±0.13	-0.24±0.25	0±0.16			0.01±0.17
NCAS	0.03±0.12				15.19±0.08	0.06±0.08				15.19±0.09	-0.03±0.15				0±0.12
NEWL	-2.74±0.15	0.01±0.14	-7.7±0.11		15.67±0.07	-2.76±0.08	0.08	-7.72±0.07		15.68±0.09	0.02±0.17	0.01±0.16	0.02±0.13		0±0.11
OMGH	-1.69±0.14				14.22±0.08	-1.69±0.08				14.22±0.11	0±0.16				0±0.13
OXFR	-5.99±0.12				17.35±0.1	-5.99±0.08				17.35±0.12	0±0.14				0±0.15
PBIL	-194.86±0.12				17.09±0.1	-194.87±0.08				17.1±0.12	0.01±0.14				0±0.15
PETE	0.23±0.12				16.63±0.09	0.23±0.08				16.63±0.1	0±0.14				0±0.13
PMTG	0.59±0.15				17.21±0.12	0.59±0.1				17.21±0.13	0±0.18				0±0.17
PMTH	-4.52±0.13				16.38±0.09	-4.52±0.09				16.38±0.11	0±0.16				0±0.15
POOL	-0.61±0.13				16.99±0.11	-0.62±0.09				16.99±0.12	0.01±0.16				0±0.16
PRAE	14.21±0.13				16.57±0.12	14.21±0.09				16.58±0.14	0±0.16				0±0.18
RICM	8.31±0.13				15.9±0.09	8.3±0.08				15.9±0.11	0.01±0.15				0±0.15
SABB	-12.04±0.13				16.14±0.11	-12.05±0.09				16.15±0.12	0.01±0.16				0±0.16
SANO	0.85±0.14				16.44±0.12	0.85±0.09				16.43±0.14	0±0.17				0±0.18
SCAO	-7.84±0.13				16.82±0.1	-7.85±0.09				16.82±0.11	0.01±0.16				0±0.14
SHOB	-2.04±0.14				15.87±0.12	-2.04±0.09				15.87±0.14	0±0.17				0±0.18
SHOE	2.77±0.12				17.4±0.1	2.79±0.08				17.41±0.13	-0.02±0.14				0±0.16
SHRE	4.71±0.13				16.14±0.1	4.71±0.09				16.15±0.12	0±0.16				0±0.15
SKEE	-7.49±0.12				17.25±0.11	-7.49±0.08				17.25±0.13	0±0.14				0±0.17
STEE	3.32±0.13	1.89±0.13	0.8±0.13		16.61±0.09	3.33±0.08	1.9±0.08	0.81±0.08		16.6±0.11	-0.01±0.15	-0.01±0.15	-0.01±0.15		0.01±0.15
SWAN	-0.48±0.12				16.31±0.09	-0.49±0.08				16.32±0.11	0.01±0.14				0±0.14
SWTG	3.82±0.17				14.15±0.12	3.85±0.09				14.14±0.13	-0.03±0.19				0.01±0.18
TAUT	-0.76±0.13				16.56±0.1	-0.77±0.09				16.56±0.12	0.01±0.16				0±0.16
TEDD	-	-	-	-	-	-	-	-	-	-	-	-	-	-	-

	CATS					1st approach					The difference (CATS – 1st approach)				
	(A)	(B)	(C)	(D)	(E)	(F)	(G)	(H)	(I)	(J)	(K)	(L)	(M)	(N)	(O)
	Offset#1	Offset#2	Offset#3	Offset#4	Trend	Offset#1	Offset#2	Offset#3	Offset#4	Trend	Offset#1	Offset#2	Offset#3	Offset#4	Trend
THUS	-0.08±0.12				13.52±0.11	-0.11±0.08				13.52±0.14	0.03±0.14				0±0.18
WARS	-45.28±0.24	-1.57±0.23	133.22±0.15		16.66±0.12	-45.28±0.09	-1.58±0.1	133.22±0.09		16.67±0.14	0±0.26	0.01±0.25	0±0.17		0±0.18
WATT	-	-	-	-	-	-	-	-	-	-	-	-	-	-	-
WEAR	-4.54±0.16				15.6±0.12	-4.54±0.11				15.6±0.16	0±0.19				0±0.2
WEIW	2.59±0.12				16.91±0.08	2.58±0.08				16.91±0.11	0.01±0.14				0±0.13
WELL	-6.2±0.13				16.79±0.12	-6.22±0.08				16.79±0.14	0.02±0.15				0±0.19
WEYB	-5.03±0.12				16.82±0.08	-5.03±0.08				16.82±0.1	0±0.14				0±0.13
YEAS	4.61±0.12				16.14±0.09	4.61±0.08				16.14±0.11	0±0.15				0±0.01

Table A-3 ΔU component offsets and trends. CATS results vs the implementation of the 1st offset correction approach.

	CATS					*1st approach*					*The difference (CATS – 1st approach)*				
	(A)	*(B)*	*(C)*	*(D)*	*(E)*	*(F)*	*(G)*	*(H)*	*(I)*	*(J)*	*(K)*	*(L)*	*(M)*	*(N)*	*(O)*
	Offset#1	*Offset#2*	*Offset#3*	*Offset#4*	*Trend*	*Offset#1*	*Offset#2*	*Offset#3*	*Offset#4*	*Trend*	*Offset#1*	*Offset#2*	*Offset#3*	*Offset#4*	*Trend*
ABER	1.02±0.86	-2.07±0.39	1.85±0.43	-2.15±0.42	0.74±0.2	0.17±0.47	-2.05±0.2	1.89±0.21	-2.12±0.18	0.74±0.42	0.85±0.98	-0.02±0.44	-0.04±0.48	-0.03±0.46	0.01±0.46
ABYW	1.77±0.42	0.94±0.46	35.13±0.6		-0.87±0.2	1.76±0.22	0.91±0.21	35.12±0.3		-0.87±0.42	0.01±0.48	0.03±0.51	0.01±0.67		0±0.47
AMER	14.62±0.42				-0.75±0.34	14.6±0.24				-0.74±0.67	0.02±0.49				-0.01±0.75
ANLX	249.21±0.39				-0.84±0.3	249.21±0.21				-0.85±0.7	0±0.44				0.01±0.76
APPL	2.13±0.45	9.17±0.47			-0.52±0.3	2.09±0.21	9.2±0.22			-0.54±0.67	0.04±0.5	-0.03±0.52			0.01±0.73
ASAP	10.04±0.43				-0.33±0.36	10.07±0.25				-0.35±0.69	-0.03±0.5				0.02±0.78
ATTL	7.99±0.42				-1.02±0.42	8.03±0.24				-1.02±0.82	-0.04±0.48				0±0.93
BARR	-9.41±0.65	28.98±0.34			-0.34±0.33	-9.19±0.31	28.98±0.16			-0.34±0.8	-0.22±0.72	0±0.37			0±0.86
BEES	8.73±0.42				0.82±0.39	8.73±0.23				0.82±0.81	0±0.48				0±0.9
BELF	6.11±0.42				-0.1±0.3	6.11±0.23				-0.1±0.64	0±0.48				0±0.71
BLAP	26.51±0.36				0.11±0.26	26.6±0.2				0.09±0.52	-0.09±0.41				0.02±0.58
BRAE	10.4±0.41				1.09±0.38	10.4±0.23				1.08±0.74	0±0.47				0.01±0.83
BREC	10.37±0.4				-0.59±0.33	10.37±0.22				-0.59±0.71	0±0.46				0±0.78
BUCK	24.84±0.37				0.52±0.35	24.82±0.2				0.51±0.72	0.02±0.42				0.01±0.8
CAML	14.67±0.67				-3.08±0.92	14.64±0.44				-3.08±1.11	0.03±0.8				0±1.44
CARI	9.54±0.4				-1.07±0.29	9.59±0.22				-1.1±0.66	-0.05±0.46				0.02±0.72
CARL	-4.55±0.38	-3.3±0.38			0.55±0.23	-4.42±0.2	-3.32±0.2			0.55±0.47	-0.13±0.43	0.02±0.43			0±0.52
CLAW	493.6±0.38	11.52±0.41			-0.81±0.31	493.56±0.21	11.54±0.23			-0.81±0.65	0.04±0.43	-0.02±0.47			0.01±0.72
DARE	-2.05±0.38	12.69±0.37			-0.24±0.24	-1.99±0.2	12.69±0.2			-0.24±0.47	-0.06±0.43	0±0.42			0±0.53
DROW	14.15±0.4				-1.3±0.35	14.15±0.22				-1.31±0.71	0±0.46				0.01±0.79
DRUM	4.33±0.39				1.07±0.33	4.34±0.21				1.06±0.66	-0.01±0.44				0.01±0.74
DUNG	24.16±0.42				-1.36±0.31	24.14±0.24				-1.36±0.66	0.02±0.48				-0.01±0.73
DUNK	14.27±2.3	-1.11±1.06	2.75±0.57		-0.97±0.35	11.51±2.39	-1.11±0.54	2.75±0.32		-0.97±0.74	2.76±3.32	0±1.19	0±0.65		0±0.82
EASN	10.84±0.42				-0.52±0.33	10.86±0.24				-0.53±0.65	-0.02±0.48				0.01±0.73
EDIN	-2.76±0.35	-0.64±0.37			1.15±0.22	-2.71±0.18	-0.65±0.19			1.16±0.46	-0.05±0.39	0.01±0.42			0±0.51

	CATS					1st approach					The difference (CATS – 1st approach)				
	(A)	(B)	(C)	(D)	(E)	(F)	(G)	(H)	(I)	(J)	(K)	(L)	(M)	(N)	(O)
	Offset#1	Offset#2	Offset#3	Offset#4	Trend	Offset#1	Offset#2	Offset#3	Offset#4	Trend	Offset#1	Offset#2	Offset#3	Offset#4	Trend
ESKD	9.43±0.46	4.03±0.46	3.41±0.74	-3.18±0.75	0.7±0.37	9.45±0.22	4.08±0.24	3.41±0.24	-3.09±0.24	0.66±0.73	-0.02±0.51	-0.05±0.52	0±0.78	-0.09±0.79	0.03±0.82
EXMO	20.82±0.53	5.08±0.52	0.53	1.73±0.52	-1.78±0.36	20.83±0.26	5.09±0.28	0.01±0.27	1.75±0.25	-1.78±0.73	-0.01±0.59	-0.01±0.59	-0.01±0.6	-0.02±0.58	0.01±0.81
FARB	28.74±0.43				-1.94±0.33	28.73±0.24				-1.93±0.68	0.01±0.49				-0.01±0.75
FAUG	15.26±0.4				1.13±0.41	15.18±0.21				1.12±0.86	0.08±0.45				0±0.95
GIGG	10.68±0.4				-0.21±0.31	10.72±0.23				-0.22±0.64	-0.04±0.46				0.02±0.71
GIRA	-2.6±0.39				1.07±0.32	-2.6±0.21				1.06±0.67	0±0.44				0±0.74
GLAS	-2.65±0.37	10.12±0.38			0.66±0.23	-2.57±0.19	10.11±0.2			0.67±0.47	-0.08±0.42	0.01±0.43			0±0.52
GORS	22.84±0.42				-1.19±0.37	22.84±0.24				-1.19±0.72	0±0.48				0±0.81
HARD	19.87±0.41				-1.05±0.3	19.89±0.23				-1.05±0.65	-0.02±0.47				0.01±0.72
HELS	7.59±0.56				-1.48±0.72	7.54±0.35				-1.48±1.01	0.05±0.66				0±1.24
HERT	5.15±0.4				-0.38±0.29	5.16±0.23				-0.39±0.59	-0.01±0.46				0.01±0.66
HOLY	23.85±0.4				-0.4±0.33	23.9±0.22				-0.42±0.67	-0.05±0.46				0.02±0.75
HOOB	1.81±0.43				1.92±0.35	1.83±0.25				1.91±0.66	-0.02±0.5				0.01±0.75
INVR	-2.31±0.35				0.88±0.23	-2.36±0.2				0.89±0.47	0.05±0.4				-0.01±0.53
KELO	19.02±0.42	4.69±0.47			-0.61±0.4	19.03±0.22	4.66±0.26			-0.6±0.77	-0.01±0.48	0.03±0.53			-0.01±0.87
KEYW	13.1±0.42				-0.82±0.44	13.08±0.23				-0.82±0.88	0.02±0.48				0±0.98
KILN	4.45±0.45				1.29±0.35	4.45±0.26				1.28±0.73	0±0.52				0.01±0.81
KING	-1.44±0.56	1.59±0.56	2.17±0.37		-0.96±0.24	-1.47±0.17	1.61±0.17	2.2±0.19		-0.97±0.47	0.03±0.59	-0.02±0.59	-0.03±0.42		0.01±0.53
KINL	0.74±0.36				0.9±0.37	0.74±0.19				0.9±0.83	0±0.41				0±0.91
KIRK	10.89±0.39				-1.01±0.35	10.91±0.21				-1±0.72	-0.02±0.44				0±0.8
KIRW	9.56±0.38				0.11±0.42	9.55±0.2				0.1±0.84	0.01±0.43				0±0.94
KLRE	4.38±0.47				0.34±0.28	4.39±0.24				0.35±0.63	-0.01±0.53				0±0.69
LEED	-2.31±0.64	1.92±0.65	0.37		-0.35±0.23	-2.32±0.17	1.92±0.17	0.01±0.2		-0.35±0.47	0.01±0.66	0±0.67	-0.01±0.42		0±0.53
LEEK	1.42				-0.4±0.35	10.04±0.24				-0.41±0.66	-0.04±0.48				0.01±0.74
LICF	16.04±0.4				-0.61±0.3	16.06±0.22				-0.61±0.63	-0.02±0.45				0.01±0.7
LINO	14.86±0.4				-0.57±0.32	14.88±0.23				-0.58±0.64	-0.02±0.46				0.01±0.72
LOCG	26.99±0.46				-0.47±0.42	27±0.27				-0.48±0.73	-0.01±0.54				0.01±0.84

	CATS					1st approach					The difference (CATS – 1st approach)				
	(A)	(B)	(C)	(D)	(E)	(F)	(G)	(H)	(I)	(J)	(K)	(L)	(M)	(N)	(O)
	Offset#1	Offset#2	Offset#3	Offset#4	Trend	Offset#1	Offset#2	Offset#3	Offset#4	Trend	Offset#1	Offset#2	Offset#3	Offset#4	Trend
LOFT	14.34±0.41				-2.35±0.39	14.34±0.23				-2.35±0.74	0±0.47				0±0.83
MACY	3.76±0.42				-0.6±0.36	3.74±0.23				-0.61±0.74	0.02±0.48				0.01±0.83
MART	88.46±0.46	-15.09±0.51			-1.95±0.33	88.44±0.24	-15.11±0.27			-1.94±0.67	0.02±0.52	0.02±0.58			0±0.74
MORP	5.83±0.67	0.5±0.44			0.47±0.39	6.03±0.38	0.5±0.24			0.51±0.7	-0.2±0.77	0±0.5			-0.05±0.8
NCAS	-59.14±0.35				0.66±0.23	-59.15±0.2				0.66±0.47	0.01±0.4				0±0.53
NEWL	-3.02±0.4	-0.5±0.38	-6.44±0.31		-0.77±0.17	-2.99±0.18	-0.49±0.17	-6.42±0.16		-0.77±0.42	-0.03±0.44	-0.01±0.42	-0.02±0.35		0.01±0.45
OMGH	11.84±0.46				0.33±0.3	11.84±0.23				0.33±0.63	0±0.52				0±0.7
OXFR	14.6±0.4				-0.88±0.33	14.6±0.22				-0.88±0.68	0±0.46				0±0.76
PBIL	25.97±0.45				-2.73±0.39	26.02±0.27				-2.76±0.71	-0.05±0.52				0.02±0.8
PETE	22.08±0.4				-0.45±0.32	22.09±0.22				-0.46±0.64	-0.01±0.46				0±0.72
PMTG	0.66±0.37				-0.72±0.24	0.66±0.21				-0.72±0.52	0±0.42				0±0.57
PMTH	6.14±0.42				-0.85±0.3	6.17±0.24				-0.86±0.64	-0.03±0.48				0.01±0.71
POOL	13.77±0.42				-0.75±0.32	13.78±0.24				-0.75±0.68	-0.01±0.49				0±0.75
PRAE	79.79±0.4				-1.67±0.32	79.79±0.22				-1.68±0.72	0±0.46				0.01±0.79
RICM	14.47±0.41				-0.19±0.32	14.5±0.23				-0.2±0.64	-0.03±0.47				0.01±0.72
SABB	71.23±0.75				-5.99±0.82	71.31±0.5				-6.03±0.91	-0.08±0.9				0.04±1.23
SANO	32.12±0.42				-1.1±0.34	32.13±0.23				-1.1±0.7	-0.01±0.48				0.01±0.77
SCAO	25.23±0.42				-0.54±0.32	25.28±0.24				-0.55±0.59	-0.05±0.48				0.01±0.67
SHOB	7.87±0.42				-0.45±0.33	7.87±0.24				-0.45±0.71	0±0.48				0±0.78
SHOE	2.89±0.4				-0.93±0.36	2.89±0.22				-0.93±0.72	0±0.46				0±0.81
SHRE	14.78±0.41				-0.57±0.31	14.79±0.24				-0.58±0.65	-0.01±0.47				0.01±0.72
SKEE	30.69±0.41				-2.2±0.4	30.69±0.23				-2.2±0.76	0±0.47				0±0.86
STEE	19.42±0.45	-0.99±0.47	2.74±0.47		-1.02±0.34	19.43±0.23	-0.95±0.25	2.82±0.24		-1.05±0.7	-0.01±0.5	-0.04±0.53	-0.08±0.53		0.03±0.78
SWAN	13.95±0.42				-0.97±0.35	13.99±0.24				-0.98±0.66	-0.04±0.48				0.01±0.74
SWTG	-10.77±0.42				-0.04±0.29	-10.77±0.18				-0.04±0.66	0±0.46				0±0.72
TAUT	12.88±0.48				-0.69±0.4	12.88±0.29				-0.69±0.72	0±0.56				0±0.82
TEDD	-	-	-	-	-	-	-	-	-	-	-	-	-	-	-

	CATS					1st approach					The difference (CATS – 1st approach)				
	(A)	(B)	(C)	(D)	(E)	(F)	(G)	(H)	(I)	(J)	(K)	(L)	(M)	(N)	(O)
	Offset#1	Offset#2	Offset#3	Offset#4	Trend	Offset#1	Offset#2	Offset#3	Offset#4	Trend	Offset#1	Offset#2	Offset#3	Offset#4	Trend
THUS	9.31±0.38				0.45±0.4	9.2±0.19				0.44±0.82	0.11±0.43				0±0.91
WARS	1022.03±0.76	13.82±0.75	-505.36±0.49		-0.74±0.35	1021.98±0.25	14.05±0.26	-505.13±0.25		-0.82±0.72	0.05±0.8	-0.23±0.79	-0.23±0.55		0.07±0.81
WATT	-	-	-	-	-	-	-	-	-	-	-	-	-	-	-
WEAR	10.82±0.43				0.25±0.35	10.83±0.25				0.24±0.69	-0.01±0.5				0.01±0.77
WEIW	18.98±0.42				-1.09±0.3	19±0.24				-1.1±0.65	-0.02±0.48				0.01±0.72
WELL	15.05±0.4				-0.89±0.41	15.04±0.22				-0.89±0.8	0.01±0.46				0±0.9
WEYB	17.95±0.42				-1.18±0.34	17.95±0.24				-1.18±0.66	0±0.48				0±0.74
YEAS	9.26±0.43				-0.56±0.34	9.3±0.24				-0.57±0.65	-0.04±0.49				0.01±0.73

APPENDIX B

NAR-ANN evaluation

To evaluate the different architectures, the Normalised Mean Square Error (NMSE) and Root Mean Squared Error (RMSE) were determined using Equation 3-10 and Equation 3-11 for each NAR-ANN model for each station. Tables below show an averaged value of NMSE of the stations used in Chapters 6, 7 and 8.

Table B-1 the average value of the Normalised Mean Square Error (NMSE) of the 87 ΔN time series in the BIGF network of GPS stations in the British Isles case study using different ANN architectures (i.e. the number of layers , and the number of neurons in these layer

NO. OF NEURONS PER LAYER	TRAINING FUNCTION	(NMSE) TRAINING	(NMSE) TESTING	(RMSE) TRAINING (mm)	(RMSE) TESTING (mm)
1 LAYER * 5 NEURONS	LM	$6.06*10^{-08}$	$7.13*10^{-08}$	0.63	0.76
1 LAYER * 10 NEURONS	LM	$5.37*10^{-08}$	$6.37*10^{-08}$	0.59	0.68
2 LAYERS * 10 NEURONS	LM	$5.30*10^{-08}$	$6.44*10^{-08}$	0.59	0.66
2 LAYERS * 20 NEURONS	LM	$4.99*10^{-08}$	$6.73*10^{-08}$	0.51	0.71
1 LAYER * 5 NEURONS	BR	$5.18*10^{-08}$	$5.25*10^{-08}$	0.56	0.57
1 LAYER * 10 NEURONS	BR	$5.18*10^{-08}$	$5.20*10^{-08}$	0.57	0.58
2 LAYERS * 10 NEURONS	BR	$5.15*10^{-08}$	$5.18*10^{-08}$	0.54	0.56
2 LAYERS * 20 NEURONS	BR	$5.15*10^{-08}$	$5.20*10^{-08}$	0.54	0.59

Table B-2 same as Table A-4, but for ΔE time series.

NO. OF NEURONS PER LAYER	TRAINING FUNCTION	(NMSE) TRAINING	(NMSE) TESTING	(RMSE) TRAINING (mm)	(RMSE) TESTING (mm)
1 LAYER * 5 NEURONS	LM	$5.28*10^{-08}$	$7.27*10^{-08}$	0.86	0.94
1 LAYER * 10 NEURONS	LM	$5.57*10^{-08}$	$7.68*10^{-08}$	0.87	0.96
2 LAYERS * 10 NEURONS	LM	$4.37*10^{-08}$	$7.08*10^{-08}$	0.61	0.89
2 LAYERS * 20 NEURONS	LM	$4.65*10^{-08}$	$5.73*10^{-08}$	0.72	0.73
1 LAYER * 5 NEURONS	BR	$4.72*10^{-08}$	$5.65*10^{-08}$	0.76	0.70
1 LAYER * 10 NEURONS	BR	$4.09*10^{-08}$	$5.66*10^{-08}$	0.51	0.72
2 LAYERS * 10 NEURONS	BR	$3.72*10^{-08}$	$4.64*10^{-08}$	0.49	0.62
2 LAYERS * 20 NEURONS	BR	$3.72*10^{-08}$	$4.64*10^{-08}$	0.49	0.58

Table B-3 same as Table A-4, but for ΔU time series.

NO. OF NEURONS PER LAYER	TRAINING FUNCTION	(NMSE) TRAINING	(NMSE) TESTING	(RMSE) TRAINING (mm)	(RMSE) TESTING (mm)
1 LAYER * 5 NEURONS	LM	$5.30*10^{-07}$	$6.64*10^{-07}$	1.72	2.15
1 LAYER * 10 NEURONS	LM	$5.24*10^{-07}$	$2.86*10^{-06}$	1.67	9.05
2 LAYERS * 10 NEURONS	LM	$5.17*10^{-07}$	$9.90*10^{-07}$	1.68	3.14
2 LAYERS * 20 NEURONS	LM	$5.07*10^{-07}$	$6.95*10^{-07}$	1.61	2.22
1 LAYER * 5 NEURONS	BR	$5.17*10^{-07}$	$5.46*10^{-07}$	1.63	1.73
1 LAYER * 10 NEURONS	BR	$5.15*10^{-07}$	$5.39*10^{-07}$	1.63	1.72
2 LAYERS * 10 NEURONS	BR	$5.13*10^{-07}$	$5.21*10^{-07}$	1.66	1.69
2 LAYERS * 20 NEURONS	BR	$5.11*10^{-07}$	$5.21*10^{-07}$	1.64	1.68

Table B-4 the average value of the Normalised Mean Square Error (NMSE) of the 847 3D displaceme in the GEONET network of GPS stations using different ANN architectures (i.e. the number of layers , and the number of neurons in these layer

NO. OF NEURONS PER LAYER	TRAINING FUNCTION	(NMSE) TRAINING	(NMSE) TESTING	(RMSE) TRAINING (mm)	(RMSE) TESTING (mm)
1 LAYER * 5 NEURONS	LM	$3.10*10^{-5}$	$8.51*10^{-5}$	1.78	5.07
1 LAYER * 10 NEURONS	LM	$9.82*10^{-6}$	$5.11*10^{-5}$	0.59	3.04
2 LAYERS * 10 NEURONS	LM	$8.22*10^{-6}$	$8.76*10^{-6}$	0.56	0.57
2 LAYERS * 20 NEURONS	LM	$8.21*10^{-6}$	$8.39*10^{-6}$	0.53	0.55
1 LAYER * 5 NEURONS	BR	$8.17*10^{-6}$	$8.50*10^{-6}$	0.52	0.53
1 LAYER * 10 NEURONS	BR	$8.10*10^{-6}$	$8.51*10^{-6}$	0.47	0.52
2 LAYERS * 10 NEURONS	BR	$8.10*10^{-6}$	$8.50*10^{-6}$	0.48	0.51
2 LAYERS * 20 NEURONS	BR	$8.10*10^{-6}$	$8.51*10^{-6}$	0.49	0.53

Table B-5 the average value of the Normalised Mean Square Error (NMSE) of the 72 IWV time series in the BIGF network of GPS stations using different ANN architectures (i.e. the number of layers , and the number of neurons in these layer

NO. OF NEURONS PER LAYER	TRAINING FUNCTION	(NMSE) TRAINING	(NMSE) TESTING	(RMSE) TRAINING (kg.m-2)	(RMSE) TESTING (kg.m-2)
1 LAYER * 20 NEURONS	LM	$7.53*10^{-06}$	$3.20*10^{-05}$	3.11	13.05
1 LAYER * 30 NEURONS	LM	$9.02*10^{-07}$	$1.17*10^{-05}$	0.42	4.78
2 LAYERS * 20 NEURONS	LM	$7.91*10^{-07}$	$9.94*10^{-07}$	0.38	0.45
2 LAYERS * 30 NEURONS	LM	$6.48*10^{-07}$	$6.98*10^{-07}$	0.33	0.30
1 LAYER * 20 NEURONS	BR	$7.93*10^{-07}$	$9.82*10^{-07}$	0.35	0.41
1 LAYER * 30 NEURONS	BR	$5.73*10^{-07}$	$6.13*10^{-07}$	0.23	0.25
2 LAYERS * 20 NEURONS	BR	$4.93*10^{-07}$	$5.24*10^{-07}$	0.20	0.27
2 LAYERS * 30 NEURONS	BR	$4.91*10^{-07}$	$5.55*10^{-07}$	0.24	0.28

The overall performance of Bayesian Regularization is better than Levenberg-Marquardt as the latter seems to be more vulnerable to overfitting than the former. This can be noticed as the difference between the training dataset and testing dataset is larger using Levenberg-Marquardt.

When the Bayesian Regularization method is used, the different architectures gives close estimates of NMSE. However, a 2-layers network with 10 neurons per layer was found to be the most optimal for both case studies in Chapter 6 (Tables A-4 to A-7) and Chapter 7 (Tables A-8), while A 2-layers network with 20 neurons per layer was found to be the most optimal the third case study in Chapter 8 (Tables A-9).

APPENDIX C

The analysis of the long-term, daily GNSS coordinate time series of the BIGF network in the British Isles

The Figures below show the corrected displacement time series, the detrended and low-frequency time series, as well as the temporal, spatial and combined analysis residuals with their corresponding thresholds of each station.

ABER Station

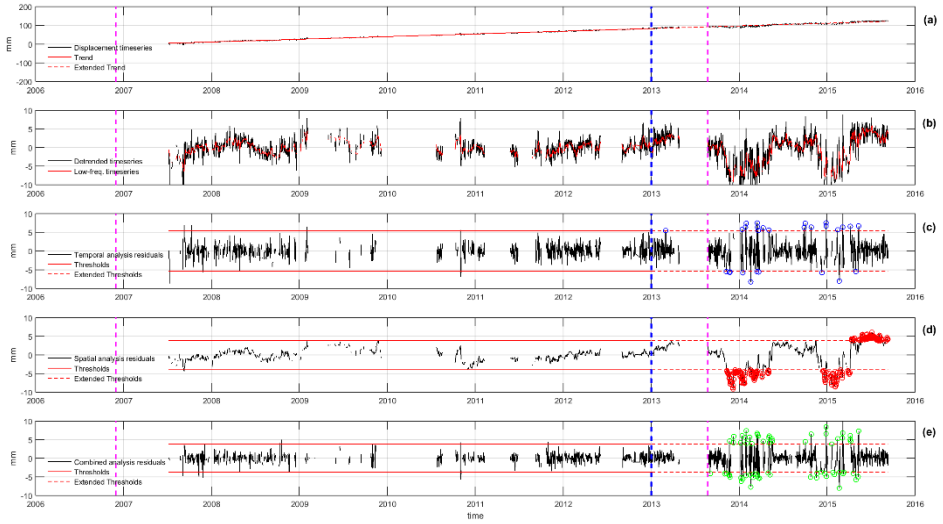


Figure C-1 ABER (ΔN) – (a) Corrected displacement time series, (b) detrended and low-frequency time series, the (c) Temporal, (d) Spatial and (e) combined analysis residuals.

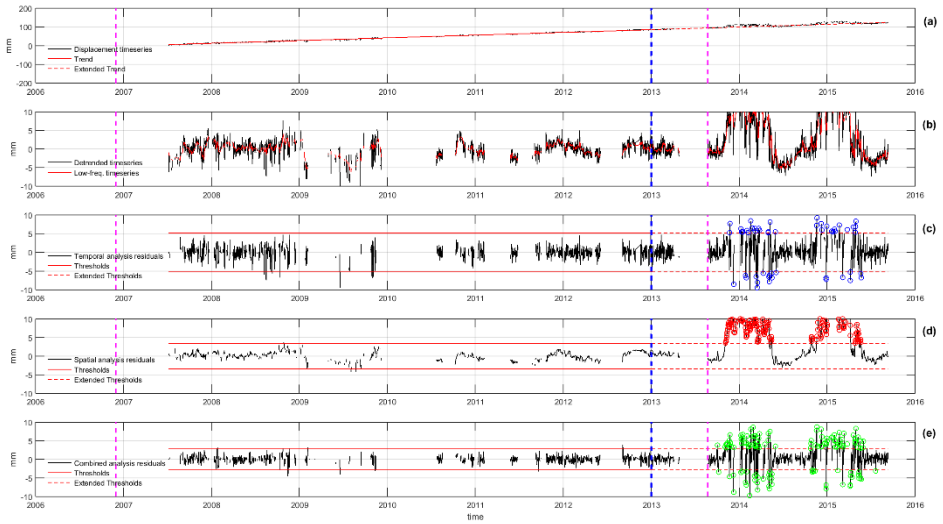


Figure C-2 Same as A-1, but for ABER (ΔE)

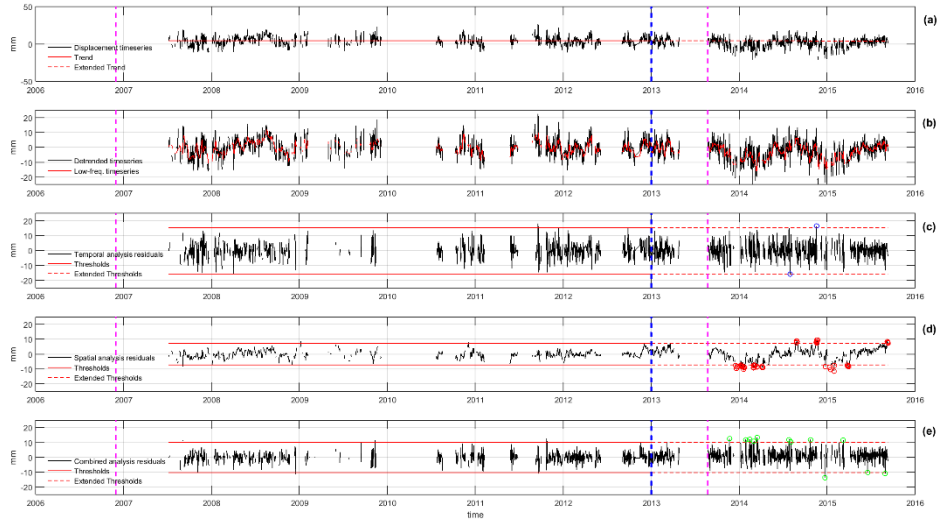


Figure C-3 Same as A-1, but for ABER (ΔU)

ABYW

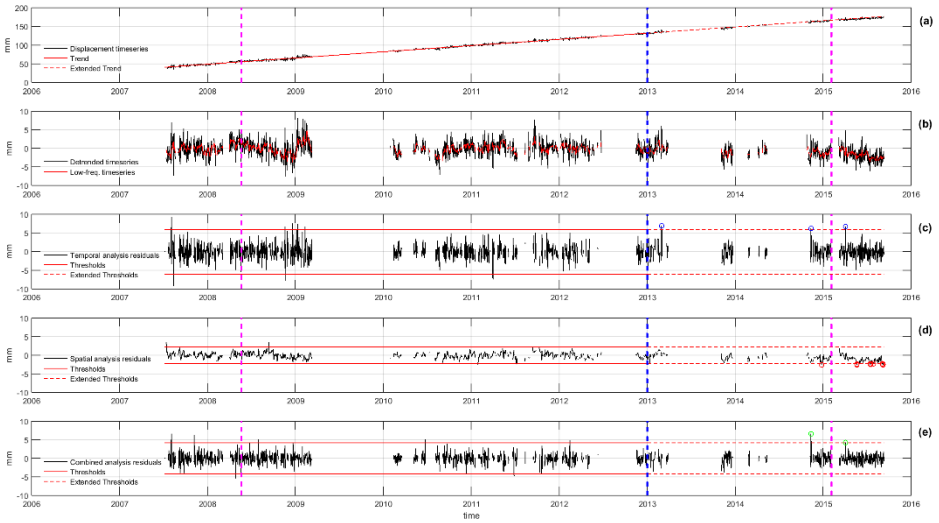


Figure C-4 ABYW (ΔN) – (a) Corrected displacement time series, (b) detrended and low-frequency time series, the (c) Temporal, (d) Spatial and (e) combined analysis residuals.

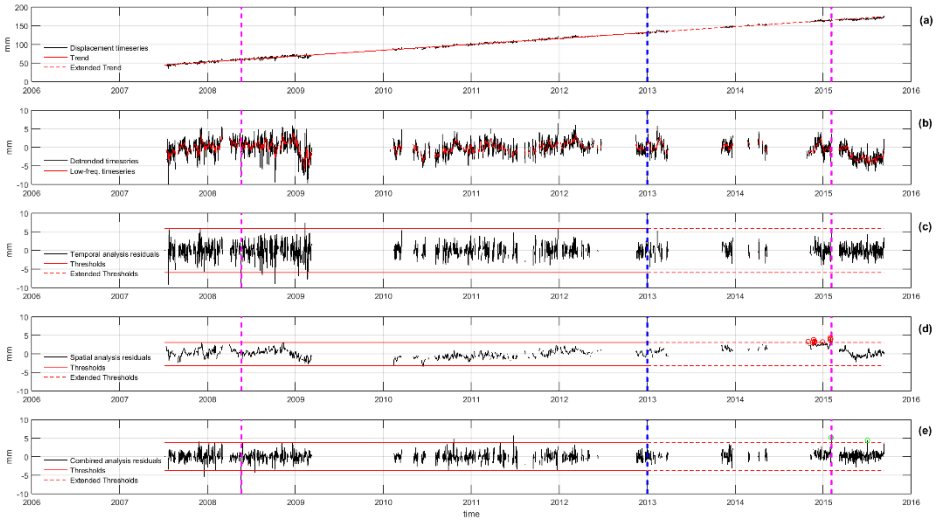


Figure C-5 Same as A-4, but for ΔE component

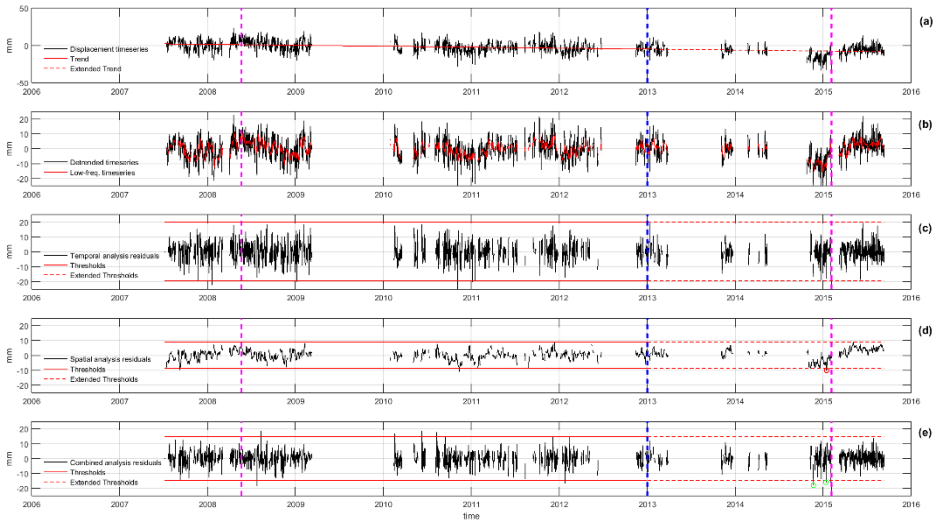


Figure C-6 Same as A-4, but for ΔU component

AMER

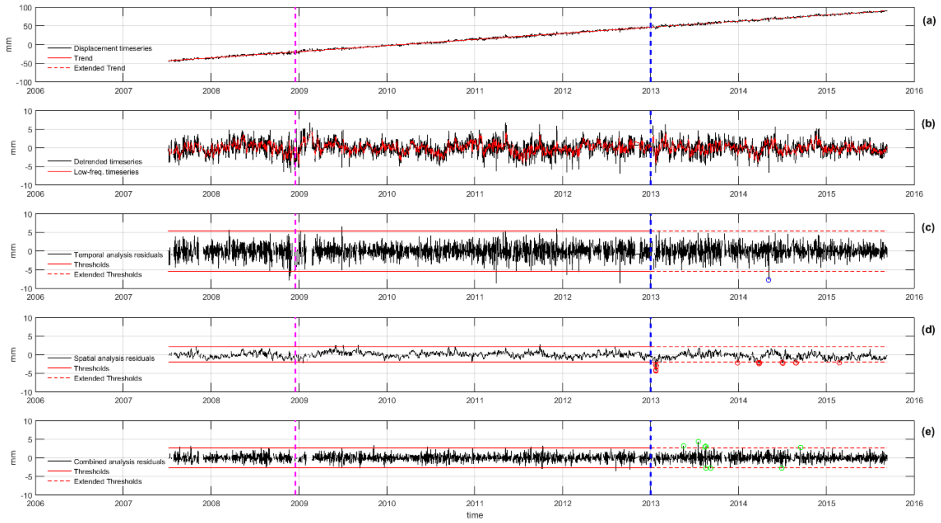


Figure C-7 AMER (ΔN) – (a) Corrected displacement time series, (b) detrended and low-frequency time series, the (c) Temporal, (d) Spatial and (e) combined analysis residuals.

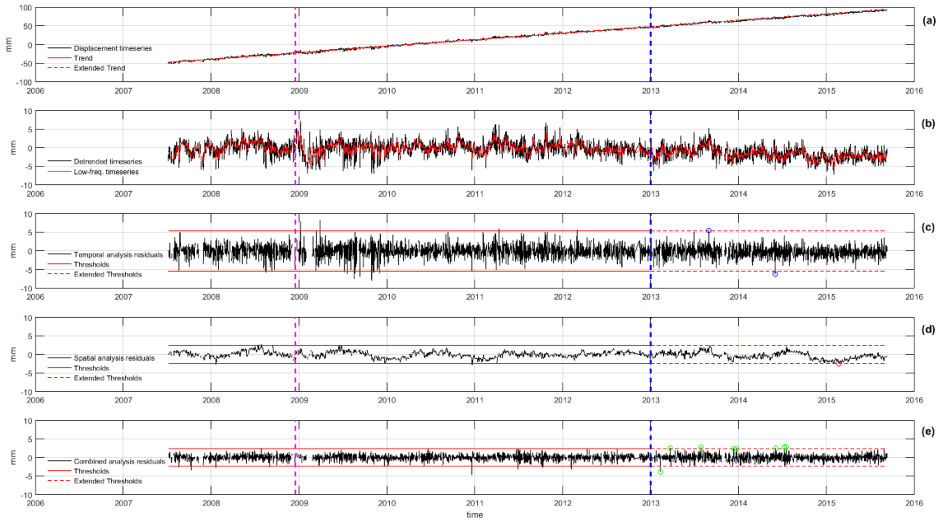


Figure C-8 Same as A-7, but for ΔE component

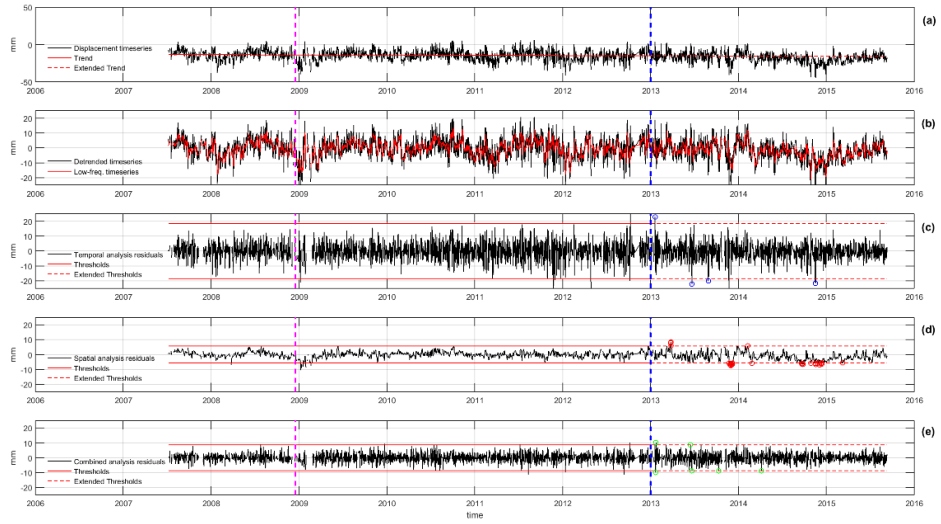


Figure C-9 Same as A-7, but for ΔU component

ANLX

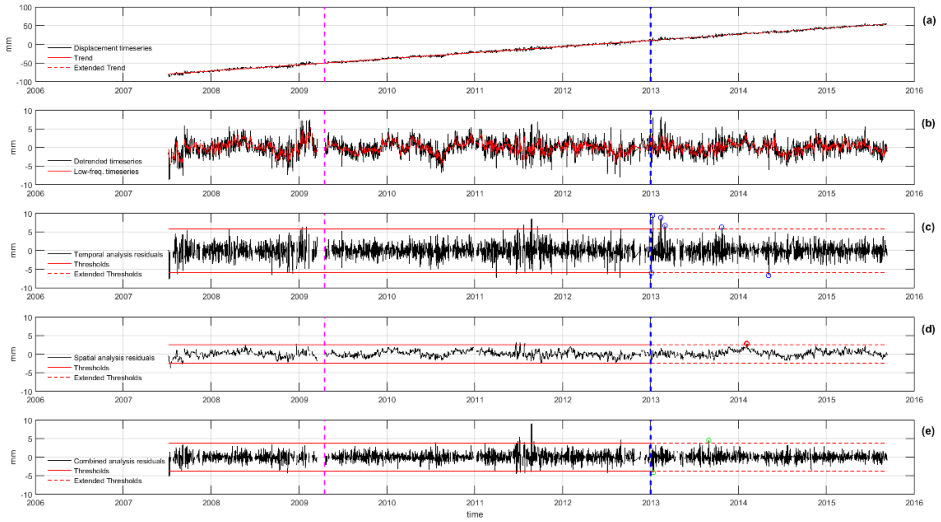


Figure C-10 ANLX (ΔN) – (a) Corrected displacement time series, (b) detrended and low-frequency time series, the (c) Temporal, (d) Spatial and (e) combined analysis residuals.

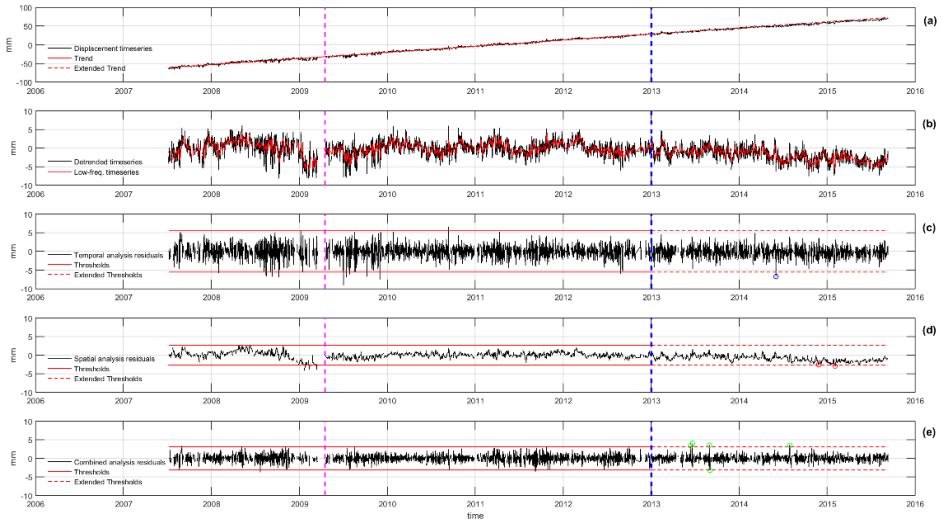


Figure C-11 Same as A-10, but for ΔE component

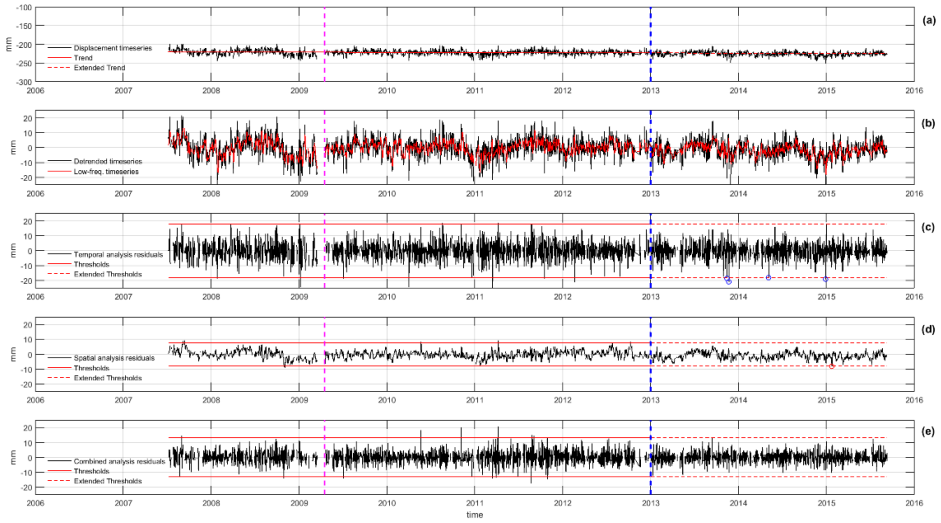


Figure C-12 Same as A-10, but for ΔU component

APPL

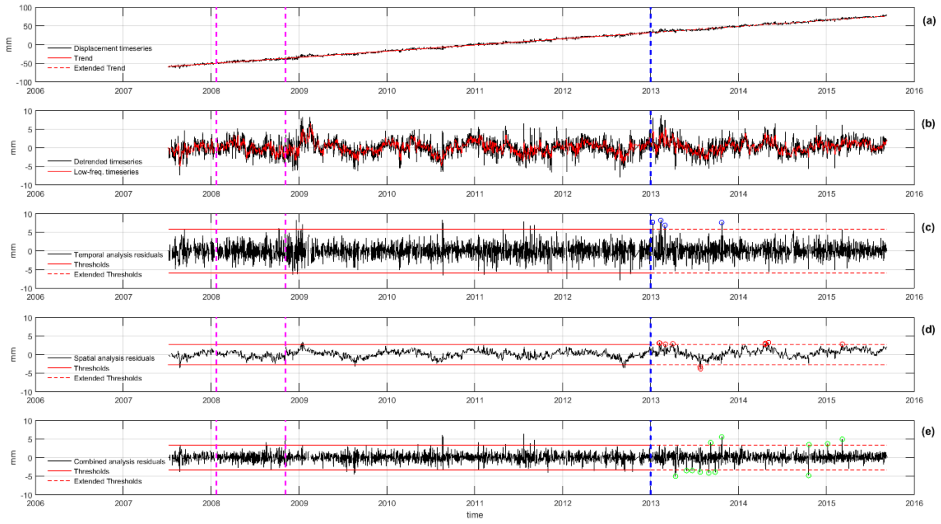


Figure C-13 APPL (ΔN) – (a) Corrected displacement time series, (b) detrended and low-frequency time series, the (c) Temporal, (d) Spatial and (e) combined analysis residuals.

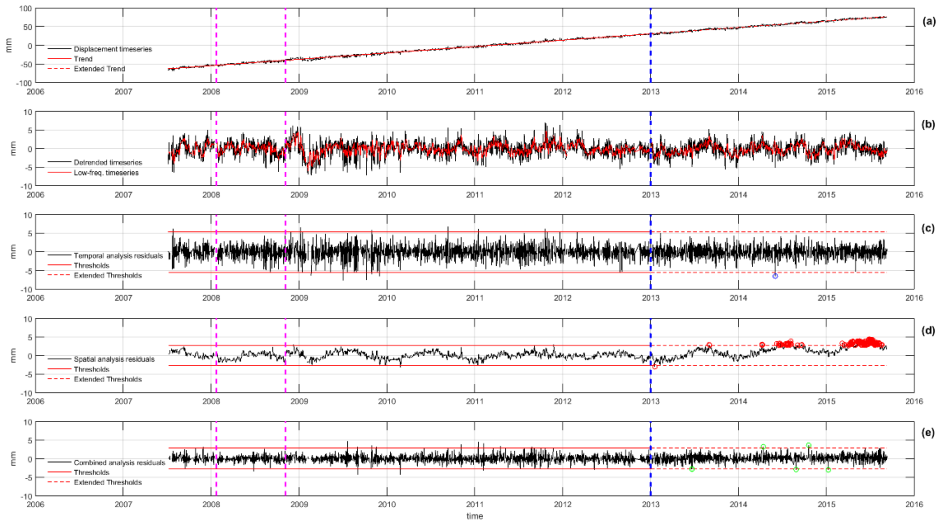


Figure C-14 Same as A-13, but for ΔE component

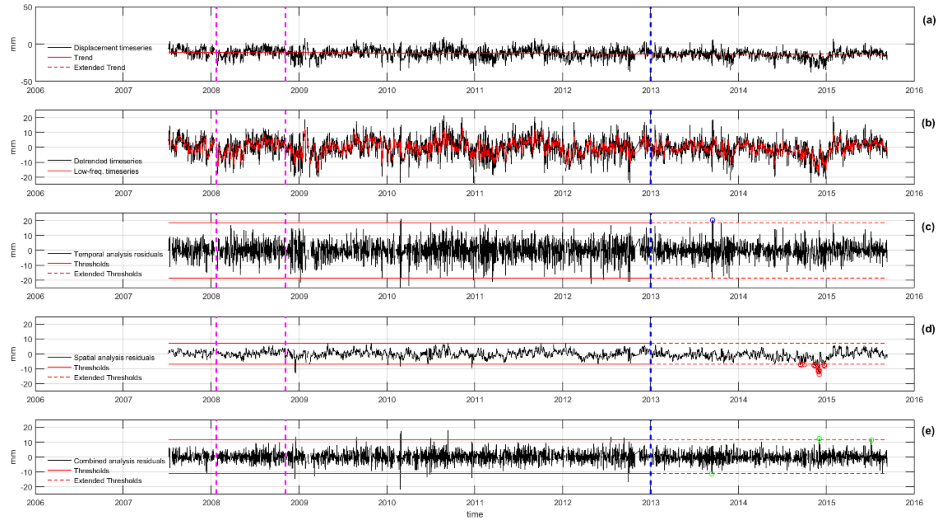


Figure C-15 Same as A-13, but for ΔU component

ASAP

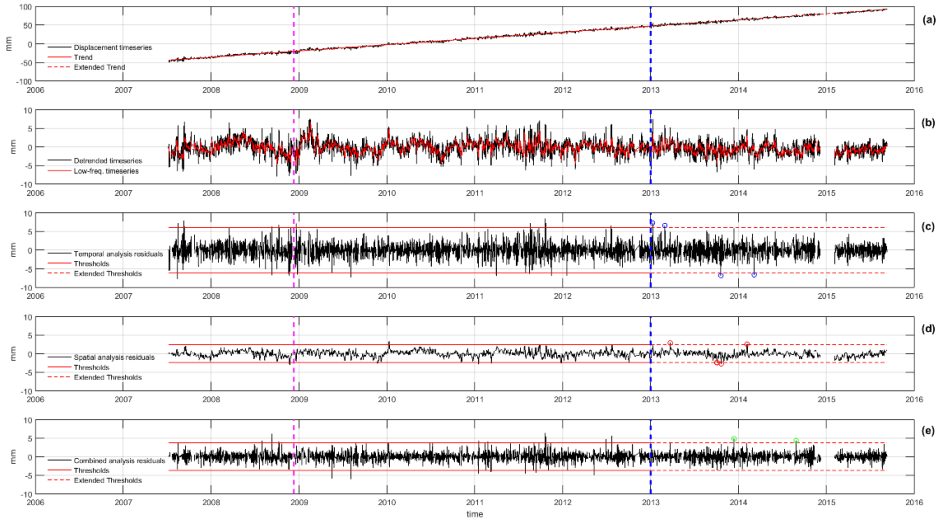


Figure C-16 ASAP (ΔN) – (a) Corrected displacement time series, (b) detrended and low-frequency time series, the (c) Temporal, (d) Spatial and (e) combined analysis residuals.

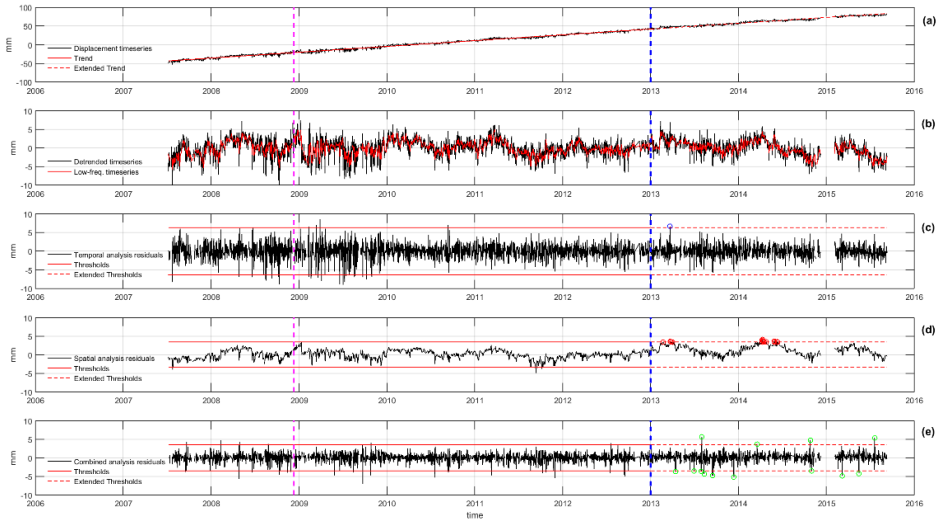


Figure C-17 Same as A-16, but for ΔE component

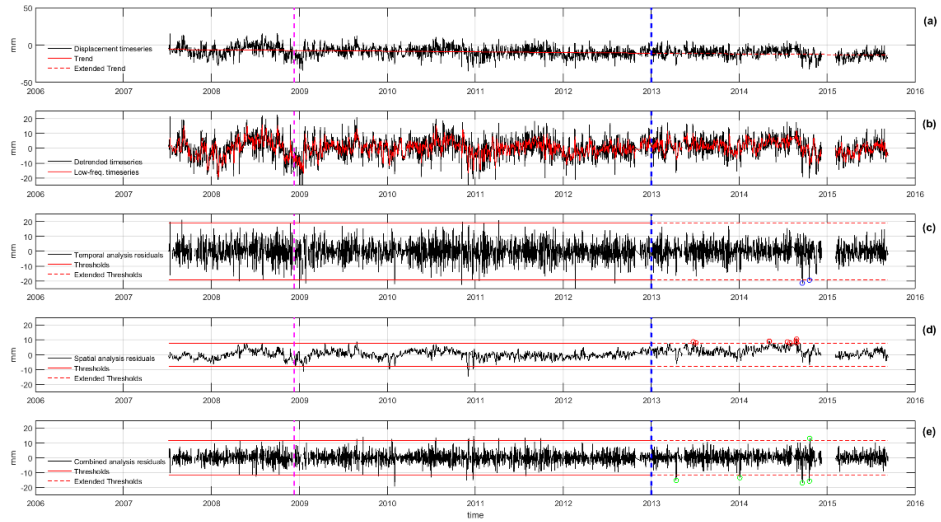


Figure C-18 Same as A-16, but for ΔU component

ATTL

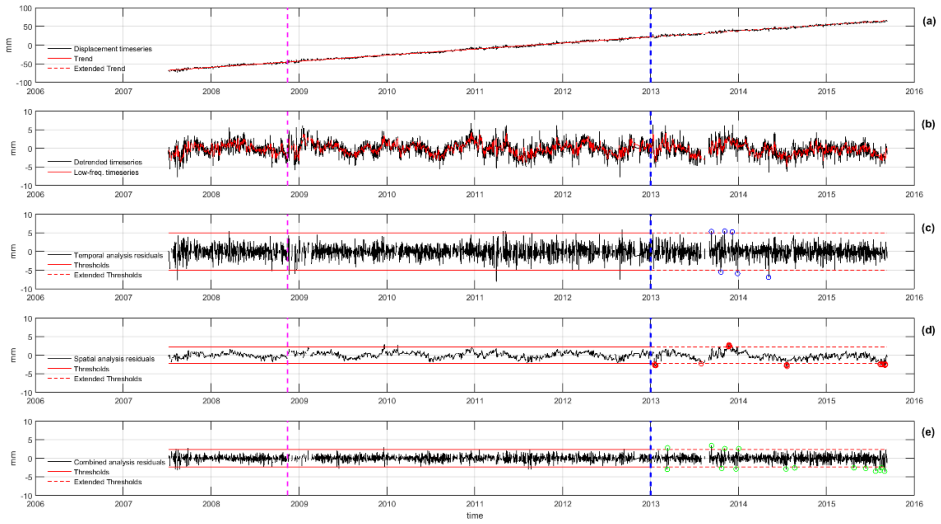


Figure C-19 ATTL (ΔN) – (a) Corrected displacement time series, (b) detrended and low-frequency time series, the (c) Temporal, (d) Spatial and (e) combined analysis residuals.

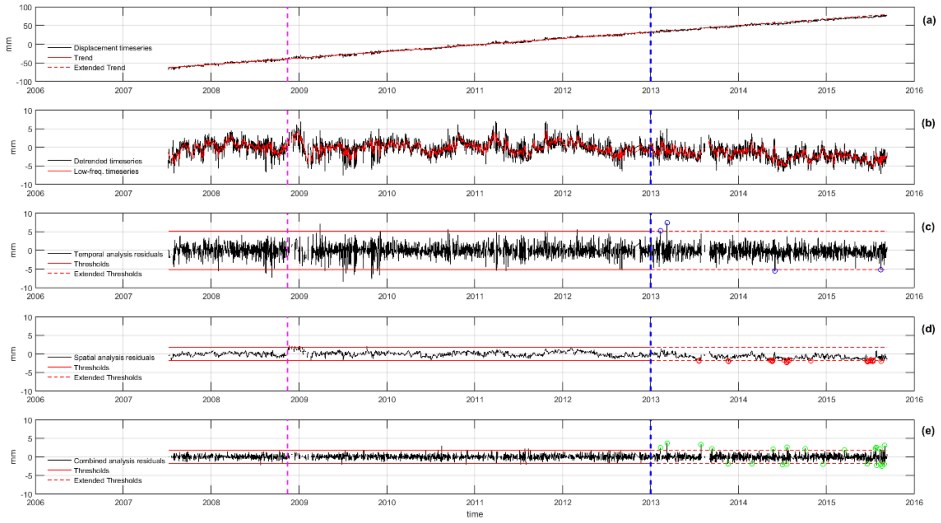


Figure C-20 Same as A-19, but for ΔE component

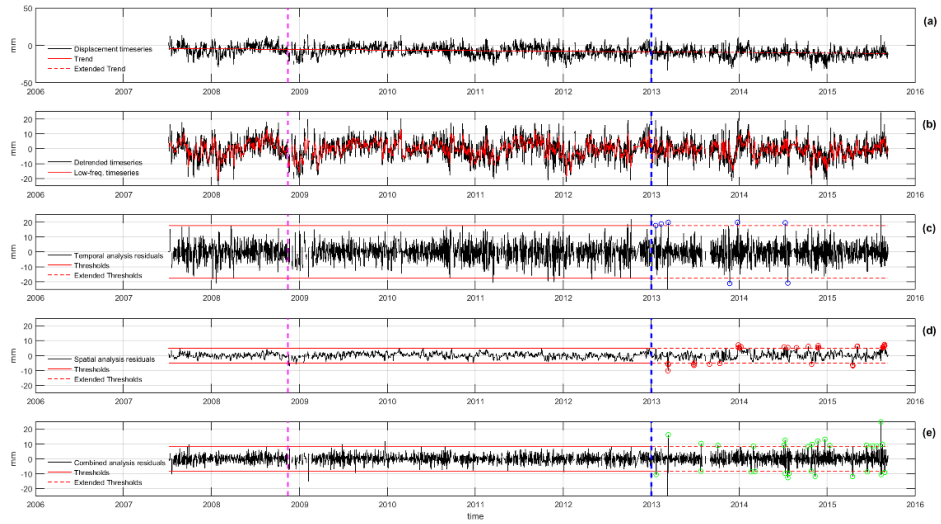


Figure C-21 Same as A-19, but for ΔU component

BARR

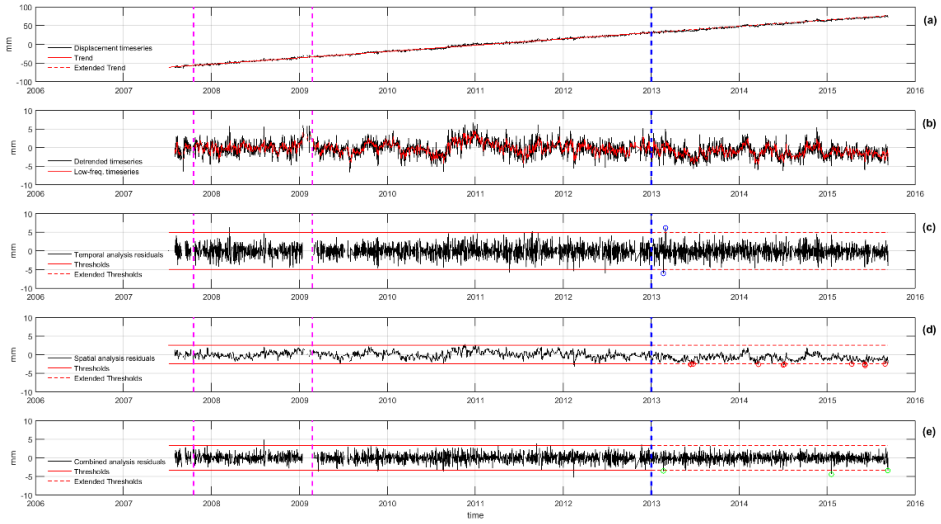


Figure C-22 BARR (ΔN) – (a) Corrected displacement time series, (b) detrended and low-frequency time series, the (c) Temporal, (d) Spatial and (e) combined analysis residuals.

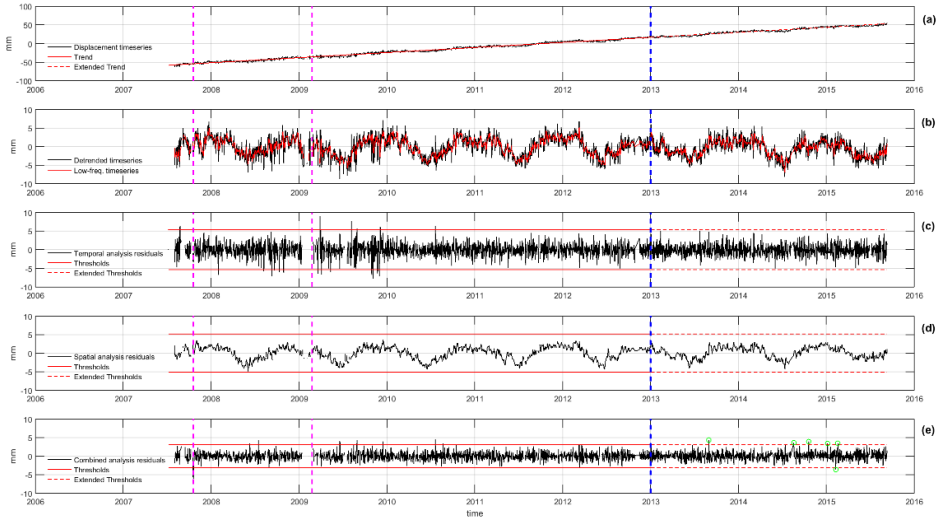


Figure C-23 Same as A-22, but for ΔE component

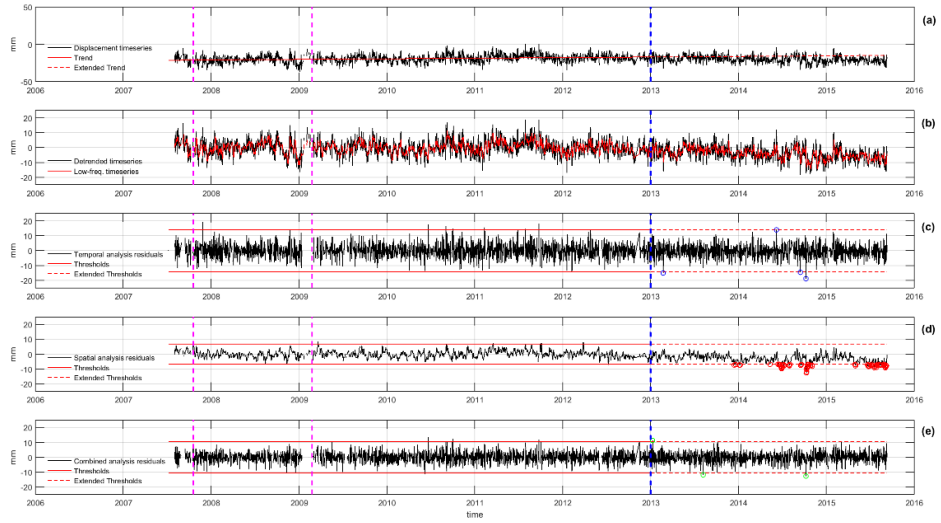


Figure C-24 Same as A-22, but for ΔU component

BEES

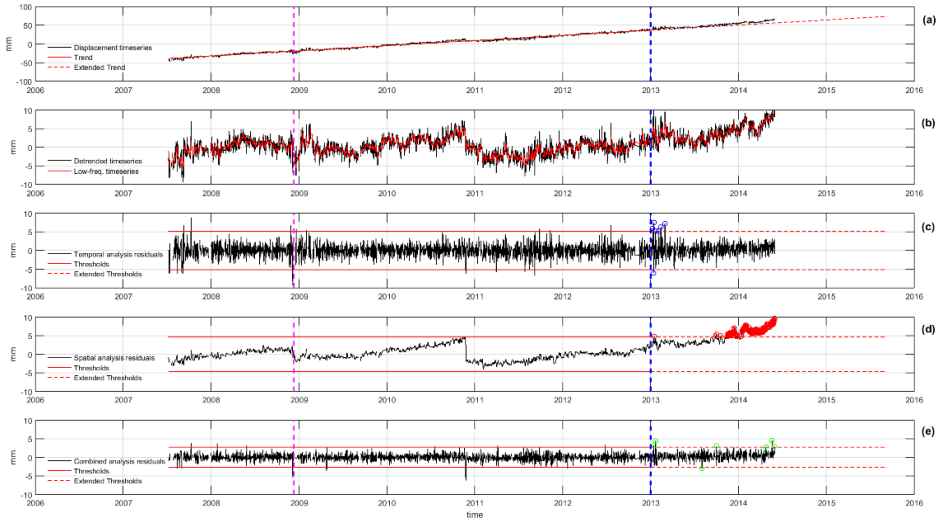


Figure C-25 BEES (ΔN) – (a) Corrected displacement time series, (b) detrended and low-frequency time series, the (c) Temporal, (d) Spatial and (e) combined analysis residuals.

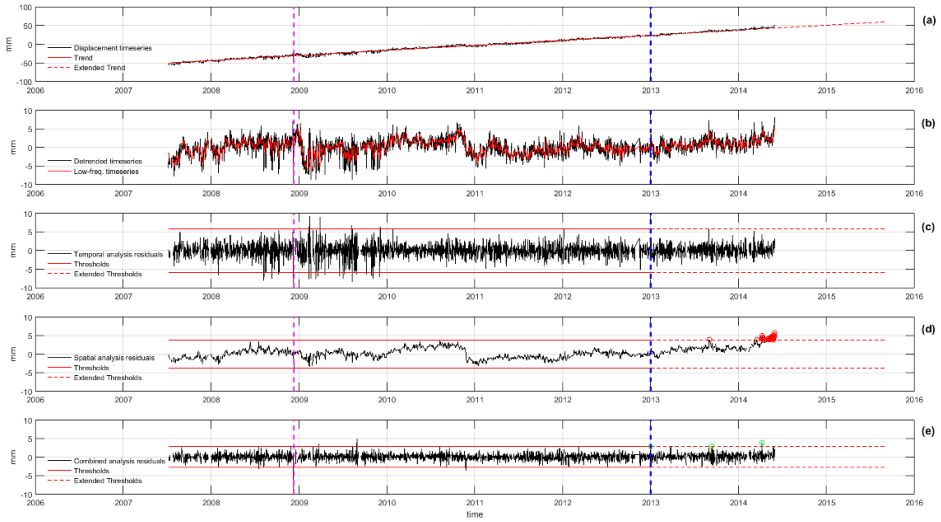


Figure C-26 Same as A-25, but for ΔE component

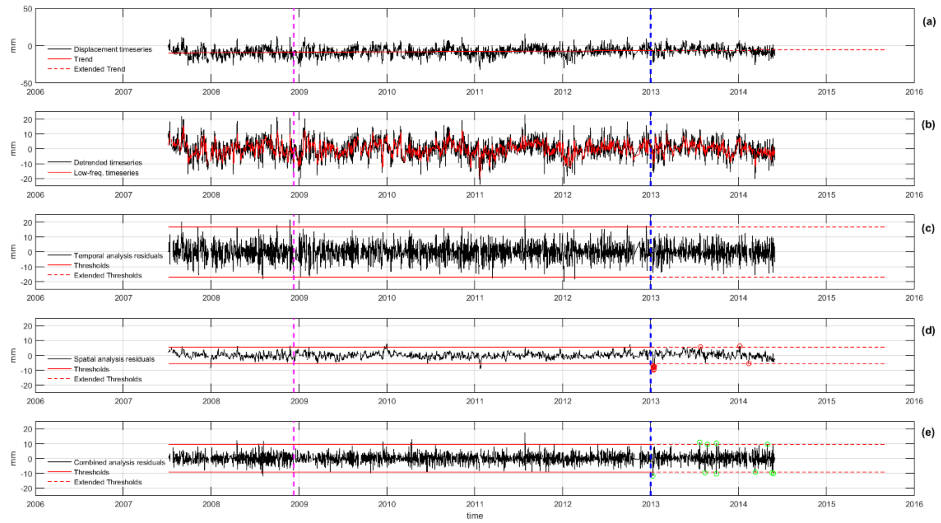


Figure C-27 Same as A-25, but for ΔU component

BELF

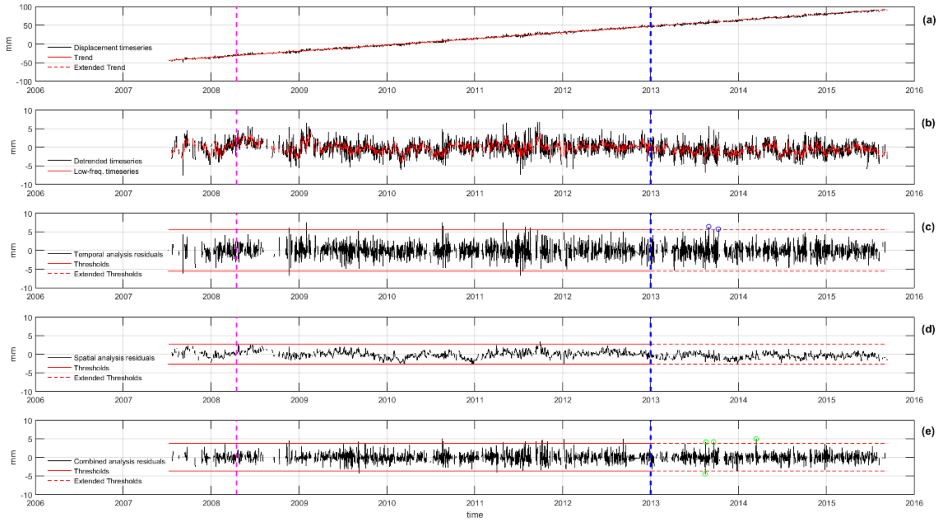


Figure C-28 BELF (ΔN) – (a) Corrected displacement time series, (b) detrended and low-frequency time series, the (c) Temporal, (d) Spatial and (e) combined analysisresiduals.

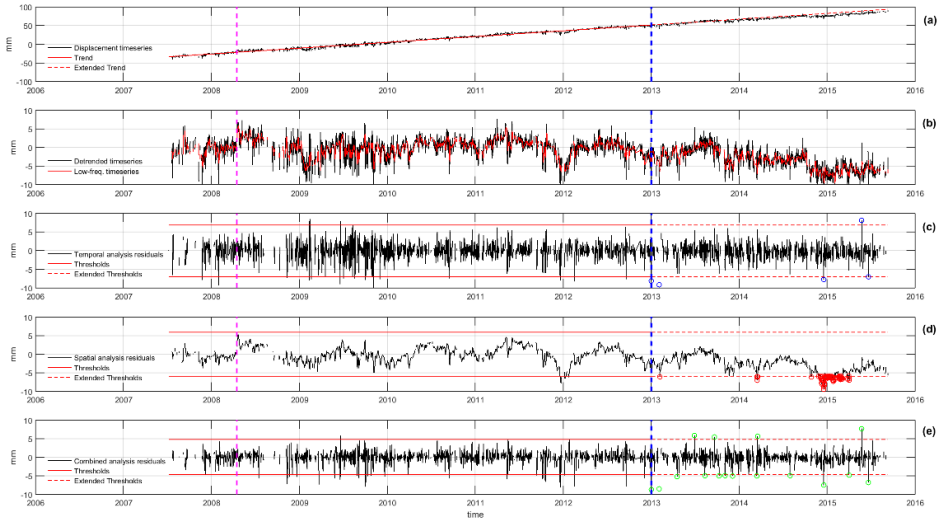


Figure C-29 Same as A-28, but for ΔE component

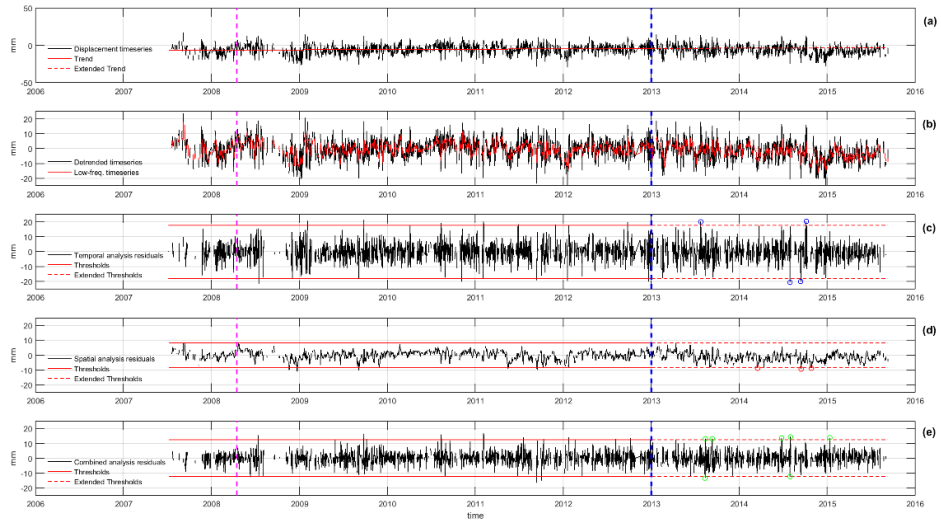


Figure C-30 Same as A-28, but for ΔU component

BLAP

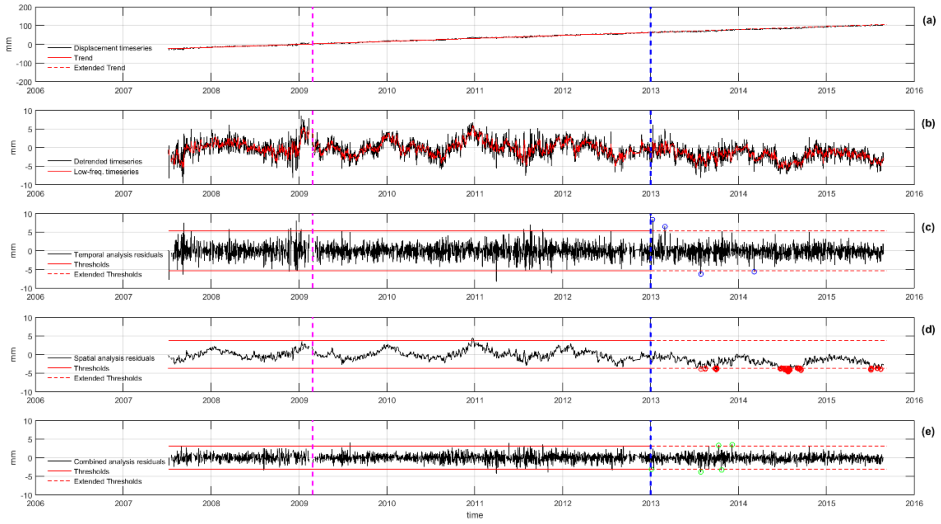


Figure C-31 BLAP (ΔN) – (a) Corrected displacement time series, (b) detrended and low-frequency time series, the (c) Temporal, (d) Spatial and (e) combined analysisresiduals.

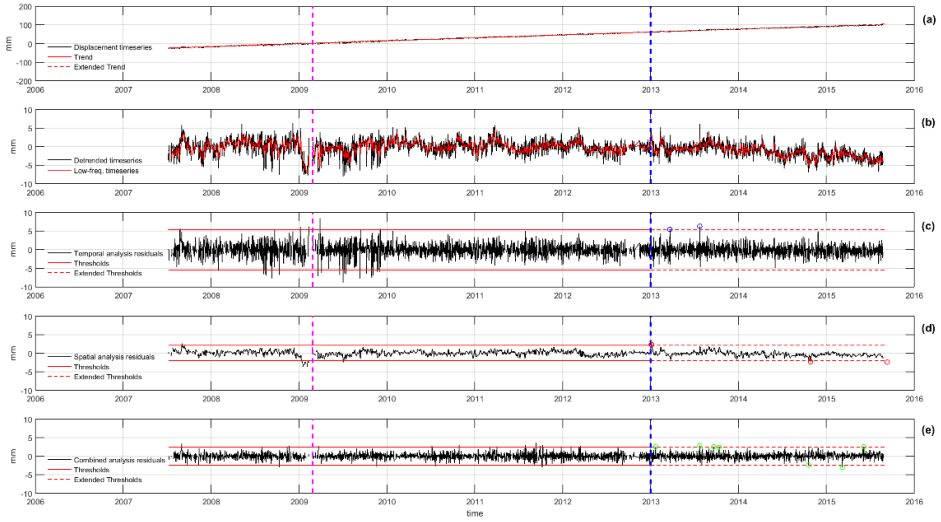


Figure C-32 Same as A-31, but for ΔE component

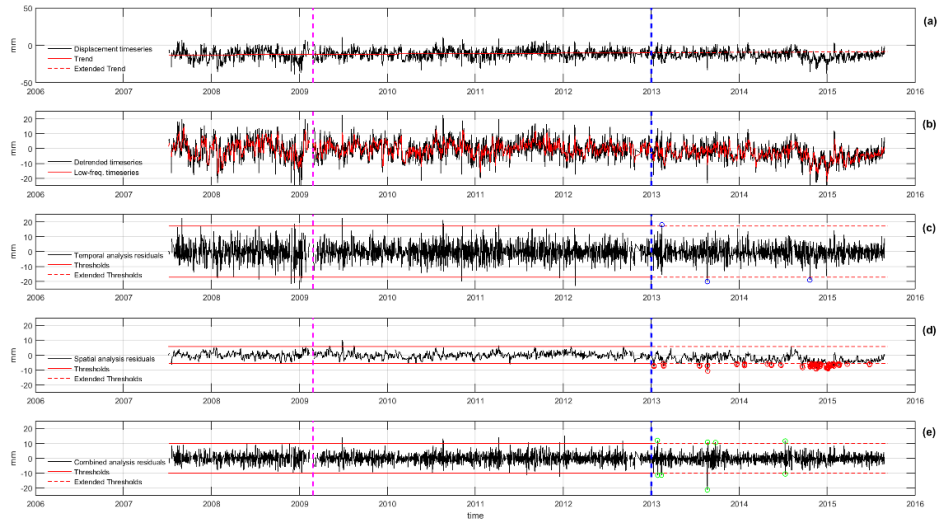


Figure C-33 Same as A-31, but for ΔU component

BRAE

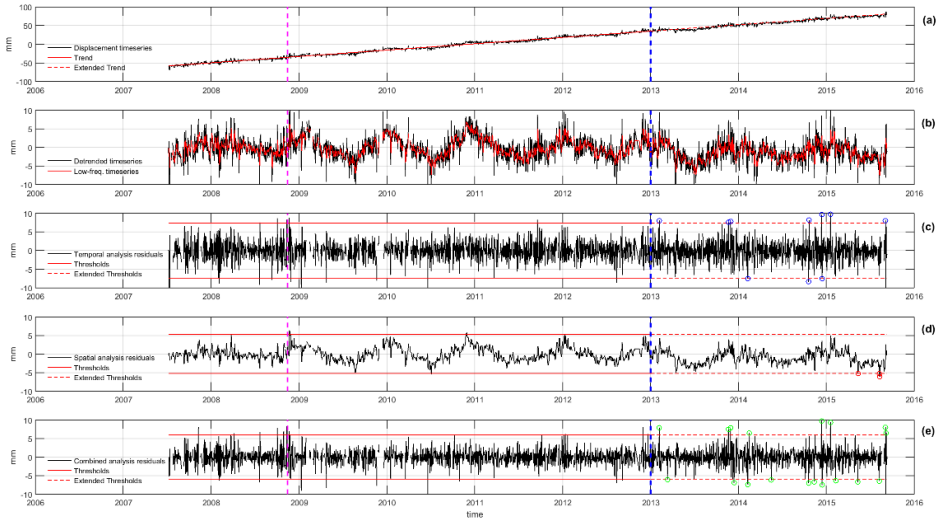


Figure C-34 BRAE (ΔN) – (a) Corrected displacement time series, (b) detrended and low-frequency time series, the (c) Temporal, (d) Spatial and (e) combined analysisresiduals.

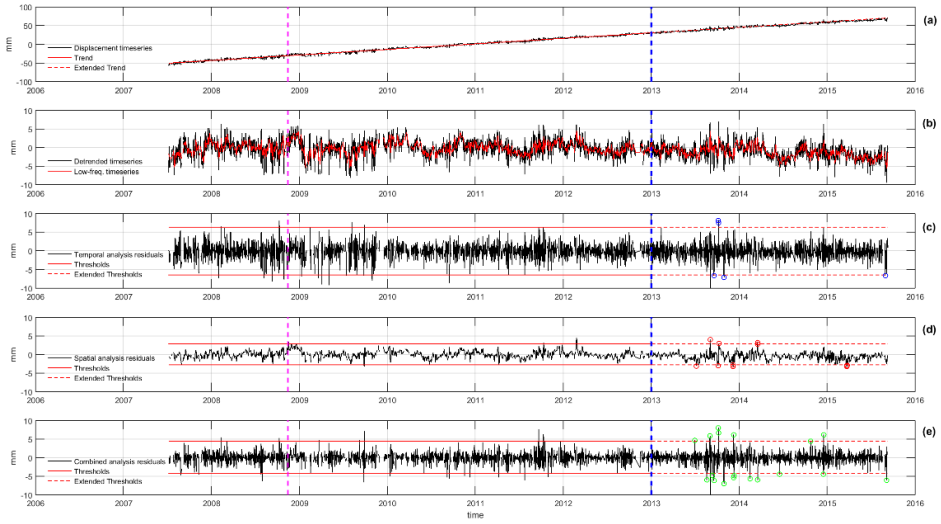


Figure C-35 Same as A-34, but for ΔE component

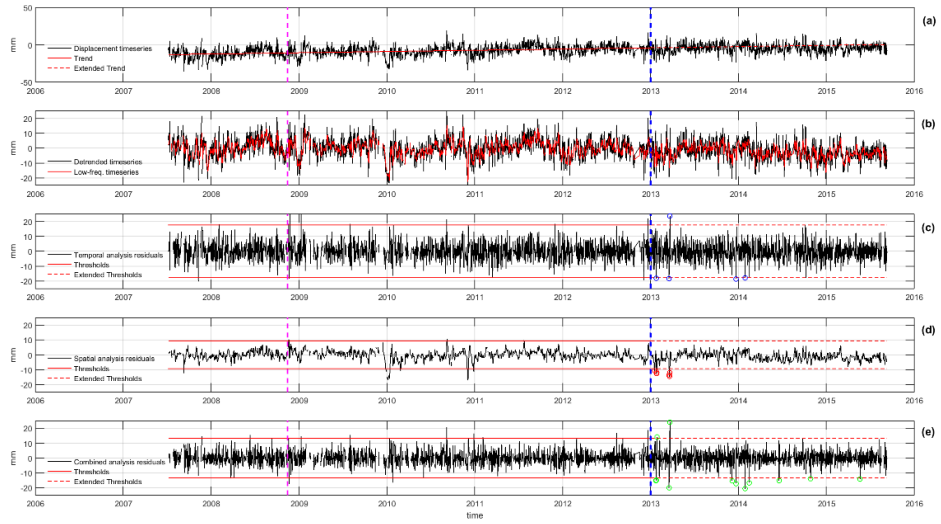


Figure C-36 Same as A-34, but for ΔU component

BREC

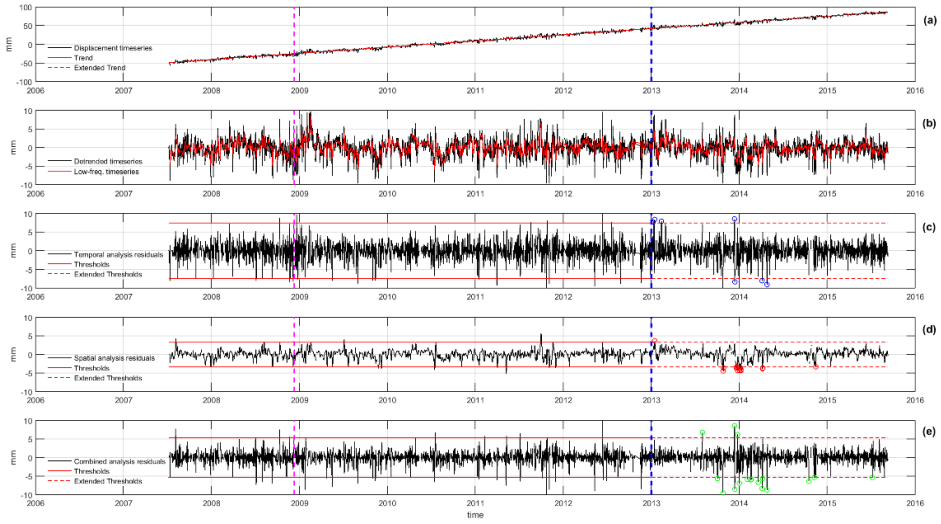


Figure C-37 BREC (ΔN) – (a) Corrected displacement time series, (b) detrended and low-frequency time series, the (c) Temporal, (d) Spatial and (e) combined analysisresiduals.

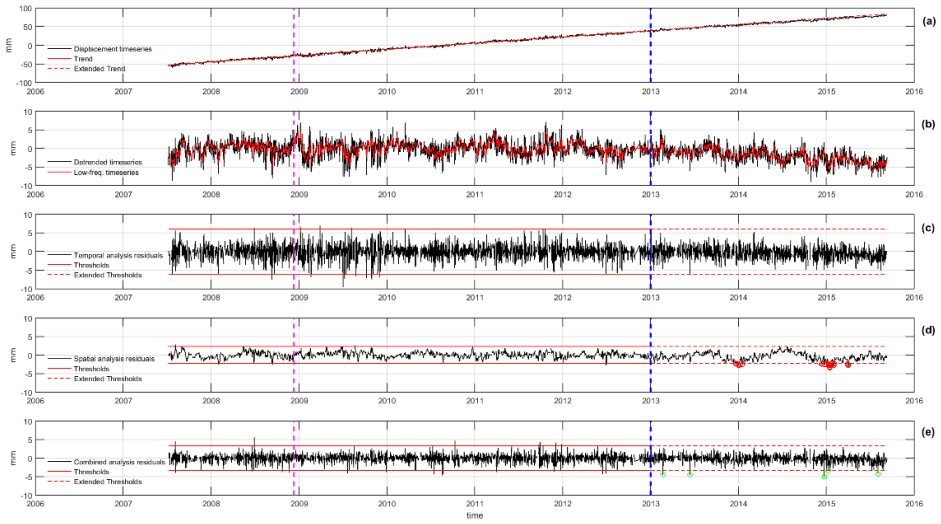


Figure C-38 Same as A-37, but for ΔE component

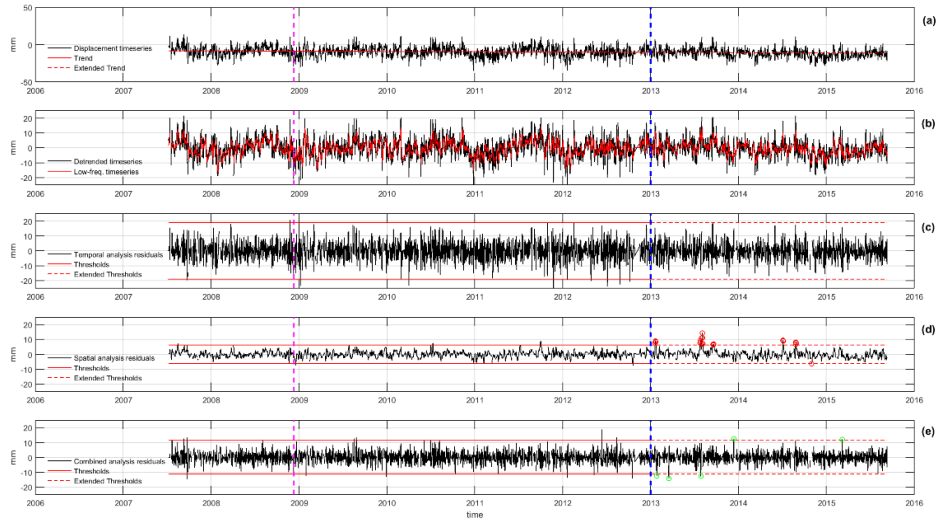


Figure C-39 Same as A-37, but for ΔU component

BUCK

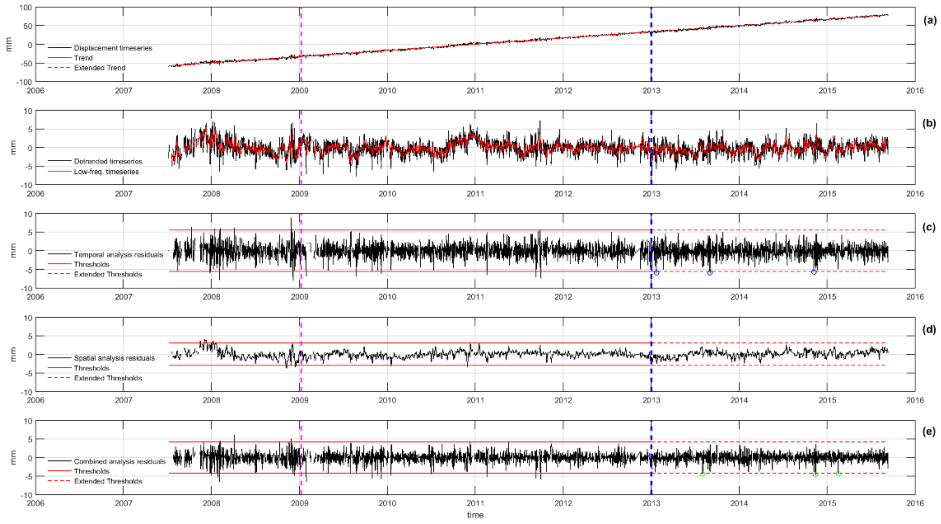


Figure C-40 BUCK (ΔN) – (a) Corrected displacement time series, (b) detrended and low-frequency time series, the (c) Temporal, (d) Spatial and (e) combined analysisresiduals.

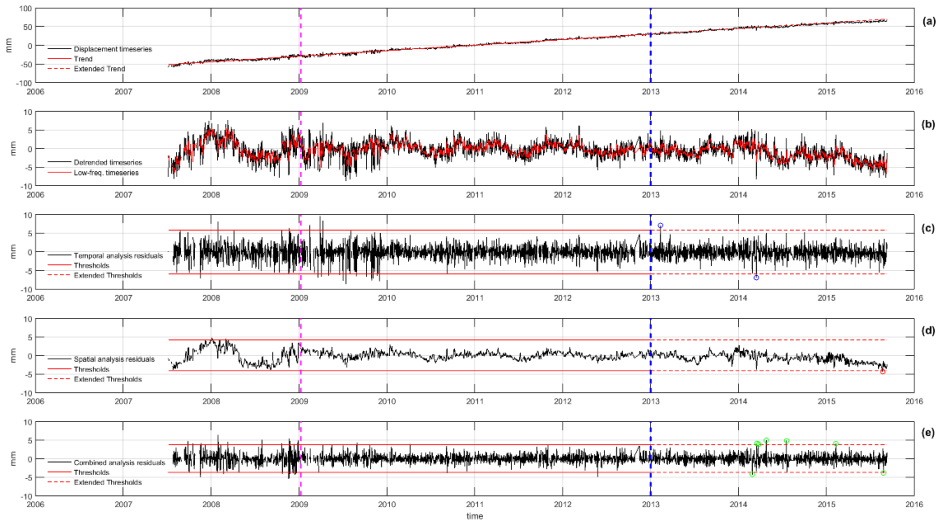


Figure C-41 Same as A-40, but for ΔE component

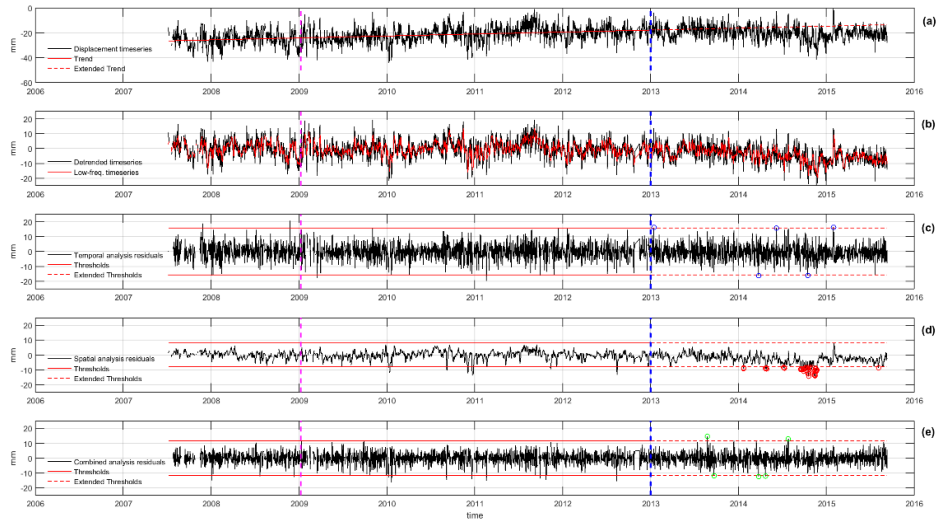


Figure C-42 Same as A-40, but for ΔU component

CAML

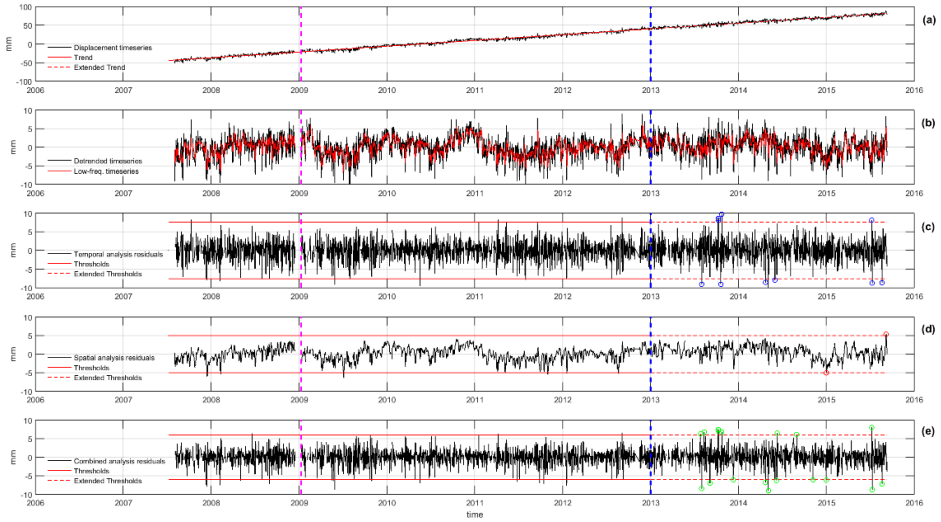


Figure C-43 CAML (ΔN) – (a) Corrected displacement time series, (b) detrended and low-frequency time series, the (c) Temporal, (d) Spatial and (e) combined analysisresiduals.

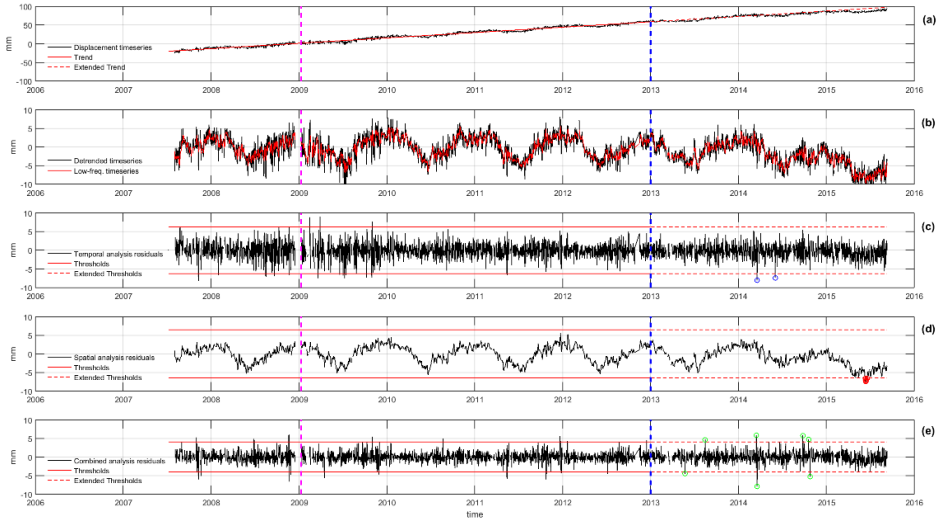


Figure C-44 Same as A-43, but for ΔE component

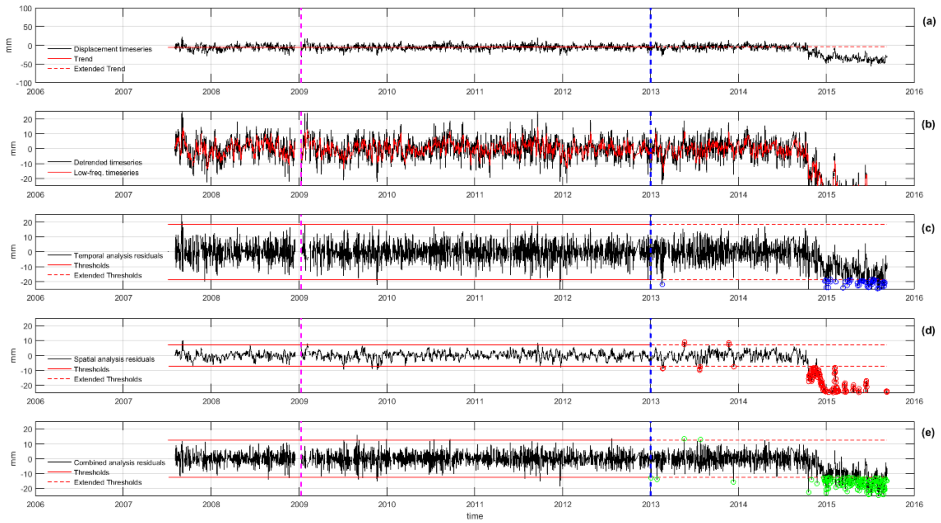


Figure C-45 Same as A-43, but for ΔU component

CARI

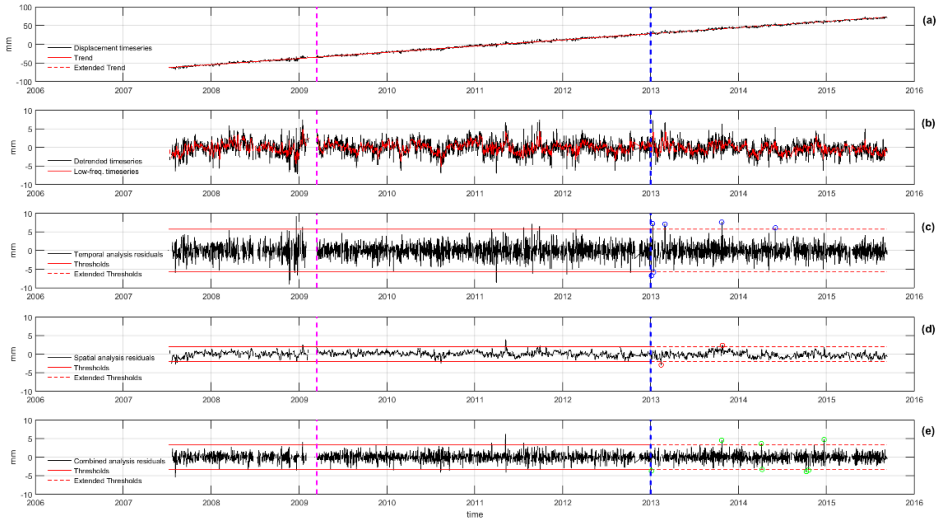


Figure C-46 CARI (ΔN) – (a) Corrected displacement time series, (b) detrended and low-frequency time series, the (c) Temporal, (d) Spatial and (e) combined analysisresiduals.

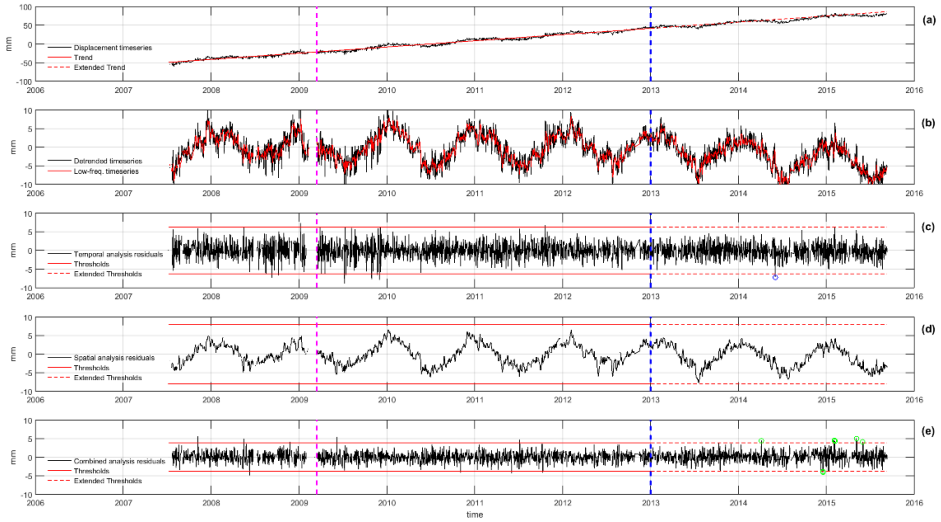


Figure C-47 Same as A-46, but for ΔE component

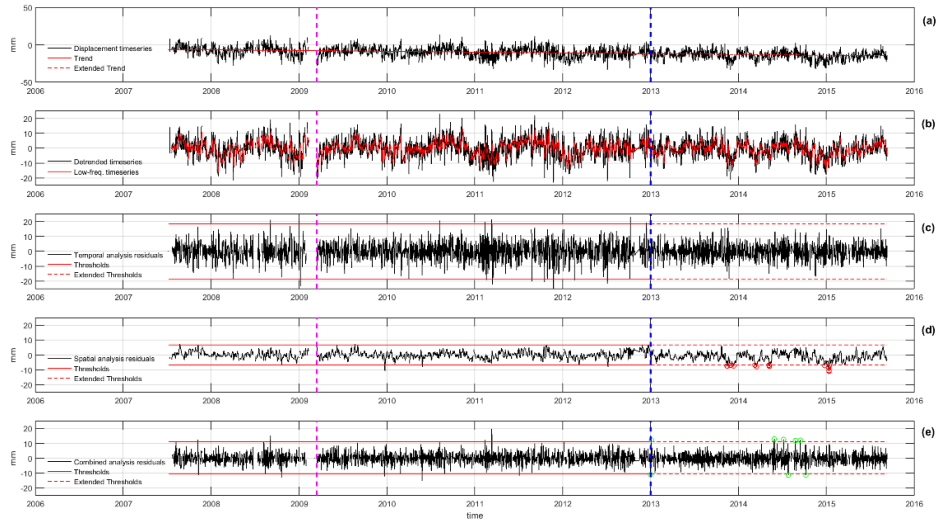


Figure C-48 Same as A-46, but for ΔU component

CARL

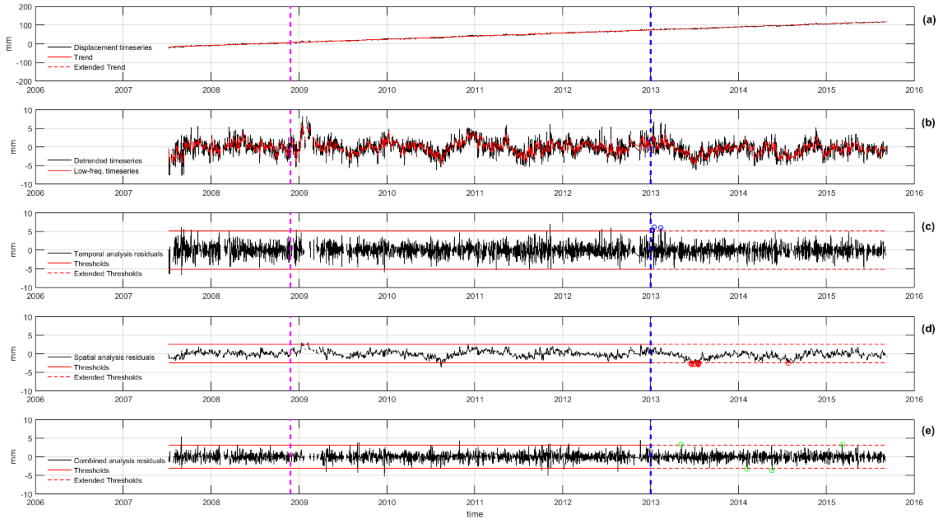


Figure C-49 CARL (ΔN) – (a) Corrected displacement time series, (b) detrended and low-frequency time series, the (c) Temporal, (d) Spatial and (e) combined analysisresiduals.

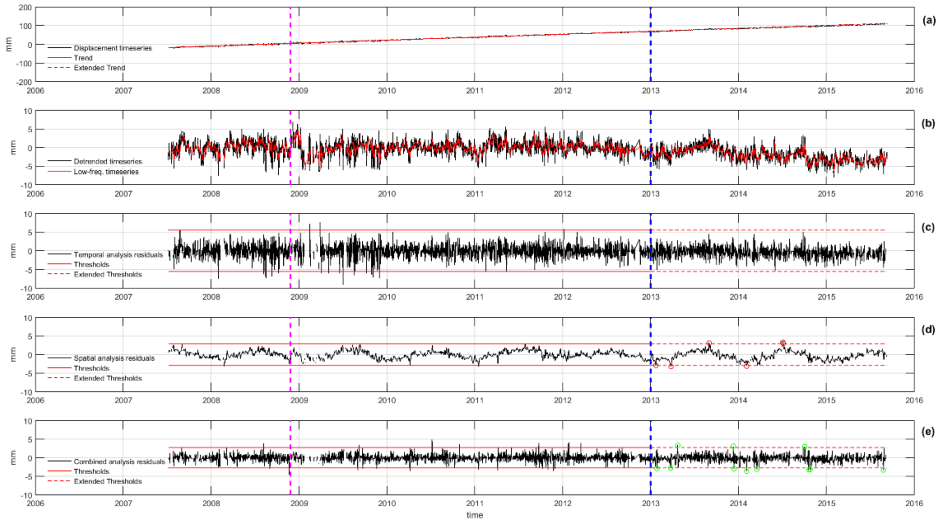


Figure C-50 Same as A-49, but for ΔE component

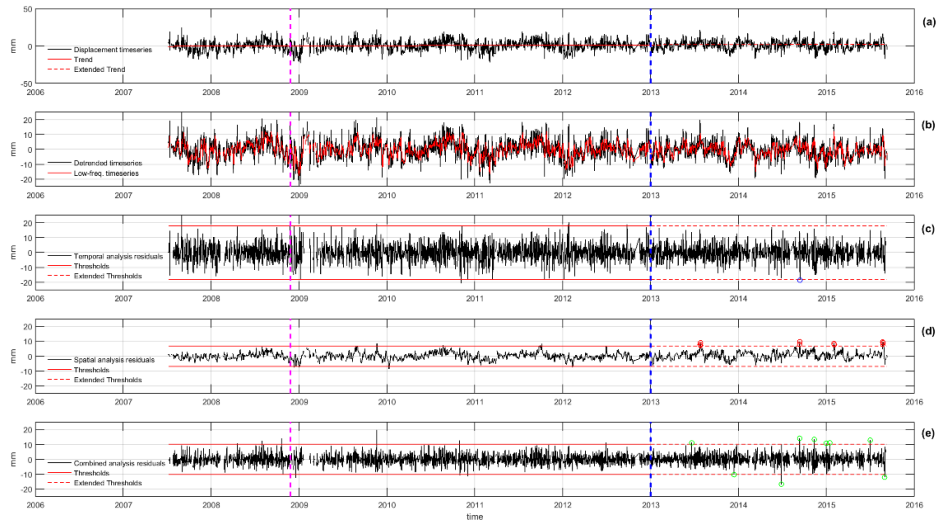


Figure C-51 Same as A-49, but for ΔU component

CLAW

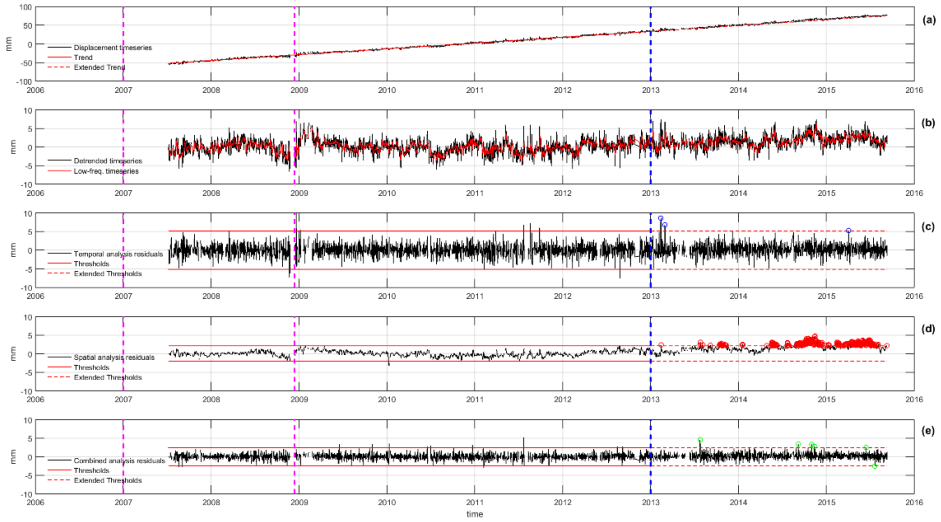


Figure C-52 CLAW (ΔN) – (a) Corrected displacement time series, (b) detrended and low-frequency time series, the (c) Temporal, (d) Spatial and (e) combined analysisresiduals.

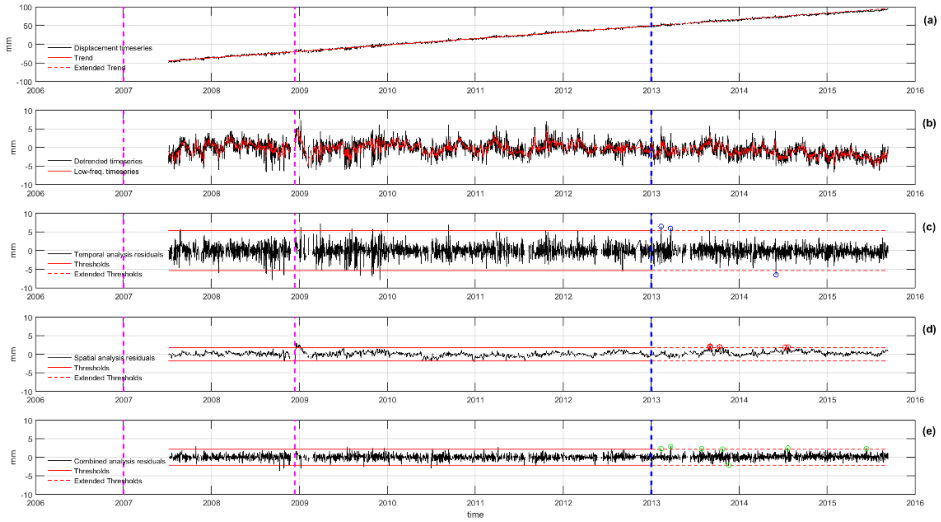


Figure C-53 Same as A-52, but for ΔE component

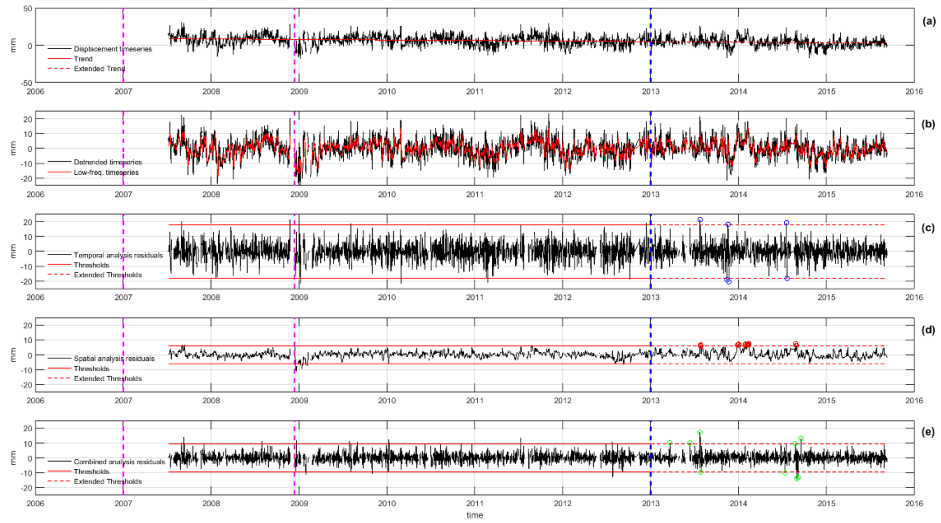


Figure C-54 Same as A-52, but for ΔU component

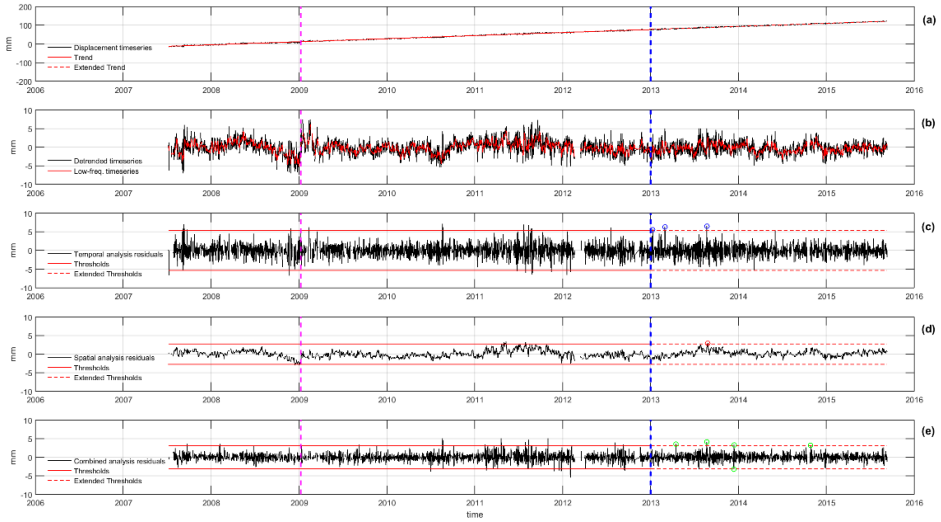


Figure C-55 DARE (ΔN) – (a) Corrected displacement time series, (b) detrended and low-frequency time series, the (c) Temporal, (d) Spatial and (e) combined analysisresiduals.

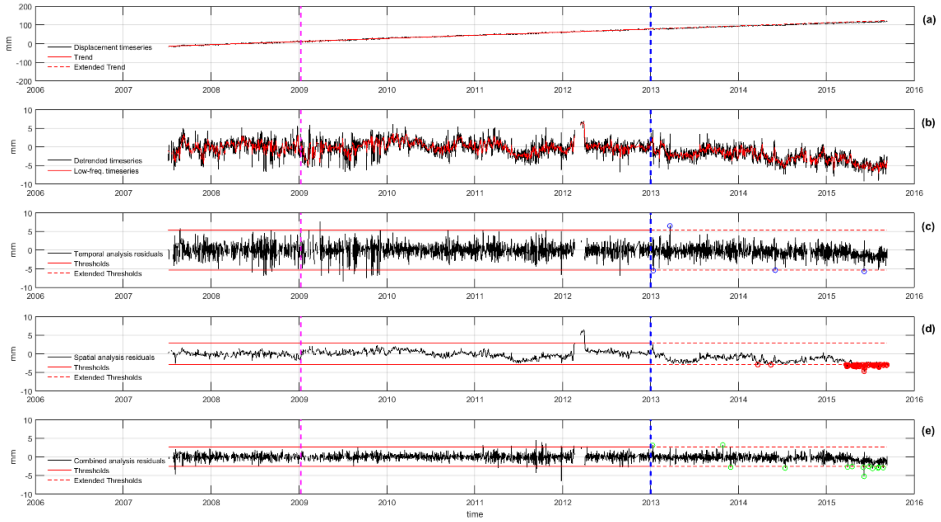


Figure C-56 Same as A-55, but for ΔE component

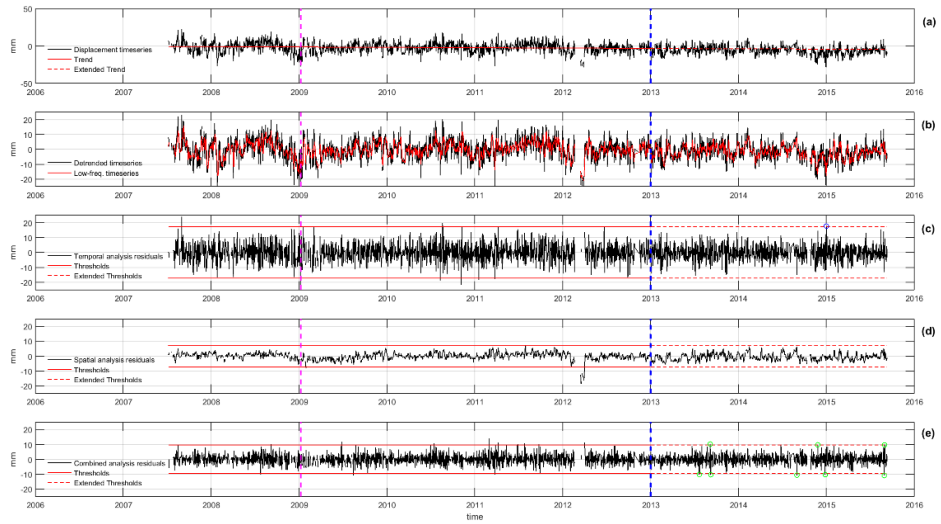


Figure C-57 Same as A-55, but for ΔU component

DROW

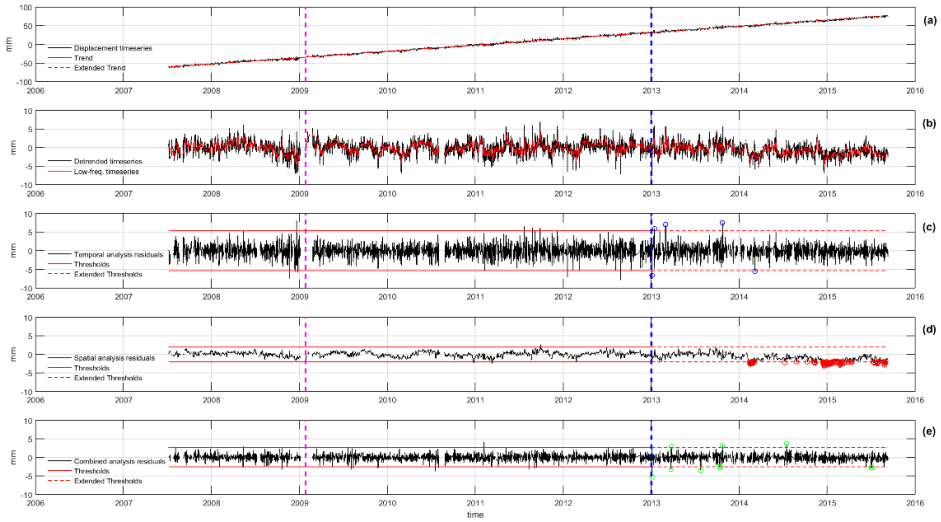


Figure C-58 DROW (ΔN) – (a) Corrected displacement time series, (b) detrended and low-frequency time series, the (c) Temporal, (d) Spatial and (e) combined analysisresiduals.

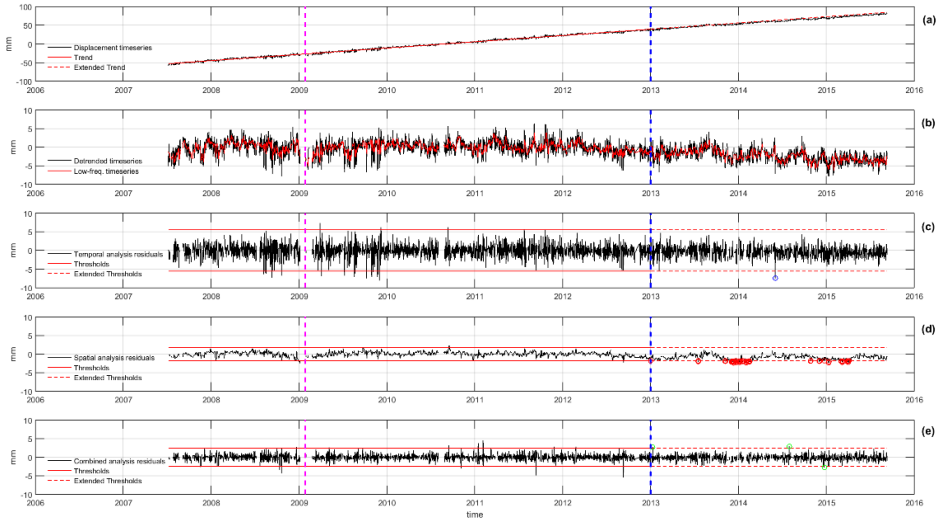


Figure C-59 Same as A-58, but for ΔE component

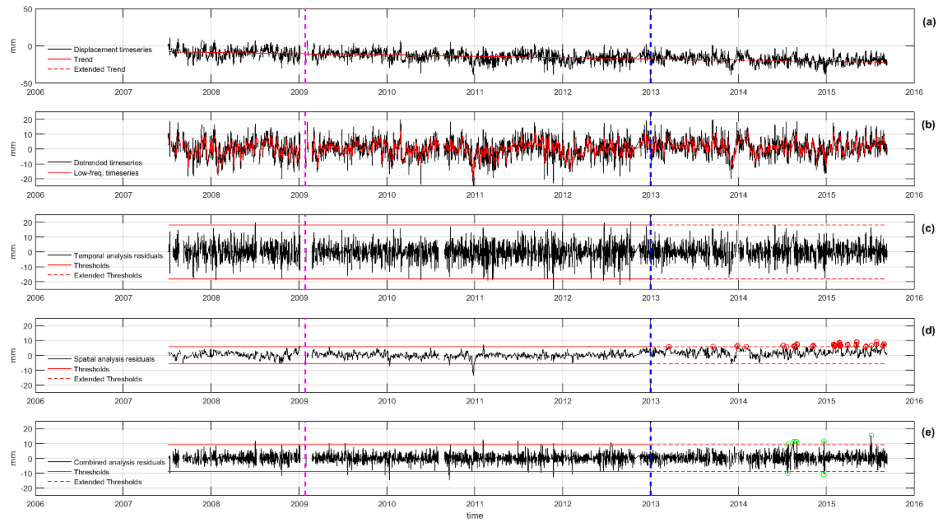


Figure C-60 Same as A-58, but for ΔU component

DRUM

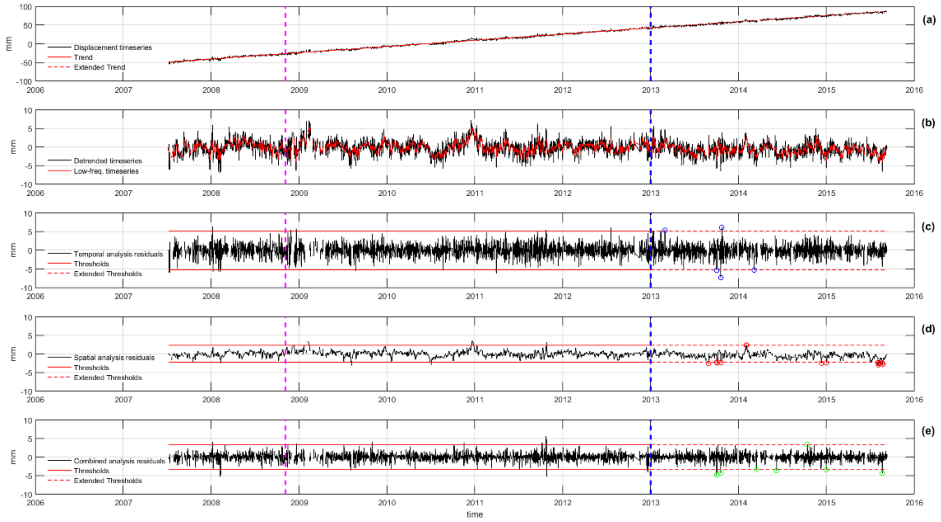


Figure C-61 DRUM (ΔN) – (a) Corrected displacement time series, (b) detrended and low-frequency time series, the (c) Temporal, (d) Spatial and (e) combined analysisresiduals.

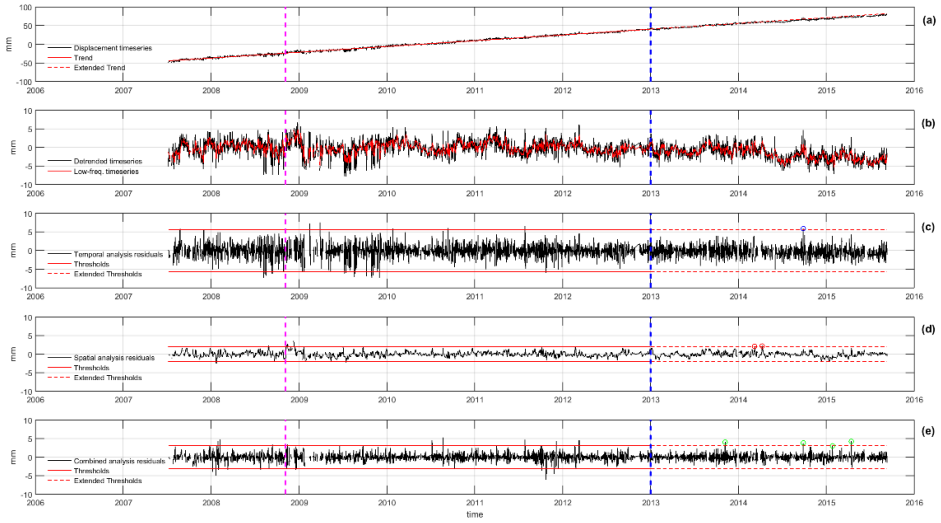


Figure C-62 Same as A-61, but for ΔE component

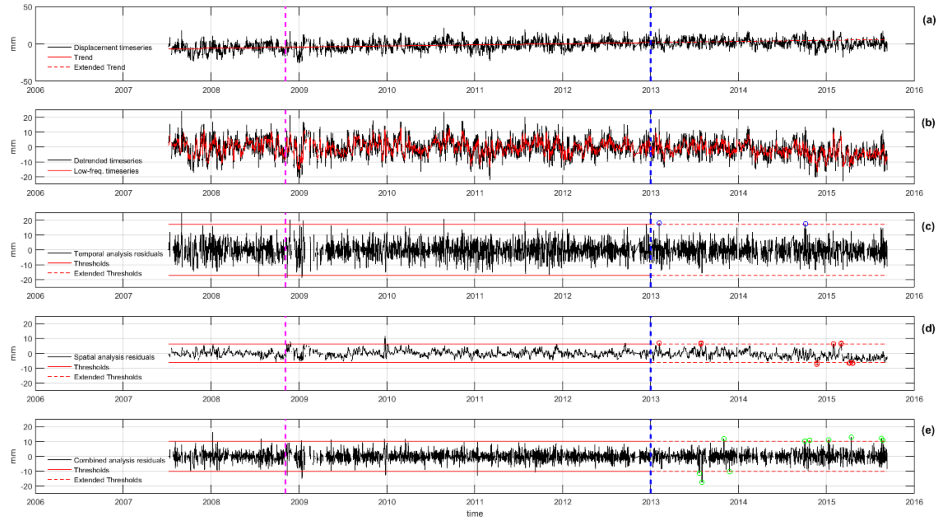


Figure C-63 Same as A-61, but for ΔU component

DUNG

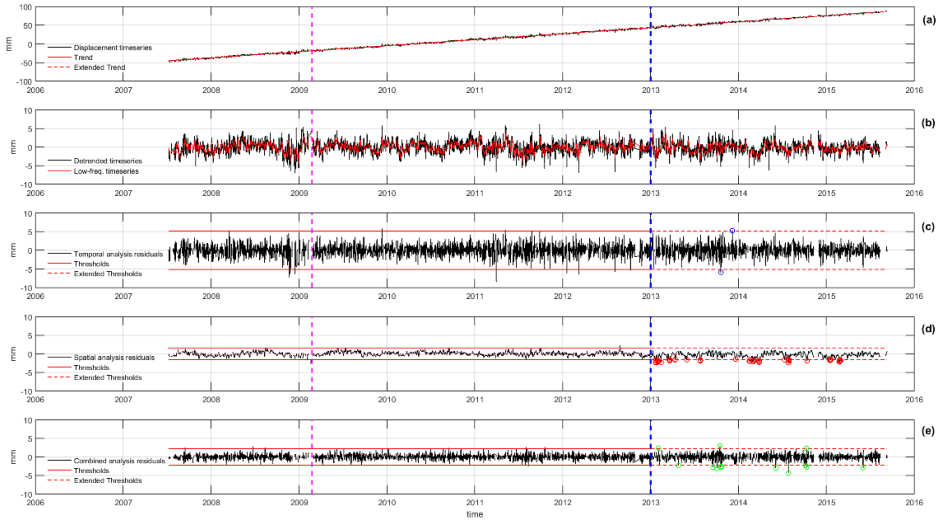


Figure C-64 DUNG (ΔN) – (a) Corrected displacement time series, (b) detrended and low-frequency time series, the (c) Temporal, (d) Spatial and (e) combined analysisresiduals.

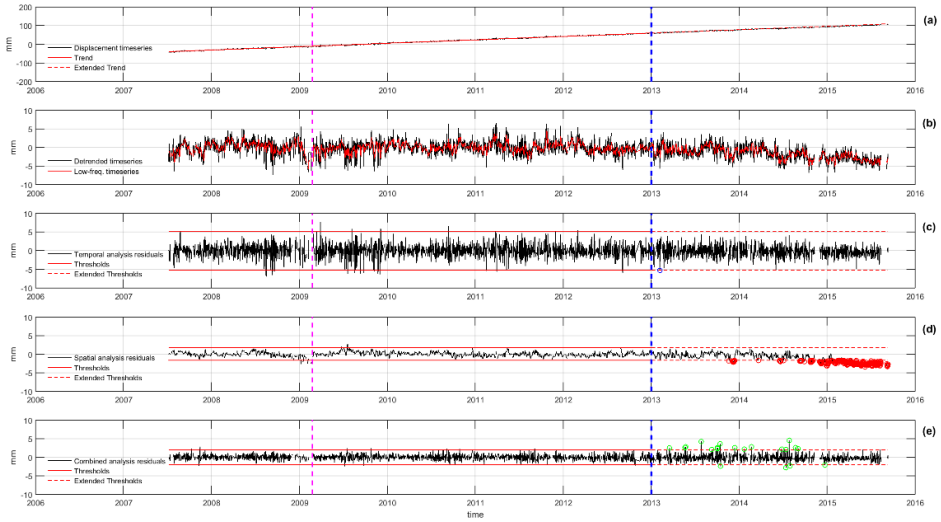


Figure C-65 Same as A-64, but for ΔE component

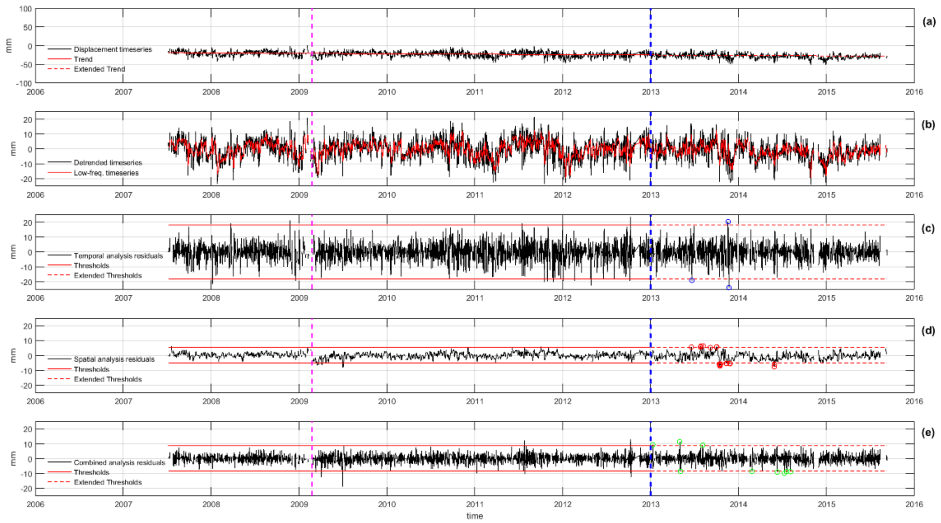


Figure C-66 Same as A-64, but for ΔU component

DUNK

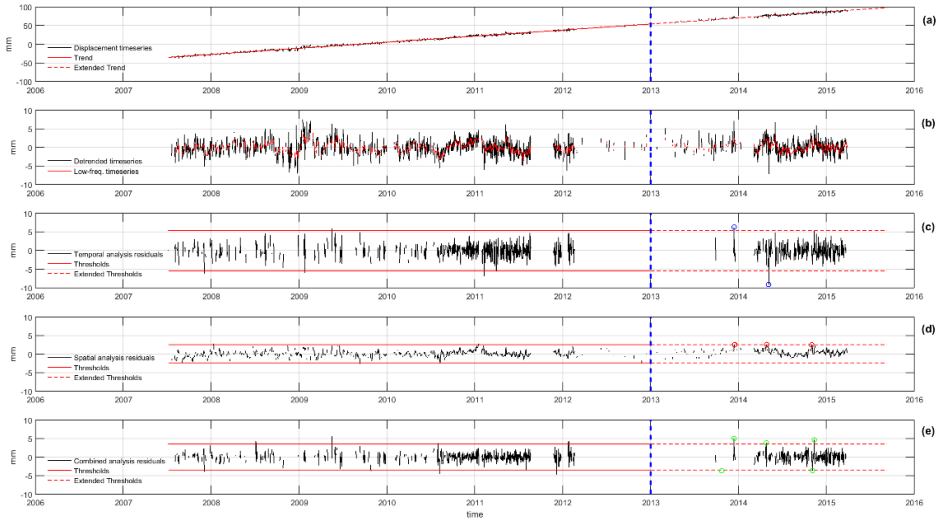


Figure C-67 DUNK (ΔN) – (a) Corrected displacement time series, (b) detrended and low-frequency time series, the (c) Temporal, (d) Spatial and (e) combined analysisresiduals.

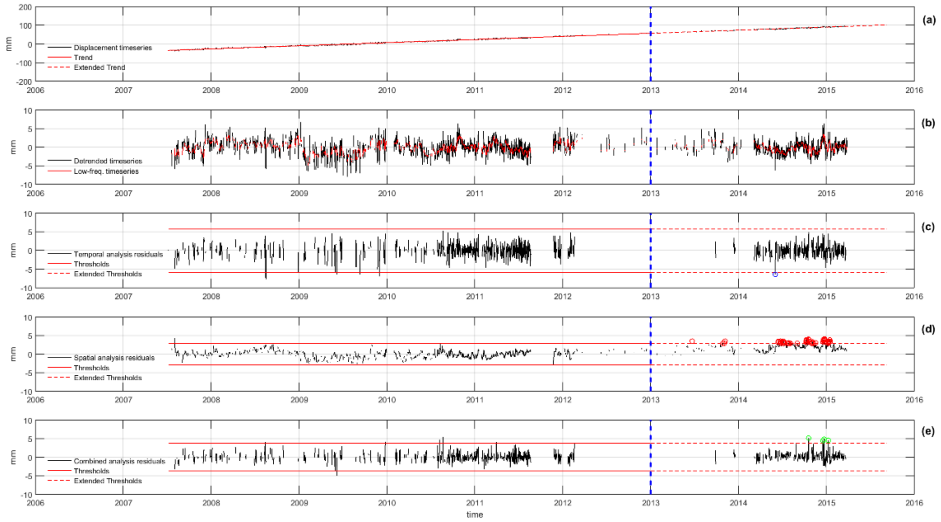


Figure C-68 Same as A-67, but for ΔE component

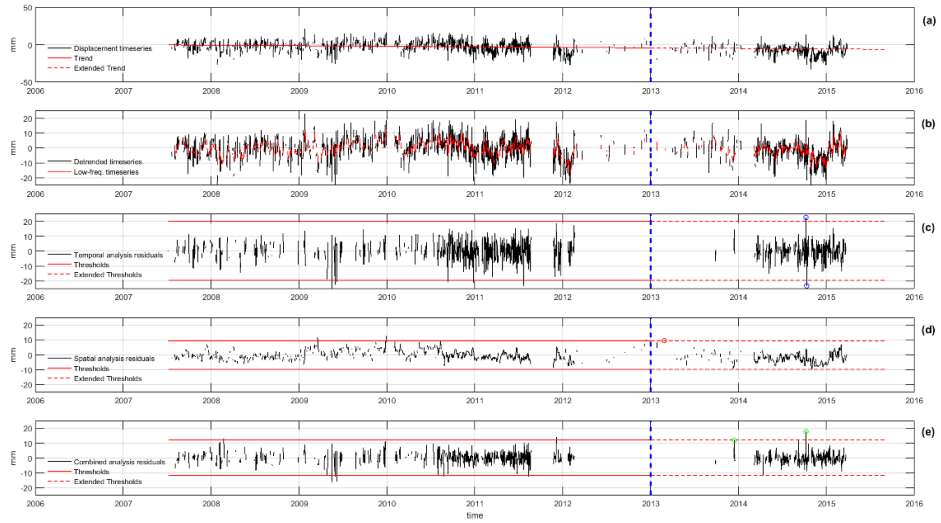


Figure C-69 Same as A-67, but for ΔU component

EASN

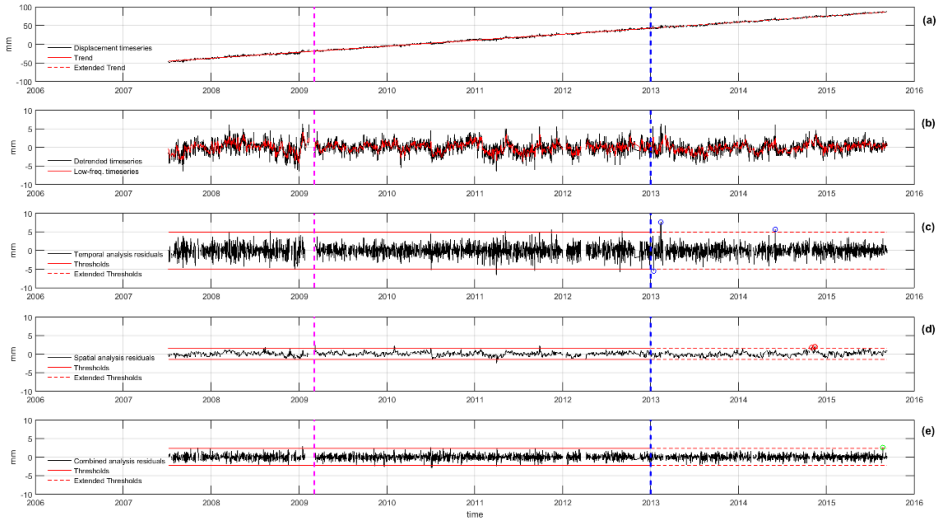


Figure C-70 EASN (ΔN) – (a) Corrected displacement time series, (b) detrended and low-frequency time series, the (c) Temporal, (d) Spatial and (e) combined analysisresiduals.

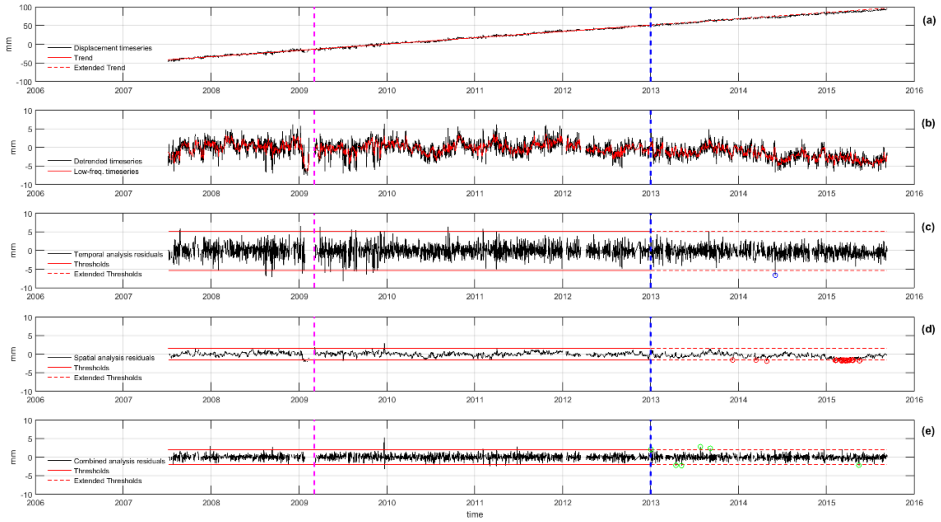


Figure C-71 Same as A-70, but for ΔE component

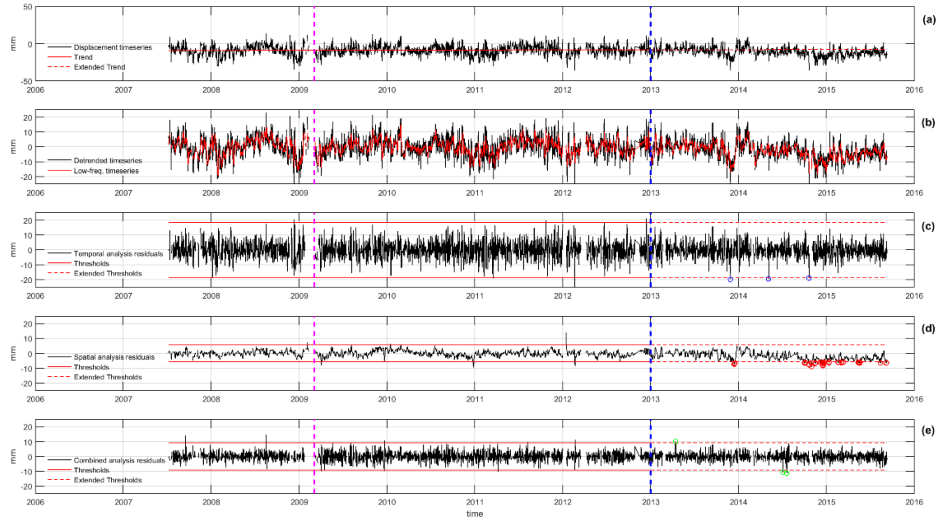


Figure C-72 Same as A-70, but for ΔU component

EDIN

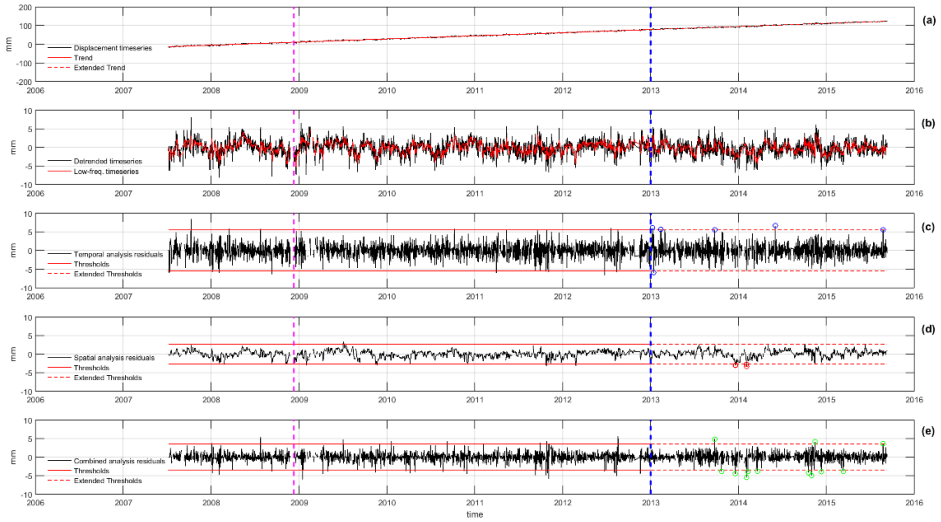


Figure C-73 EDIN (ΔN) – (a) Corrected displacement time series, (b) detrended and low-frequency time series, the (c) Temporal, (d) Spatial and (e) combined analysisresiduals.

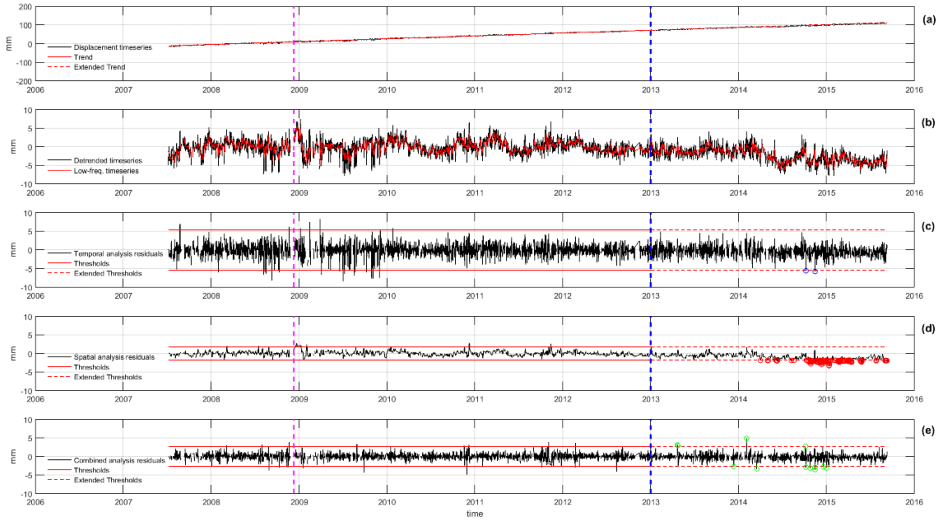


Figure C-74 Same as A-73, but for ΔE component

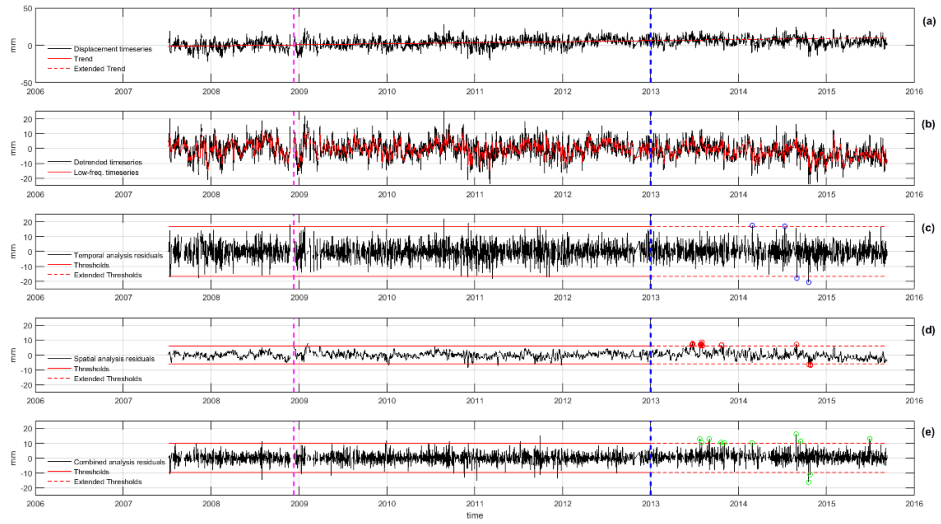


Figure C-75 Same as A-73, but for ΔU component

ESKD

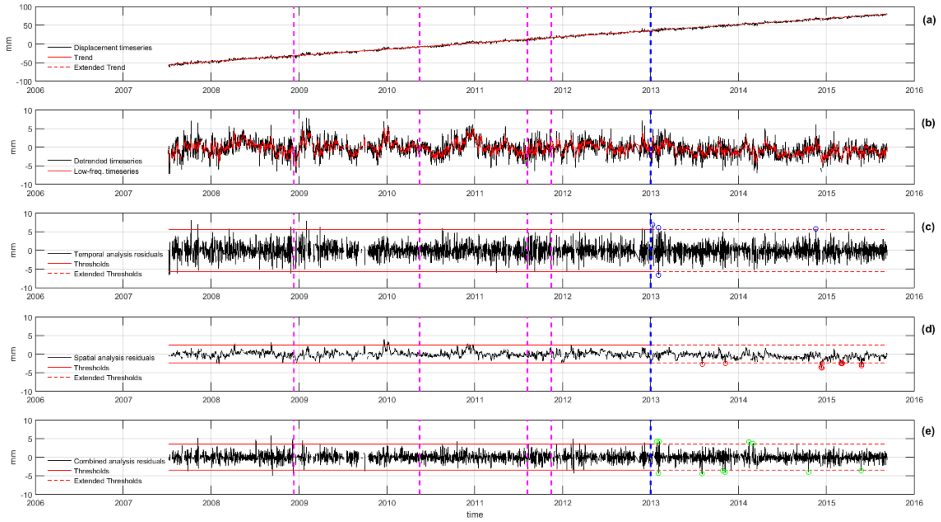


Figure C-76 ESKD (ΔN) – (a) Corrected displacement time series, (b) detrended and low-frequency time series, the (c) Temporal, (d) Spatial and (e) combined analysisresiduals.

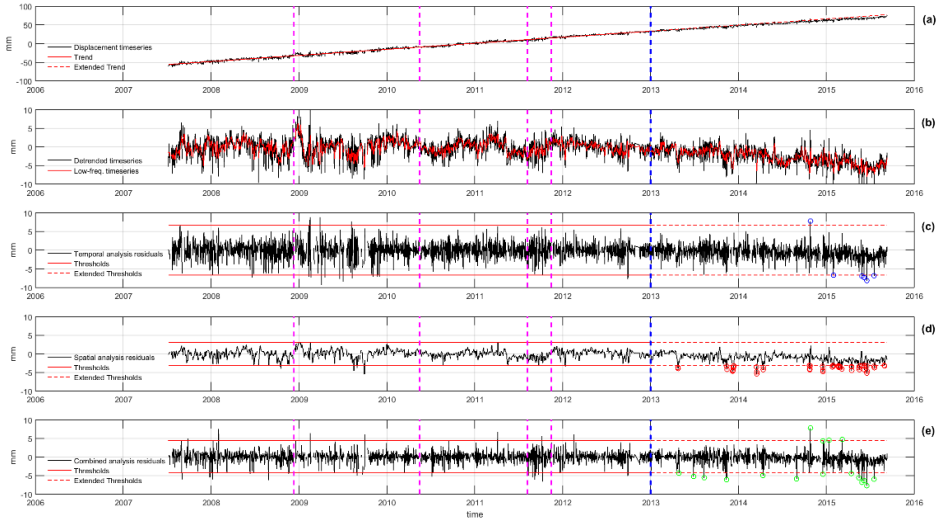


Figure C-77 Same as A-76, but for ΔE component

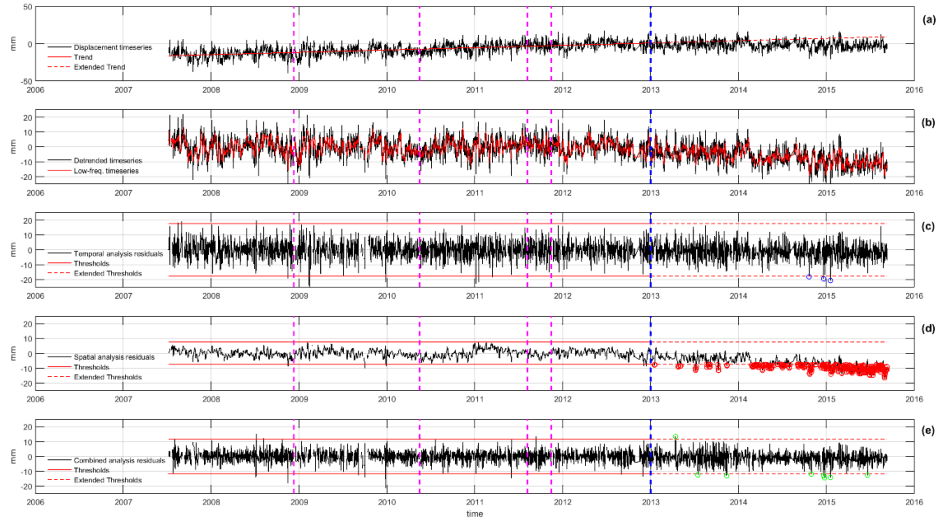


Figure C-78 Same as A-76, but for ΔU component

EXMO

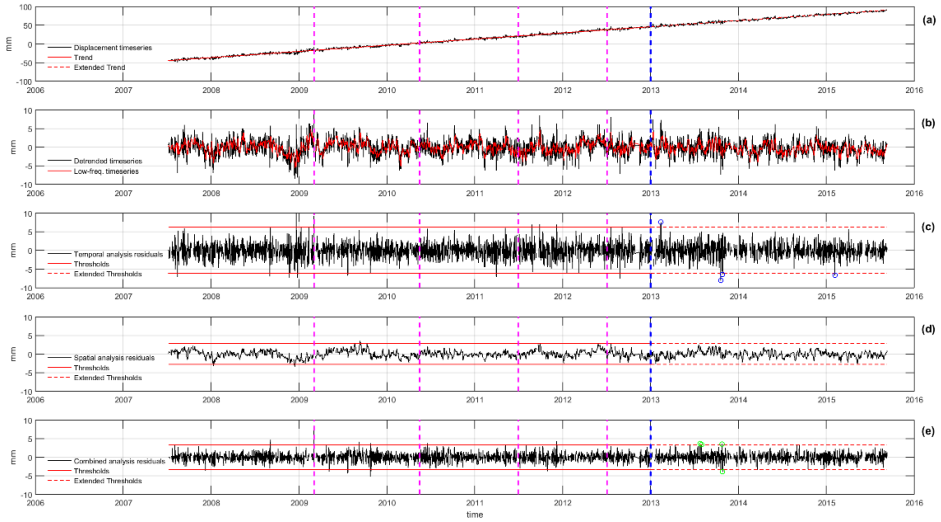


Figure C-79 EXMO (ΔN) – (a) Corrected displacement time series, (b) detrended and low-frequency time series, the (c) Temporal, (d) Spatial and (e) combined analysisresiduals.

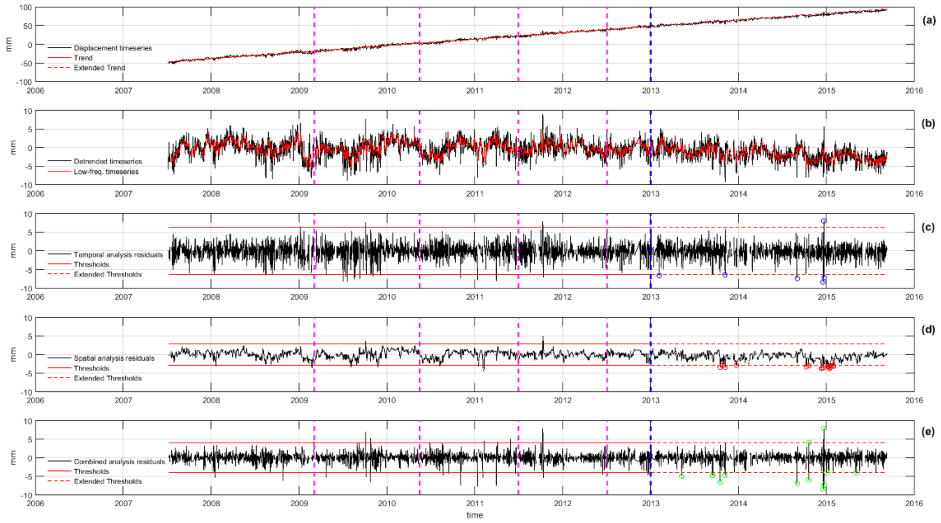


Figure C-80 Same as A-79, but for ΔE component

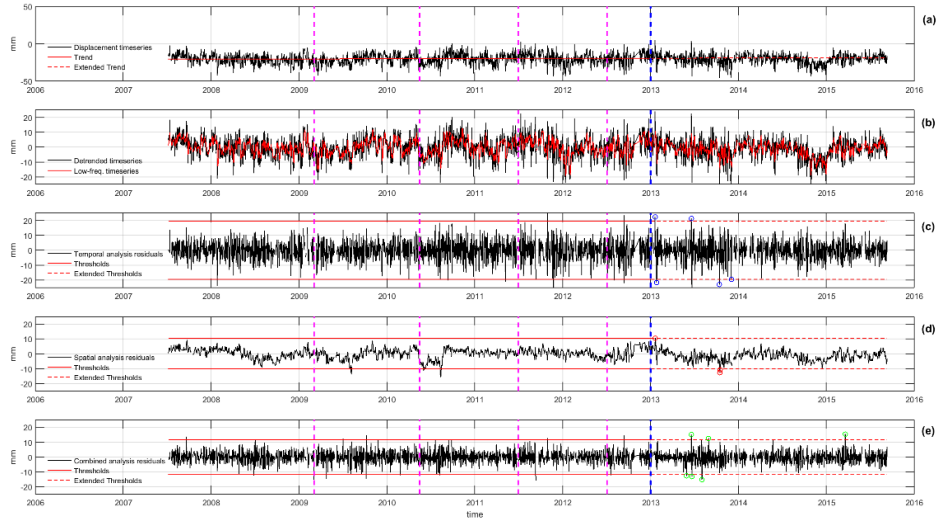


Figure C-81 Same as A-79, but for ΔU component

FARB

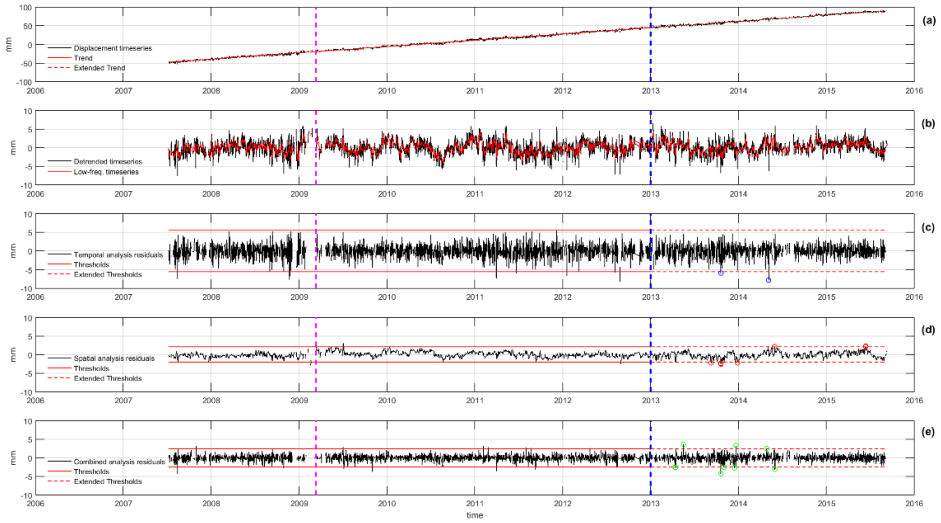


Figure C-82 FARB (ΔN) – (a) Corrected displacement time series, (b) detrended and low-frequency time series, the (c) Temporal, (d) Spatial and (e) combined analysisresiduals.

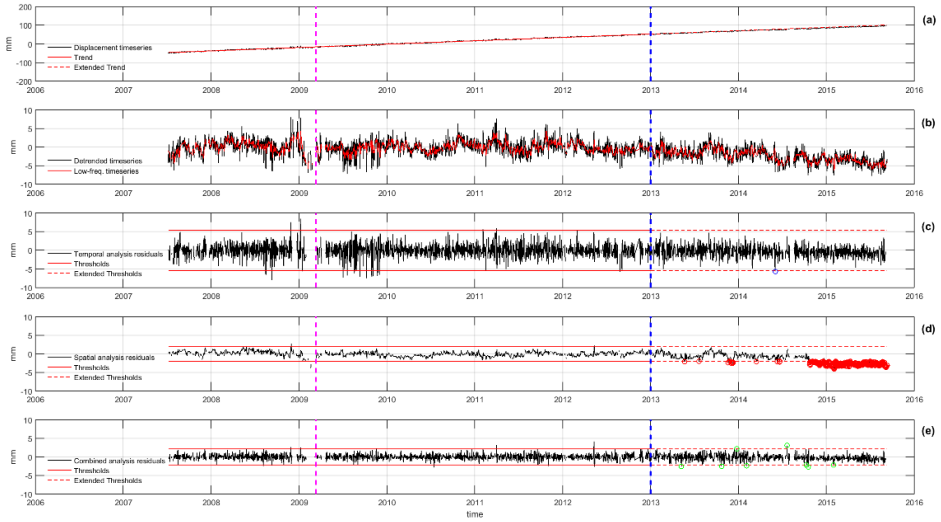


Figure C-83 Same as A-83, but for ΔE component

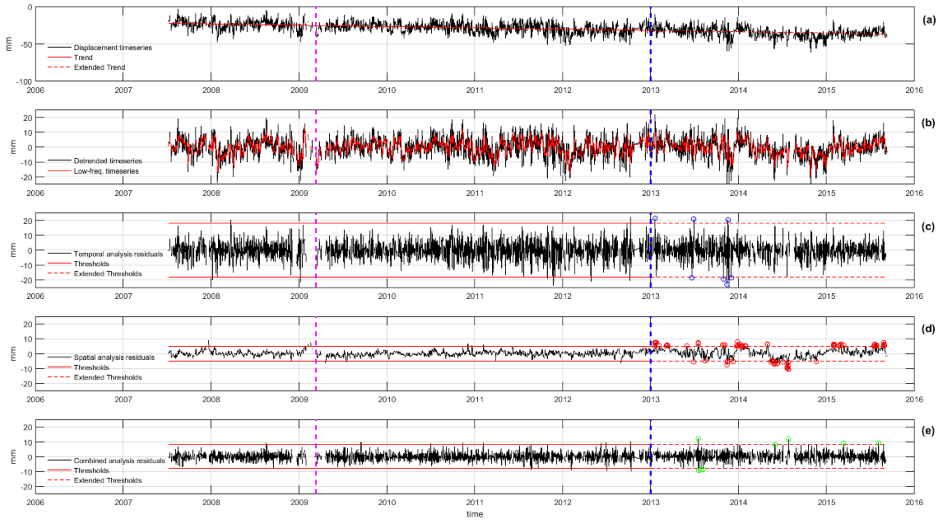


Figure C-84 Same as A-83, but for ΔU component

FAUG

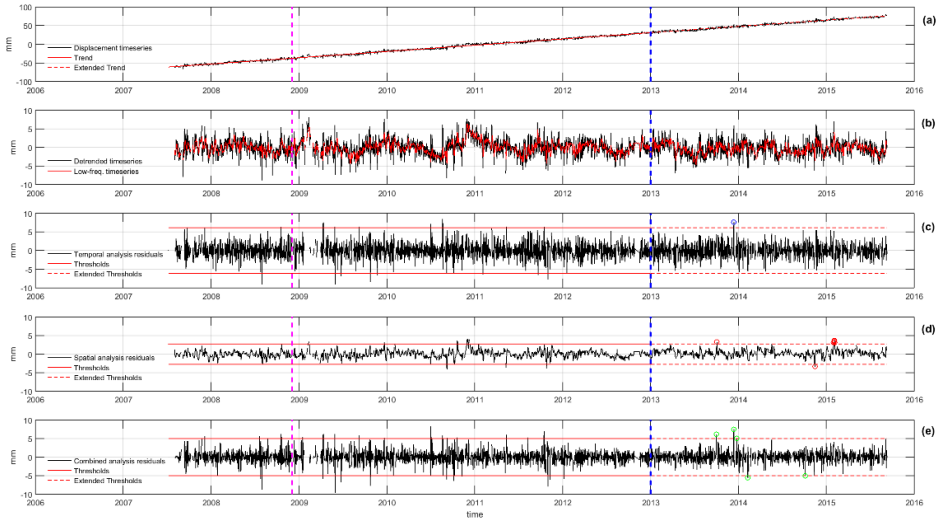


Figure C-85 FAUG (ΔN) – (a) Corrected displacement time series, (b) detrended and low-frequency time series, the (c) Temporal, (d) Spatial and (e) combined analysisresiduals.

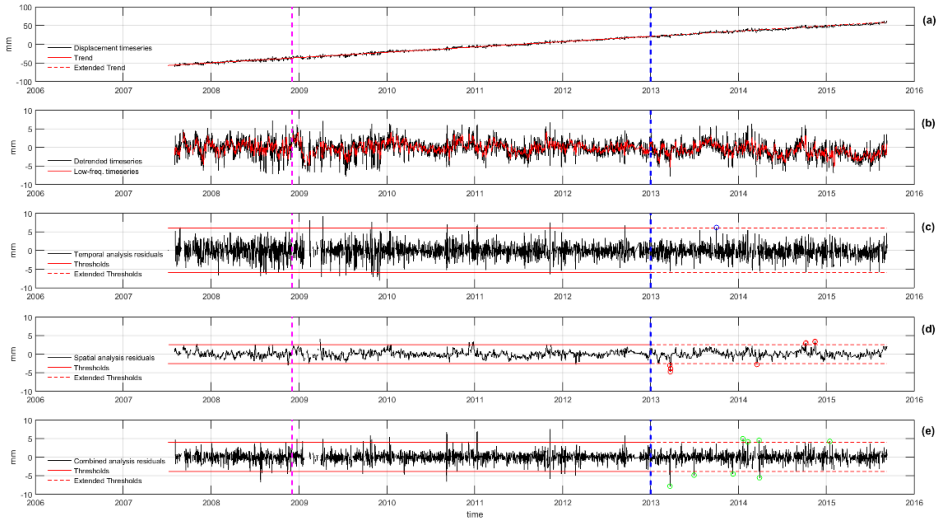


Figure C-86 Same as A-85, but for ΔE component

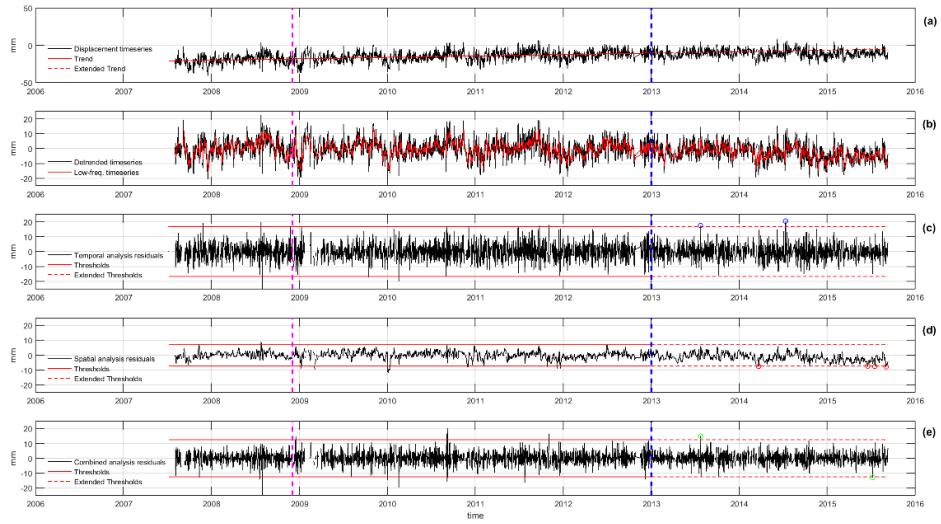


Figure C-87 Same as A-85, but for ΔU component

GIGG

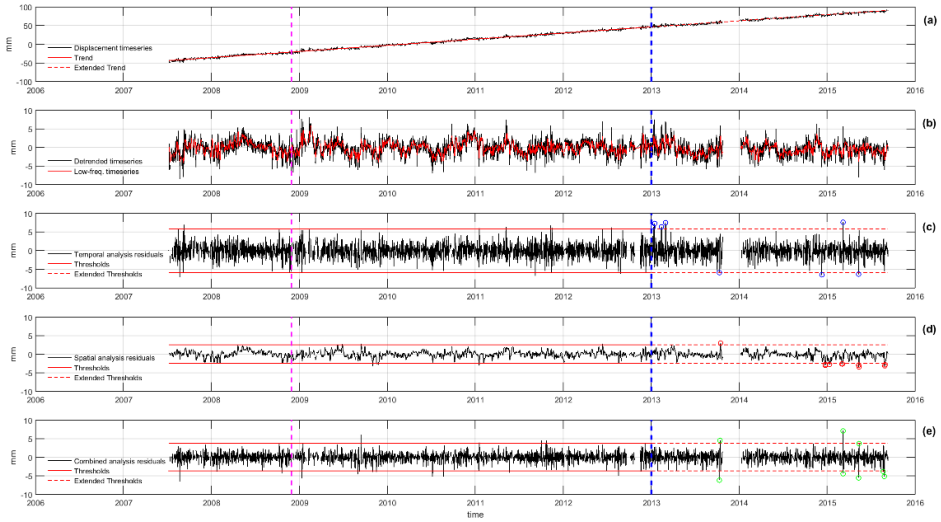


Figure C-88 GIGG (ΔN) – (a) Corrected displacement time series, (b) detrended and low-frequency time series, the (c) Temporal, (d) Spatial and (e) combined analysisresiduals.

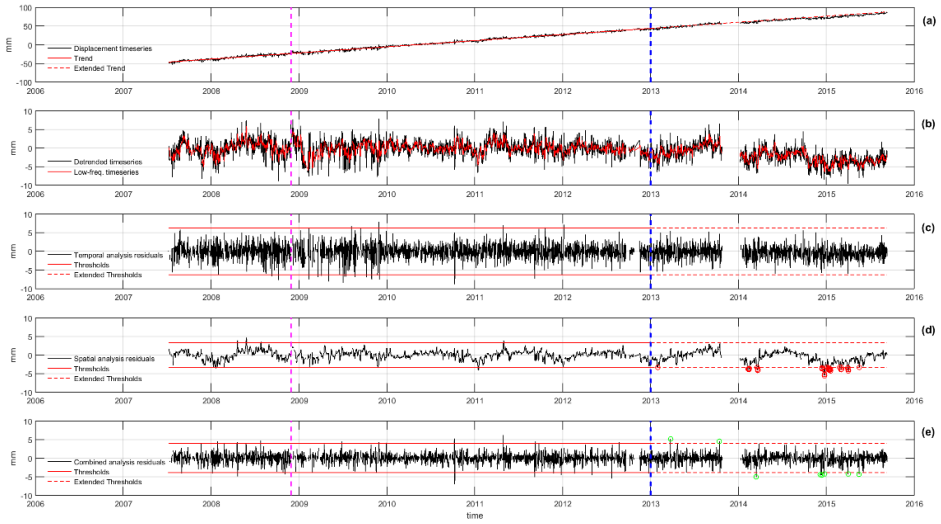


Figure C-89 Same as A-88, but for ΔE component

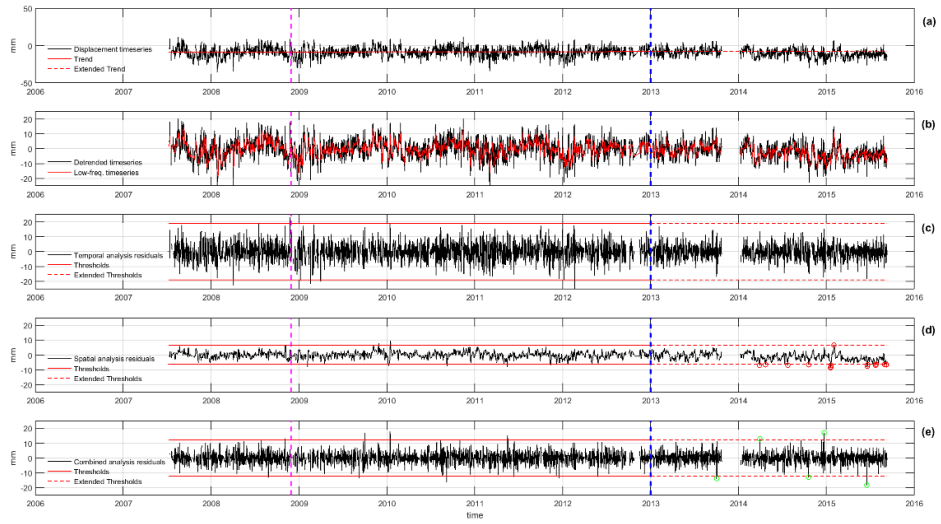


Figure C-90 Same as A-88, but for ΔU component

GIRA

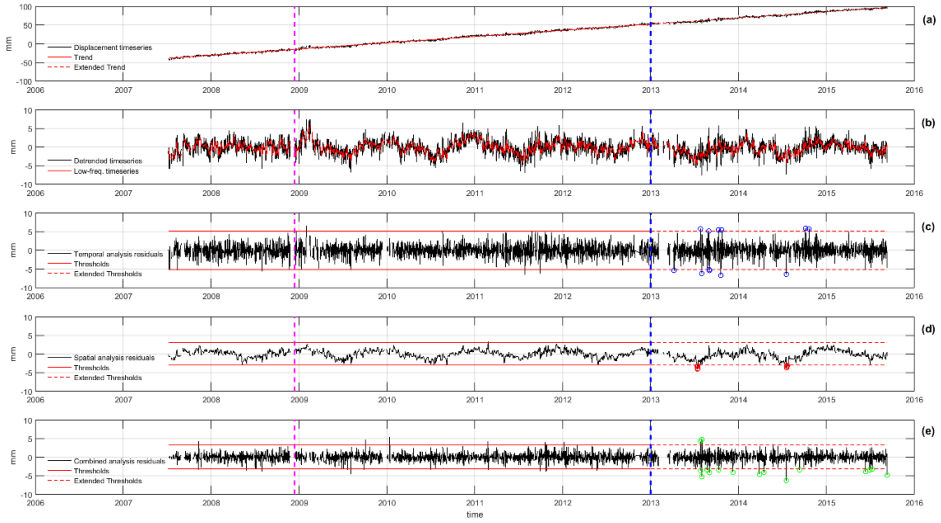


Figure C-91 GIRA (ΔN) – (a) Corrected displacement time series, (b) detrended and low-frequency time series, the (c) Temporal, (d) Spatial and (e) combined analysisresiduals.

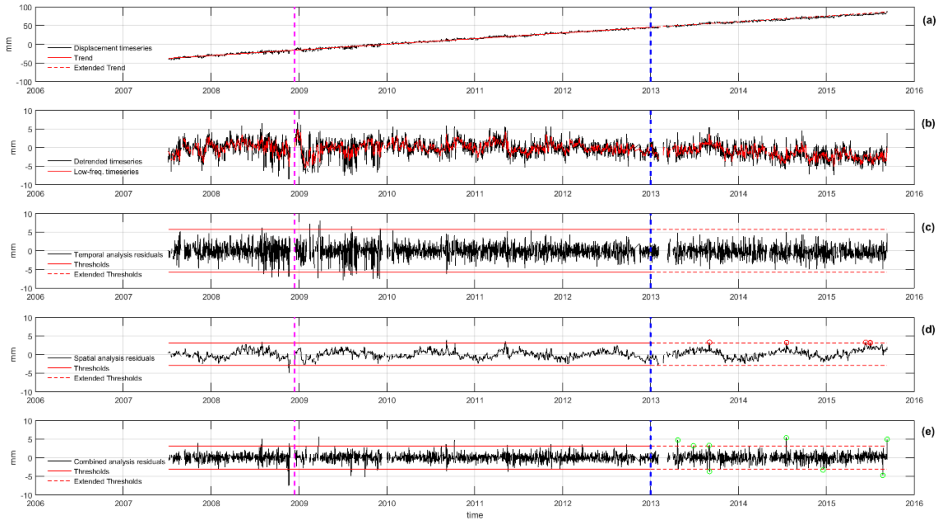


Figure C-92 Same as A-91, but for ΔE component

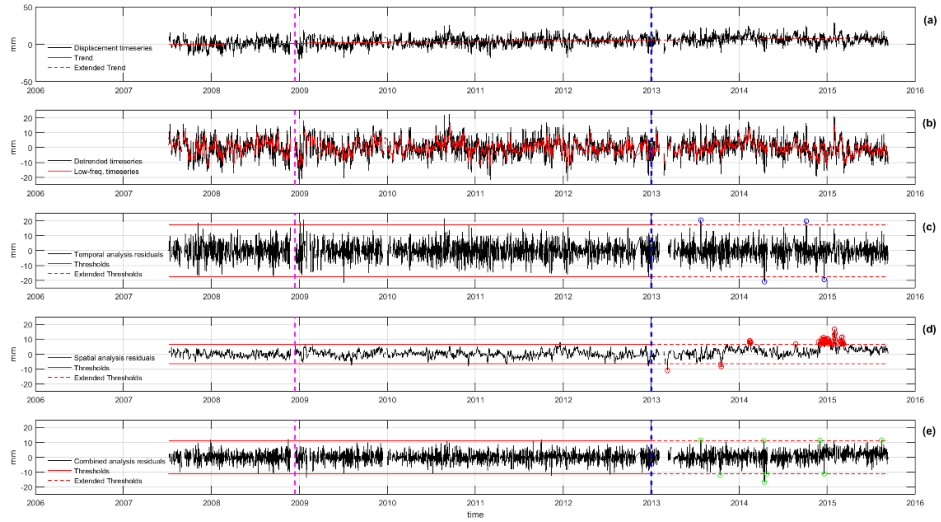


Figure C-93 Same as A-91, but for ΔU component

GLAS

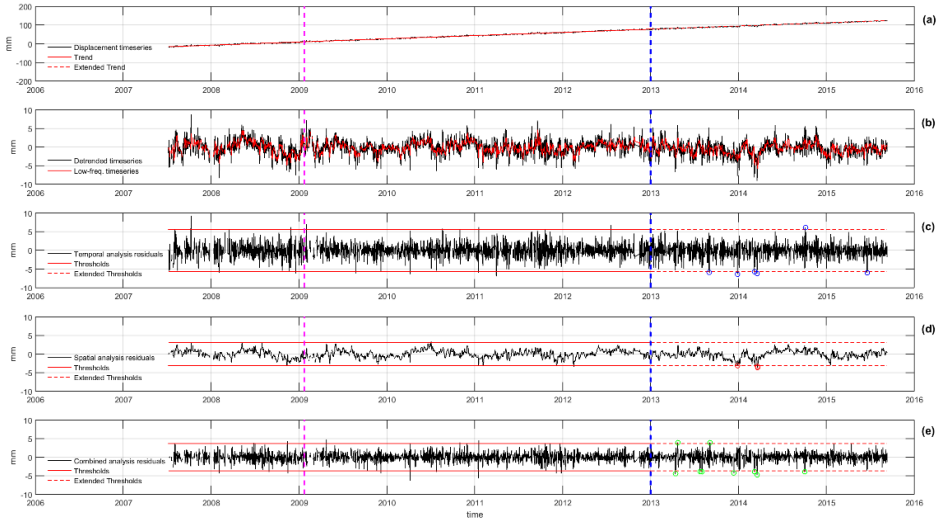


Figure C-94 GLAS (ΔN) – (a) Corrected displacement time series, (b) detrended and low-frequency time series, the (c) Temporal, (d) Spatial and (e) combined analysisresiduals.

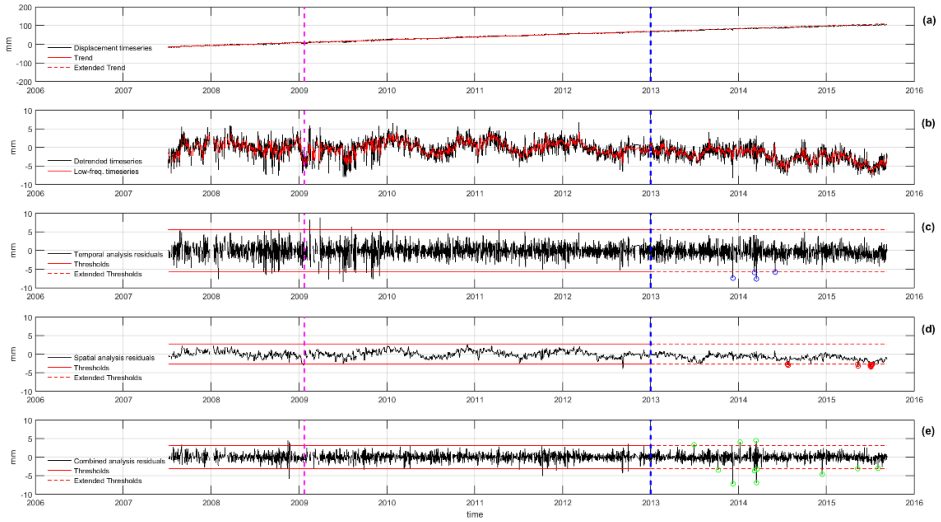


Figure C-95 Same as A-94, but for ΔE component

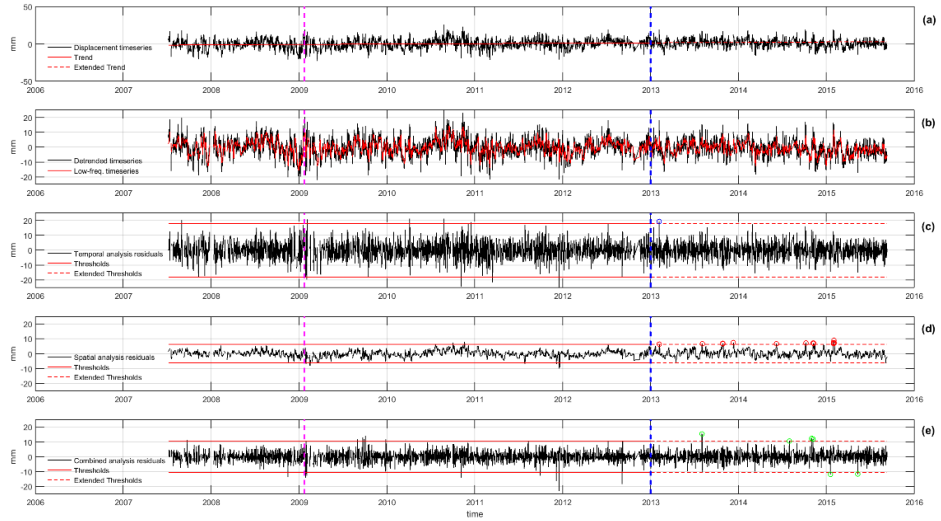


Figure C-96 Same as A-94, but for ΔU component

GORS

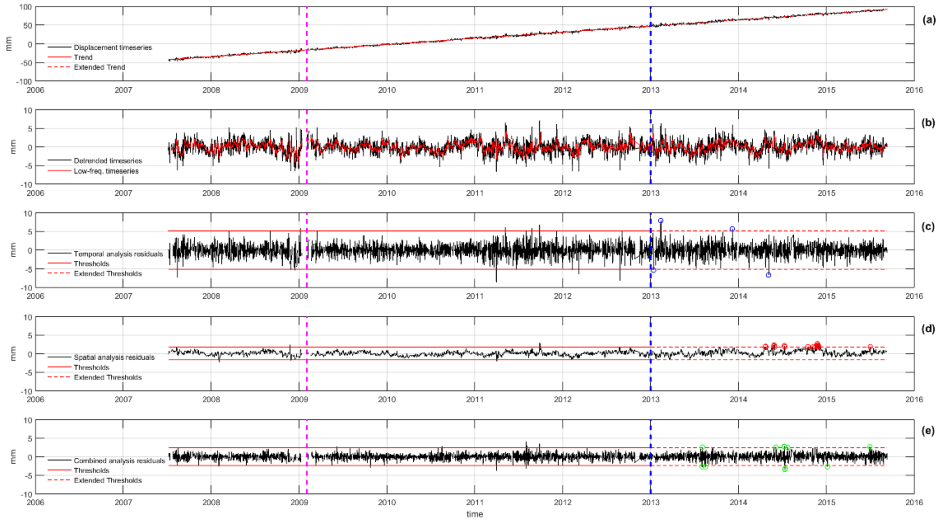


Figure C-97 GORS (ΔN) – (a) Corrected displacement time series, (b) detrended and low-frequency time series, the (c) Temporal, (d) Spatial and (e) combined analysisresiduals.

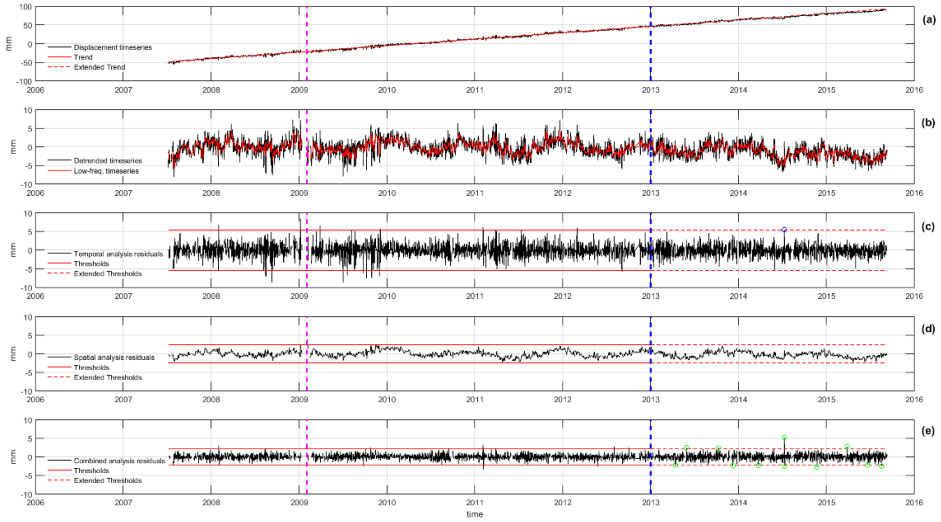


Figure C-98 Same as A-97, but for ΔE component

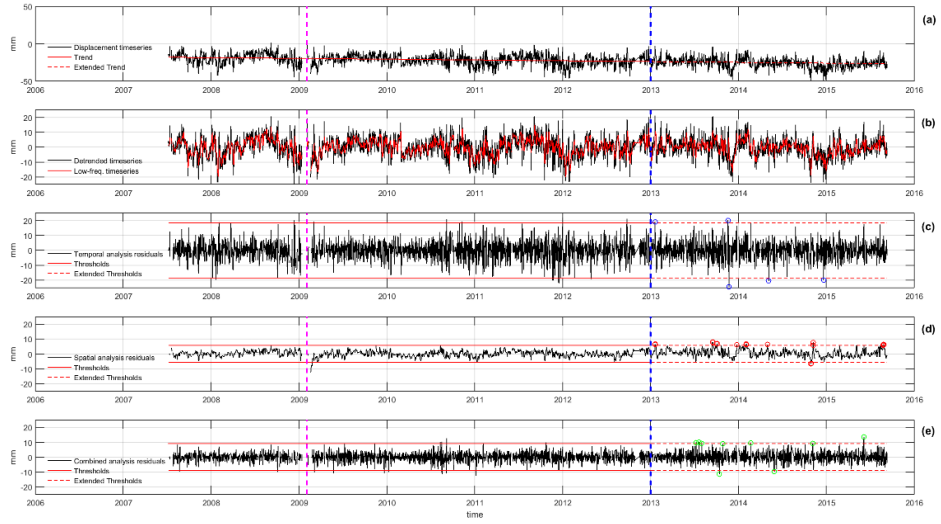


Figure C-99 Same as A-97, but for ΔU component

HARD

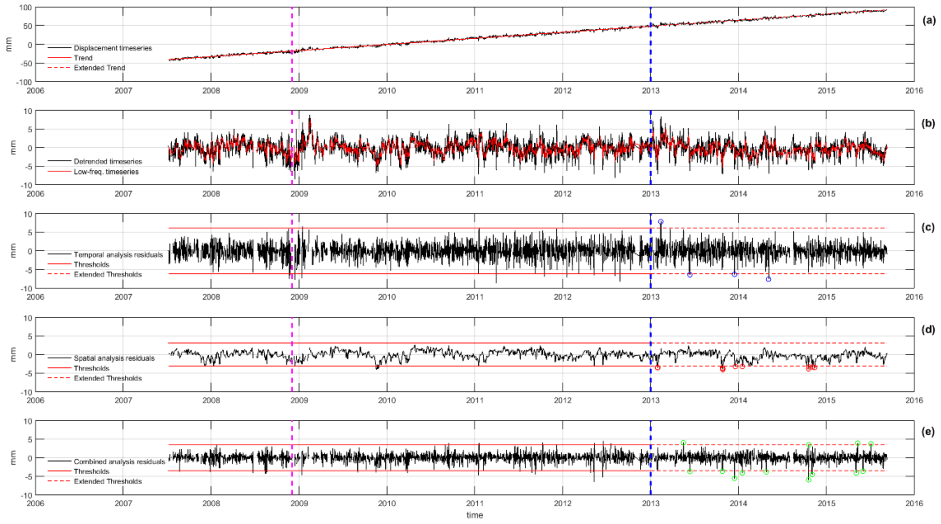


Figure C-100 HARD (ΔN) – (a) Corrected displacement time series, (b) detrended and low-frequency time series, the (c) Temporal, (d) Spatial and (e) combined analysisresiduals.

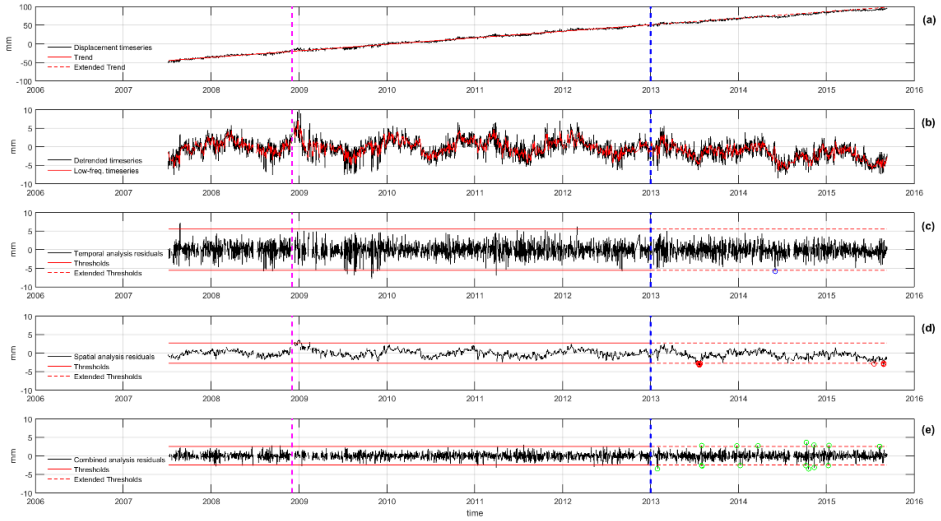


Figure C-101 Same as A-100, but for ΔE component

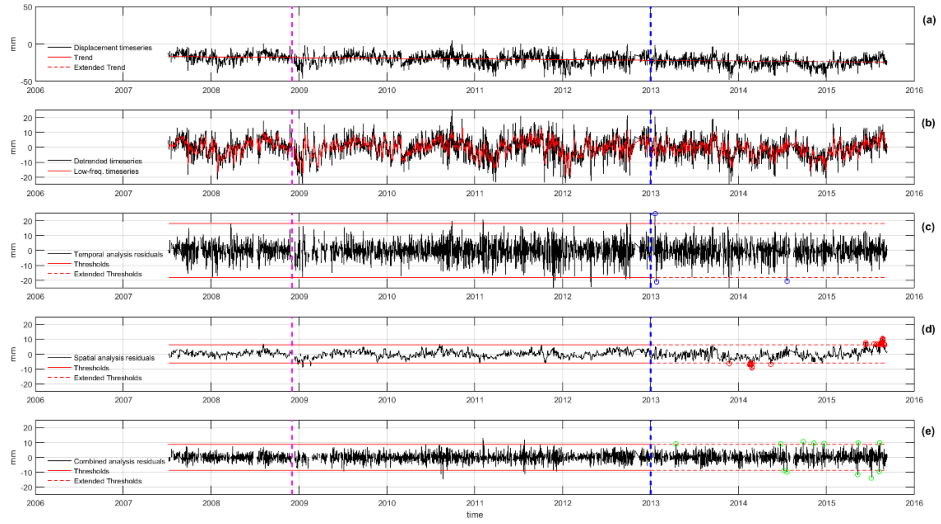


Figure C-102 Same as A-100, but for ΔU component

HELS

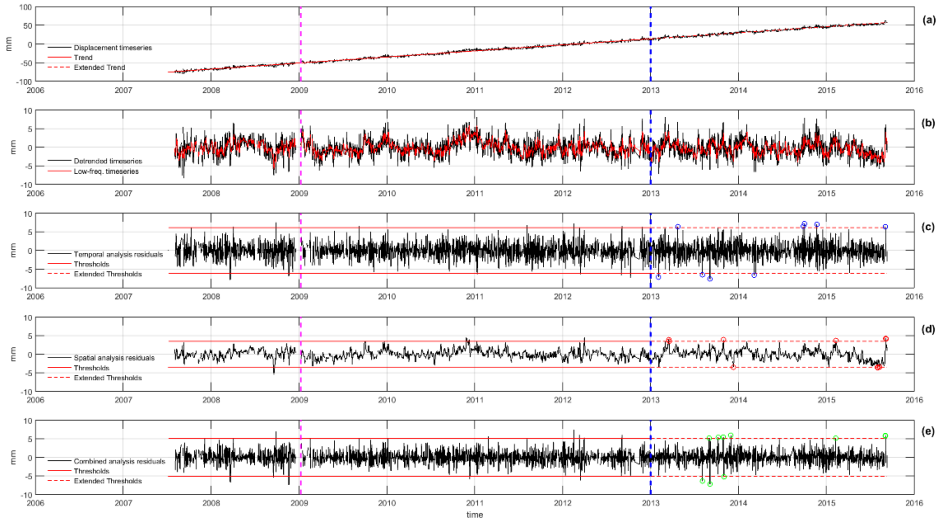


Figure C-103 HELS (ΔN) – (a) Corrected displacement time series, (b) detrended and low-frequency time series, the (c) Temporal, (d) Spatial and (e) combined analysisresiduals.

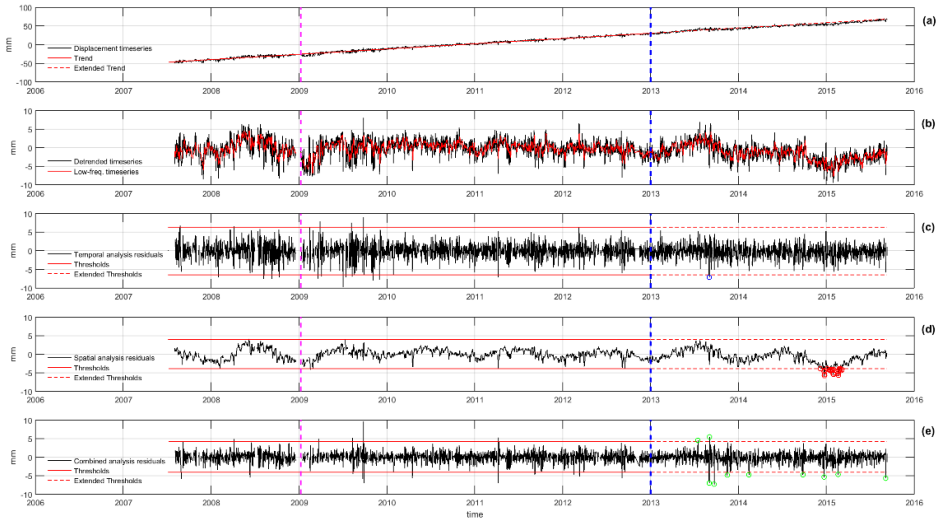


Figure C-104 Same as A-103, but for ΔE component

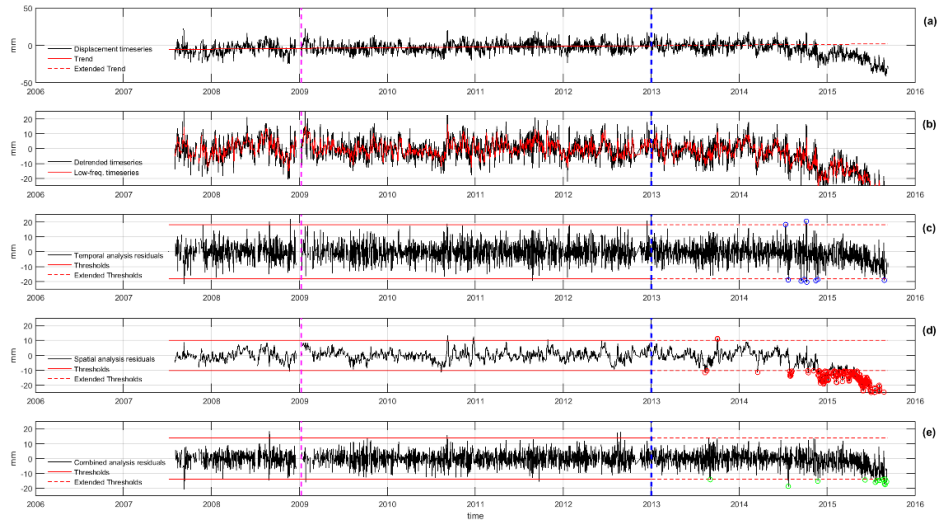


Figure C-105 Same as A-103, but for ΔU component

HERT

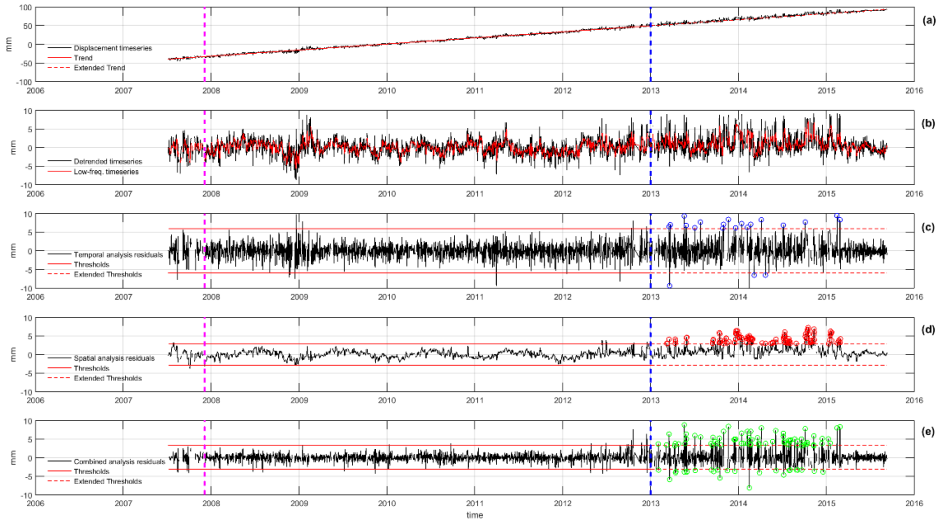


Figure C-106 HERT (ΔN) – (a) Corrected displacement time series, (b) detrended and low-frequency time series, the (c) Temporal, (d) Spatial and (e) combined analysisresiduals.

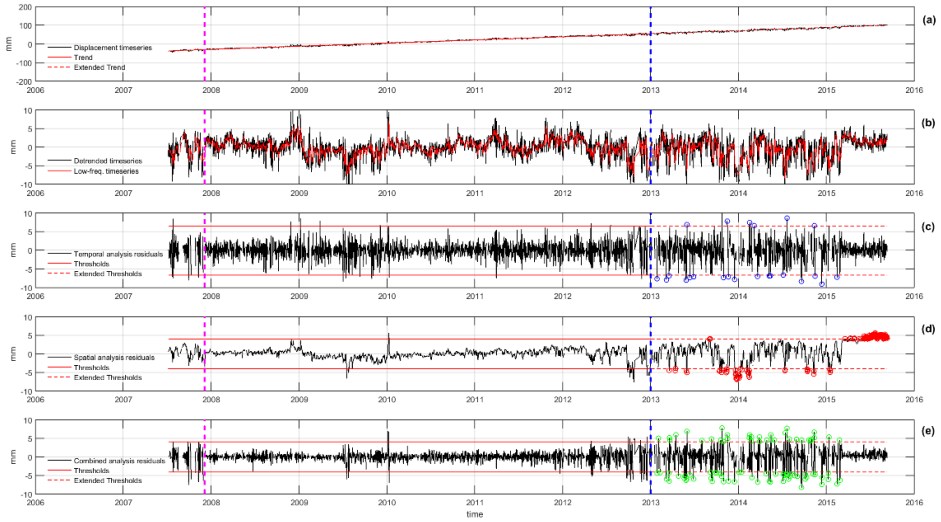


Figure C-107 Same as A-106, but for ΔE component

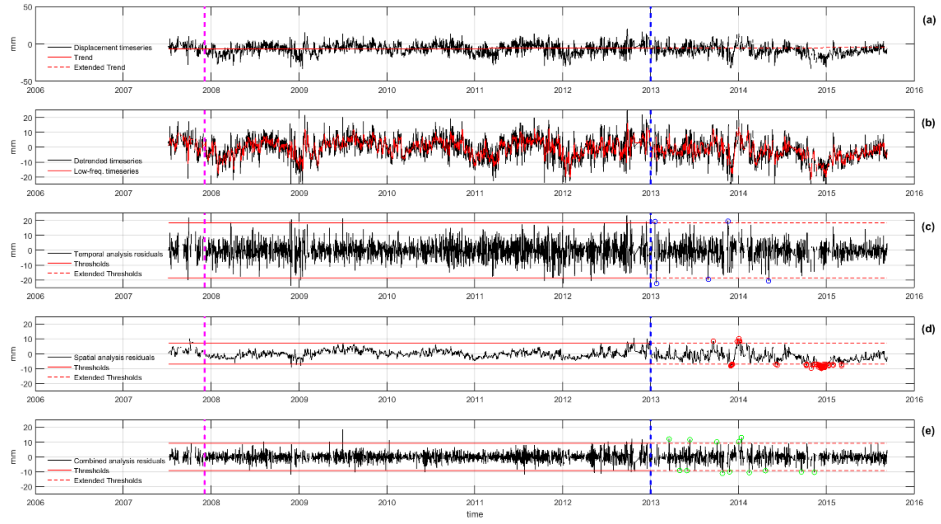


Figure C-108 Same as A-106, but for ΔU component

HOLY

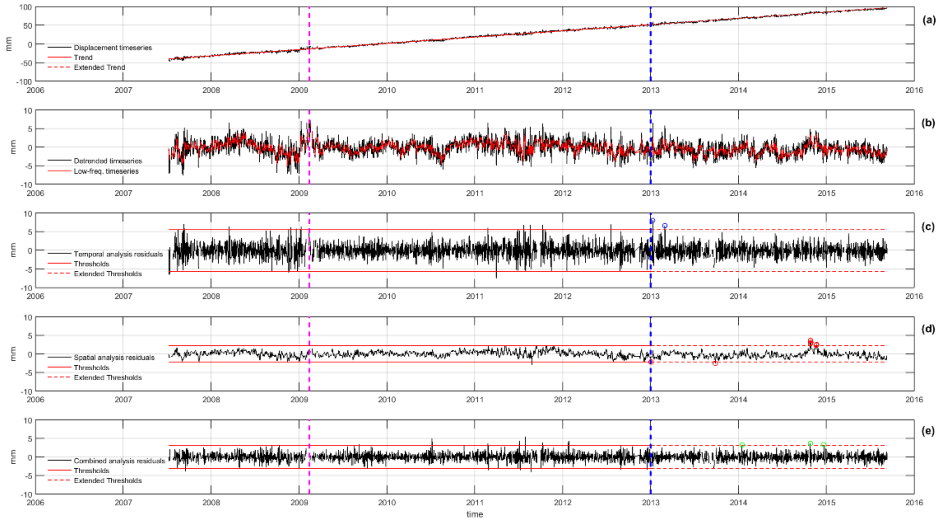


Figure C-109 HOLY (ΔN) – (a) Corrected displacement time series, (b) detrended and low-frequency time series, the (c) Temporal, (d) Spatial and (e) combined analysisresiduals.

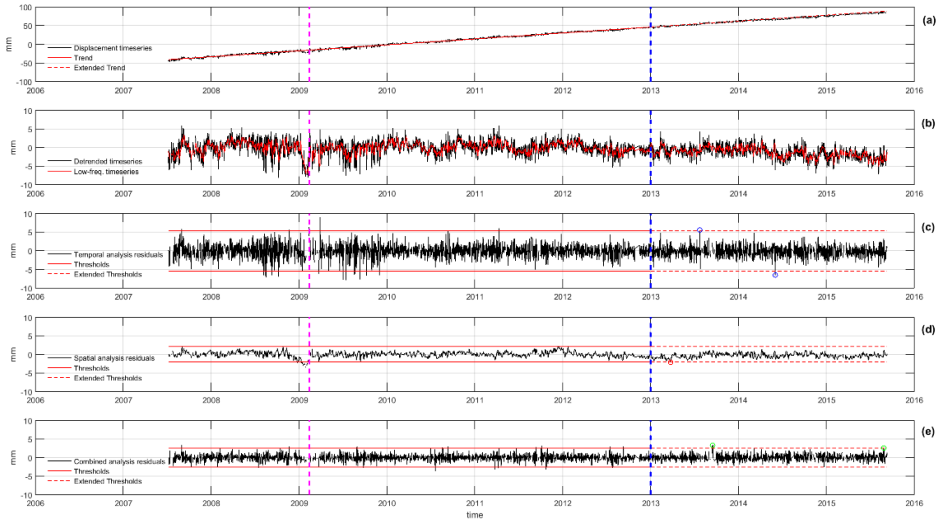


Figure C-110 Same as A-109, but for ΔE component

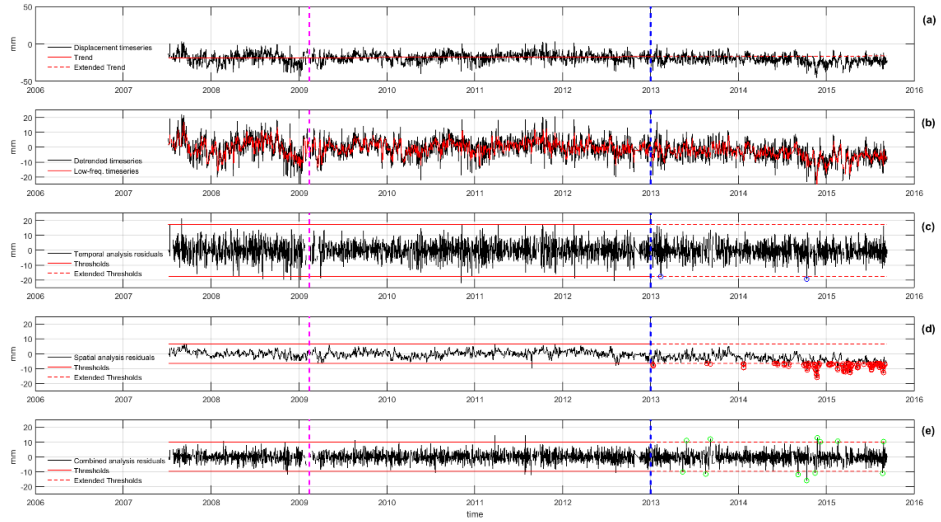


Figure C-111 Same as A-109, but for ΔU component

HOOB

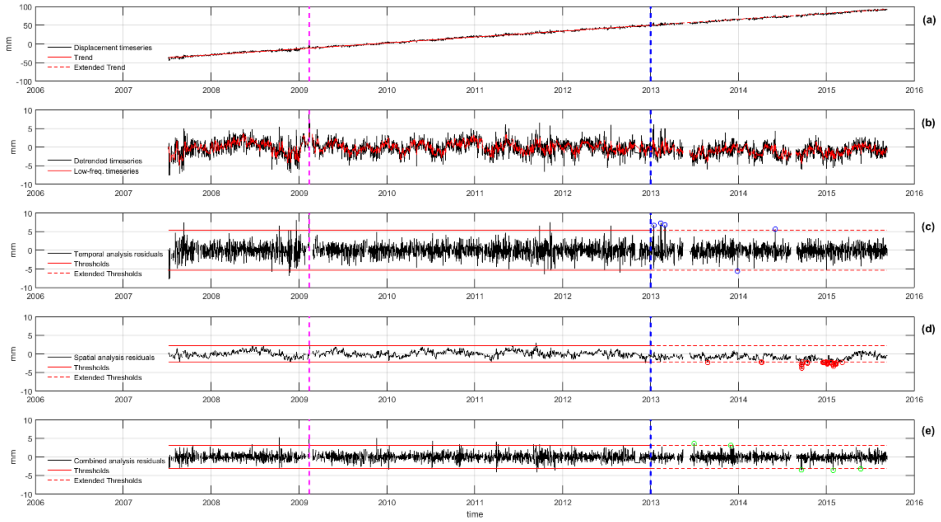


Figure C-112 HOOB (ΔN) – (a) Corrected displacement time series, (b) detrended and low-frequency time series, the (c) Temporal, (d) Spatial and (e) combined analysisresiduals.

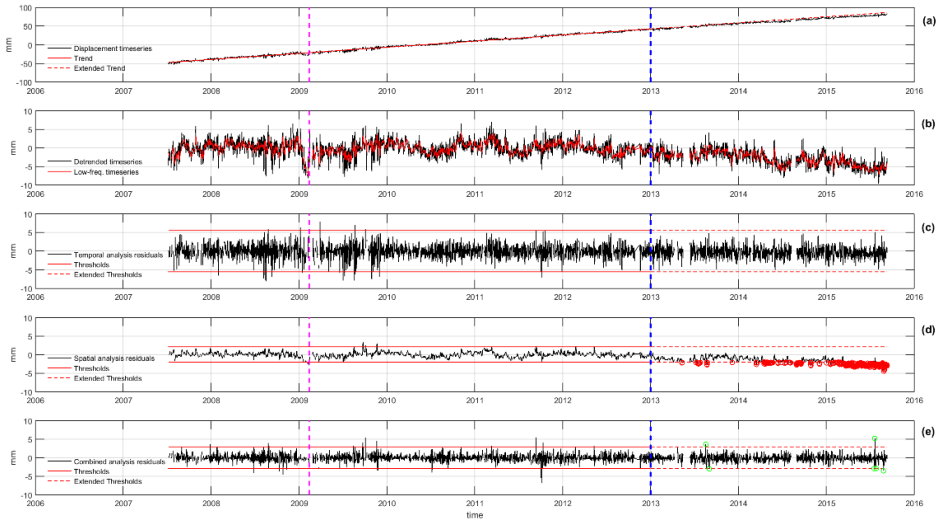


Figure C-113 Same as A-112, but for ΔE component

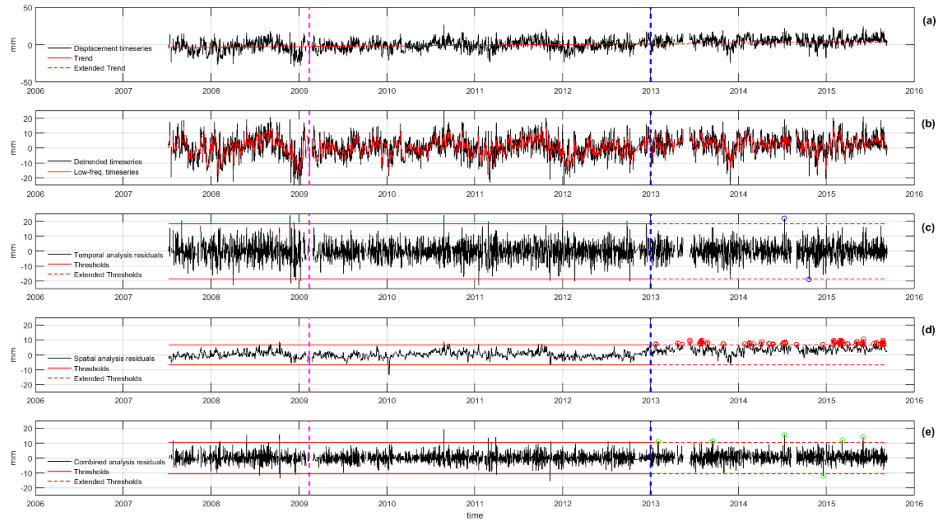


Figure C-114 Same as A-112, but for ΔU component

INVR

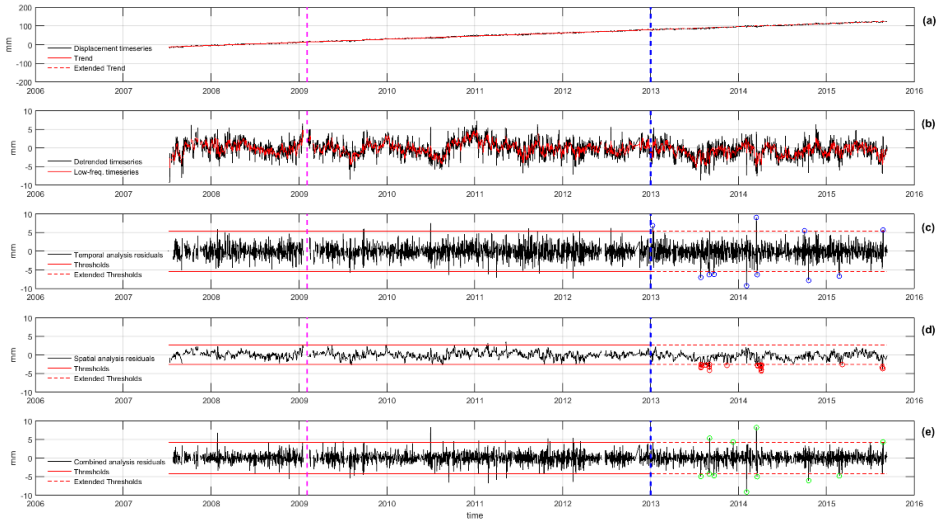


Figure C-115 INVR (ΔN) – (a) Corrected displacement time series, (b) detrended and low-frequency time series, the (c) Temporal, (d) Spatial and (e) combined analysisresiduals.

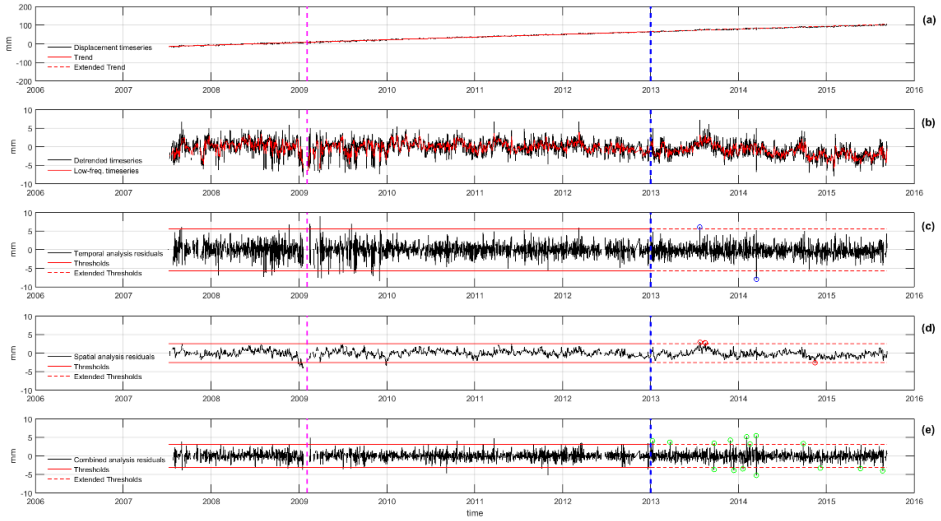


Figure C-116 Same as A-115, but for ΔE component

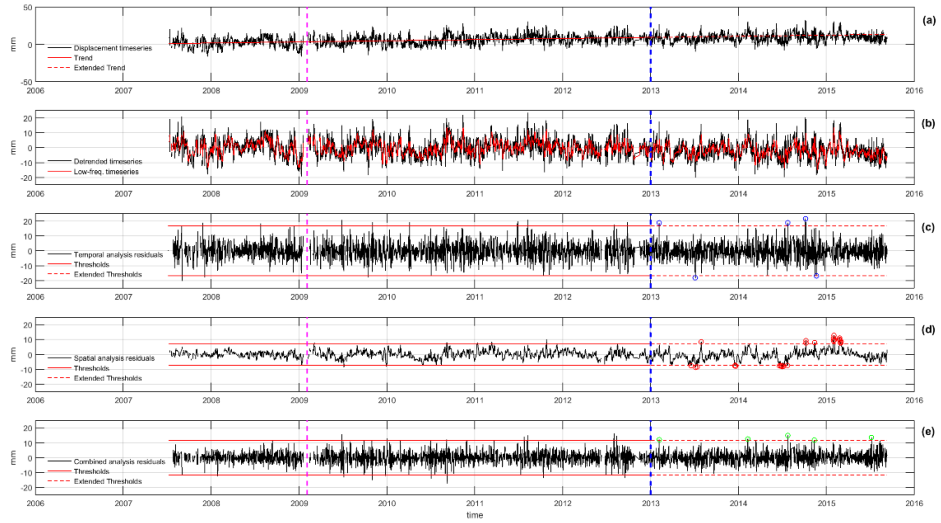


Figure C-117 Same as A-115, but for ΔU component

KELO

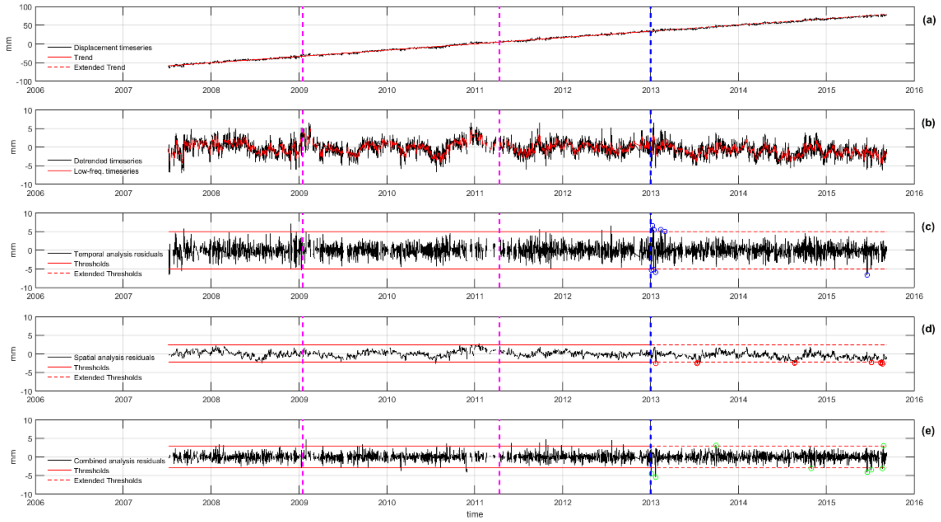


Figure C-118 KELO (ΔN) – (a) Corrected displacement time series, (b) detrended and low-frequency time series, the (c) Temporal, (d) Spatial and (e) combined analysisresiduals.

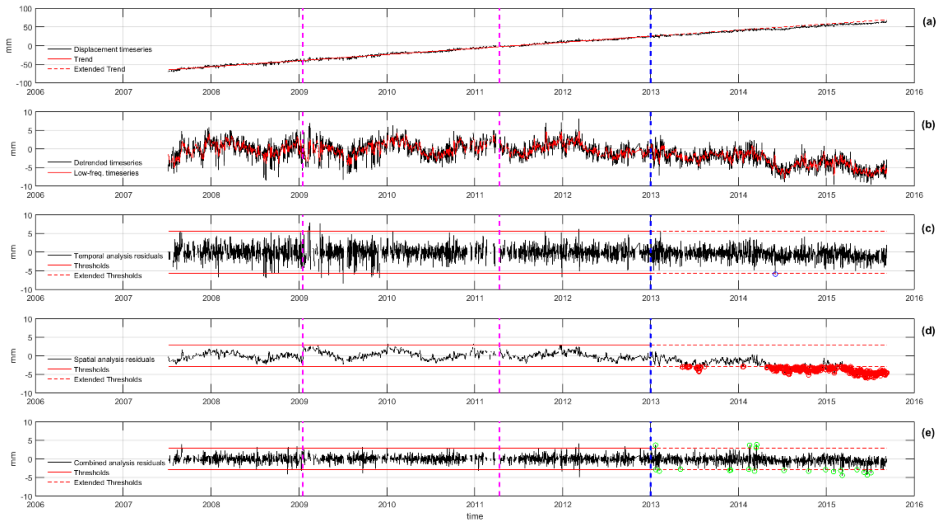


Figure C-119 Same as A-118, but for ΔE component

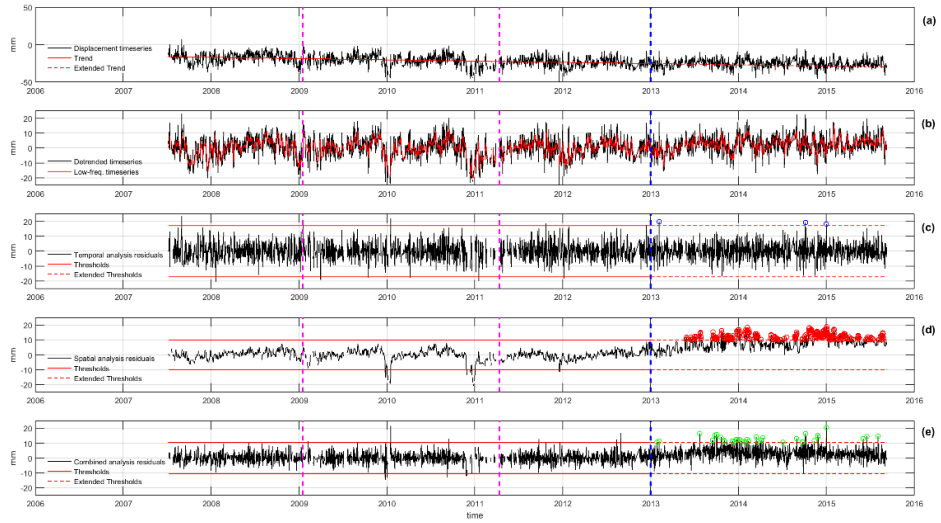


Figure C-120 Same as A-118, but for ΔU component

KEYW

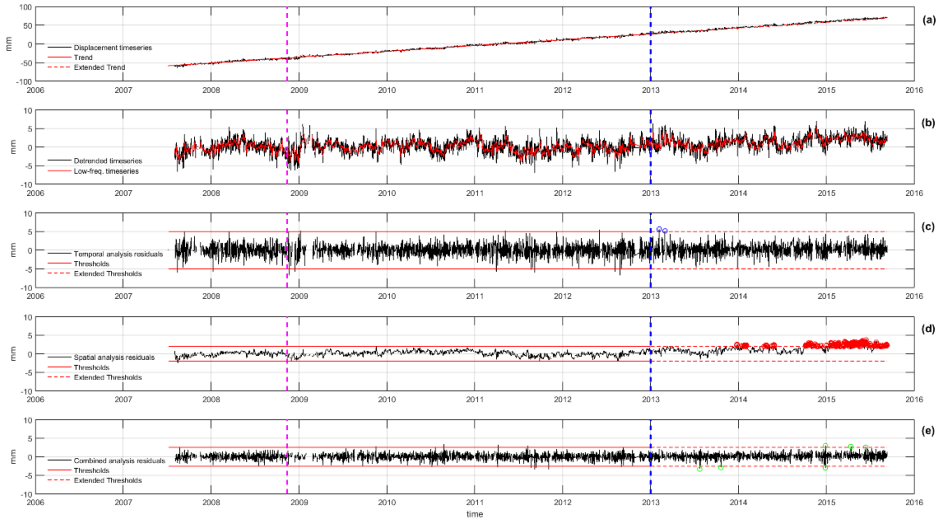


Figure C-121 KEYW (ΔN) – (a) Corrected displacement time series, (b) detrended and low-frequency time series, the (c) Temporal, (d) Spatial and (e) combined analysisresiduals.

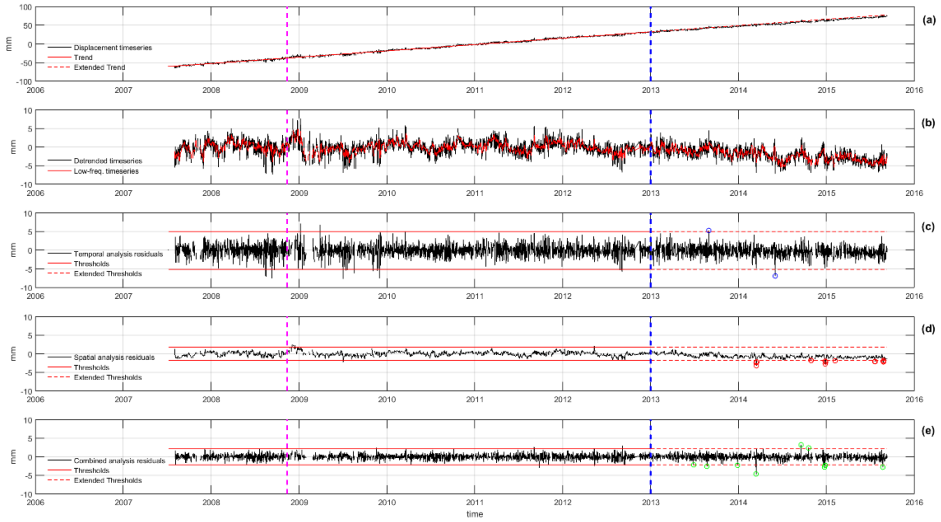


Figure C-122 Same as A-121, but for ΔE component

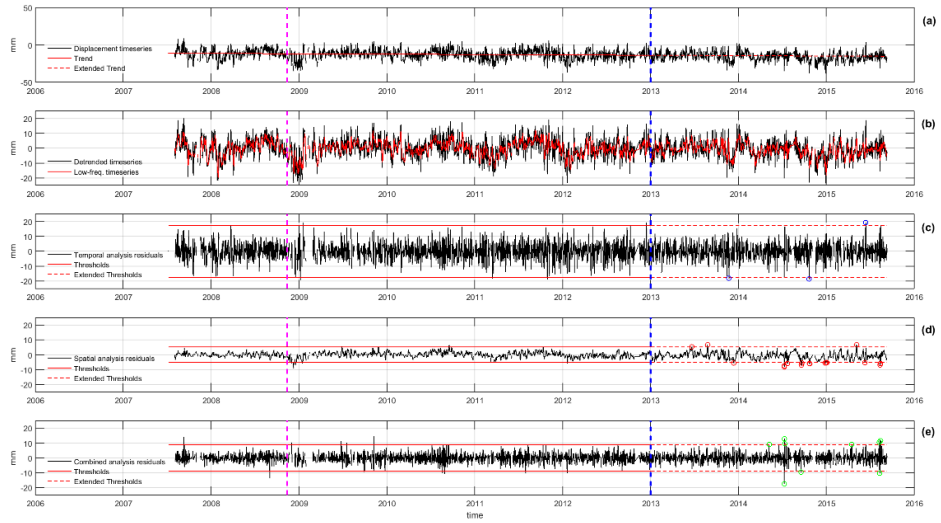


Figure C-123 Same as A-121, but for ΔU component

KILN

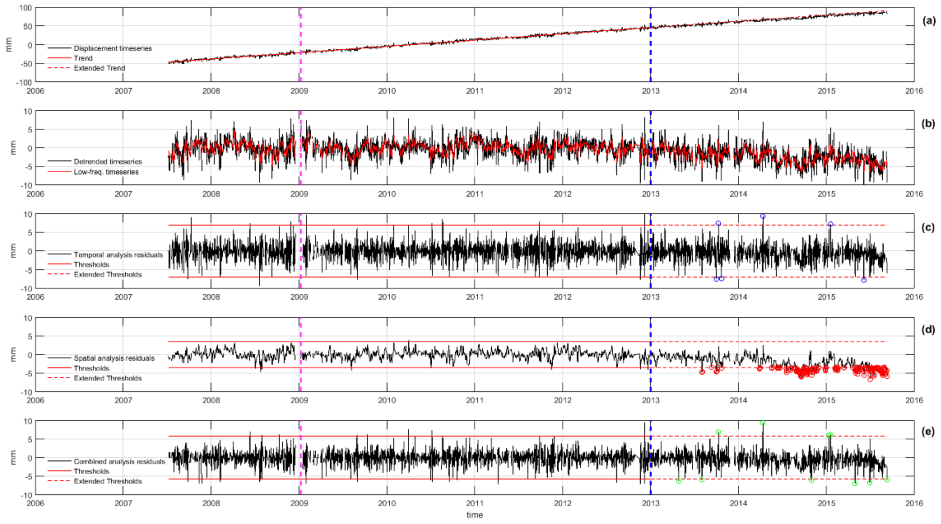


Figure C-124 KILN (ΔN) – (a) Corrected displacement time series, (b) detrended and low-frequency time series, the (c) Temporal, (d) Spatial and (e) combined analysisresiduals.

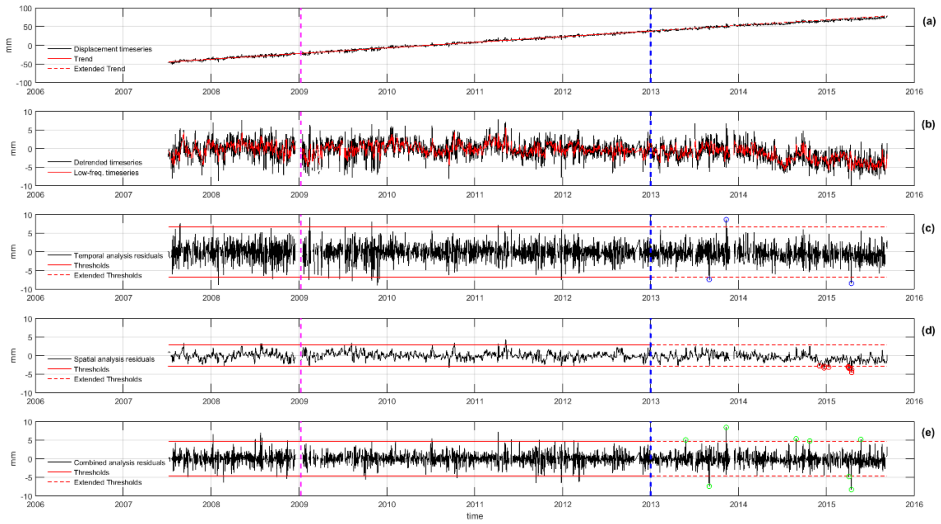


Figure C-125 Same as A-124, but for ΔE component

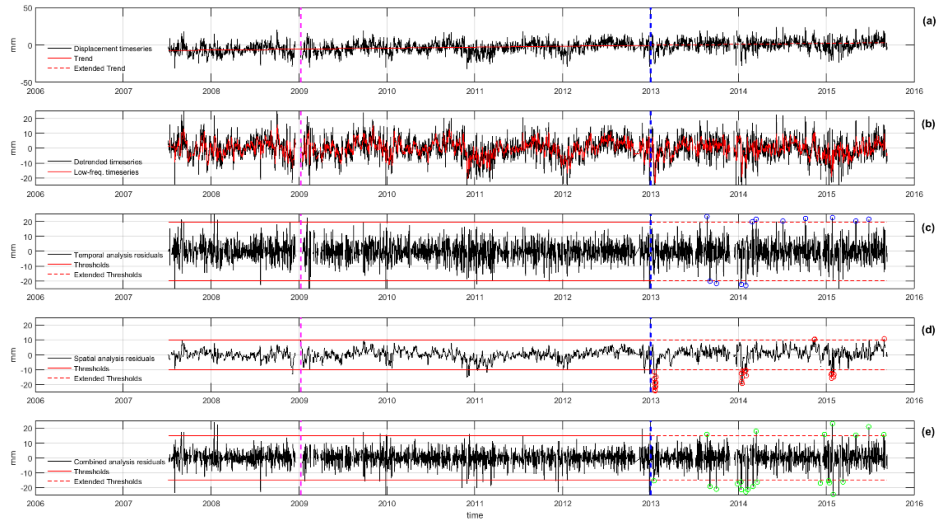


Figure C-126 Same as A-124, but for ΔU component

KING

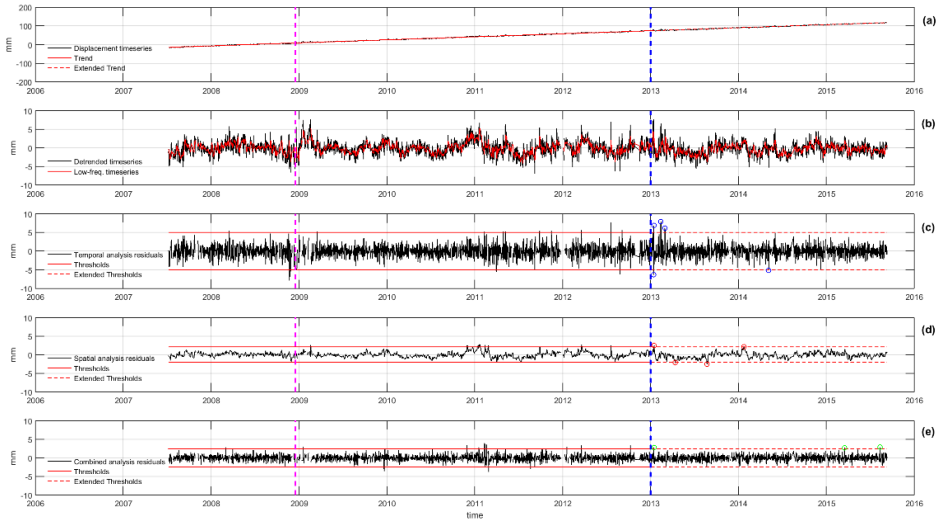


Figure C-127 KING (ΔN) – (a) Corrected displacement time series, (b) detrended and low-frequency time series, the (c) Temporal, (d) Spatial and (e) combined analysisresiduals.

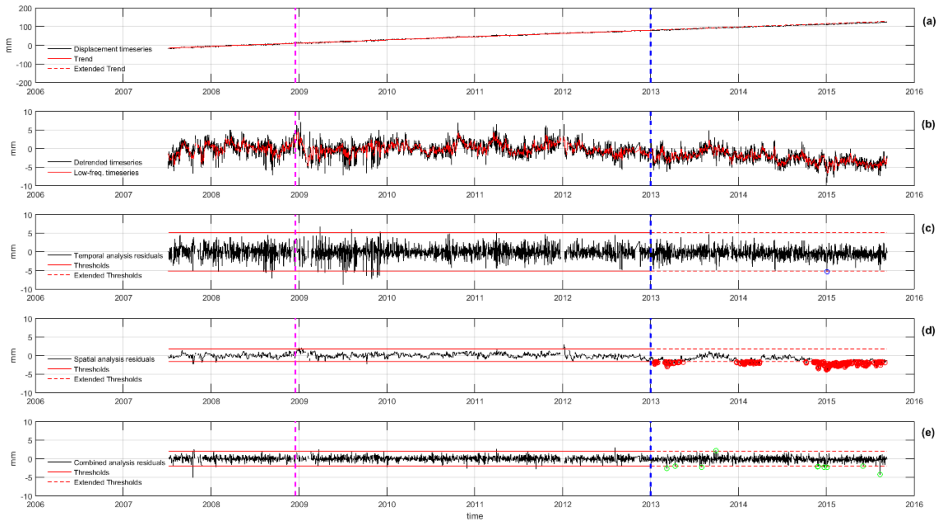


Figure C-128 Same as A-127, but for ΔE component

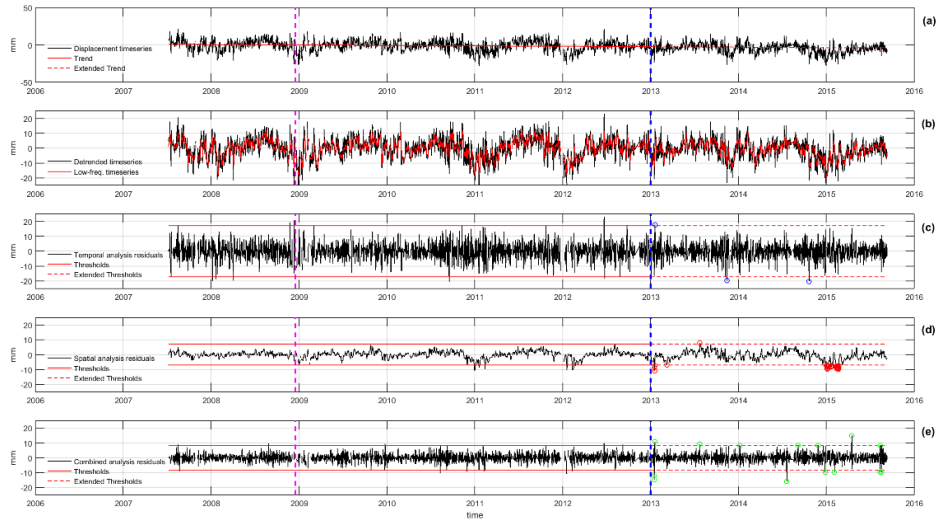


Figure C-129 Same as A-127, but for ΔU component

KINL

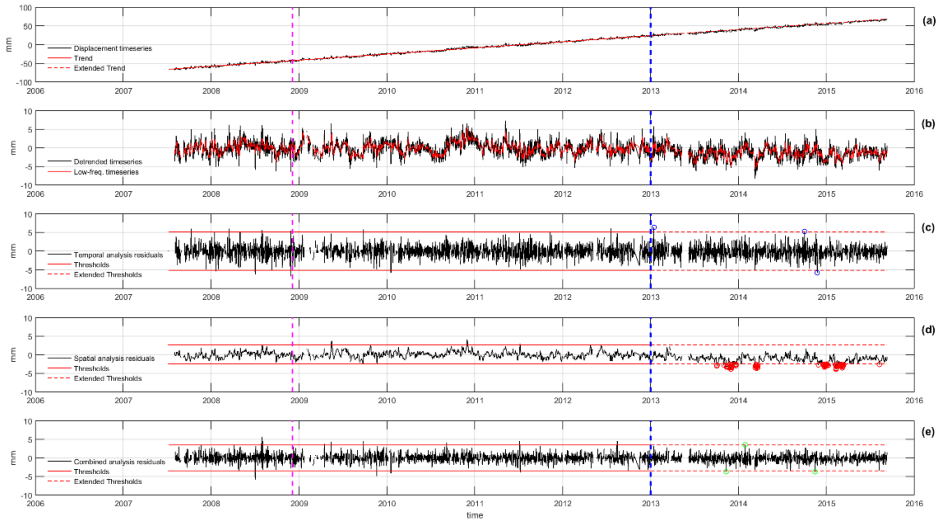


Figure C-130 KINL (ΔN) – (a) Corrected displacement time series, (b) detrended and low-frequency time series, the (c) Temporal, (d) Spatial and (e) combined analysisresiduals.

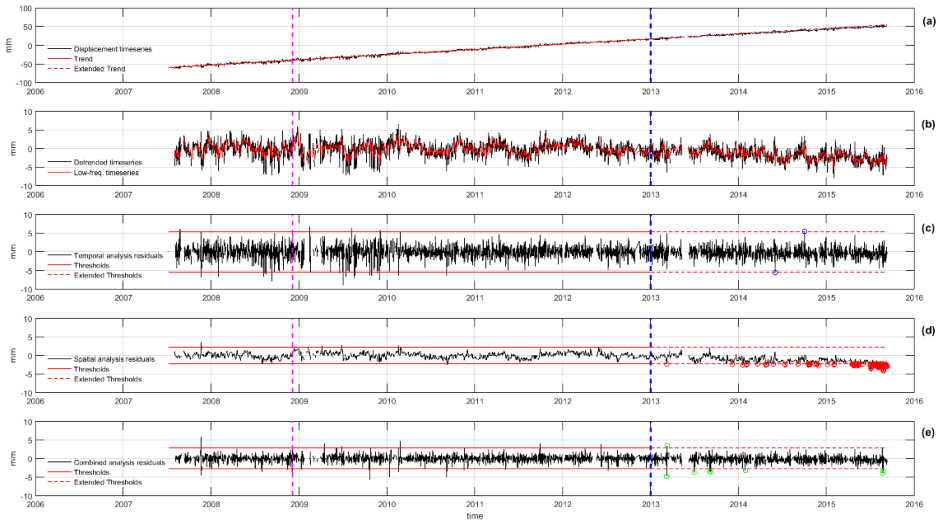


Figure C-131 Same as A-130, but for ΔE component

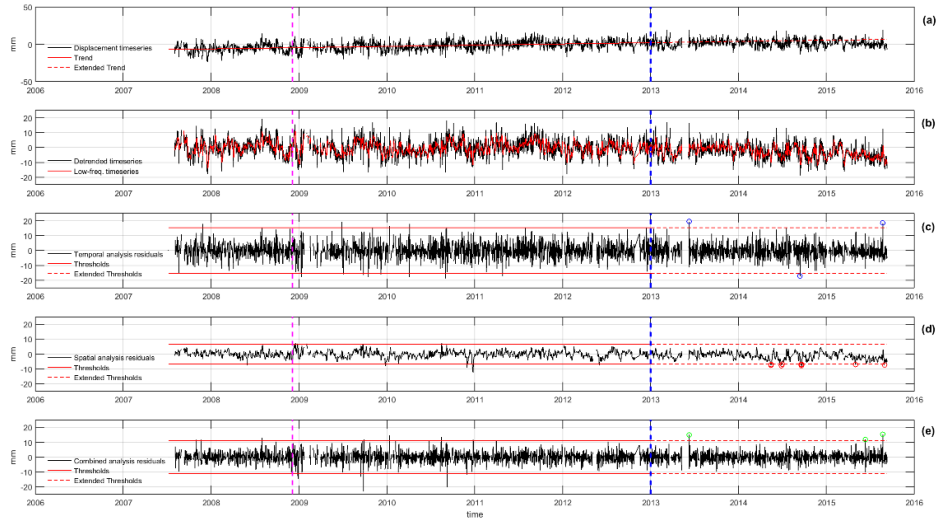


Figure C-132 Same as A-130, but for ΔU component

KIRK

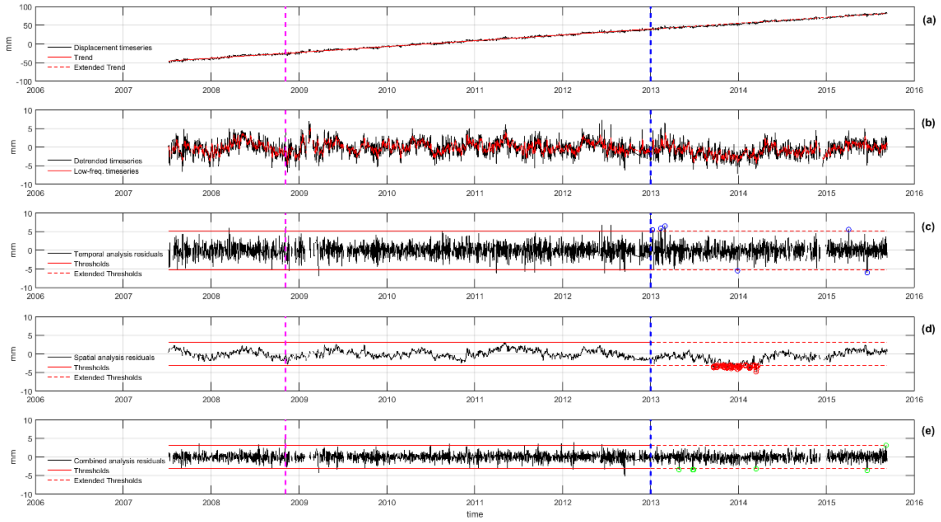


Figure C-133 KIRK (ΔN) – (a) Corrected displacement time series, (b) detrended and low-frequency time series, the (c) Temporal, (d) Spatial and (e) combined analysisresiduals.

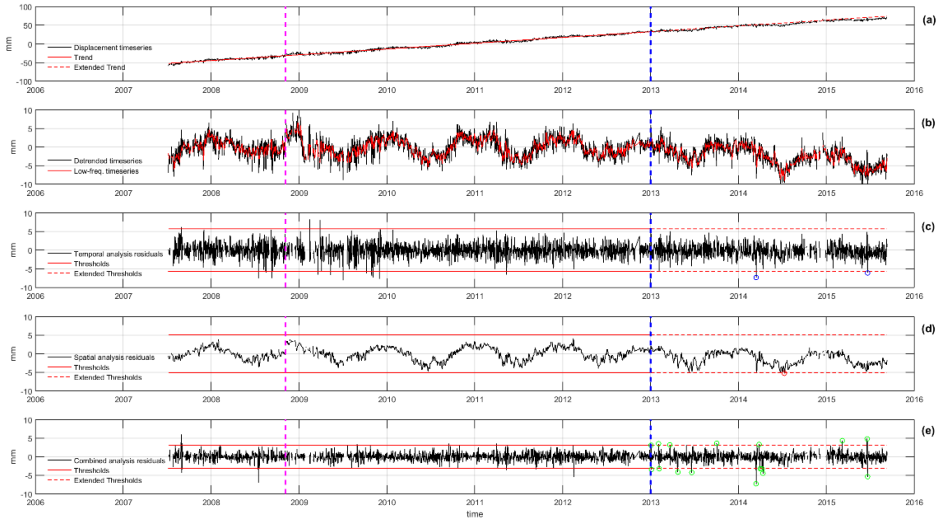


Figure C-134 Same as A-133, but for ΔE component

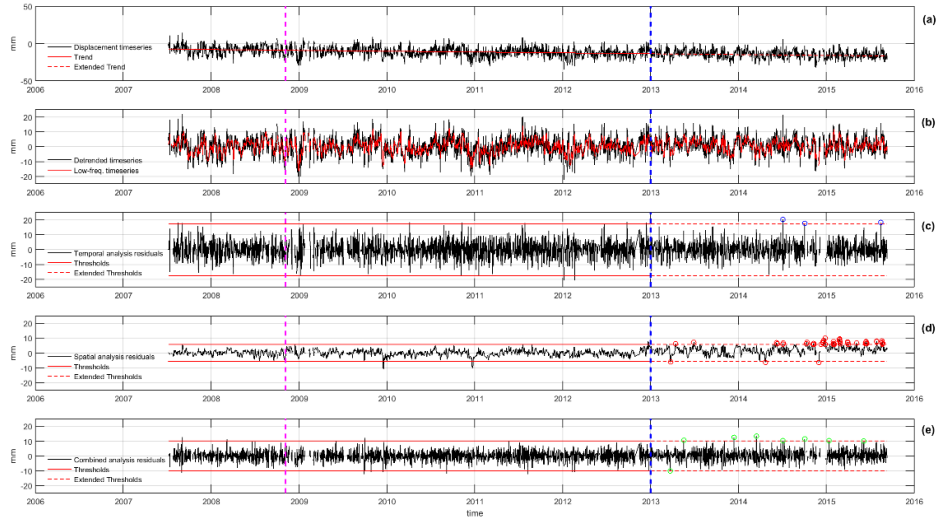


Figure C-135 Same as A-133, but for ΔU component

KIRW

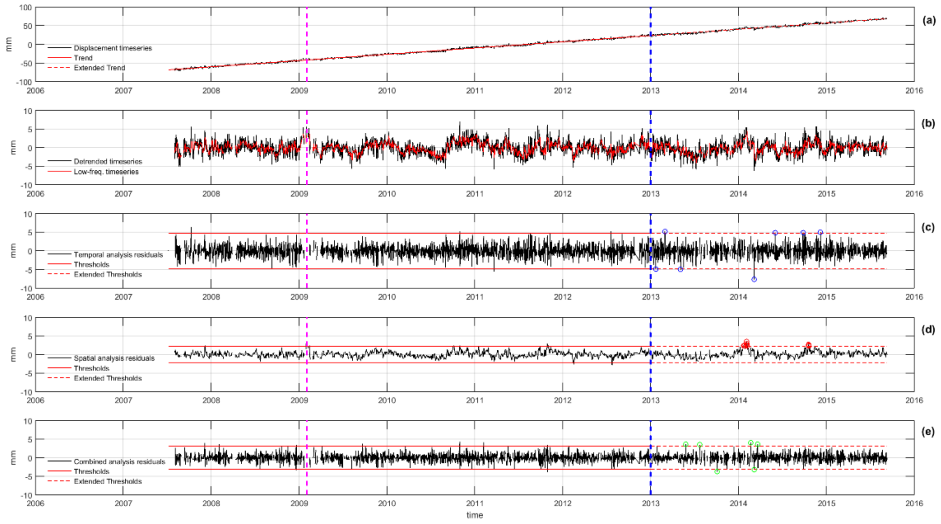


Figure C-136 KIRW (ΔN) – (a) Corrected displacement time series, (b) detrended and low-frequency time series, the (c) Temporal, (d) Spatial and (e) combined analysisresiduals.

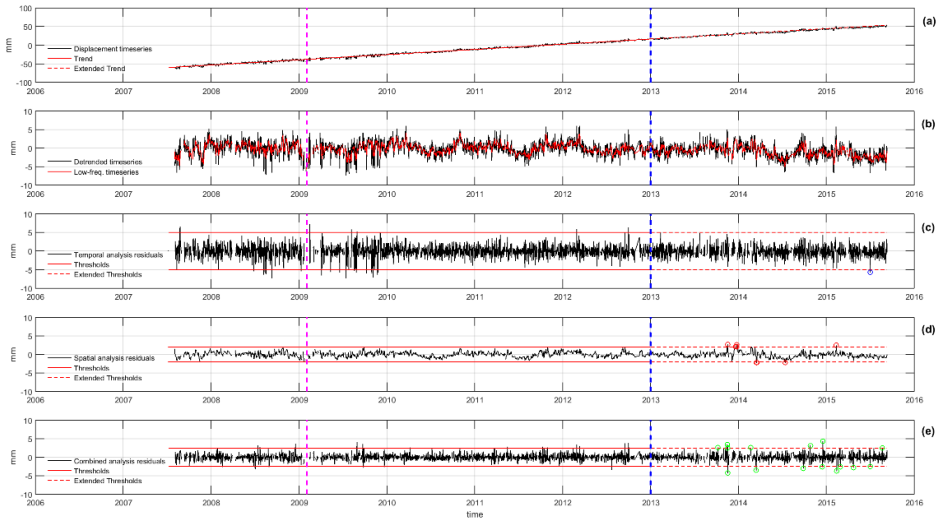


Figure C-137 Same as A-136, but for ΔE component

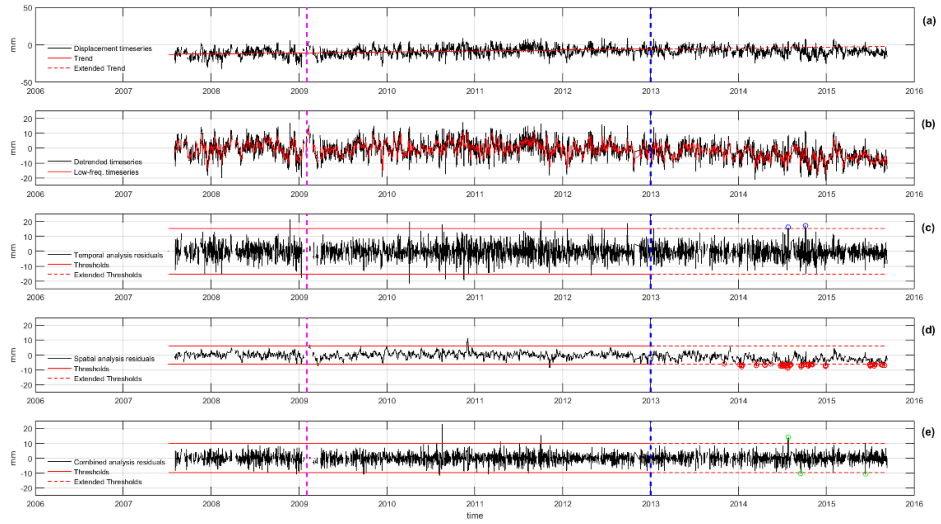


Figure C-138 Same as A-136, but for ΔU component

KLRE

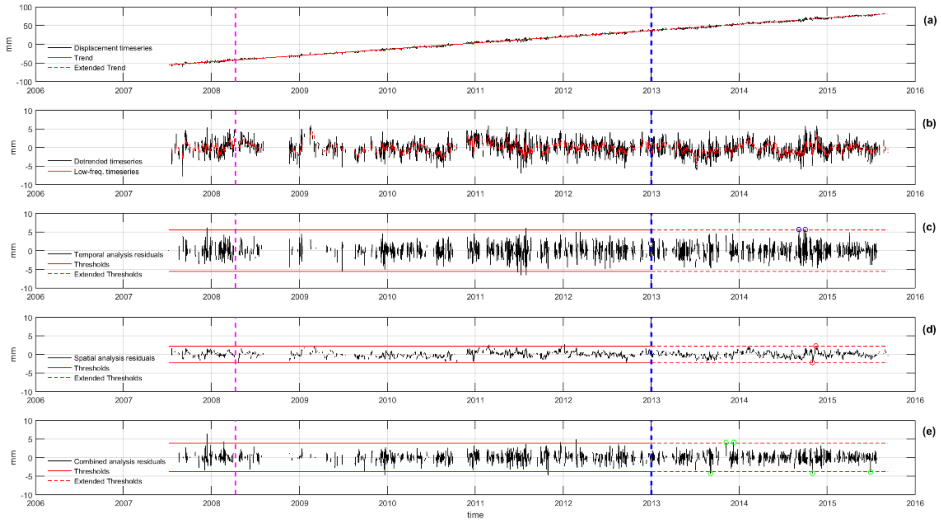


Figure C-139 KLRE (ΔN) – (a) Corrected displacement time series, (b) detrended and low-frequency time series, the (c) Temporal, (d) Spatial and (e) combined analysisresiduals.

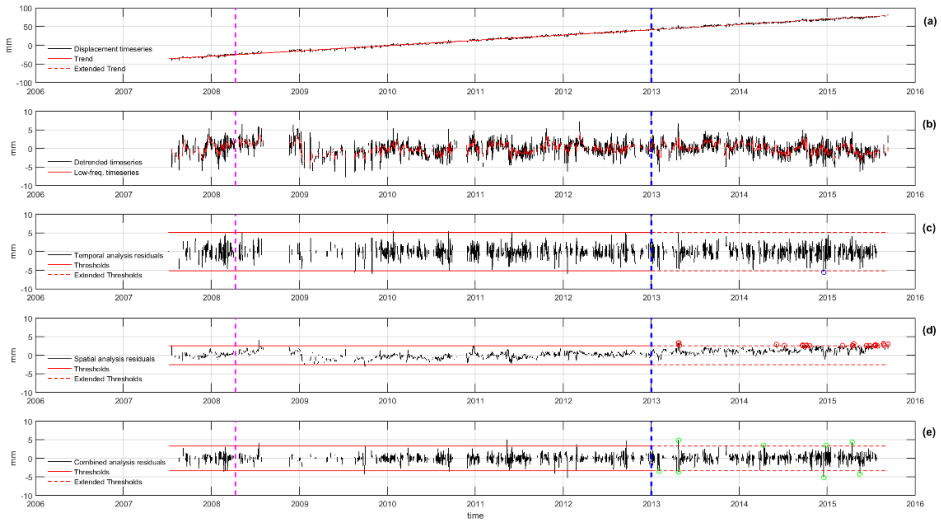


Figure C-140 Same as A-140, but for ΔE component

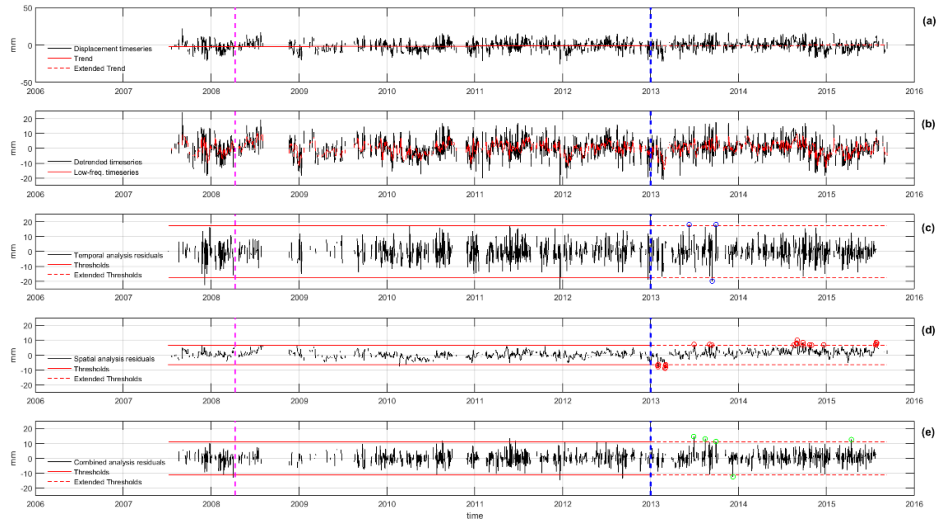


Figure C-141 Same as A-140, but for ΔU component

LEED

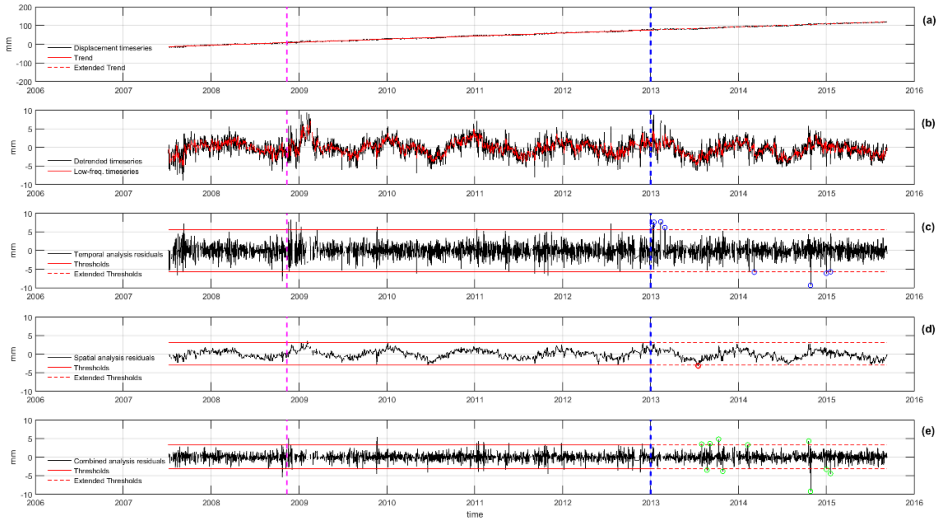


Figure C-142 LEED (ΔN) – (a) Corrected displacement time series, (b) detrended and low-frequency time series, the (c) Temporal, (d) Spatial and (e) combined analysisresiduals.

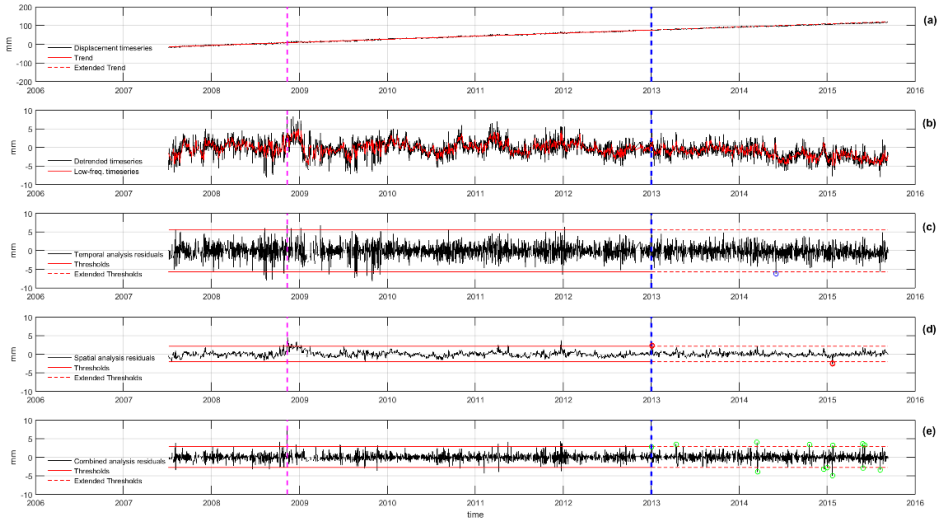


Figure C-143 Same as A-142, but for ΔE component

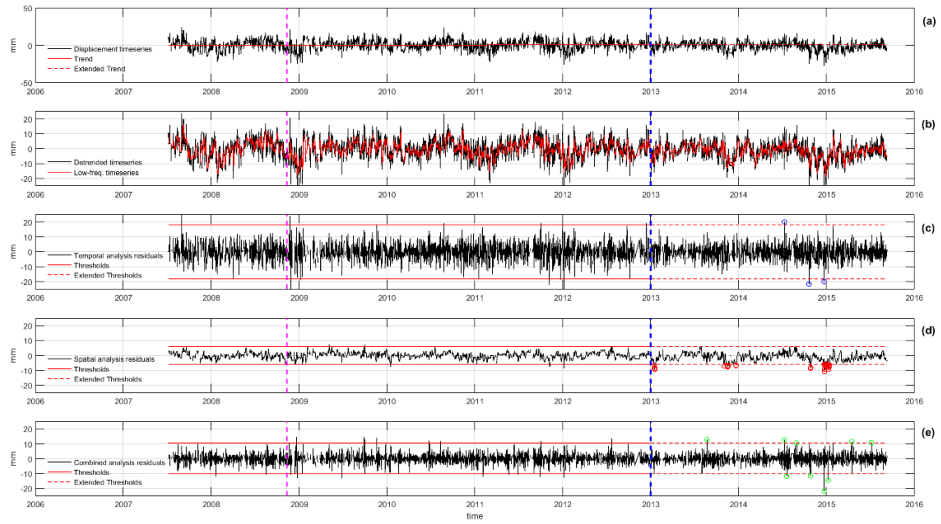


Figure C-144 Same as A-142, but for ΔU component

LEEK

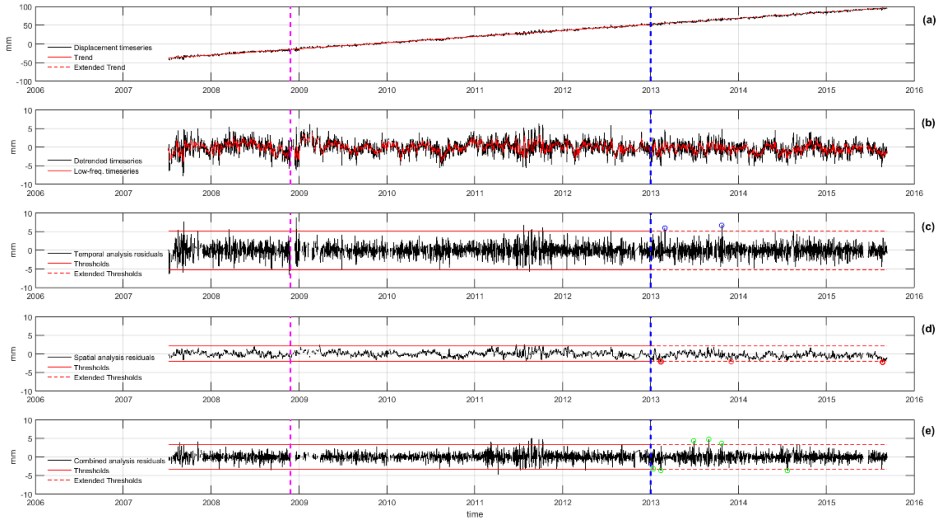


Figure C-145 LEEK (ΔN) – (a) Corrected displacement time series, (b) detrended and low-frequency time series, the (c) Temporal, (d) Spatial and (e) combined analysisresiduals.

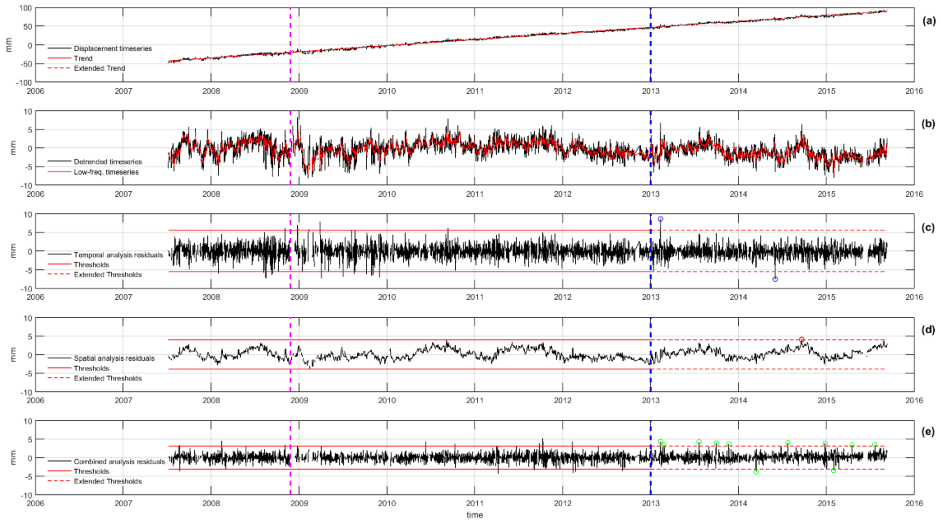


Figure C-146 Same as A-145, but for ΔE component

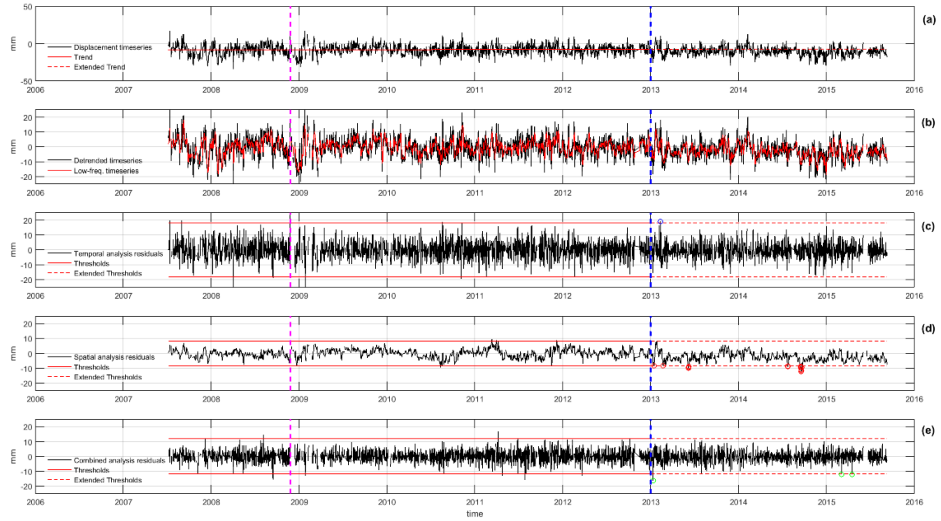


Figure C-147 Same as A-145, but for ΔU component

LICF

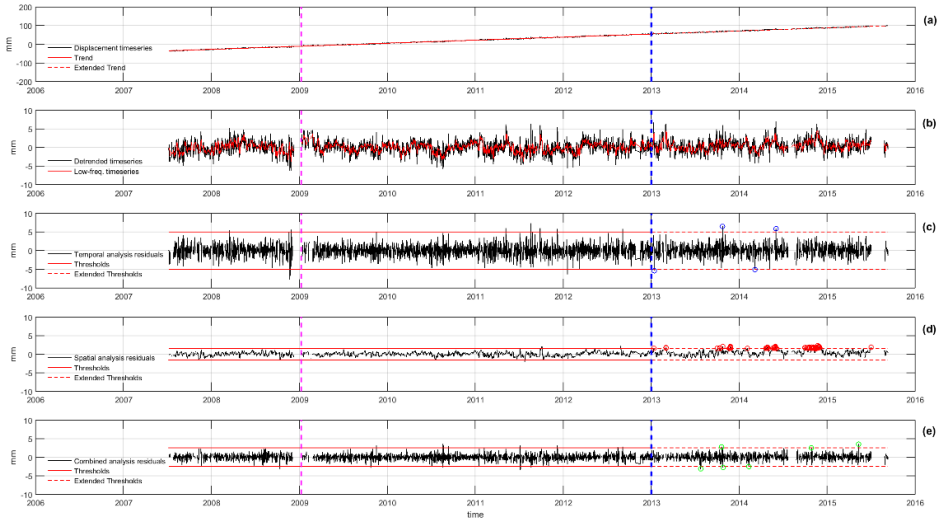


Figure C-148 LICF (ΔN) – (a) Corrected displacement time series, (b) detrended and low-frequency time series, the (c) Temporal, (d) Spatial and (e) combined analysisresiduals.

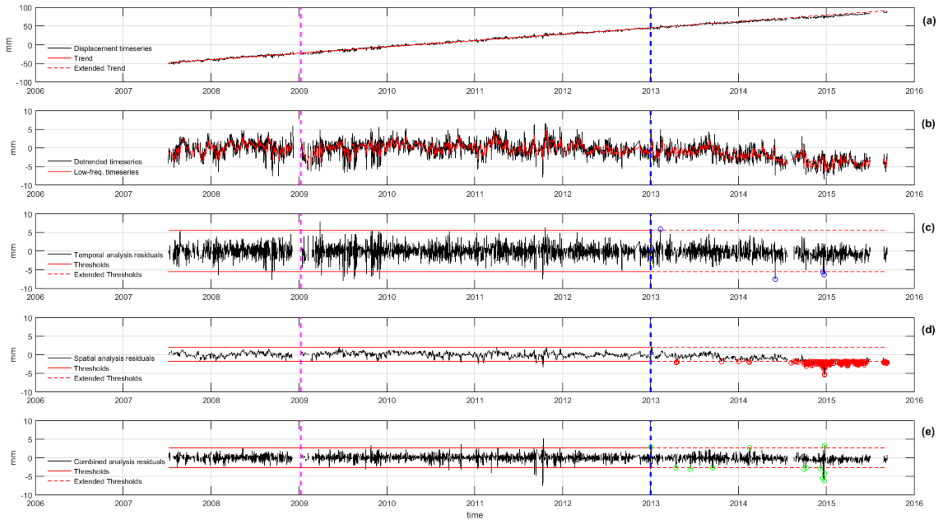


Figure C-149 Same as A-148, but for ΔE component

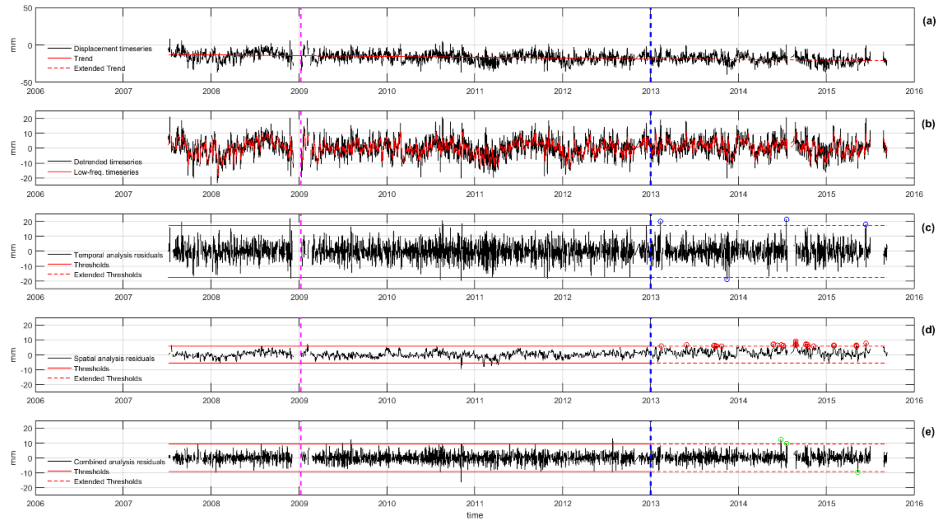


Figure C-150 Same as A-148, but for ΔU component

LINO

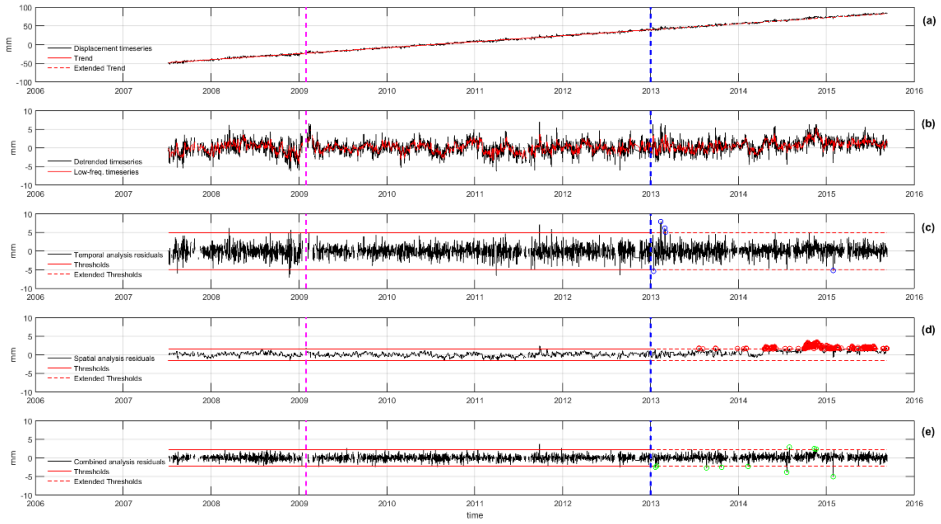


Figure C-151 LINO (ΔN) – (a) Corrected displacement time series, (b) detrended and low-frequency time series, the (c) Temporal, (d) Spatial and (e) combined analysisresiduals.

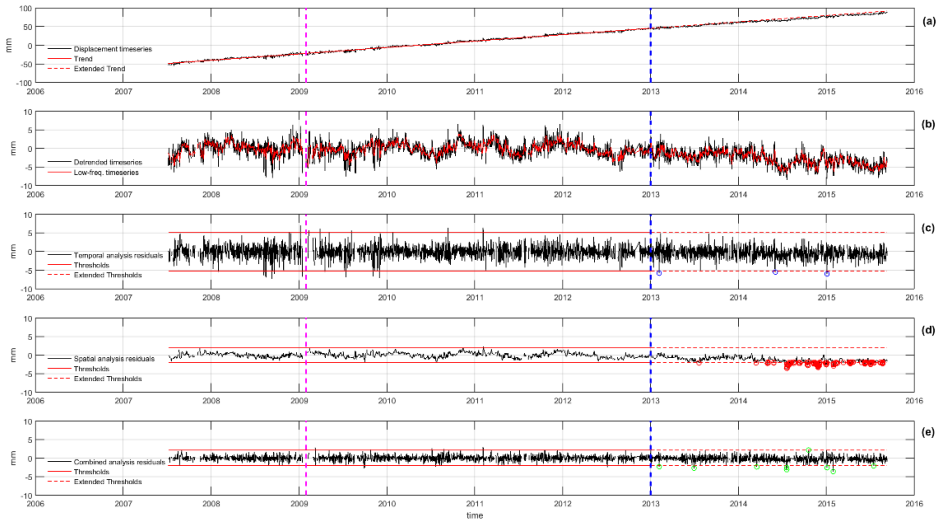


Figure C-152 Same as A-151, but for ΔE component

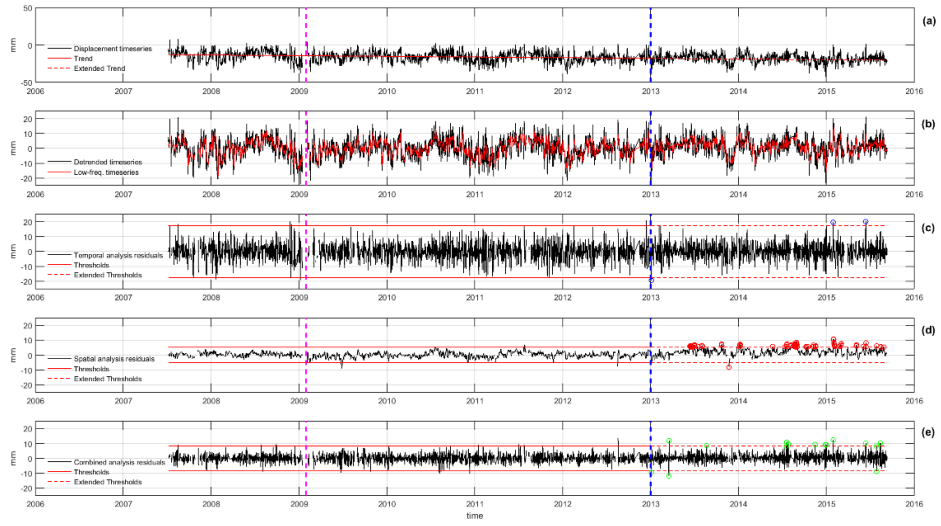


Figure C-153 Same as A-151, but for ΔU component

LOCG

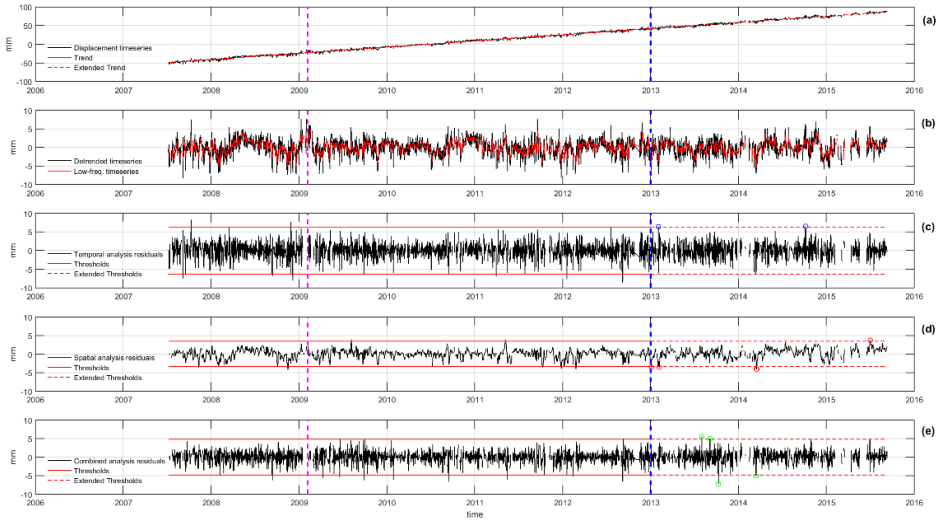


Figure C-154 LOCG (ΔN) – (a) Corrected displacement time series, (b) detrended and low-frequency time series, the (c) Temporal, (d) Spatial and (e) combined analysisresiduals.

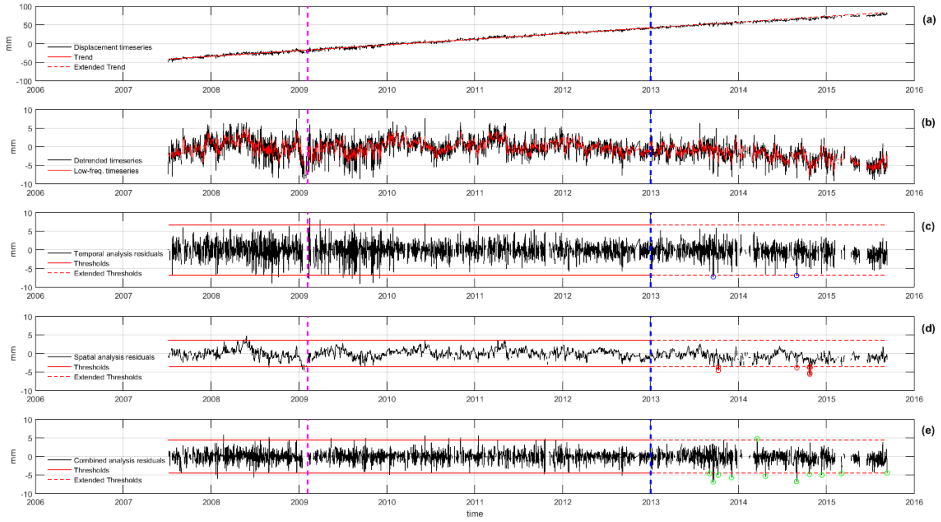


Figure C-155 Same as A-154, but for ΔE component

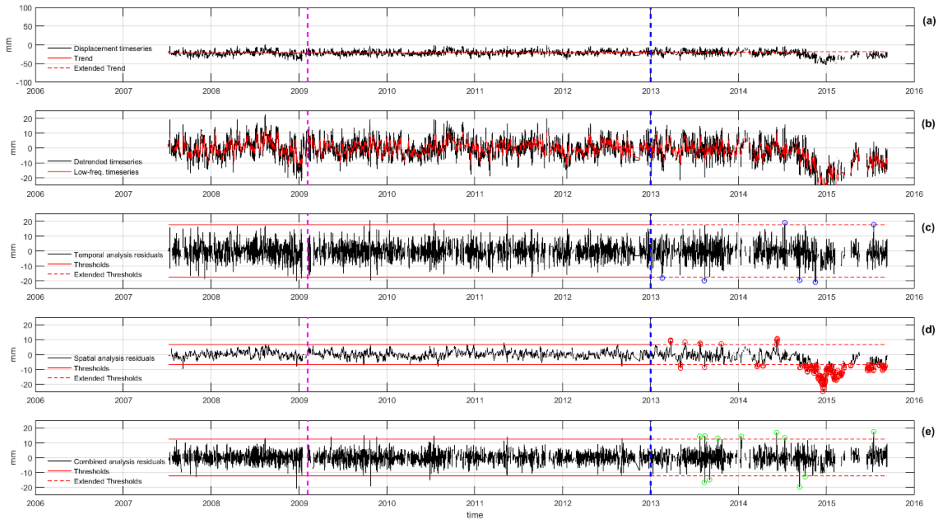


Figure C-156 Same as A-154, but for ΔU component

LOFT

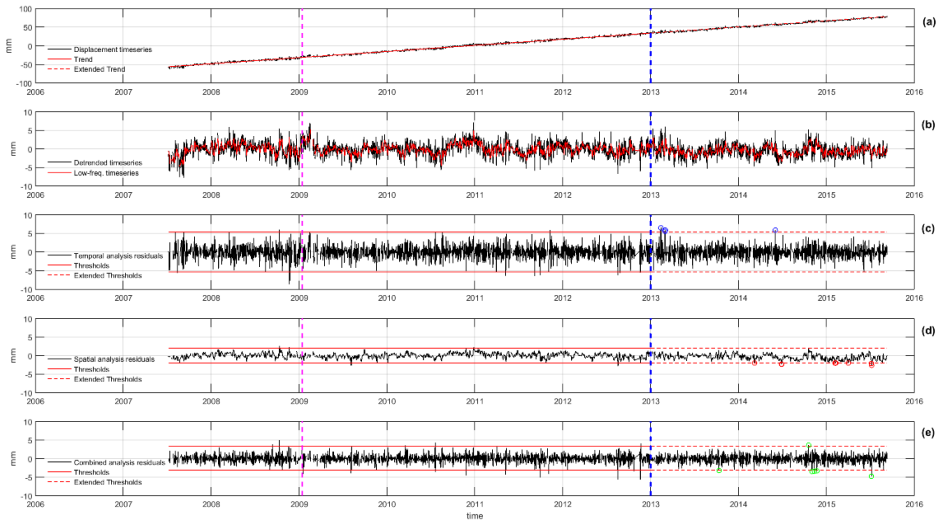


Figure C-157 LOFT (ΔN) – (a) Corrected displacement time series, (b) detrended and low-frequency time series, the (c) Temporal, (d) Spatial and (e) combined analysisresiduals.

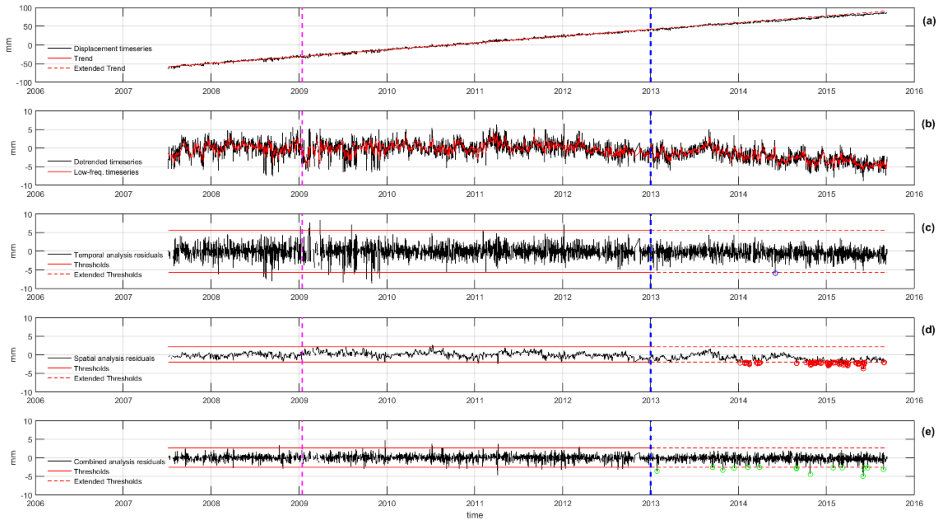


Figure C-158 Same as A-157, but for ΔE component

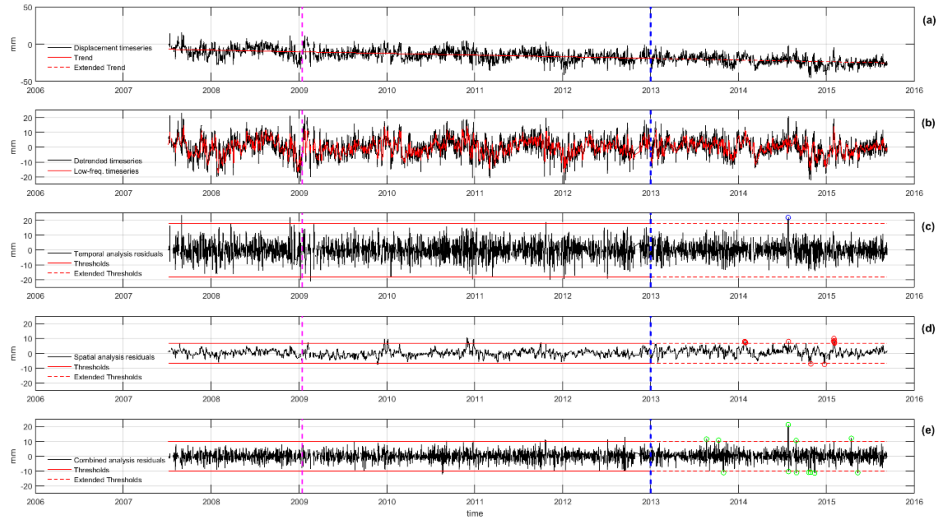


Figure C-159 Same as A-157, but for ΔU component

MACY

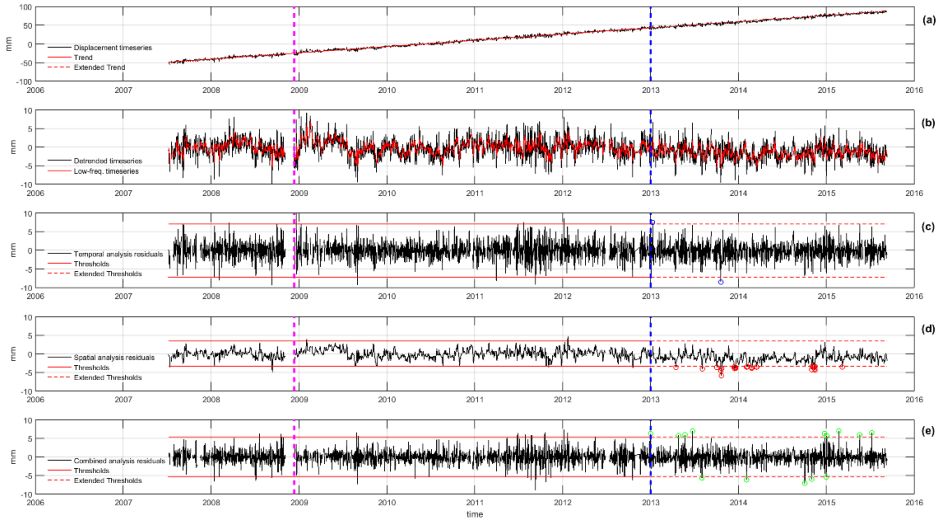


Figure C-160 MACY (ΔN) – (a) Corrected displacement time series, (b) detrended and low-frequency time series, the (c) Temporal, (d) Spatial and (e) combined analysisresiduals.

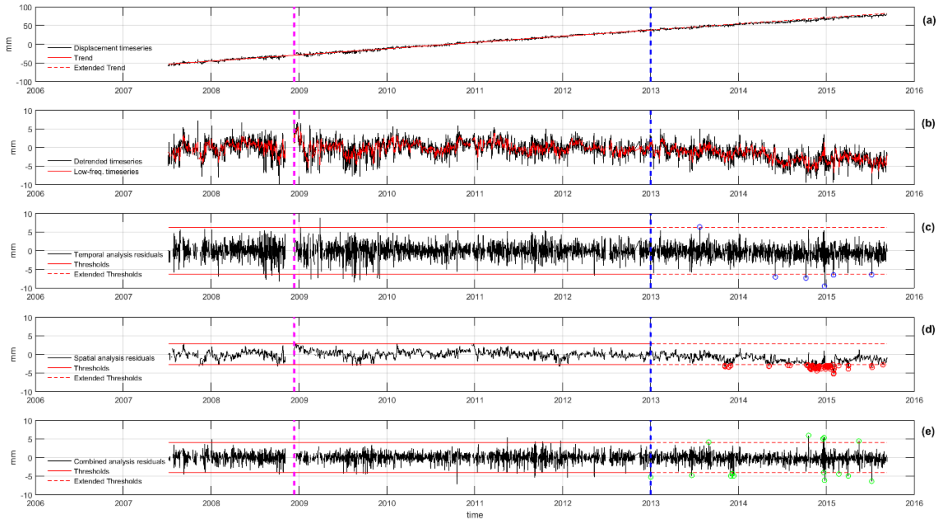


Figure C-161 Same as A-160, but for ΔE component

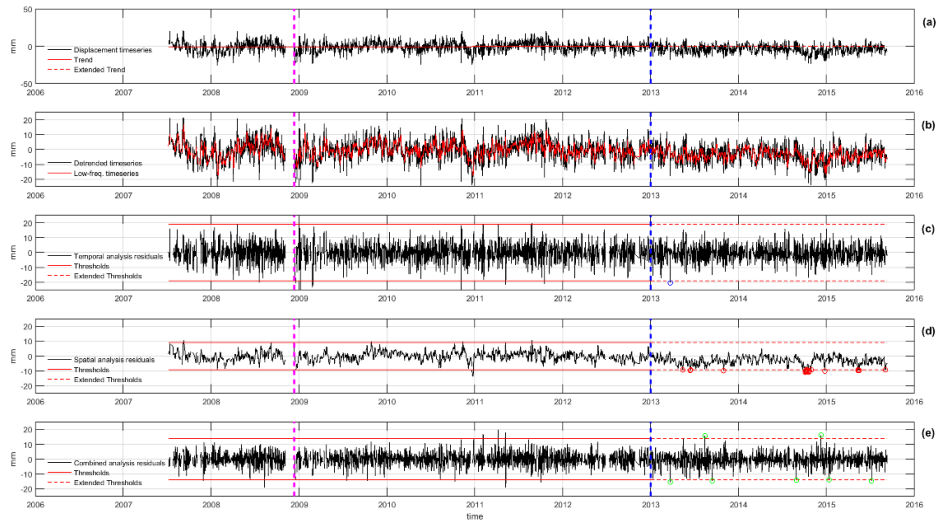


Figure C-162 Same as A-160, but for ΔU component

MART

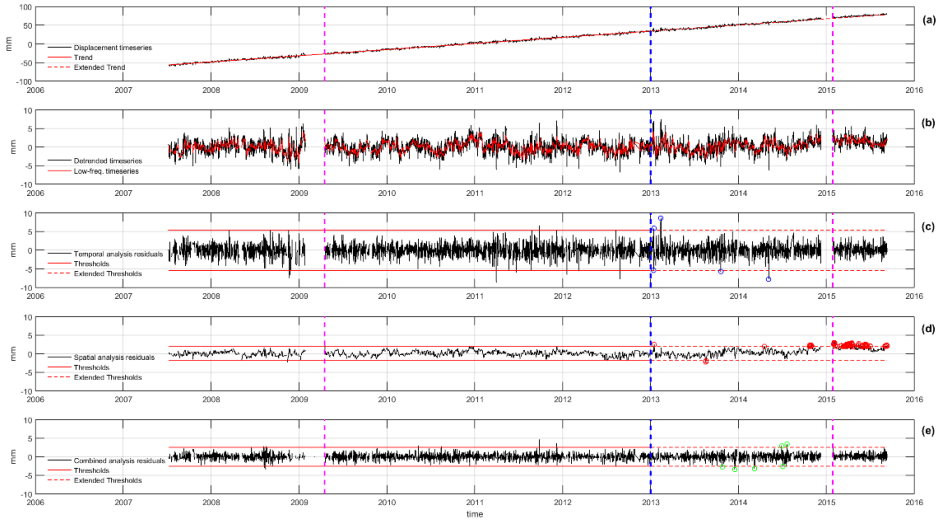


Figure C-163 MART (ΔN) – (a) Corrected displacement time series, (b) detrended and low-frequency time series, the (c) Temporal, (d) Spatial and (e) combined analysisresiduals.

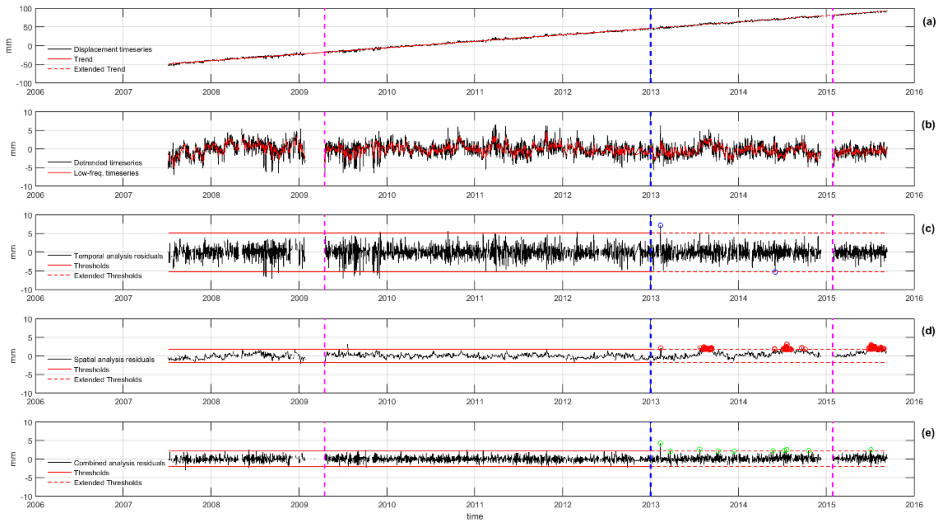


Figure C-164 Same as A-163, but for ΔE component

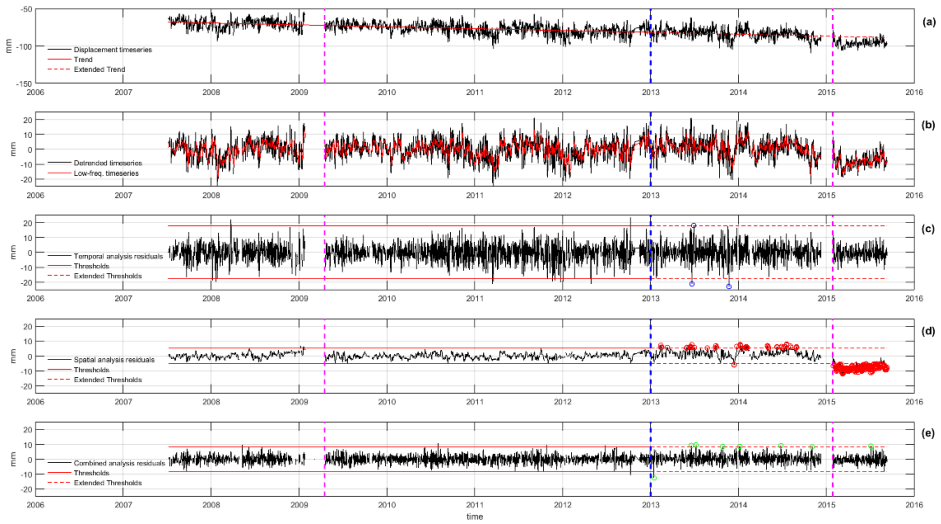


Figure C-165 Same as A-163, but for ΔU component

MORP

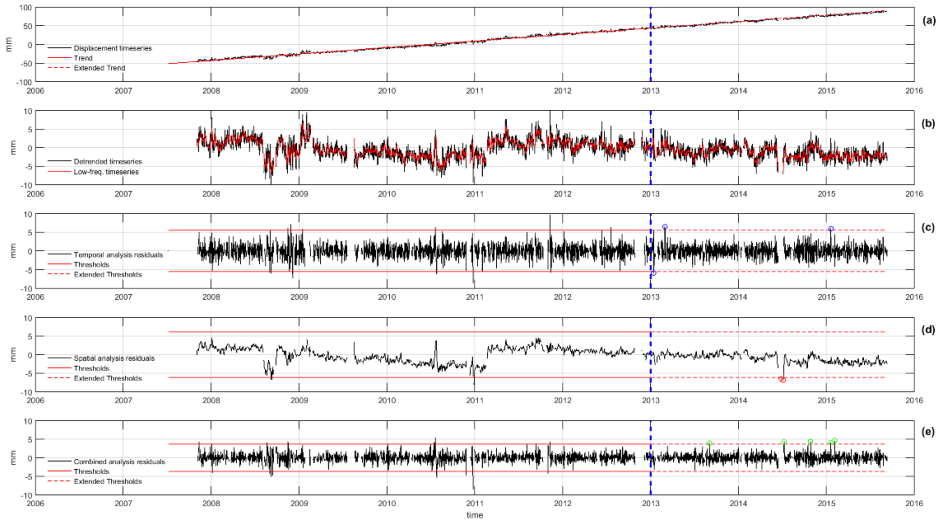


Figure C-166 MORP (ΔN) – (a) Corrected displacement time series, (b) detrended and low-frequency time series, the (c) Temporal, (d) Spatial and (e) combined analysisresiduals.

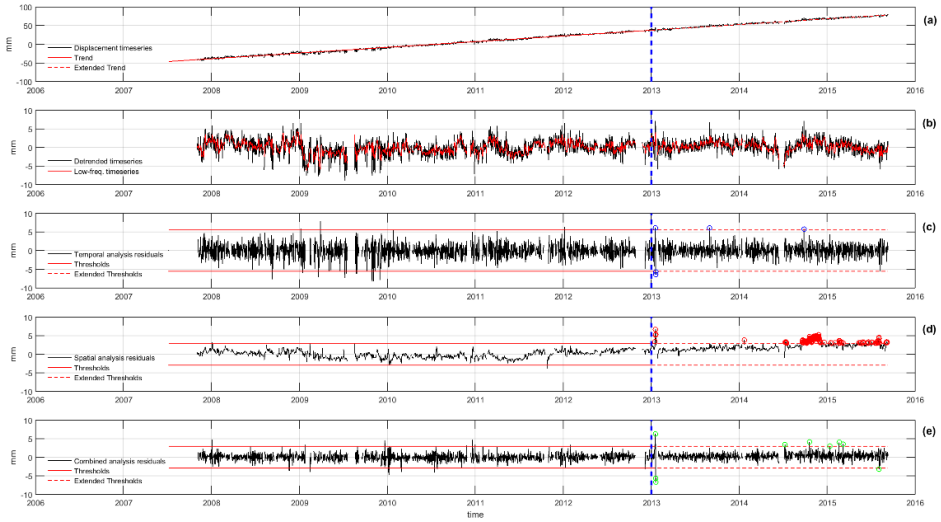


Figure C-167 Same as A-166, but for ΔE component

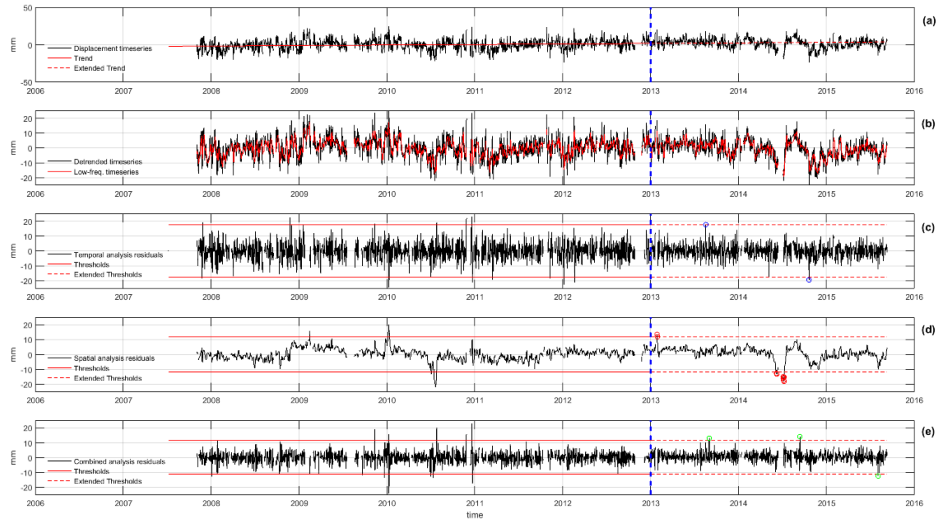


Figure C-168 Same as A-166, but for ΔU component

NCAS

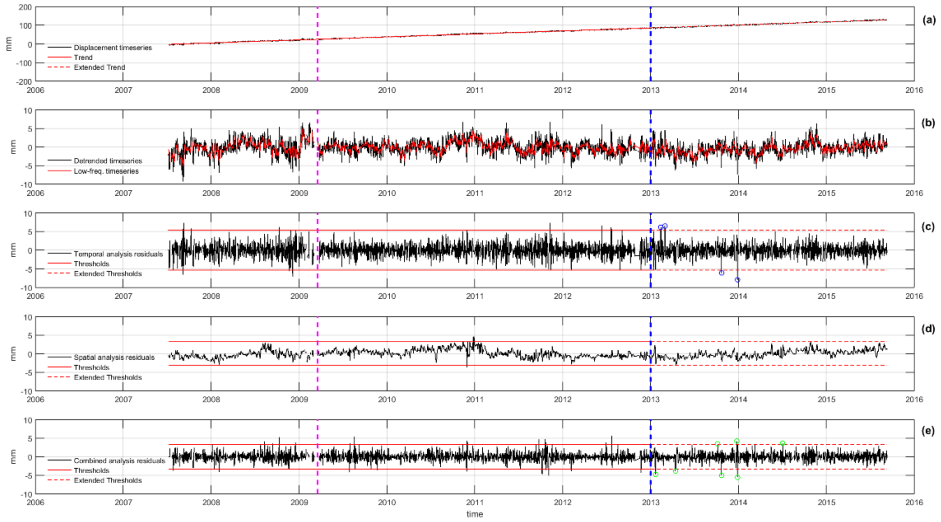


Figure C-169 NCAS (ΔN) – (a) Corrected displacement time series, (b) detrended and low-frequency time series, the (c) Temporal, (d) Spatial and (e) combined analysisresiduals.

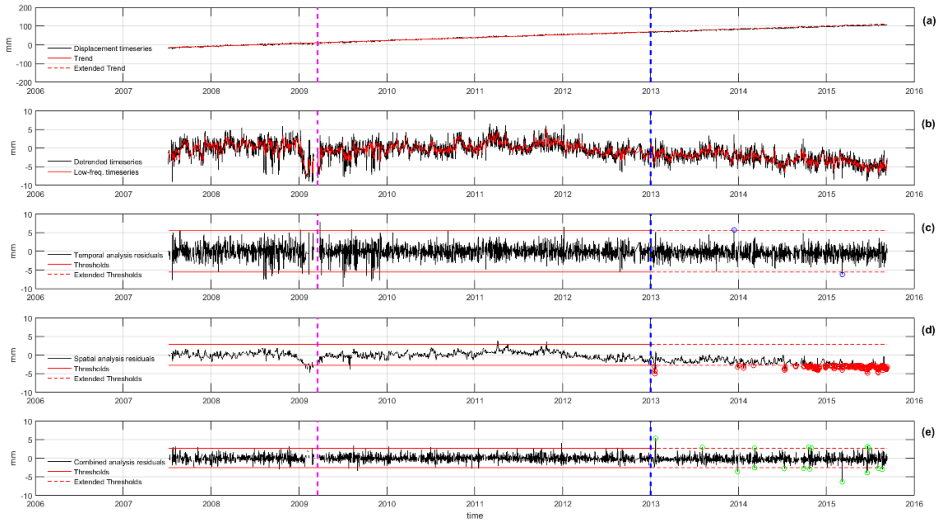


Figure C-170 Same as A-169, but for ΔE component

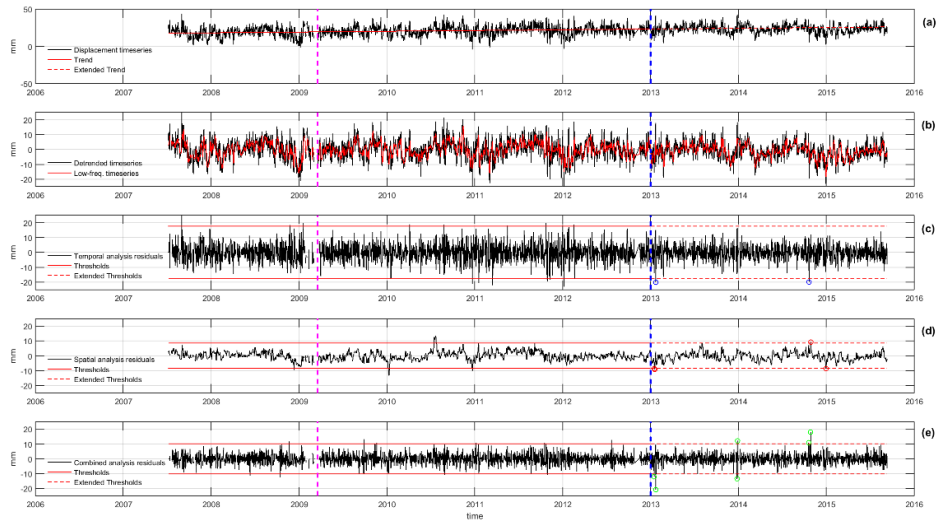


Figure C-171 Same as A-169, but for ΔU component

NEWL

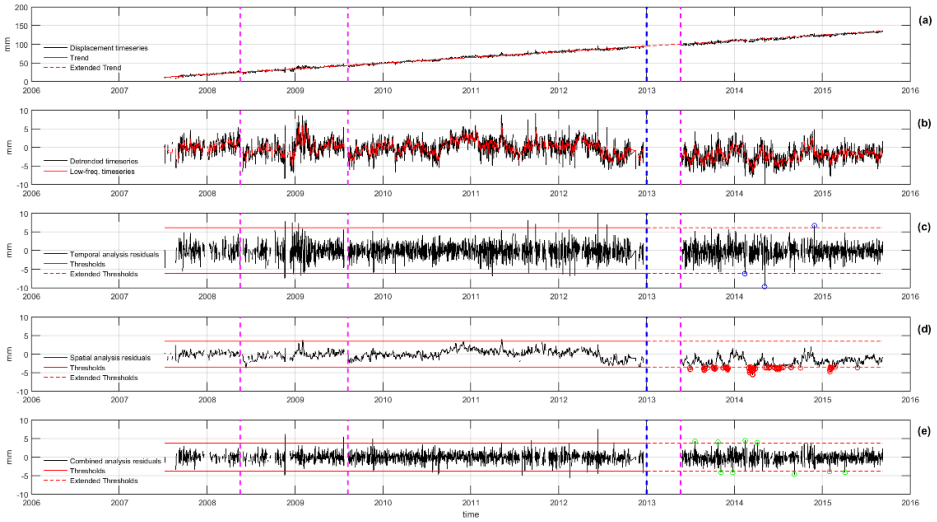


Figure C-172 NEWL (ΔN) – (a) Corrected displacement time series, (b) detrended and low-frequency time series, the (c) Temporal, (d) Spatial and (e) combined analysisresiduals.

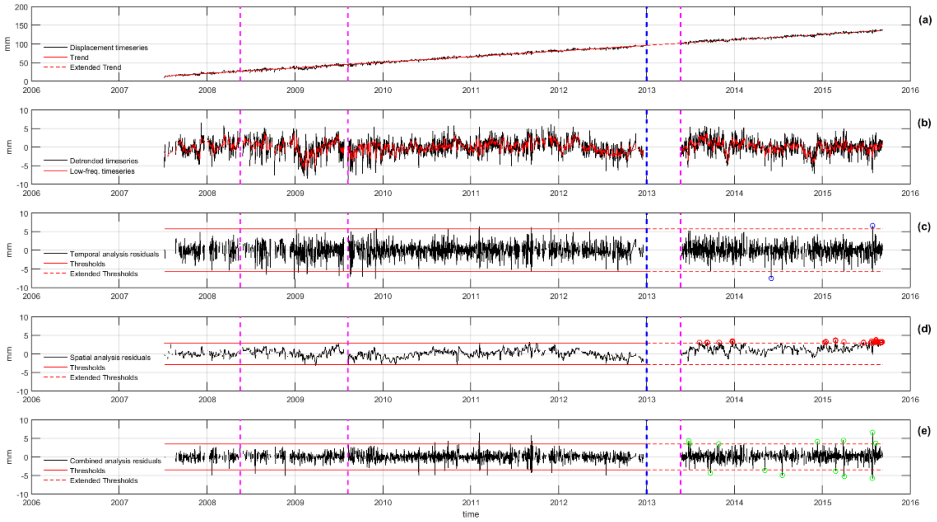


Figure C-173 Same as A-172, but for ΔE component

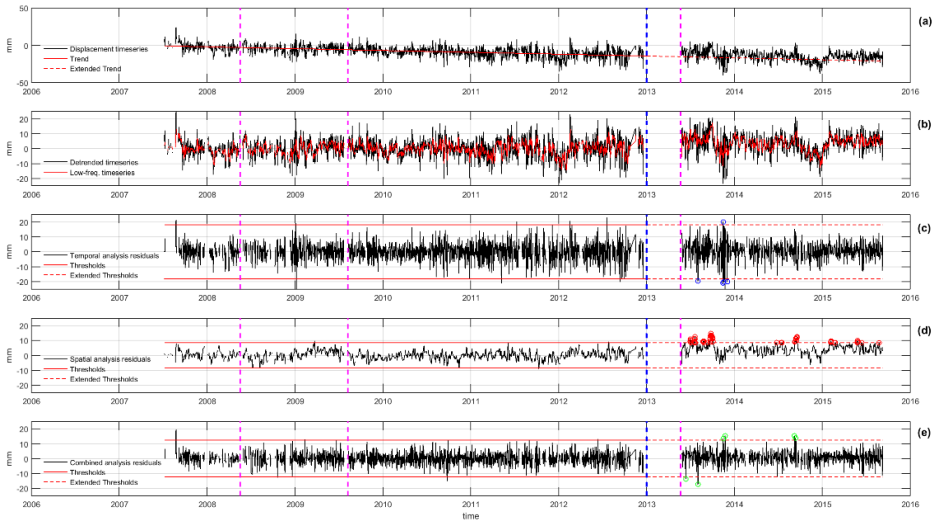


Figure C-174 Same as A-172, but for ΔU component

OMGH

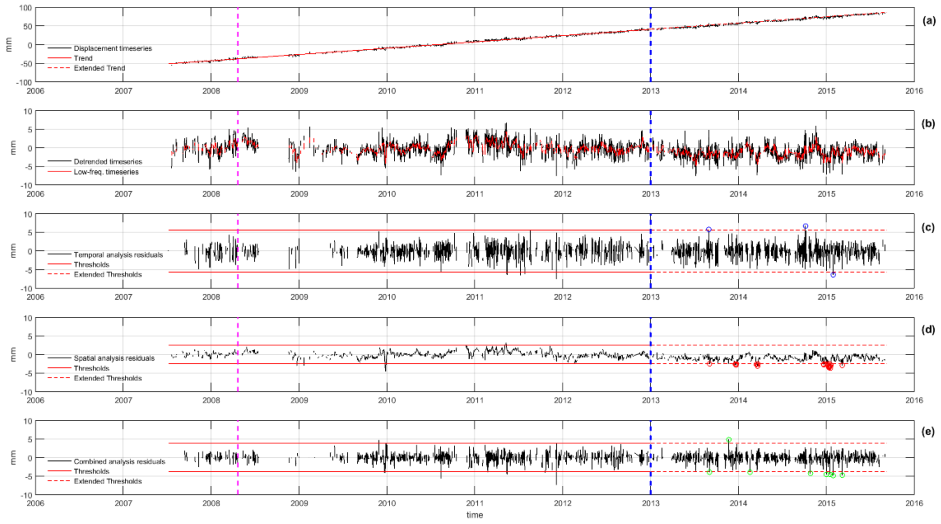


Figure C-175 OMGH (ΔN) – (a) Corrected displacement time series, (b) detrended and low-frequency time series, the (c) Temporal, (d) Spatial and (e) combined analysisresiduals.

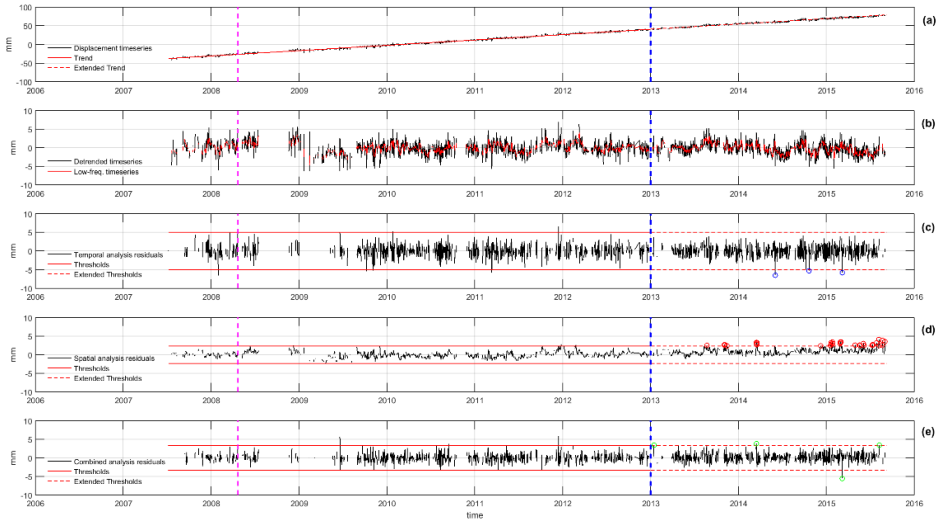


Figure C-176 Same as A-175, but for ΔE component

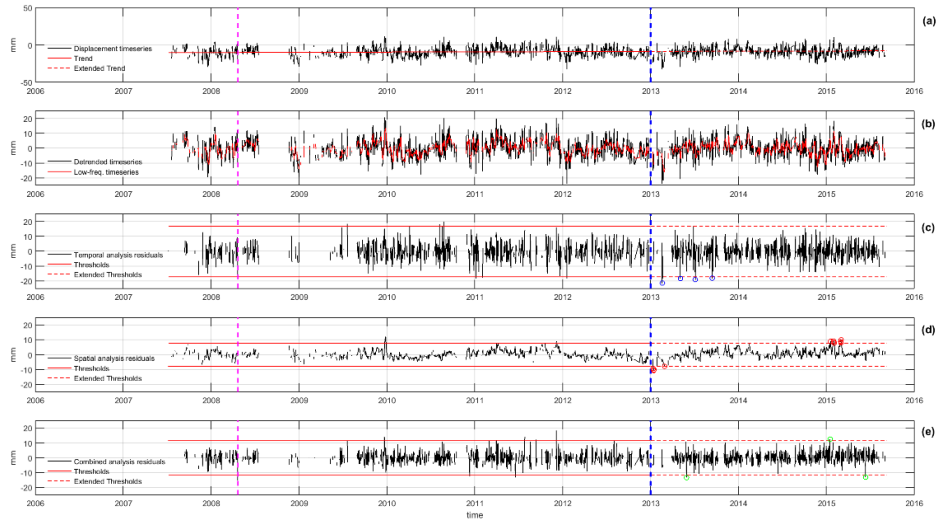


Figure C-177 Same as A-175, but for ΔU component

OXFR

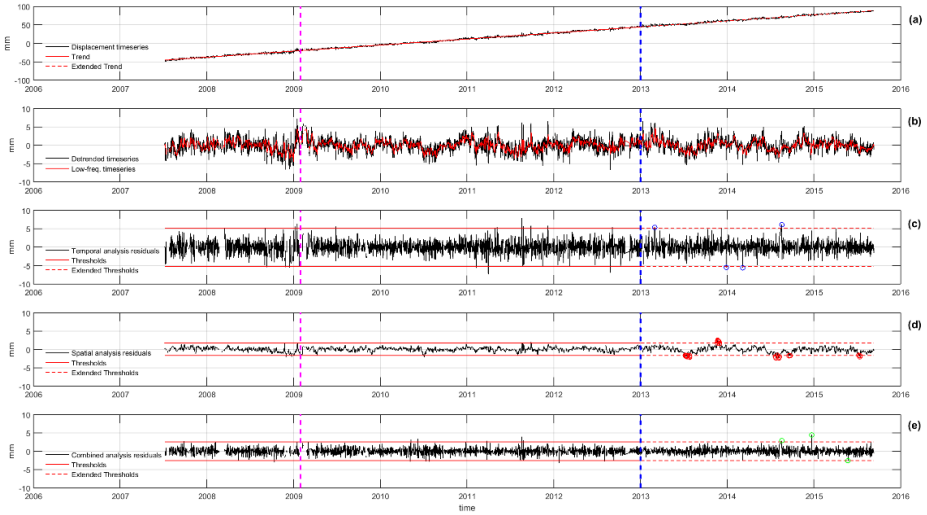


Figure C-178 OXFR (ΔN) – (a) Corrected displacement time series, (b) detrended and low-frequency time series, the (c) Temporal, (d) Spatial and (e) combined analysisresiduals.

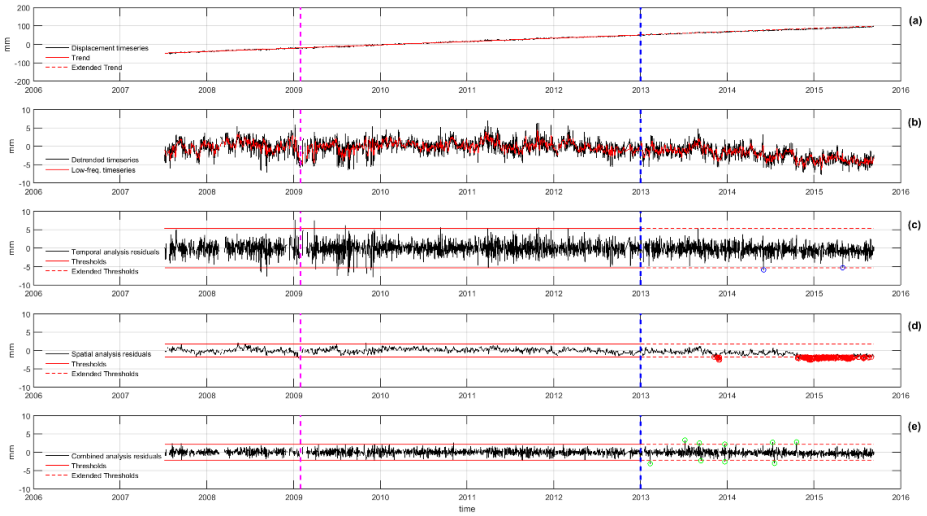


Figure C-179 Same as A-178, but for ΔE component

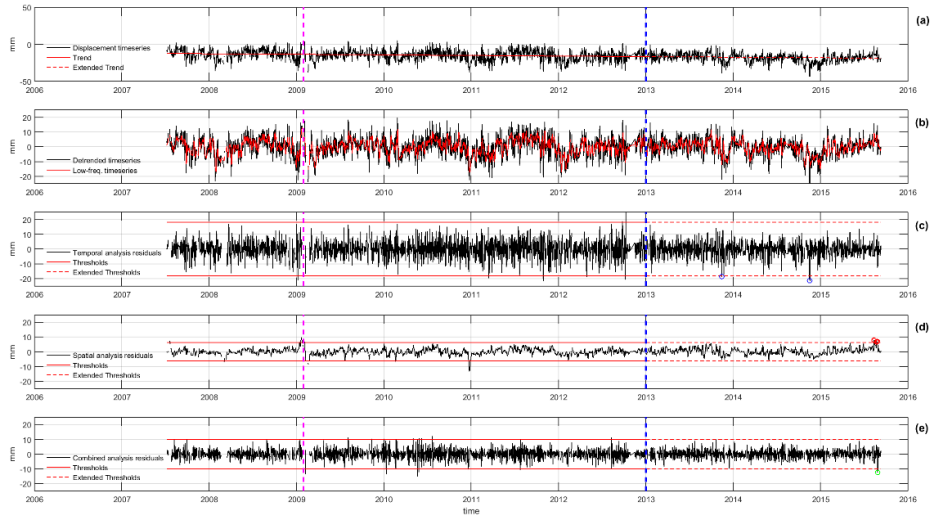


Figure C-180 Same as A-178, but for ΔU component

PBIL

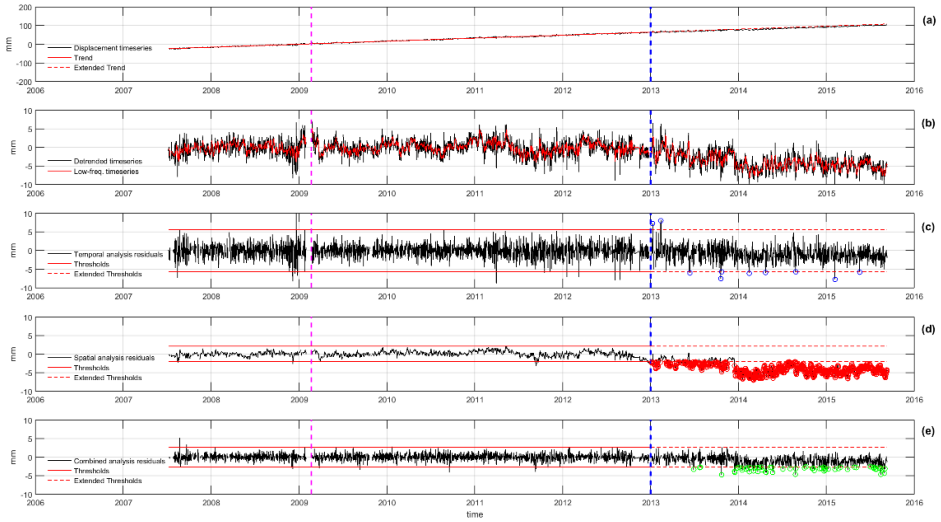


Figure C-181 PBIL (ΔN) – (a) Corrected displacement time series, (b) detrended and low-frequency time series, the (c) Temporal, (d) Spatial and (e) combined analysisresiduals.

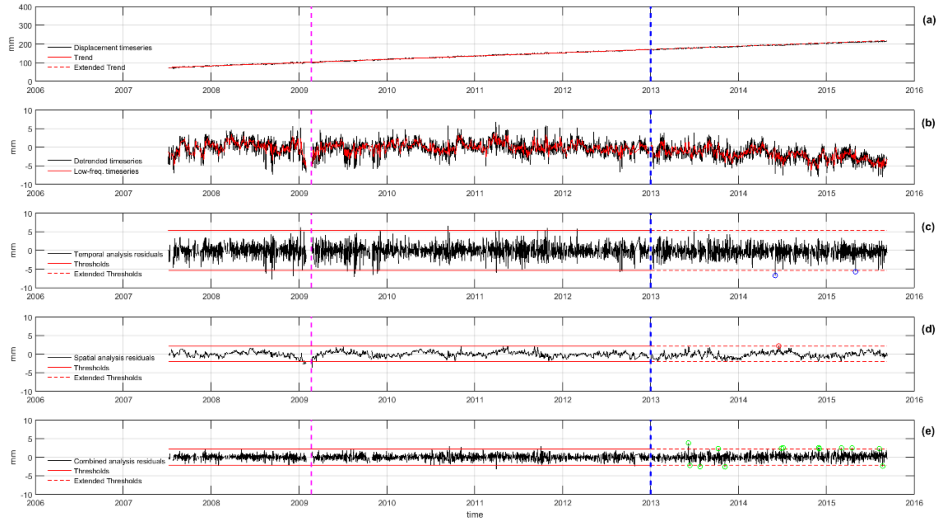


Figure C-182 Same as A-181, but for ΔE component

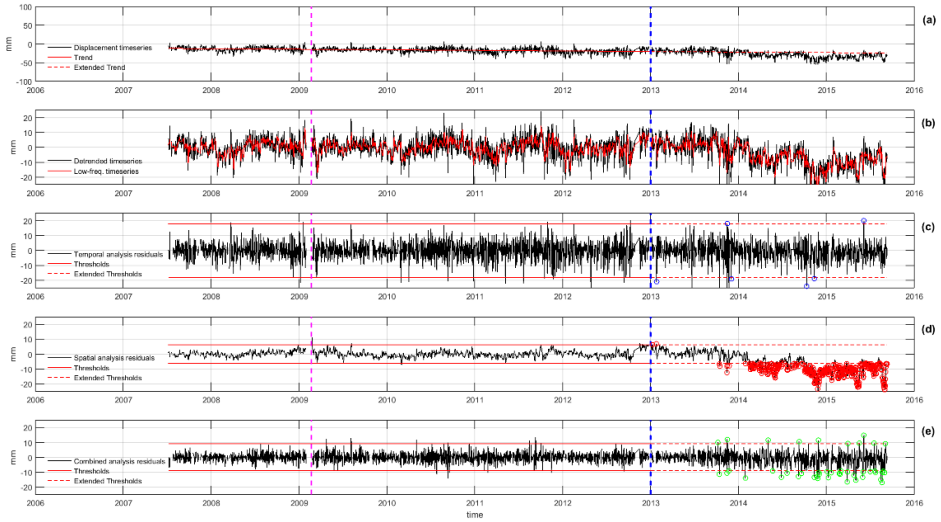


Figure C-183 Same as A-181, but for ΔU component

PETE

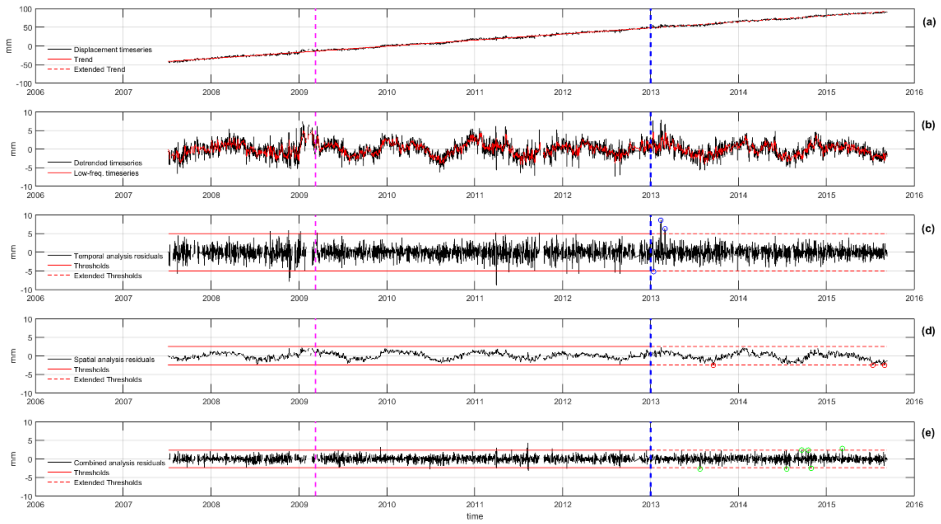


Figure C-184 PETE (ΔN) – (a) Corrected displacement time series, (b) detrended and low-frequency time series, the (c) Temporal, (d) Spatial and (e) combined analysisresiduals.

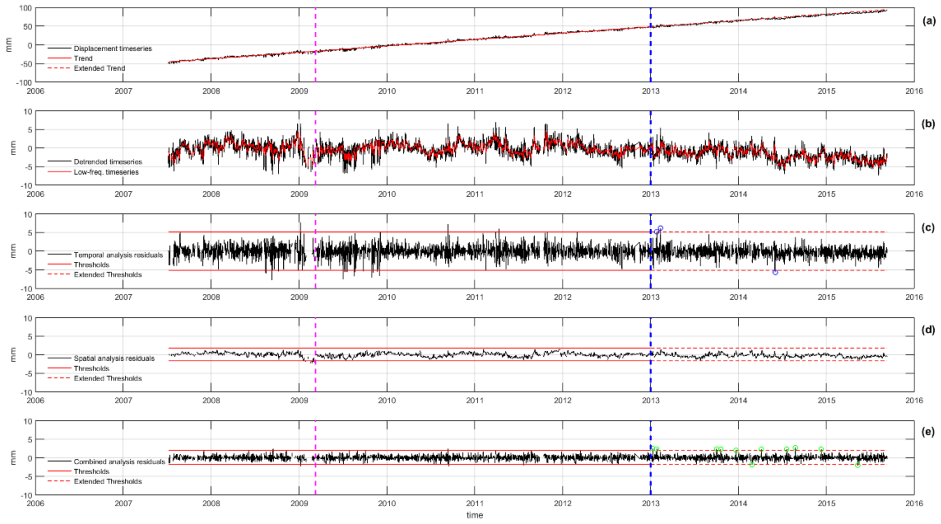


Figure C-185 Same as A-184, but for ΔE component

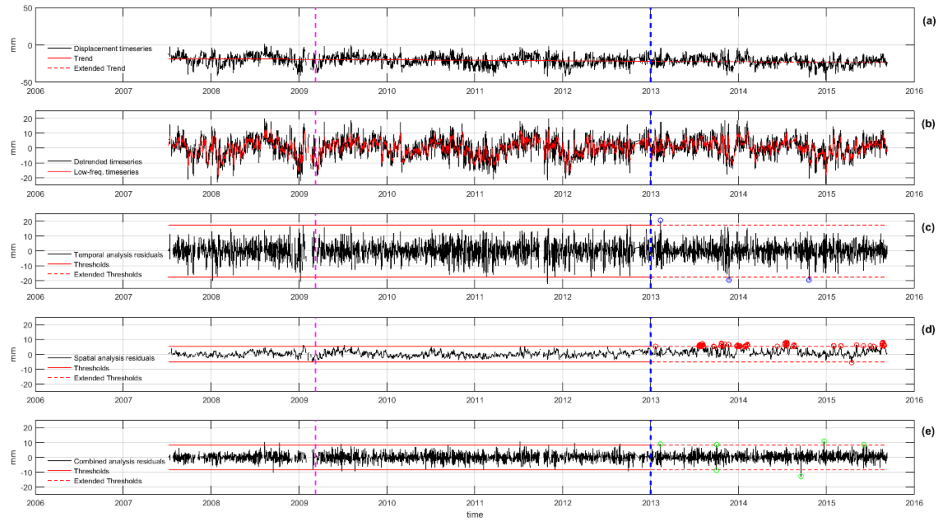


Figure C-186 Same as A-184, but for ΔU component

PMTG

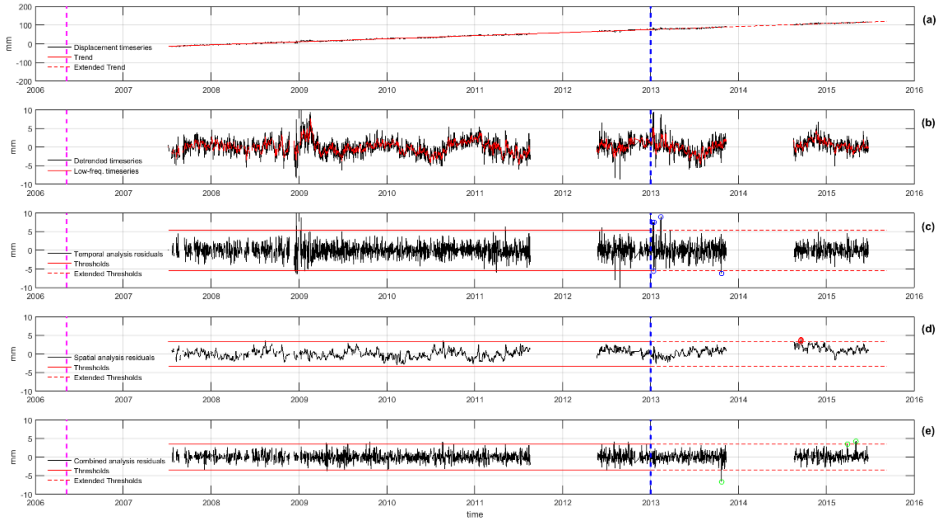


Figure C-187 PMTG (ΔN) – (a) Corrected displacement time series, (b) detrended and low-frequency time series, the (c) Temporal, (d) Spatial and (e) combined analysisresiduals.

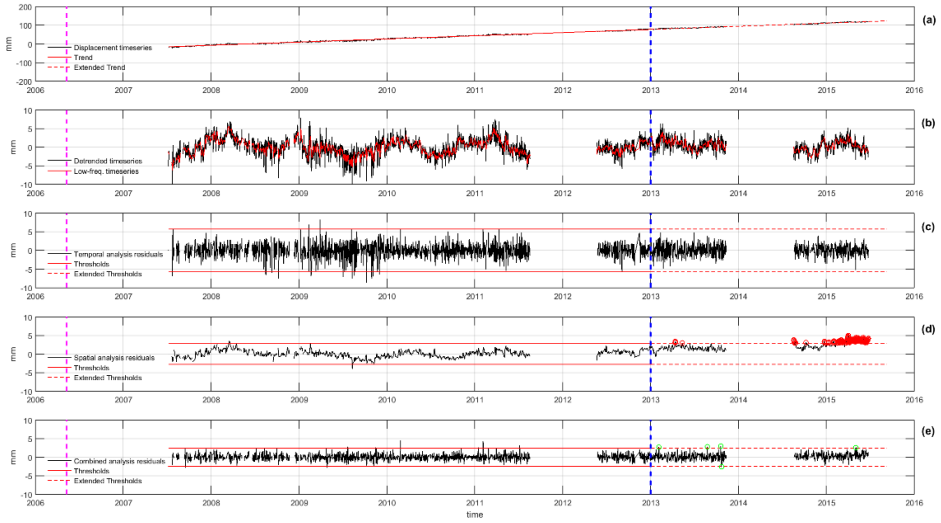


Figure C-188 Same as A-187, but for ΔE component

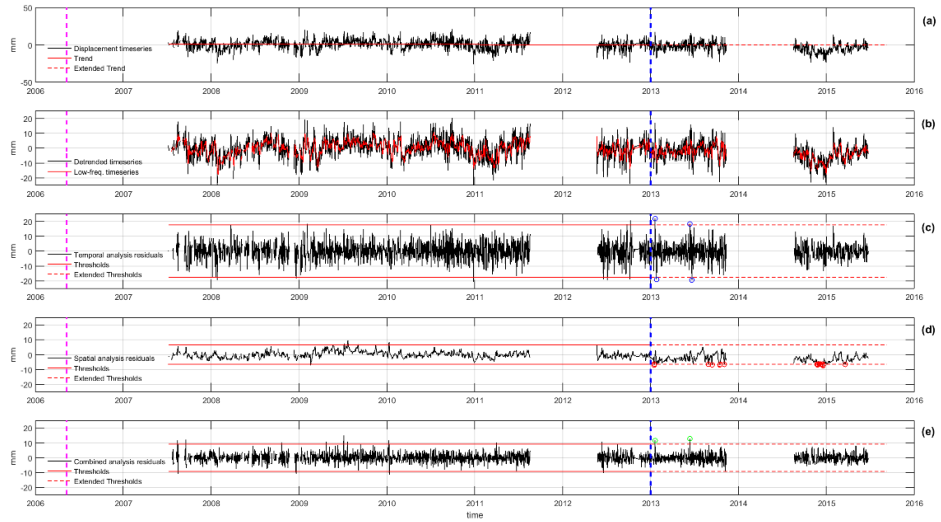


Figure C-189 Same as A-187, but for ΔU component

PMTH

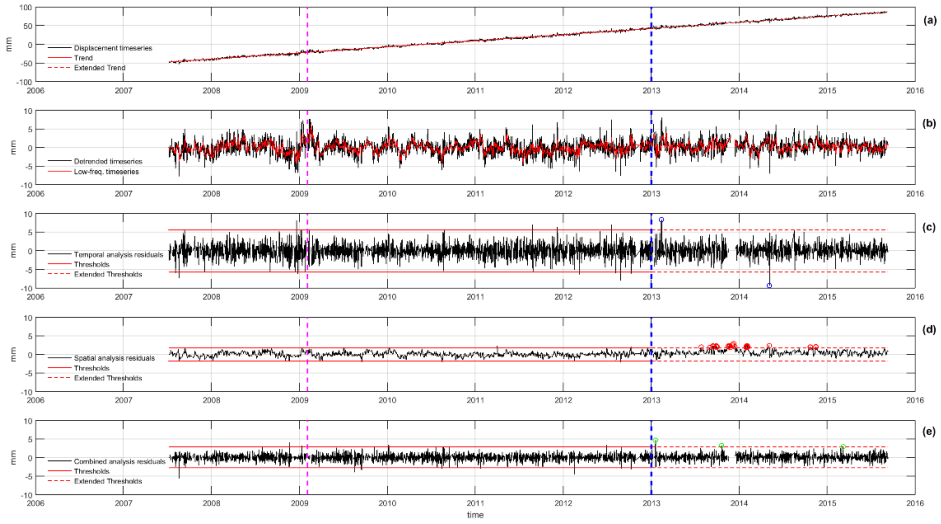


Figure C-190 PMTH (ΔN) – (a) Corrected displacement time series, (b) detrended and low-frequency time series, the (c) Temporal, (d) Spatial and (e) combined analysisresiduals.

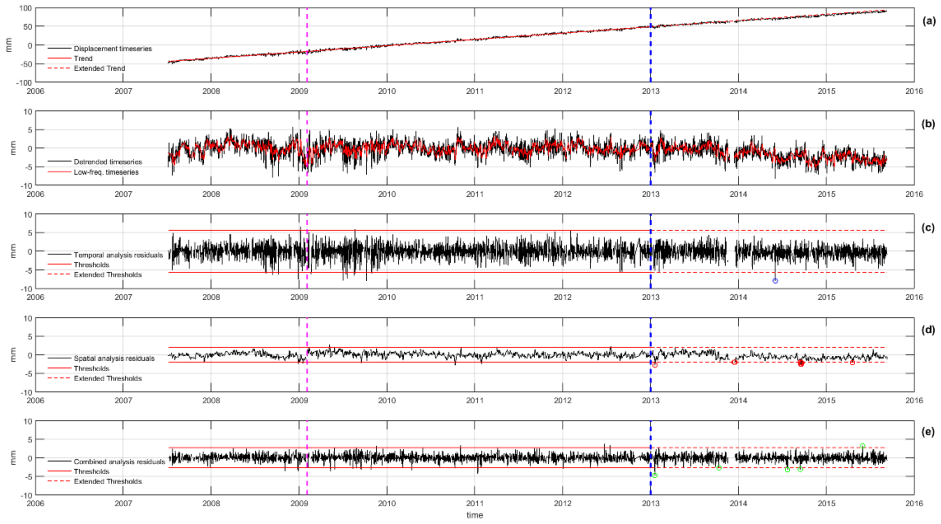


Figure C-191 Same as A-190, but for ΔE component

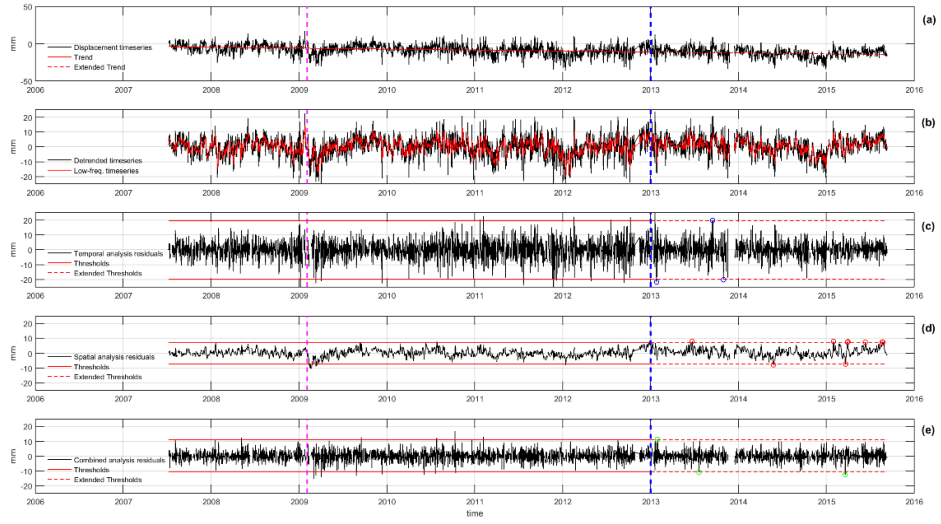


Figure C-192 Same as A-190, but for ΔU component

POOL

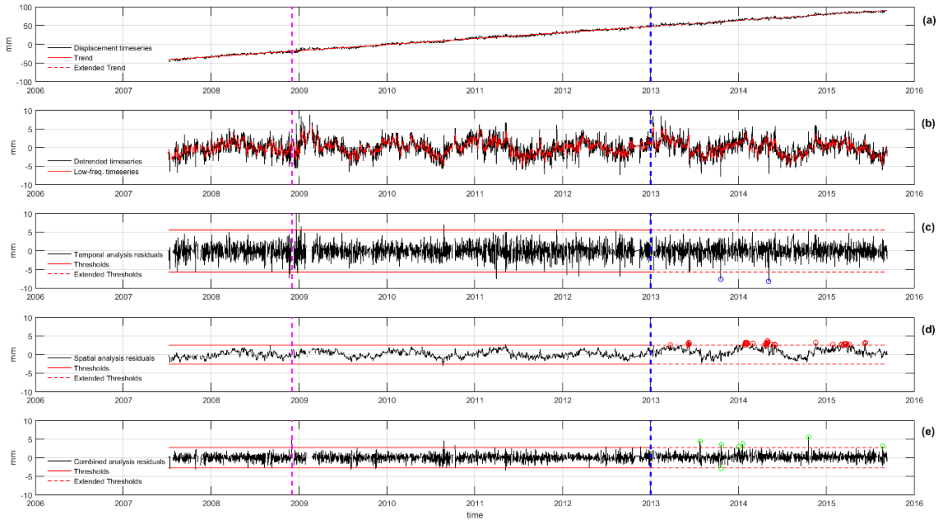


Figure C-193 POOL (ΔN) – (a) Corrected displacement time series, (b) detrended and low-frequency time series, the (c) Temporal, (d) Spatial and (e) combined analysisresiduals.

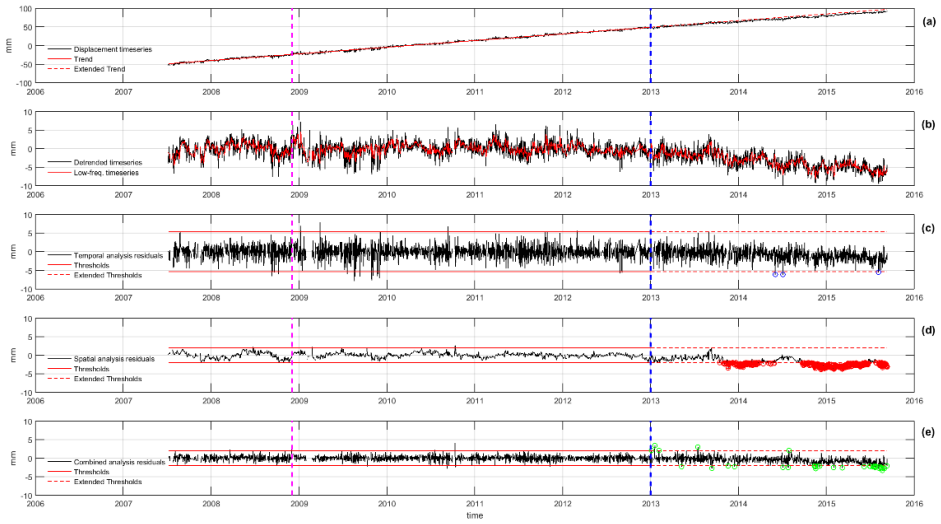


Figure C-194 Same as A-193, but for ΔE component

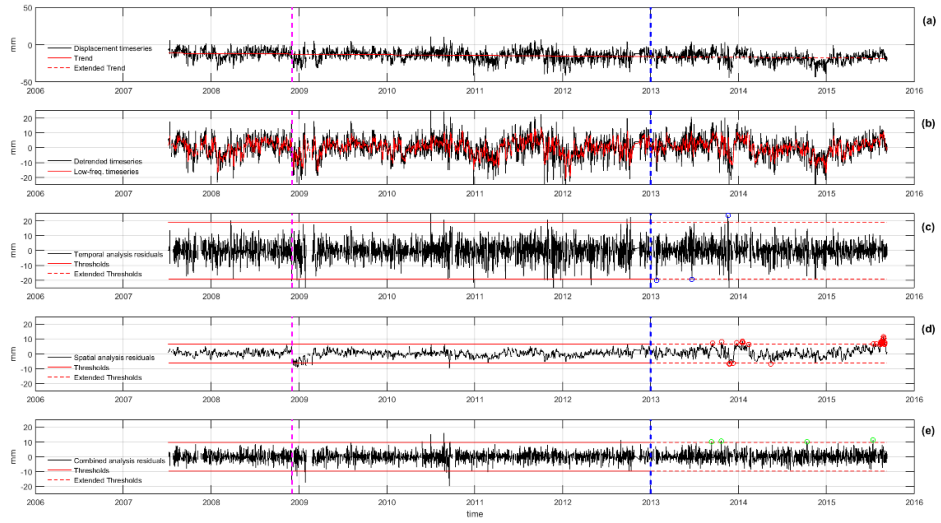


Figure C-195 Same as A-193, but for ΔU component

PRAE

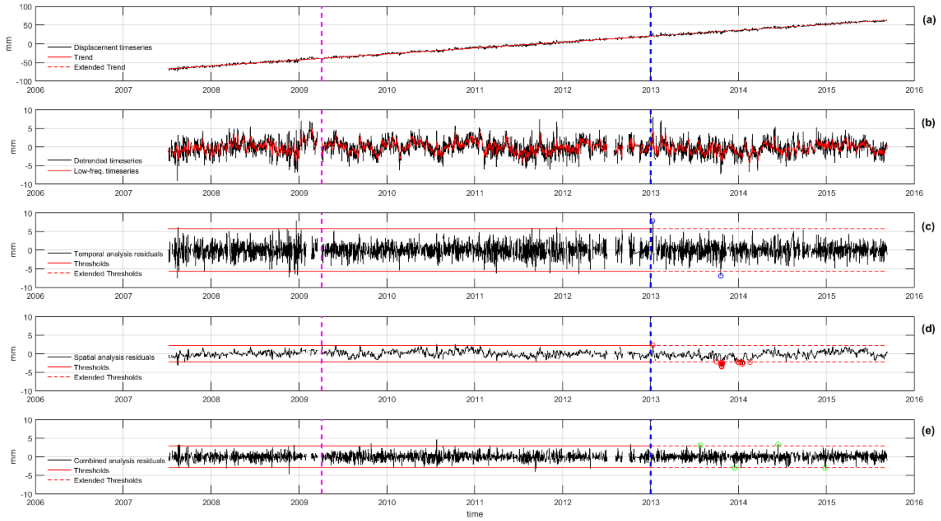


Figure C-196 PRAE (ΔN) – (a) Corrected displacement time series, (b) detrended and low-frequency time series, the (c) Temporal, (d) Spatial and (e) combined analysisresiduals.

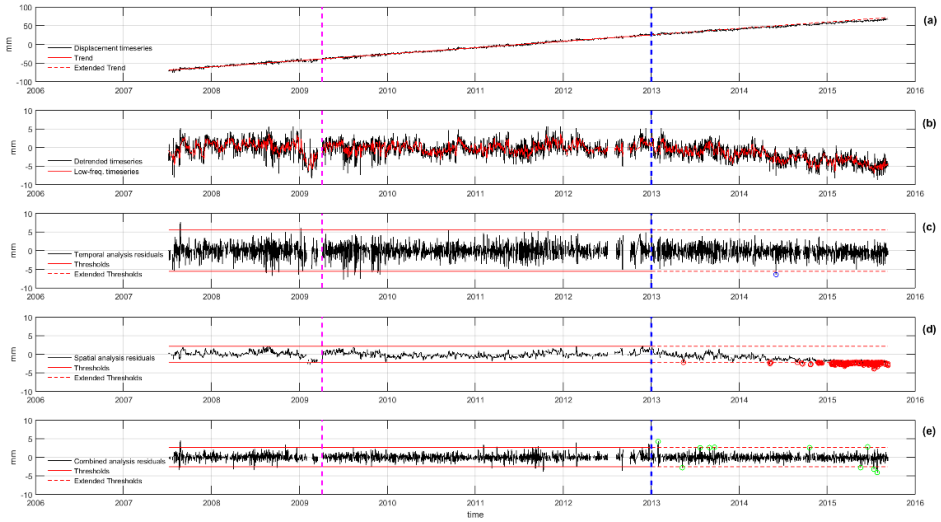


Figure C-197 Same as A-196, but for ΔE component

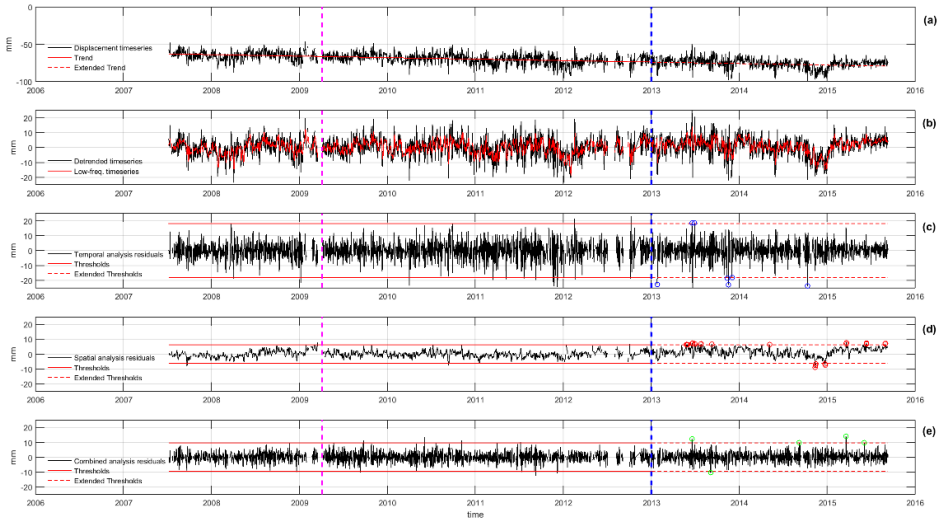


Figure C-198 Same as A-196, but for ΔU component

RICM

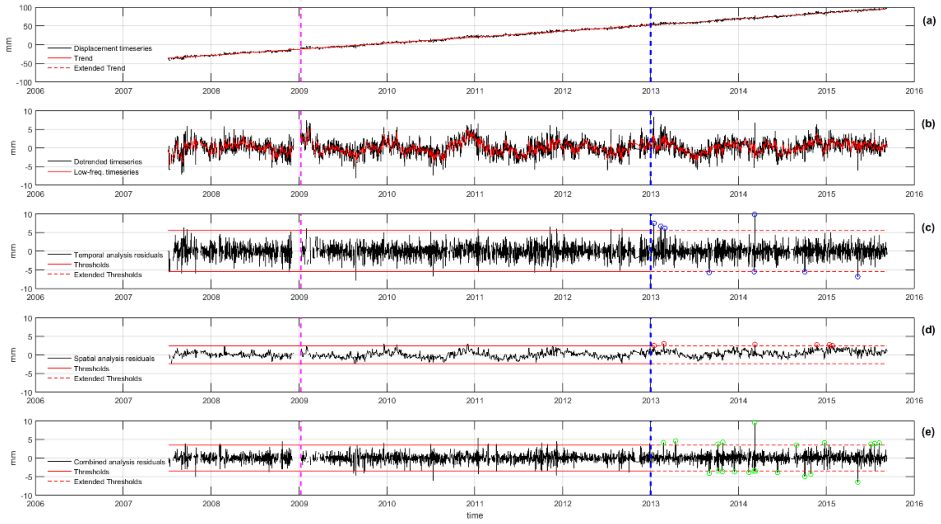


Figure C-199 RICM (ΔN) – (a) Corrected displacement time series, (b) detrended and low-frequency time series, the (c) Temporal, (d) Spatial and (e) combined analysisresiduals.

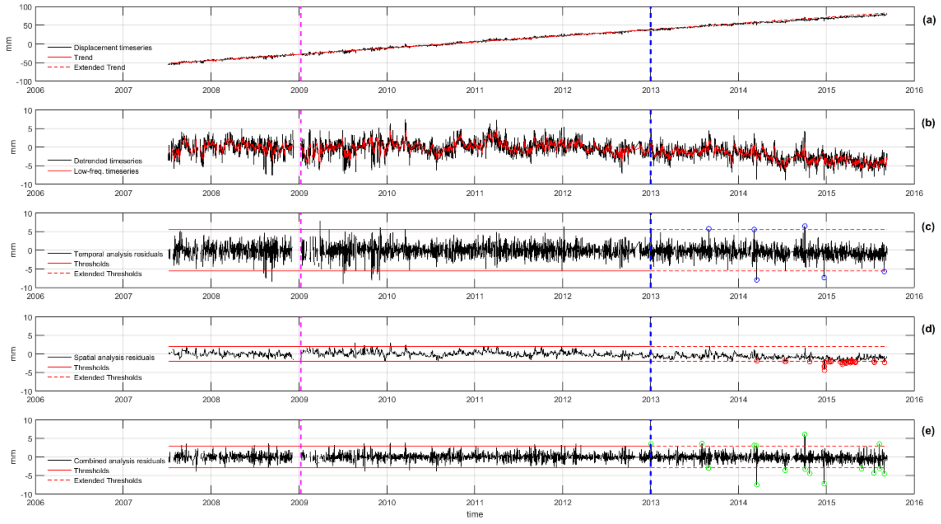


Figure C-200 Same as A-199, but for ΔE component

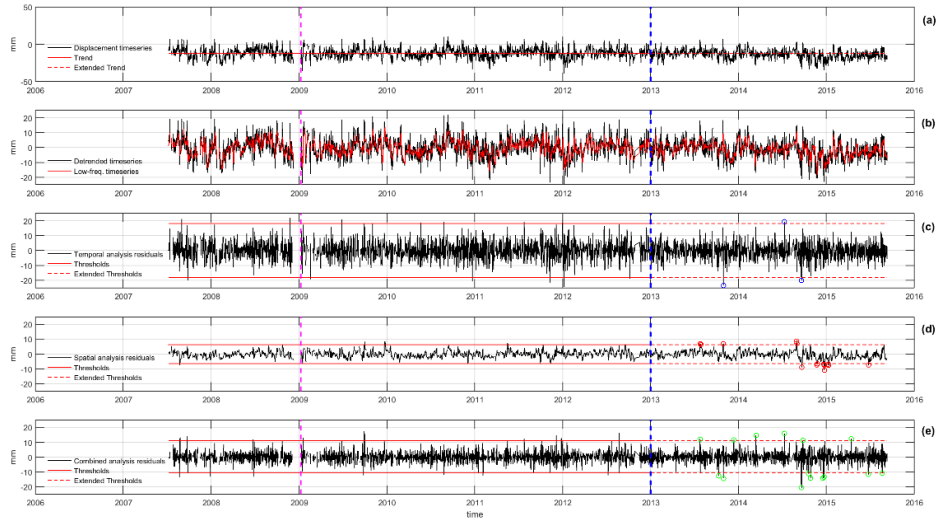


Figure C-201 Same as A-199, but for ΔU component

SABB

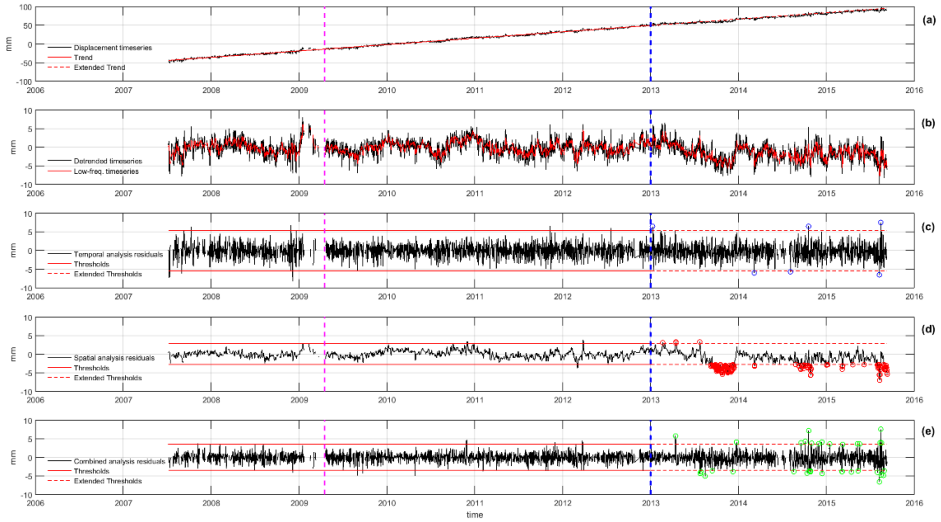


Figure C-202 SABB (ΔN) – (a) Corrected displacement time series, (b) detrended and low-frequency time series, the (c) Temporal, (d) Spatial and (e) combined analysisresiduals.

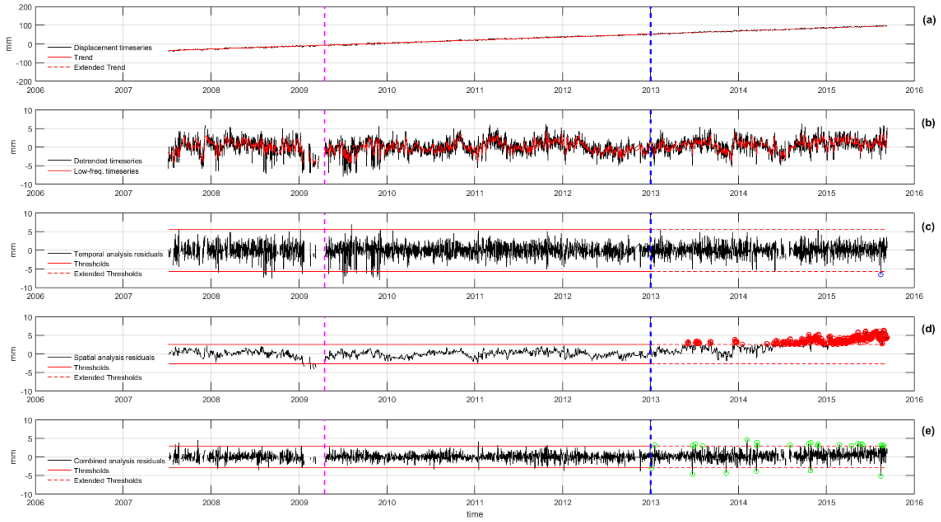


Figure C-203 Same as A-202, but for ΔE component

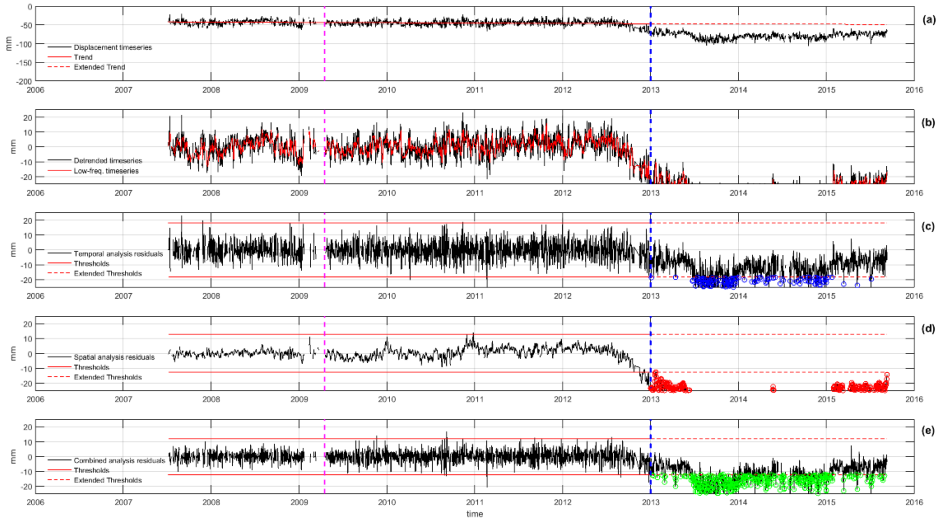


Figure C-204 Same as A-204, but for ΔU component

SANO

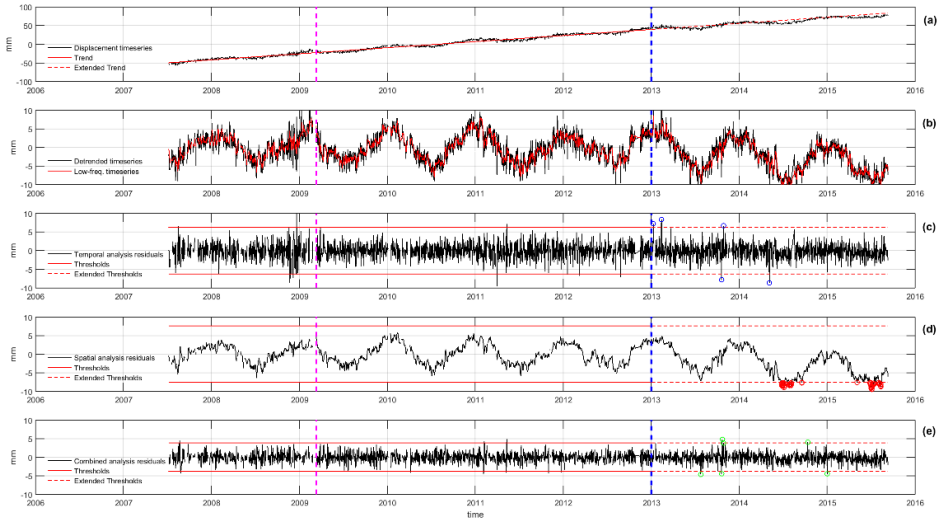


Figure C-205 SABB (ΔN) – (a) Corrected displacement time series, (b) detrended and low-frequency time series, the (c) Temporal, (d) Spatial and (e) combined analysisresiduals.

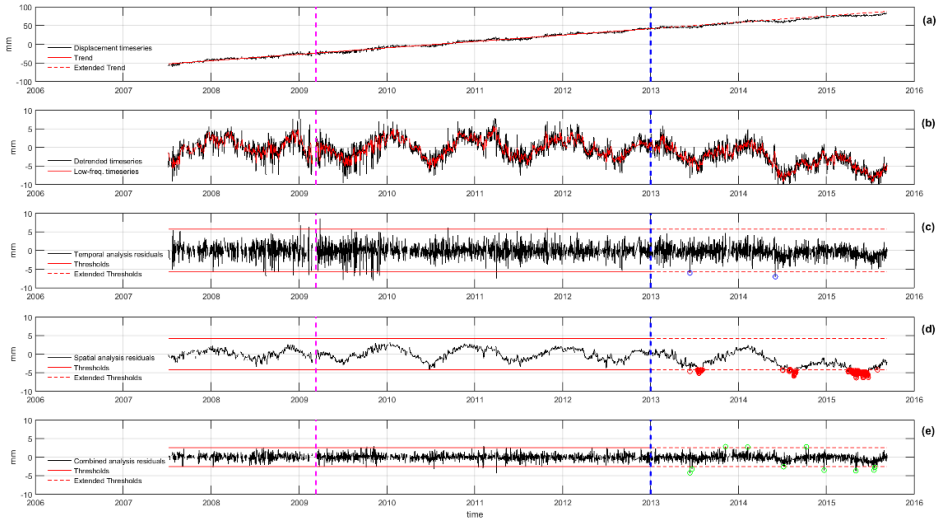


Figure C-206 Same as A-206, but for ΔE component

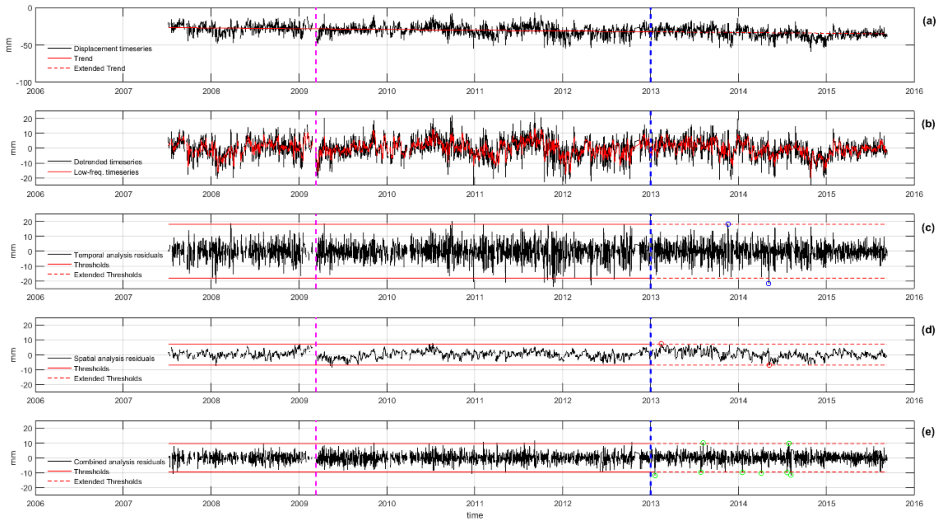


Figure C-207 Same as A-206, but for ΔU component

SCAO

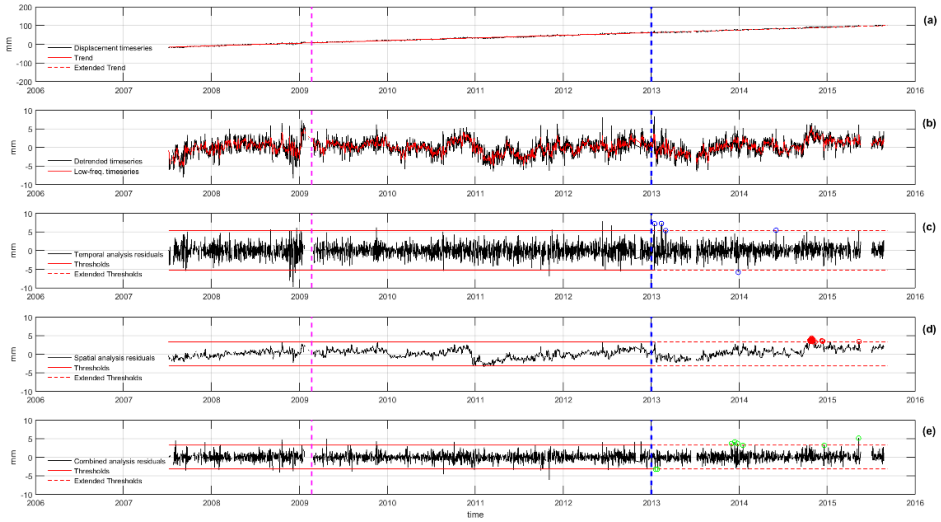


Figure C-208 SCAO (ΔN) – (a) Corrected displacement time series, (b) detrended and low-frequency time series, the (c) Temporal, (d) Spatial and (e) combined analysisresiduals.

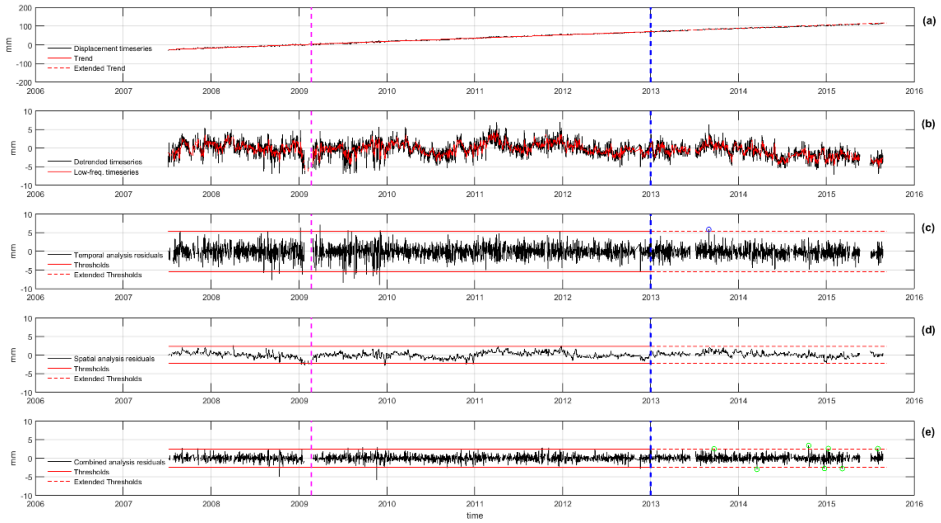


Figure C-209 Same as A-208, but for ΔE component

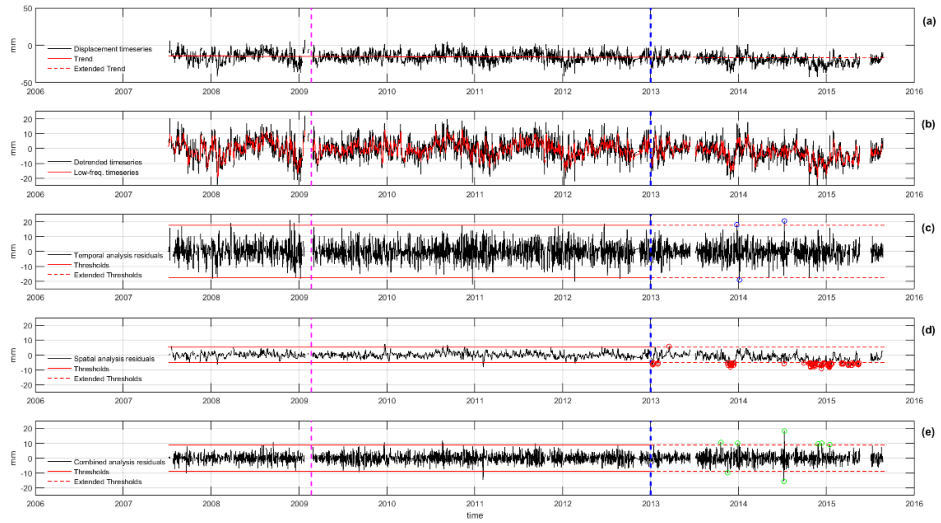


Figure C-210 Same as A-208, but for ΔU component

SHOB

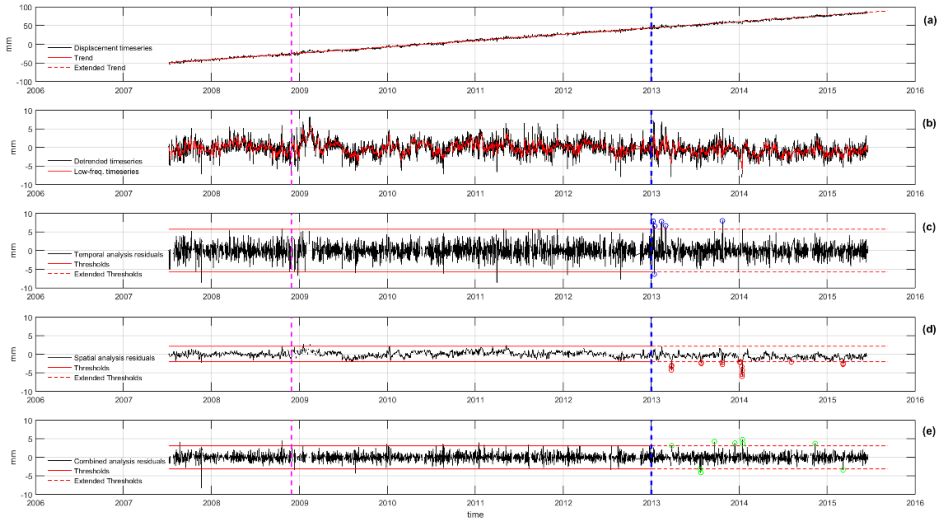


Figure C-211 SHOB (ΔN) – (a) Corrected displacement time series, (b) detrended and low-frequency time series, the (c) Temporal, (d) Spatial and (e) combined analysisresiduals.

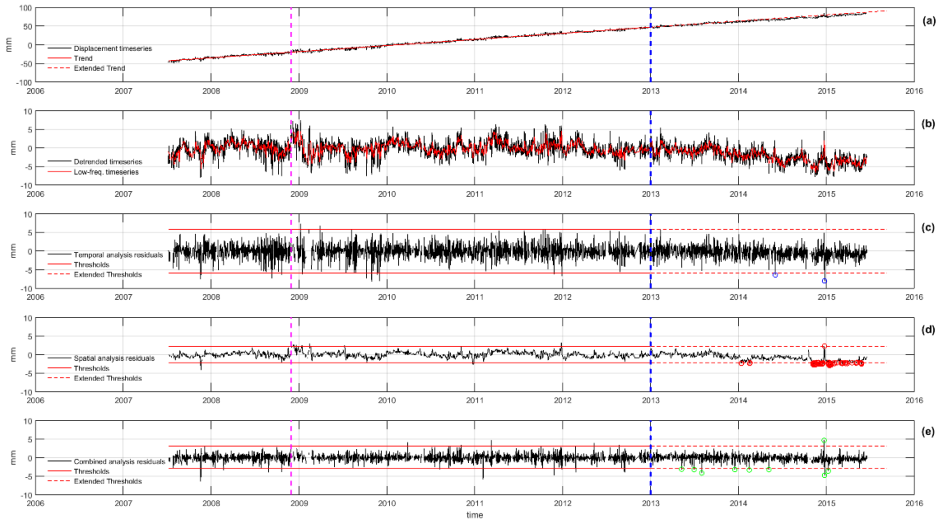


Figure C-212 Same as A-211, but for ΔE component

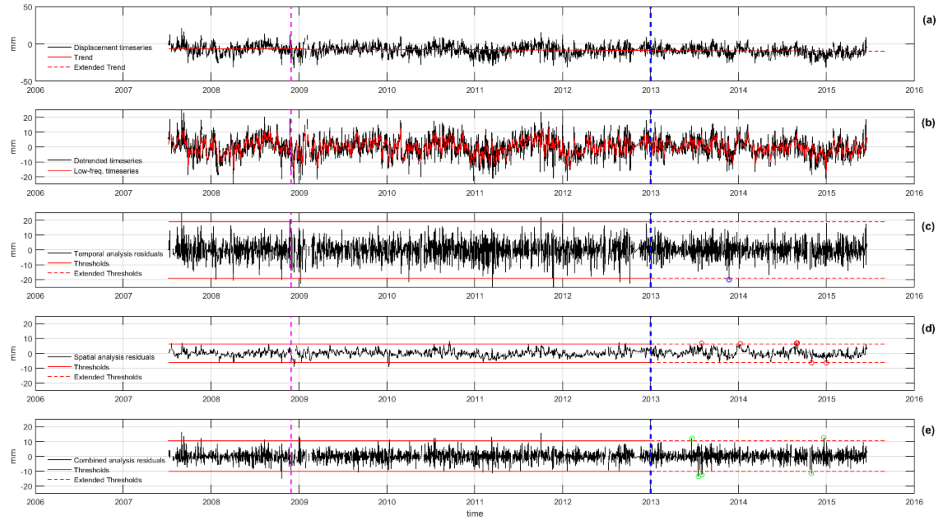


Figure C-213 Same as A-211, but for ΔU component

SHOE

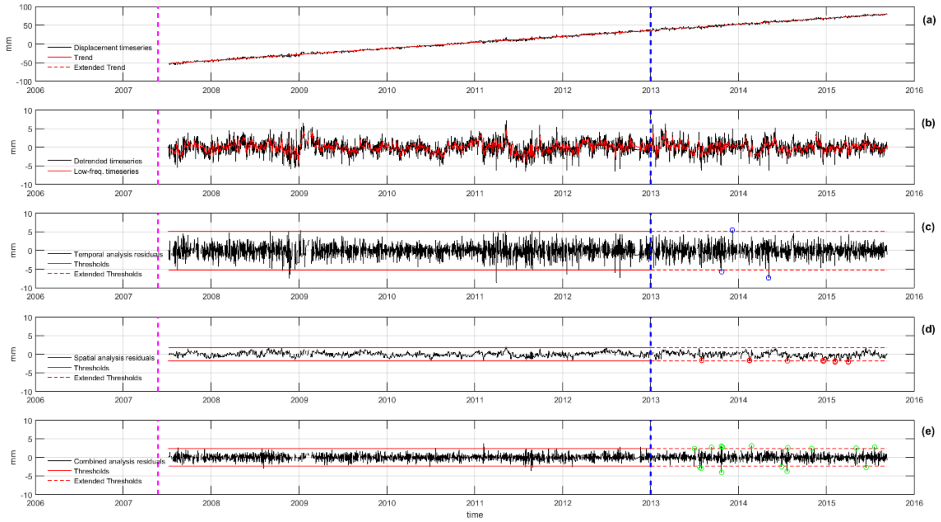


Figure C-214 SHOE (ΔN) – (a) Corrected displacement time series, (b) detrended and low-frequency time series, the (c) Temporal, (d) Spatial and (e) combined analysisresiduals.

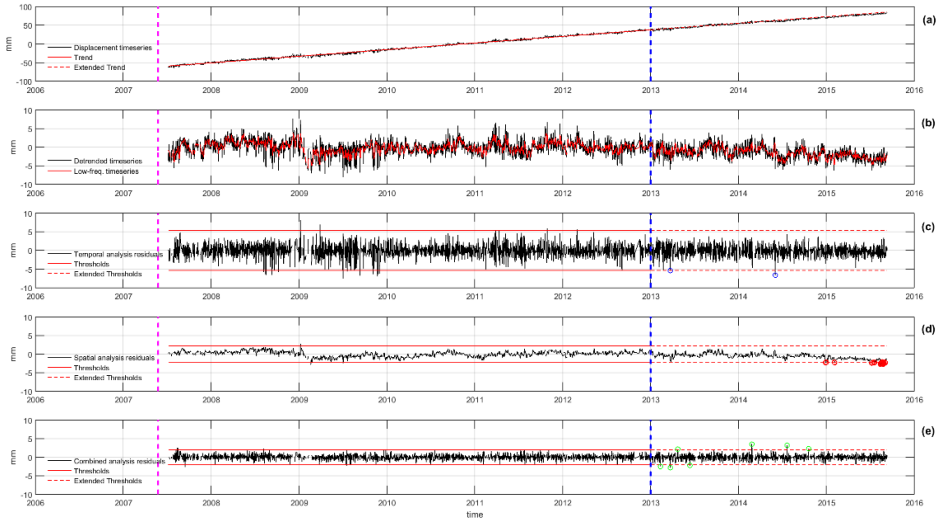


Figure C-215 Same as A-214, but for ΔE component

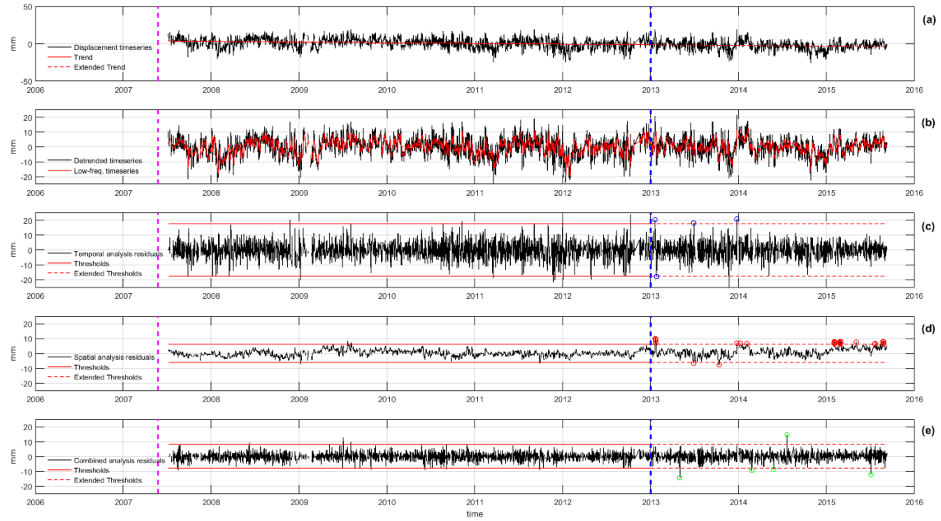


Figure C-216 Same as A-214, but for ΔU component

SHRE

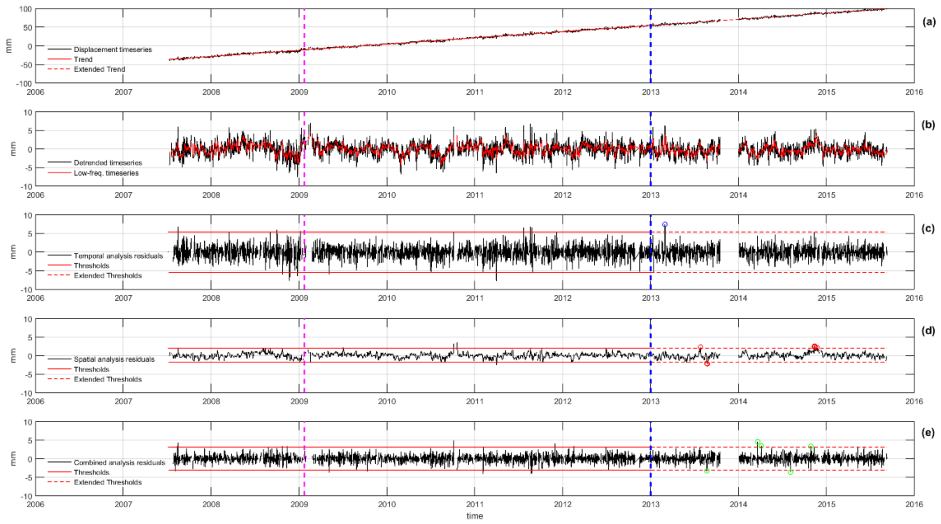


Figure C-217 SHRE (ΔN) – (a) Corrected displacement time series, (b) detrended and low-frequency time series, the (c) Temporal, (d) Spatial and (e) combined analysisresiduals.

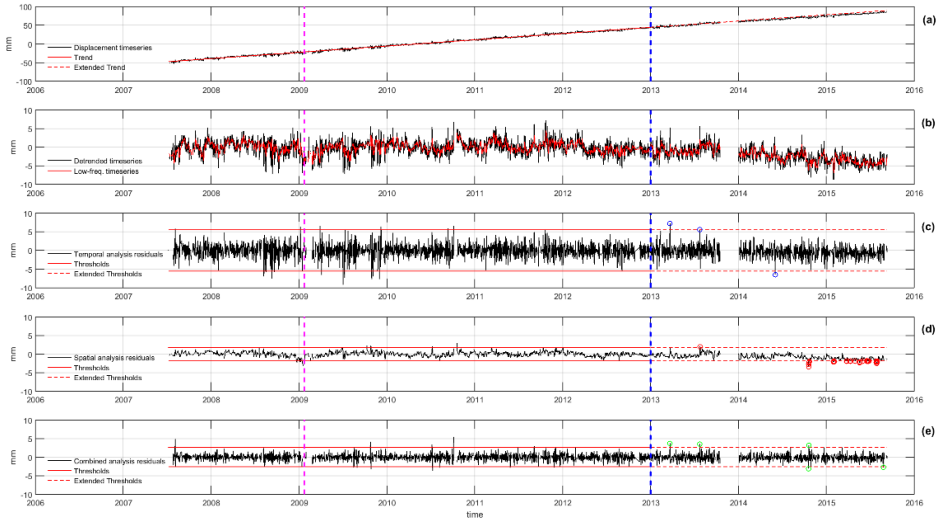


Figure C-218 Same as A-217, but for ΔE component

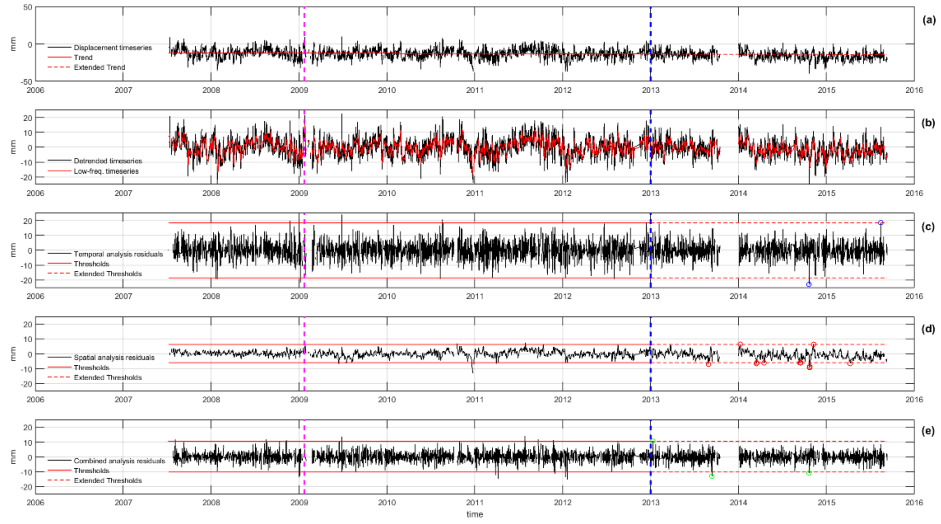


Figure C-219 Same as A-217, but for ΔU component

SKEE

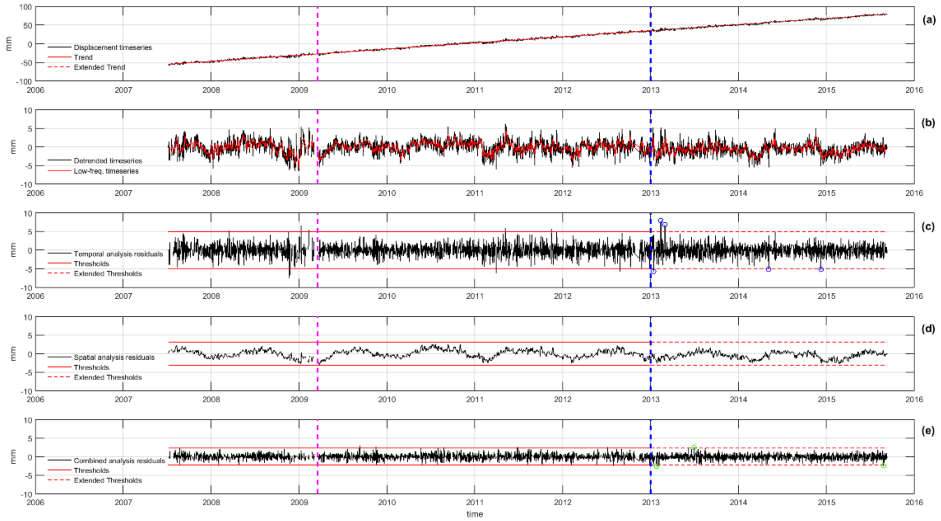


Figure C-220 SKEE (ΔN) – (a) Corrected displacement time series, (b) detrended and low-frequency time series, the (c) Temporal, (d) Spatial and (e) combined analysisresiduals.

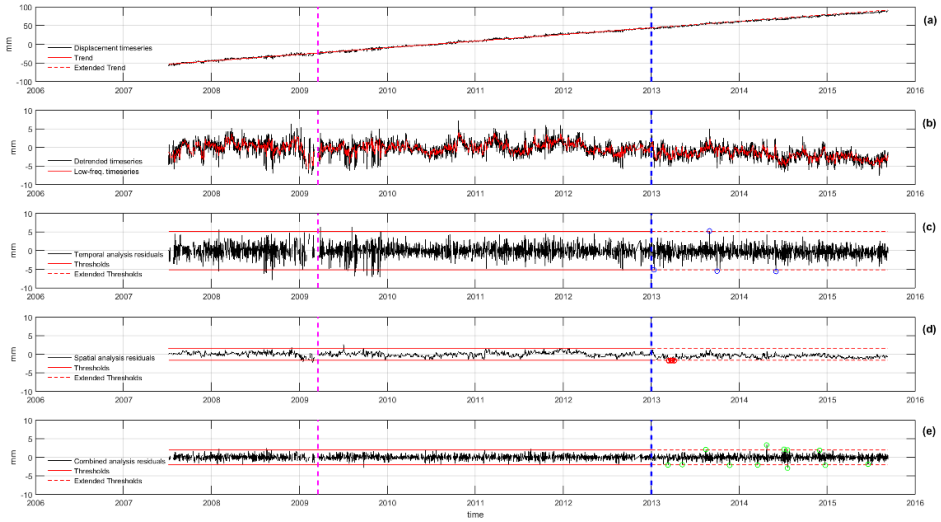


Figure C-221 Same as A-220, but for ΔE component

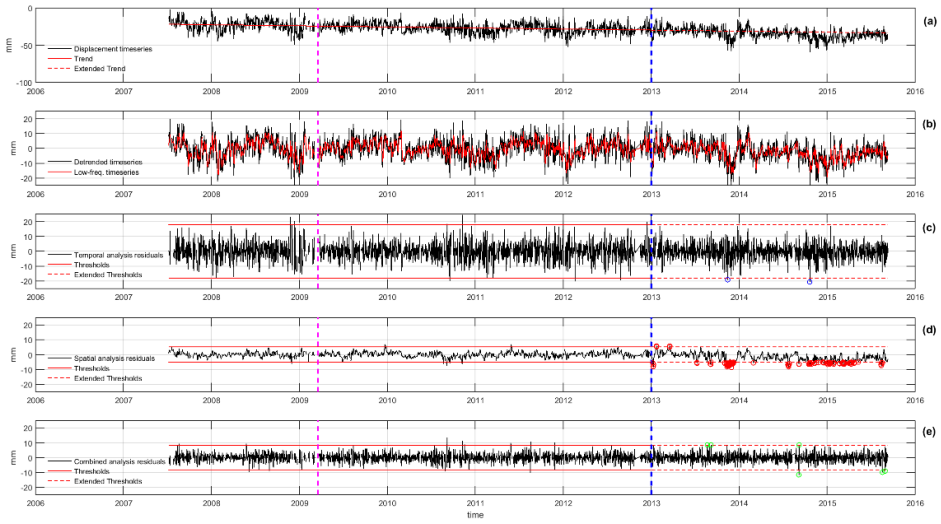


Figure C-222 Same as A-220, but for ΔU component

STEE

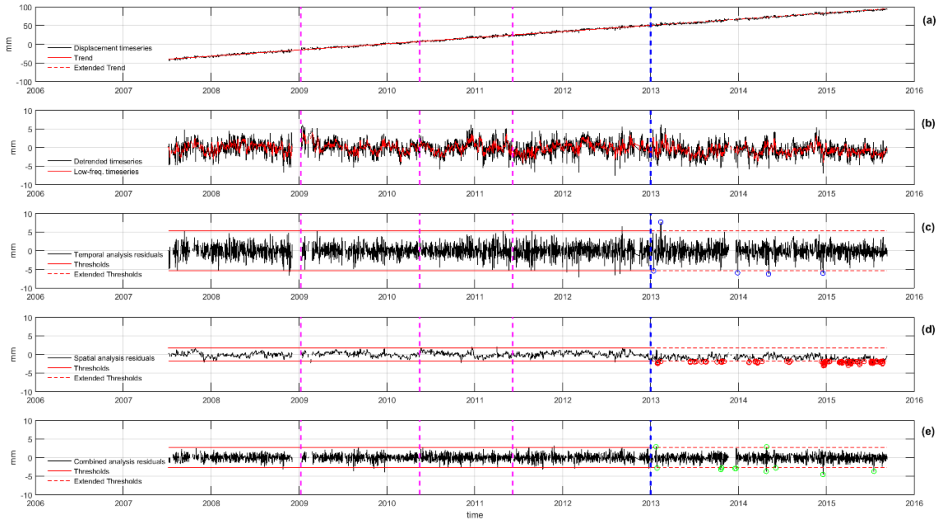


Figure C-223 STEE (ΔN) – (a) Corrected displacement time series, (b) detrended and low-frequency time series, the (c) Temporal, (d) Spatial and (e) combined analysisresiduals.

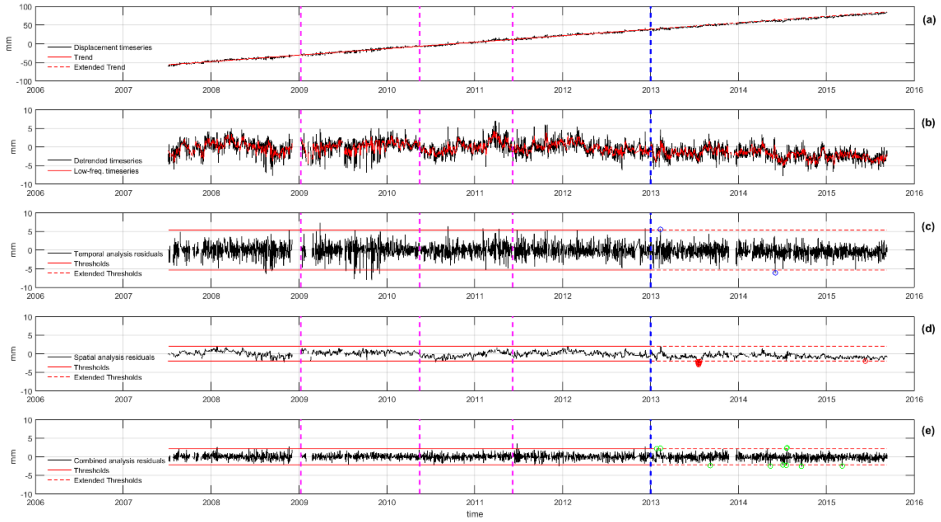


Figure C-224 Same as A-223, but for ΔE component

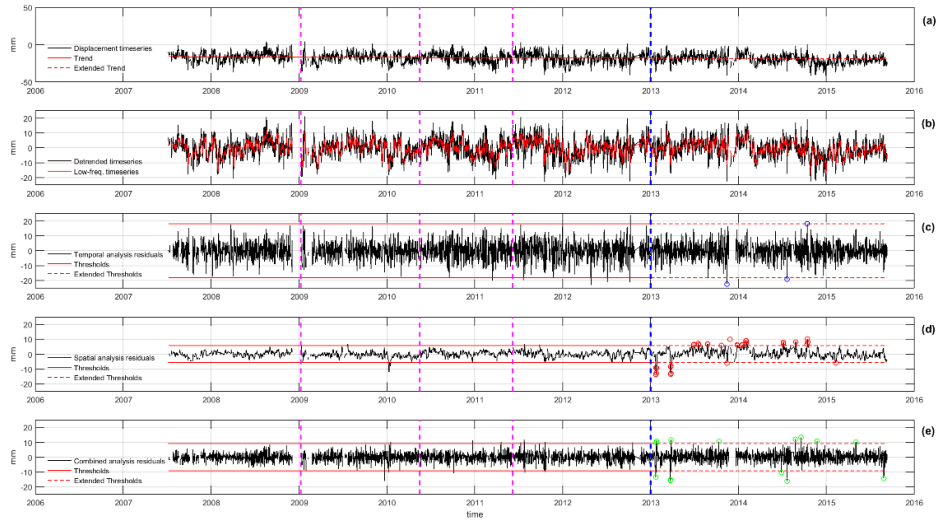


Figure C-225 Same as A-223, but for ΔU component

SWAN

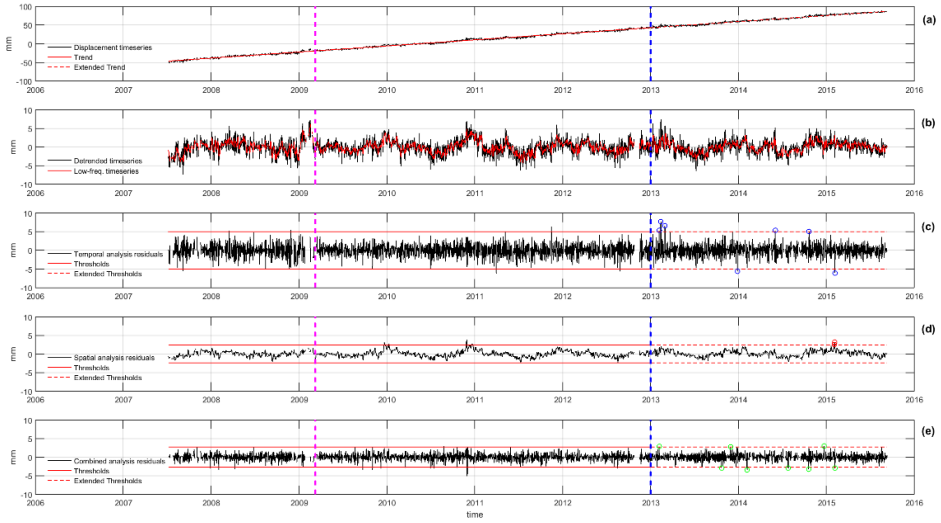


Figure C-226 SWAN (ΔN) – (a) Corrected displacement time series, (b) detrended and low-frequency time series, the (c) Temporal, (d) Spatial and (e) combined analysisresiduals.

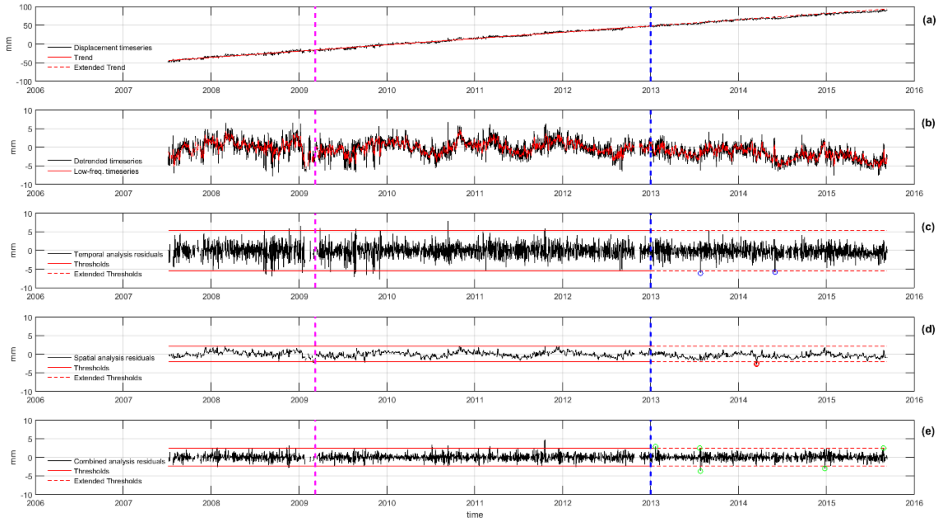


Figure C-227 Same as A-226, but for ΔE component

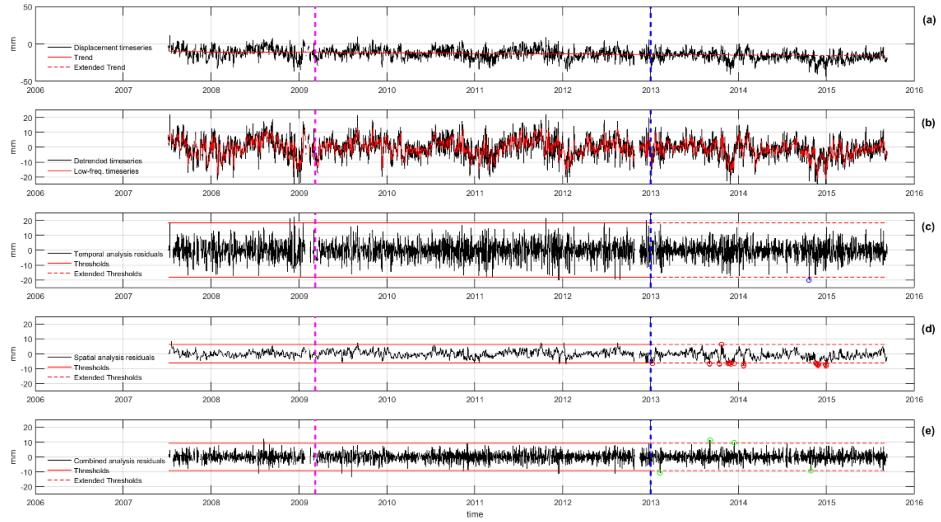


Figure C-228 Same as A-226, but for ΔU component

SWTG

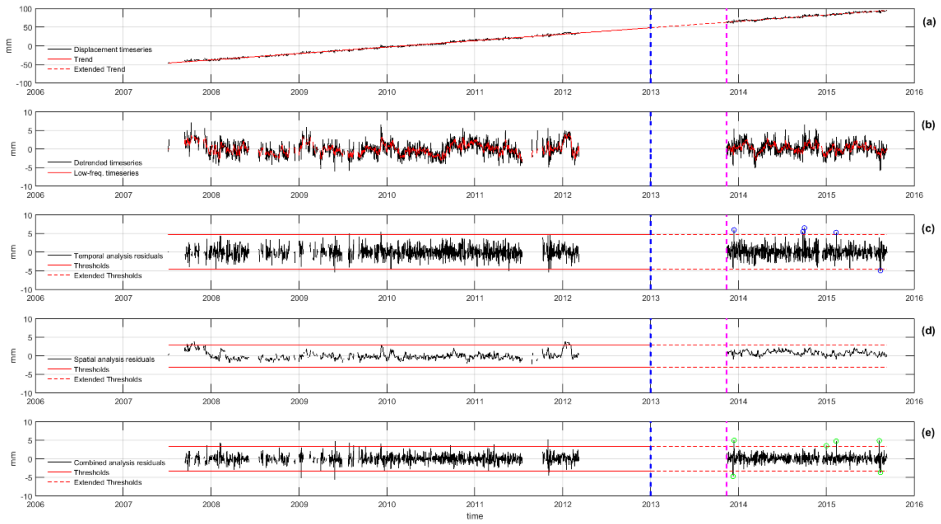


Figure C-229 SWTG (ΔN) – (a) Corrected displacement time series, (b) detrended and low-frequency time series, the (c) Temporal, (d) Spatial and (e) combined analysisresiduals.

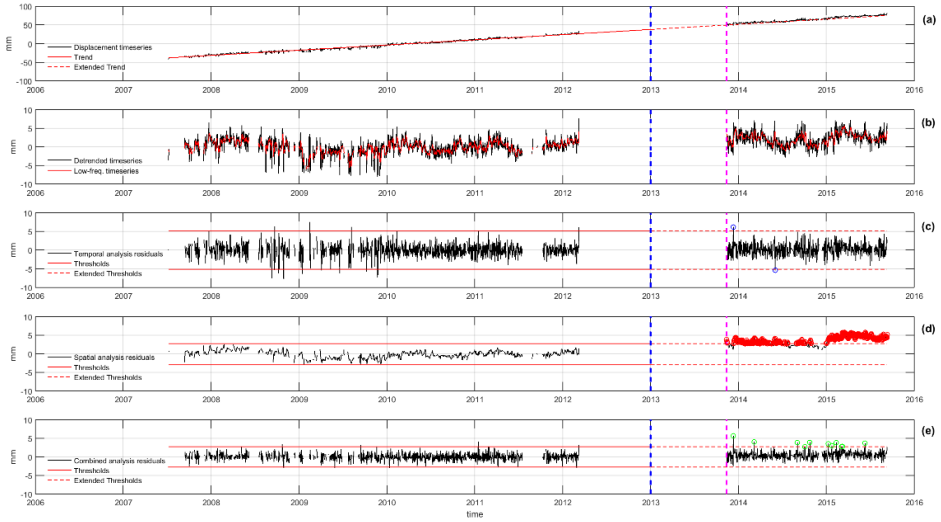


Figure C-230 Same as A-229, but for ΔE component

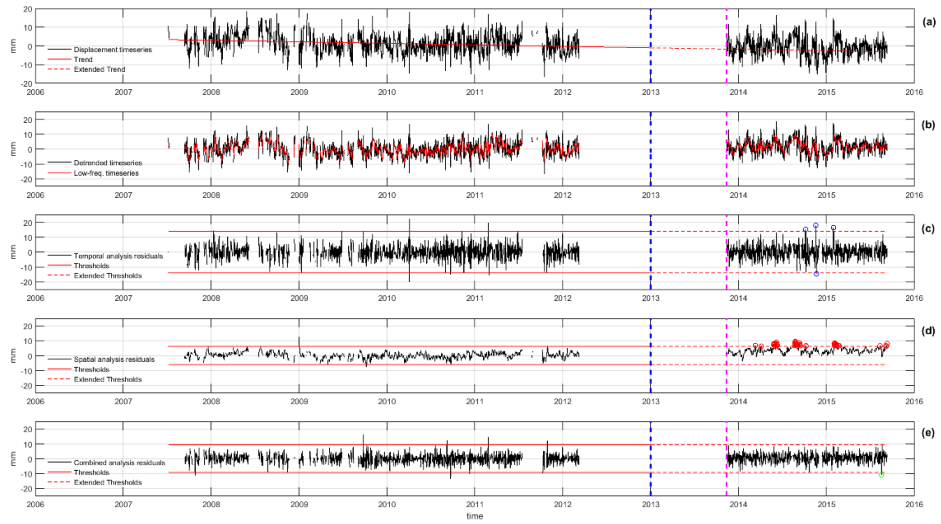


Figure C-231 Same as A-229, but for ΔU component

TAUT

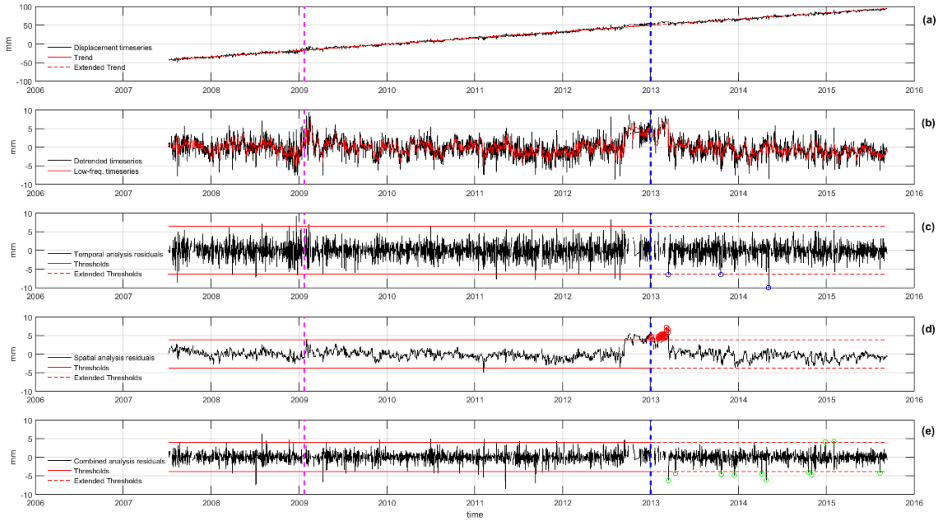


Figure C-232 TAUT (ΔN) – (a) Corrected displacement time series, (b) detrended and low-frequency time series, the (c) Temporal, (d) Spatial and (e) combined analysisresiduals.

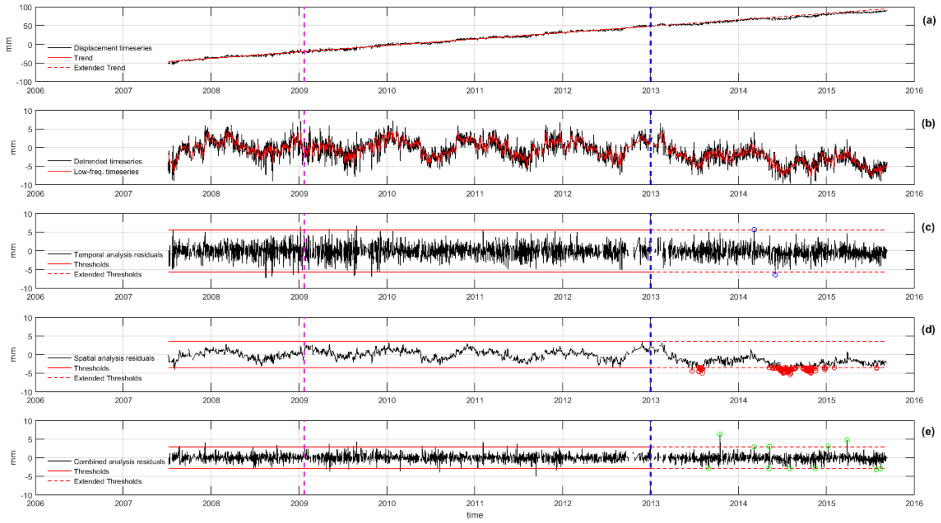


Figure C-233 Same as A-232, but for ΔE component

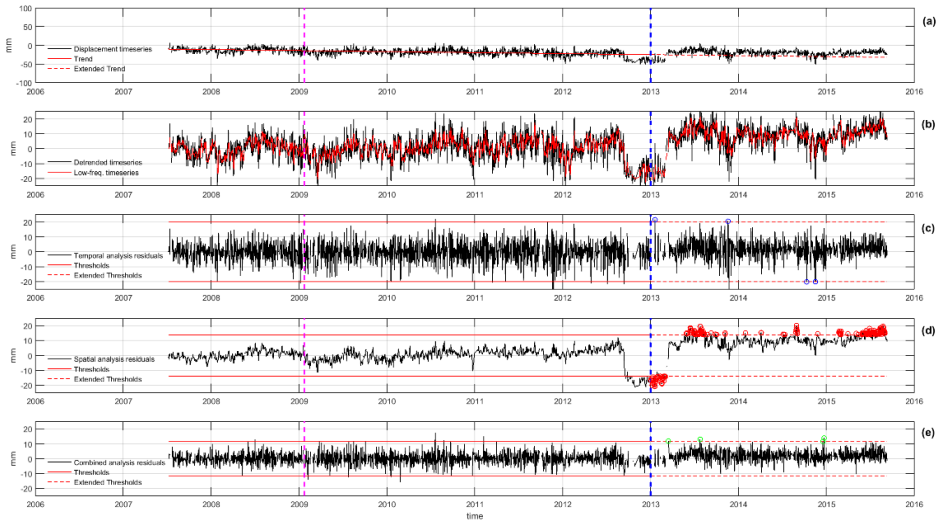


Figure C-234 Same as A-232, but for ΔU component

TEDD

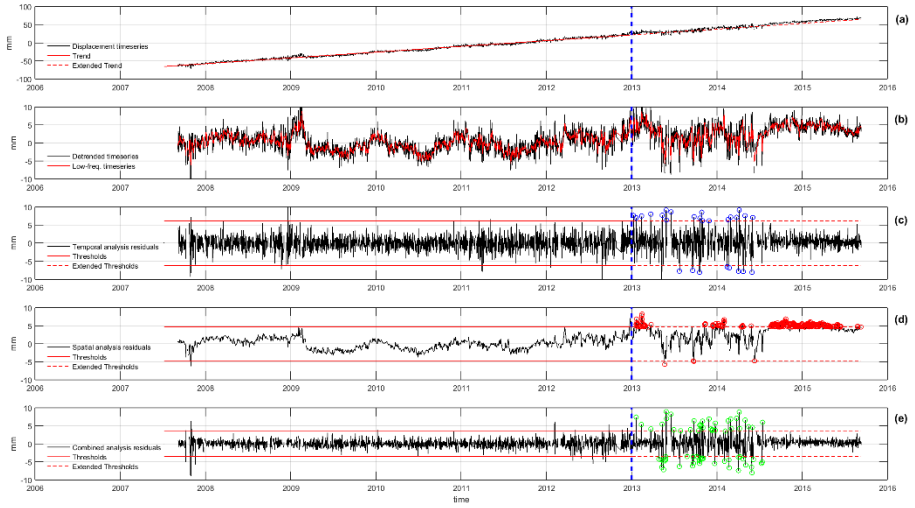


Figure C-235 TEDD (ΔN) – (a) Corrected displacement time series, (b) detrended and low-frequency time series, the (c) Temporal, (d) Spatial and (e) combined analysisresiduals.

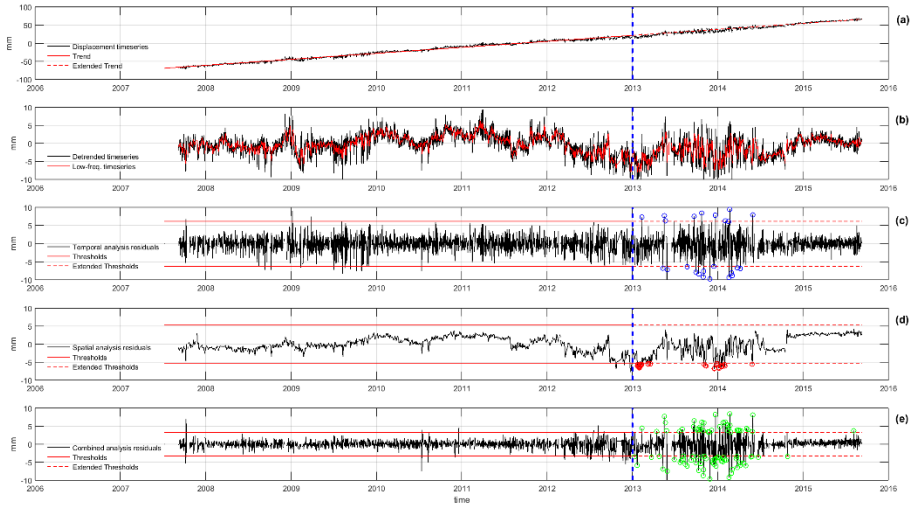


Figure C-236 Same as A-235, but for ΔE component

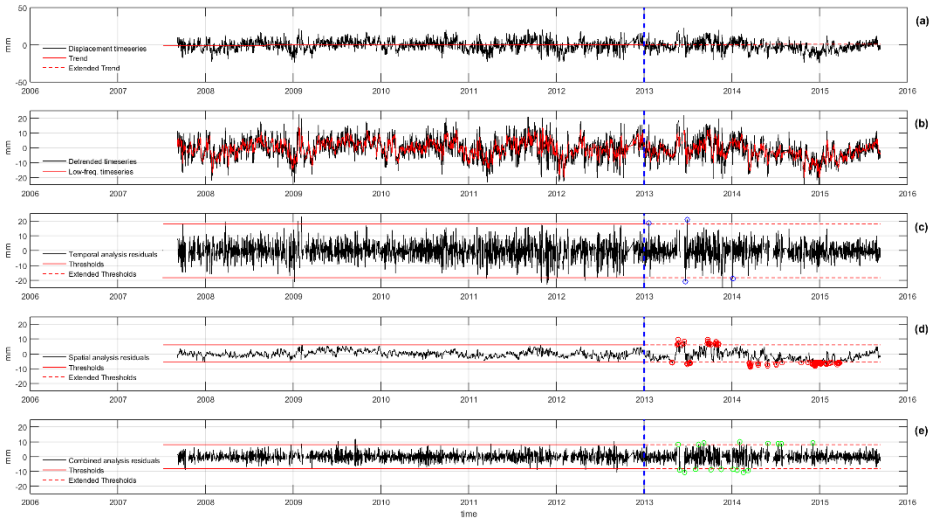


Figure C-237 Same as A-235, but for ΔU component

THUS

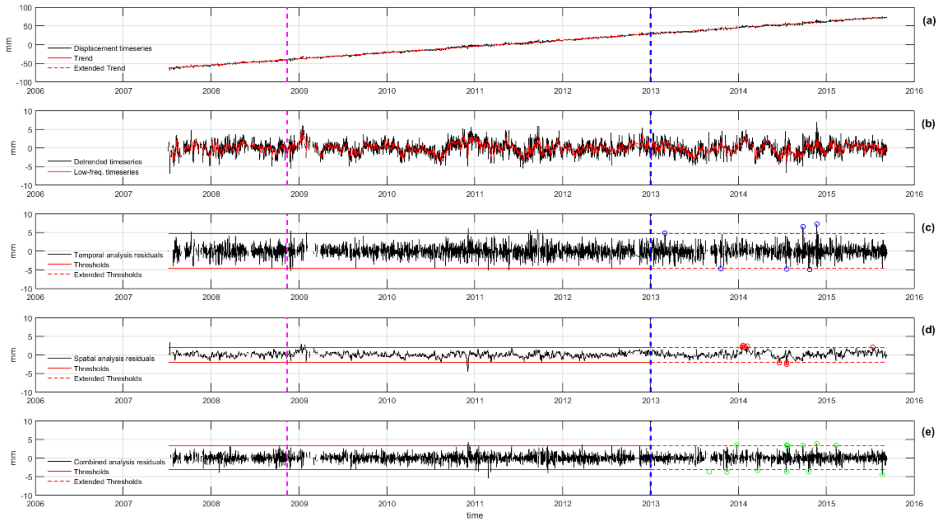


Figure C-238 THUS (ΔN) – (a) Corrected displacement time series, (b) detrended and low-frequency time series, the (c) Temporal, (d) Spatial and (e) combined analysisresiduals.

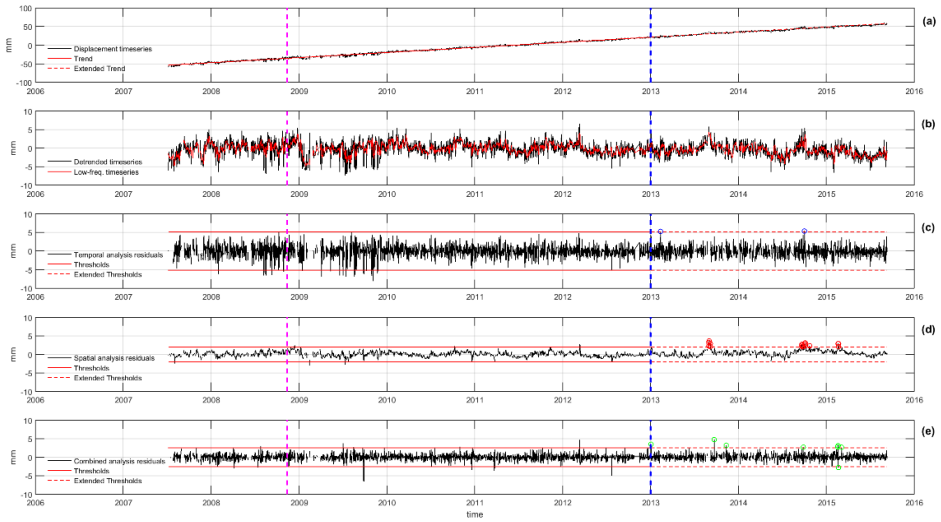


Figure C-239 Same as A-238, but for ΔE component

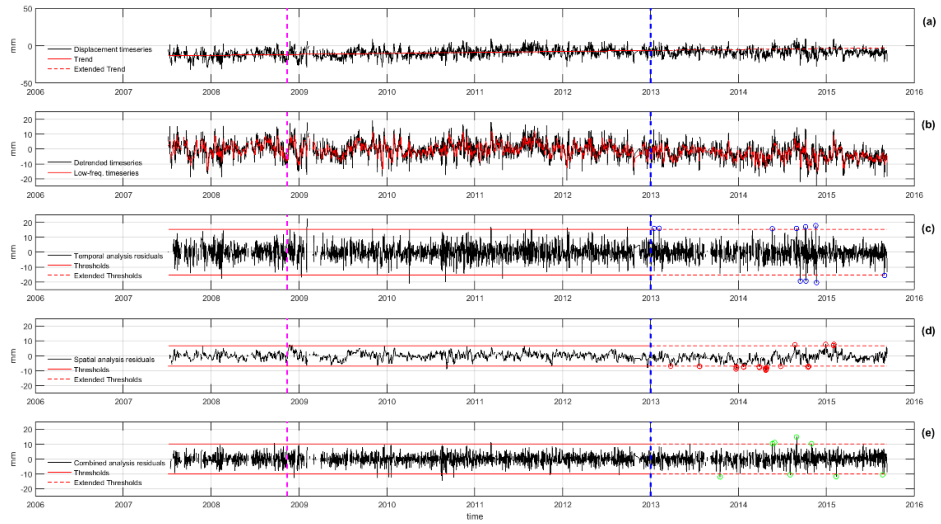


Figure C-240 Same as A-238, but for ΔU component

WARS

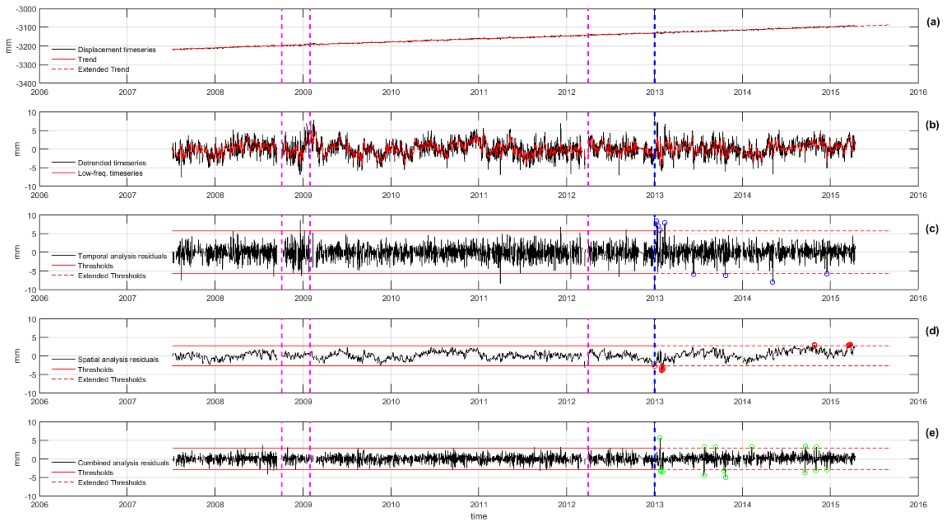


Figure C-241 WARS (ΔN) – (a) Corrected displacement time series, (b) detrended and low-frequency time series, the (c) Temporal, (d) Spatial and (e) combined analysisresiduals.

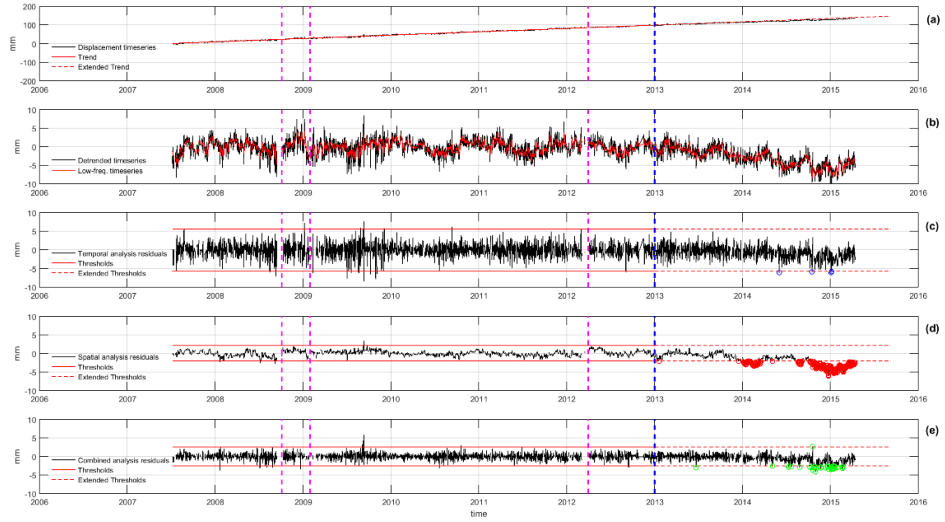


Figure C-242 Same as A-241, but for ΔE component

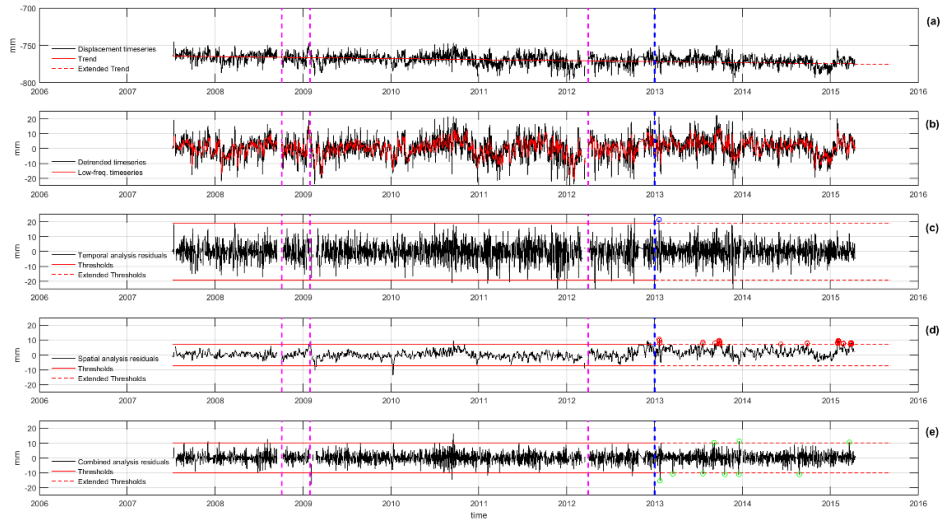


Figure C-243 Same as A-241, but for ΔU component

WATT

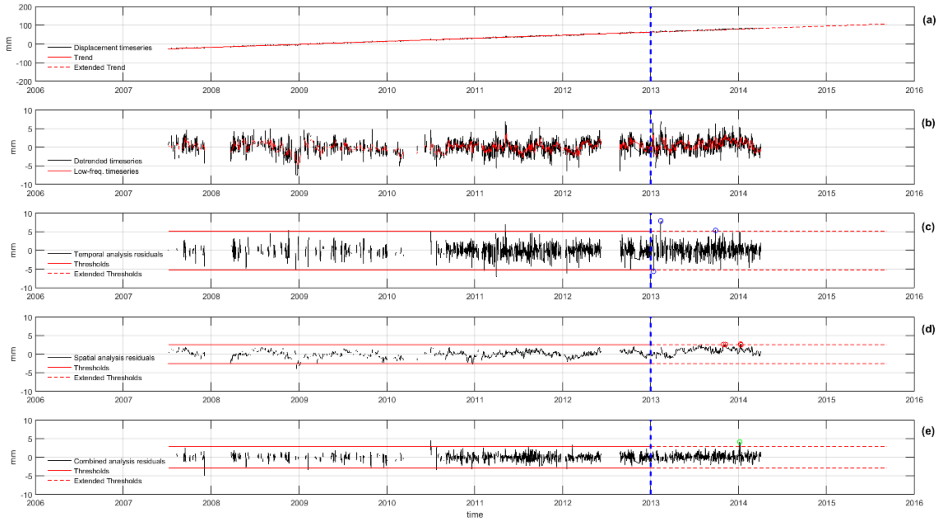


Figure C-244 WATT (ΔN) – (a) Corrected displacement time series, (b) detrended and low-frequency time series, the (c) Temporal, (d) Spatial and (e) combined analysisresiduals.

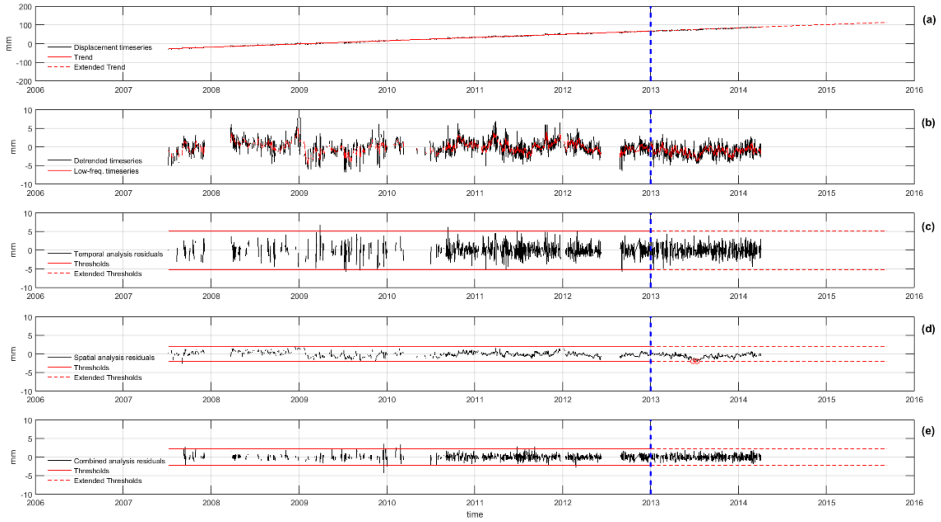


Figure C-245 Same as A-244, but for ΔE component

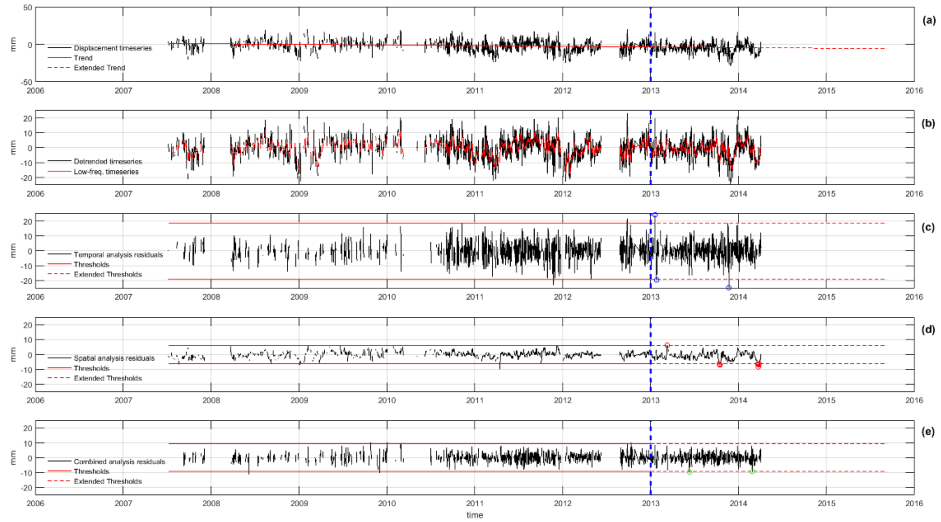


Figure C-246 Same as A-244, but for ΔU component

WEAR

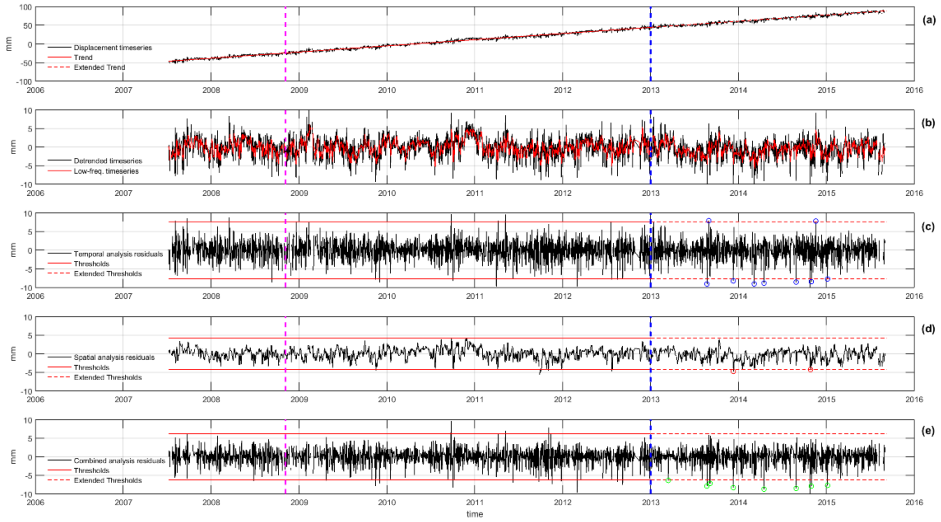


Figure C-247 WEAR (ΔN) – (a) Corrected displacement time series, (b) detrended and low-frequency time series, the (c) Temporal, (d) Spatial and (e) combined analysisresiduals.

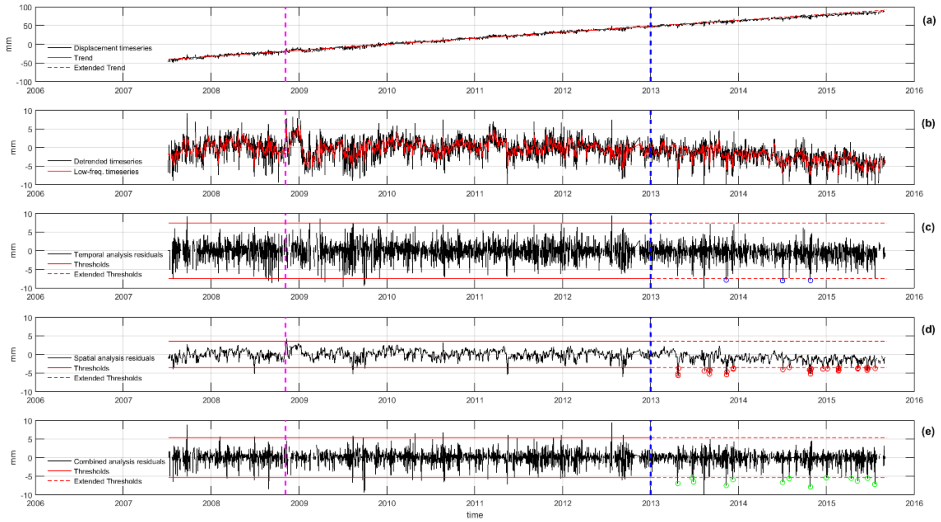


Figure C-248 Same as A-247, but for ΔE component

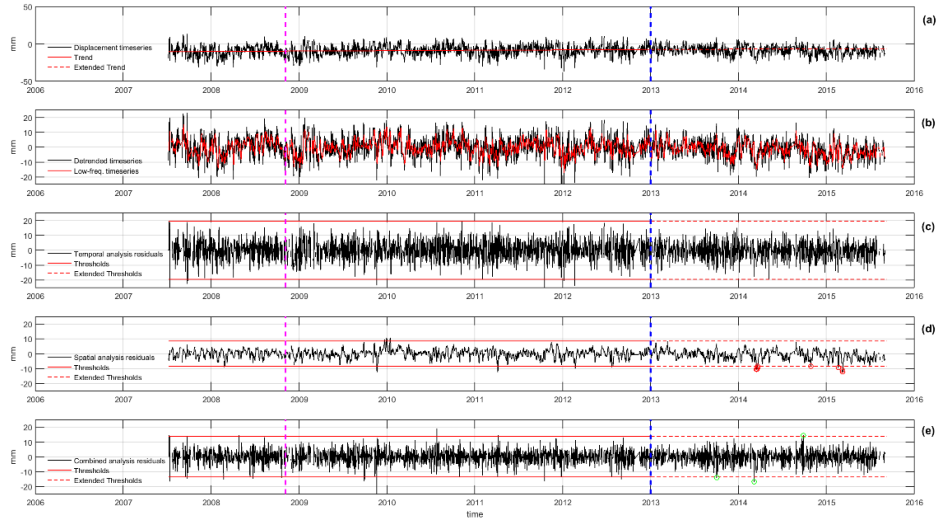


Figure C-249 Same as A-247, but for ΔU component

WEIW

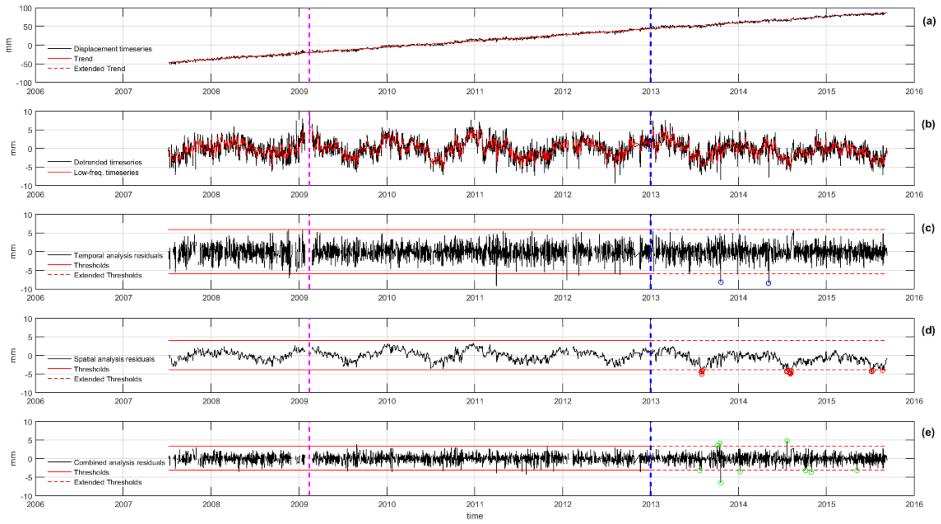


Figure C-250 WEIW (ΔN) – (a) Corrected displacement time series, (b) detrended and low-frequency time series, the (c) Temporal, (d) Spatial and (e) combined analysisresiduals.

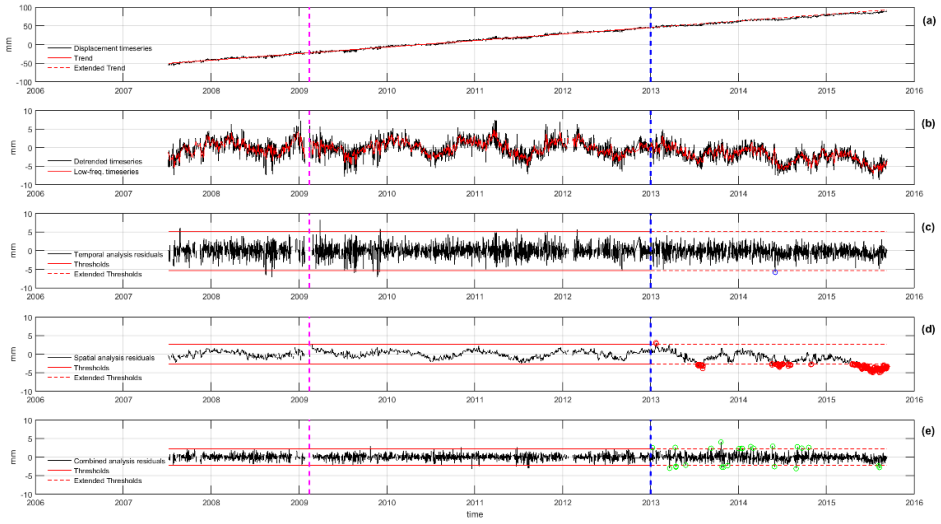


Figure C-251 Same as A-250, but for ΔE component

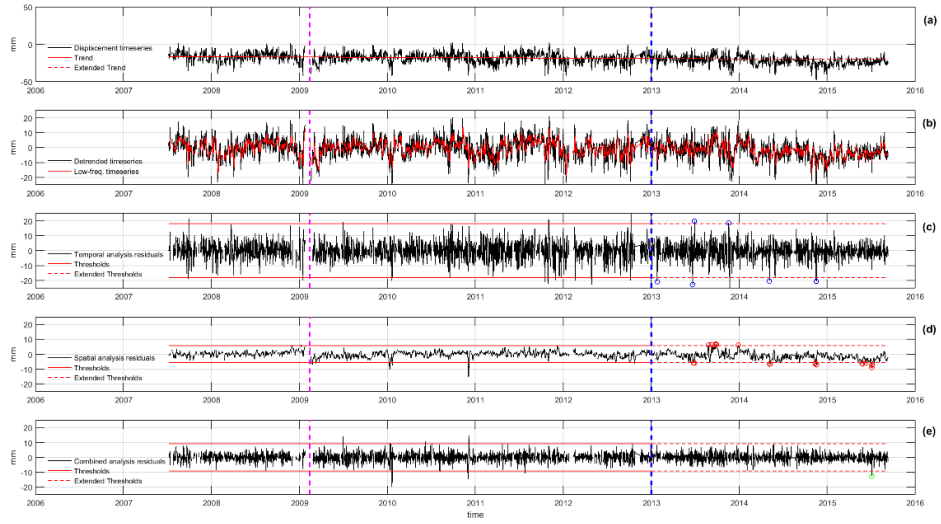


Figure C-252 Same as A-250, but for ΔU component

WELL

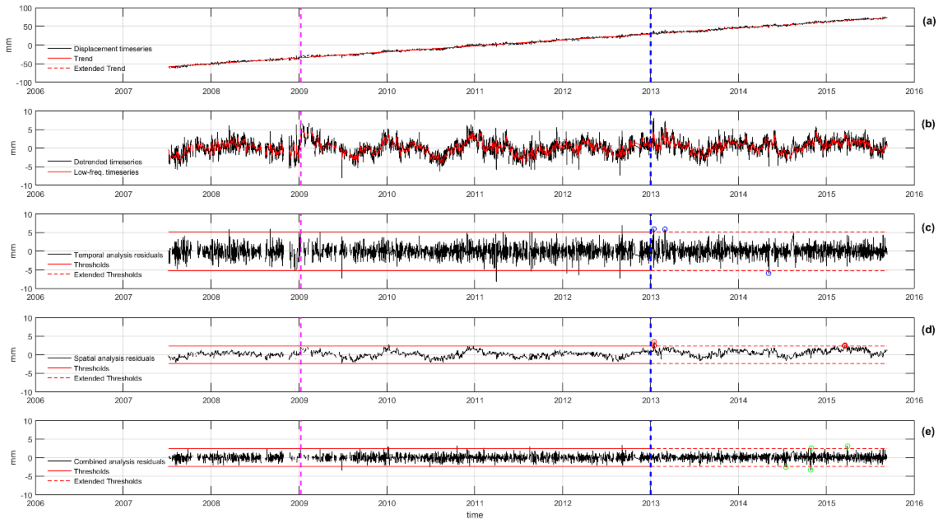


Figure C-253 WELL (ΔN) – (a) Corrected displacement time series, (b) detrended and low-frequency time series, the (c) Temporal, (d) Spatial and (e) combined analysisresiduals.

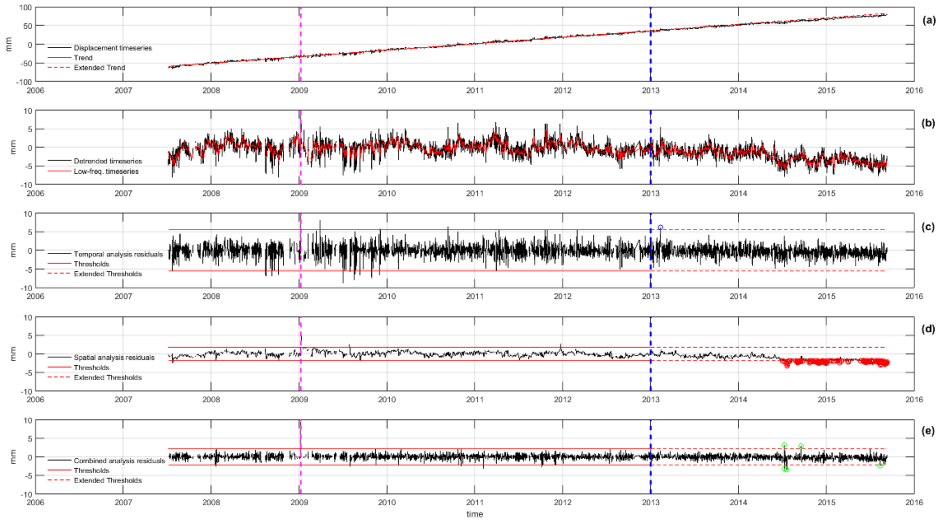


Figure C-254 Same as A-253, but for ΔE component

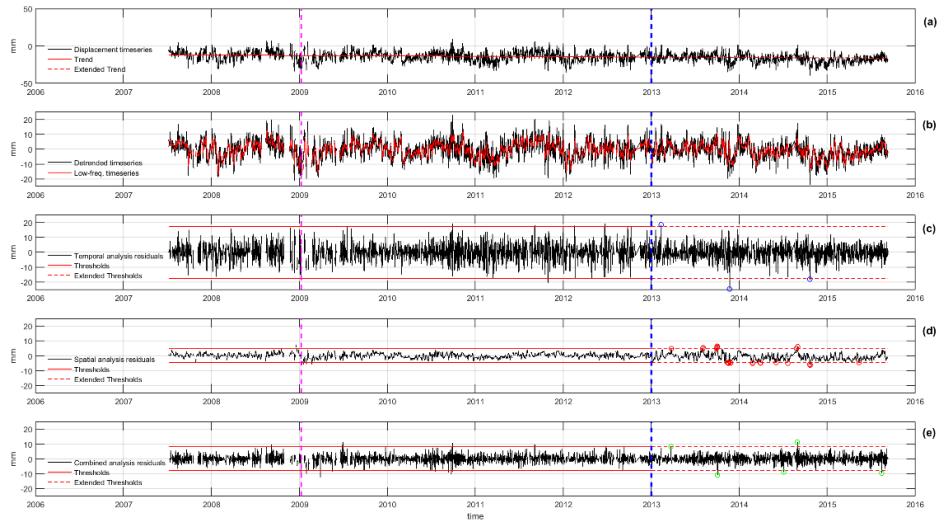


Figure C-255 Same as A-253, but for ΔU component

WEYB

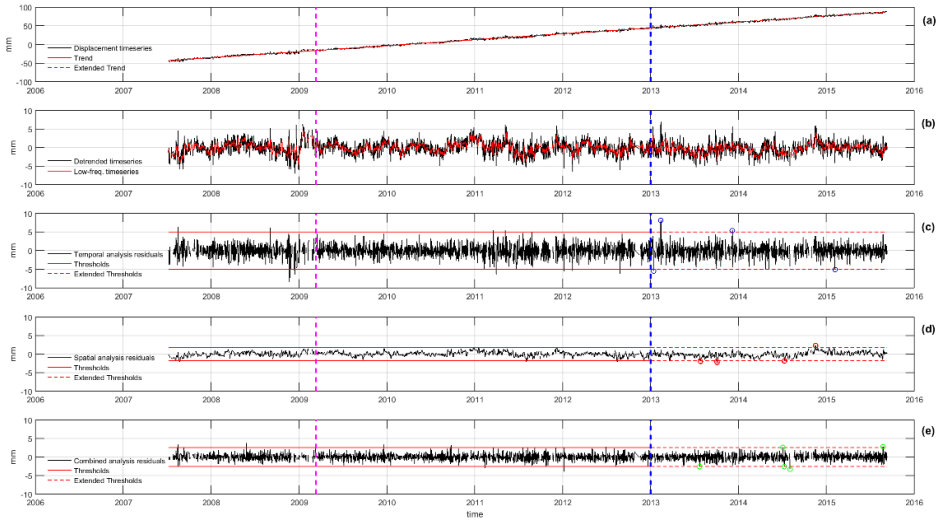


Figure C-256 WEYB (ΔN) – (a) Corrected displacement time series, (b) detrended and low-frequency time series, the (c) Temporal, (d) Spatial and (e) combined analysisresiduals.

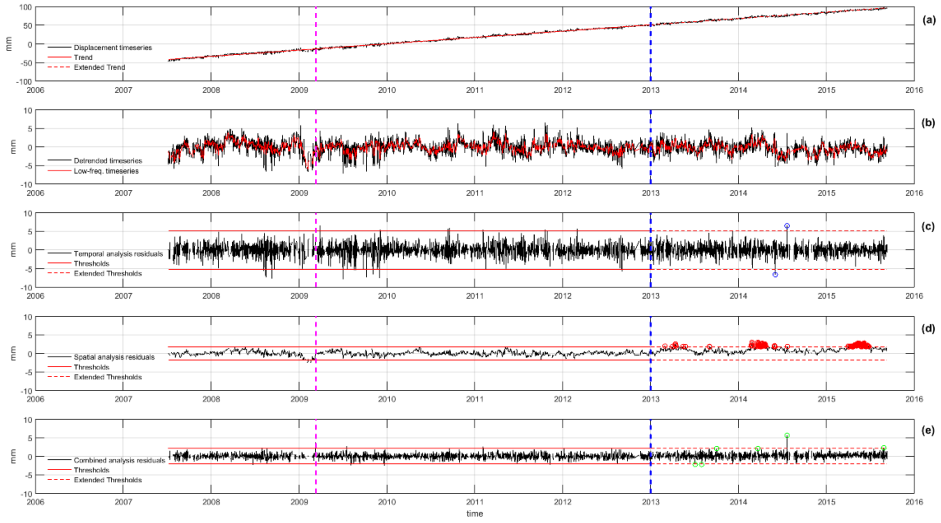


Figure C-257 Same as A-256, but for ΔE component

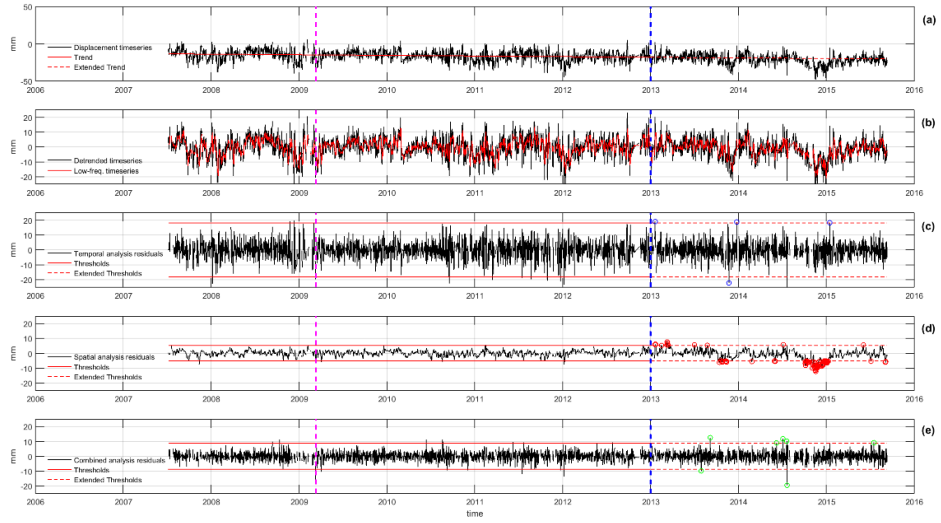


Figure C-258 Same as A-256, but for ΔU component

YEAS

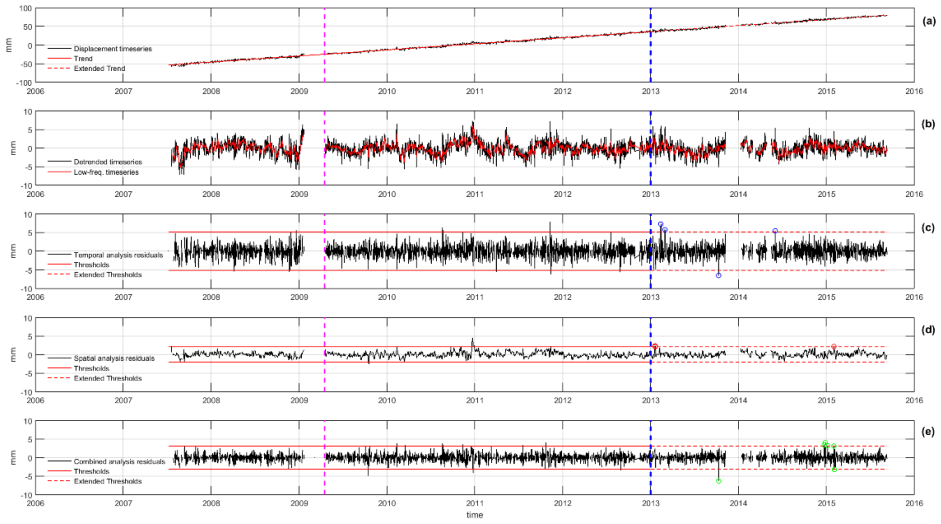


Figure C-259 YEAS (ΔN) – (a) Corrected displacement time series, (b) detrended and low-frequency time series, the (c) Temporal, (d) Spatial and (e) combined analysisresiduals.

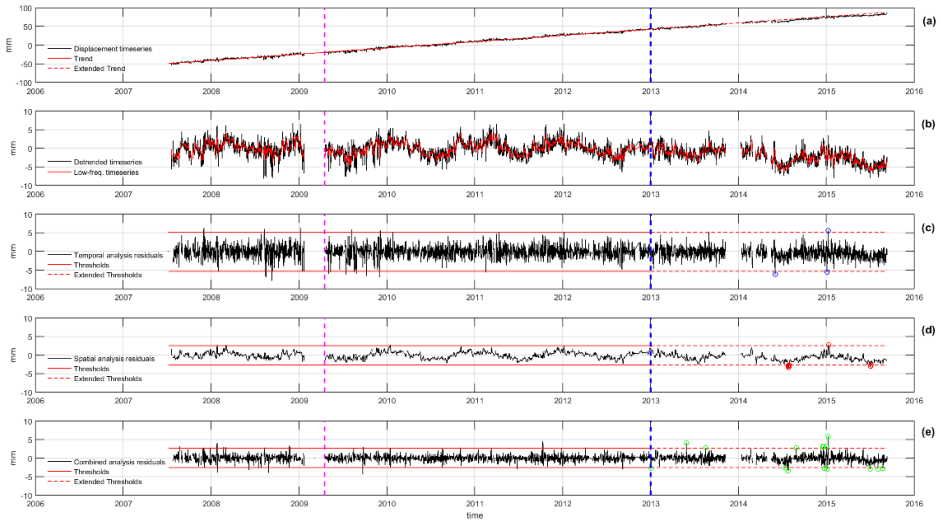


Figure C-260 Same as A-259, but for ΔE component

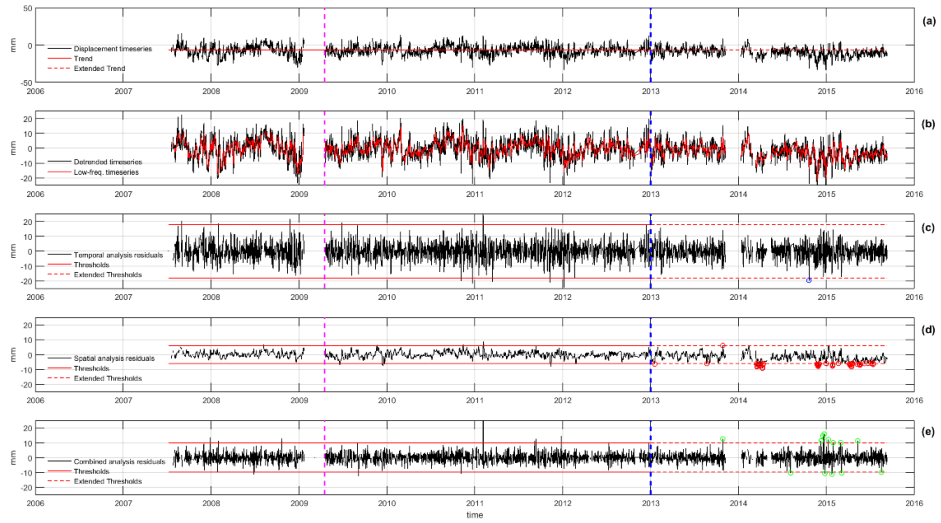


Figure C-261 Same as A-559, but for ΔU component

APPENDIX D

The days on which meteorological events were detected by the multiple algorithm approach.

Table D-1 shows that the number of days considered as having meteorological events is always higher from the temporal analysis algorithm; roughly three times higher than for the spatial analysis algorithm and two times higher than for the combined analysis algorithm. It can also be seen from this table that, in some cases, the number of hours or stations flagged using 1 cycle / day as the cut off frequency is higher than the rest, while in other cases, it is the other way around (i.e. the number of hours or stations flagged using 0.25 cycle / day as the cut off frequency is higher than the rest). Moreover, the table shows that the average number of hours for a meteorological event that were flagged by the combined analysis algorithm is the shortest (i.e. 2 hours). In order to further understand this performance, examples will, therefore, be shown using the 0.25, 0.5 and 1 cycle/day cut-off frequencies.

Table D-1 The days on which meteorological events were detected by the Temporal (T), spatial (S) and (c) combined analysis algorithms along with the number of hours (Hrs) and the number of stations (Stn) on each day using different cut-off frequencies.

	0.25 cycle/day						0.5 cycle/day						1 cycle/day					
	T		S		C		T		S		C		T		S		C	
Date	Hrs	Stn	Hrs	Stn	Hrs	Stn	Hrs	Stn	Hrs	Stn	Hrs	Stn	Hrs	Stn	Hrs	Stn	Hrs	Stn
01/01/2013							2	25					2	32				
02/01/2013	4	15					3	14					3	14				
03/01/2013	2	3					2	3					2	3				
05/01/2013					1	2	1	12			1	3	2	15			2	4
06/01/2013	4	11			2	5	4	12			1	2	6	13			1	2

Table 8-2 continued

	0.25 cycle/day						0.5 cycle/day						1 cycle/day					
	T		S		C		T		S		C		T		S		C	
Date	Hrs	Stn	Hrs	Stn	Hrs	Stn	Hrs	Stn	Hrs	Stn	Hrs	Stn	Hrs	Stn	Hrs	Stn	Hrs	Stn
07/01/2013			2	2					1	2								
08/01/2013	10	27					13	27			1	1	13	28			1	1
09/01/2013	9	14					7	15					4	9				
10/01/2013			1	2														
26/01/2013	2	5					6	15			1	3	7	28			1	3
27/01/2013	5	27					7	36					8	40				
28/01/2013	1	3					1	10					2	15				
29/01/2013	8	22					8	26					9	34			1	1
30/01/2013	6	21					7	19					7	17				
31/01/2013	1	1					2	11					2	13				
03/02/2013													1	5				
04/02/2013	1	4					4	16					5	18				
05/02/2013			2	5					1	4					1	4		
14/02/2013							1	1					2	4				
07/03/2013			1	1														
09/03/2013					2	2					2	4					2	4
12/03/2013			3	6					2	6					2	6		
13/04/2013	12	56					13	51					13	43				
14/04/2013	4	14	1	1			5	18	1	1	1	6	5	19	1	1	1	6
18/04/2013							1	15					2	21				
25/04/2013	1	2					1	7					1	10				
26/04/2013	2	4					2	6					3	9				
02/05/2013			2	1					4	1					4	1		
04/05/2013	1	1					2	4					2	6				
08/05/2013	4	12			2	5	6	21			2	5	7	26			2	5
09/05/2013	1	4					1	4					1	4				
12/05/2013	4	16					6	22					5	24				
15/05/2013											1	2					1	1
19/05/2013	4	8			1	3	4	8					4	8			1	2
20/05/2013	4	8	3	7	2	2	5	16	2	6	2	2	4	14	2	6	1	1
10/06/2013	1	3					2	4					1	4				
11/06/2013	12	40			2	5	11	38			3	5	11	36			4	6
12/06/2013	3	5					7	15					7	17				
15/06/2013	2	6					2	7					3	11			1	2
19/06/2013									1	1					1	1		
20/06/2013	3	3	12	12	6	9	3	3	7	10	5	5	3	3	6	10	3	4
21/06/2013	2	10					4	25			1	3	5	25			1	3
22/06/2013	7	28			2	4	8	35			2	4	9	38			2	3
27/06/2013	9	11			1	4	7	11			1	6	5	9			1	3
28/06/2013	13	49			1	4	13	53			2	7	14	55			2	7
29/06/2013	5	28					5	27			1	3	5	25				
30/06/2013					1	4	2	6			1	4	2	6			1	4
02/07/2013													1	1				
03/07/2013			3	3					2	3			2	7	2	3		
04/07/2013					1	1					1	1					1	1
06/07/2013	7	15			4	11	8	18			5	11	8	17			5	8
07/07/2013							1	4										
08/07/2013															1	2		
09/07/2013			4	3					4	5					4	5		

Table 8-2 continued

	0.25 cycle/day						0.5 cycle/day						1 cycle/day					
	T		S		C		T		S		C		T		S		C	
Date	Hrs	Stn	Hrs	Stn	Hrs	Stn	Hrs	Stn	Hrs	Stn	Hrs	Stn	Hrs	Stn	Hrs	Stn	Hrs	Stn
10/07/2013									1	5					2	5		
13/07/2013	3	6					2	6					3	6	1	4		
14/07/2013																	1	3
15/07/2013	1	4					1	4					1	4				
18/07/2013															1	3		
21/07/2013							1	1										
22/07/2013											1	2					1	2
23/07/2013					1	2					1	4					1	1
25/07/2013					2	3			3	2	2	3			3	2	2	3
27/07/2013	6	17					5	14					4	10				
28/07/2013	1	2					2	10					5	13				
31/07/2013	9	18					9	18					7	15				
01/08/2013					1	3	1	3			1	3	1	3			1	3
02/08/2013	8	21			1	4	9	28			1	4	9	34			2	5
05/08/2013	6	23					6	29	2	2			6	26	4	2		
06/08/2013	4	19					2	15					2	15				
13/08/2013																	1	1
15/08/2013					1	1					1	1					1	1
16/08/2013	14	47			3	13	13	48			4	7	11	46			3	4
17/08/2013	6	29			2	7	9	31			4	10	9	31			4	10
18/08/2013							1	2					2	4				
21/08/2013	3	7			1	1	5	12			4	9	6	13			4	8
22/08/2013			5	5					3	5					3	5		
23/08/2013					2	5					2	5					1	2
24/08/2013											1	1					1	1
25/08/2013											1	1					2	2
28/08/2013	1	8	1	3			1	8					1	8				
29/08/2013					1	1	1	1			1	1	1	5				
30/08/2013	6	32			1	2	6	32			3	6	6	32			3	9
31/08/2013	7	34			1	2	7	34			1	2	7	32			1	2
03/09/2013	1	1																
05/09/2013							2	1					2	1				
06/09/2013	2	2	4	4	4	5	2	4	4	5	1	4	4	3	4	8	1	4
11/09/2013	15	57					14	51			1	1	14	42			1	1
12/09/2013	13	57			10	26	13	59			10	24	13	59			9	22
13/09/2013	5	29			1	4	5	36			1	6	5	37			1	4
14/09/2013	8	16					6	15					5	16				
15/09/2013	22	69					22	69					22	69			1	1
17/09/2013	3	19					4	23					5	24				
19/09/2013	4	15					7	18					7	23				
20/09/2013													1	1				
21/09/2013	14	55					13	47					13	47	1	2		
24/09/2013			3	6			1	2	3	6			1	2	3	6		
25/09/2013	2	6			1	1	2	10			1	1	2	10			1	5
26/09/2013			1	1					2	1								
30/09/2013			5	1					6	3					4	3		
01/10/2013			1	1	1	4			3	3	1	4	1	1	6	6	1	4
02/10/2013	1	1	10	7					7	7					7	7		
03/10/2013							1	2					1	2				

Table 8-2 continued

	0.25 cycle/day						0.5 cycle/day						1 cycle/day					
	T		S		C		T		S		C		T		S		C	
Date	Hrs	Stn	Hrs	Date	Hrs	Stn	Hrs	Date	Hrs	Stn	Hrs	Date	Hrs	Stn	Hrs	Date	Hrs	Stn
04/10/2013	2	7					3	6					3	6				
07/10/2013					1	2					1	1					1	1
08/10/2013					1	3					2	6					2	3
09/10/2013	1	2					1	3					1	3				
10/10/2013			1	1														
11/10/2013	1	1					1	4					3	8				
12/10/2013	2	6					3	9					3	8				
13/10/2013													1	1				
14/10/2013			5	3					6	3					5	3		
16/10/2013	11	31					13	31			1	2	13	31			1	3
18/10/2013	2	9					2	12					2	12				
19/10/2013							1	4					2	6				
21/10/2013	1	2			1	1	2	12			1	1	3	15			1	1
22/10/2013	1	1					1	1					1	1				
23/10/2013	8	32					7	35					7	35				
25/10/2013	2	4					2	9	2	1	1	1	2	13	2	1	1	6
26/10/2013	5	14			2	2	9	35			3	3	12	39			4	7
27/10/2013	1	3															1	1
28/10/2013	5	10					4	17					4	17				
29/10/2013			2	2					1	2					1	2		
30/10/2013							2	6			3	5	3	17			3	8
02/11/2013					1	1					3	5					4	6
04/11/2013	3	8					4	10					4	10				
05/11/2013							1	2					2	5				
06/11/2013	1	1					1	8					2	10				
07/11/2013	7	25					10	24					10	23			1	3
08/11/2013			5	2					2	2					2	1		
10/11/2013	4	23					4	23					4	25				
11/11/2013	17	63					17	62					17	56	1	3		
12/11/2013	13	27			1	1	8	28			1	2	8	29			1	2
13/11/2013			7	7					5	8					5	8		
16/11/2013					1	1					1	1	1	3			1	1
17/11/2013	3	9					3	9					3	9				
20/11/2013													1	2				
26/11/2013	7	13					3	4					1	2				
27/11/2013	2	2					1	1										
29/11/2013									1	1					1	1		
04/12/2013													4	13				
05/12/2013					1	1					1	1						
10/12/2013													1	1				
11/12/2013													1	3				
12/12/2013	16	49			2	2	15	50	3	2	4	7	15	48	4	2	4	7
13/12/2013	3	15	5	6	1	3	4	15	4	5	1	1	4	16	3	5	1	1
14/12/2013	2	7			1	1	6	26			1	1	6	36			1	1
15/12/2013	9	26					14	44					15	45				
18/12/2013	2	4					4	35					4	40				
19/12/2013													1	4				
21/12/2013							1	3					1	3				
24/12/2013	1	4					5	36					5	40				

Table 8-2 continued

	0.25 cycle/day						0.5 cycle/day						1 cycle/day					
	T		S		C		T		S		C		T		S		C	
Date	Hrs	Stn	Hrs	Date	Hrs	Stn	Hrs	Date	Hrs	Stn	Hrs	Date	Hrs	Stn	Hrs	Date	Hrs	Stn
26/12/2013	1	6					1	13					1	13				
27/12/2013	1	2					1	3			2	4	1	4			2	4
02/01/2014	1	4					1	5					1	5				
03/01/2014													1	4				
05/01/2014	6	31					7	33					7	32				
11/01/2014	1	1					2	8					2	10				
12/01/2014	8	22					5	13					5	13				
13/01/2014							1	7					3	18				
24/01/2014	4	9			2	4	4	33			2	3	4	36			2	3
25/01/2014	5	11					5	18					5	23	1	2		
26/01/2014													3	8				
01/02/2014	2	12					4	19					4	20				
08/02/2014													1	1				
14/02/2014	2	8					1	3					1	3				
19/02/2014													1	3				
20/02/2014	2	8					2	17			1	1	4	20			1	1
27/02/2014	2	2	1	1			2	6	1	1			5	18	1	1	1	1
07/03/2014	7	53					6	52					6	52				
08/03/2014	5	26					5	33					5	37				
10/03/2014	2	6					4	8					4	11				
14/03/2014			3	3					2	3					1	3		
20/03/2014	7	37					7	35	1	1			7	36	2	1		
05/04/2014													1	1				
06/04/2014	6	24			2	4	6	27			2	4	5	24			2	4
07/04/2014	5	12			1	1	6	14			1	2	6	14			1	2
11/04/2014	1	2					2	4					2	4				
12/04/2014	3	8					5	9	1	1			5	12	1	1		
18/04/2014									1	4					1	1		
20/04/2014													1	1				
25/04/2014	3	7					3	7					3	8				
26/04/2014	3	5			7	21	6	16			7	21	8	17			10	26
28/04/2014									1	1					1	1		
30/04/2014			4	1					2	1					2	1		
01/05/2014			2	1														
03/05/2014			3	4					2	4					1	4		
06/05/2014	2	6					3	9					5	10				
08/05/2014							1	2										
09/05/2014	1	2					1	2					1	4				
17/05/2014	3	7					4	7	3	2			4	8	3	2		
18/05/2014			9	6					9	4					9	4		
21/05/2014	1	1					2	6					2	7				
22/05/2014							2	4					3	6			1	1
29/05/2014			4	4					6	5					7	7		
30/05/2014			13	5					13	5					13	5		
06/06/2014			3	1					3	1					5	1		
07/06/2014							2	7					3	10				
10/06/2014	2	4					3	8					3	8				
14/06/2014			6	2					3	1					1	1		

Table 8-2 continued

	0.25 cycle/day						0.5 cycle/day						1 cycle/day					
	T		S		C		T		S		C		T		S		C	
Date	Hrs	Stn	Hrs	Date	Hrs	Stn	Hrs	Date	Hrs	Stn	Hrs	Date	Hrs	Stn	Hrs	Date	Hrs	Stn
26/06/2014			1	4	1	2			1	4	2	3					1	1
02/07/2014	2	5			2	3	4	13			2	2	5	15			2	2
03/07/2014			2	4					4	6					3	6		
04/07/2014	8	26			4	8	11	28	2	2	5	13	11	29	2	2	4	13
05/07/2014	11	25	9	2			10	27	9	2			9	24	9	6		
09/07/2014			2	4					3	4					2	4		
10/07/2014			24	7					24	12					24	8		
11/07/2014			7	9	2	2			9	11	1	3			10	12	1	3
12/07/2014					1	1			2	3	1	1	1	3	2	3		
13/07/2014	1	1	1	3	1	4	1	1	7	6	1	4	1	1	6	9		
14/07/2014	9	30			1	2	12	40			1	2	12	39			1	2
16/07/2014	1	1			2	3	1	1			2	3	2	3			3	4
17/07/2014					4	5	1	2			4	6	2	3			4	6
18/07/2014	8	13			6	11	11	19			5	10	11	18			5	10
19/07/2014	6	10					6	11					7	11			1	1
22/07/2014			2	1					1	1					1	1		
23/07/2014			1	2					2	2					2	2		
24/07/2014											1	4			1	2	1	4
25/07/2014															1	2		
26/07/2014					4	4					4	4					3	3
27/07/2014					2	2	2	1			2	5	3	4			2	5
29/07/2014					12	24					11	24					10	28
02/08/2014	5	14					4	17					3	12			1	1
03/08/2014	4	15			1	3	6	17	1	1	1	5	6	19	1	1	2	6
04/08/2014											1	1					1	1
07/08/2014	2	3																
25/08/2014					1	2					1	2					1	2
27/08/2014	9	32			1	5	9	35			2	13	10	37			2	17
28/08/2014	15	38			14	38	15	39			14	43	16	39			13	46
29/08/2014	1	3			1	2	2	9			1	4	3	12			1	4
30/08/2014	3	9			4	6	4	13			4	6	4	16			5	7
31/08/2014	3	8			9	24	4	8			9	27	7	10			9	31
01/09/2014	7	12					7	8			2	5	8	10			2	7
05/09/2014	5	7	2	1	2	4	7	11	5	2	1	1	7	11	8	6	1	3
06/09/2014	1	7					1	4							1	1		
07/09/2014			7	1					7	1					7	1		
08/09/2014			2	1					1	1								
11/09/2014			11	2	1	2			7	3					7	3		
17/09/2014			2	1					1	1					1	1		
19/09/2014			1	3					3	5					3	5		
20/09/2014	5	15	9	5			6	16	5	6			7	16	5	6		
21/09/2014	7	26					4	14					2	7				
22/09/2014			4	3					5	6					5	6		
23/09/2014	1	1	2	4	4	12	2	4			3	4	2	4			2	3
24/09/2014	5	23					5	24					5	25				
25/09/2014	15	57					13	54	1	3			12	53	1	3		
26/09/2014	7	28			2	3	7	27			4	7	7	27			4	9

Table 8-2 continued

	0.25 cycle/day						0.5 cycle/day						1 cycle/day					
	T		S		C		T		S		C		T		S		C	
Date	Hrs	Stn	Hrs	Date	Hrs	Stn	Hrs	Date	Hrs	Stn	Hrs	Date	Hrs	Stn	Hrs	Date	Hrs	Stn
27/09/2014	2	10					4	7					4	7				
29/09/2014																	1	3
30/09/2014					1	1											1	3
01/10/2014	8	21			1	1	7	19			1	2	5	19			1	2
02/10/2014									1	2					1	2		
03/10/2014							2	4					2	4				
04/10/2014	10	43					11	42					11	42				
06/10/2014	3	5			1	6	5	13			1	6	6	16			1	5
07/10/2014			16	2					15	3					11	3		
15/10/2014					1	1					2	2					2	2
17/10/2014	6	26					7	26					7	25				
18/10/2014	1	8	2	2			1	6	2	2			1	4	2	2		
19/10/2014	1	1					1	4					2	5			1	3
20/10/2014															1	3		
21/10/2014	4	36					6	44					6	46				
22/10/2014	11	41	6	6	2	4	10	38	5	6	2	4	10	35	4	6	1	4
23/10/2014	2	5			1	1	2	6			2	2	2	6			1	1
24/10/2014	7	23	7	6	1	1	7	21	4	6			7	22	2	9		
25/10/2014	1	6																
26/10/2014	6	28			1	1	6	37			2	2	6	38			2	2
28/10/2014	15	31			1	2	15	31	1	1	2	5	16	31	1	2	2	5
29/10/2014	6	10					6	12	1	2			5	12	2	2		
30/10/2014	8	20					9	20					9	20				
01/11/2014	11	55			3	3	11	54			1	1	11	51			2	2
02/11/2014							2	4					2	7				
03/11/2014			2	2					1	2					1	2		
06/11/2014	9	23					4	15					3	16				
07/11/2014	1	2																
11/11/2014			2	2					1	2					1	2		
13/11/2014													1	4				
14/11/2014	1	6					1	8					3	9				
22/11/2014			3	4					2	4					2	4		
23/11/2014	6	16					5	14					5	14				
24/11/2014	2	8																
25/11/2014					1	2												
02/12/2014													1	4				
07/12/2014							1	3					3	7				
09/12/2014	3	18					4	26					4	26				
10/12/2014							1	4					2	6				
16/12/2014	6	60					8	56					8	57				
17/12/2014	4	32					2	19					2	15				
18/12/2014	1	2																
19/12/2014	12	45					11	45					11	45				
21/12/2014													1	1				
24/12/2014							3	9					6	19				
29/12/2014	2	4					2	7					2	7				
30/12/2014	4	12					4	10					2	7				
31/12/2014	3	9	1	1			3	9					4	9			1	1
01/01/2015	1	2					2	3					2	3				

Table 8-2 continued

	0.25 cycle/day						0.5 cycle/day						1 cycle/day					
	T		S		C		T		S		C		T		S		C	
Date	Hrs	Stn	Hrs	Date	Hrs	Stn	Hrs	Date	Hrs	Stn	Hrs	Date	Hrs	Stn	Hrs	Date	Hrs	Stn
02/01/2015	11	50					10	48					10	48				
03/01/2015													2	6				
04/01/2015					2	2	2	5			2	2	2	5			2	2
06/01/2015					1	1	1	4			1	1	1	6			1	4
07/01/2015	2	2					4	19					7	26				
08/01/2015	3	12					5	17					5	17				
09/01/2015	9	49					8	46					9	46				
10/01/2015	8	31					10	45					10	53				
12/01/2015							1	1					2	3				
13/01/2015	2	6			1	1	2	7			1	1	2	7			1	1
15/01/2015					1	1					2	3	3	13			1	1
23/01/2015	1	6					2	6					1	6				
24/01/2015							1	2					3	11				
25/01/2015							1	4					2	6				
26/01/2015	2	3					6	20			1	2	7	32				
18/02/2015	2	7					2	6					1	6				
19/02/2015	2	4					2	4					2	4				
22/02/2015							2	2					2	2				
26/02/2015	12	55					13	59					13	59				
28/02/2015	4	10					4	23					5	27				
01/03/2015							1	2					1	2				
06/03/2015	1	3					2	6					2	7				
07/03/2015	5	11					8	14					6	11				
08/03/2015	10	28					11	36					12	39				
09/03/2015	9	51					12	51					13	51				
10/03/2015	1	5					3	9					3	9				
11/03/2015	10	46					10	43					10	43				
12/03/2015	6	19	1	4			6	17	1	4			7	16	1	4		
13/03/2015									2	1					2	1		
21/03/2015	2	1					1	1										
26/03/2015							1	2					1	2				
28/03/2015	4	17					3	13			1	2	3	12			1	2
30/03/2015	3	15					2	7										
31/03/2015													1	5				
10/04/2015							2	4					2	4				
11/04/2015							4	7					5	14				
12/04/2015					1	4	1	1			1	2	2	5			1	2
13/04/2015	2	7	5	2			3	8	3	2			5	9	1	1		
14/04/2015					2	2					2	2	1	4			3	2
15/04/2015	9	20			8	13	9	24			8	15	9	24			5	10
16/04/2015									2	3					3	3		
23/04/2015			3	1					3	1					1	1		
24/04/2015													1	4				
03/05/2015							1	1					2	2				
04/05/2015	3	9					9	18					10	19				
05/05/2015	7	31					6	32					7	39				

Table 8-2 continued

	0.25 cycle/day						0.5 cycle/day						1 cycle/day					
	T		S		C		T		S		C		T		S		C	
Date	Hrs	Stn	Hrs	Date	Hrs	Stn	Hrs	Date	Hrs	Stn	Hrs	Date	Hrs	Stn	Hrs	Date	Hrs	Stn
10/05/2015											1	2					2	3
11/05/2015	3	9	6	2	4	15	3	13	7	2	5	17	5	20	7	2	5	18
12/05/2015			1	1									1	4				
14/05/2015			2	2					3	2					3	2		
15/05/2015	14	57	1	2			14	58	1	2			14	58	1	1		
16/05/2015	9	25					8	33					9	33				
18/05/2015	3	9					6	18					6	20				
21/05/2015																	1	1
22/05/2015	1	1					2	6					3	7			1	1
23/05/2015	7	9	3	1			5	9	3	1			5	8	3	2		
24/05/2015	14	27			2	4	15	36			2	3	16	42			2	2
27/05/2015	1	1					1	1										
30/05/2015	4	8					4	6					2	2				
31/05/2015	14	50					13	52					12	52				
01/06/2015	1	6											1	2				
02/06/2015					1	1	2	6			3	4	2	10			3	3
05/06/2015	12	27			6	10	13	36			7	12	10	30			8	13
06/06/2015	3	14					3	11					2	11				
11/06/2015	8	14					4	5					4	5				
12/06/2015	6	8					3	4	1	1					2	1		
13/06/2015	1	1	14	4					12	4					10	4		
14/06/2015			2	1														
16/06/2015	1	1			1	1	1	1			1	1	1	1			1	1
17/06/2015	16	39	12	9	7	14	15	36	6	9	7	12	15	36	4	9	6	11
18/06/2015	11	35	2	3	3	5	11	32			3	5	10	31			1	1
20/06/2015					1	1					1	1						
22/06/2015							1	5					2	5				
24/06/2015									1	1					1	2		
26/06/2015	3	4			2	3	5	9			3	3	3	10			4	3
27/06/2015													1	3				
28/06/2015	2	4			3	3	5	31			3	6	7	38			3	5
30/06/2015									1	3	2	1					2	1
01/07/2015					1	2					1	2					2	6
02/07/2015	6	25			2	2	7	28			2	2	7	29			2	2
03/07/2015	12	42	1	2			13	41					12	36				
04/07/2015	15	45			1	2	16	42			2	7	14	46	1	1	2	7
05/07/2015	2	6					2	6			1	1	2	6			1	1
06/07/2015	7	25					7	25					7	26				
07/07/2015							1	1					1	5				
09/07/2015	6	12					4	11					3	8				
10/07/2015	4	5																
13/07/2015	2	6					1	9					3	12				
16/07/2015	2	5					1	1					1	1				
17/07/2015	1	3			2	4	5	10			2	4	5	10			2	8
18/07/2015							1	1					1	2				
19/07/2015			2	2	1	1			3	2	1	1			5	7		
20/07/2015	12	26	6	4	1	1	12	24	7	5	1	1	13	24	7	5	2	2
21/07/2015	1	3					1	3					1	3				

Table 8-2 continued

	0.25 cycle/day						0.5 cycle/day						1 cycle/day					
	T		S		C		T		S		C		T		S		C	
Date	Hrs	Stn	Hrs	Date	Hrs	Stn	Hrs	Date	Hrs	Stn	Hrs	Date	Hrs	Stn	Hrs	Date	Hrs	Stn
26/07/2015	1	6					1	8					1	5				
02/08/2015	8	9					6	9					5	6				
03/08/2015					2	7					2	7					4	9
04/08/2015					1	5					2	6					3	9
05/08/2015							1	1					1	1				
06/08/2015			1	2														
08/08/2015	4	9					5	6					5	6				
09/08/2015	3	9			1	4	2	9			3	8	2	8			2	6
10/08/2015											1	2					2	5
11/08/2015	1	3	17	7					16	8					15	6		
12/08/2015			9	14					9	7					9	7		
13/08/2015	11	12					4	7					2	6				
14/08/2015	8	8					3	6	1	3			1	1	1	3		
15/08/2015	8	15					5	10					5	10				
17/08/2015					1	3												
18/08/2015			18	12	2	8	1	1	21	11	1	4			22	10		
19/08/2015	7	13	11	8	9	27	6	14	13	10	9	25	7	15	13	8	7	24
20/08/2015					1	1					1	1					1	2
21/08/2015					1	4			1	1	2	6			2	1	1	4
22/08/2015									2	1					4	2		
23/08/2015	4	8			4	5	7	16	2	1	4	8	9	18	2	1	4	8
24/08/2015											2	1					2	1
25/08/2015	10	28					10	37					11	38				
26/08/2015	6	11	3	2	6	9	7	17	3	2	7	13	9	19	3	2	7	12
31/08/2015	10	14					8	13					7	11				
12/09/2015	2	2	1	1	1	2	4	5			1	2	5	8			1	2
15/09/2015					2	7					2	8					2	8
16/09/2015					1	2					1	2					1	2
21/09/2015	1	1					4	10					4	10				
23/09/2015							1	3			1	1	2	4			1	1
Average	5	16	5	3	2	5	5	17	4	3	2	5	5	17	4	4	2	5
Max	22	69	24	14	14	38	22	69	24	12	14	43	22	69	24	12	13	46
Count	244		83		117		279		98		137		299		104		146	

Example 1: Stations considered as having meteorological events using different cut-off frequencies.

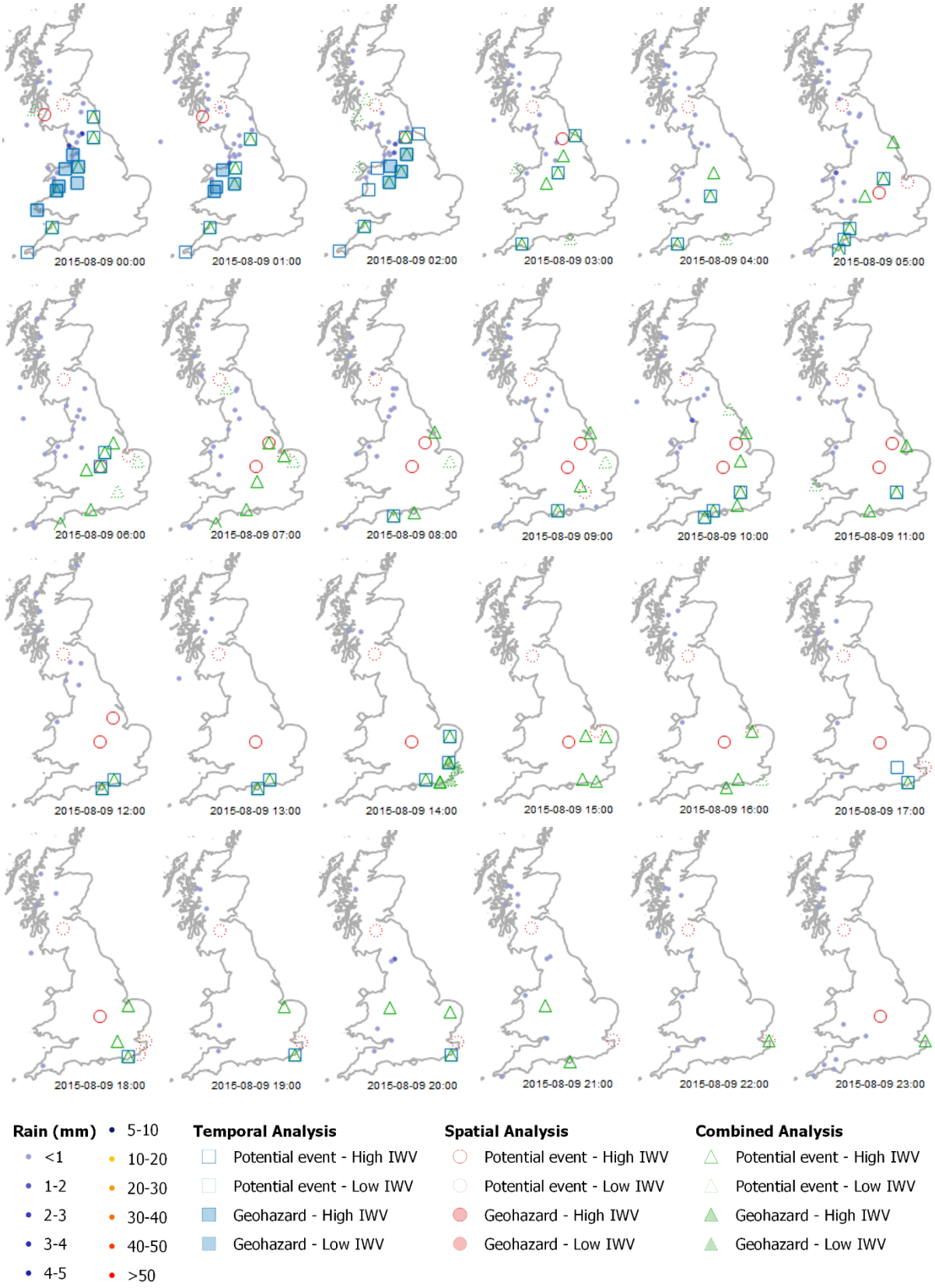


Figure D-1 Rain gauge readings (coloured dots) and stations considered as having either potential events (hollow symbols)or meteorological events (filled symbols), with 0.25 cycle/day as a cut-off frequency.

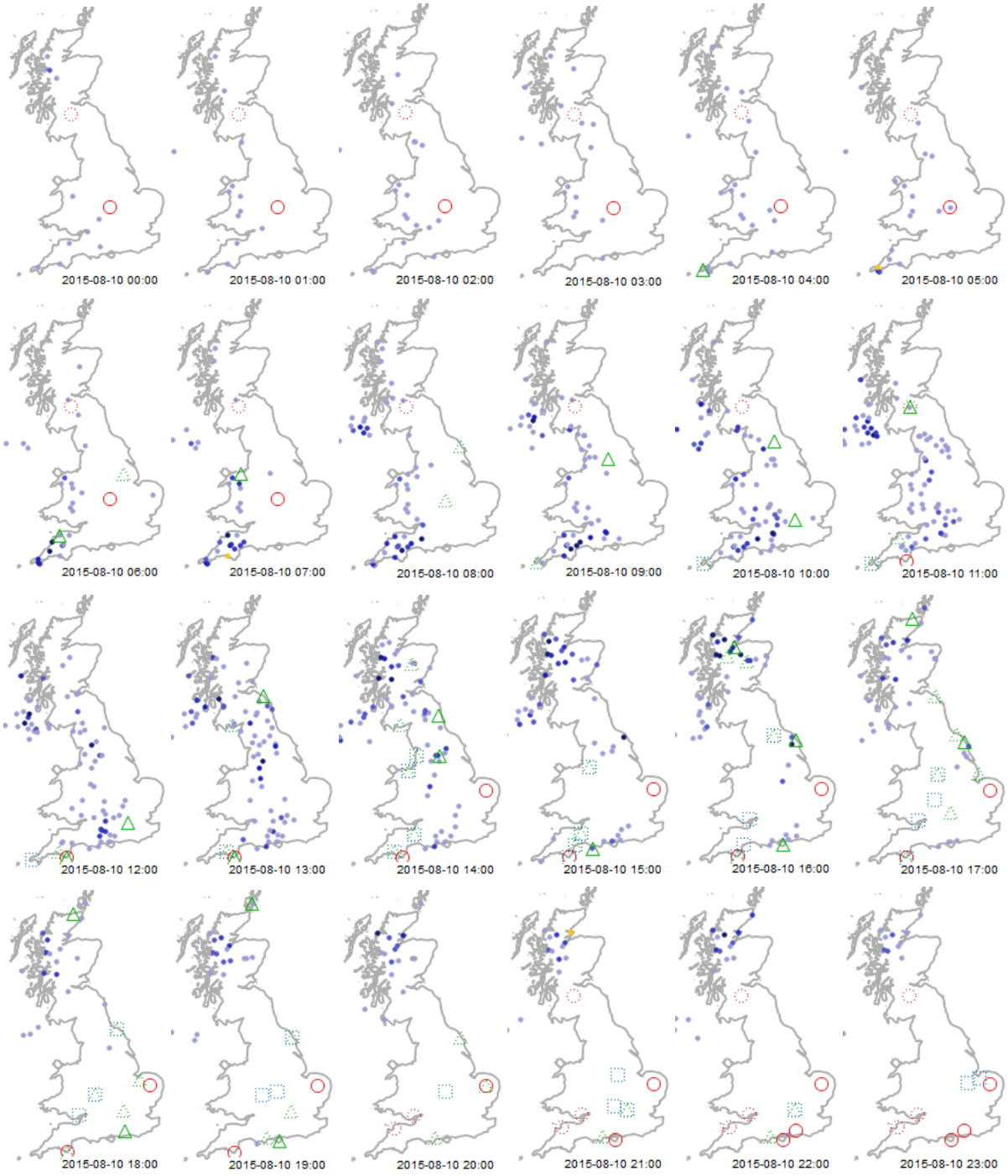


Figure D-1 (continued showing the 10th Aug 2015)

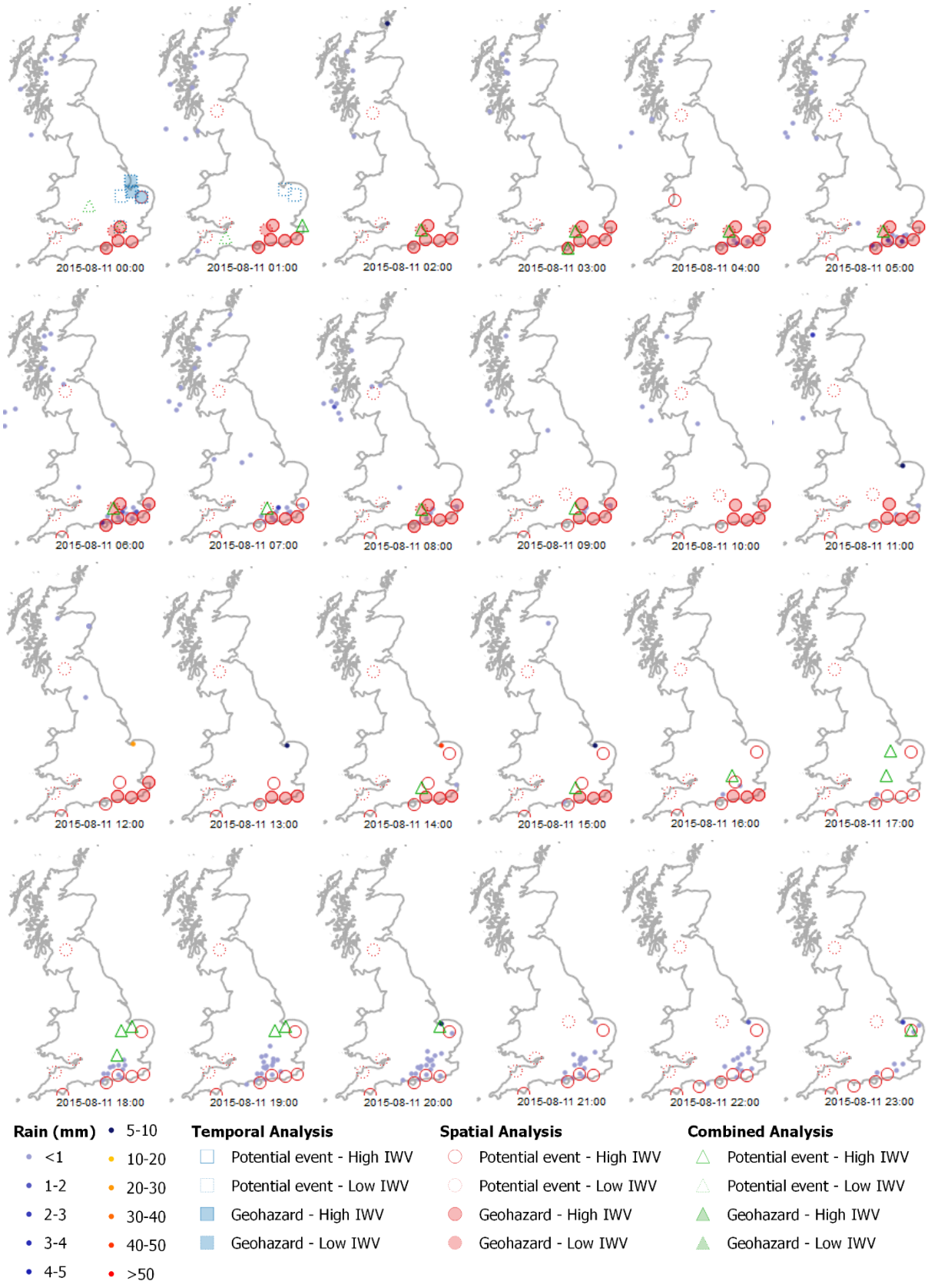


Figure D-1 (continued showing the 11th Aug 2015)



Figure D-1 (continued showing the 12th Aug 2015)

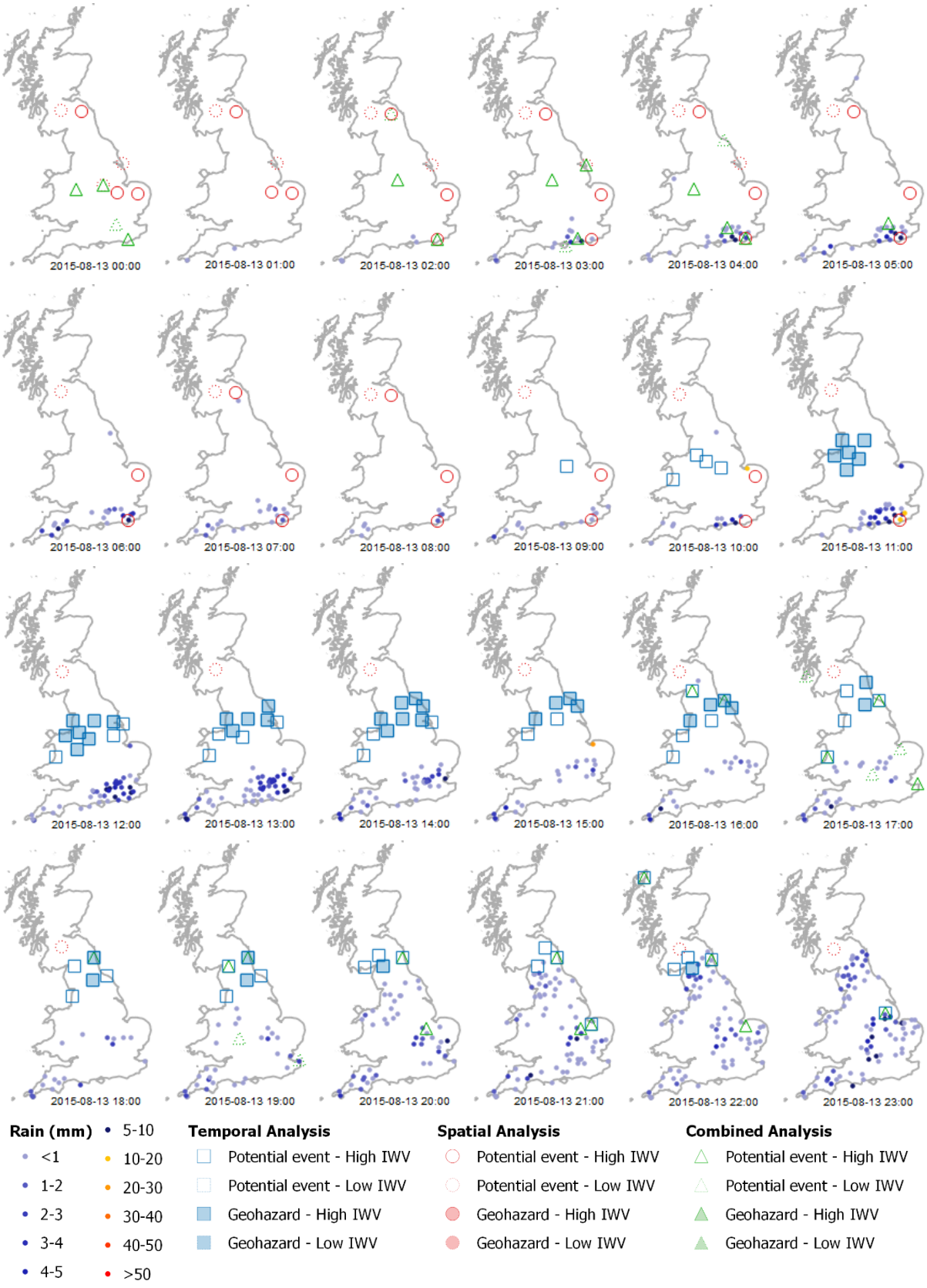


Figure D-1 (continued showing the 13th Aug 2015)

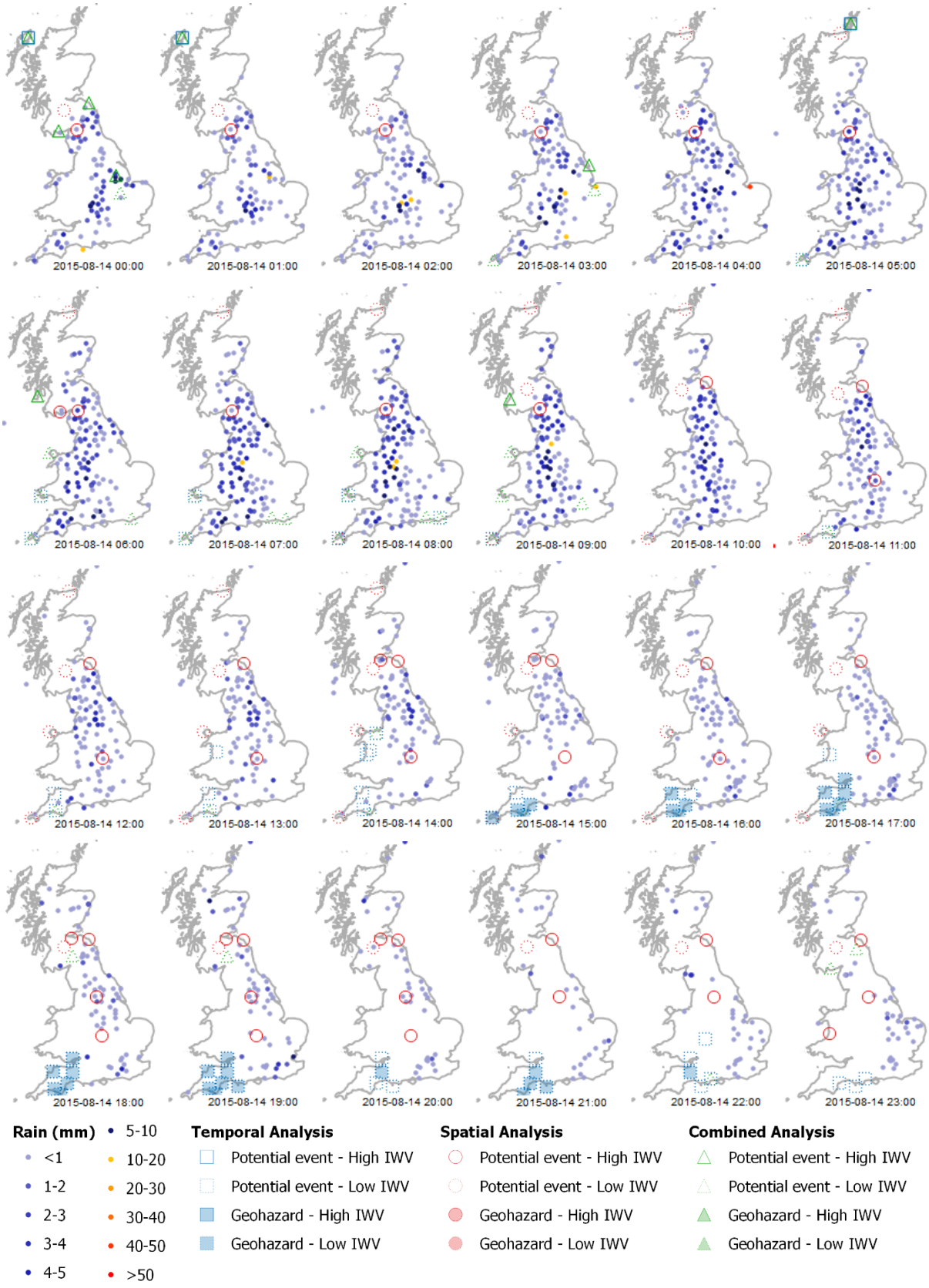


Figure D-1 (continued showing the 14th Aug 2015)

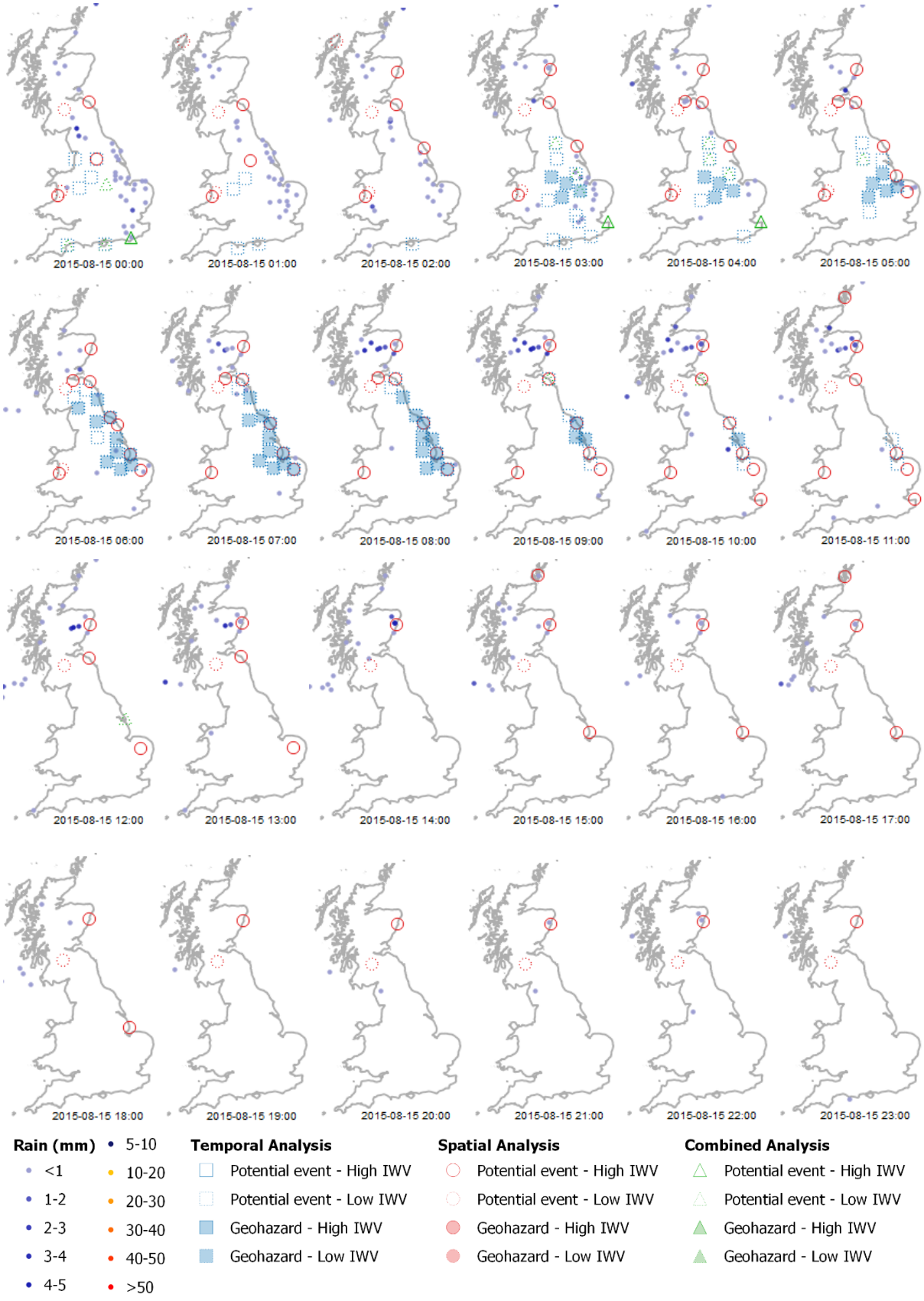


Figure A- D-1 (continued showing the 15th Aug 2015)

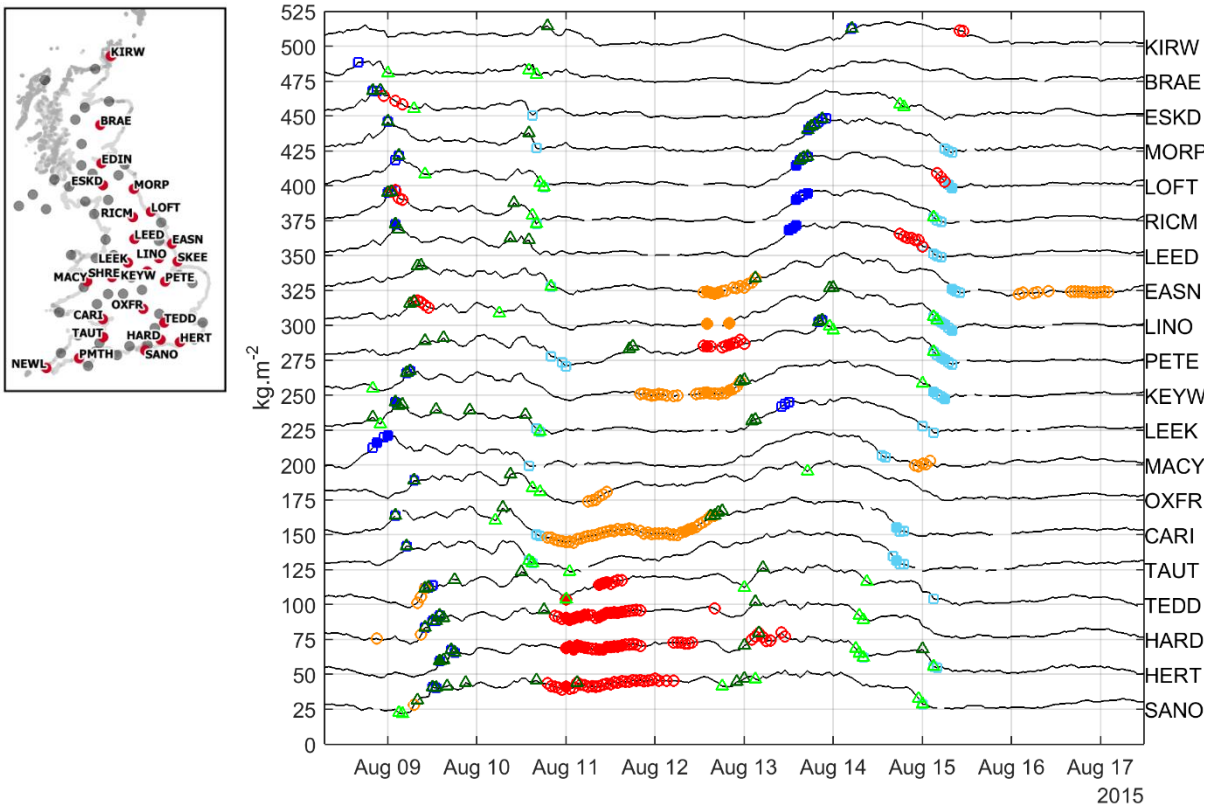


Figure D-2 The IWV time series of 20 stations along with epochs considered as having either potential events (hollow) or meteorological events (filled) using the temporal (high IWV: dark blue, and low IWV: light blue), the spatial (high IWV: red, and low IWV: orange), and the combined (high IWV: dark green, and low IWV: light green) analysis algorithms, with 0.5 cycle/day as a cut off frequency (y-axis grid:25 kg.m^{-2}).

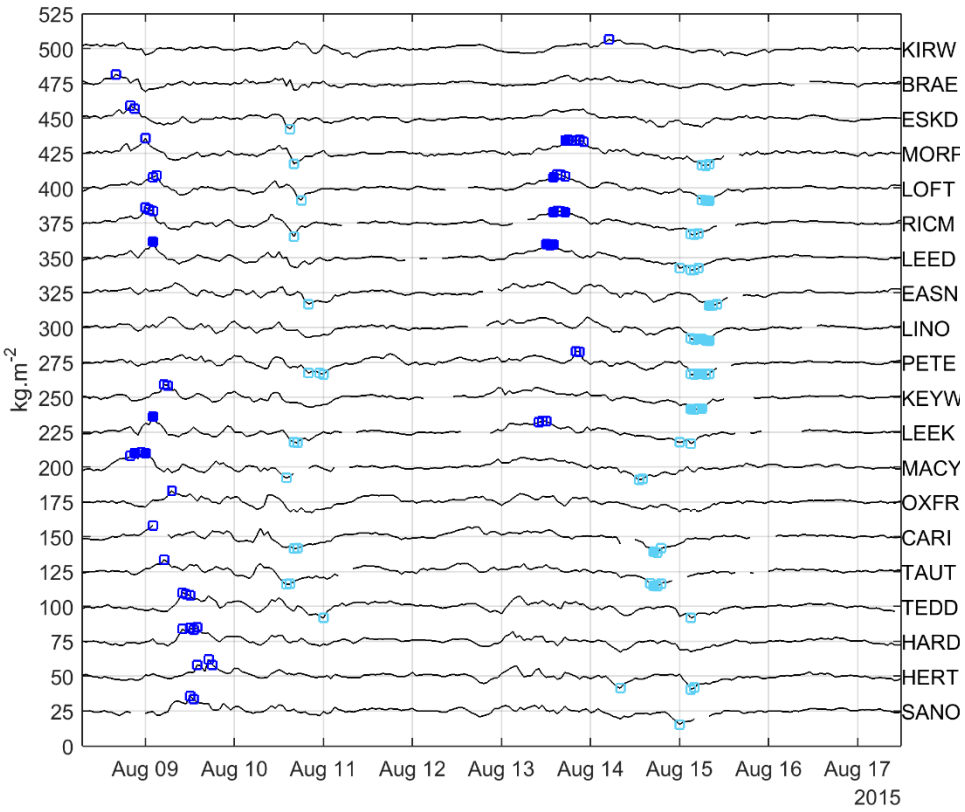


Figure D-3 Same as Figure D-2 but showing the temporal analysis residuals only.

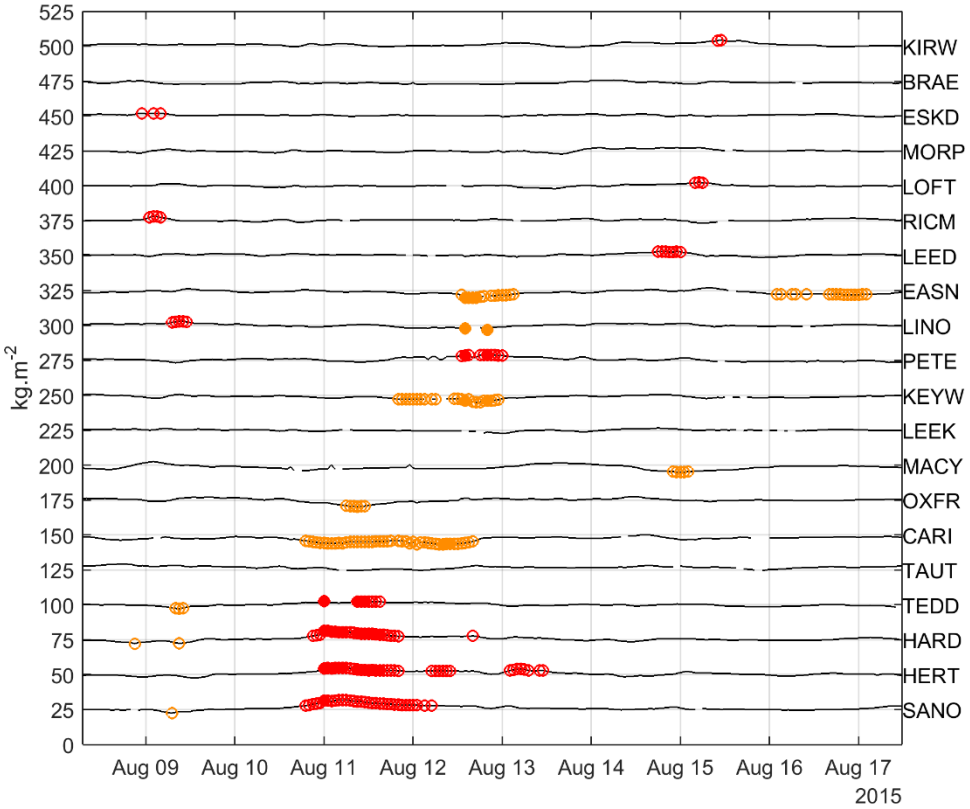


Figure D-4 Same as Figure D-2 but showing the spatial analysis residuals only.

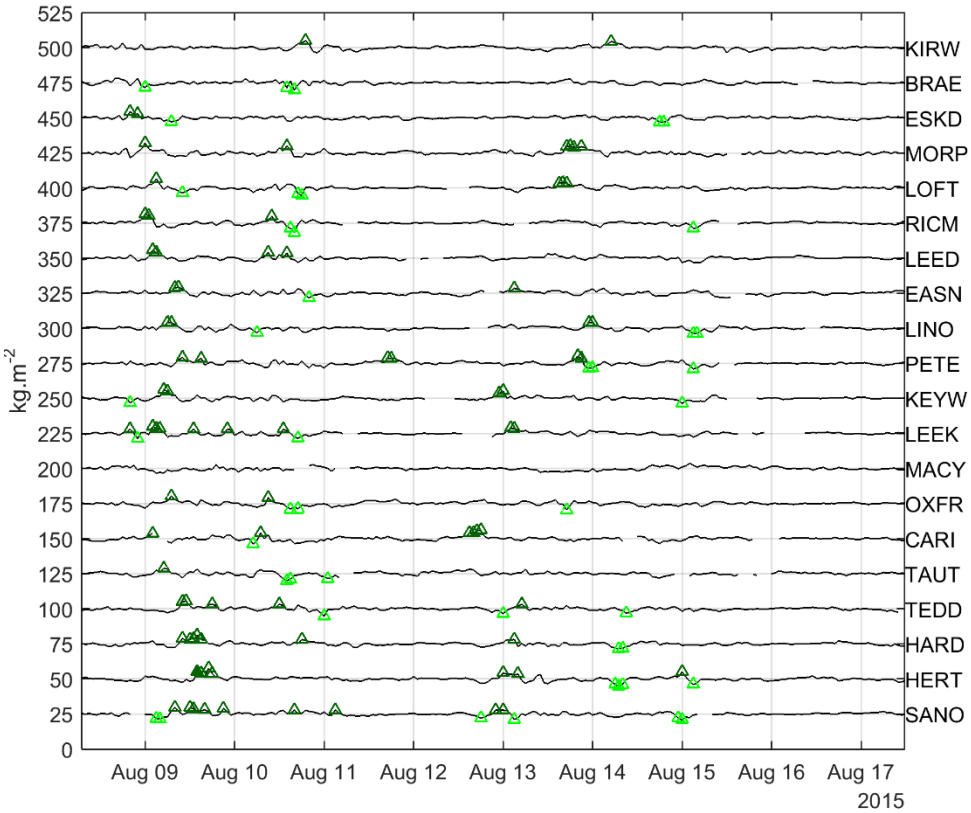


Figure D-5 Same as Figure D-2 but showing the combined analysis residuals only.

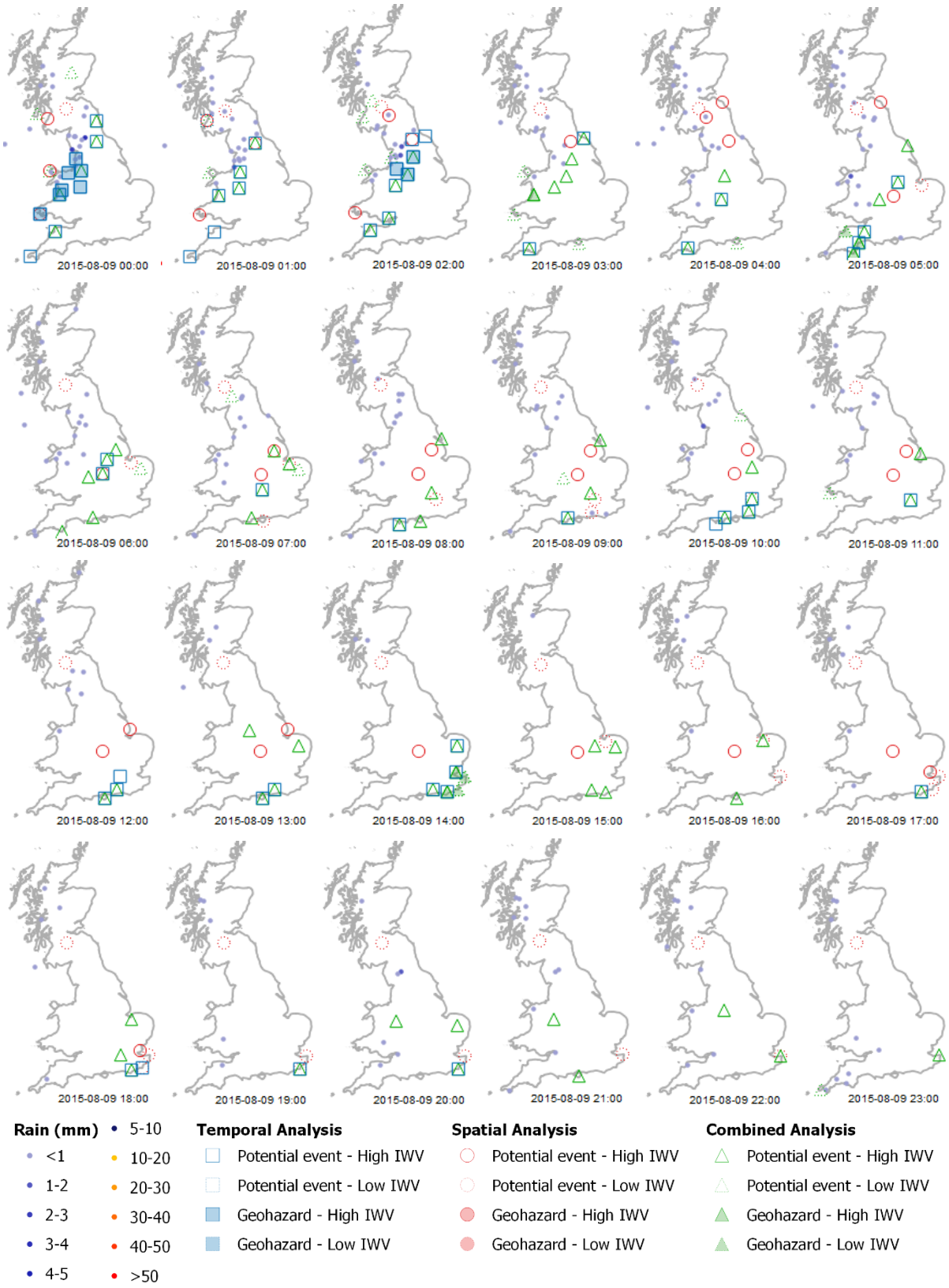


Figure D-6 Rain gauge readings (coloured dots) and stations considered as having either potential events (hollow symbols) or meteorological events (filled symbols), with 0.5 cycle/day as a cut-off frequency.

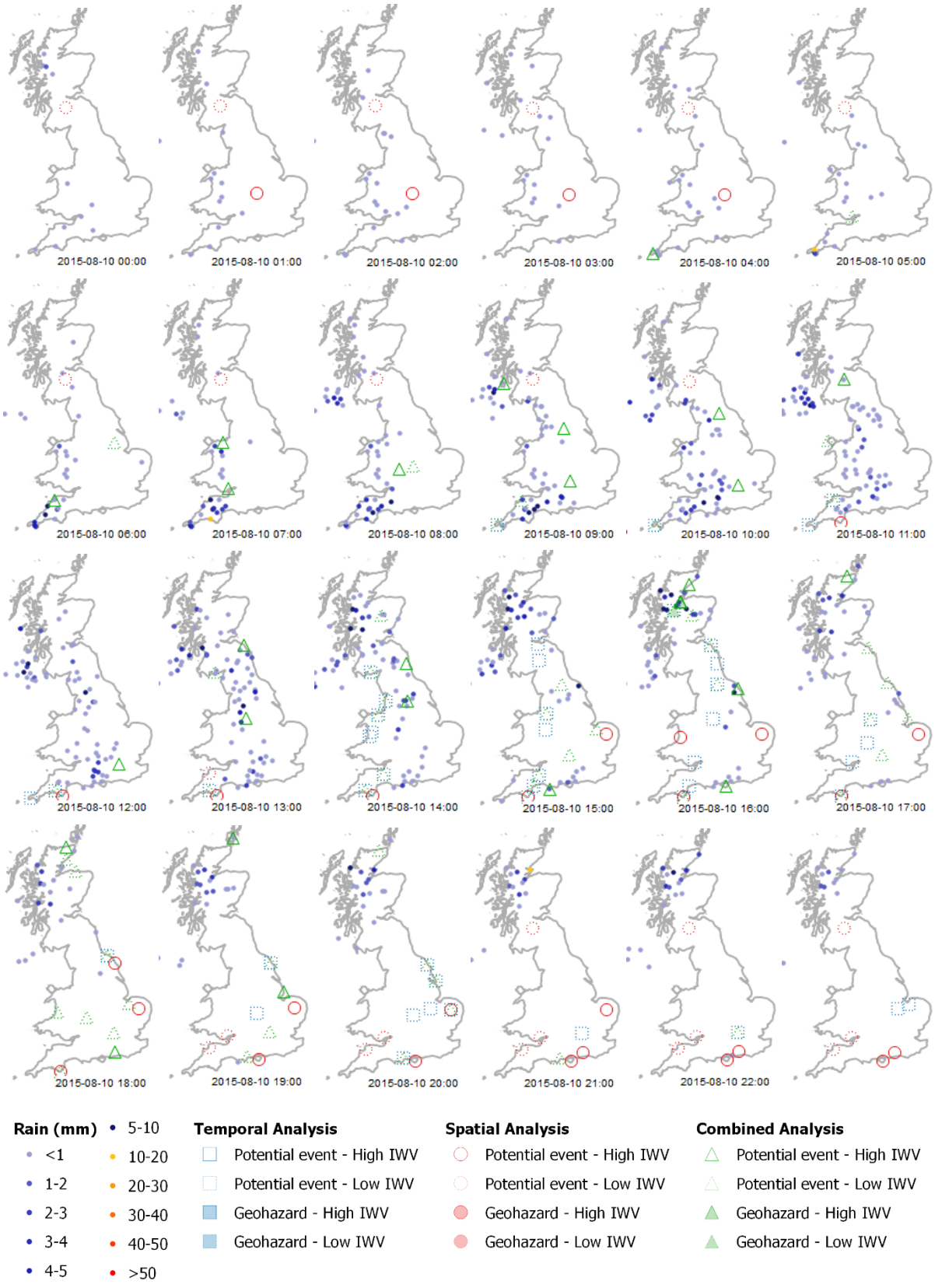


Figure D-6 (continued showing the 10th Aug 2015)

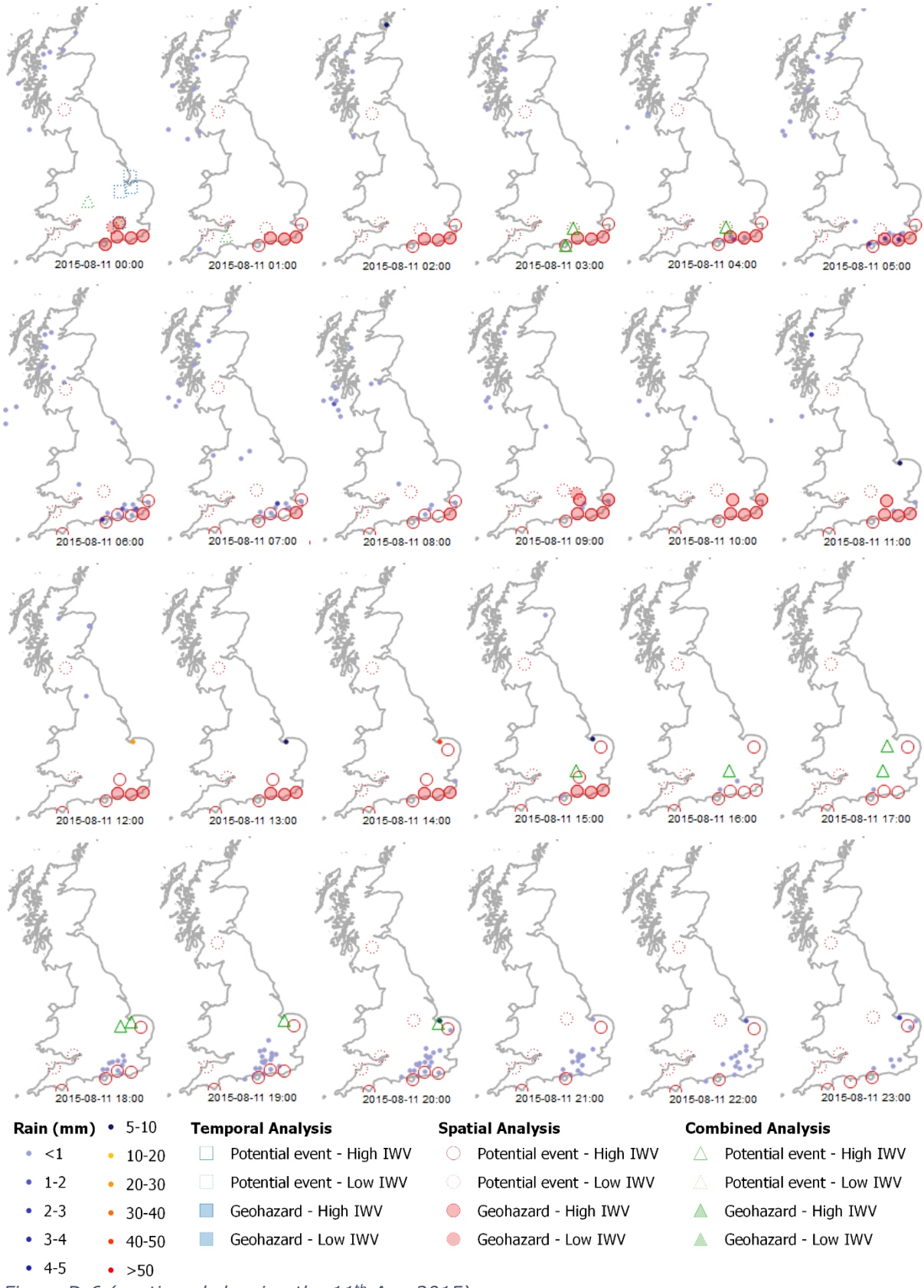


Figure D-6 (continued showing the 11th Aug 2015)

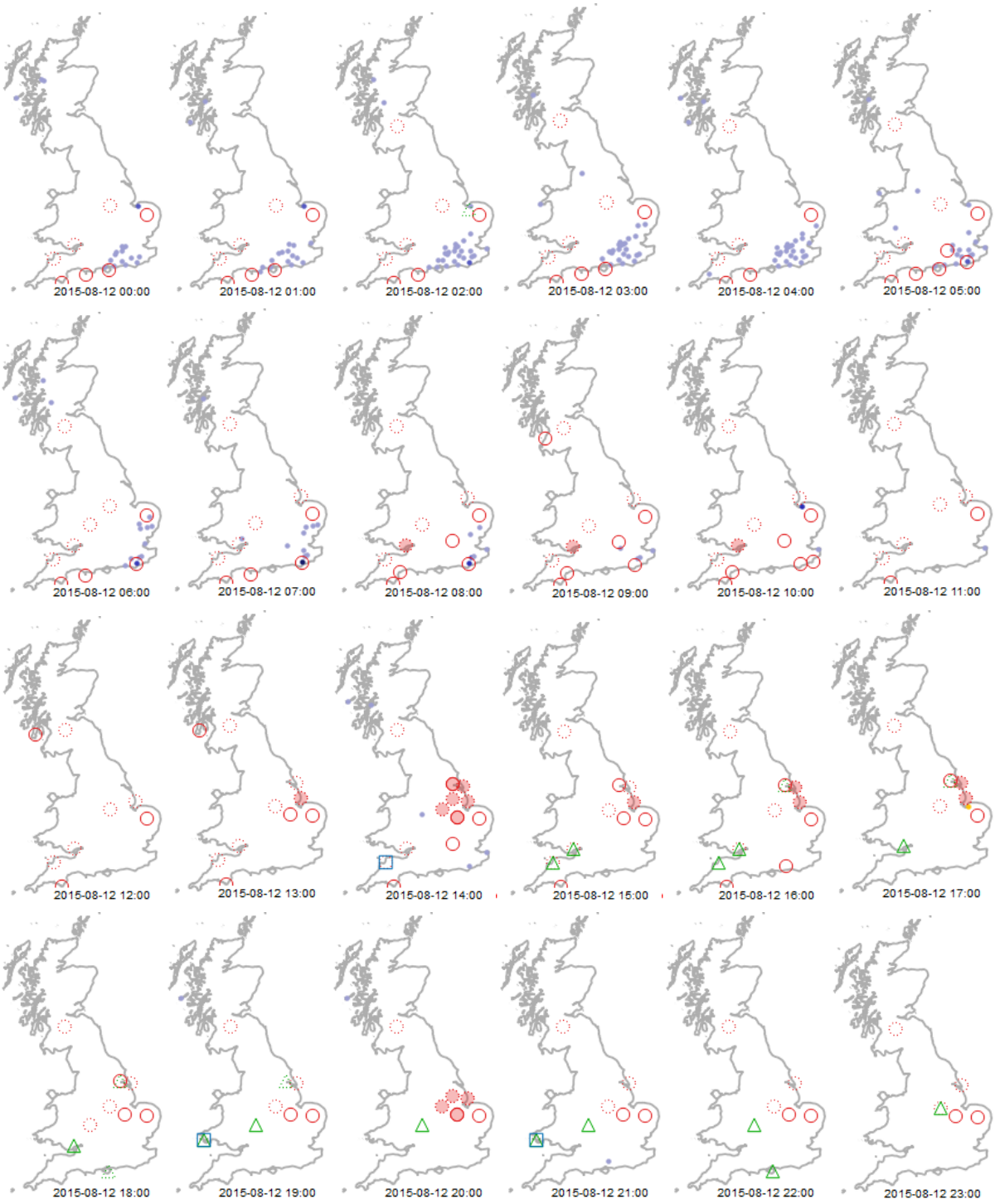


Figure D-6 (continued showing the 12th Aug 2015)

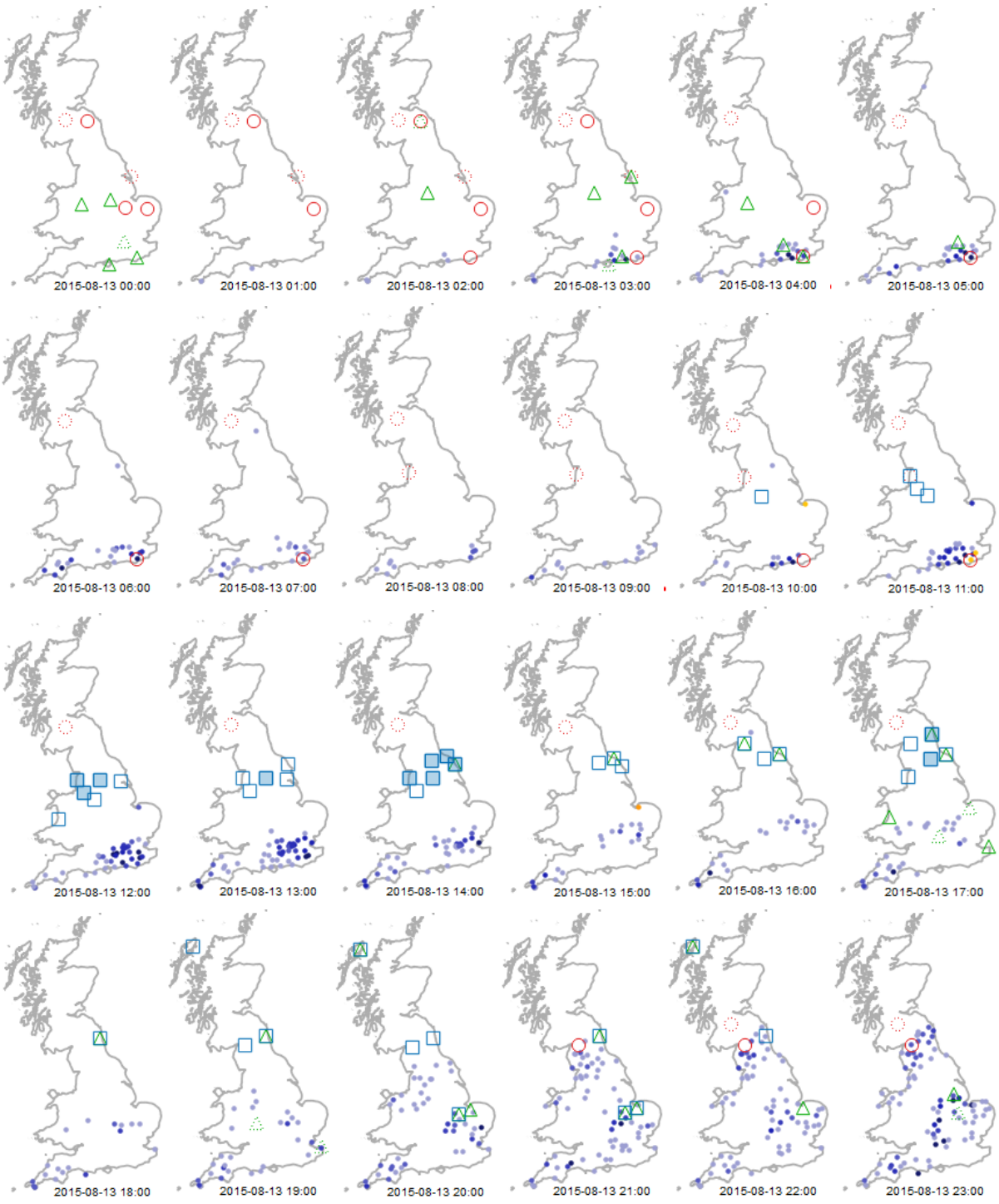


Figure D-6 (continued showing the 13th Aug 2015)

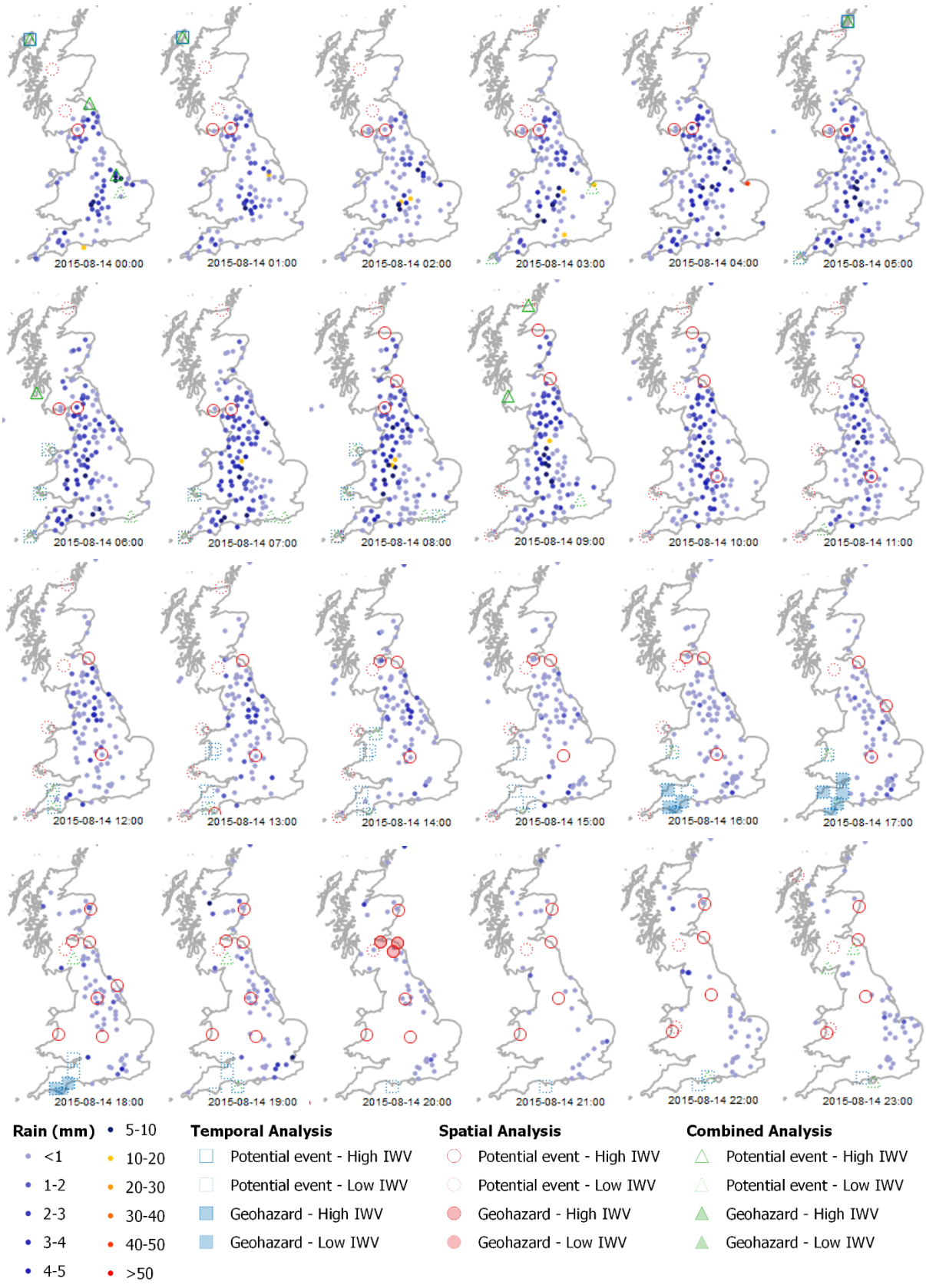


Figure D-6 (continued showing the 14th Aug 2015)

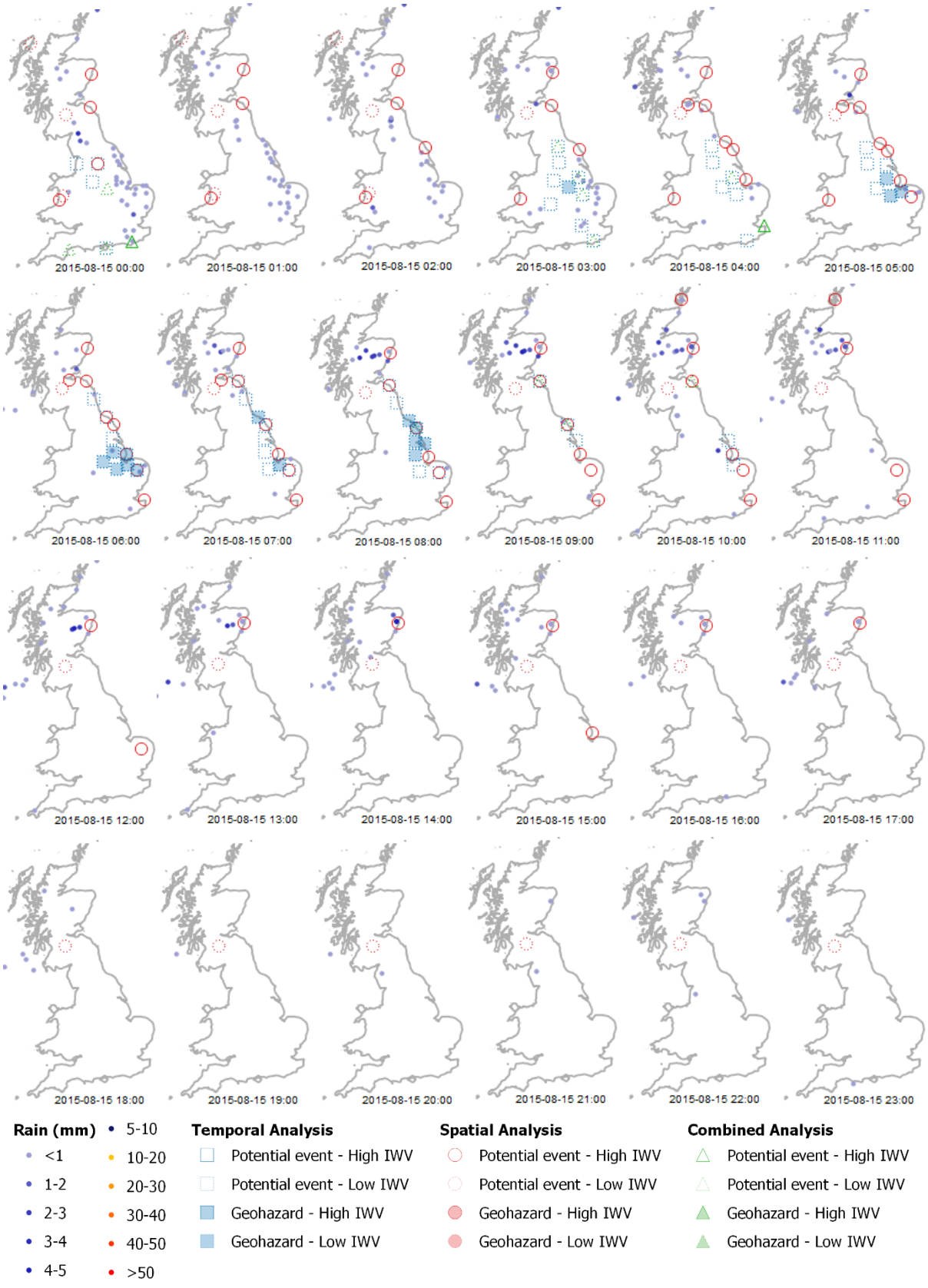


Figure D-6 (continued showing the 15th Aug 2015)

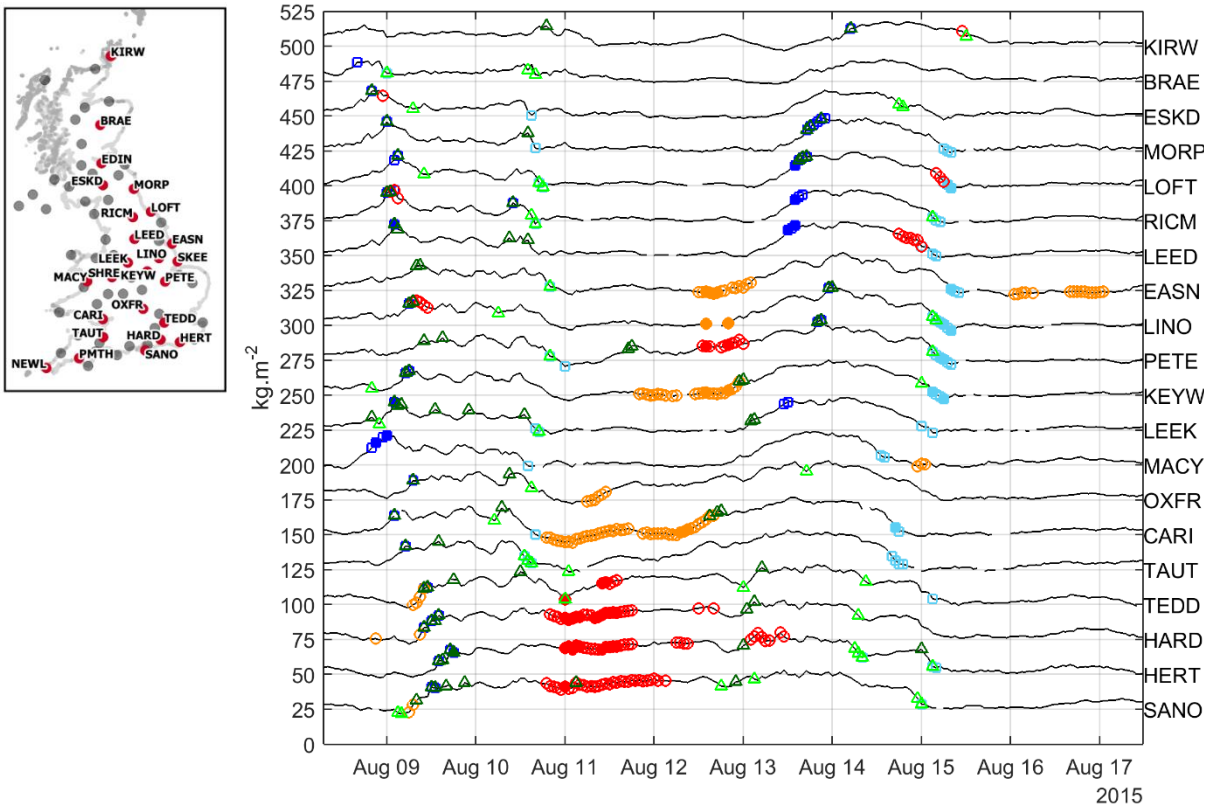


Figure D-7 The IWV time series of 20 stations along with epochs considered as having either potential events (hollow) or meteorological events (filled) using the temporal (high IWV: dark blue, and low IWV: light blue), the spatial (high IWV: red, and low IWV: orange), and the combined (high IWV: dark green, and low IWV: light green) analysis algorithms, with 1 cycle/day as a cut off frequency (y-axis grid:25 kg.m^{-2}).

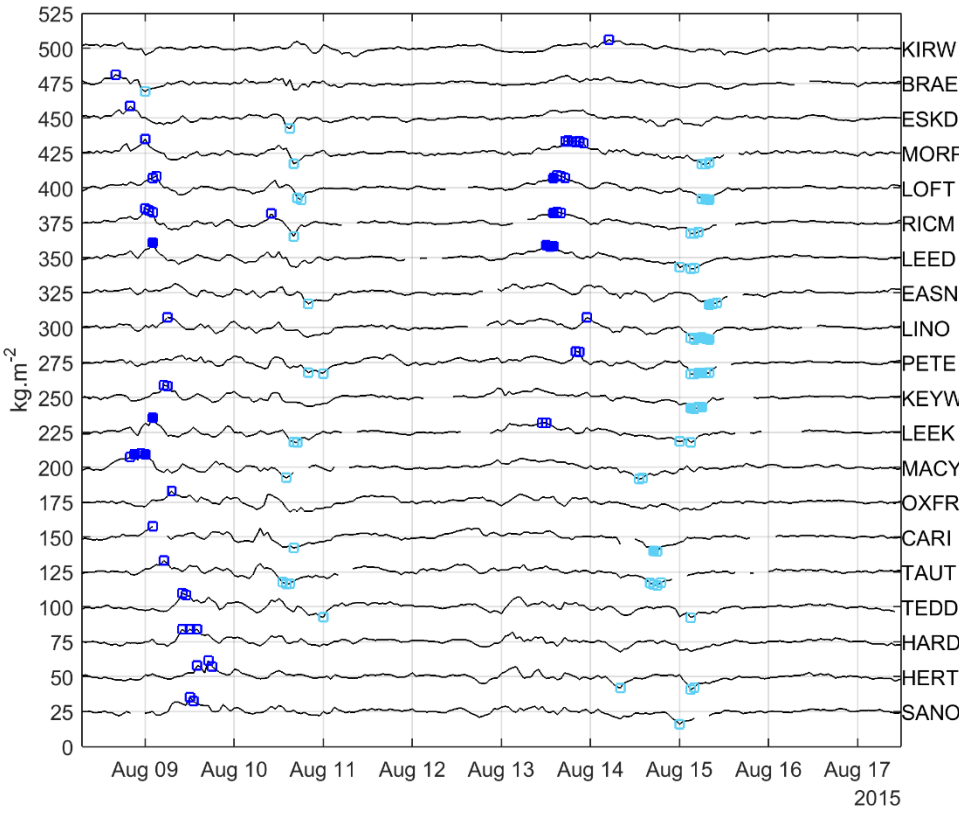


Figure D-8 Same as Figure D-7 but showing the temporal analysis residuals only.

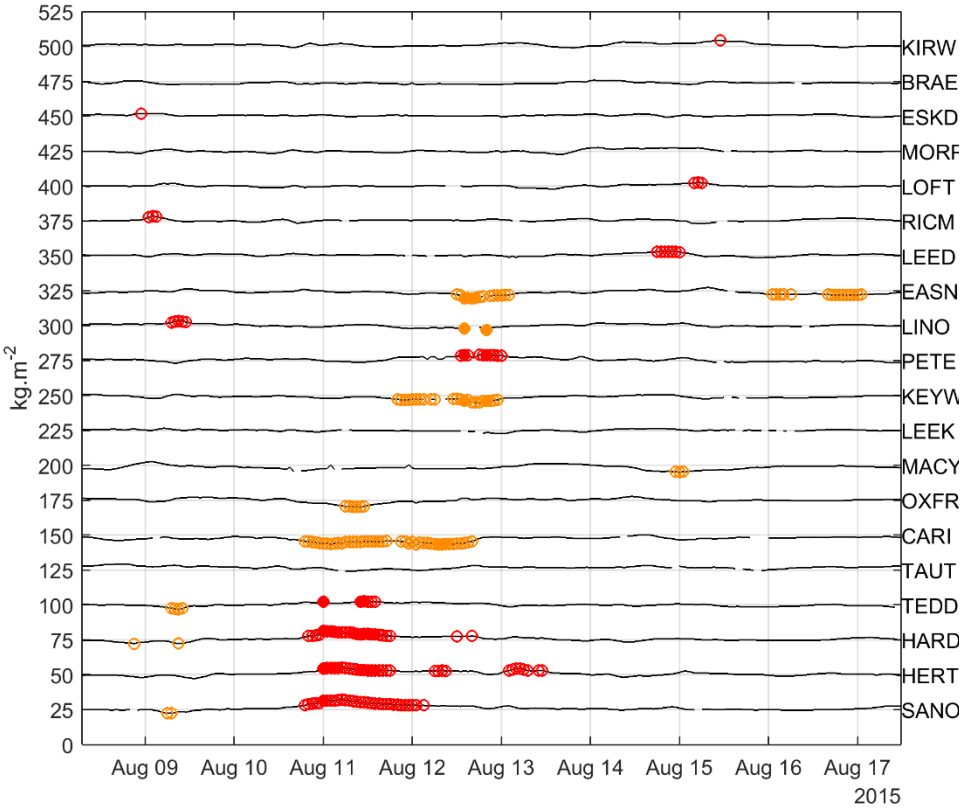


Figure D-9 Same as Figure D-7 but showing the spatial analysis algorithm residuals only.

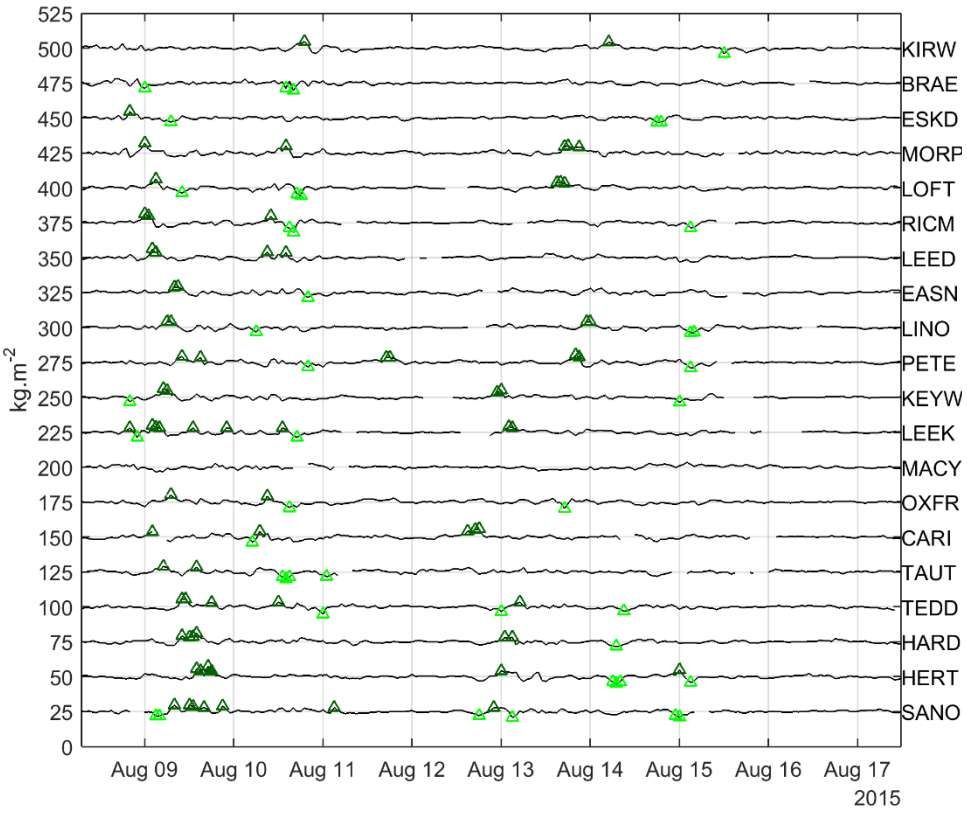


Figure D-10 Same as Figure D-7 but showing the combined analysis residuals only.

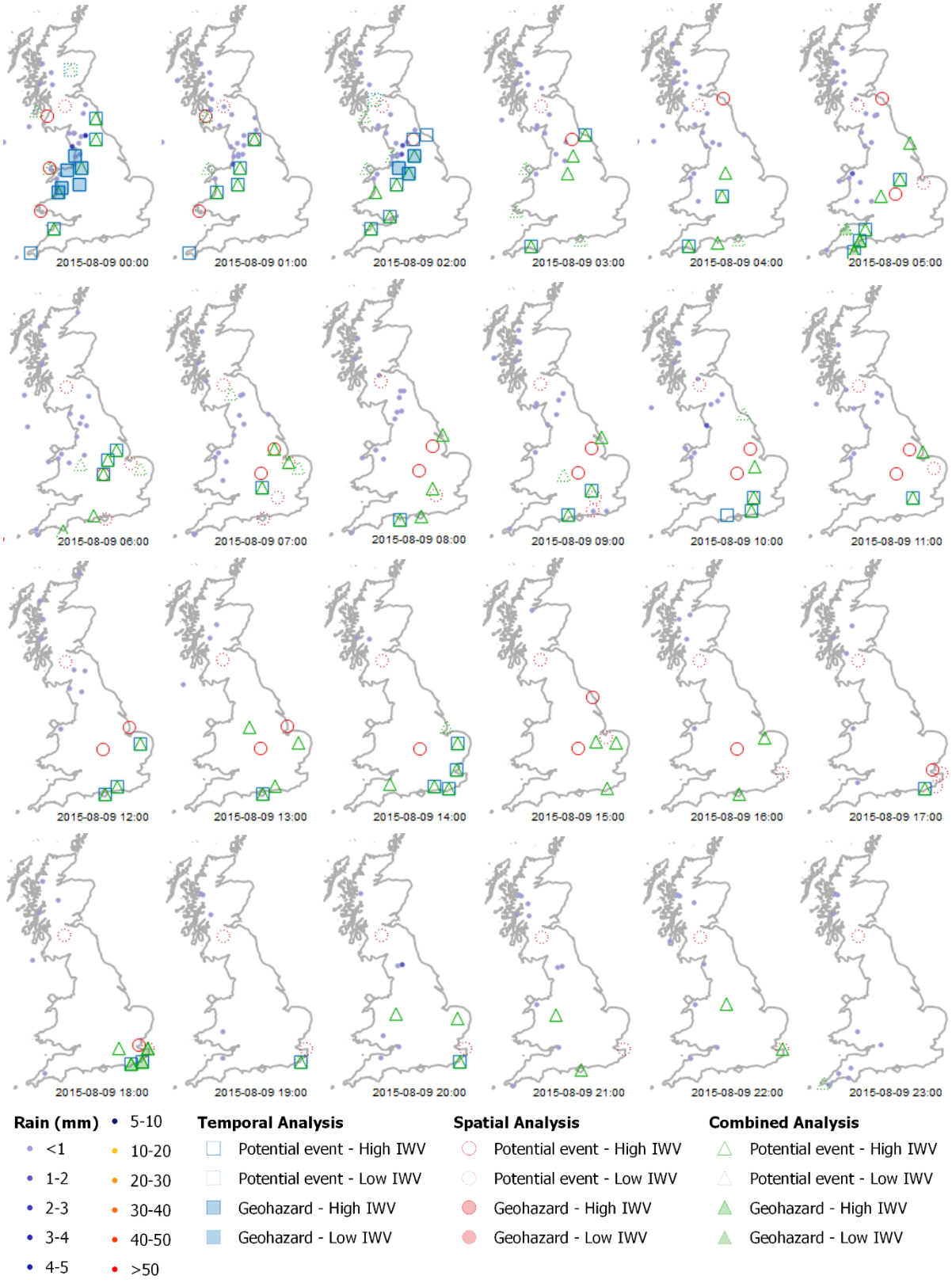


Figure D-11 Rain gauge readings (coloured dots) and stations considered as having either potential events (hollow symbols) or meteorological events (filled symbols), with 1 cycle/day as a cut-off frequency.

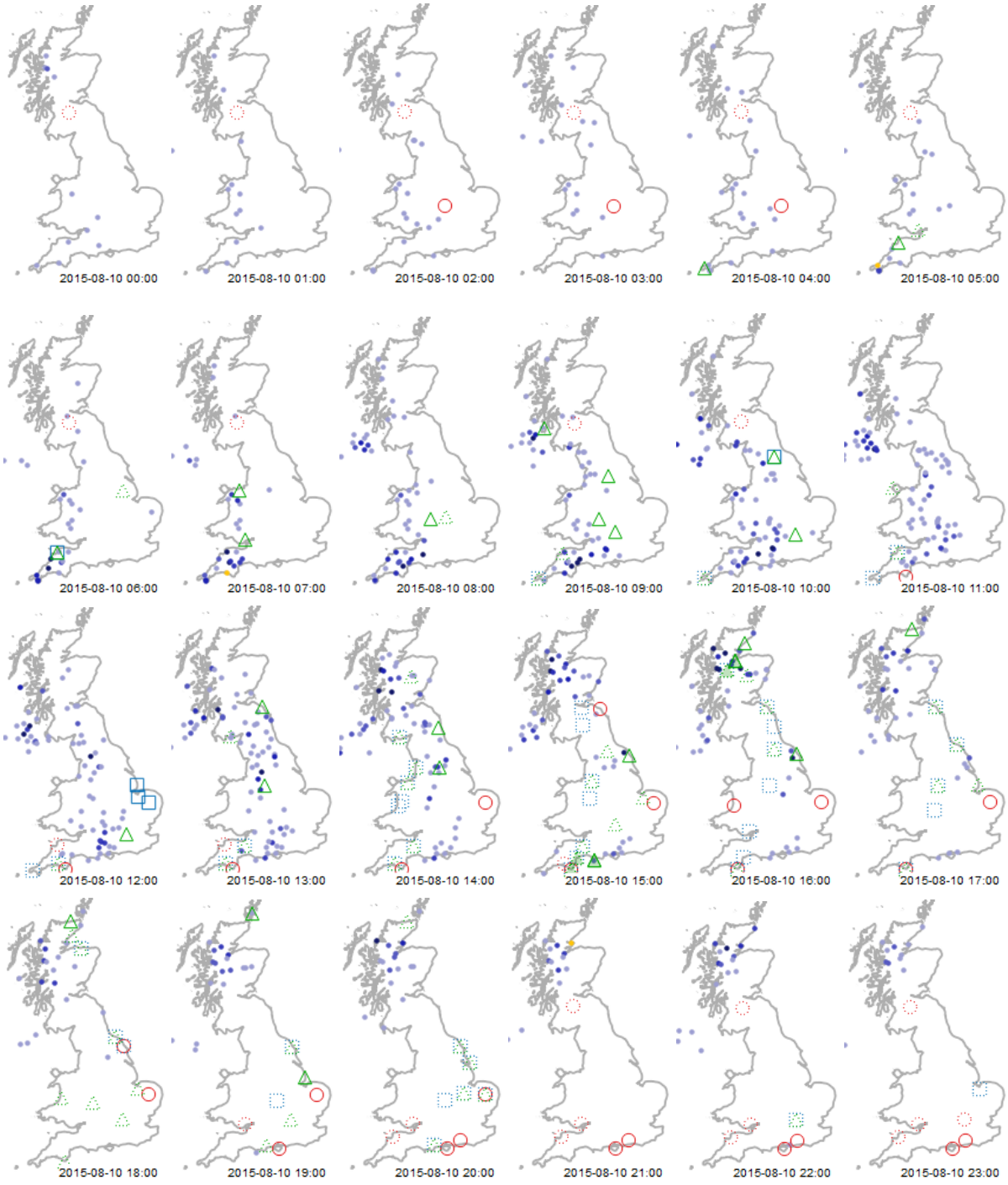


Figure D-11(continued showing the 10th Aug 2015)

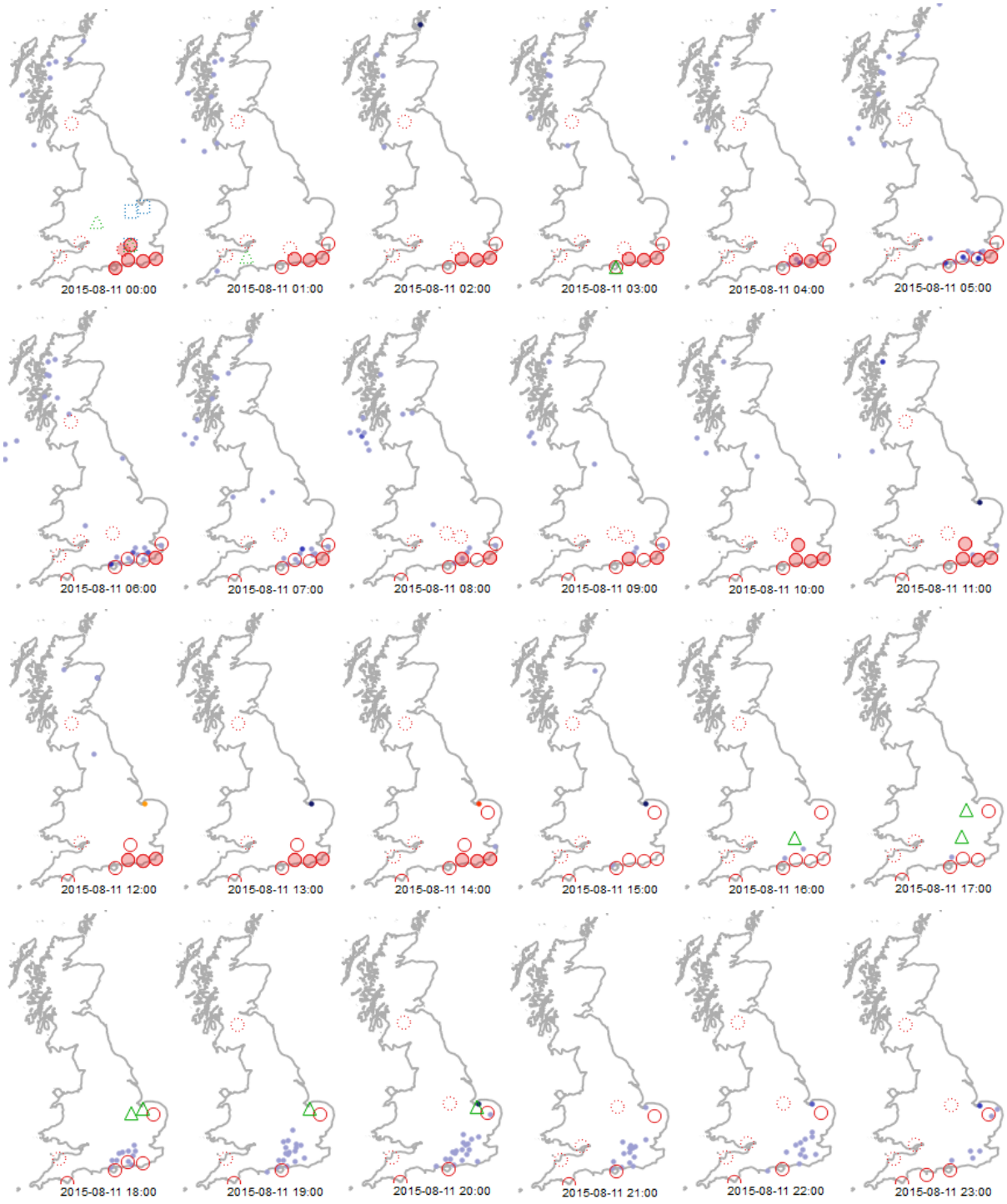


Figure D-11 (continued showing the 11th Aug 2015)

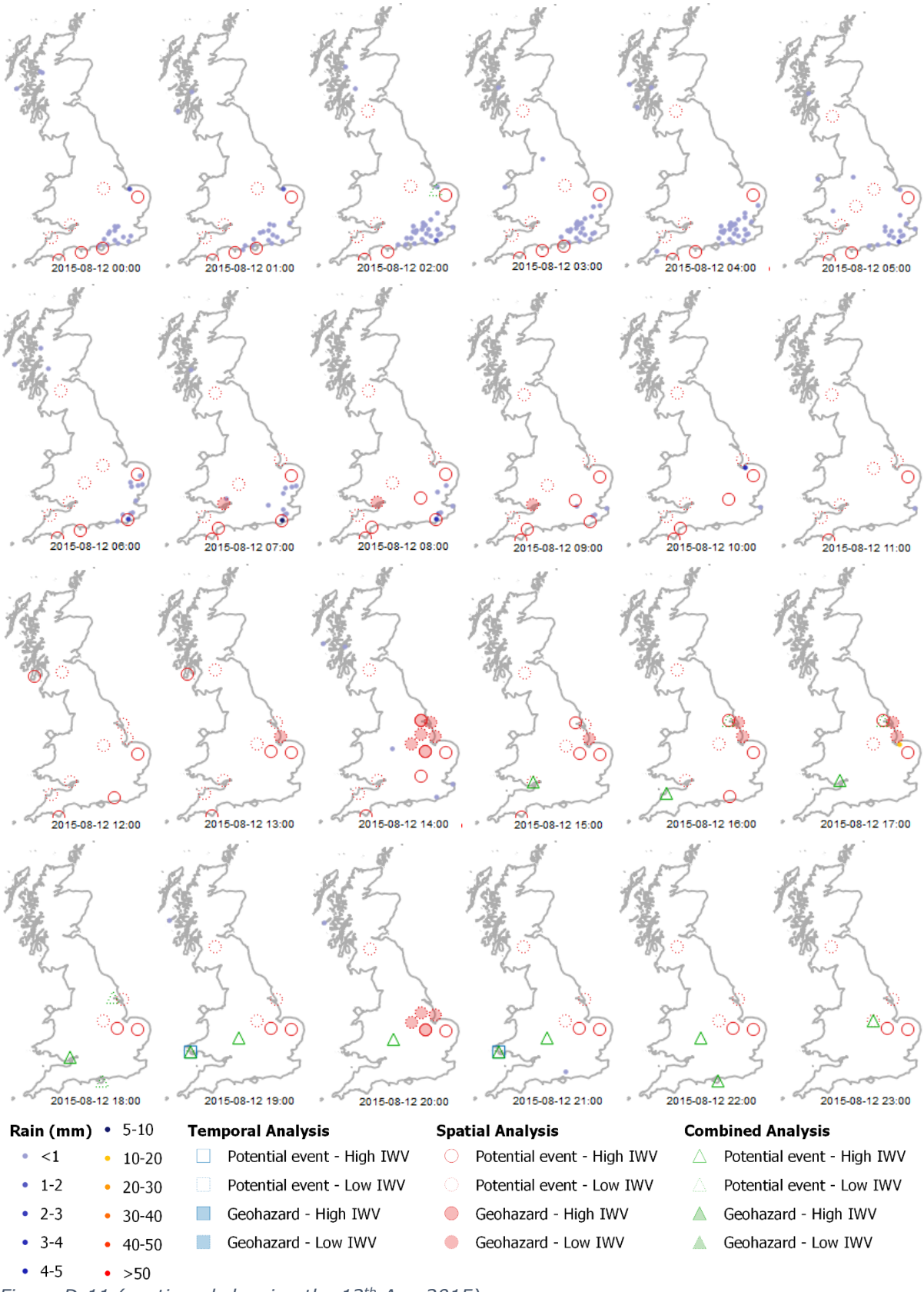


Figure D-11 (continued showing the 12th Aug 2015)

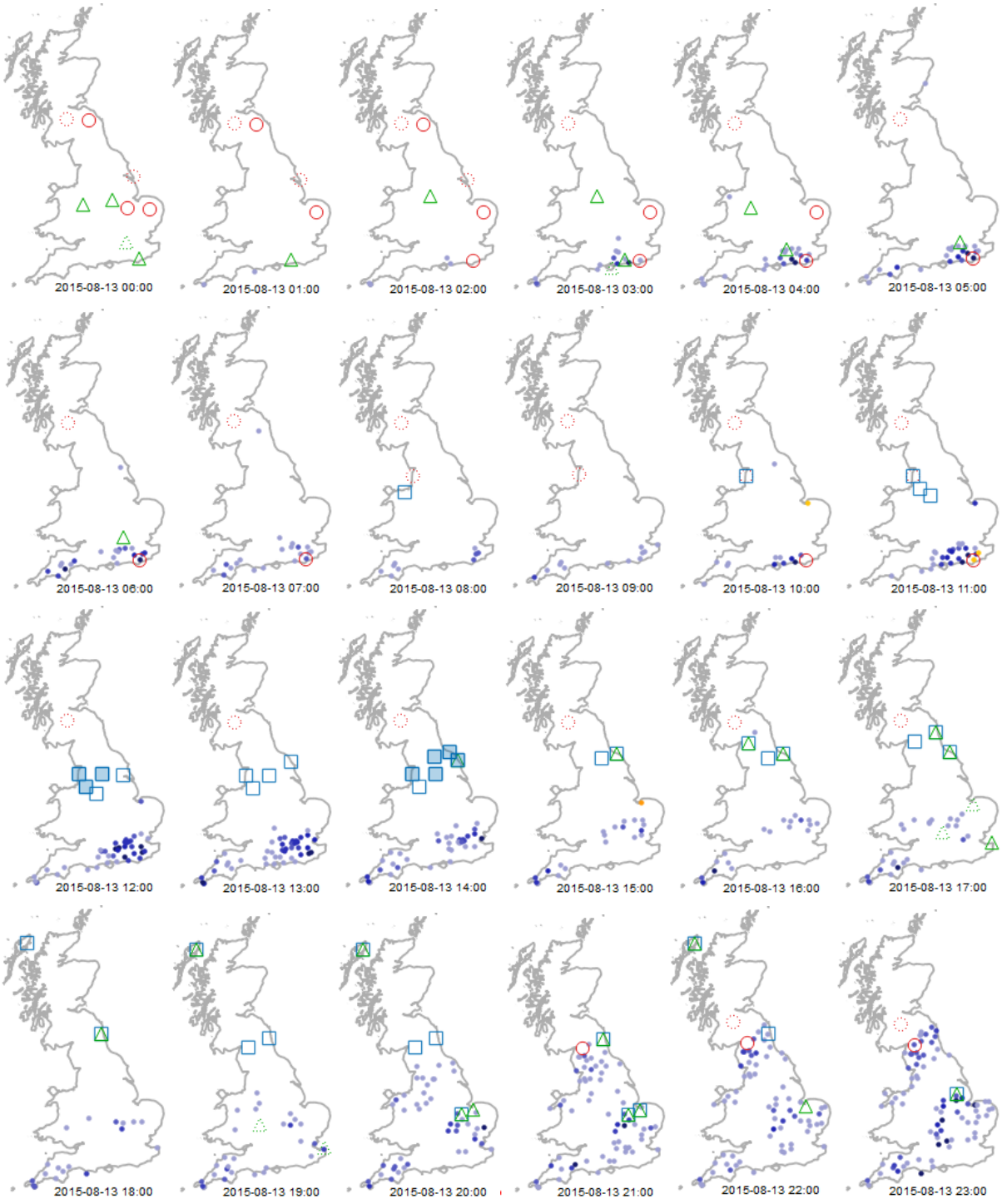


Figure D-11 (continued showing the 13th Aug 2015)

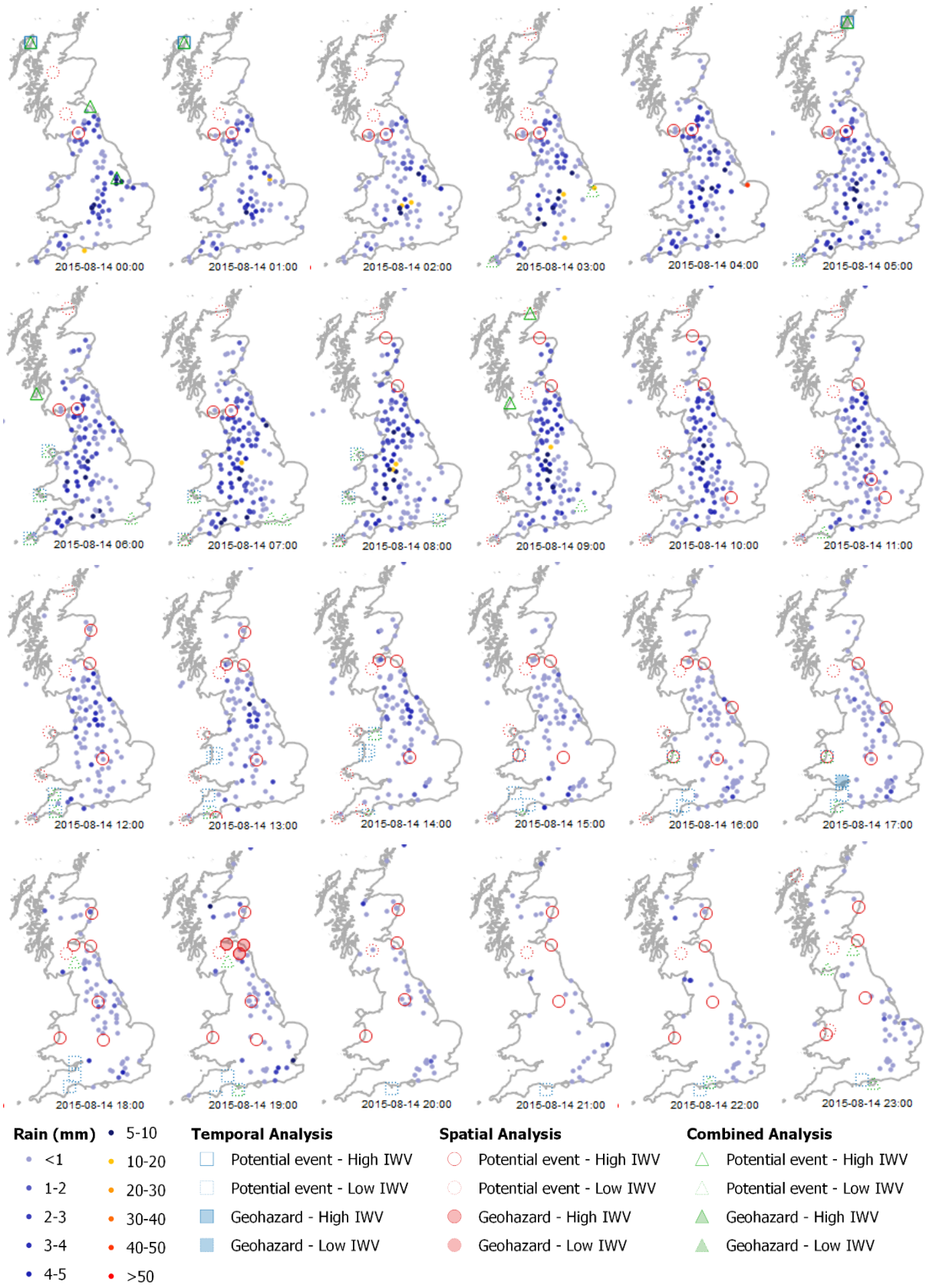


Figure D-11 (continued showing the 14th Aug 2015)

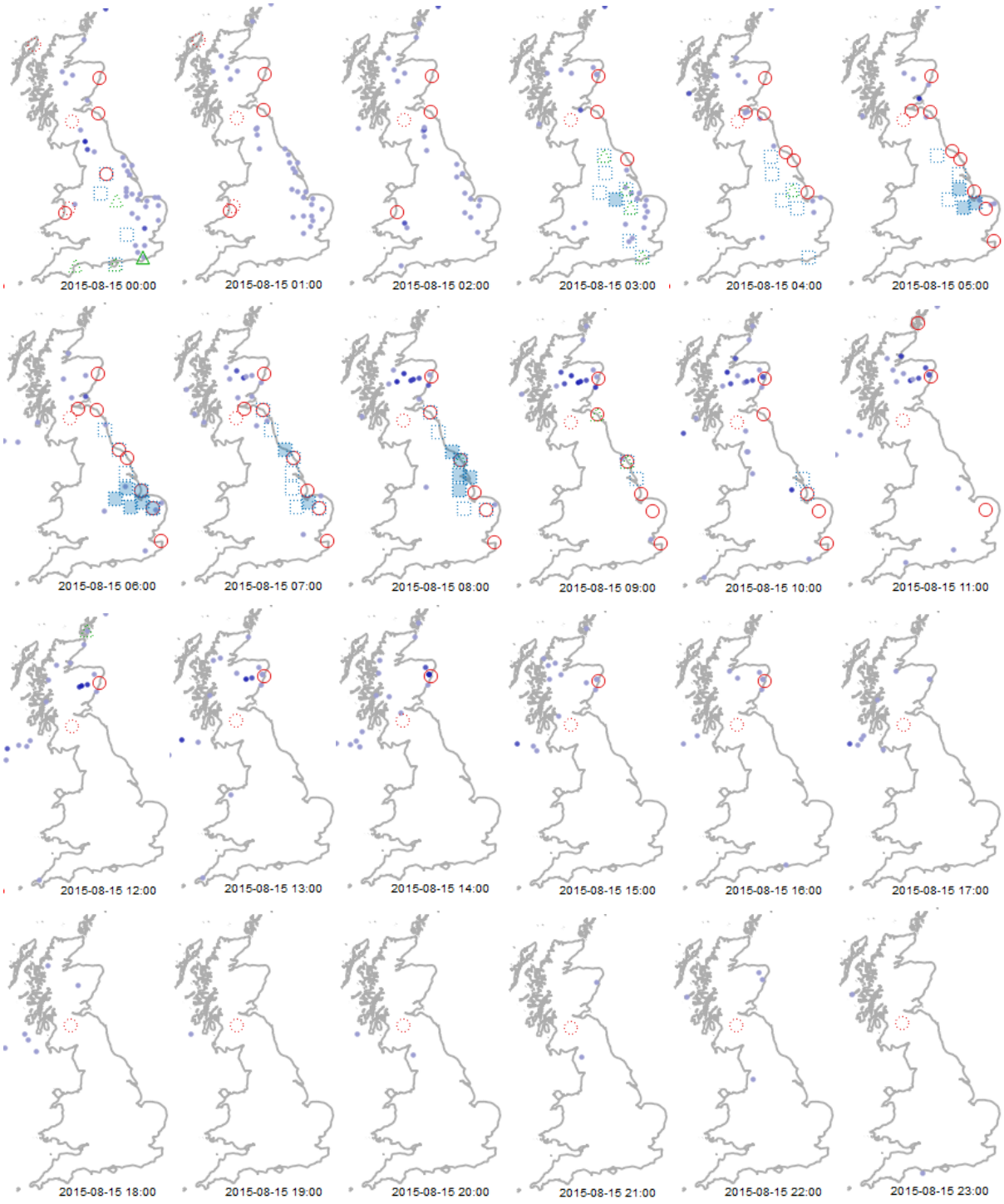


Figure D-11 (continued showing the 15th Aug 2015)

Example 2: Stations considered as having meteorological events using different cut-off frequencies

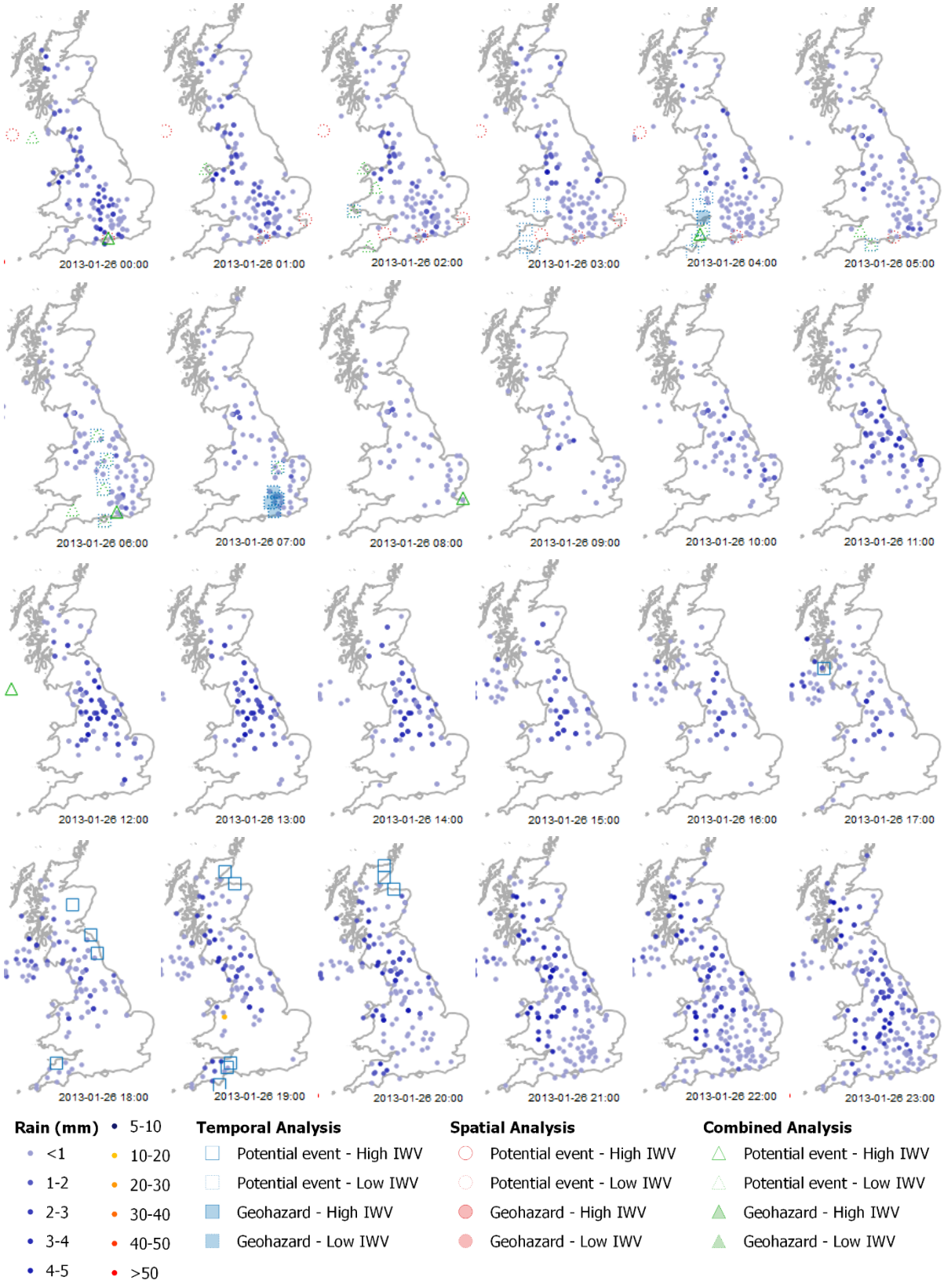


Figure D-12 Rain gauge readings (coloured dots) and stations considered as having either potential events (hollow symbols) or meteorological events (filled symbols), with 0.25 cycle/day as a cut-off frequency.

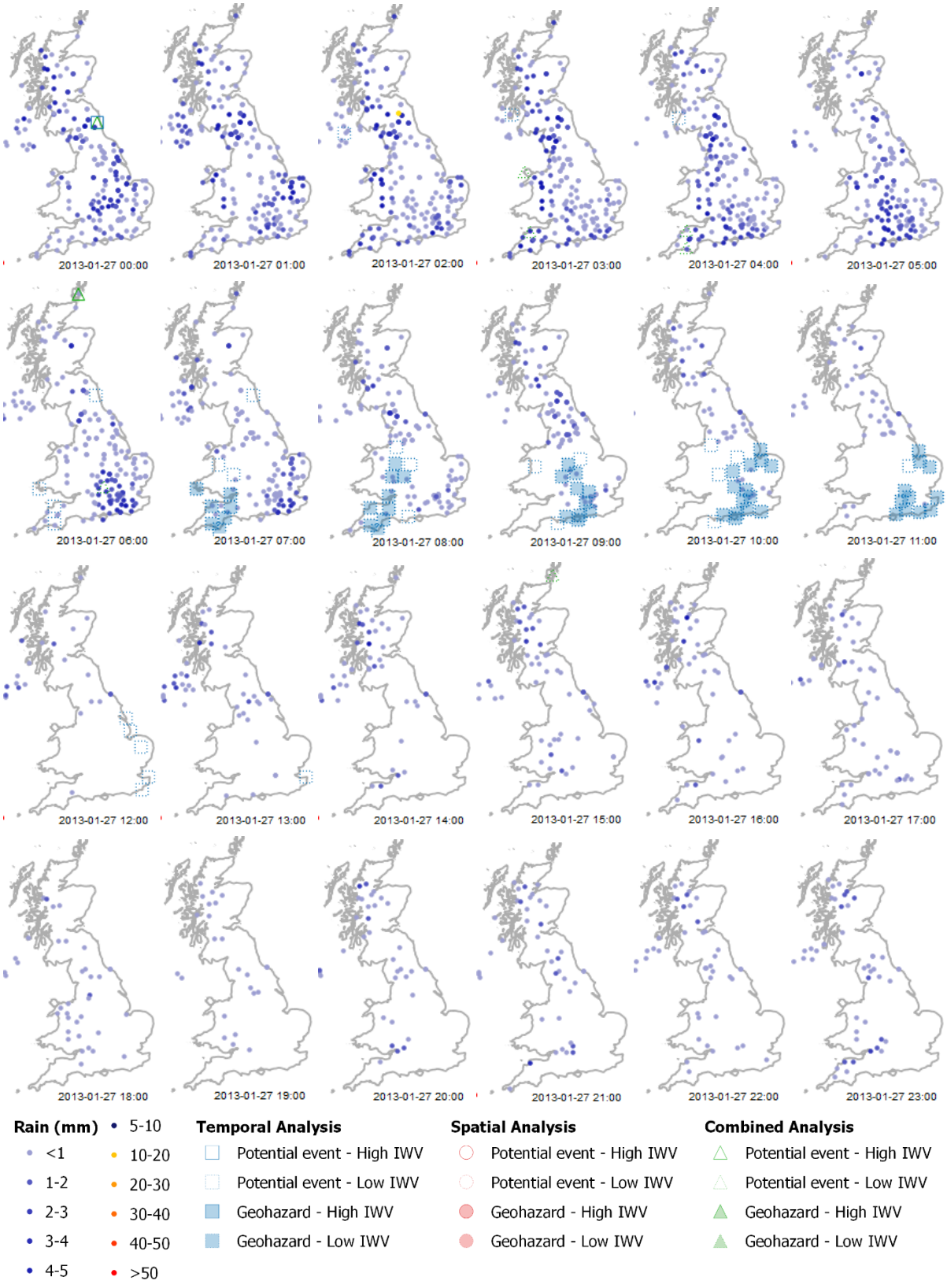


Figure D-12 (continued showing the 27th Jan 2013)

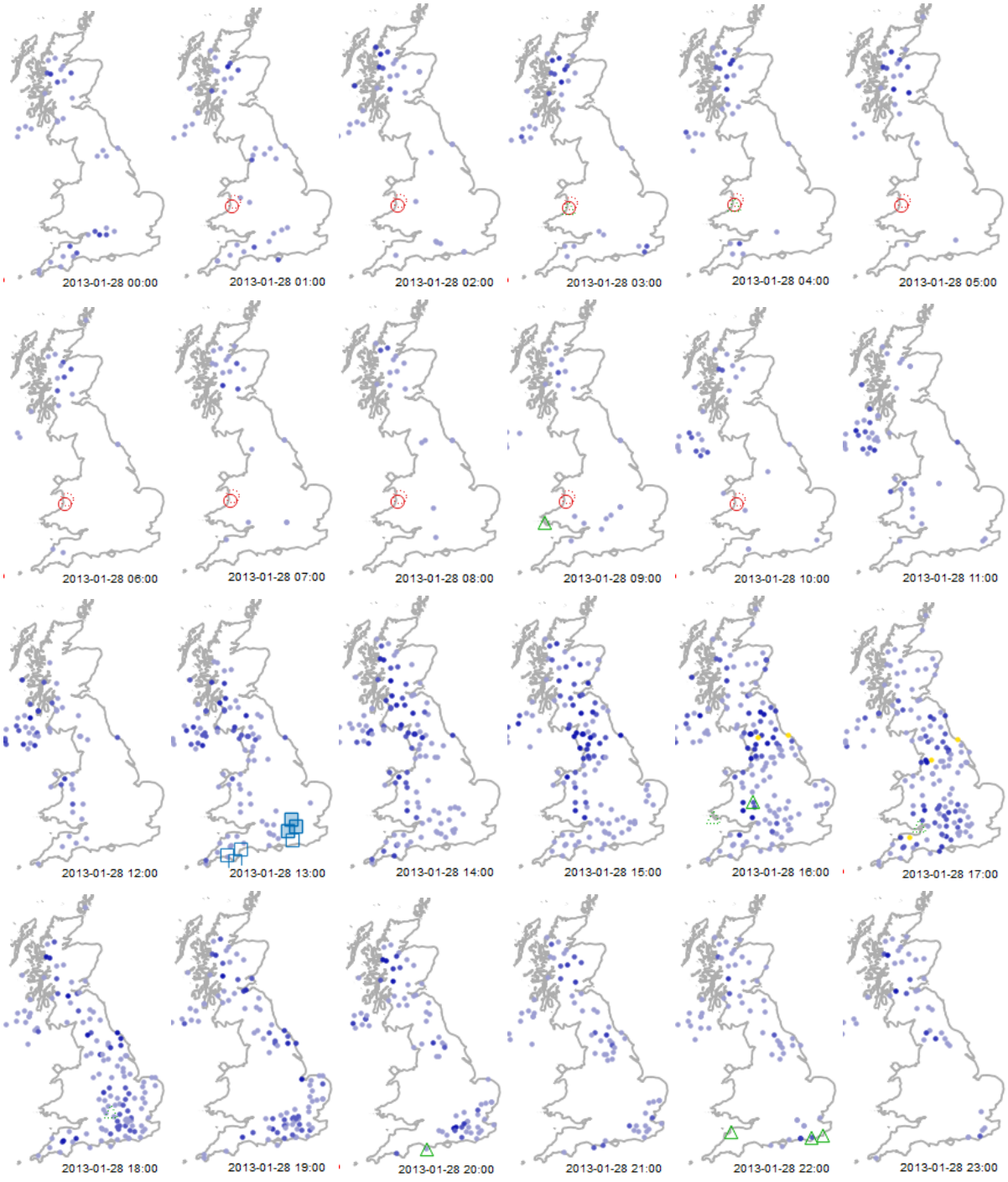


Figure D-12 (continued showing the 28th Jan 2013)

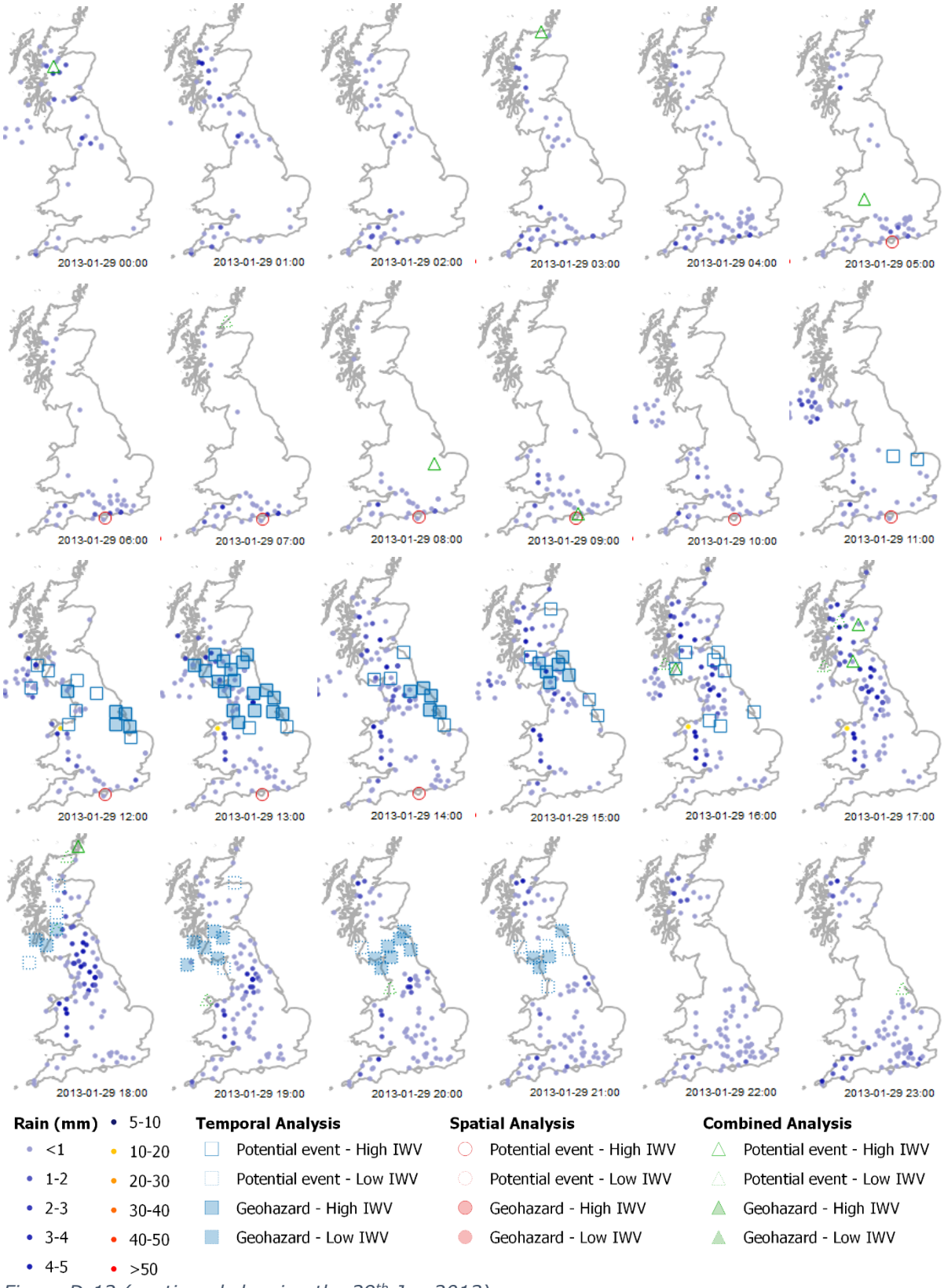


Figure D-12 (continued showing the 29th Jan 2013)

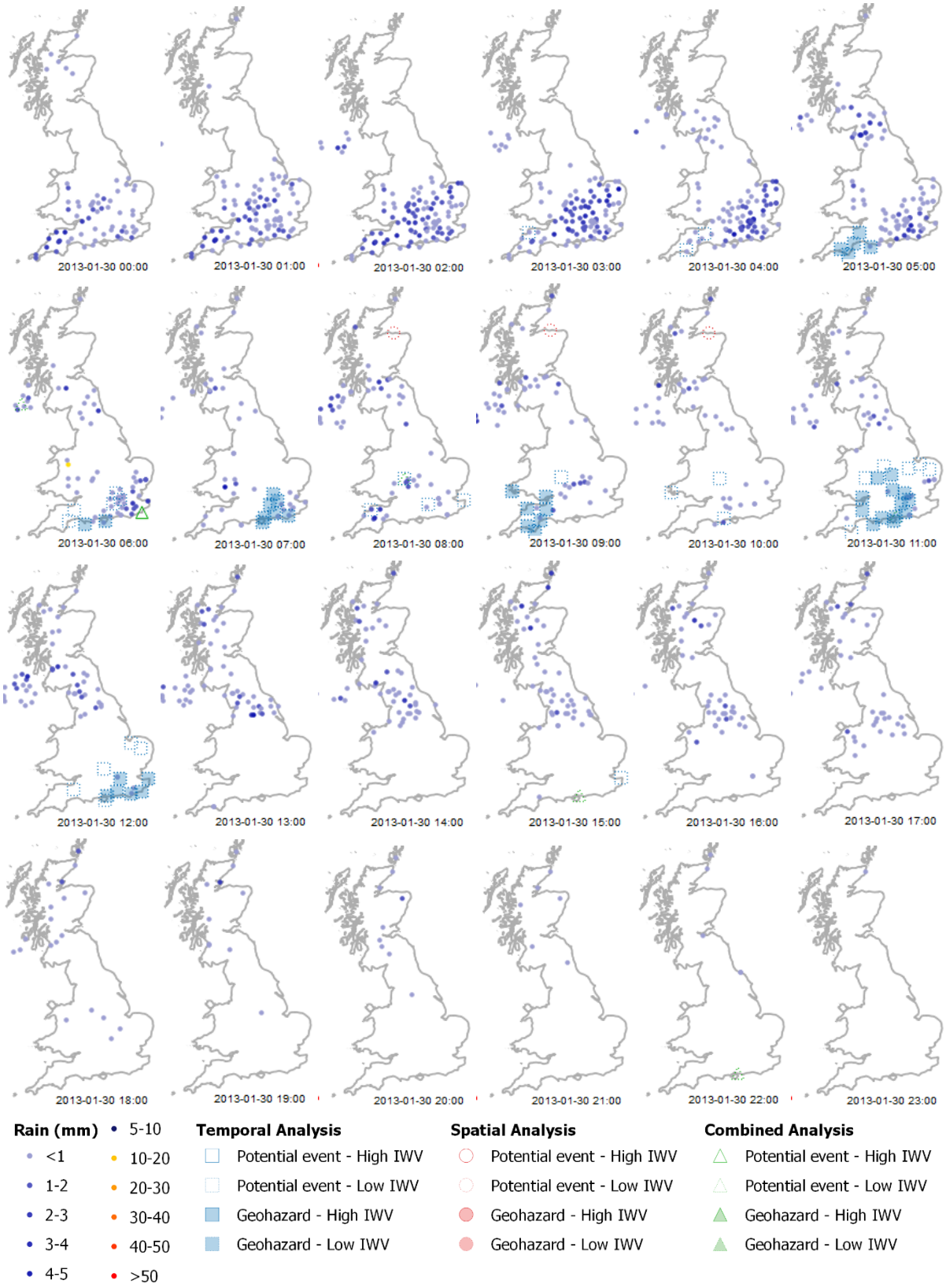


Figure D-12 (continued showing the 30th Jan 2013)

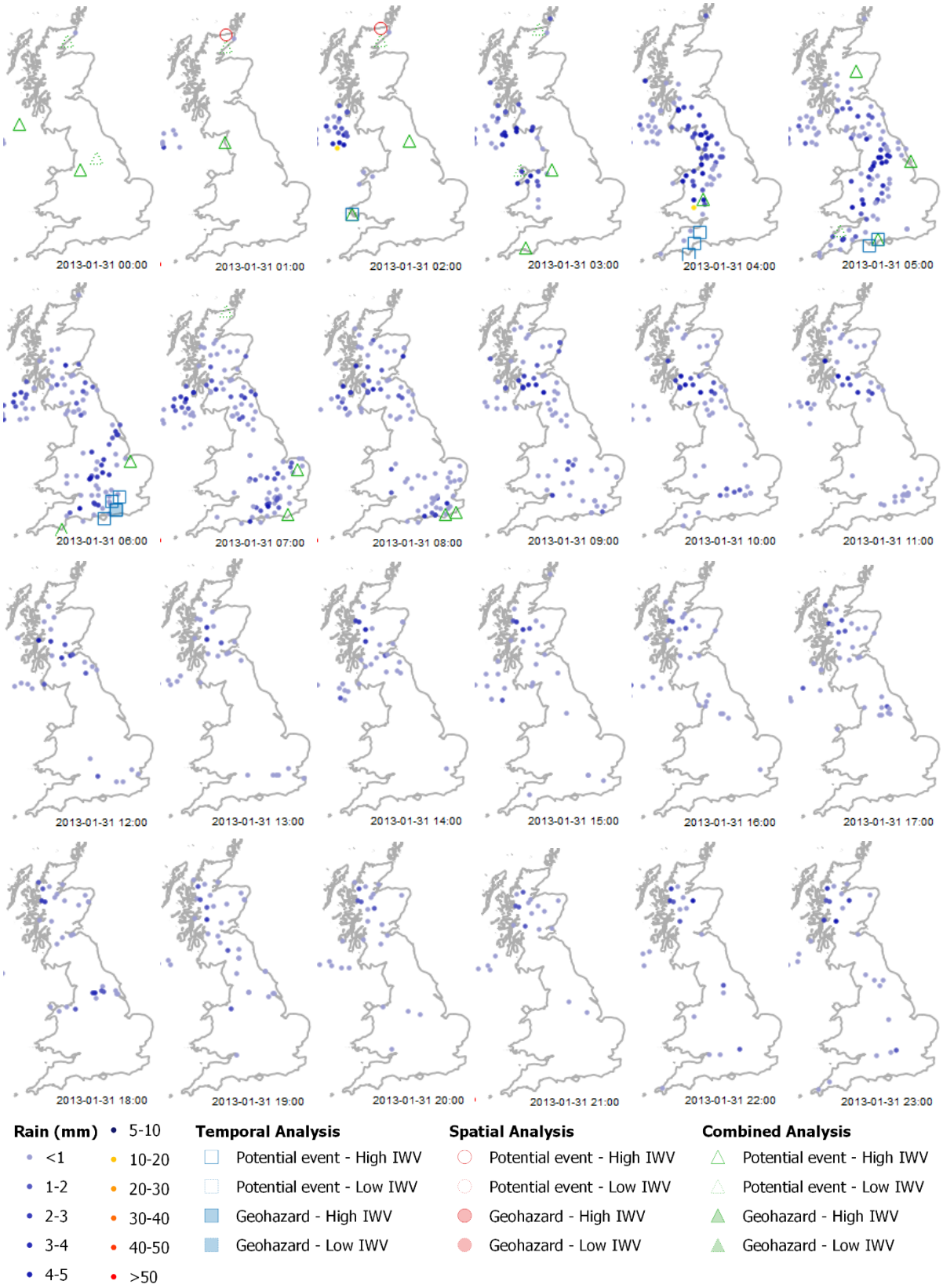


Figure D-12 (continued showing the 31st Jan 2013)

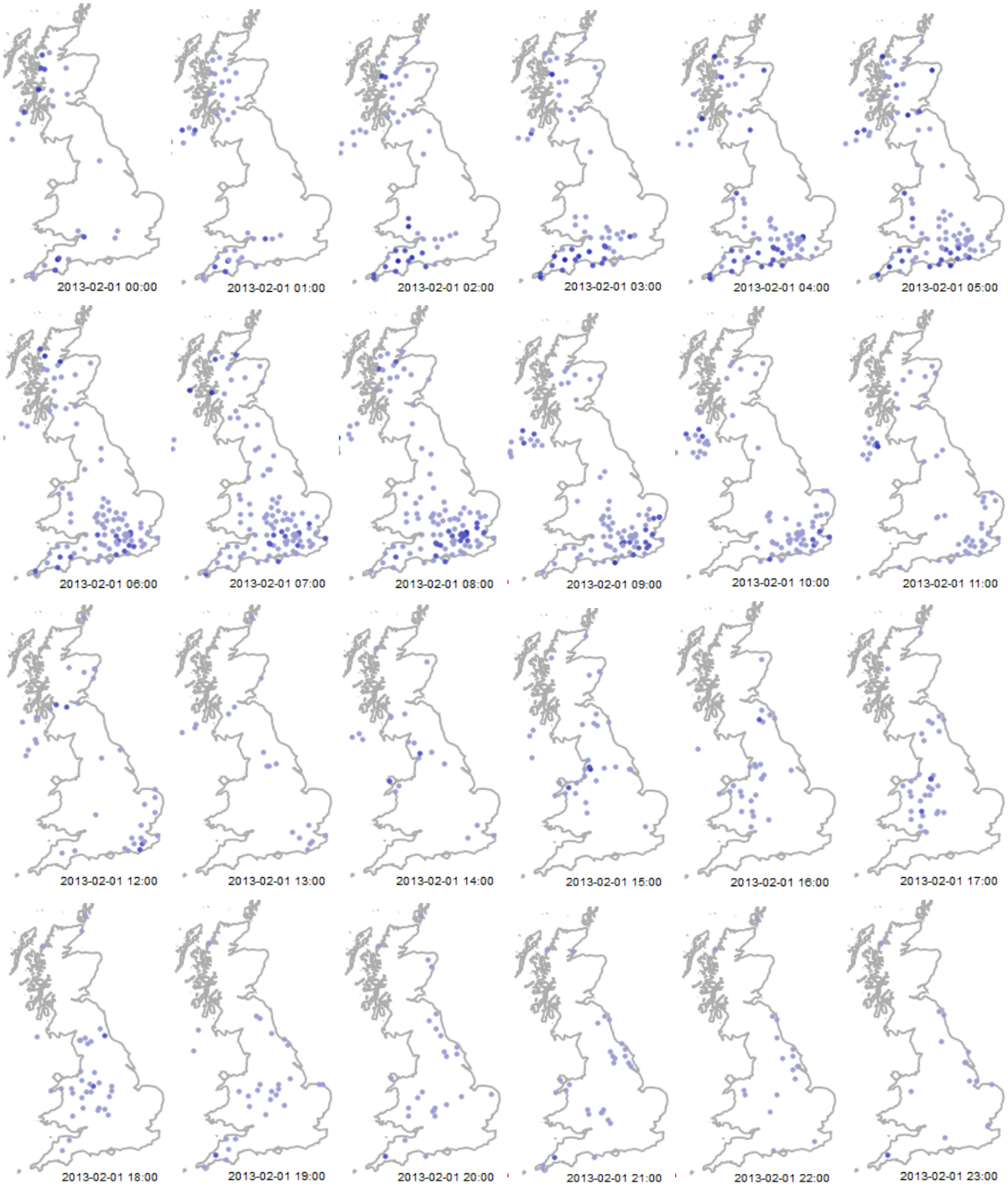


Figure D-12 (continued showing the 1st Feb 2013)

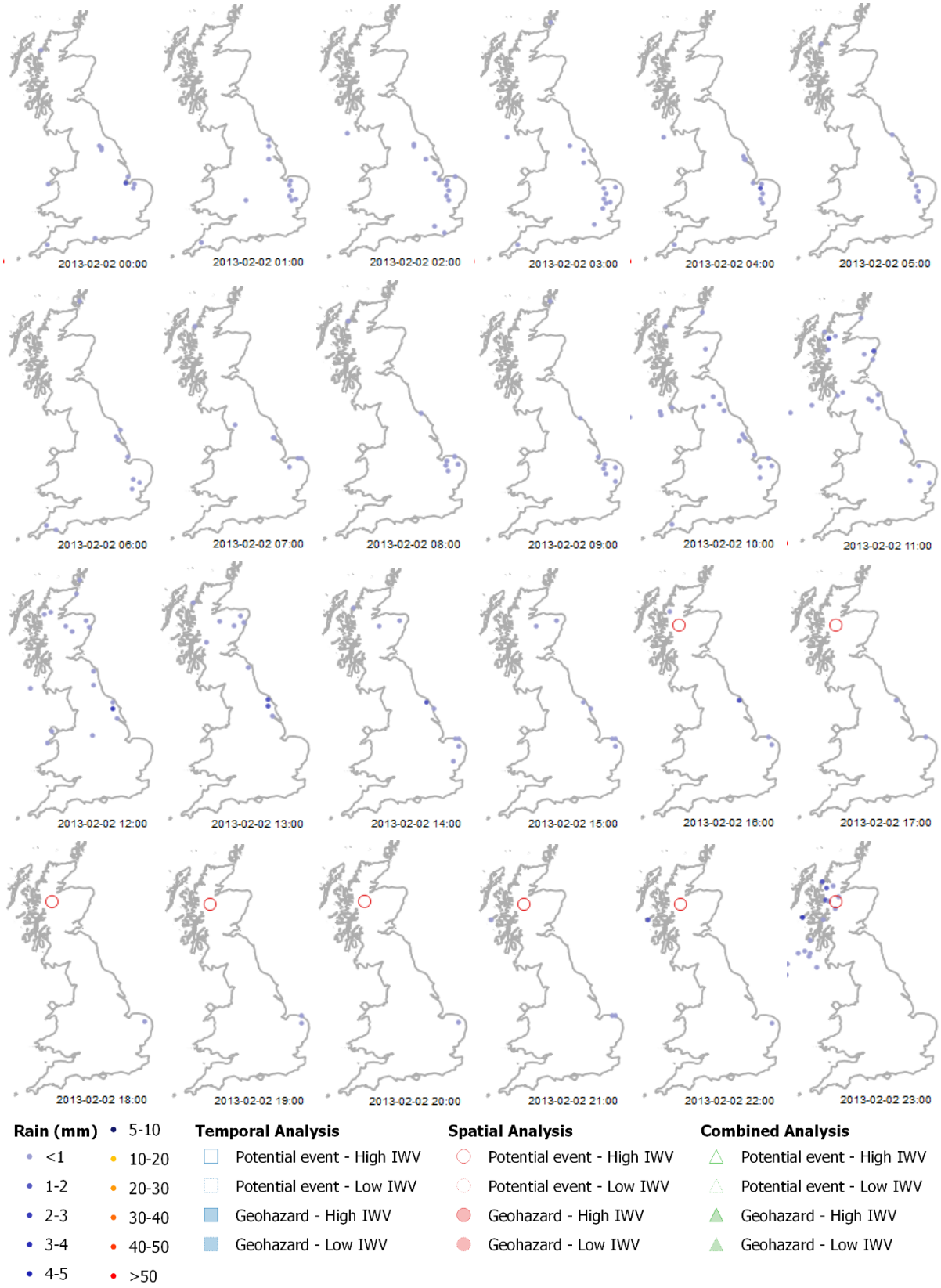


Figure D-12 (continued showing the 2nd Feb 2013)

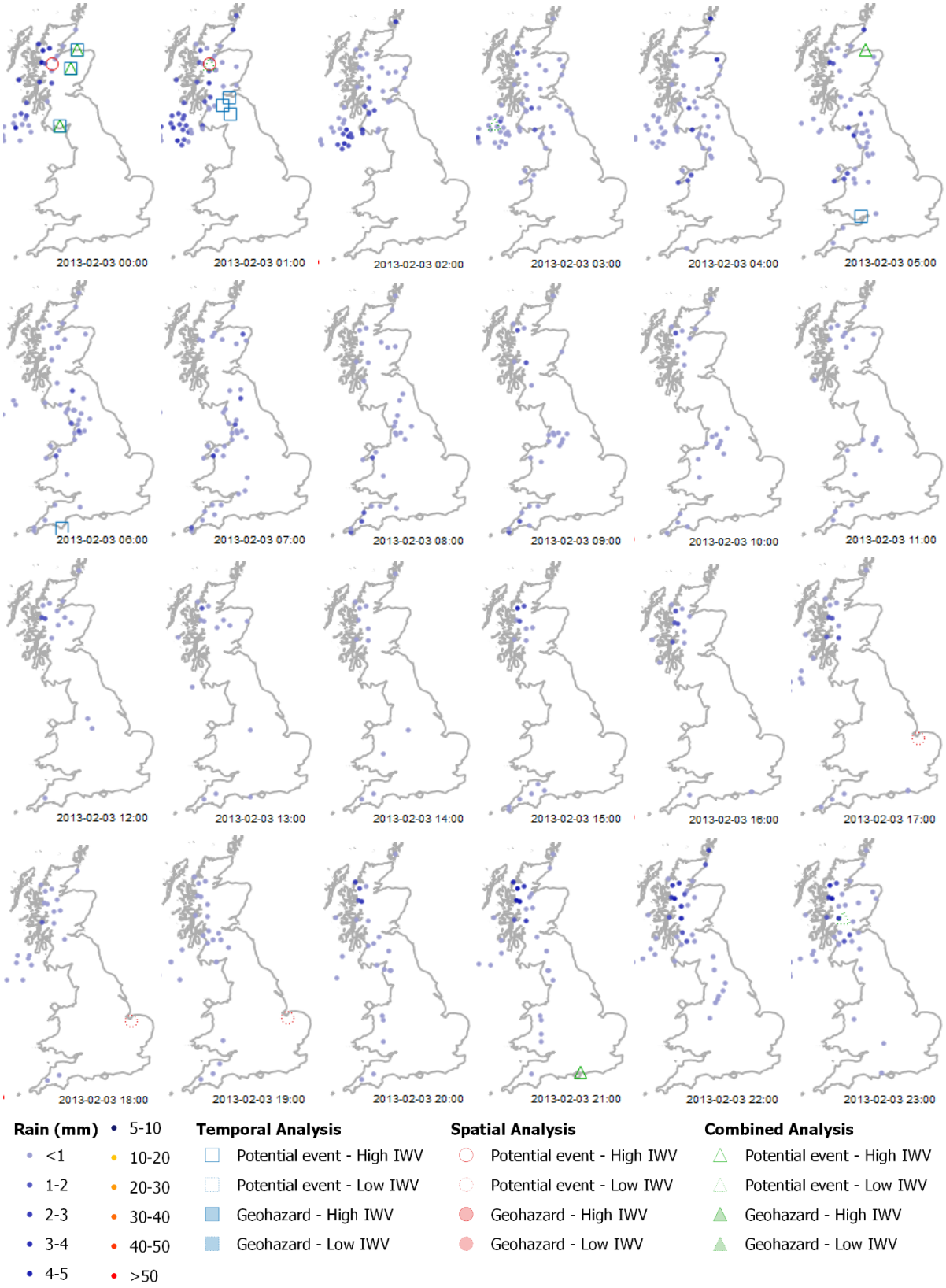


Figure D-12 (continued showing the 3rd Feb 2013)

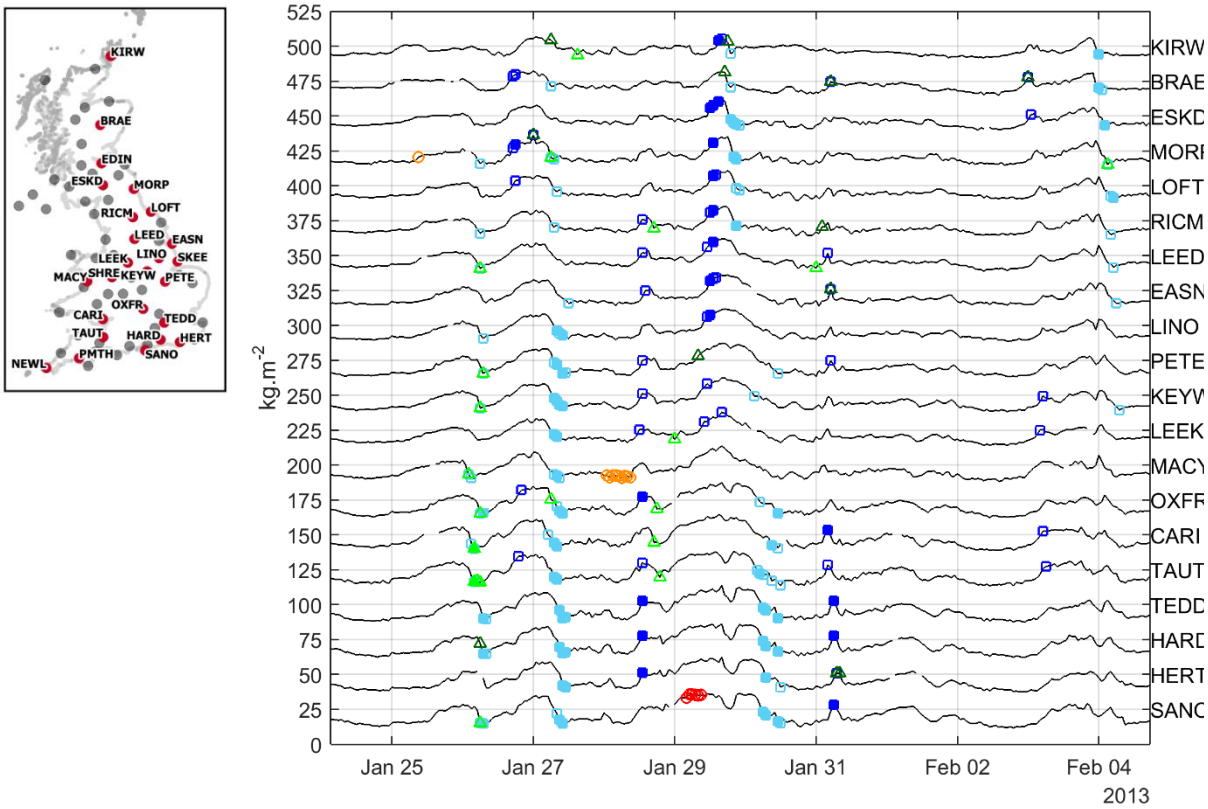


Figure D-13 The IWV time series of 20 stations along with epochs considered as having either potential events(hollow) or meteorological events (filled) using the temporal (high IWV: dark blue, and low IWV: light blue), the spatial (high IWV: red, and low IWV: orange), and the combined (high IWV: dark green, and low IWV: light green) analysis algorithms, with 0.5 cycle/day as a cut off frequency (y-axis grid:25 kg.m^{-2}).

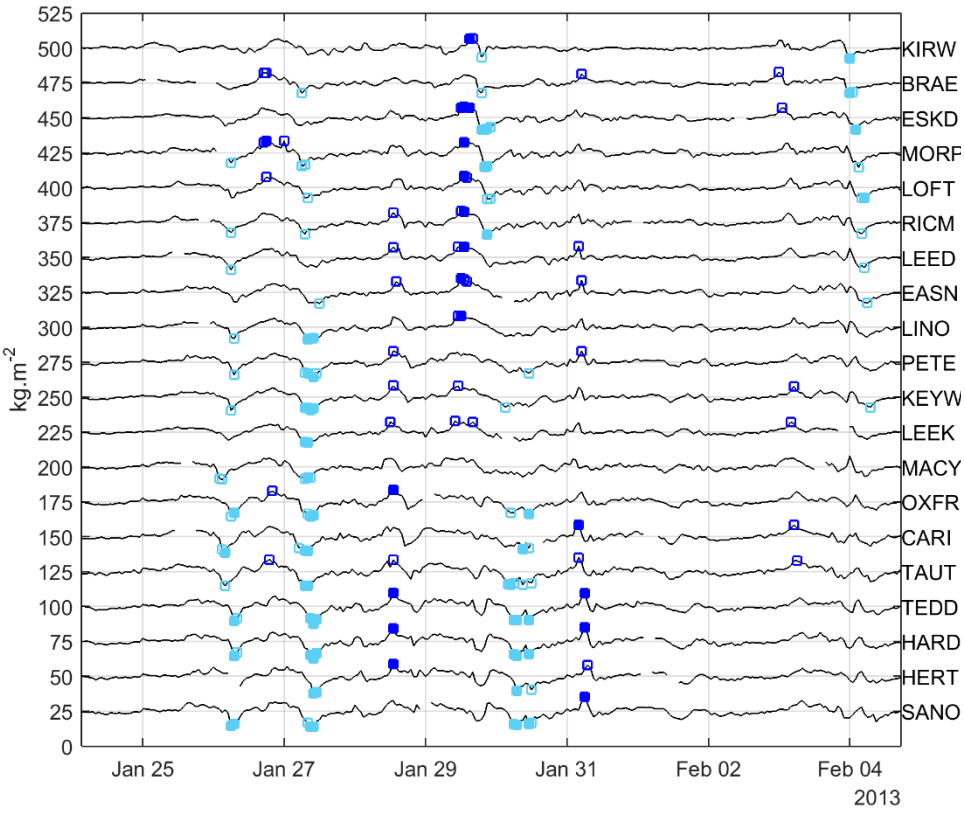


Figure D-14 Same as Figure D-13 but showing the temporal analysis residuals only.

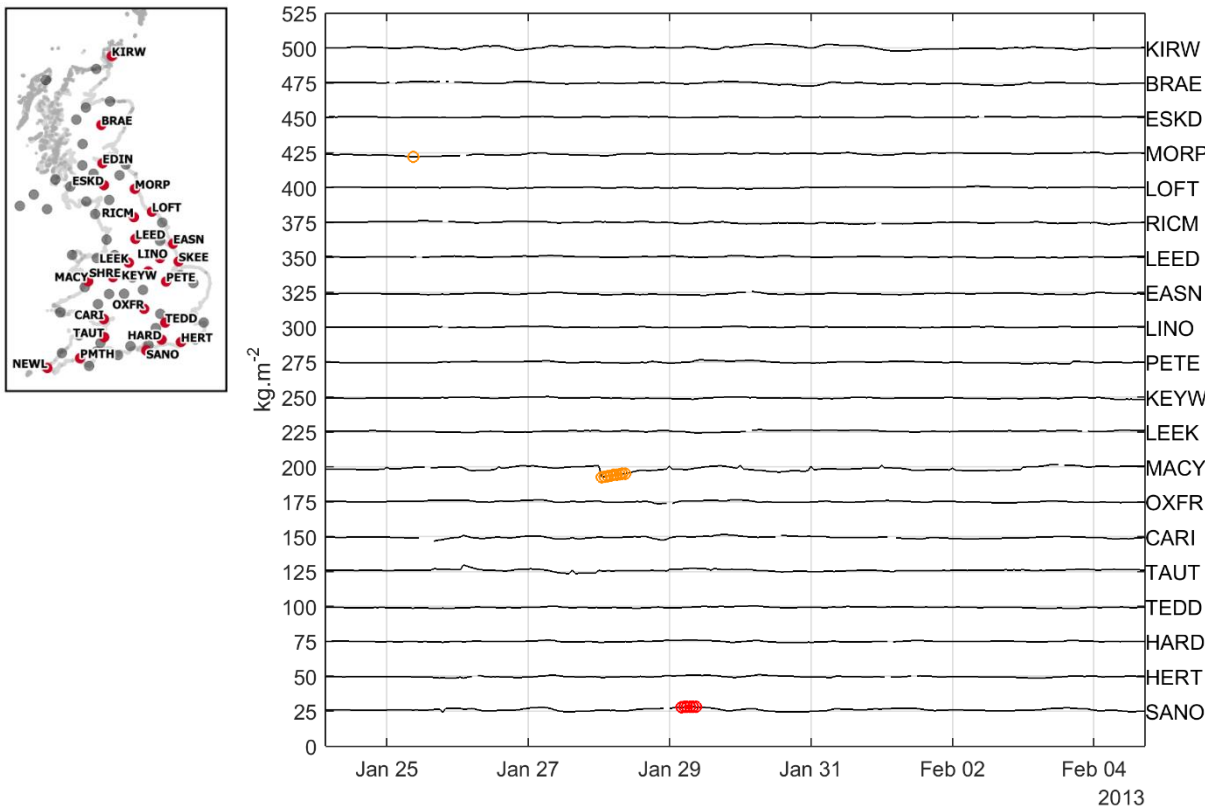


Figure D-15 Same as Figure D-13 but showing the temporal analysis residuals only.

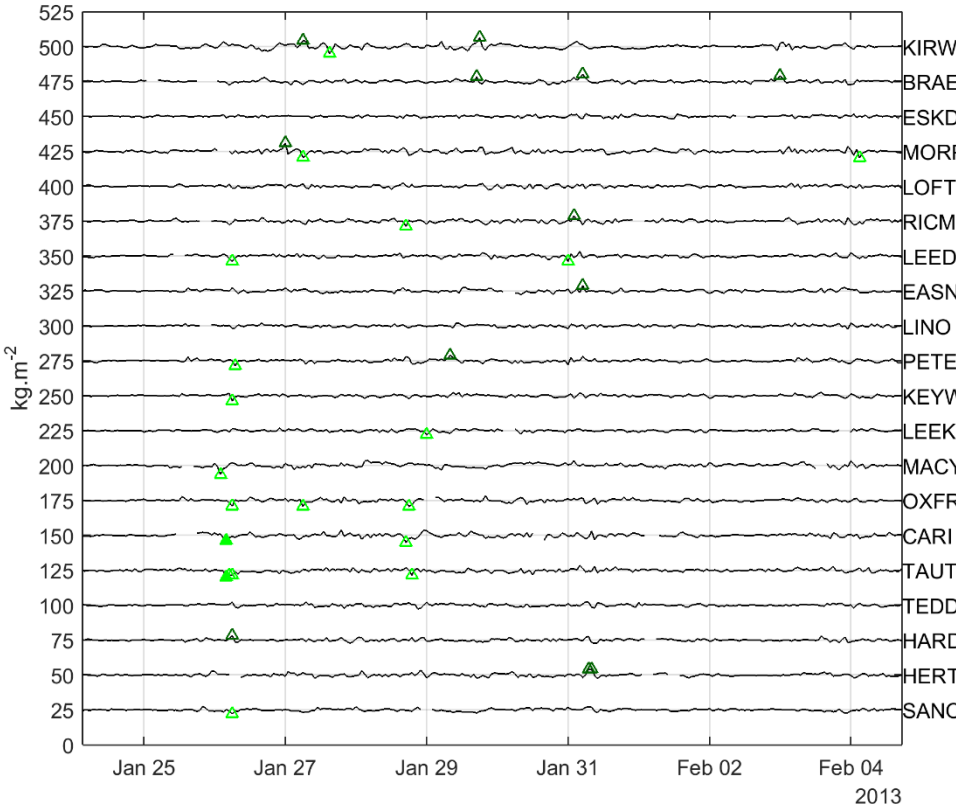


Figure D-16 Same as Figure D-13 but showing the combined analysis residuals only.

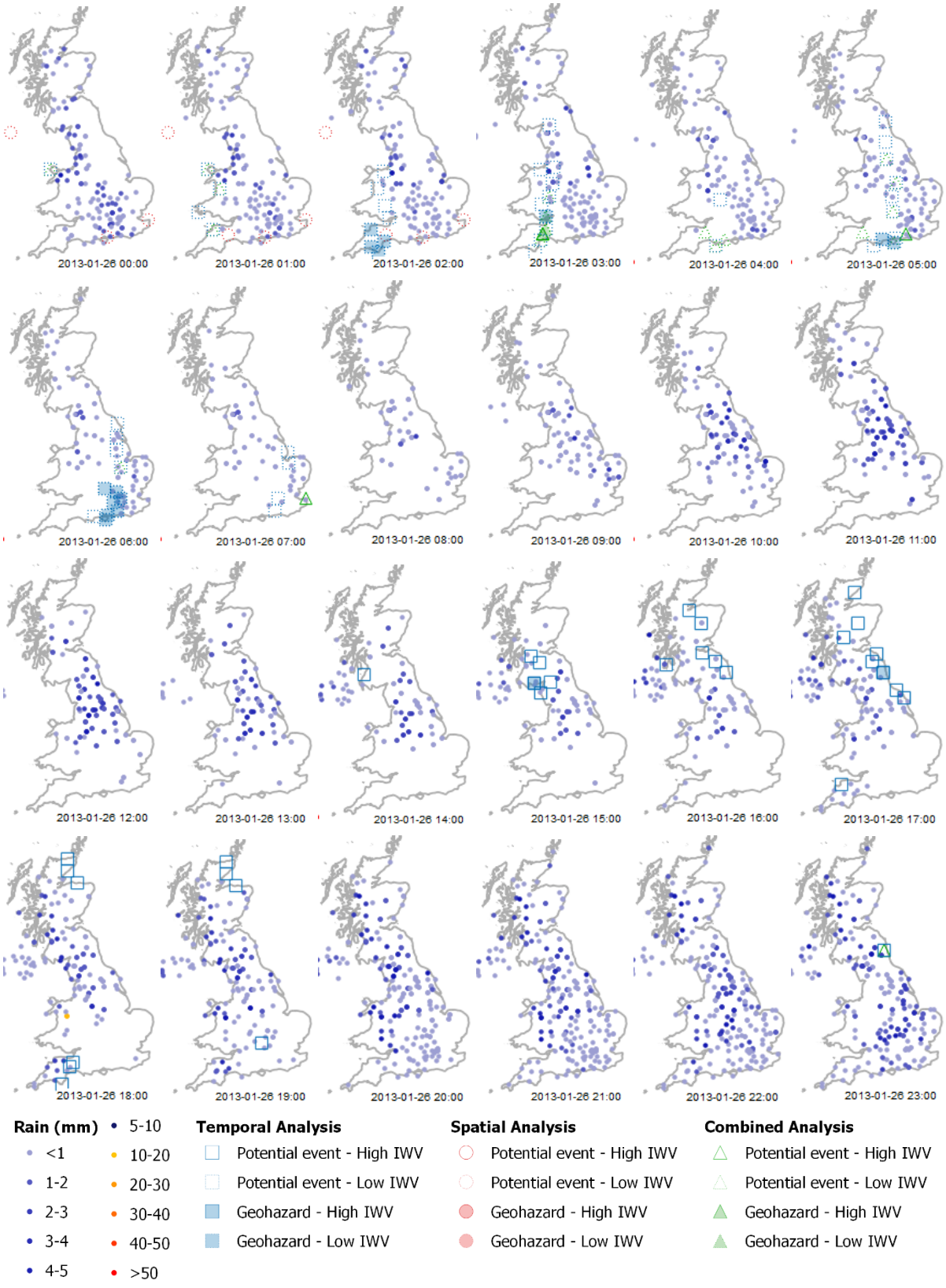


Figure D-17 Rain gauge readings (coloured dots) and stations considered as having either potential events (hollow symbols) or meteorological events (filled symbols), with 0.5 cycle/day as a cut-off frequency.

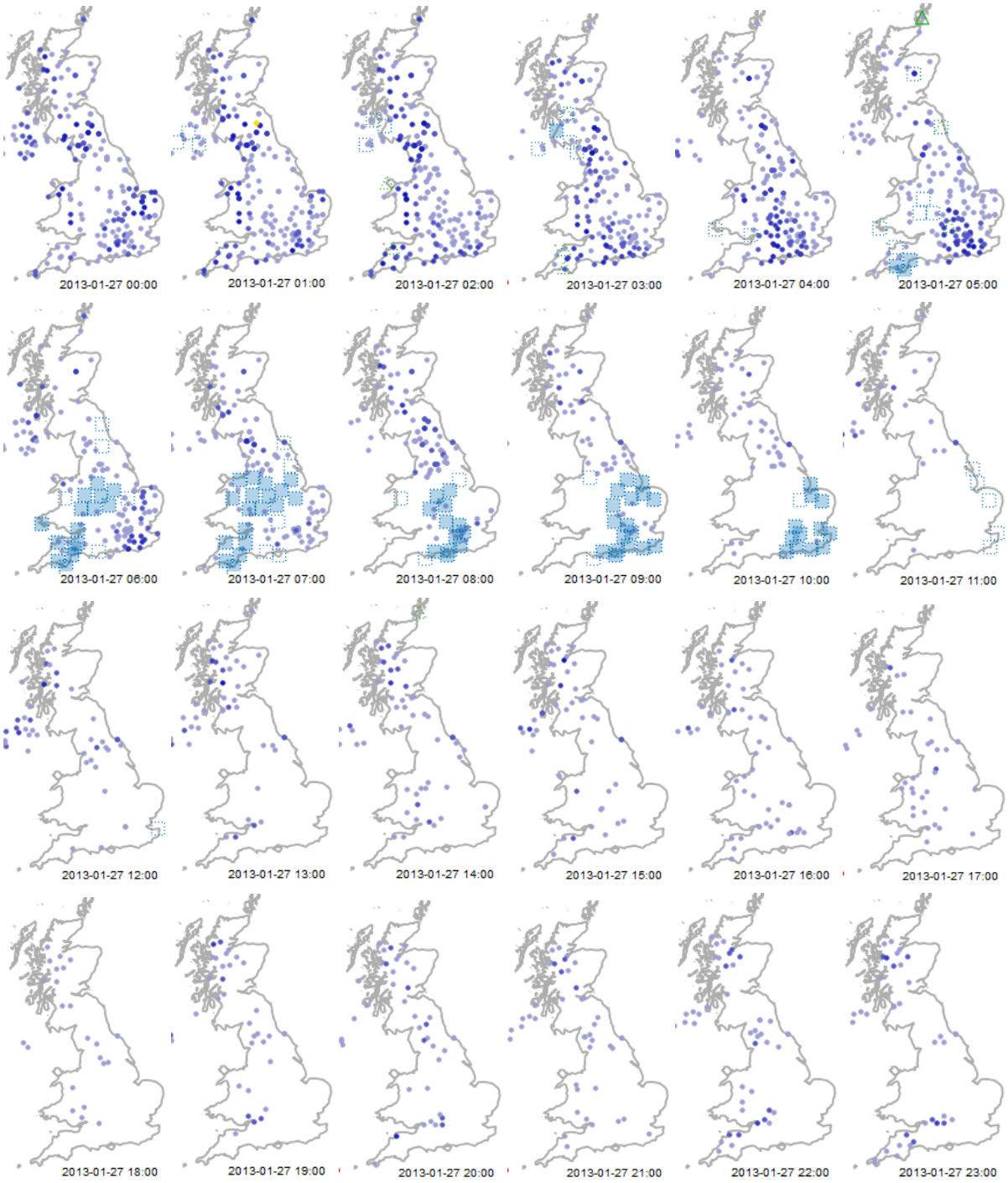


Figure D-17(continued showing the 27th Jan 2013)

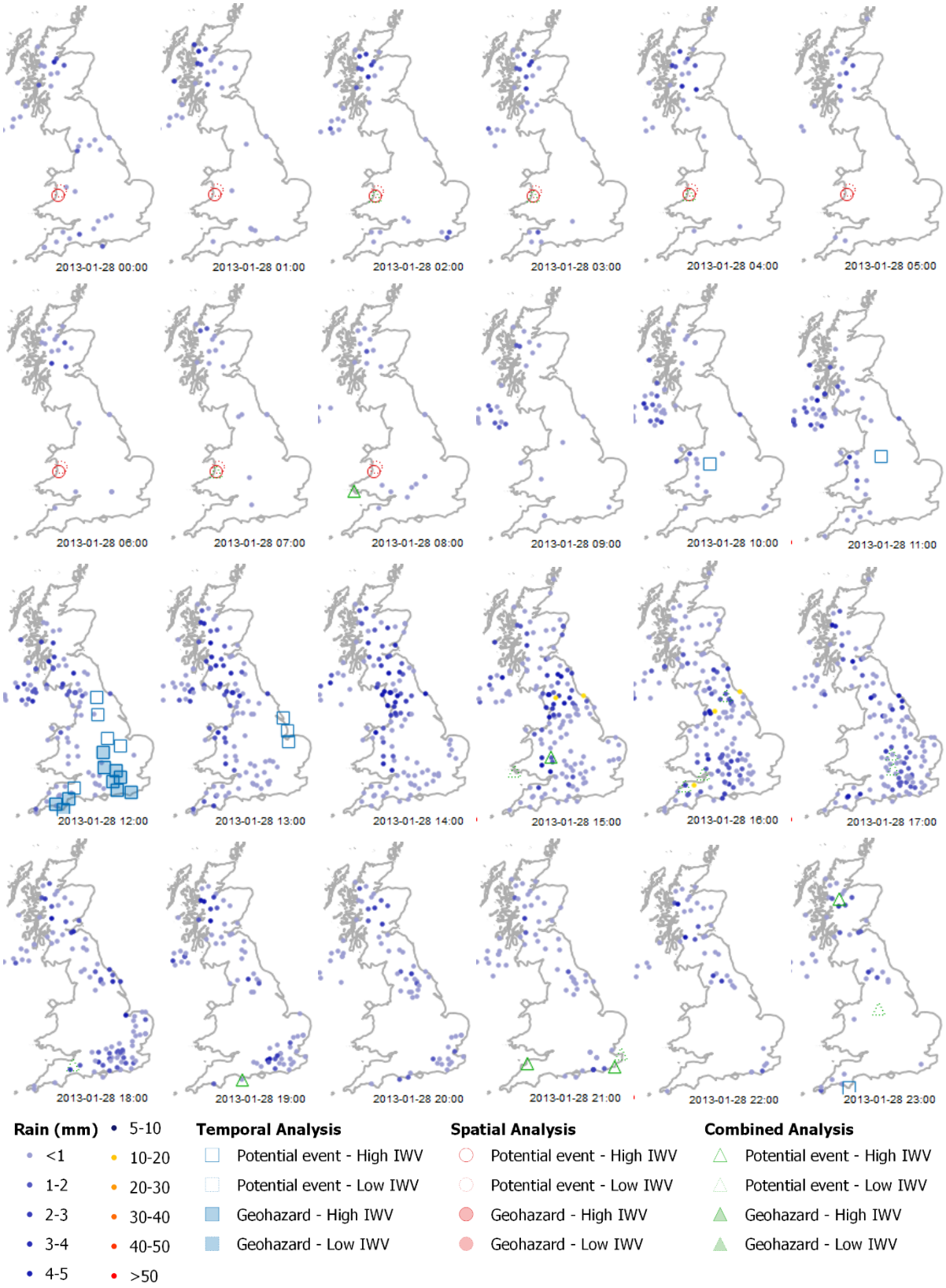


Figure D-17(continued showing the 28th Jan 2013)

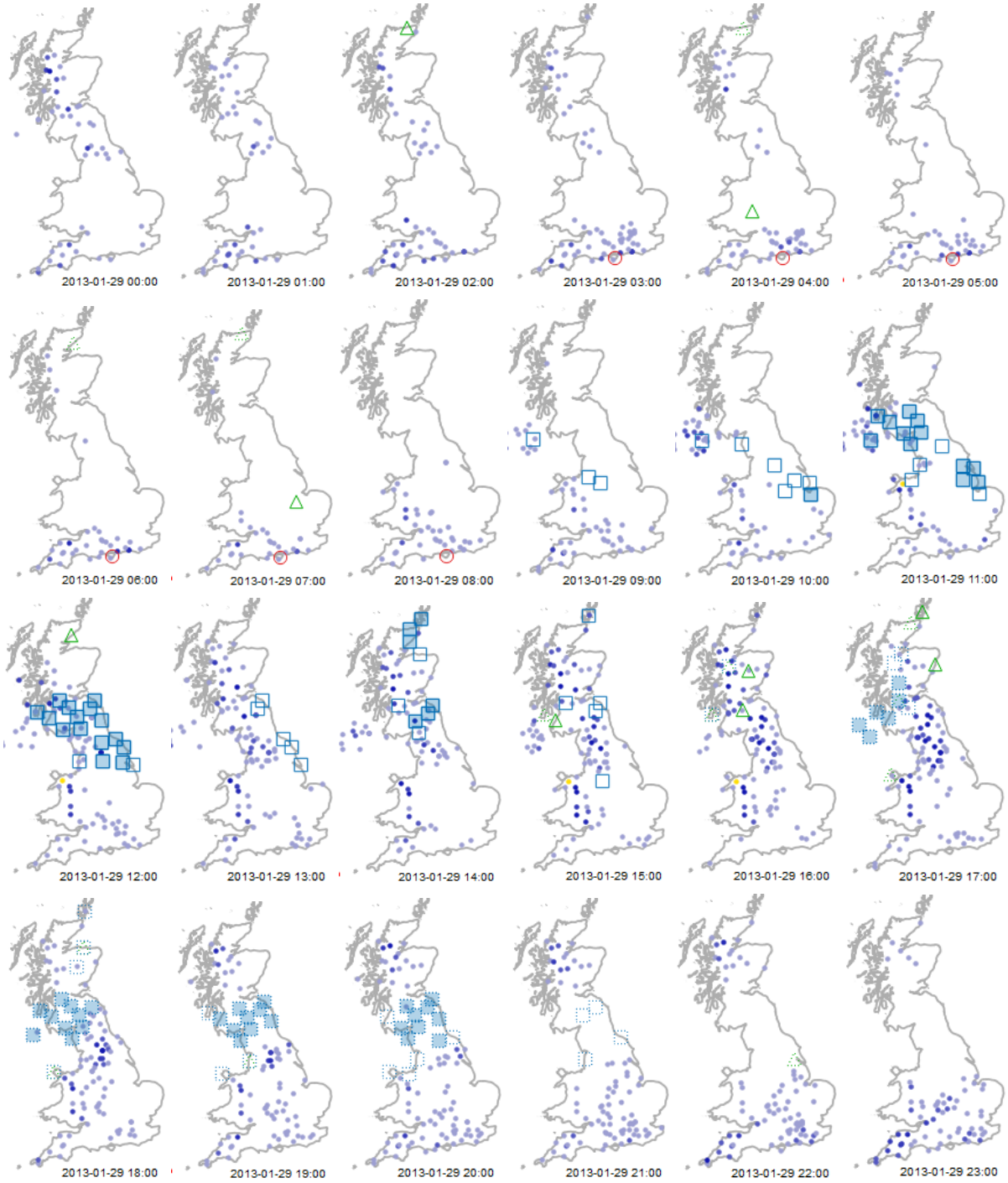


Figure D-17(continued showing the 29th Jan 2013)

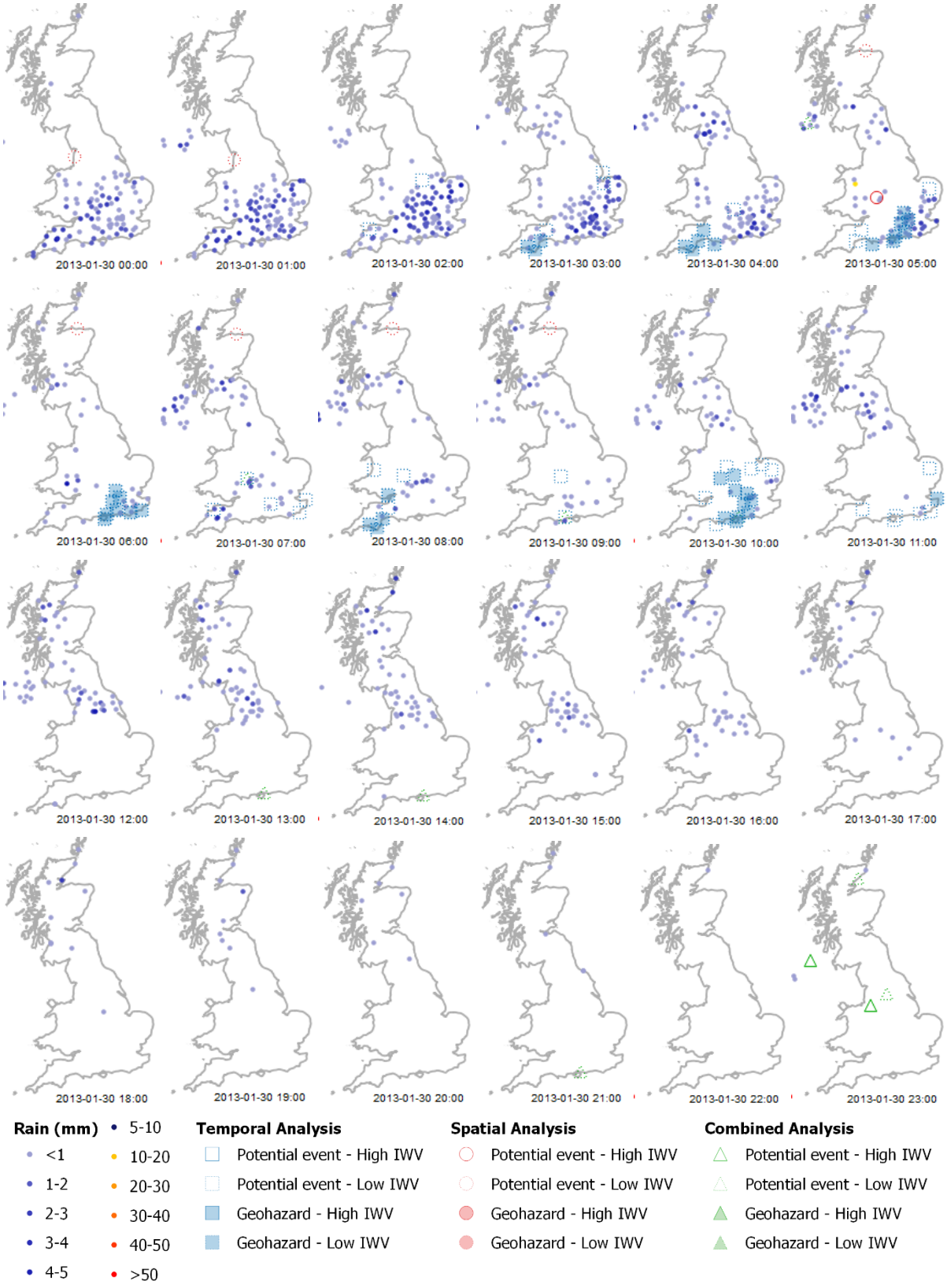


Figure D-17(continued showing the 30th Jan 2013)

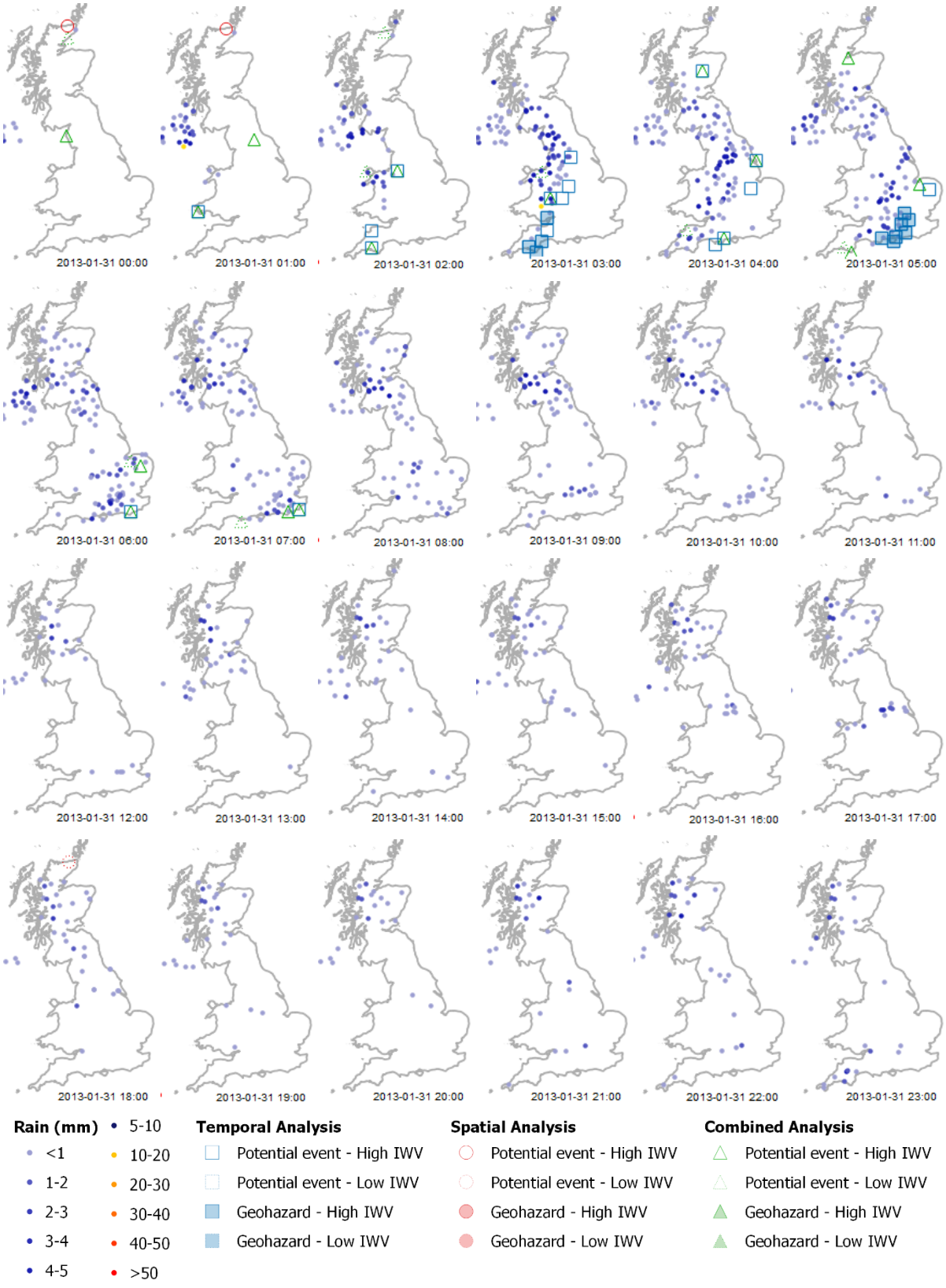


Figure D-17(continued showing the 31st Jan 2013)

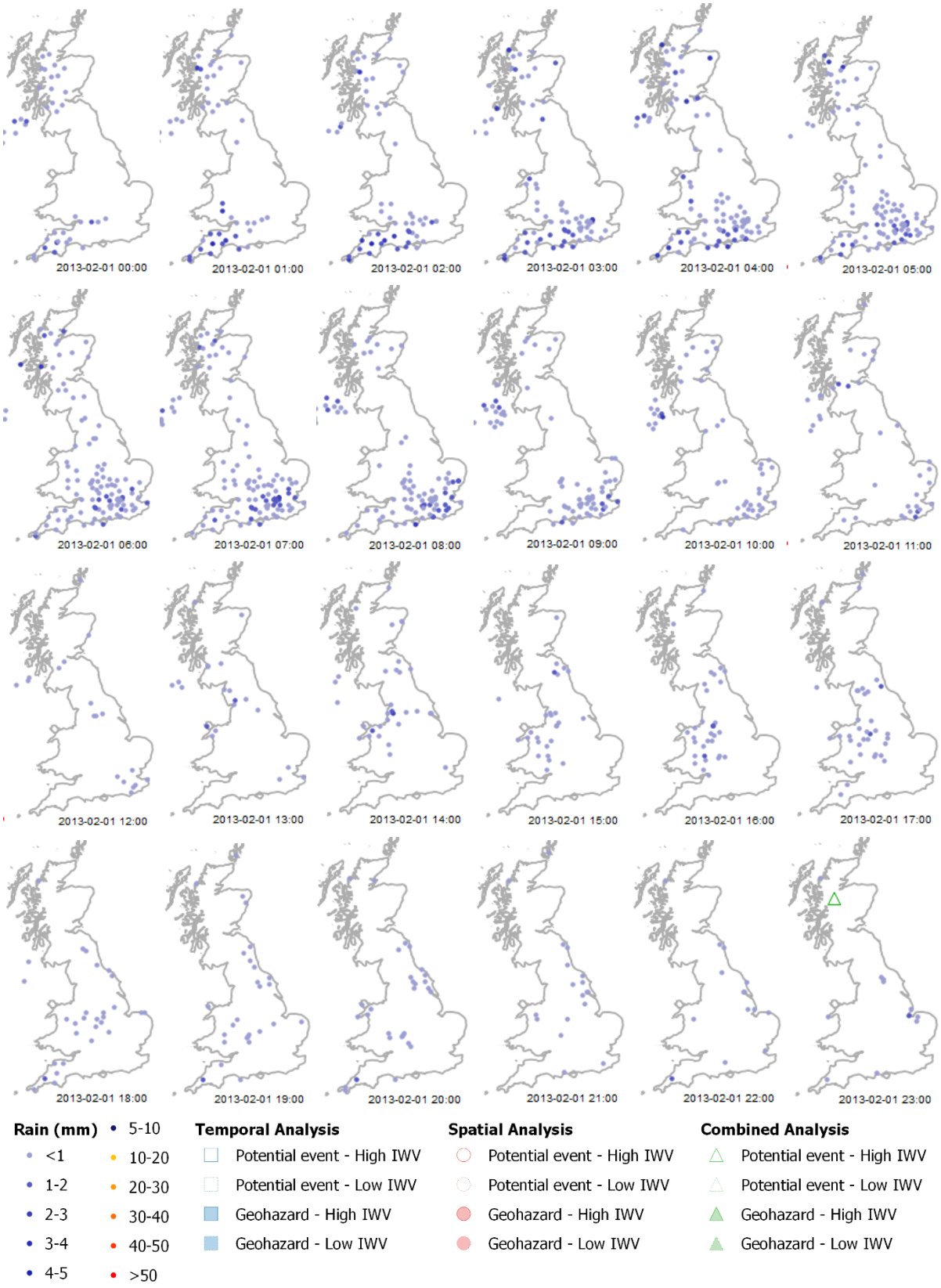


Figure D-17(continued showing the 1st Feb 2013)

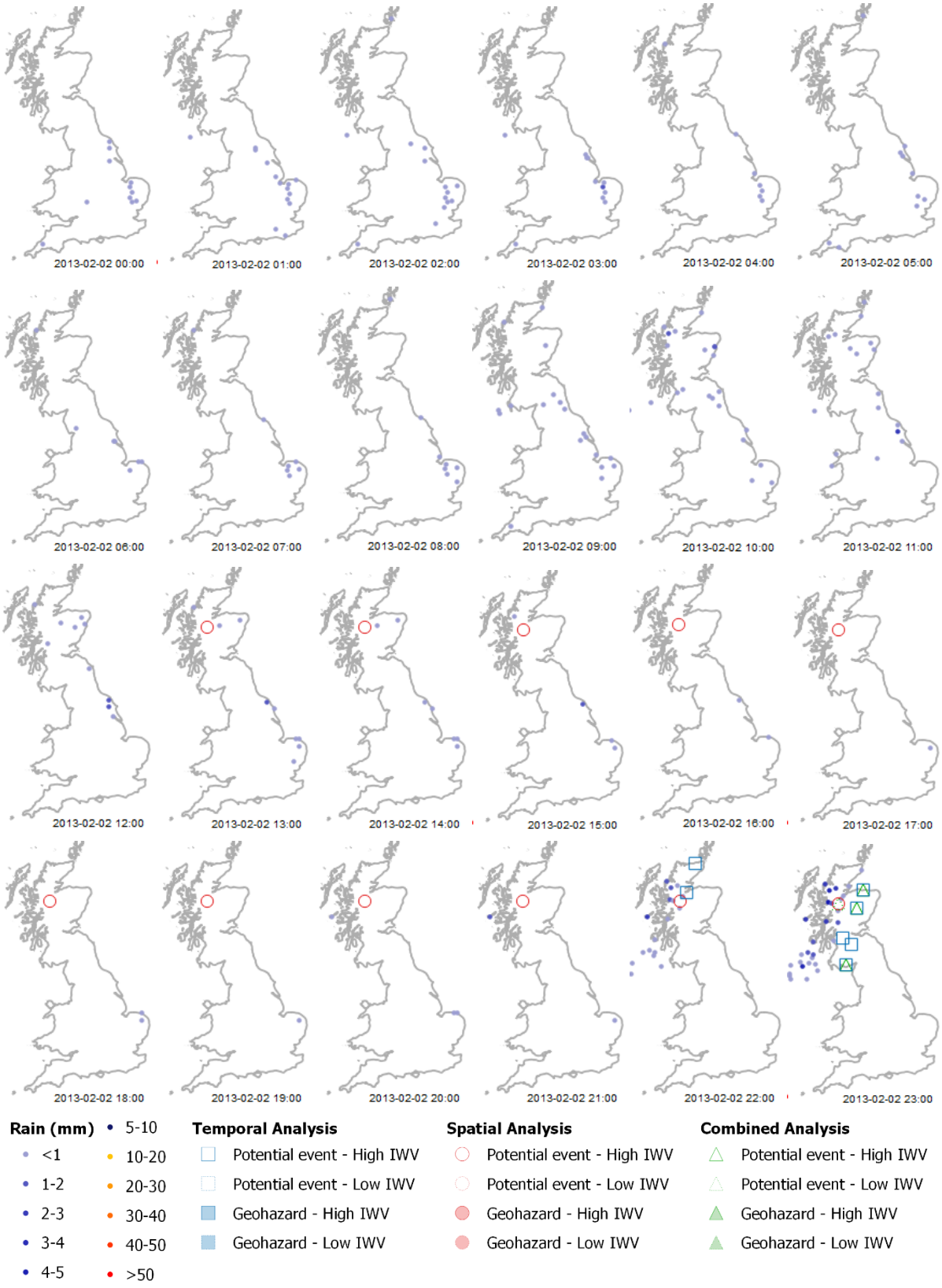


Figure D-17(continued showing the 2nd Feb 2013)

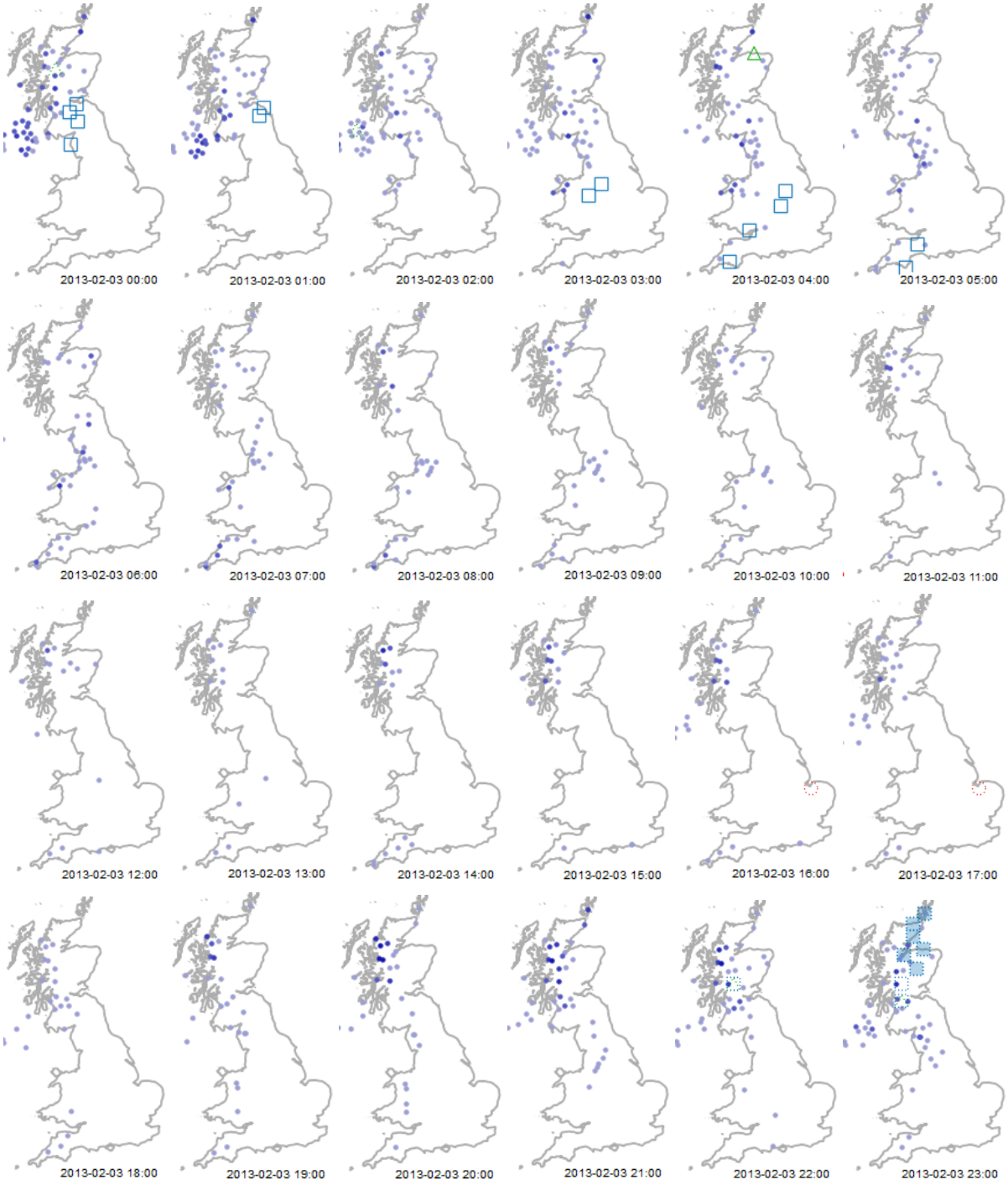


Figure D-17(continued showing the 3rd Feb 2013)

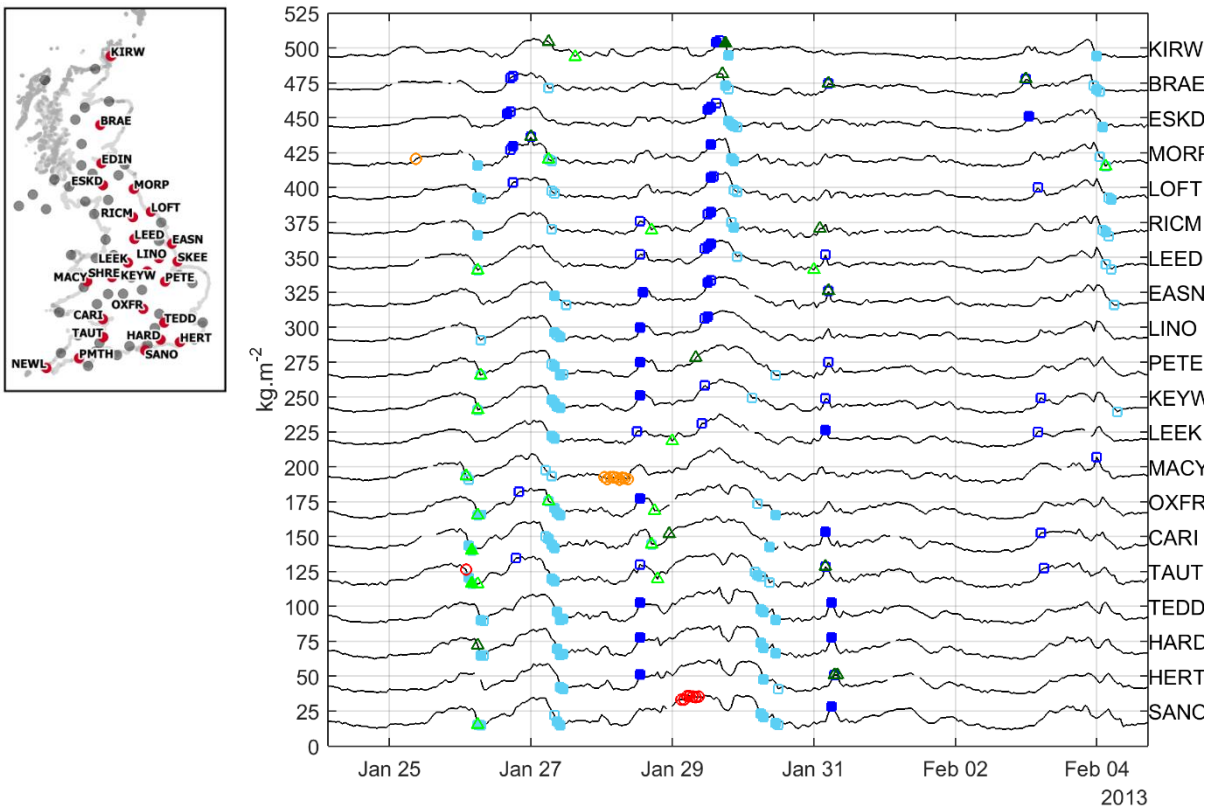


Figure D-18 The IWV time series of 20 stations along with epochs considered as having either potential events (hollow) or meteorological events (filled) using the temporal (high IWV: dark blue, and low IWV: light blue), the spatial (high IWV: red, and low IWV: orange), and the combined (high IWV: dark green, and low IWV: light green) analysis algorithms, with using 1 cycle/day as a cut off frequency (y-axis grid:25 kg.m^{-2}).

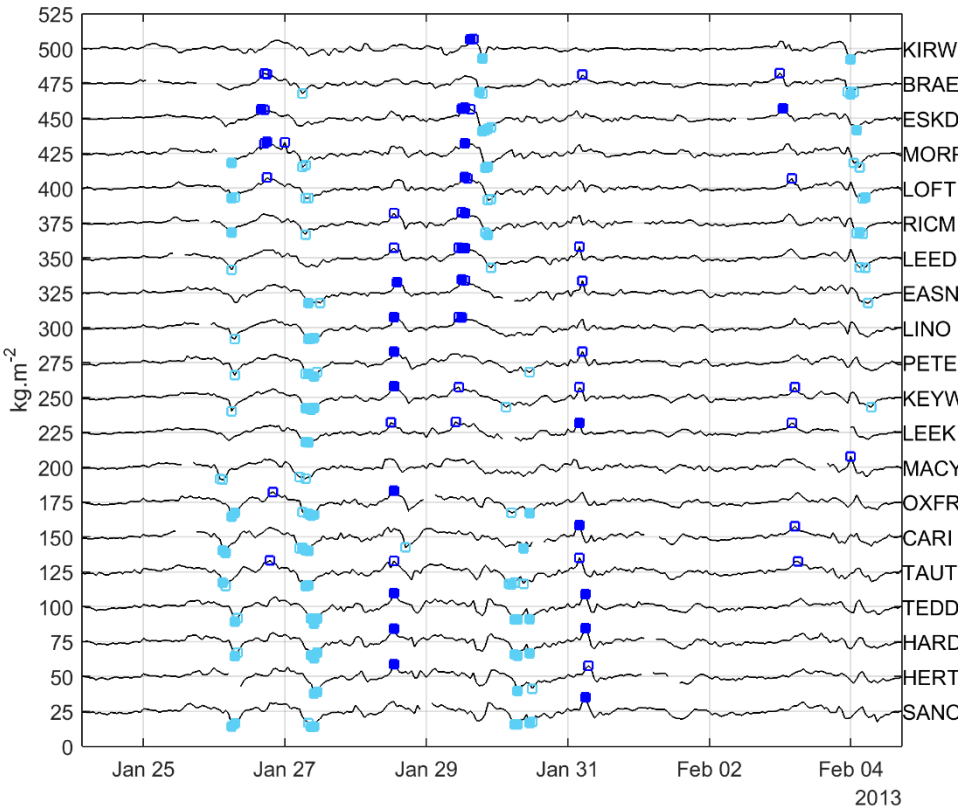


Figure D-19 Same as Figure D-18 but showing the temporal analysis residuals only.

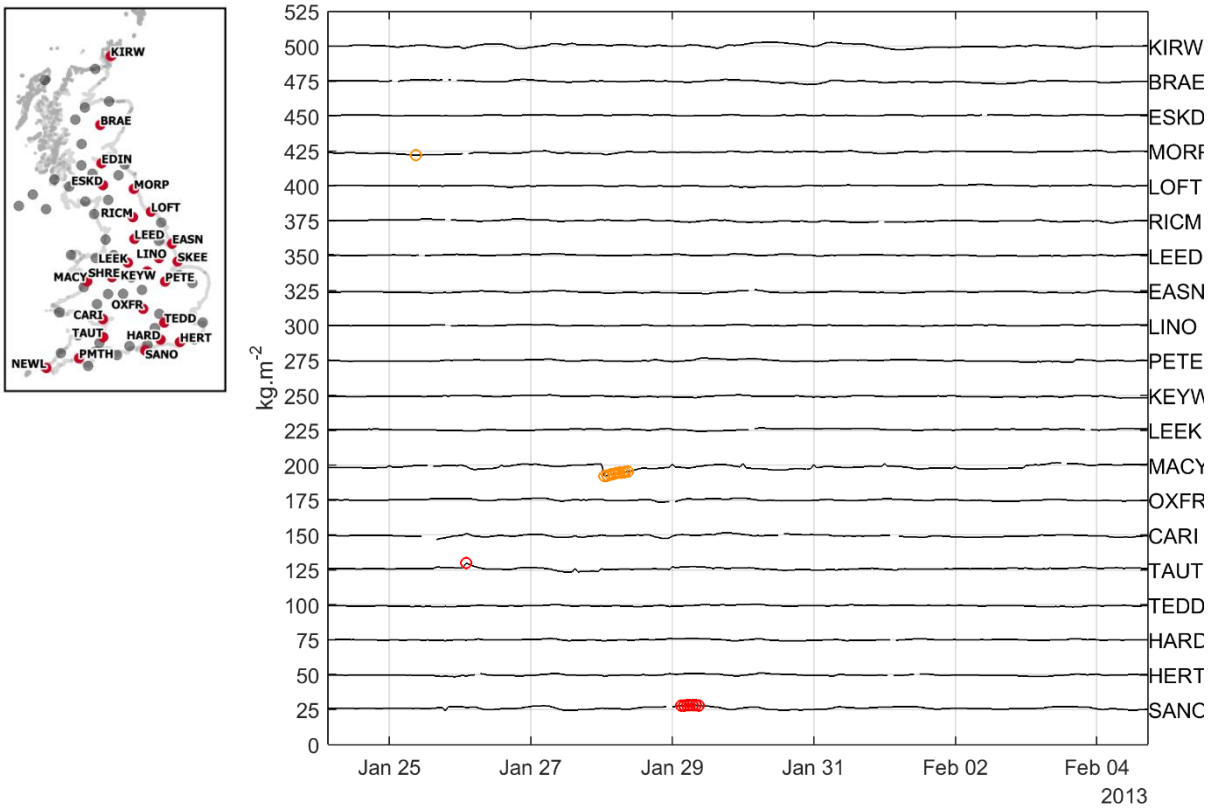


Figure D-20 Same as Figure D-18 but showing the spatial analysis residuals only.

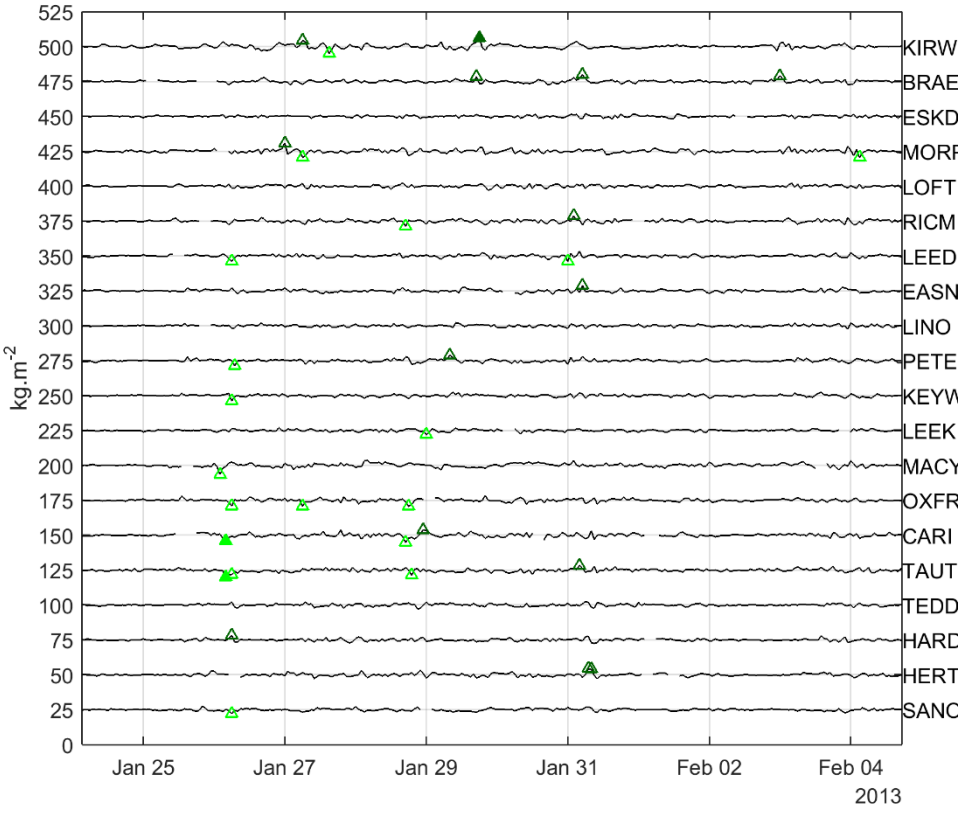


Figure D-21 Same as Figure D-18 but showing the combined analysis residuals only.

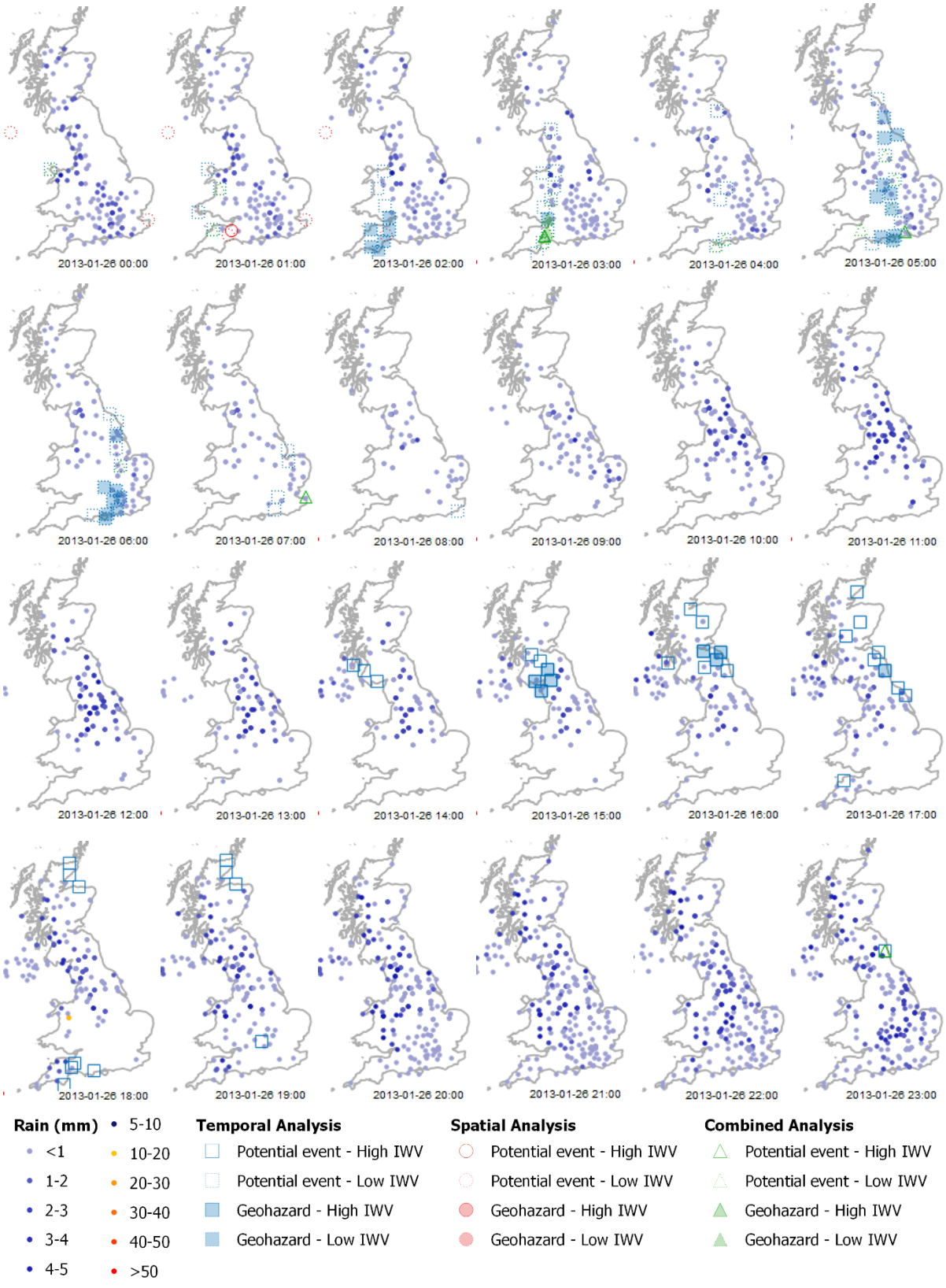


Figure D-22 Rain gauge readings (coloured dots) and stations considered as having either potential events (hollow symbols) or meteorological events (filled symbols), with 1 cycle/day as a cut-off frequency.

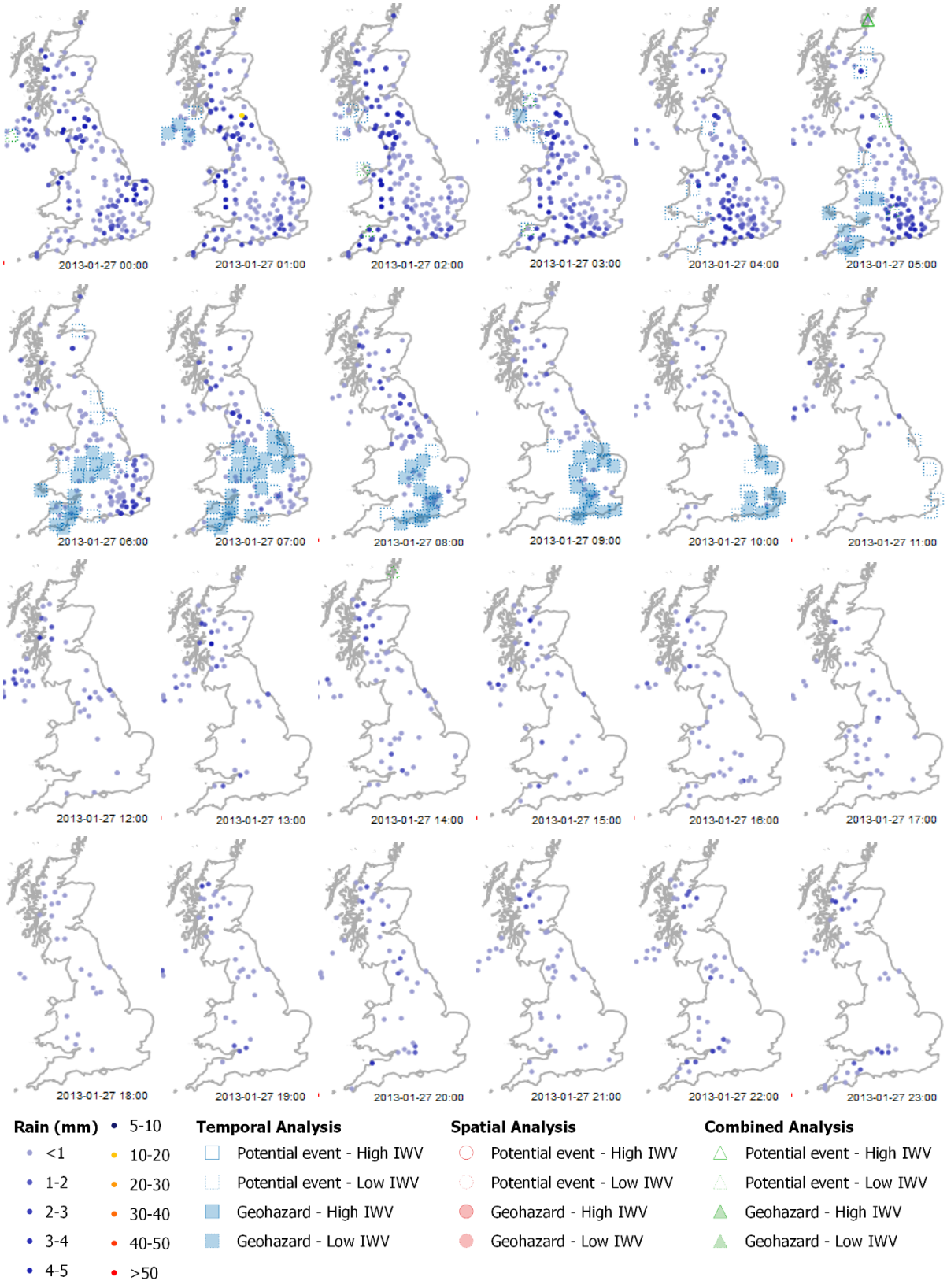


Figure D-22 (continued showing the 27th Jan 2013)

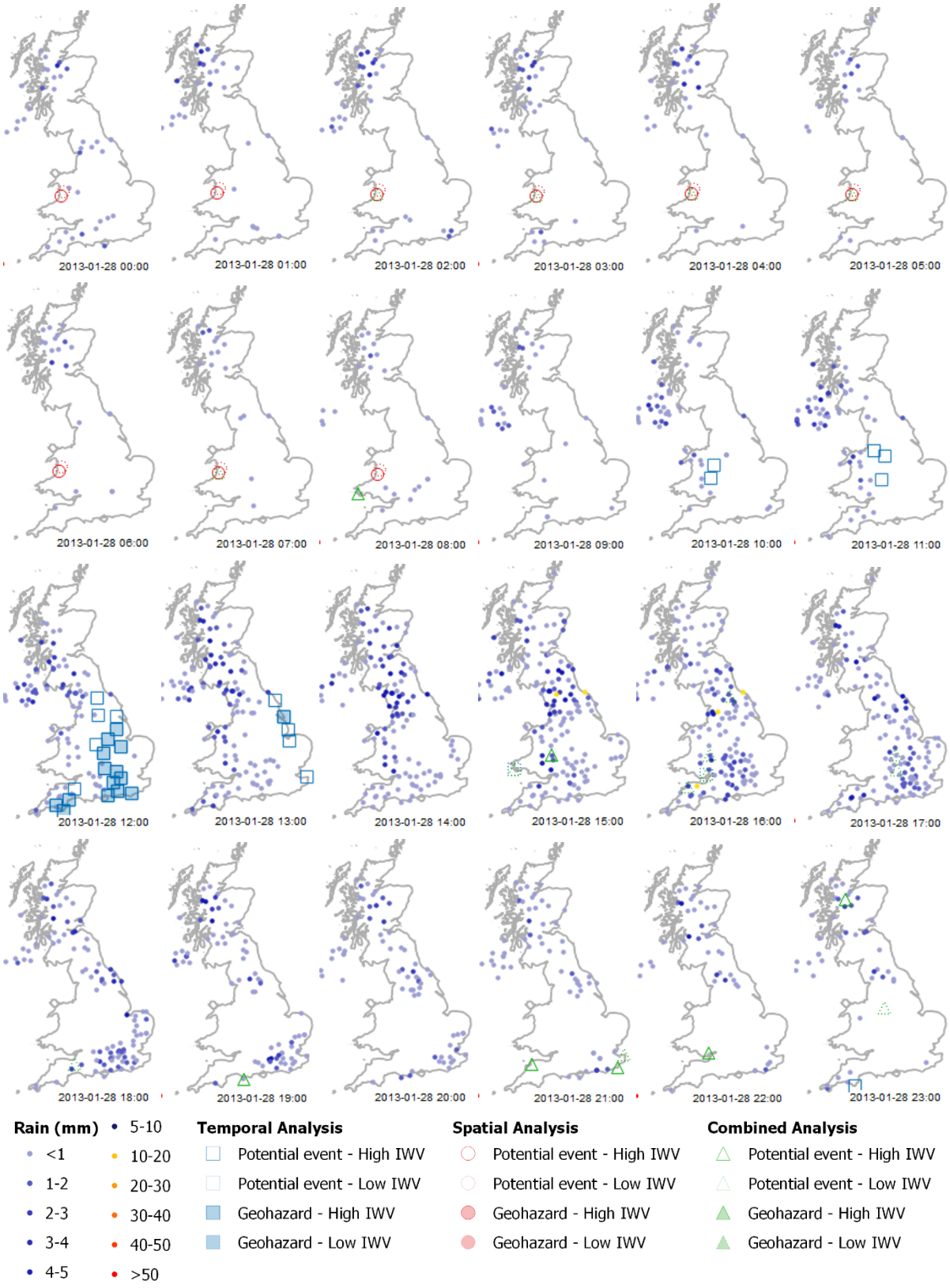


Figure D-22 (showing the 28th Jan 2013continued)

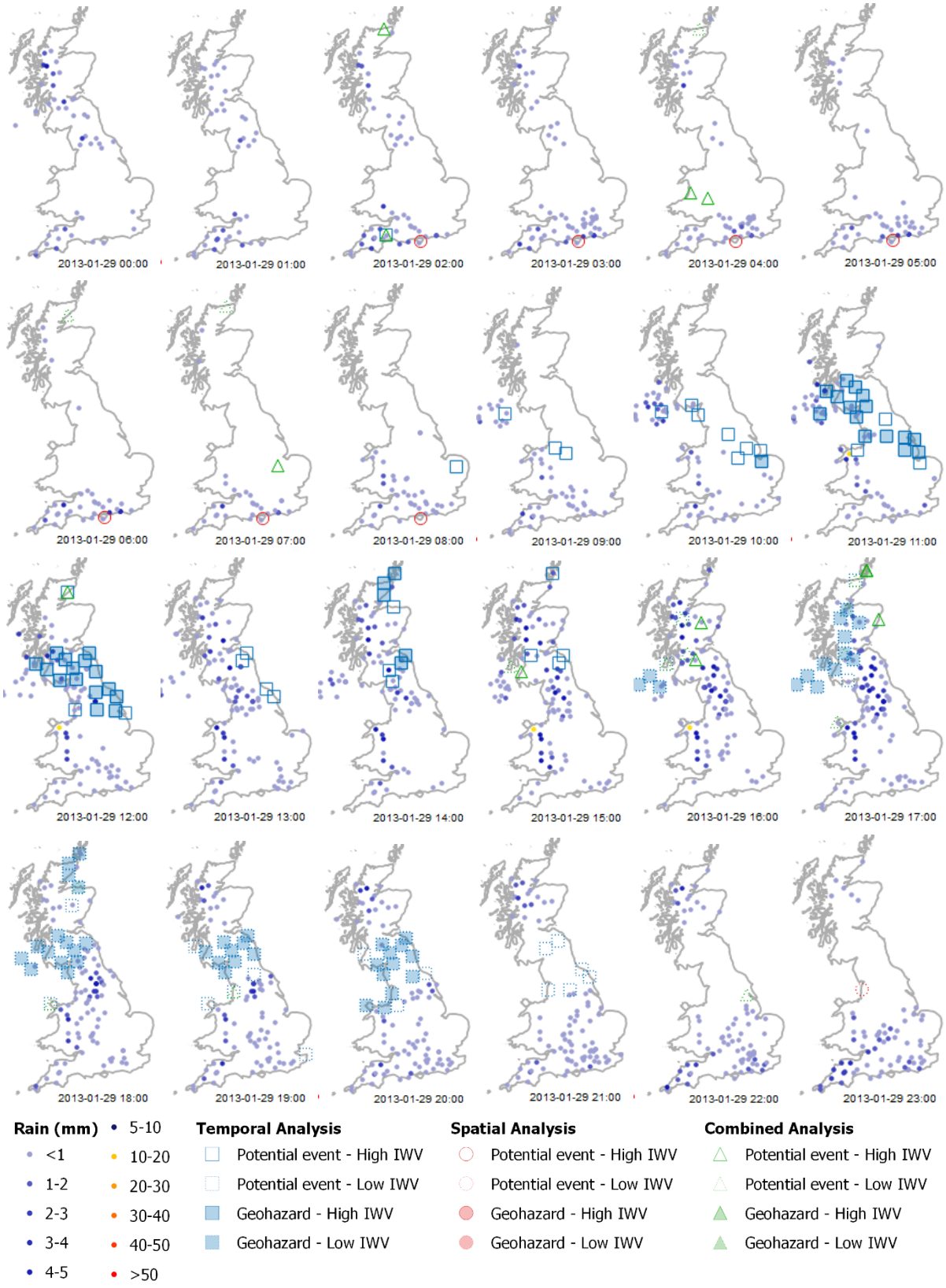


Figure D-22 (continued showing the 29th Jan 2013)

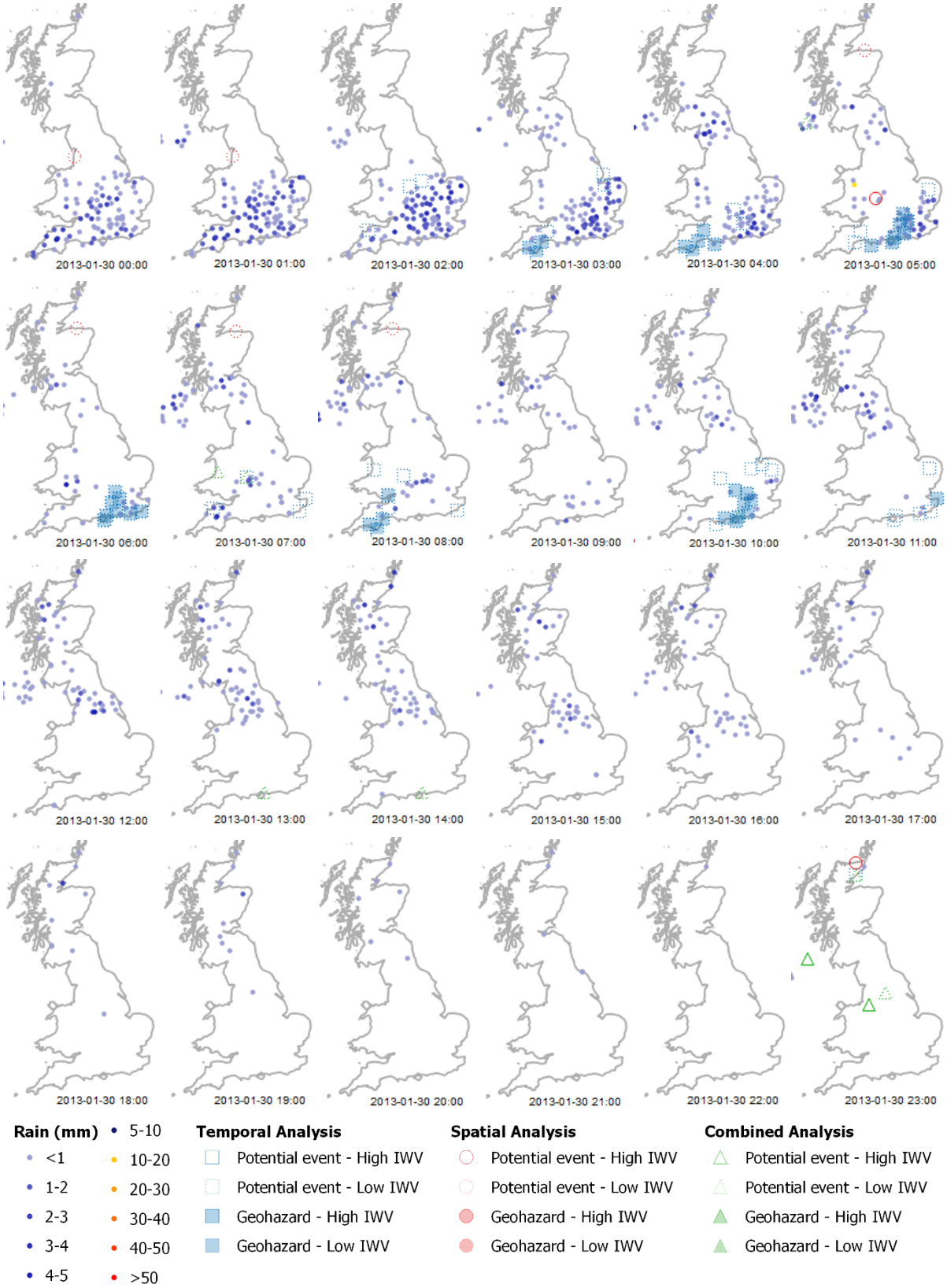


Figure D-22 (continued showing the 30th Jan 2013)

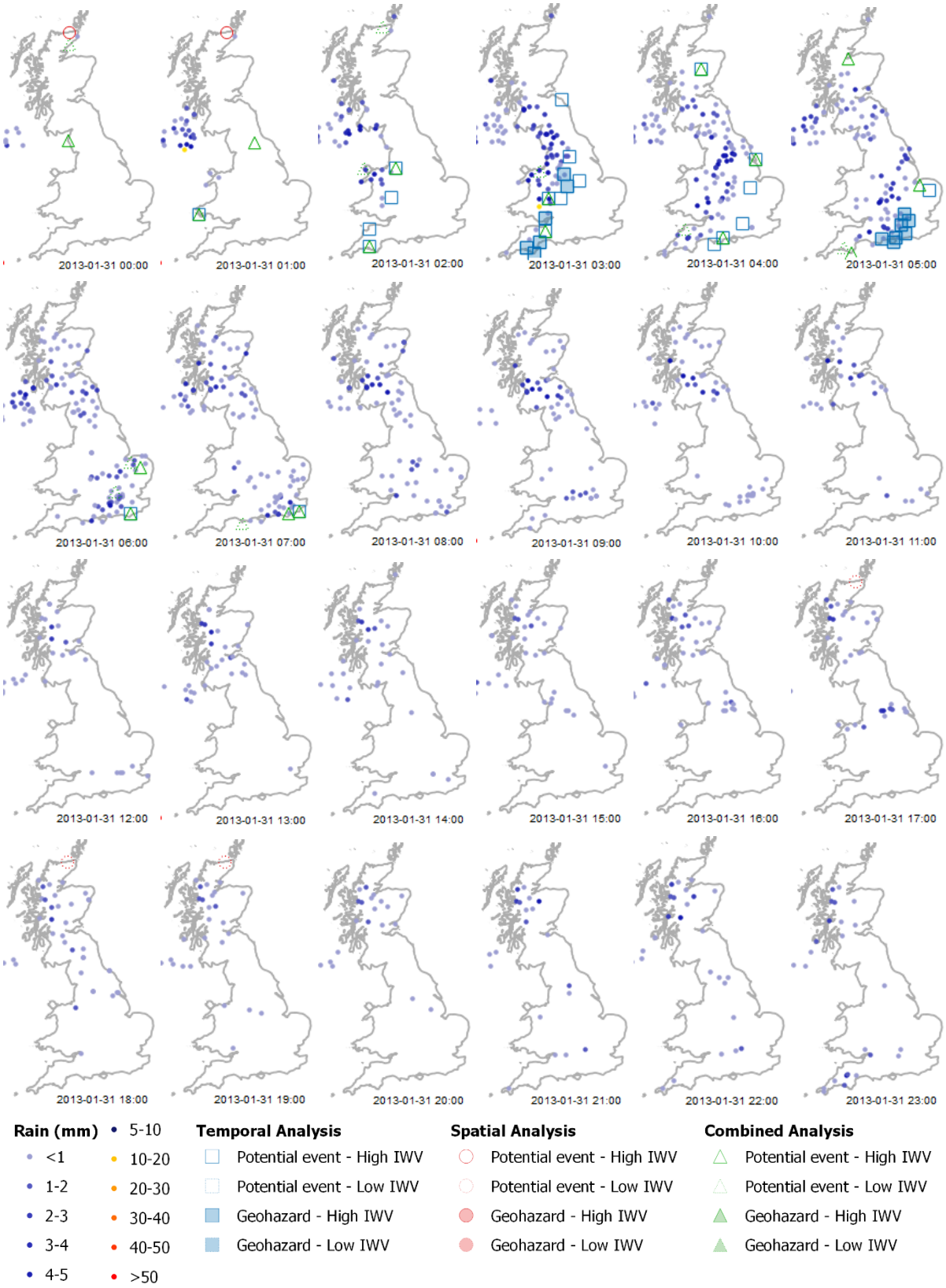


Figure D-22 (continued showing the 31st Jan 2013)

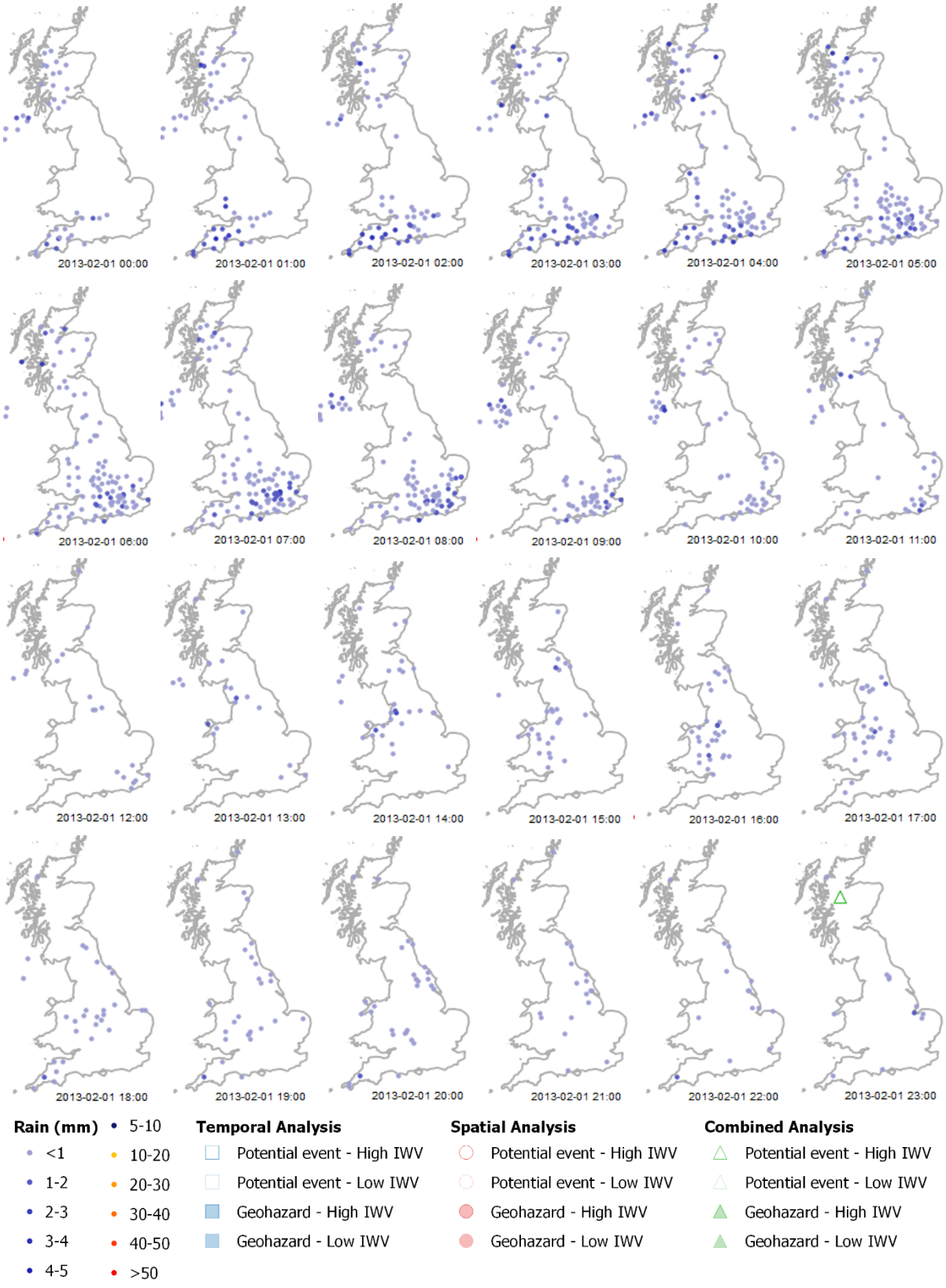


Figure D-22 (continued showing the 1st Feb 2013)

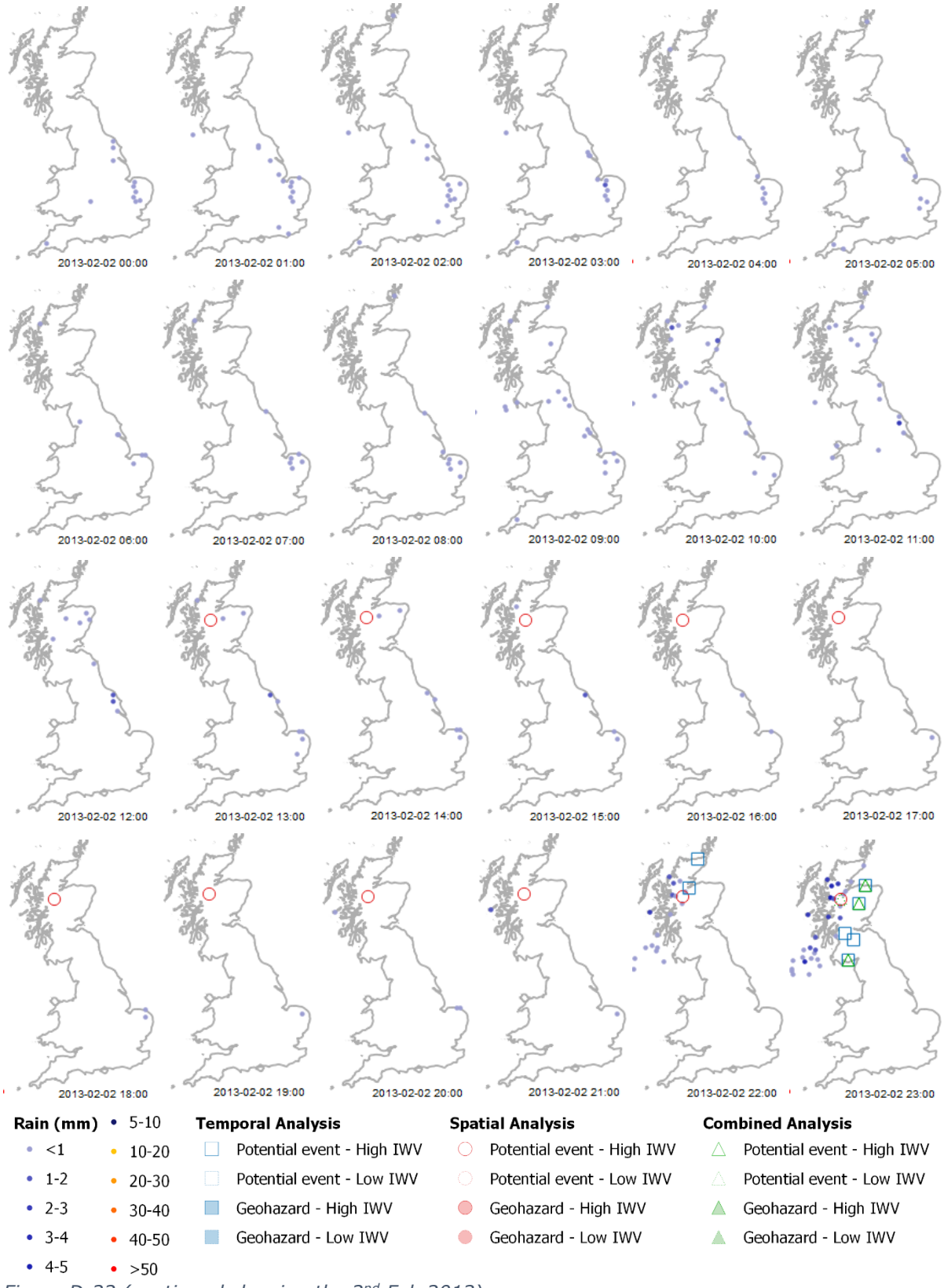


Figure D-22 (continued showing the 2nd Feb 2013)

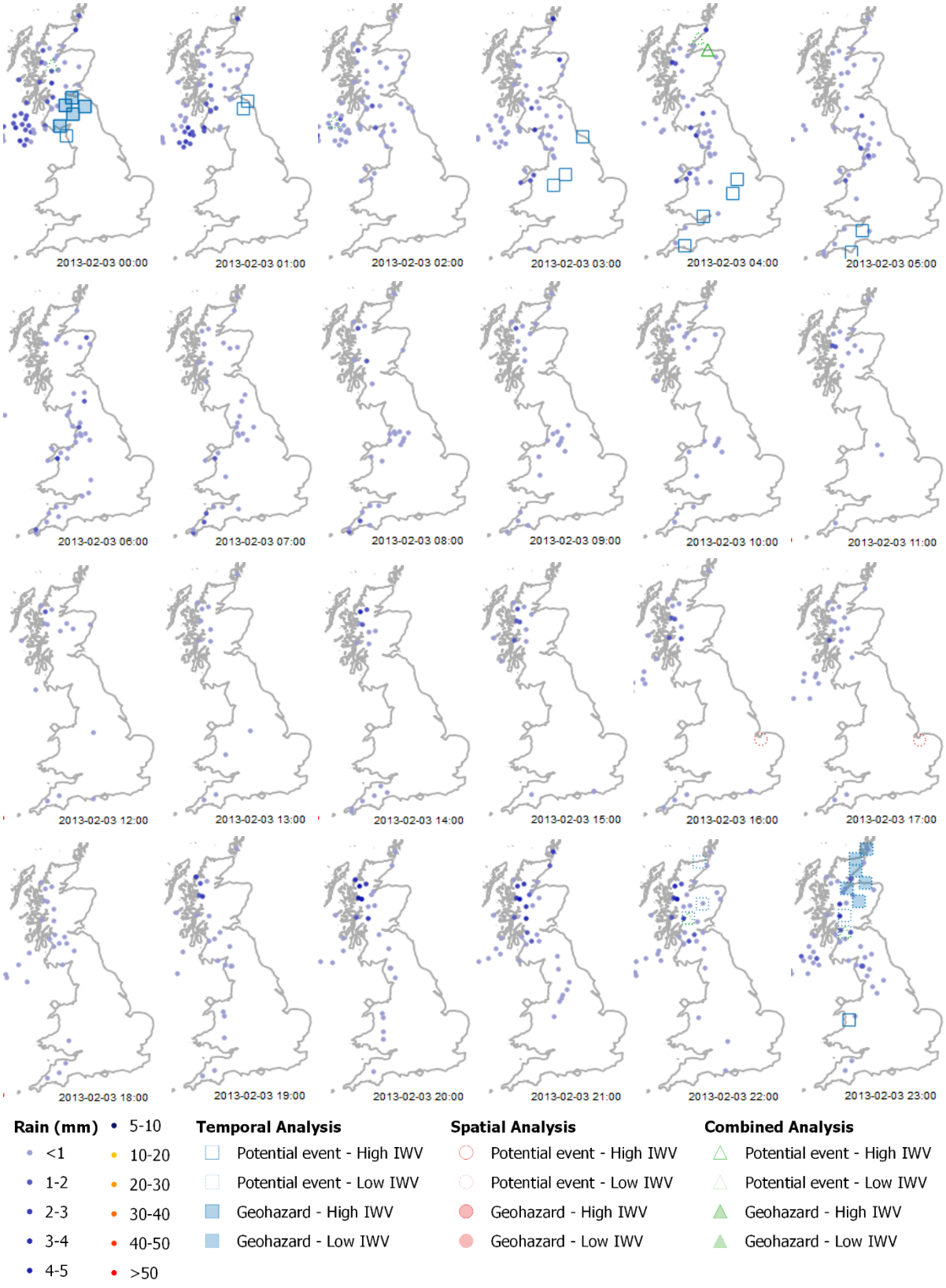


Figure D-22 (continued showing the 3rd Feb 2013)